Highlights of Spanish Astrophysics XI

La Laguna, Tenerife, 5-9 sept. 2022

Eds. M. Manteiga, L. Bellot, P. Benavidez, A. de Lorenzo-Cáceres,
M. A. Fuente, M. J. Martínez, M. Vázquez-Acosta, C. Dafonte

ISBN: 978-84-09-50197-7

Highlights of Spanish Astrophysics XI, Proceedings of the XV Scientific Meeting of the Spanish Astronomical Society held on September 4–9, 2022, in La Laguna, Spain. M. Manteiga, L. Bellot, P. Benavidez, A. de Lorenzo-Cáceres, M. A. Fuente, M. J. Martínez, M. Vázquez- Acosta, C. Dafonte (eds.), 2023

PREFACE

We are glad to present the Proceedings of the XV Scientific Meeting of the Sociedad Española de Astronomía (SEA) under the title "Highlights of Spanish Astrophysics XI", an initiative that the Society started in printed format, back in 1998, after the III Scientific Meeting held in La Laguna. After four difficult years caused by the covid-19 pandemic, with the 2020 Scientific Meeting held online, the Spanish astronomical community gathered again in La Laguna in September 2022, retaking our biennial meetings.

The Meeting, with more than 500 enthusiastic people registered, was especially stimulating in several aspects:

- We have a very active young community of Ph.D. students and postdocs. They presented extremely interesting papers in all areas. Being aware that a research career is a long-distance race, we can say without complacency that the future of astronomy in Spain is assured.

- Spanish research centres are involved in major international scientific and instrumental projects, on the ground and in space. It is much easier to make a list of projects in which our community is not involved! Although bureaucracy and financial difficulties do not ease the way for progress on these initiatives, the community is stubborn and its achievements are there for all to see.

- As far as SEA is concerned, we are already close to 1000 members, practically all the people –staff, postdocs and PhD students– working in astronomy in Spain, according to the V SEA Report on human resources presented during the Meeting. The SEA Board, its commissions and working groups will continue working to contribute to the cohesion of Spanish astronomy, serving the community to the extent of their possibilities and competences, always in the spirit of channelling the aspirations of the collective and its individual members. There is a lot of work to be done, such as, for example, that the percentage of 28% of women, practically unchanged since we have data, will increase over time.

That being said, it is now the time to say thanks. We would like to express our gratitude to all the people involved in the preparation phase, in the day-to-day conference happening, and also in the "post-processing" of the scientific information acquired. We owe it to all of them that the event was a great success.

We are very grateful to our host institution, the Instituto de Astrofísica de Canarias, and its Director, Prof. Rafael Rebolo, for their support in all aspects, logistics and financial; without their help the meeting would not have had the quality standards we enjoyed. We also appreciate the willingness of the Universidad de la Laguna, which allowed us to hold our sessions on its premises.

We thank the Scientific Organizing Committee (SOC) for the careful reading of the manuscripts and the effort to fit the program in the best possible way so that we could all somehow participate. The SOC was made up of the following persons: Luis Bellot (IAA), Paula Benavidez (UA), Asunción Fuente (OAN), Álvaro Labiano (ESAC), Nanda Rea (IEEC), Mónica Vázquez-Acosta (IAC), Gustavo Yepes (UAM), Adriana de Lorenzo Cáceres (IAC) and Minia Manteiga (UDC, Chair).

We also thank the Local Organizing Committee (LOC) for the continuous work before and

during the meeting, and for their availability to help in any circumstance and at any time. The LOC was composed of the following persons, all of them researchers at the Instituto de Astrofísica de Canarias: Íñigo Arregui, Giuseppina Battaglia, Claudio Dalla Vecchia, Martín Gómez, Jonay González, Elena Khomenko, Adriana de Lorenzo Cáceres, Ignacio Martín, Savita Mathur, Hannu Parvianen, Helmut Dannerbauer, and María Jesús Martínez González (Chair).

Finally, we are very grateful to our conference proceedings referees, who have diligently undertaken the work of critical reading, at the cost of their time. Our referees were: Santiago Pérez-Hoyos (UPV/EHU), Ricardo Hueso (UPV/EHU), Mónica Vázquez-Acosta (IAC), José Acosta Pulido (IAC), Gustavo Yepes (UAM), Ana Ulla (UVIGO), Juan Antonio Belmonte (IAC), Luis Bellot (IAA), Carlos Dafonte (UDC), Francisco Garzón (IAC), Arturo Manchado (IAC), Adriana de Lorenzo Cáceres (IAC), Miguel Cerviño (CAB), Asunción Fuente (OAN), José Antonio Caballero (CAB) and Paula Benavidez (UA). Minia Manteiga, responsible for the editing process, does not want to fail to thank the help provided by Ángel Gómez and Daniel Garabato (UDC) in the final compilation of the volume.

Benjamín Montesinos
SEA President

Minia Manteiga
SEA Vicepresident
SOC Coordinator

Contents

Highlights of Spanish Astrophysics XI, Proceedings of the XV Scientific Meeting of the Spanish Astronomical Society held on September 4–9, 2022, in La Laguna, Spain. M. Manteiga, L. Bellot, P. Benavidez, A. de Lorenzo-Cáceres, M. A. Fuente, M. J. Martínez, M. Vázquez- Acosta, C. Dafonte (eds.), 2023

Barium stars and their white-dwarf companions, a key to understanding evolved binaries.

Escorza, A.[1]

[1] European Southern Observatory, Alonso de Córdova 3107, Vitacura, Santiago, Chile
ana.escorza@eso.org

Abstract

A rich zoo of peculiar objects forms when evolved stars with extended and loosely-bound convective envelopes, such as Asymptotic Giant Branch (AGB) stars, undergo gravitational interaction in binary systems. For example, Barium (Ba) stars are main-sequence and red-giant stars that accreted mass from the outflows of a former AGB companion. This companion is now a dim and, in most cases, not directly detectable, white dwarf (WD). The orbital properties of barium stars can help us constrain interaction mechanisms in binary systems with giant components, and their chemical abundances are a tracer of the nucleosynthesis processes that took place inside the former AGB star. This contribution presents the most recent observational constraints concerning the orbital and stellar properties of Ba stars, which have increased in quantity and quality in the past few years thanks to long-term radial-velocity monitoring programs and to the accurate distances provided by the Gaia mission. However, until recently, important uncertainties affected the properties of their faint white dwarf companions, which contain key information about the formation of Ba stars. Combining radial-velocity data with Hipparcos and Gaia astrometry, we accurately measured the orbital inclinations of these binary systems and obtained the absolute masses of these otherwise hidden white dwarfs. The stellar and orbital properties of Ba stars, including the WD companion masses, are essential for our understanding of these systems and are important input parameters for binary evolution and AGB nucleosynthesis models.

1 Introduction

About half of the stars in our Galaxy are born with a companion, forming so-called binary systems. In these systems, the two components are gravitationally bound and orbit one another during their evolution. Interactions between the two stars, which can range from subtle tidal effects to common envelope evolution and mergers, including different forms of mass transfer such as wind pollution or Roche-Lobe Overflow, can have large effects on their individual evolutionary pathways. Additionally, binary interactions affect not only the fate of these orbiting stars but also the evolution of the orbital parameters of the system.

Unfortunately, many aspects of interaction physics in binaries are not yet well understood, and investigating the products that result from interacting systems is crucial to unravel the physical mechanisms involved. These statements apply to binary systems all across the Hertzsprung-Russell (HR) diagram, but here, we focus on low- and intermediate-mass systems, with components with initial masses between 1 and 5 $M_{\odot}$.

One of the prototypical families of post-interaction binaries in the mentioned mass range is Barium (Ba) stars. Ba stars are main-sequence or giant stars that show a surface enhancement of several heavy elements (including barium, which gives them their name) that should not yet be overabundant at these evolutionary stages [4]. These elements are synthesized by the slow-neutron-capture-process (s-process) of nucleosynthesis in the interior of late Asymptotic Giant Branch (AGB) stars [27]. Currently, it is widely accepted that these elements were transferred from a former AGB companion during a phase of mass transfer in the system [34]. This former AGB star, having already evolved into a cool white dwarf (WD), is currently too dim to be directly detected in most systems [44]. However, the orbital motion of the Ba star and its WD companion is detectable, and understanding the observed orbital properties of Ba-star systems, as well as the stellar properties of Ba stars and their polluters, is a key to the interaction history of these systems [24, 25].

This manuscript is mainly a summary of my Ph.D. Thesis [15], which was awarded the *Premio SEA Tesis* in 2021 and the opportunity to contribute to these proceedings. However, in order to make this contribution up to date, it also includes the part of my current work that is directly related to the thesis. The manuscript presents the most recent stellar and orbital observational constraints collected with the aim of shedding light on some of the open questions concerning Ba stars. With this purpose, we exploit the synergy between Hipparcos and Gaia data, broadband photometry, high-resolution spectroscopy, radial-velocity monitoring programs, and state-of-the-art stellar and binary evolutionary models. In Sect. 2, we describe the methodology followed to accurately locate Ba stars on the Hertzsprung-Russell (HR) diagram and determine their masses [12]. Section 3 presents the orbital properties of main-sequence and giant Ba stars [26, 13] and in Sect. 4, we present and discuss the masses of the faint WD companions [16]. In Sect. 5, we compare all these observations with binary evolution models [14] in order to investigate the evolution of these systems along the Red Giant Branch (RGB), and finally, in Sect. 6, we discuss the potential of this work and present a sample of very well-known Ba star systems that can be used to constrain binary evolution and nucleosynthesis models.

2 The HERMES-Gaia HR diagram of Barium stars

With the availability of the revolutionary parallaxes and distances provided by the Gaia mission [19, 20, 21], it is possible to construct Hertzsprung-Russell diagrams with unprecedented accuracy. Additionally, by comparing the position of stars in the HR diagram with evolutionary tracks, the evolutionary masses of single or apparently single stars can also be determined [40]. Figure 1 shows a schematic representation of the methodology used to accurately locate Ba stars on the HR diagram and determine their masses. We use a grid search method to find the MARCS atmospheric model [22] that best fits the spectral energy distribution of each

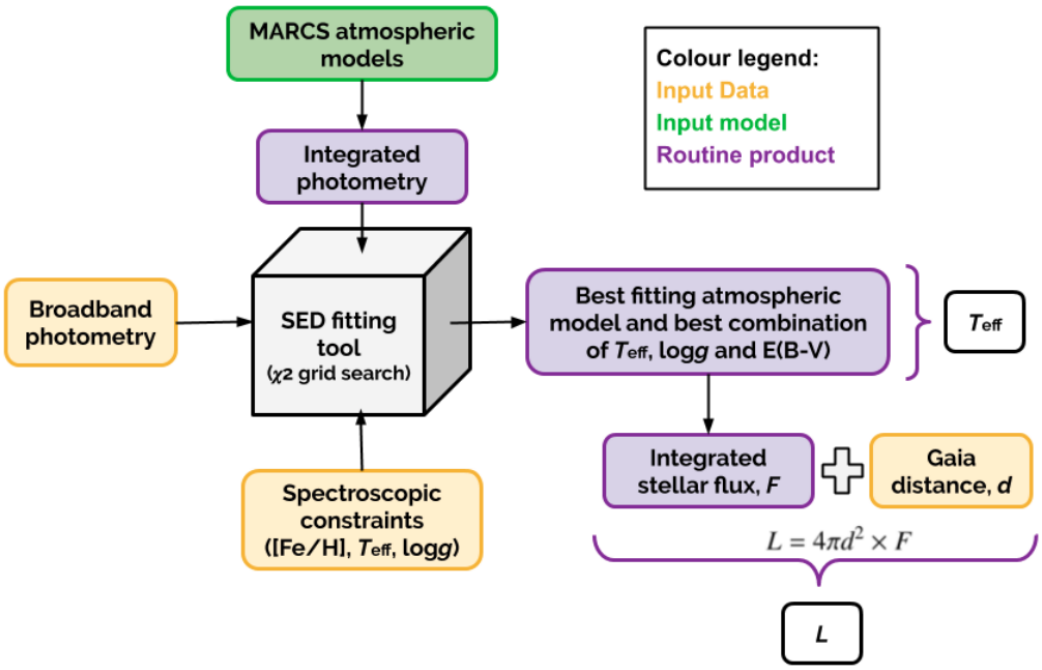

Figure 1: Schematic representation of the methodology used in [12, 13, 26, 30, 31] among others to accurately locate Ba and related stars on the Hertzsprung-Russell (HR) diagram. Broadband photometric data is compared to synthetic photometry, obtained by integrating MARCS atmospheric models [22] with the response curve of different broadband filters. Spectroscopic constraints are also considered in order to determine the best-fitting model and the line-of-sight extinction value. Finally, combining the integrated flux with the Gaia distance [2], the luminosity is derived and used together with the temperature obtained in the previous step to design an HR diagram like that of Ba stars shown in Fig. 2. Figure from [15].

star in the sample. Initially, we applied this method to over 400 Ba and related stars found in the literature and obtained some interesting mass distributions and preliminary results [12]. However, our extensive tests showed that there are important degeneracies, mainly between the temperature and the line-of-sight extinction and between the metallicity and the mass, that cannot be lifted using only broadband photometry. Because of this, at a later stage, we included constraints obtained from HERMES [37, 38] high-resolution spectra in our methodology [30, 31, 26, 13]. We showed that having independent knowledge of the metallicity is crucial, in order to use a grid of evolutionary tracks of the corresponding metallicity.

Once the best combination of stellar parameters and line-of-sight extinction is found, the stellar fluxes, integrated from the spectral energy distributions, are combined with the Gaia distances [2] to determine the accurate luminosities. We compared the location of Ba stars on the HR diagram with STAREVOL evolutionary models [41], computed for this specific sample (left panel in Fig. 2) and also determined the most probable evolutionary mass for each target, taking into account the timescale of the different evolutionary phases and

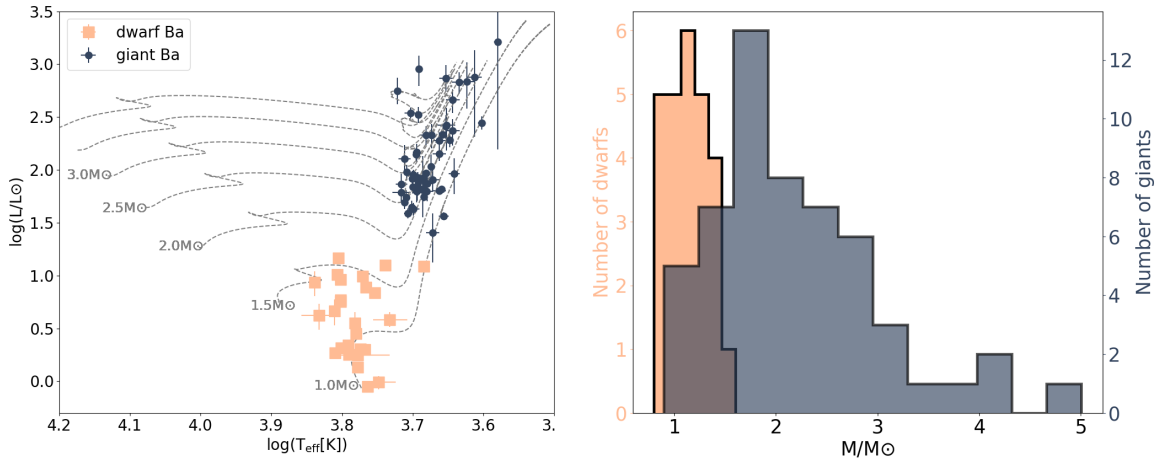

Figure 2: **Left:** Hertzsprung-Russell diagram of dwarf (squares) and giant (circles) Ba stars. STAREVOL tracks are over-plotted and used for mass determination. **Right:** Mass distribution of dwarf and giant Ba stars. Figures adapted from [13].

of tracks with different initial masses. We concluded that Ba giants have masses from 1 to 5 $M_\odot$, with their mass distribution peaking around 2 $M_\odot$, while main-sequence Ba stars cover a much narrower mass range than their giant counterparts, from 0.9 to 1.6 $M_\odot$ (right panel in Fig. 2), opening questions about the observational biases against hotter main-sequence polluted objects. Additionally, the deficit of low-mass barium giants was associated to binary interaction between the evolving Ba star and its WD companion, given the fact that low-mass stars reach large radii at the tip of the red giant branch. This was investigated by [14] and it is discussed in Sect. 5.

3 The $e \log P$ diagram of Barium stars

Giant Ba stars have been intensively investigated since their discovery, but main-sequence Ba stars were discovered later and are much less sampled and studied than their giant counterparts [35]. Since the polluting episode is expected to happen when the Ba star is still in the main-sequence phase [25], the properties of these systems are essential to have a complete picture of the formation and evolution of Ba stars. Recently, we presented the largest systematic study of the orbital properties of main-sequence Ba stars and a thorough comparison of these properties to those of the Ba giants [13]. This work was based on radial-velocity data. We combined recent radial-velocity measurements from HERMES [37, 38] and SALT-HRS [5, 9] high-resolution spectra with archival radial-velocity data from CORAVEL [3].

Fig. 3 shows the two main orbital parameters, the period and the eccentricity, of main-sequence and giant Ba stars in an eccentricity-period diagram or $e \log P$ diagram. Main-sequence Ba stars show orbital periods between 200 and 11 000 days and eccentricities over the whole range from 0 to over 0.8, similar to Ba giants. We note that the observational

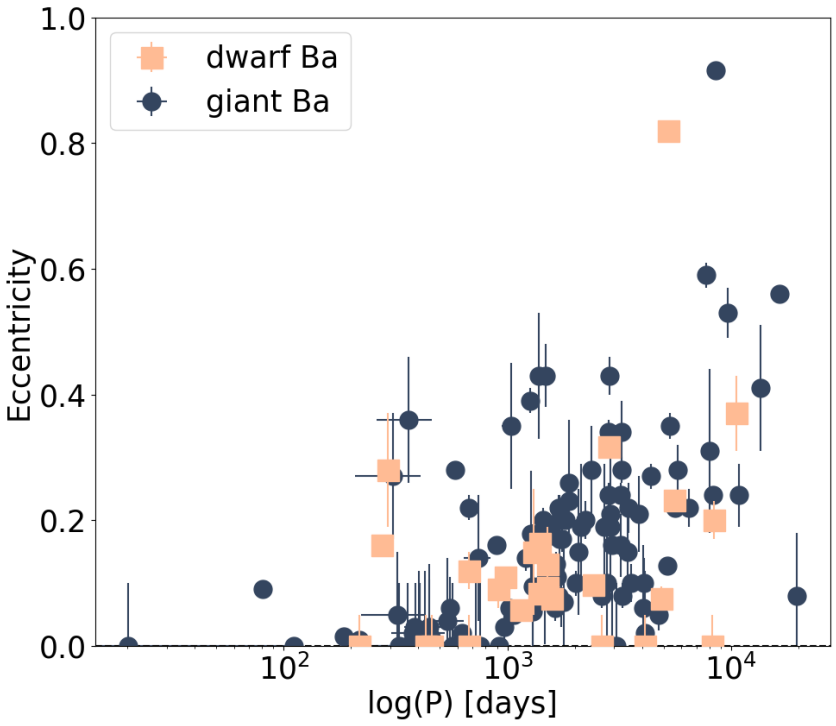

Figure 3: $e \log P$ diagram of dwarf (squares) and giant (circles) Ba stars. Figure adapted from [13].

effort behind Fig. 3 is enormous, and that some of these systems have been part of multi-decade radial-velocity monitoring programs with different instruments, especially with the CORAVEL spectrometers and the HERMES spectrograph.

The orbital properties of Ba stars are not well understood [36]. Binary evolution and interaction models predict that systems with periods below 3000–5000 days should have negligible eccentricities after interacting with an AGB star [23]. However, the region of the $e \log P$ diagram occupied by Ba stars is also populated by several other families of post-mass-transfer evolved binaries, making this figure one of the biggest unresolved puzzles concerning evolved low- and intermediate-mass binaries.

4 The masses of the white dwarf companions

As mentioned above, the white dwarf companions of Ba stars are dim, cool, and difficult to observe via direct methods. However, they contain key information about binary interaction processes, about the s-process of nucleosynthesis, and about the formation of Ba stars. Recently, we combined the radial-velocity data used to determine the orbits presented in Fig. 3 with Hipparcos and Gaia astrometry and with the Hipparcos-Gaia catalogue of accelerations (HGCA; [6, 7]) in order to use the dynamical information of these systems to determine the

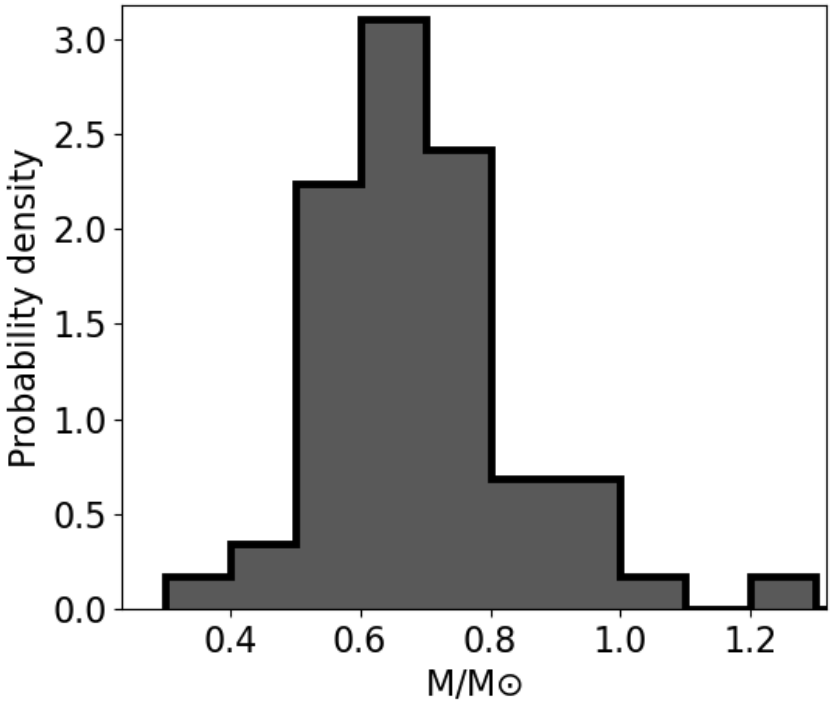

Figure 4: Mass distribution of the WD companions of Ba star. Data from [16]

masses of the faint companions. We used the software package ORVARA [8], designed to simultaneously fit a single Keplerian model to any combination of radial-velocity and astrometric data using a parallel-tempering Markov chain Monte Carlo method. Adopting Gaussian priors for the Ba star masses (obtained as described in Sect. 2) and for the parallaxes (from Gaia EDR3 [21] or from the Gaia DR3 non-single-star catalogue [18] when available), and assuming uninformative priors for the orbital elements and the WD masses, we determined new orbital inclinations and companion masses for 60 Ba star systems. This combination of data allowed us to constrain new orbits and improve the orbits for the longest-period systems. Additionally, we unravelled a new triple system that was not known before (HD 218356) and constrained the orbits and the masses of the two companions, and we discovered a neutron star candidate accompanying a thought-to-be Ba star that is probably a normal giant (56 UMa, [17]).

Figure 4 shows the WD mass distribution obtained. The weighted average is slightly more massive than that of field WDs, and there is an excess of WDs with masses higher than 0.7 - 0.8 $M_{\odot}$ considering the 1σ uncertainties. This indicates that they might come from AGB stars that are more massive than 3 $M_{\odot}$ [33], and these AGB stars would be more massive than what the abundance ratios on Ba star atmospheres and theoretical models of the s-process of nucleosynthesis seem to expect [32, 30, 10].

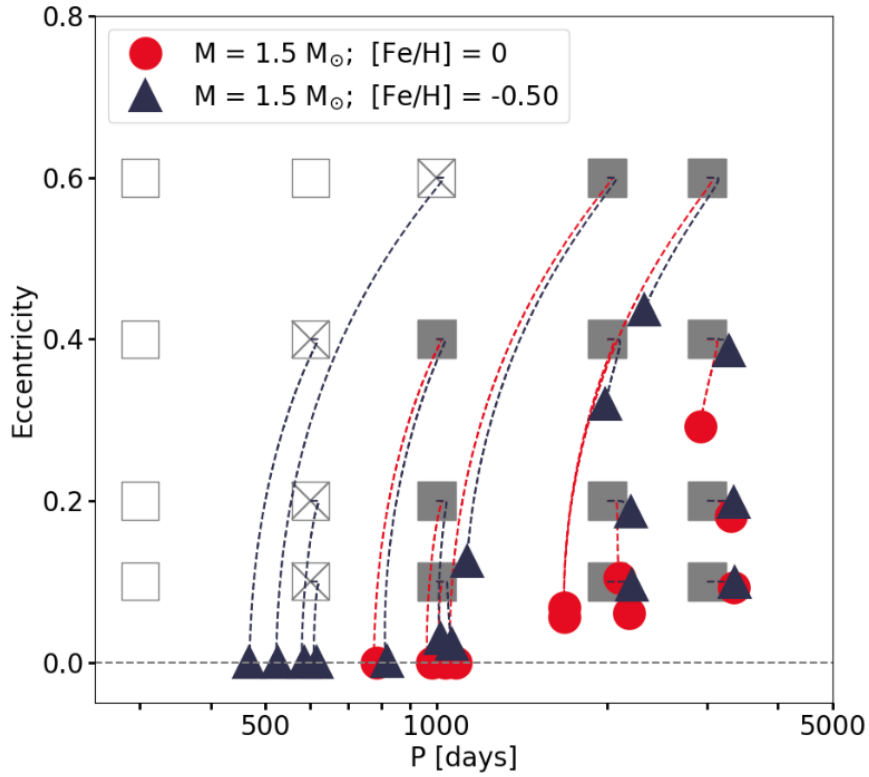

Figure 5: Evolution of the period and the eccentricity of binary systems formed by a main-sequence Ba star of 1.5 $M_\odot$ with solar (red circles) or subsolar (blue triangles) metallicity. The squares represent the initial orbital elements, the lines show the evolution of these elements as the Ba star evolves along the red-giant branch, and the coloured symbols show the orbital parameters at the moment of He-core ignition. Empty squares indicate systems that merge at both metallicities due to binary interaction. Those with a cross only merge at solar metallicity, and the systems with shaded squares reach core-He burning stage at both metallicities. Figure from [14].

5 The evolution of Ba stars along the Red Giant Branch

The distributions of masses, periods, and eccentricities presented above provide strong constraints to theoretical studies. Here, we focus on the comparison between main-sequence and giant Ba stars, which allows us to investigate the evolution of the binary orbit between these two phases [14]. Our detailed binary evolution models, computed with the BINSTAR code [42, 11], showed that a second stage of binary interaction, this time between the main-sequence Ba star and its WD companion, also takes place in some of these systems, affecting the distribution of orbits and masses observed among Ba giants. Our models suggest that main-sequence Ba stars of less than 2 $M_\odot$ in systems with periods below 500 to 1000 days (depending on mass and metallicity) will merge with their WD companions and never become core-He-burning giants. As an example, Fig. 5 shows the evolution, on an eccentricity-period

Table 1: List of Ba stars with well-constrained orbital parameters (we list here the period, the eccentricity, the semimajor axis, and the inclination and refer to [26, 13, 16] for the remaining parameters), Ba star and WD masses, and recently determined chemical abundances from high-resolution spectra.

Star ID	P [days]	e	a [AU]	i [°]	$M_{\rm Ba}$	$M_{\rm WD}$	Abund.
BD-14°2678	3481 ± 205	0.25 ± 0.05	7.0 ± 0.5	93 ± 18	3.0 ± 0.2	0.67 ± 0.10	[39]
HD 5424	1906 ± 17	0.19 ± 0.05	3.7 ± 0.4	30 ± 3	1.3 ± 0.4	0.52 ± 0.11	[30, 39]
HD 16458	2017 ± 15	0.10 ± 0.03	4.2 ± 0.5	61 ± 12	1.90 ± 0.10	0.74 ± 0.15	[30]
HD 20394	2248 ± 8	0.16 ± 0.06	4.6 ± 0.5	31 ± 3	2.0 ± 0.2	0.49 ± 0.1	[39]
HD 27271	1681.1 ± 1.0	0.224 ± 0.007	4.2 ± 0.3	103 ± 5	2.9 ± 0.2	0.70 ± 0.09	[30]
HD 40430	6147 ± 278	0.26 ± 0.02	9.4 ± 0.8	23.4 ± 0.6	2.3 ± 0.2	0.7 ± 0.12	[39]
HD 43389	1688.4 ± 1.4	0.083 ± 0.017	4.0 ± 0.7	111 ± 3	1.8 ± 0.4	0.76 ± 0.25	[30, 39]
HD 49841	897.5 ± 1.9	0.162 ± 0.015	2.8 ± 0.1	109 ± 19	2.85 ± 0.10	0.82 ± 0.16	[39]
HD 50082	2883 ± 6	0.19 ± 0.02	5.1 ± 0.9	63 ± 3	1.6 ± 0.3	0.56 ± 0.18	[30]
HD 51959	11195 ± 475	0.30 ± 0.05	11.8 ± 1.0	163.2 ± 0.8	1.2 ± 0.1	0.51 ± 0.08	[39]
HD 53199	8233 ± 175	0.255 ± 0.010	11.7 ± 0.5	103 ± 7	2.5 ± 0.1	0.64 ± 0.05	[39]
HD 58121	1217 ± 5	0.135 ± 0.019	3.4 ± 0.5	121 ± 4	2.6 ± 0.5	0.67 ± 0.19	[39]
HD 59852	3477 ± 80	0.14 ± 0.08	6.6 ± 0.8	26 ± 4	2.5 ± 0.3	0.62 ± 0.15	[39]
HD 87080	274.31 ± 0.05	0.162 ± 0.016	1.05 ± 0.10	60 ± 12	1.38 ± 0.15	0.70 ± 0.18	[1]
HD 88562	1451.0 ± 1.0	0.203 ± 0.013	2.9 ± 0.3	87 ± 9	1.0 ± 0.1	0.48 ± 0.09	[30, 39]
HD 91208	1770 ± 3	0.178 ± 0.018	4.2 ± 0.4	134 ± 2	2.3 ± 0.2	0.83 ± 0.14	[39]
HD 95193	1652 ± 5	0.13 ± 0.02	4.12 ± 0.15	81 ± 25	2.7 ± 0.1	0.71 ± 0.08	[39]
HD 104979	18518 ± 1205	0.12 ± 0.04	21.1 ± 1.7	147.8 ± 1.6	2.7 ± 0.2	0.94 ± 0.14	[29]
HD 107541	3583 ± 47	0.09 ± 0.04	5.5 ± 0.8	128 ± 3	1.1 ± 0.2	0.55 ± 0.16	[39]
HD 107574	1384.8 ± 1.5	0.083 ± 0.005	2.99 ± 0.12	166.3 ± 0.4	1.11 ± 0.05	0.74 ± 0.06	[29]
HD 119185	25385 ± 5114	0.61 ± 0.08	23 ± 3	98 ± 13	1.7 ± 0.2	0.65 ± 0.08	[39]
HD 123949	8544 ± 12	0.9167 ± 0.0007	10.8 ± 0.9	122 ± 72	1.3 ± 0.3	0.78 ± 0.15	[30, 39]
HD 139195	5296 ± 14	0.32 ± 0.02	8.8 ± 0.3	97.6 ± 1.1	2.6 ± 0.1	0.66 ± 0.05	[43]
HD 143899	1461.8 ± 1.2	0.18 ± 0.04	3.66 ± 0.15	124.6 ± 2.5	2.4 ± 0.1	0.66 ± 0.06	[39]
HD 178717	2912 ± 14	0.46 ± 0.03	5.2 ± 0.8	35 ± 4	1.6 ± 0.9	0.53 ± 0.16	[30]
HD 180622	4045 ± 30	0.08 ± 0.04	6.9 ± 1.2	100 ± 6	1.8 ± 0.3	0.80 ± 0.25	[39]
HD 183915	4344 ± 20	0.41 ± 0.04	7.1 ± 1.2	174.3 ± 0.3	1.8 ± 1.0	0.61 ± 0.19	[39]
HD 200063	1743 ± 8	0.07 ± 0.04	4.3 ± 0.5	115 ± 5	2.0 ± 1.3	0.95 ± 0.26	[39]
HD 201824	2922 ± 23	0.30 ± 0.04	5.5 ± 1.1	59 ± 66	1.7 ± 0.4	0.78 ± 0.28	[39]
HD 204075	2367 ± 9	0.26 ± 0.05	6.0 ± 0.4	133 ± 5	4.5 ± 0.3	0.67 ± 0.10	[43, 39]
HD 205011	2846 ± 5	0.23 ± 0.02	5.3 ± 0.9	74 ± 5	1.8 ± 0.3	0.61 ± 0.19	[43]
HD 210946	1521 ± 0.9	0.109 ± 0.011	3.9 ± 0.5	114 ± 8	1.8 ± 0.5	0.86 ± 0.26	[39]
HD 216219	3948 ± 23	0.09 ± 0.05	6.2 ± 0.4	33.5 ± 1.8	1.45 ± 0.10	0.63 ± 0.08	[28]

diagram, of two grids of 20 models each. All the systems modelled for this plot start their evolution with a main-sequence Ba star of 1.5 $M_\odot$ and a WD companion. The grid plotted in red corresponds to systems with solar metallicity, while the dark blue one shows systems with sub-solar metallicity. The squares represent the initial orbital elements of the modelled binary systems when the Ba star was a main-sequence star. The lines show the evolution of these elements along the giant branch of the Ba star, and the coloured symbols show the final orbital parameters at the onset of He-core burning. We show that depending on the metallicity, the Ba stars in many of these systems (those without a corresponding final symbol) will never ignite their helium cores. As mentioned before, we concluded that even though we observe such Ba star systems in the main-sequence phase, these systems will likely merge and not become part of the Ba giant population.

6 Conclusions and discussion

Despite the efforts to describe the properties and evolution of Ba stars, further research is necessary to entirely understand their formation and evolution. From the observational side, identifying main-sequence Ba stars with higher masses is needed to complete the full evolutionary picture. Additionally, larger samples should be built, making use of large spectroscopic surveys. Of course, further theoretical research is also necessary. The orbital properties of this family of post-interaction binary systems cannot be properly explained yet, and the exact mass-transfer mechanism responsible for the pollution of Ba stars is not well-defined. In any case, the observational constraints presented in [15] and in this contribution are important for future investigation of interaction mechanisms in low- and intermediate-mass binary systems as well as of AGB nucleosynthesis models. To help with this purpose, we have collected in Table 1 a sample of well-known Ba stars that can be used to constrain the mentioned models. The table only includes systems with well-constrained orbits, masses available for both the Ba star and the WD, and stellar parameters and individual abundances determined from high-resolution high signal-to-noise spectra. The table lists their main orbital parameters (period P, eccentricity e, semimajor axis a, and inclination i) determined as described in Sects. 3 and 4, the Ba star masses determined as described in Sect. 2, and the WD masses determined as described in Sect. 4. In order to ensure the quality of the orbital inclinations and the WD masses, we only included systems with a significant orbital acceleration in the HGCA (see [16] for more details). Since the work summarized here did not focus on the chemistry of Ba stars, we list in the last column of the table recent references where the individual chemical abundances of several elements, including s-process elements, were determined from high-quality spectra.

These are exceptional times for stellar and binary evolution research. New telescopes, instruments, surveys, and theories keep coming, providing new pieces to solve this and many other puzzles. Low- and intermediate-mass stars are very common, and they are major contributors of carbon, nitrogen, many heavy elements, and dust to their host galaxies, and since at least half of them evolve in binary systems, nucleosynthesis and interaction physics are essential to our understanding of stellar evolution and the chemical evolution of galaxies.

Acknowledgments

The author wants to thank the Spanish Astronomy Society for awarding their 2021 Thesis Prize to the work summarized in this contribution. The PhD Thesis was mainly funded by the Fonds voor Wetenschappelijk Onderzoek Vlaanderen (FWO) under contract ZKD1501-00-W01 and by the Belgian Science Policy Office under contract BR/143/A2/STARLAB for the first year. The HERMES spectrograph is supported by the Fund for Scientific Research of Flanders (FWO), the Research Council of KU Leuven, Belgium, the Fonds National de la Recherche Scientifique (F.R.S.-FNRS), the Royal Observatory of Belgium, the Observatoire de Genève, and the Thüringer Landessternwarte Tautenburg. This work has made use of data from the European Space Agency (ESA) mission Gaia processed by the Gaia Data Processing and Analysis Consortium (DPAC). Funding for the DPAC has been provided by national institutions, in particular the institutions participating in the Gaia Multilateral Agreement. This research has also made use of the SIMBAD database, operated at CDS,

Strasbourg, France.

References

[1] Allen, D. M. & Barbuy, B. 2006, A&A, 454, 895

[2] Bailer-Jones, C. A. L., Rybizki, J., Fouesneau, M., et al. 2018, ApJ, 156, 58

[3] Baranne, A., Mayor, M., & Poncet, J. L. 1979, Vistas Astron., 23, 279

[4] Bidelman, W. P. & Keenan, P. C. 1951, ApJ, 114, 473

[5] Bramall, D. G., Sharples, R., Tyas, L., et al. 2010, Proc. SPIE, 7735, 77354F

[6] Brandt, T. D. 2018, ApJS, 239, 31

[7] Brandt, T. D. 2021, ApJS, 254, 42

[8] Brandt, T. D., Dupuy, T. J., Li, Y., et al. 2021, AJ, 162, 186

[9] Crause, L. A., Sharples, R. M., Bramall, D. G., et al. 2014, Proc. SPIE, 9147, 91476T

[10] Cseh, B., Lugaro, M., D'Orazi, V., et al. 2018, A&A, 620, A146

[11] Davis, P. J., Siess, L., & Deschamps, R. 2013, A&A, 556, A4

[12] Escorza, A., Boffin, H. M. J., Jorissen, A., et al. 2017, A&A, 608, A100

[13] Escorza, A., Karinkuzhi, D., Jorissen, A., et al. 2019, A&A, 626, A128

[14] Escorza, A., Siess, L., Van Winckel, H., & Jorissen, A. 2020, A&A, 639, A24

[15] Escorza, A. 2020, PhD thesis, KU Leuven and Université Libre de Bruxelles

[16] Escorza, A. & De Rosa, R. J. 2023, arXiv e-prints, arXiv:2301.04232

[17] Escorza, A., Karinkuzhi, D., Jorissen, A., et al. 2023, A&AL, accepted.

[18] Gaia Collaboration, Arenou, F., Babusiaux, C., et al. 2022, arXiv e-prints, arXiv:2206.05595

[19] Gaia Collaboration, Brown, A. G. A., Vallenari, A., et al. 2018, A&A, 616, A1

[20] Gaia Collaboration, Brown, A. G. A., Vallenari, A., et al. 2021, A&A, 649, A1

[21] Gaia Collaboration, Brown, A. G. A., Vallenari, A., et al. 2016, A&A, 595, A1

[22] Gustafsson, B., Edvardsson, B., Eriksson, K., et al. 2008, A&A, 486, 951

[23] Izzard, R. G., Dermine, T., & Church, R. P. 2010, A&A, 523, A10

[24] Jorissen, A., Van Eck, S., Mayor, M., & Udry, S. 1998, A&A, 332, 877

[25] Jorissen, A. 2004, in Asymptotic Giant Branch Stars. Springer, 2004., 461–518

[26] Jorissen, A., Boffin, H. M. J., Karinkuzhi, D., et al. 2019, A&A, 626, A127

[27] Käppeler, F., Gallino, R., Bisterzo, S., & Aoki, W. 2011, Reviews of Modern Physics, 83, 157

[28] Karinkuzhi D., Goswami A., 2014, MNRAS, 440, 1095

[29] Karinkuzhi, D. & Goswami, A. 2015, MNRAS, 446, 2348

[30] Karinkuzhi, D., Van Eck, S., Jorissen, A., et al. 2018, A&A, 618, A32

[31] Karinkuzhi, D., Van Eck, S., Goriely, S., et al. 2021, A&A, 645, A61

[32] Lugaro, M., Karakas, A. I., Stancliffe, R. J., & Rijs, C. 2012, ApJ, 747, 2

[33] Marigo, P., Bossini, D., Trabucchi, M., et al. 2022, ApJS, 258, 43

[34] McClure, R. D. 1984, ApJ, 280, L31

[35] North, P., Jorissen, A., & Mayor, M. 2000, in IAU Symposium, Vol. 177, 269

[36] Pols, O. R., Karakas, A. I., Lattanzio, J. C., & Tout, C. A. 2003, in Astronomical Society of the Pacific Conference Series, Vol. 303

[37] Raskin, G., van Winckel, H., Hensberge, H., et al. 2011, A&A, 526, A69

[38] Raskin, G., van Winckel, H., Hensberge, H., et al. 2011, A&A, 526, A69

[39] Roriz, M. P., Lugaro, M., Pereira, C. B., et al. 2021, MNRAS, 507, 1956

[40] Serenelli, A., Weiss, A., Aerts, C., et al. 2021, A&ARv, 29, 4

[41] Siess, L. 2006, A&A, 448, 717

[42] Siess, L., Izzard, R. G., Davis, P. J., & Deschamps, R. 2013, A&A, 550, A100

[43] Smiljanic R., Porto de Mello G. F., da Silva L., 2007, A&A, 468, 679

[44] Webbink, R. F. 1986, Highlights of Astronomy, 7, 185

Highlights of Spanish Astrophysics XI, Proceedings of the XV Scientific Meeting of the Spanish Astronomical Society held on September 4–9, 2022, in La Laguna, Spain. M. Manteiga, L. Bellot, P. Benavidez, A. de Lorenzo-Cáceres, M. A. Fuente, M. J. Martínez, M. Vázquez- Acosta, C. Dafonte (eds.), 2023

Challenges and projects to progress toward gender equality in the Spanish astronomical community.

Rodríguez-Baras, M.[1,†], Agís-González, B.[2], Barrado-Izagirre, N.[3], Bonoli, S.[4], Cerviño, M.[5], de Lorenzo-Cáceres, A.[6], Manjavacas, E.[7], Martínez-Núñez, S.[8], Ospina, N.[9], Pintos-Castro, I.[10], Rebollido, I. [11], Rouco Escorial, A. [12,13], Suso, J.[14], Varela, J.[10], and Vidal-García, A.[1]

[1] Observatorio Astronómico Nacional (OAN), Alfonso XII, 3, 28014, Madrid, Spain
[2] Instituto de Astrofísica de Andalucía-CSIC, Glorieta de la Astronomía s/n, 18008, Granada, Spain
[3] UPV/EHU, Escuela de Ingeniería de Bilbao, Física Aplicada, Bilbao, Spain
[4] Donostia International Physics Center (DIPC), Manuel Lardizabal Ibilbidea, 4, San Sebastián, E-20018 Donostia, Spain; Ikerbasque, Basque Foundation for Science, E-48013 Bilbao, Spain
[5] Centro de Astrobiología (CAB), CSIC-INTA, Carretera de Ajalvir km 4, E-28850 Torrejón de Ardoz, Madrid, Spain
[6] Instituto de Astrofísica de Canarias, Calle Vía Láctea s/n, E-38205 La Laguna, Tenerife, Spain; Departamento de Astrofísica, Universidad de La Laguna, E-38200 La Laguna, Tenerife, Spain
[7] AURA for the European Space Agency (ESA), ESA Office, Space Telescope Science Institute, 3700 San Martin Dr., Baltimore, MD 21218, USA
[8] Instituto de Física de Cantabria (CSIC-Universidad de Cantabria), 39005, Santander, Spain
[9] Department of Theoretical Physics, University Autónoma Madrid, 28049 Madrid, Spain
[10] Centro de Estudios de Física del Cosmos de Aragón (CEFCA), Plaza San Juan 1, 44001, Teruel, Spain
[11] Space Telescope Science Institute, 3700 San Martń Dr., Baltimore, MD 21218, USA
[12] Center for Interdisciplinary Exploration and Research in Astrophysics (CIERA) and Department of Physics and Astronomy, Northwestern University, Evanston, IL 60208, USA
[13] European Space Agency (ESA), European Space Astronomy Centre (ESAC), Camino Bajo del Castillo s/n, 28692 Villanueva de la Cañada, Madrid, Spain
[14] Observatorio Astronómico de la Univ. de Valencia, C/ Catedrático José Beltrán, 2, 46980, Paterna, Valencia, Spain
[†] mujer-y-astronomia@sea-astronomia.es

Abstract

In the last decades important improvements have been made towards better access and working conditions for women in science. However, we are still far from reaching gender equality in the scientific field. We still suffer from gender stereotypes during childhood, subtle gender bias in academic and scientific evaluations, unequal work-life responsibilities, gender pay gap and challenging glass ceilings, among many other factors, that prevent real equal opportunities in the development of women's careers.

The Women and Astronomy Committee of the Spanish Astronomical Society works to progress towards gender equality in the Spanish astronomical community by organizing and promoting activities that raise awareness on this issue and contribute to eliminating gender inequality factors in the scientific and research environment.

In this proceedings paper, we summarize the report presented by the Committee at the XV Spanish Astronomical Society meeting in September 2022 in La Laguna (Tenerife). First of all, we present the report of our activities during the 2020-2022 period. Then, we have identified a number of key areas where we need especially to work now. We present our upcoming projects classified in the following lines of work: early stages of the research career, increasing awareness and providing tools to the community, actions at the institutional level, work-family balance, addressing harassment, and diversity and LBTI+ initiatives.

1 Introduction

The situation of gender inequality in the scientific field is currently well-diagnosed (e.g. [1]), both as the reflection of gender inequality factors in society and as the result of specific issues in the scientific context. The Spanish research environment, and particularly the Spanish astronomical community, follows this general trend, with some progress seen over the last years, although there is still much room for improvement [2].

In this context, the Women and Astronomy Committee[1] (CMyA, in its Spanish acronym) of the Spanish Astronomical Society (SEA) was founded in 2010 with the aim of collaborating in a better diagnosis of the existing inequalities in the Spanish astronomical community and their causes, as well as to organize activities that contribute to their elimination. Throughout its history, the CMyA has organized activities along different lines: scientific outreach focused on increasing the visibility of Spanish women astronomers, specific analysis of the causes for inequality throughout the different stages of the scientific career, creation of networks among Spanish women astronomers, increasing community awareness on this issue, etc.

The SEA held its XV biannual scientific meeting last September 2022 in Tenerife, Spain. In this conference the CMyA presented the report of its activities during the period 2020-2022, as well as the key projects that intends to carry out over 2022-2024, in order to promote the involvement of the community. This paper of the conference proceedings is a summary

[1] https://www.sea-astronomia.es/comision-mujer-y-astronomia

of the CMyA oral contribution. Due to our usual work context, several of the references provided are in Spanish.

2 Summary of CMyA activities in 2020-2022

Over the past two years, a total of 19 people (17 women and 2 men) have been part of the core group of the CMyA, currently composed of 13 members. The committee's bylaws have been renewed, and are published in its webpage. The CMyA holds monthly meetings, and organizes its activity through different working groups. The CMyA can also count on the support of the so-called Extended Group, made up of SEA members who wish to receive information on gender and science and collaborate with particular activities, which currently has around 60 members. The minutes of the CMyA meetings are available for all members of the Extended Group, as well as for all SEA members under request.

The activities carried out in this two-years period are classified in five main areas:

1. **Outreach**. In the framework of February 11, International Day of Women and Girls in Science, the CMyA organizes activities aimed at giving visibility to women astronomers and to promote scientific interest among children and young girls. These past two years we have celebrated the fourth and fifth editions of the activity *Chat with a Woman Astronomer*, an annual online activity in which for twelve hours anyone can chat with professional woman astronomers to ask questions about astronomy or their professional careers. More than 50 woman astronomers participate each year, chatting with hundreds of people and dozens of schools. The CMyA also organizes creativity contests for children (short stories in 2021, videos in 2022), publishing the winning entries on the SEA website and its social networks. We also highlighted the work of women astronomers at the banner of the SEA main webpage and helped other institutions to advertise their own activities. All the information can be found in the CMyA webpage.

2. **Analysis**. In 2021 we conducted a survey among SEA members, with the goal of obtaining a detailed diagnosis of the situation of gender inequality in the Spanish astronomical community and its effect on scientific careers. The survey was answered by 225 people (25% of SEA members), of which 34% were women. The results, which show the existence of the so-called "scissors" diagram, were provided for SEA human resources studies. We also carried out a specific study on the possible gender-differentiated effect of COVID-19 lockdown on the number of astronomical publications. No biases were found against women in 2020 with respect to previous years, although the study should be extended to 2021 and 2022. Results were published in 2021 SEA Summer Newsletter.

3. **Awareness-raising**. In 2020 we organized a colloquium at the 2020 Spanish Astronomical Society online meeting where we presented an open document with information, statistics, resources and tools for SEA members to better understand the factors of gender inequality in our work environment and be able to contribute to mitigating or eliminating them in their daily work. The document will be updated on an ongoing basis. In March 2022, under the "synergies" SEA scheme, we organised the online

meeting entitled "Gender inequality in Science: diagnosis and debate for progress toward real equality". The event included a talk that reviewed the current situation of gender inequality in science with updated data, both in general in the world and in the specific case of Spanish astronomy. This was followed by a round table discussion with female experts in the field and a debate with the audience, aimed at complementing the analysis with the various opinions and experiences in the community. The event was attended by more than 90 people.

4. **Mentoring.** Under the motto "Walking together Towards the Sky", we launched the first edition of the Mentoring program (see Manjavacas et al. in this Proceeding series), with more than 50 women participating as either mentors (25) or mentees (27). The Mentoring program included two training sessions for mentors, and different small workshop sessions targeting common issues for young female astronomers (i.e. impostor syndrome). Peer mentoring sessions for both mentors and mentees were held every two to three months, with a specific goal of building networks and sharing experiences. As the second edition of the Mentoring program starts, most of the participants in the previous year decided to continue (∼80%), and a survey among the participants showed a high fraction of satisfaction, with an average score of 9 out of 10.

5. **Communication and collaborations**. We have dedicated important efforts to make visible the role of women in astronomy and to raise awareness about the importance of advancing towards equality, both in professional environments (e.g. contributed talk at the European Astronomical Society -EAS- meeting in June 2022) and in the media (numerous interventions and publications in radio and newspapers). Our involvement also includes collaborating in different actions with other institutions, such as the EAS "Inclusion and diversity" working group (since January 2022), or the working groups on mentoring of both the IAU (since 2022) and the Spanish Ministry of Science and Innovation (since May 2022).

3 Challenges in the first stages of the academy

The effects of gender inequality in scientific careers are observed in two different types of segregations: a horizontal one and a vertical one. The horizontal segregation describes the fact that, even in countries where there is gender parity among university students, there is an imbalance among academic disciplines, with men outnumbering women in science and engineering disciplines. This is the result of gender stereotypes associated with science that are transmitted since childhood and throughout pre-university education, and whose effects are detectable from a very early age [3]. In Spain, studies also show the influence of these effects (e. g. [4]). A Vertical segregation implies that women who decide to embark on a professional scientific career are less likely to reach the highest and decision-making positions than their male counterparts, which is reflected in the well-known scissors diagram [1, 2].

The effect of both phenomena can be seen in Figure 1, which shows the evolution between 2002 and 2022 of the percentage of women in the field of Astronomy and Astrophysics in Spain, according to the latest report on human resources in Astronomy and Astrophysics of

the Spanish Astronomical Society [5]. There is no gender parity (at least 40-60%) even in the undergraduate stage, and the numbers worsen in the subsequent stages. The evolution over the last 20 years is particularly worrying, since not only there is no significant growth of the women percentage, but in recent years there is also an important decrease at the undergraduate and graduate stages, which will constitute the scientific community in the coming decades.

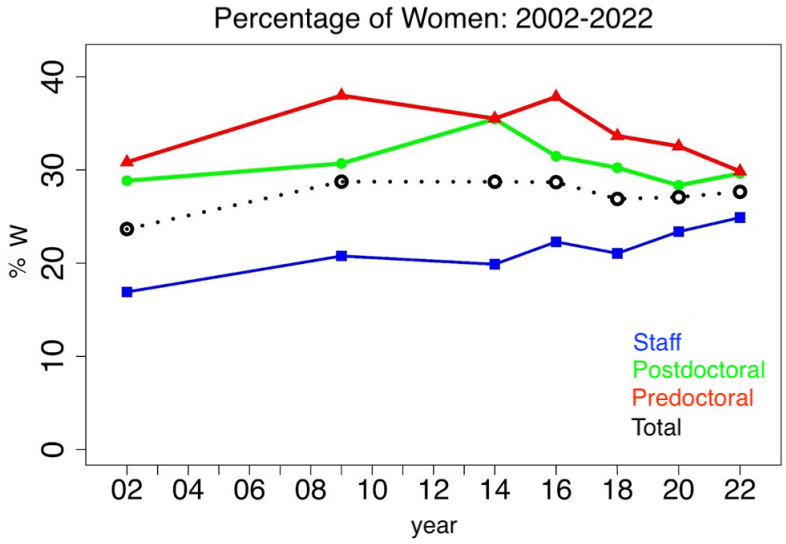

Figure 1: Evolution between 2002 and 2022 of the percentage of women in the field of astronomy and astrophysics in Spain. Different colours correspond to different stages of the scientific career, and the total number is indicated in black.

Women scientists in the early stages of their careers suffer the consequences of both horizontal and vertical segregation. On the one hand, they carry the effects of a stereotypical upbringing that has left them less self-confident and in the minority among their peers. On the other hand, they try to compete in a work environment in which they are judged more harshly [6], have fewer reference figures to follow and will encounter more obstacles to progress (e.g. [7]). To overcome this situation, it is essential to create support and communication networks, and to promote greater self-confidence in young women astronomers.

In this context, in 2021/2022 we launched the first edition of the SEA Mentoring program for young women astronomers (see Sec. 1 and Manjavacas et al. in this Proceedings series), which is currently starting its second edition. This program generates mentor-mentee pairs, composed of a junior and a senior female astronomers, to promote the transmission of knowledge and experience, as well as professional orientation. Furthermore, the program also includes a specific training program for mentors, peer-mentoring sessions for mentors and mentees so that they can share their experiences, and specific thematic sessions, such as one about the impostor syndrome. All of this also generates a solid network of collaboration and support among Spanish women astronomers.

4 Increasing awareness and providing tools to the community

Gender inequality in science today is not only a consequence of past inertia, but the result of current factors of inequality that require active and direct action for their disappearance. All of us (women, men, non-binary) can play a relevant role in this process, detecting the manifestations of gender inequality in our daily work and carrying out small daily actions that contribute to the creation of more egalitarian work environments.

In this line of action, in recent years the CMyA has organised training activities focused on providing information, data and tools to promote awareness and actions by SEA members with respect to gender equality. Two examples are the colloquium on the open document with tools, organised and published in 2020, and the synergy with a round table of experts, organised in 2022 (see Sec. 2).

These previous activities have provided the community with an overview of the current situation of inequality and its general causes. We now consider that it is convenient to go a step further and to address separately the different aspects that make up this multifaceted situation, providing more detailed and complete information and the opportunity to specifically discuss each of them. We are therefore organizing a training course on gender, inclusion and science for 2023, with 10 online seminars on different topics taught by experts in the corresponding subjects. The subjects to be covered are the following:

1. Introduction: advances and challenges to reach gender equality in science.
2. University education with gender perspective.
3. Subtle gender bias in the scientific career.
4. Gender diversity and inclusion.
5. Inclusive language.
6. Harassment.
7. Inclusion of gender perspective in scientific projects.
8. How to be an ally.
9. Equality plans in scientific institutions.
10. Glass ceiling.

5 Actions at the institutional level

The involvement of institutions is essential to advance towards equality, since they have the capacity to apply measures to modify unequal work dynamics in a general, effective and lasting manner. In particular, the implementation of affirmative action policies is necessary, i.e. measures and strategies aimed at eliminating situations, prejudices, behaviour and cultural

and social practices that prevent an undervalued or discriminated social group from achieving a real situation of equal opportunities. This is established in the Spanish Constitution itself, which states that (Article 9.2) "It is the responsibility of the public authorities to promote the conditions so that the freedom and equality of the individual and of the groups in which she/he is integrated are real and effective; to remove the obstacles that prevent or hinder their fullness and to facilitate the participation of all citizens in political, economic, cultural and social life".

Furthermore, the Spanish legislation [8] establishes that it is mandatory for all companies with more than 50 employees to have a Gender Equality Plan, defined as "An ordered set of measures, adopted after carrying out a diagnosis of the situation, aimed at achieving equal treatment and opportunities between women and men in the company and eliminating discrimination based on sex". To ensure its effectiveness, a Gender Equality Plan must include: (i) A detailed diagnosis of the gender equality situation in the corresponding institution, with statistics dis-aggregated by sex. (ii) Adequate affirmative action policies for the improvement of gender equality within the institution, appropriate to the circumstances and timeframe considered by the gender equality plan. Their implementation and application should be accessible to all staff members. (iii) Financial resources and qualified personnel for the implementation of the measures considered. (iv) Periodic evaluation of the measures, based on indicators to check their degree of adequacy and compliance.

Aiming to create an inclusive work environment and to help mitigate the inequalities previously mentioned, there are some examples of affirmative actions at institutional level that can be implemented in the different areas:

1. Dynamics in the workplace. It is essential to create an inclusive and gender-equal institutional environment. Possible measures:

- Improvement of the visibility of women's work (seminars given by women, networking between women, promote outreach activities with gender parity).
- Use of inclusive language in all communications.
- Explicit and active condemnation of sexist attitudes.
- Ensuring work-life balance (see Sec. 6).

2. Promotion, evaluation, and selection processes. The existence of unintentional subtle gender bias hinders objectivity in evaluation processes. Some possible measures to ensure objectivity and avoid discriminatory attitudes:

- Specific training on gender equality and subtle bias for those who participate as reviewers in selection processes.
- Consideration of the influence of work-life balance factors (e.g. maternity leave) for men and women in the criteria applied in selection, hiring and promotion processes.
- Gender parity composition (at least 40-60%) in selection, scientific and time allocation committees, PhD tribunals, project evaluation panels, etc.
- Whenever possible, blind evaluations.

• Transparency, clarity and publicity in the evaluation and selection criteria.

3. Conferences and workshops. These events are a fundamental scenario for publicizing scientific work and creating collaborative networks. It is therefore important to guarantee gender equality in their organization and course. Possible measures:

• Gender parity composition (at least 40-60%) in scientific and local organizing committees (SOC and LOC).

• Gender parity among invited speakers.

• Work-family measures: Childcare service provided during the conference, financial assistance for researchers travelling with minors, etc.

• Provide the option to attend remotely, to facilitate the attendance of those who cannot travel (also convenient in ecological terms).

4. Workload distribution. It is important to ensure that measures adopted for parity do not result in an excessive workload for women scientists. The extra participation of women in parity committees should be compensated by a discharge of responsibilities in other areas.

The SEA is not an ordinary scientific institution, but a collaborative society of astronomers in Spain. Therefore, its capacity to implement institutional measures is lower, and it has little direct influence on the working conditions of its members. However, it also has the capacity to act, both through the direct application of measures in its normal operation and through the example it can set for other ordinary institutions. For this reason, the CMyA, with the support of the SEA management board, considers the following lines of action:

- Update of the SEA's Gender Equality Plan. Compliance and evaluation of measures.
- Ensuring the use of inclusive language in the SEA official email communications, official documents, forms, web, etc.
- Systematisation of the human resources statistics dis-aggregated by gender.
- Gender parity among the speakers participating in SEA's conferences and events.

6 Work-life/work-family balance

When talking about work-family balance, it is relevant to take into account that this is a transversal issue, related to the overall work-life balance. Considering the case of Spain, the data show that nowadays the distribution of household work and the care of children and dependents continues to be very unbalanced, with women dedicating many more hours than men [9]. Therefore, the labor consequences derived from work-family balance are also suffered mainly by women, generating an important factor of inequality. Thus, although the final goal must be to achieve a general work-life balance, we focus mainly in the work-family aspect,

as it is still a gender inequality cause. It is clear that an improvement of the work-family balance is necessarily linked to the concept of *co-responsibility*.

To improve the work-family balance in the work environment we consider measures taken at three different levels:

- **Governmental level: laws and regulations.** States have the capacity to establish legislative and regulatory frameworks to produce better work-family balance possibilities, as well as a more balanced distribution of the associated responsibilities. State action is essential, since its measures are more lasting and produce greater social transformation. In addition, they reach the entire population, without depending on the specific work environment in which people work. In Spain, important steps have been taken in recent years, such as an increase in the number of weeks of maternity and paternity leaves (16 weeks in each case). There are also specific regulations for public employees (a specific gender equality plan [10] and additional measures such as flexible working hours [11], the possibility of reduced working hours, etc.). However, there is still much room for improvement to achieve a good work-life balance and an equilibrium in the distribution of responsibilities.

- **Institutional level: gender equality plans and group policies.** Institutional equality plans can and should include measures to facilitate work-family reconciliation. Some examples would be creche grants, after-school activity grants, technological facilities, measures aimed at facilitating flexible working hours, etc. Furthermore, the issue of work-family balance can be taken into account in smaller groups and daily contexts, such as the organization of a research group. This can be done independently of the corresponding institution work-life policies, and it has a great effect, even if it is in a short-range environment. Some of the possible measures are: ensuring digital disconnection outside working hours, schedule working meetings exclusively during working hours (with no time extensions), flexible working plans to take into account possible personal circumstances of any group member (not only family-care), ensuring that no member of the group misses out on participation or leadership opportunities due to family circumstances (e.g. maternity leave), etc.

- **Personal level: co-responsibility and self-care** Last but not least, work-life, and specially work-family balance implies a personal responsibility inside one's own family. It is necessary to deconstruct some of the ideas learned in the childhood about family roles. The article *What Causes the Child Penalty? Evidence from Adopting and Same-Sex Couples* [12], compares the "child penalty" between heterosexual couples and same-sex couples, showing that the penalty is lower in same-sex couples. It therefore considers that the variation is due to the different family roles associated with gender. The definition of the different roles inside a couple is obviously an internal decision, but the traditional social tendency to assign women greater responsibility for caregiving must be taken into account by both partners in order to build real co-responsibility. In this regard, some websites and citizen platforms, such as the so-called Club de Malas Madres (Bad Mothers Club), provide videos related with work-life balance, self-care and motherhood, among other resources.

The CMyA has a work-family balance working group, focused on discussing measures to improve work-family balance that can be implemented at the SEA level. We also distribute information on measures that can be taken in the work environments of SEA members.

7 Addressing harassment

Harassment is one of the least openly discussed issues when considering labor rights and equality, and nevertheless it has devastating consequences. According to a survey by the Spanish Ministry of Science and Innovation conducted in 2021, 8.6% of female researchers admitted having suffered sexual harassment[13]. And yet this number probably does not reflect the full reality of the problem, both because of the difficulty many victims have in becoming aware of their situation and, if they do, the reluctance to acknowledge it publicly. Aware and concerned about this, the CMyA has decided to take actions to give visibility to this problem, with the aim of mitigating its consequences and creating a space in which to provide support and advice to victims.

According to the Spanish penal code, harassment can be defined as a situation in which, without necessarily involving explicit or non-explicit threats or the direct use of violence, a person *harasses* another in a repeated and insistent way, altering the victim's life and attempting against his/her integrity, regardless of the intention. The Spanish penal code also defines different types of harassment (e.g. [8], art. 7), as well as their sanctions (e.g. [14], art 184): workplace harassment, harassment based on gender, on sexual orientation, psychological harassment and sexual harassment, among others.

Harassment situations are more likely to occur in hierarchical environments[15], especially those in which some people are heavily dependent on others in higher positions, as is the case in academia. In addition, the risk of harassment increases in environments where there are more men than women, as is the case of many scientific fields. The book *"Acoso: MeToo en la ciencia Española"* [15], published in 2021, reflects through testimonies how the hierarchical system present in Science encourages harassment situations to occur.

There are several concerns regarding harassment that should be taken into account. A particularly striking one is the self-identification of the victim. In many cases, victims are not able to identify their situation as harassment, due to its subtle and non-explicit characteristics and the scarce knowledge that still exists on this subject. In this regard, the existence of harassment protocols is an essential tool to help identify and deal with these situations. Fortunately, many Spanish institutions now have anti-harassment protocols, but it is still necessary to increase the knowledge of their staff about them.

Another key issue is the concern of victims that their testimony will not be considered or believed, and the repercussions that a report may have on their professional career due to the hierarchical structure of academia. It is also important the discouraging nature of the complicated bureaucracy associated with reporting, and the feeling of lack of support during the process.

To help address and mitigate this problem, the CMyA has decided to implement in the coming years a series of actions:

- Compiling the anti-harassment protocols of Spanish scientific institutions and publish them on the CMyA website, to promote awareness and provide easy access to them.
- Revising SEA's gender equality plan to include anti-harassment measures.
- Providing SEA members with a confidential point of contact at which to provide information and accompaniment on harassment issues.
- Creating "violet contacts" at SEA scientific meetings to contact and report possible situations of harassment that may occur.
- Including a session on harassment in the training course organized for 2023 (Sec. 4).

8 Diversity and inclusion: LBTI+ initiatives

In order to further strengthen the diversity, equity and inclusion of Women in Astronomy, we have created a new LBTI+ working group within the CMyA, following the initiatives proposed in the equality plans of both the General State Agency ([10] Eje 6, Medida 6) and the Superior Council for Scientific Research 3rd equality plan (Eje 6, Medida 4). The new LBTI+ group will pay special attention to the well-being of the LBTI+ female astronomers, as they can suffer situations of special vulnerability (a.k.a. multiple types of discrimination or intersectionality). In this regard, we want to boost the LBTI+ visibility and to make the SEA members aware of their vulnerable situation.

The equality plans presented by AGE and CSIC propose a study of the situation of the LGTBI+ collective. We aim to include a section on the gender perspective in future sociological and human resources studies to analyze the situation of the LGTBI+ collective in the SEA. This action has also been launched by the European Astronomy Society (EAS).

We also promote a series of very simple actions, such as:

- Apart from working on the visibility of the collective every day of the year, we plan to introduce a small logo on the SEA website during the month of June, the month of Pride. This initiative has also been carried out by other European institutions, such as the University of Amsterdam or the University of Heidelberg, and also in the USA.
- For the sake of the diversity of our society, we will include a session focused on the richness of gender and identity within the training course we are organizing for 2023 (see Section 4), with the main goal of training and updating SEA members regarding the evolution of society and the new generations of SEA in relation to gender identity.
- Organization of talks where the efforts of the LBTI+ community in Astronomy are made visible, highlighting the intersectionality of the problems they suffer.
- Creating an area in the SEA website to store informative, formative and practical material that relates science and LBTI+, such as links to websites like PRISMA (Association for Affective-Sexual and Gender Diversity in Science, Technology and Innovation).

It is worth mentioning that the SEA does not currently have a commission focused on LGTBI+ issues. Here we are approaching this topic in an intersectional way, focusing on women and science. We are aware that this may not be enough, but if we are able to make this gains strength, we will propose the creation of a new LGTBI+ commission.

9 Conclusions

The CMyA will continue in the next years working along the lines described above, pushing for a real gender equality within our community. The contribution of the whole community at all levels, from individuals to group leaders and institute directors, will be essential for a real step forward in this direction.

References

[1] She Figures 2021. Gender in research and innovation: statistics and indicators. EU publications.

[2] Científicas en Cifras 2021. Unidad de Mujer y Ciencia. Ministerio de Ciencia e Innovación. España.

[3] Bian, Leslie et al., 2017, Science, Vol. 355, Issue 6323

[4] Ayuso, Fillola et al., 2021, IEEE Transactions on Education, Vol. 64, Issue 1

[5] Quinto Informe de Recursos Humanos en Astronomía y Astrofísica en España. SEA 2022.

[6] Moss-Racusin, Corinne A. et al., 2012, *PNAS*, Vol. 109, Issue 41.

[7] Caplar, Neven et al., 2017, Nature Astronomy, Volume 1, id. 0141

[8] Ley Orgánica 3/2007, para la igualdad efectiva de mujeres y hombres, BOE-A-2007-6115

[9] Mujeres y hombres en España. Instituto Nacional de Estadística. 2021.

[10] III Plan para la Igualdad de Género en la Administración General del Estado. BOE-A-2021-2.

[11] Instrucciones sobre jornada laboral de la AGE, BOE-A-2019-2861.

[12] Martin Eckhoff Andresen and Emily Nix, *Journal of Labor Economics* 2022 40:4, 971-1004

[13] Estudio sobre la situación de las jóvenes investigadoras en España. Ministerio de Ciencia e Innovación, 2021.

[14] Ley Orgánica 11/1999, de 30 de abril. BOE-A-1999-9744

[15] Bernardo Alvarez, A., 2021, Acoso. Me Too en la Ciencia Española, Next Door Publishers. 2021.

Highlights of Spanish Astrophysics XI, Proceedings of the XV Scientific Meeting of the Spanish Astronomical Society held on September 4–9, 2022, in La Laguna, Spain. M. Manteiga, L. Bellot, P. Benavidez, A. de Lorenzo-Cáceres, M. A. Fuente, M. J. Martínez, M. Vázquez- Acosta, C. Dafonte (eds.), 2023

Observing black holes with mm-VLBI and the EHT.

Martí-Vidal, I.[1,2]

[1] Dpt. Astronomia i Astrofísica, Universitat de València (Spain)
[2] Observatori Astronòmic, Universitat de València (Spain)

Abstract

The Very Long Baseline Interferometry (VLBI) technique allows us to synthesize virtual telescopes with optical apertures as large as the Earth's diameter (and beyond). With these apertures, when observing at millimeter wavelengths, it is possible to obtain images of the radio universe with a diffraction limit of just a few tens of micro-arcseconds, which is high enough to resolve the "photon rings" of the closest supermassive black holes (SMBH) to the Earth. In these proceedings, we discuss about the challenges of doing VLBI at such short wavelengths and the scientific exploitation of this kind of observations, with an emphasis on the results published by the Event Horizon Telescope (EHT) Collaboration for SgrA* and M87*.

1 Introduction

One of the most exotic predictions of the Theory of General Relativity (GR) is the existence of event horizons in black holes. These are regions where time and space exchange their metric signs, still observers cease to exist as seen from distant reference frames, and two causally-disconnected parts of the Universe meet. The direct observation of black holes at the spatial scales of their event horizons is a way to probe the edge of space and time, which marks the frontier of the Universe that can be accessible to us. Monitoring black holes at these spatial scales may allow, in a longer term, to probe how matter, magnetism, space and time interact and behave in these extreme regions, to test GR (and/or alternative theories of spacetime) in gory detail.

Just a few decades ago, the enterprise of imaging black holes at the scales of their event horizons was in the realm of fiction. The pioneering works of Jean-Pierre Luminet [24] gave us a glance of how these images would look like under ideal conditions, while the more realistic simulations by Heino Falcke [16] demonstrated the feasability of getting observational signatures of the presence of an event horizon (the so-called "black hole shadow") via high-resolution observations at radio wavelengths with the Very Long Baseline Interferometry (VLBI) technique.

The World had to wait many years of technological developments in Radio Astronomy to have stable and sensitive VLBI receivers at millimeter wavelengths; short enough to provide the spatial resolutions needed to image the scales of the event horizons of the closest supermassive black holes (SMBH) to the Earth, specifically those at the center of galaxy M87 (known as M 87*) and our Galactic Center (known as Sgr A*). Here, the critical roles of Shep Doeleman in the american side (Harvard/MIT), and Anton J. Zensus and Thomas Krichbaum in the european side (MPIfR), together with other several pioneers of millimeter-VLBI, cannot be stressed enough.

Two main teams (in California and Europe) were responsible of the development of the first VLBI receivers at 230 GHz (wavelength of 1.3 mm) starting in the 80s−90s decades of the last century, with the first reported VLBI detection at this frequency (actually, at 215 GHz, between the IRAM-30m telescope at Pico Veleta in Spain and the Plateau de Bure interferometer, the current NOEMA, in the french Alps) from year 1995 [20]. The mm-VLBI technology has improved relatively fast since then. In Spain, for instance, the Centro Astronómico de Yebes (CAY), part of the Instituto Geográfico Nacional (IGN), has become a World-leading institution in the development of mm-wave heterodyne receivers.

Shep Doeleman, the founding director of the Event Horizon Telescope (EHT), was the PI of the first VLBI observations of Sgr A* and M 87* at 230 GHz, originally made with just three stations (CARMA in California, SMT in Arizona and JCMT in Hawaii), but good enough to extract some important structural information from the underlying SMBH images (e.g., [4, 5]).

Some years later, with the arrangement of the EHT, new VLBI observations of M 87* and Sgr A* at 230 GHz were finally taken, with an array large and sensitive enough to bring imaging capabilities: the first scientific observations of the modern version of the Event Horizon Telescope took place in April 2017 (see the distribution of EHT stations in Figure 1, left). And, finally, a few years after those observations were taken, the first images of these black holes were revealed to the World by the EHT Collaboration [6, 13].

In the following sections, we will briefly describe how VLBI works and will discuss about the challenges inherent to the mm-wave VLBI observations. Then, we will discuss about the theory behind the images of black holes at the scales of their event horizons, and will briefly summarize some of the main results reported by the EHT Collaboration.

2 Astronomical Interferometry in a nutshell

VLBI is based on the *Aperture Synthesis* technique (e.g., [28]), which enables the combination of a set of small telescopes, in order to "synthesize" a large virtual telescope. Such large synthesized apertures are key to achieve the diffraction-limited high angular resolutions needed to image black holes at the scales of their event horizons (a few tens of μas).

The small telescopes that are combined in the Aperture Synthesis are equiped with heterodyne receivers, which coherently sample different points of the frontwave coming from the observed source. The signals of all these telescopes are recorded and combined (correlated) among all pairs of telescopes, in such a way that it is possible to use all these cross-correlations

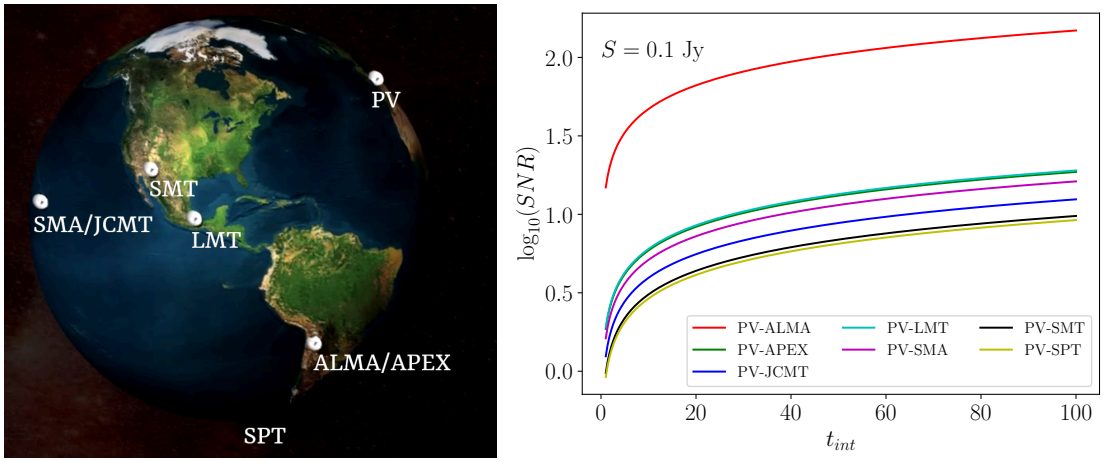

Figure 1: **Left**, array distribution of the EHT in the observing campaign of year 2017. **Right**, theoretical SNR of all the baselines associated to IRAM-30m (PV) in year 2017, assuming a perfect atmosphere and a correlated flux density of 0.1 Jy.

to synthesize the optical aperture of one single "virtual" telescope, with a size equivalent to the maximum distance among the individual elements of the interferometer. The very basic concepts of this technique are sketched in Figure 2. Let us ellaborate on this figure:

In panel **(a)**, we show a set of individual small telescopes (in red) and a giant telescope (in yellow), as large as the space occupied by the set of red telescopes. Panel **(b)** shows the optical aperture (in Fourier space) generated by the interferometer (in red) and the giant telescope (in yellow). For the giant telescope, the aperture is equal to the autocorrelation of its pupile (which we assume to be a perfect circle of size equal to that of the primary reflector surface); for the interferometer, the aperture is determined by the relative positions among all the pairs of telescopes, as seen from the direction to the source. We notice that the interferometer acts like a severe "mask" applied to the whole aperture (since there are only a few points measured in Fourier space!). That mask filters out a large fraction of the spatial frequencies of the observed source structure.

In panel **(c)**, we show the Point Spread Function (PSF, i.e., the instrumental response to a point source) of the giant telescope (i.e., having a full aperture), which is equal to an Airy disc (the sidelobes of the Airy disc are far too weak to be seen with the color palette of this figure). In panel **(d)**, we show (using a similar contrast for the color palette) the PSF corresponding to the sparse aperture of the interferometer, which (due to the large masked regions in Fourier space, see panel **(b)** in red) suffers from relatively large artifacts (i.e., very high sidelobes and secondary peaks). Ellaborated image reconstruction algorithms are needed to get rid of all the convolution artifacts produced by these so-called "dirty" interferometric PSFs (see, e.g. [7, 14]).

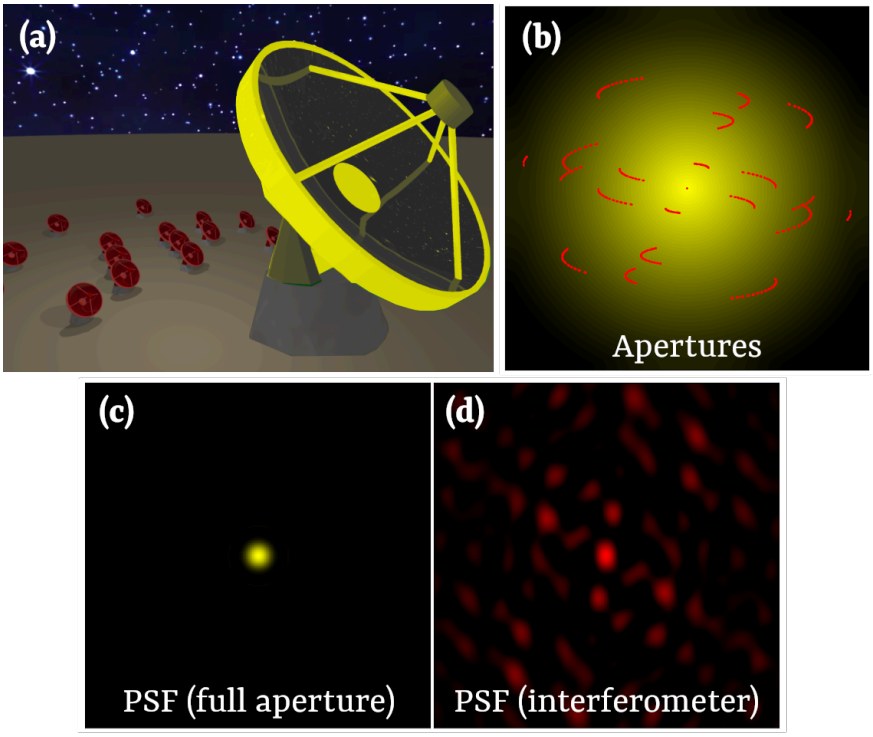

Figure 2: Sketch of how Aperture Synthesis works. **(a)** array distribution (red) and giant telescope with an equivalent resolution (yellow). **(b)** apertures of the interferometer (red) and the giant telescope (yellow). **(c)** and **(d)**, PSFs of the two instruments.

3 The challenge of VLBI at millimeter wavelengths

Observing with VLBI at very high frequencies (millimeter wavelengths) adds some extra problems to the Aperture Synthesis technique described in the previous section. The main problem of mm-VLBI is the relatively low sensitivity of the antenna receivers. It is technically challenging to properly amplify and mix the wideband high-frequency signals, adding a minimum thermal noise across the full signal chain. On the one hand, the reflector surfaces of the antennas have to be built with an extremely high precision (tens of microns), which limits the effective surface of big radiotelescopes. On the other hand, the heterodyne technology at such high frequencies is not very efficient, compared to centimeter wavelengths.

An additional problem (which combines very badly with the first one) is the relatively short coherence time of the atmosphere at these high frequencies[1]. In VLBI, there is a rule of thumb about the coherence time (not very accurate; just valid for order-of-magnitude discussions): for a given observation, *the coherence time in minutes is equivalent to the observing wavelength in centimeters*. That is, for the EHT (observing wavelength of 1 mm)

[1]The coherence time can be defined as the integration time of the interferometric observables, such that the random variations of the atmosphere over each station introduce a loss of 10% in the cross-correlated signal.

the coherence time is of the order of just a few seconds (actually, in [7] there is a more precise estimate of the coherence time of the EHT baselines, which can easily reach more than 20 seconds in most cases).

These two problems combined (i.e., the short coherence time and the limited sensitivity, which implies the need of long integration times to have good detections) prevented the possibility of obtaining VLBI images at 1 mm for many years; until the EHT came online on April 2017. The game changer that allowed to extract the maximum potential of the EHT antennas was the addition of the ALMA telescope to the EHT array (see [18, 26, 25] for details). Figure 1 (right) shows the theoretical SNR of a typical observation (correlated flux density of 100 mJy) for all baselines associated to Pico Veleta (PV), as a function of the integration time (if no atmospheric effects were present). The baseline to ALMA is so sensitive, that there are clear detections after an integration time of just one second (or even a fraction of a second!), which allows to correct for the rapid atmospheric effects, in a way similar to the adaptive optics of optical telescopes. Once these effects are corrected for the whole array (thanks to the baselines to ALMA), much longer integration times can be applied to the whole EHT, ensuring good detections across all the antenna pairs. The interested reader will find more details about the data calibration and analysis in the EHT publications [6, 7].

4 Black hole images at the highest resolutions

What do we see when we observe a black hole with a spatial resolution similar to the size of its event horizon? The first answer to this question came from Jean-Pierre Luminet [24], who realized that the image of the accretion disc could be heavily deformed by the space curvature (the well-known gravitational lensing effect) and, in addition to this, the image of a *ring* would appear around the black hole, as a result of the presence of the so-called *photon sphere* of the black hole. The photon sphere is the region around a black hole where closed photon orbits can exist. Since these orbits are all unstable, photons that orbit arbitrarilly close to the photon sphere can eventually escape from that region (after performing a given number of orbits around the black hole) and propagate in direction to the Earth, to be (much) later sampled by the EHT antennas.

The size of the ring associated to the photon sphere encodes precise information about the mass of the black hole, to the point that it can be used either to estimate the mass/distance relation of the black hole, or (if that quantity is already known) to test GR and the spacetime metric of the SMBH.

In Figure 3 (top left), we show an image similar to the results published in [24], where we have used a geometrically thin disc around a Schwarzschild black hole. The inner radius of the disck is set at the innermost stable circular orbit (ISCO). The vertical orange line marks the spin axis of the accretion disc and the dashed blue line marks the edge of the event horizon. The ring image of the photon sphere (about 2.6 times larger than the size of the event horizon) is clearly seen in the image, surrounded (after a small gap) by the image of the accretion disc.

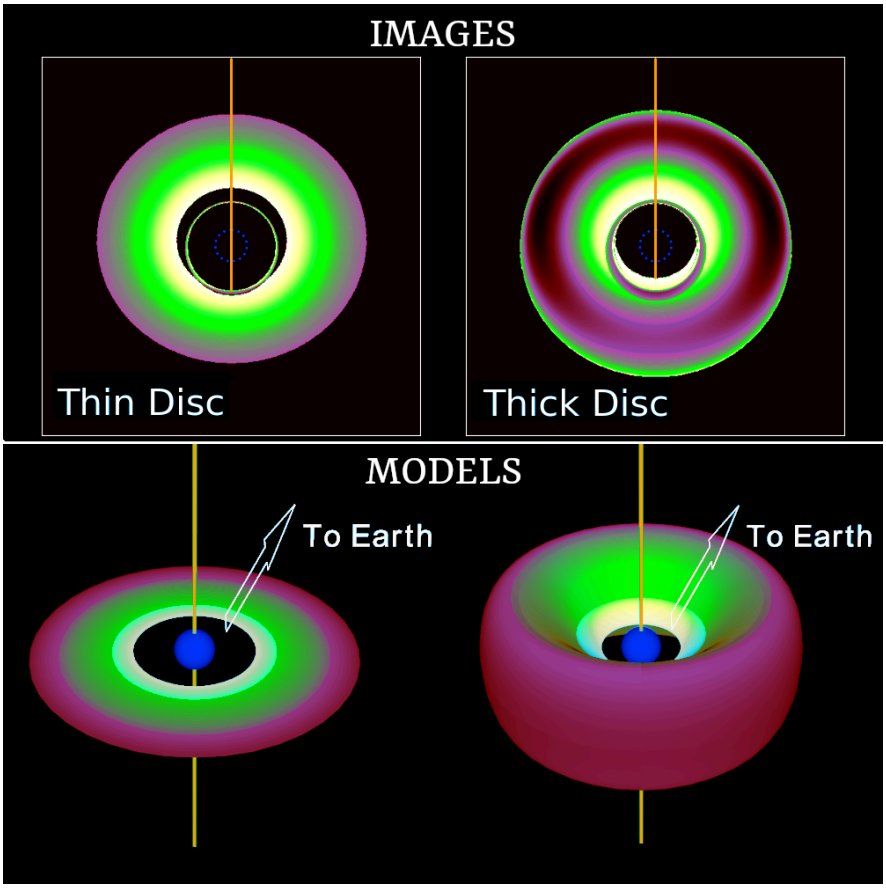

Figure 3: Simulated images of Schwarzschild black holes surrounded by accretion discs. The color palette helps identify the origin of the light rays in the images. **Bottom panels**, disc models used in the simulation; **top panels**, black hole images (Doppler boosting has been disconnected, for clarity). **Left**, the case of a geometrically thin disc; **right**, the case of a geometrically thick (but optically thin) disc. The event horizons are shown as dashed blue lines (top panels) and blue spheres (bottom panels).

However, in real black holes, the accretion discs may not be geometrically thin, especially if the discs are radiatively inneficient (e.g., [27]). These thick geometries add an extra complexity to the images of the black holes, mixing the ring image from the photon sphere with the emission from the disc.

To further complicate this, black holes can also rotate, deforming the photon spheres and the ring images, in ways that depend on the orientation to the observer. In a rotating black hole, there is also an *ergosphere*, where space is being rotationally dragged at superluminal speeds (with respect to distant observers), heavily affecting the dynamics of the accretion and, as a consequence, the black hole images. If the rotation of the black hole is high (Kerr rotation parameter, a, close to unity), the ISCO, the ergosphere, and the photon sphere may even coexist spatially, at similar distances to the black hole. In Figure 4 (left panel) we

show how the size of the ISCO, the ergosphere, and the radii of the photon orbits depend on the black hole rotation (a parameter). Notice that the retrograde (marked as +) orbits are always larger than the prograde ones (marked as −). The red and blue shaded regions give the range of sizes of the radial photon orbits and "Ergorad" refers to the (equatorial) radius of the ergosphere.

In the same Figure 4 (right panel), we show a representation of the Kerr metric for $a = 0.9$, showing the retrograde (prograde) photon spheres in dark (light) orange, together with some representative photon orbits at those regions (frame-dragging effects, which introduce strong precession in the orbits, are not included, for clarity). The white orbit shown corresponds to the photons with no angular momentum with respect to the rotation axis of the black hole. The ergospheres (outer and inner), the event horizons (outer and inner) and the physical singularity are shown (respectively) in green, red, light grey, dark grey and blue.

When all these effects are properly taken into account, the conclusion is clear: detecting (and measuring the size of) the ring associated to the photon sphere is not an easy task. Strong contamination from the accretion disc must be taken into account, which in turn depends on many unknown parameters: from the amount of rotation of the black hole (and the orientation of the spin axis with respect to the Earth) to the brightness distribution of its accretion disc. In the next sections, we give a very brief description of the strategy followed by the EHT Collaboration to "calibrate" the effect of the accretion disc in the image of M 87* (and Sgr A*).

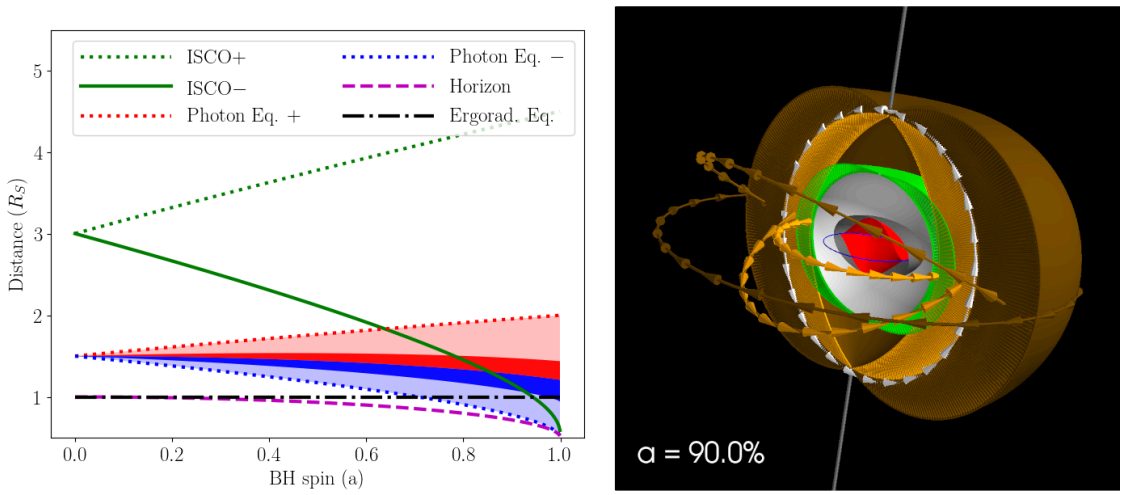

Figure 4: **Left**, size of the ISCO (in green; retrograde + and prograde −), photon orbits (red/blue for retrograde/prograde) even horizon (magenta) and ergosphere at the equator (black), as a function of Kerr rotation parameter, a. **Right**, sketch of the phton sphere (retrograde/prograde in dark/light orange) and other peculiar surfaces (see text) for a Kerr black hole with $a = 0.9$.

5 The EHT images of M 87* and Sgr A*

Several active galactic nuclei (AGN) were observed during the EHT campaign of April 2017. Results have been published for some of them (e.g., [23, 22, 21]). In any case, the two most important targets of the whole campaign were M 87* and Sgr A*. The image of M 87* was published about two years after the observations were taken (this gives an idea of the complexity of the calibration and analysis of mm-VLBI data), while it took five years to publish the results on Sgr A* (this gives an idea of the additional complexity in the analysis of this source, for reasons that are discussed in Section 5.2).

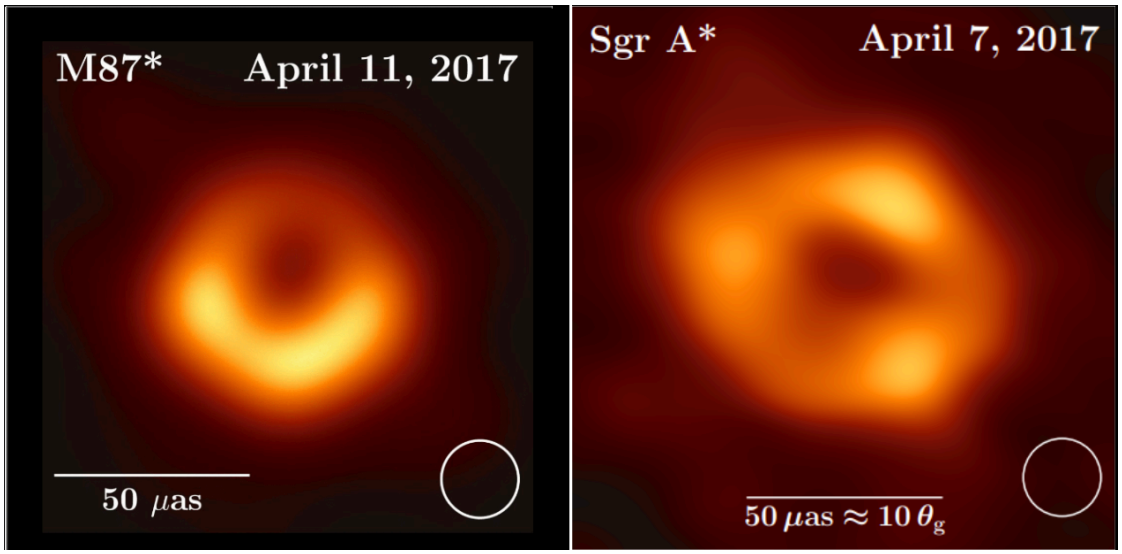

Figure 5: Images of M 87* (left) and Sgr A* (right) published by the EHT Collaboration [6, 13]

5.1 M 87*

The image of M 87* (shown in Figure 5, left) was the first observational confirmation of the *shadow* predicted in [16]. The central brightness depression (the shadow) is surrounded by an assymmetric ring, which is (partially) associated to the photon sphere around the black hole. Actually, only about 10−30% of the brightness in the M 87* image may be related to the photon sphere (e.g., [8, 3]).

By using a large set of realistic simulations of M 87* (with different rotations, orientations, levels of accretion, etc.), the EHT Collaboration estimated the expected range of biases between the size of the observed M 87* image and the size of the underlying photon sphere ring. Adding this "disc contamination" into the analysis and error budget allowed to have a relatively precise estimate of the ring angular size, $\theta_{\rm ring} \sim 42\,\mu$as [8, 9, 10], which in turn could be used to estimate the mass of M 87* (given its known distance), giving the value of $M_{\rm M87*} = (6.5 \pm 0.7) \times 10^9\,{\rm M}_\odot$. This value could then be compared to other independent

estimates, based on either the gas or the stellar bulk dynamics at the central region of the galaxy. The results, which are compatible with the mass estimate of M 87* coming from the stellar dynamics, can be understood as the first confirmation of GR using the most extreme gravitational lensing effect detected to date (i.e., the ring image of a photon sphere).

5.1.1 Polarization: magnetic field and jet launching

Two years after the publication of the M 87* image in total intensity, the EHT Collaboration published its *polarized* version [11, 12], which encodes precise information about the magnetic field geometry at the innermost side of the accretion disc. This information made it possible to constrain the parameter space of the accretion considerably, which also helps to better characterize the "disc contamination" on the estimate of the ring size. These constrains from the polarization also provide valuable information on the physics of accretion and jet launching in M 87*. From the results in [12], the launching of the relativistic jet in M 87* is very likely related to the Blandford-Znajek mechanism [2], where the poloidal component of the magnetic field in the disc, coupled to the presence of an ergosphere, originates an extraction of rotational energy from the black hole by the magnetic field, which is transferred to a plasma propagating along the jet at relativistic speeds. In Figure 6, we show the polarized image of M 87* (corresponding to the observations on April 11, 2017) and a sketch of the magnetic field geometry that could originate the BZ process.

The curly distribution of the polarization angle along the ring (which is represented by the lines of the "wind plot" shown in Figure 6, left) is a combination of the (poloidal dominated) magnetic field in the disc and the light-ray bending due to the space curvature produced by the SMBH.

5.2 SgrA*

Even though the angular scales of the images of M 87* and Sgr A* look similar (see Figure 5), their linear scales are completely different. On the one hand, M 87* is located at a distance of $\sim 16.8^{+0.8}_{-0.7}$ Mpc (e.g., [1]), which translates (for a gravitational size of $\theta_g = 3.8 \pm 0.4\,\mu$as [10]) into a gravitational radius of ∼64 AU. On the other hand, Sgr A* is at a distance of only ~ 8 kpc, which translates (for a gravitational size of $\theta_g = 9.6^{+2.8}_{-1.4}\,\mu$as [15]) into a gravitational radius of ∼0.04 AU (i.e., ∼ 1600 times smaller than M 87*). The dynamical times in both black holes are thus completely different. While in M 87* the dynamical scale is of several days (which means that the image of the ring is not expected to change much during an observation epoch of just several hours), the variability timescale of Sgr A* is just of a few minutes, which means that the image of Sgr A* may change completely, many times, during one single observing epoch of a few hours. In addition to this, the interstellar scattering produced by all the medium of the galactic disc situated between Sgr A* and the Earth, affects the spatial frequencies of the black hole image, which is an effect that also has to be taken into account during the analysis.

One of the basic tenets of the Aperture Synthesis technique is that the source structure should remain stable during the several hours needed to fill (by means of the Earth rotation)

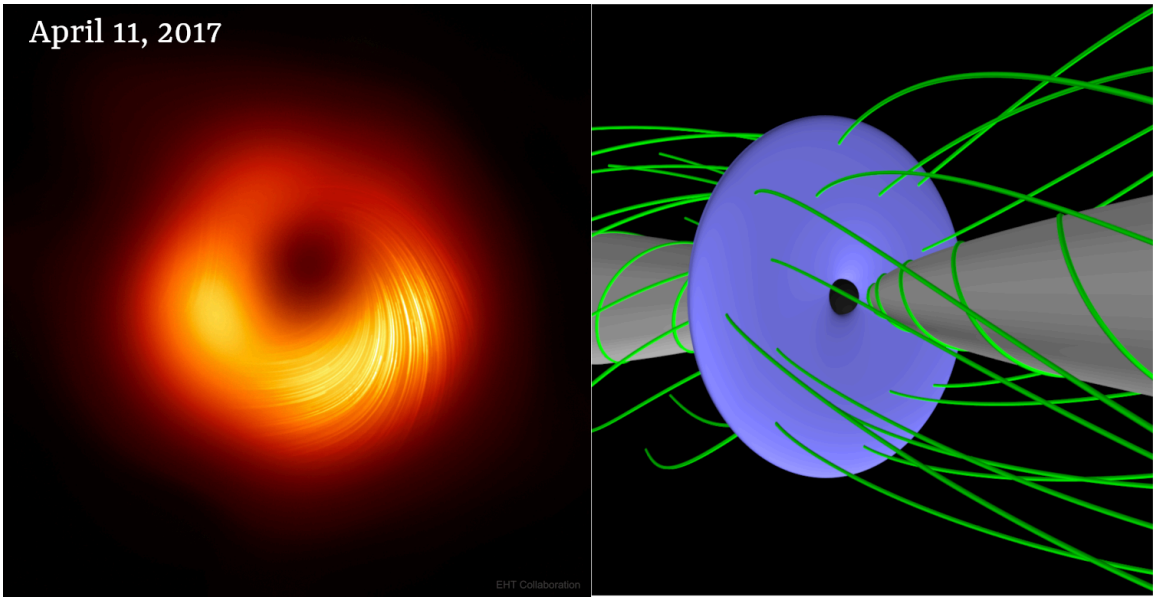

Figure 6: **Left**, "wind plot" version of the polarized image of M 87*, published by the EHT Collaboration in 2021 [11, 12]. **Right**, sketch of an accretion disc with poloidal magnetic field that gets "rolled up" due to the rotation of the central black hole.

the synthesized aperture of the interferometer. Therefore, the rapid variability of the image of Sgr A* required the development of a complete set of new algorithms (as well as a whole suite of simulations and tests) to confidently reconstruct an average image of Sgr A* (e.g., [14]). All these extra works delayed the publication of the long-awaited image of our Galactic Center by several years!

But the prize was worth the long waiting time. The distance to (and the mass of) Sgr A* are known with much higher precision than those of M 87*, thanks to the precision astrometry monitoring works on the Sgr A* field (see [17, 19] and references therein). This means that an estimate of the ring size of Sgr A* can provide more stringent tests of GR than that of M 87*, as well as restrictive tests of alternative spacetime metrics of the black hole. In one of the papers of the EHT Collaboration [15], several of such tests are presented, which combined with those on M 87*, have become a consistent test of GR covering several orders of magnitude in the mass of the black holes.

6 Conclusions

The images of M 87* and Sgr A* published by the EHT Collaboration in 2019 and 2022 represent an inflection point in observational Astrophysics. Before April 2019, the immediate neighbourhood of an event horizon could only be imagined and simulated. Now, thanks to the EHT, it has become routinely possible to observe the innermost side of the accretion discs in SMBH and the regions where light is bent in orbits around the edge of space and time.

And this is just the beginning for the EHT. The images shown in Figure 5 are the first frames of a great movie that now starts to be recorded; a movie where we will see how black holes feed and produce their relativistic jets, one of the most energetic and misterious phenomena in the Universe.

Acknowledgments

This work has been partialy supported by the GenT program of Generalitat Valenciana (Project CIDEGENT/2018/021) and by MICINN Project PID2019-108995GB-C22.

References

[1] Bird, S., Harris, W. E., Blakeslee, J. P. & Flynn, C. 2010, A&A, 524, 71

[2] Blandford, R. D. & Znajek, R. L. 1977, MNRAS, 179, 433

[3] Broderick, A. E., Pesce, D. W., Gold, R., et al. 2022, ApJ, 935, 61

[4] Doeleman, S. S., Fish, V. L., Schenck, D. E., et al. 2012, Science, 338, 6105, 355

[5] Doeleman, S. S., Weintroub, J., Rogers, A. E. E., et al. 2008, Nature, 455, 7209, 78

[6] EHT Collaboration 2019, ApJL, 875, 1

[7] EHT Collaboration 2019, ApJL, 875, 3

[8] EHT Collaboration 2019, ApJL, 875, 4

[9] EHT Collaboration 2019, ApJL, 875, 5

[10] EHT Collaboration 2019, ApJL, 875, 1

[11] EHT Collaboration 2021, ApJL, 910, 12

[12] EHT Collaboration 2021, ApJL, 910, 13

[13] EHT Collaboration 2022, ApJL, 930, 12

[14] EHT Collaboration 2022, ApJL, 930, 14

[15] EHT Collaboration 2022, ApJL, 930, 17

[16] Falcke, H., Melia, F. & Agol, E. ApJL, 528, 13

[17] Ghez, A. M., Salim, S., Weinberg, N. N., et al. 2008, ApJ, 689, 2

[18] Goddi, C., Crew, G. B., Impellizzeri, V., et al. 2019, The Messenger, 177, 25

[19] GRAVITY Collaboration 2018, A&A, 618, L10

[20] Greve, A., Torres, M., Wink, J. E., et al. 1995, A&A, 299, L33

[21] Issaoun, S., Wielgus, M., Jorstad, S., et al. 2022, ApJ, 934, 145

[22] Janssen, M., Falcke, H., Kadler, M., et al. 2021, Nature Astronomy, 5, 1017

[23] Kim, J-Y., Krichbaum, T. P., Broderick, A. E., et al. 2020, A&A, 640, 69

[24] Luminet, J.-P. 1979, A&A, 75, 228

[25] Martí-Vidal, I., Roy, A., Conway, J. & Zensus, A.$\frac{1}{2}$J. 2016, A&A, 587, 143

[26] Matthews, L. D., Crew, G. B., Doeleman, S. S., et al. 2018, PASP, 130, 983

[27] Narayan, R., Sadowski, A., Penna, R. F. & Kulkarni, A. K. 2012, MNRAS, 426, 3241

[28] Thompson, A. R., Moran, J. M. & Swenson, G. W. 2017, *Interferometry and Synthesis in Radio Astronomy*, Springer (3rd edition)

Highlights of Spanish Astrophysics XI, Proceedings of the XV Scientific Meeting of the Spanish Astronomical Society held on September 4–9, 2022, in La Laguna, Spain. M. Manteiga, L. Bellot, P. Benavidez, A. de Lorenzo-Cáceres, M. A. Fuente, M. J. Martínez, M. Vázquez- Acosta, C. Dafonte (eds.), 2023

The role of ESO observations in the Dark Energy Survey.

Sevilla-Noarbe, I[1], and on behalf of the Dark Energy Science Collaboration

[1] Centro de Investigaciones Energéticas Medioambientales y Tecnológicas (CIEMAT), Madrid, Spain

Abstract

The Dark Energy Survey is a large scale program to study the properties of dark energy through photometric observations of a large volume of the southern sky, in the optical and near-infrared, from the CTIO Blanco telescope in Chile. It ended its observations in 2019 and is currently preparing its final results, which include more than 500 nights of observations. It has already provided independent constraints on several cosmological parameters and models for half of the data, and in particular, its results have been combined with the Planck observatory measurements creating the most precise set of values to date. ESO instruments, both spectroscopic and photometric, have provided a fundamental input to many of these results, especially for redshift calibration and infrared complementary data. We briefly review these various contributions.

1 Introduction: the Dark Energy Survey

The Dark Energy Survey (DES) is a photometric survey of the Southern sky that took place during 570 nights from the Blanco 4 meter telescope in Cerro Pachón, Chile. Its goal is to pin down the nature of dark energy starting from the recommendations of the Dark Energy task force [14], using several probes: measurement of the redshift-distance relationship through supernovae Ia and the baryon acoustic oscillation peak (BAO); the combination of large scale structure distribution of galaxies and the weak lensing effect of these on the images of background galaxies and the number of clusters as a function of mass and redshift. In addition, other cosmological parameters and fundamental physics parameters can be explored by detecting strong lensing systems and measuring H_0, finding counterparts to gravitational wave events, and with the exploration of the Galactic neighborhood, ascertain the nature of dark matter. The instrument used to carry out DES is the Dark Energy Camera (DECam [7]) which uses for this survey the *grizY* bands (Figure 1). In reality, two types of surveys are combined in DES, one covers 5000 square degrees in a homogeneous fashion in the five bands, plus a time domain survey returning to the same areas every few days to detect transient phenomena which are potential supernova of type Ia of potential cosmological interest (Figure 2).

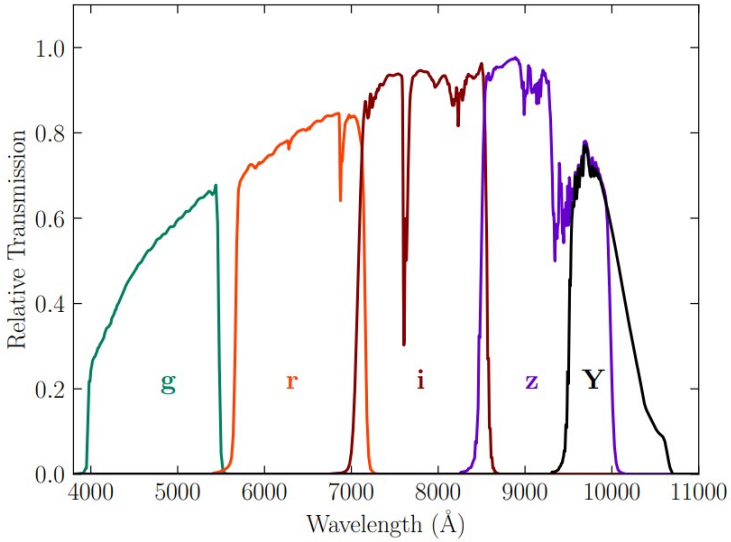

Figure 1: Standard bandpasses for DECam, valid for both data releases from DES. The need for ESO observations comes from a higher spectral resolution and blue and infrared (beyond Y) coverage.

.

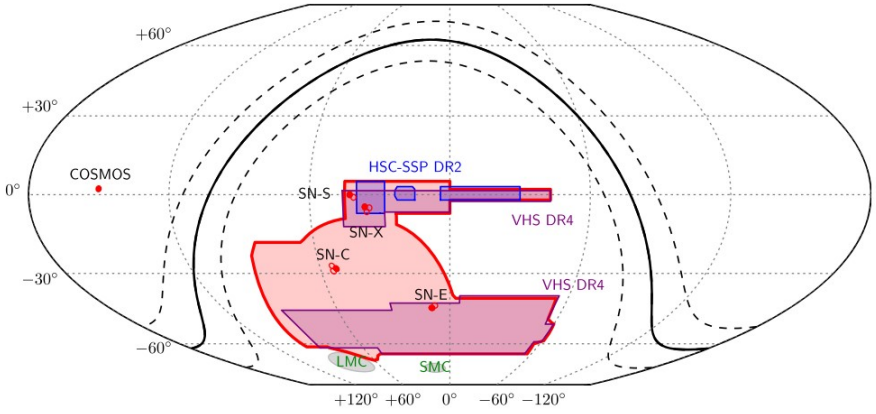

Figure 2: Layout of the wide field and supernova surveys of DES. From [11].

.

It ended on January 2019 and the participants of the international collaboration managing it are currently analyzing the complete data set (Year 6 or Y6). The main findings for the first half of the data set (Y3) are summarized in [18, 16, 19], and point to the ΛCDM cosmological model as being compatible with the data, with cosmological parameters in line with those found by the Planck satellite [20] measuring the cosmic microwave background at a vastly different redshift (see Figure 3, left).

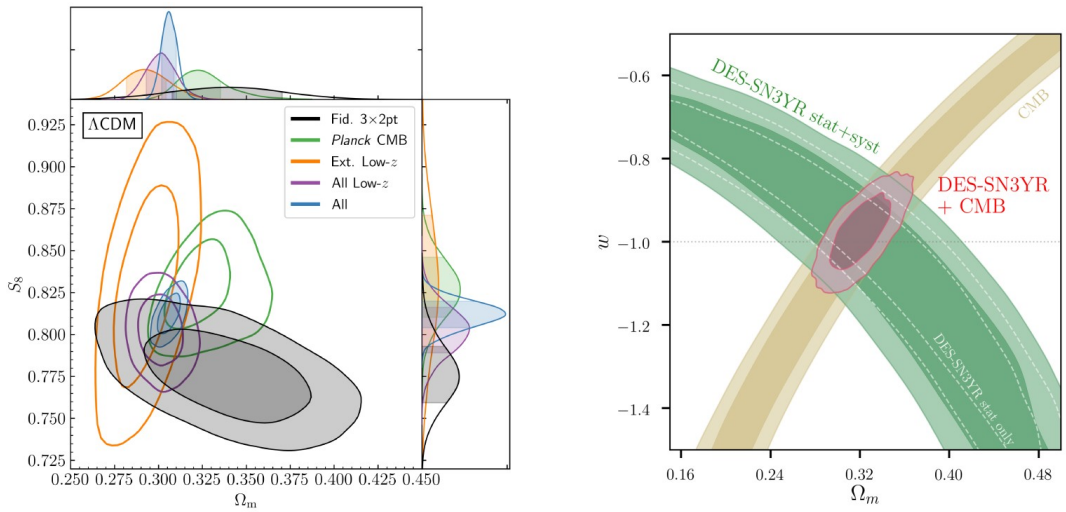

Figure 3: Left: The Y3 key project results on the $S8 - \Omega_M$ parameter plane. The gray contour corresponds exclusively to the combination of DES large scale structure and weak lensing data (the 3x2pt probe). In green, the prediction, assuming the ΛCDM model, from the Planck analysis. Right: Parameter constraints for a constant equation of state value in the $w - \Omega_M$ space using three years worth of supernovae Ia detections. Contours are 68% confidence intervals.

The data used in these results have been made public through successive data releases in 2017 (DR1, [15], for Y3 data) and 2021 (DR2, [17], covering the complete data set of Y6), and the latest cosmology-tuned catalogs as well for Y3 at [11, 8].

2 The Dark Energy Survey and ESO collaborations

Despite DECam being such a powerful instrument, it is restricted to the visible and near infrared wavelengths, and the need for imaging for measuring the shapes of the objects for instance, limits the spectral resolution to broad band photometry. This restricts the information one is able to get out from individual sources, which would be accessible through dedicated spectroscopic observations. In order to alleviate this, observations from other state of the art instruments are necessary, and in particular, ESO instruments have been able to close this gap either by direct observation proposals on competitive time allocation calls or by usage of the vast archival information in the form of spectral and photometric catalogs.

In the following sections, we go through a few examples that demonstrate the pivotal role that ESO has played in obtaining these cosmological constraints.

2.1 X-SHOOTER spectra for supernovae

One of the core results from DES is the measurement of cosmological constraints from supernovae Ia data, effectively extending the original dark energy detections from the late 1990s. In [16], the first results from a combination of spectroscopically confirmed supernovae from the DES sample plus a low redshift subsample from the literature, are discussed, finding $\Omega_M = 0.331 \pm 0.038$ for a ΛCDM model, and an equation of state for dark energy compatible with the cosmological constant both for the wCDM and $w_0 w_a$CDM models.

A fundamental element in the compilation of these supernova data sets is to have spectroscopic redshifts for the largest amount of these transients as possible, in order to construct the Hubble diagram. As detailed in [13], a devoted follow-up program partnered up with DES (OzDES, [5]) mainly focused on low to intermediate redshift transients. However, in order to cover the faintest objects to avoid any selection bias due to OzDES not being able to access these, a large spectroscopic follow-up campaign complemented de OzDES observations. In particular, a $\sim$ 14-night program was awarded at the VLT with the X-SHOOTER instrument. Thanks to this, 89 candidates on faint host galaxies (Figure 4, left) were followed up and those identified as Ia, added to the Hubble diagram of [16]. As can be seen in Figure 4 (right) the VLT spectra represent a significant fraction of the supernovae used at redshifts $z > 0.4$.

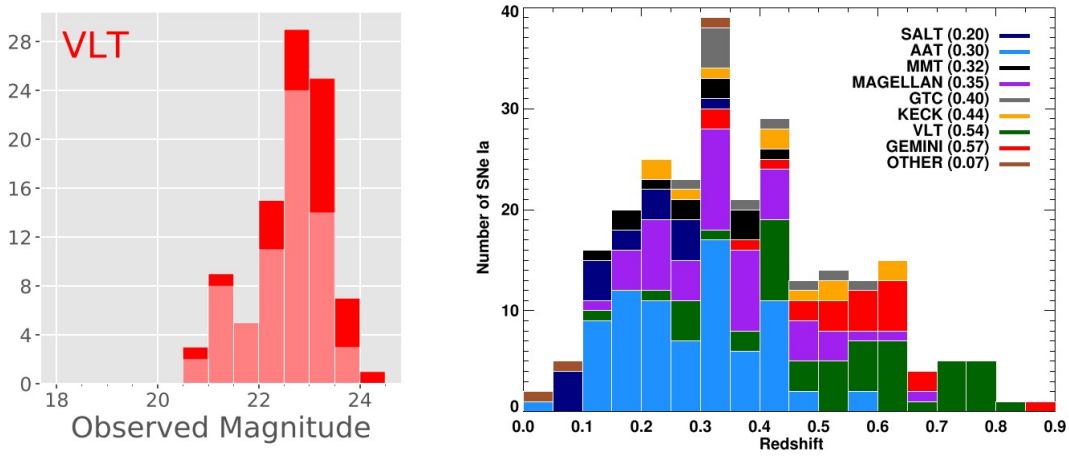

Figure 4: (left) The i-band magnitude distributions of the spectroscopically observed transients using VLT for the work in [13]. The lighter shaded histogram corresponds to confirmed supernovae of type Ia (right) Redshift histogram of all 251 spectroscopically confirmed SNe Ia in the first three seasons of DES (from [13]). The VLT data is an important contributor in the high redshift range.

2.2 MUSE data cubes for time delay cosmography

Time delay cosmography is a technique that allows the measurement of the Hubble parameter from the measurement of the time varying luminosity from objects whose light is being deflected by an intervening strong lensing system ([21]). An external collaboration of DES, the STRIDES project [23], has exploited the strong lens systems found in DES data, and obtained very relevant results to the current Hubble parameter tension research. A single system in DES data with these rare characteristics has already found 4% constraints to the Hubble parameter [12]. In order to make these complex measurements, external complementary spectra have to be obtained: the velocity dispersions of the lensing system, which can give an accurate estimate of the mass model, and the redshift distribution of objects in the line of sight of the time varying object that we are using to measure its delay.

In [3], these spectroscopic campaigns are detailed for two strong lensing systems, including DES 0408-5354, which was used in [12]. Observations using the MUSE instrument [1] at the VLT as part of an ESO program were used during two nights. The DES image for this system is shown in Figure 5 (left), whereas the redshifts for the ensemble of objects measured by MUSE's IFU is shown on the right. This distribution of objects along the line of sight, plus the measurement of the width of the spectral lines for the G1 lensing object, provides key information for the model parameters to be fitted in the extraction of cosmological information.

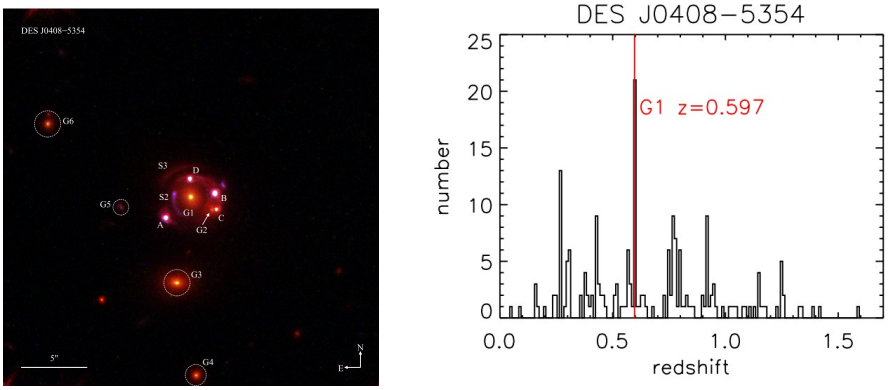

Figure 5: (left) The image of the DESJ0408-5354 system, from [12] (right) Redshift histogram 101 objects in the vicinity of this system, taken by MUSE. G1 corresponds to the central lensing system, from [3]

.

2.3 VIPERS data for accurate redshift distributions

Galaxy samples used for cosmological inference in photometric surveys need a well characterized N(z), or redshift distribution. In the DES BAO analysis, the project leads used the archival ESO VIPERS data [22] as a reference. This catalog was built with the intention of providing a complete set of galaxies with spectroscopic information for the range of redshifts

in $0.5 < z < 1.2$, which is precisely the range of interest for DES BAO studies at the depth that the survey operated. Out of the $\sim$ 90000 galaxies over 23.5 square degrees of the catalog, a subselection of them are a subsample over that area of the complete DES BAO sample. We can then use the redshift distribution of said sample as a representation of how the true N(z) looks like for that sample, within statistical errors, given the characteristics of VIPERS (Figure 6).

In addition, we can also use VIPERS to validate our photometric redshift estimates from the DNF code [24].

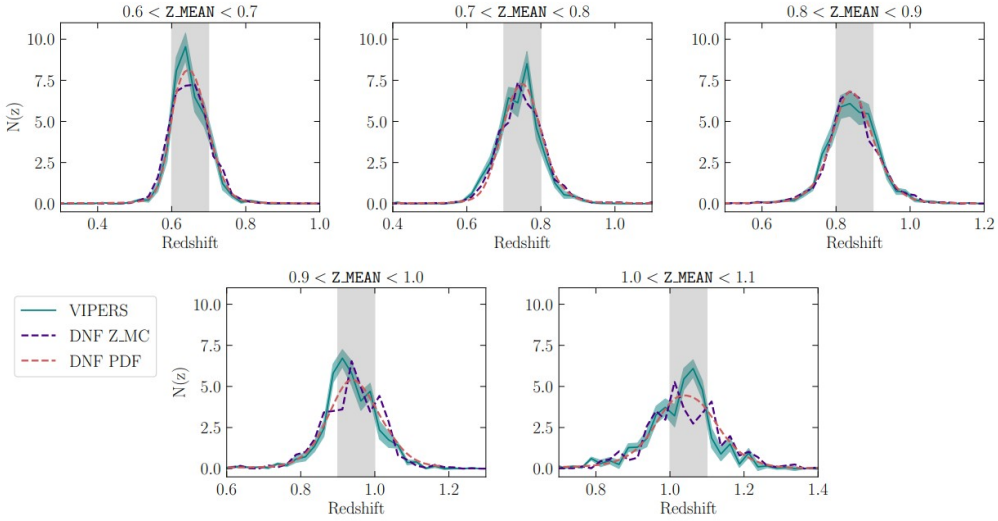

Figure 6: N(z) sample comparison for the different DES BAO redshift bins, using the DNF estimates and the spectroscopic dataset. From [4].

.

2.4 Infrared photometry from VISTA

Besides spectroscopic observations, DES can be complemented with imaging in other wavelengths towards bluer or redder parts of the spectrum. The blue and ultraviolet are useful, in broad terms, for understanding the physics of the nearby Universe, as well as for instrumental purposes (to fine tune calibration). In the case of dark energy studies, we can use infrared data to understand better the estimation of photoz at higher redshifts.

In particular, DES has benefitted from a close collaboration with the VHS survey [2], using the VISTA telescope and camera, with whom it has had a close cooperation since the

start, with early access to data releases and members belonging to both collaborations. This survey spans a very large area which, despite not covering completely the DES footprint, does provide complementary infrared information that helps with object classification and selection of stars for PSF extraction [8][11], especially through the use of the Ks band, at least for the brighter sources at $i < 21$. VISTA adds the J, H and Ks infrared bands spanning wavelengths from 1 micron to beyond 2 microns.

In addition, in the supernova fields, DES has produced very deep coadd images [9] to serve a multitude of purposes but, in particular, to provide very accurate redshifts for objects in those regions using u band from DECam, and deep VISTA data (Figure 7). These practically noise 'free' objects in these deep fields, can be stored as reference objects for synthetic simulations to be injected in other parts of the wide footprint [6]. The estimated redshifts using the main survey's optical filters for those same injected objects can be used to make a mapping between the main survey less accurate redshifts and their true counterparts in the deep fields, so that a probability that a given wide survey galaxy belongs to one type of galaxy or another can be created [10]. In this way a complete N(z) distribution can be built profiting from the deep field information, using this link to the wide field observations.

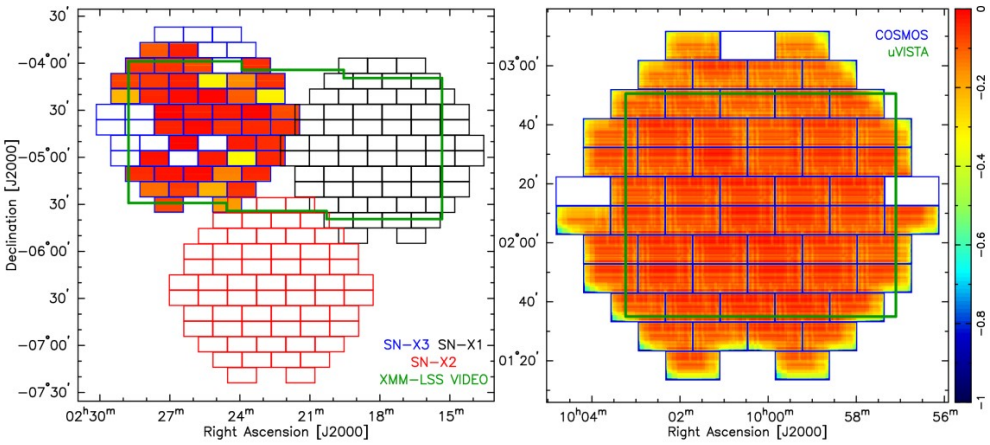

Figure 7: Location and layout of a few supernova fields of DES, with an overlay of pointings from ESO VISTA surveys. From [9].

3 Summary

The Dark Energy Survey has been able to profit from the state of the art astronomical facilities, complementing its observations with spectroscopic data and imaging in infrared wavelengths. This has been approached from three different angles:

- Through participation in competitive calls for observation time.
- Through the use of archival data.

- Through direct agreeements or close collaborations with ESO-linked surveys. For instance, since their early data releases, a close collaboration with the KiDS survey has been established to understand the root cause for the slight differences seen in the measurement of the $S8 - \Omega_M$ parameters.

The examples shown in this contribution show some cases from different areas of cosmology where ESO data has been a core contribution to obtaining some of the most constraining results on cosmological parameters to date.

Acknowledgments

Funding for the DES Projects has been provided by the U.S. Department of Energy, the U.S. National Science Foundation, the Ministry of Science and Education of Spain, the Science and Technology Facilities Council of the United Kingdom, the Higher Education Funding Council for England, the National Center for Supercomputing Applications at the University of Illinois at Urbana-Champaign, the Kavli Institute of Cosmological Physics at the University of Chicago, the Center for Cosmology and Astro-Particle Physics at the Ohio State University, the Mitchell Institute for Fundamental Physics and Astronomy at Texas A&M University, Financiadora de Estudos e Projetos, Fundação Carlos Chagas Filho de Amparo à Pesquisa do Estado do Rio de Janeiro, Conselho Nacional de Desenvolvimento Científico e Tecnológico and the Ministério da Ciência, Tecnologia e Inovação, the Deutsche Forschungsgemeinschaft and the Collaborating Institutions in the Dark Energy Survey.

The Collaborating Institutions are Argonne National Laboratory, the University of California at Santa Cruz, the University of Cambridge, Centro de Investigaciones Energéticas, Medioambientales y Tecnológicas-Madrid, the University of Chicago, University College London, the DES-Brazil Consortium, the University of Edinburgh, the Eidgenössische Technische Hochschule (ETH) Zürich, Fermi National Accelerator Laboratory, the University of Illinois at Urbana-Champaign, the Institut de Ciències de l'Espai (IEEC/CSIC), the Institut de Física d'Altes Energies, Lawrence Berkeley National Laboratory, the Ludwig-Maximilians Universität München and the associated Excellence Cluster Universe, the University of Michigan, NSF's NOIRLab, the University of Nottingham, The Ohio State University, the University of Pennsylvania, the University of Portsmouth, SLAC National Accelerator Laboratory, Stanford University, the University of Sussex, Texas A&M University, and the OzDES Membership Consortium.

Based in part on observations at Cerro Tololo Inter-American Observatory at NSF's NOIRLab (NOIRLab Prop. ID 2012B-0001; PI: J. Frieman), which is managed by the Association of Universities for Research in Astronomy (AURA) under a cooperative agreement with the National Science Foundation.

The DES data management system is supported by the National Science Foundation under Grant Numbers AST-1138766 and AST-1536171.

The DES participants from Spanish institutions are partially supported by MICINN under grants ESP2017-89838, PGC2018-094773, PGC2018-102021, SEV-2016-0588, SEV-2016-

0597, and MDM-2015-0509, some of which include ERDF funds from the European Union. IFAE is partially funded by the CERCA program of the Generalitat de Catalunya. Research leading to these results has received funding from the European Research Council under the European Union's Seventh Framework Program (FP7/2007-2013) including ERC grant agreements 240672, 291329, and 306478. We acknowledge support from the Brazilian Instituto Nacional de Ciência e Tecnologia (INCT) do e-Universo (CNPq grant 465376/2014-2).

This manuscript has been authored by Fermi Research Alliance, LLC under Contract No. DE-AC02-07CH11359 with the U.S. Department of Energy, Office of Science, Office of High Energy Physics.

References

[1] Bacon, R., Accardo, M., Adjali, L. et al. 2010, Proc. SPIE, 7735, 773508

[2] Banerji, M., Jouvel, S., Lin, H. et al. 2015, MNRAS, 446, 2523

[3] Buckley-Geer, E., Lin, H., Rusu, C.E. et al. 2020, MNRAS, 498, 3241

[4] Carnero-Rosell, A., Rodríguez-Monroy, M., Crocce, M. et al. 2022, MNRAS, 509, 778

[5] Childress, M.J., Lidman, C., Davis, T.M., et al. 2017, MNRAS, 472, 273

[6] Everett, S., Yanny, B., Kuropatkin, N. et al. 2022, ApJS, 258, 15

[7] Flaugher, B., Diehl, H.T., Honscheid, K., et al. 2015, AJ, 5, 150

[8] Gatti, M., Sheldon, E., Amon, A., et al. 2021, MNRAS, 504, 4312

[9] Hartley, W., Choi, A., Amon, A. et al. 2022, MNRAS, 509, 354

[10] Myles, J., Alarcon, A., Amon, A. et al. 2021, MNRAS, 505, 4249

[11] Sevilla-Noarbe, I., Bechtol, K., Carrasco-Kind, M. et al. 2021, ApJS, 254, 24

[12] Shajib, A.J., Birrer, S., Treu, T. et al. 2020, MNRAS, 494, 6072

[13] Smith, M., D'Andrea, C., Sullivan, M., et al. 2020, AJ, 160, 267

[14] The Dark Energy Task Force arXiv:astro-ph/0609591

[15] The DES Collaboration 2018, ApJS, 239, 18

[16] The DES Collaboration 2019, ApJL, 872, L30

[17] The DES Collaboration 2021, ApJS, 255, 20

[18] The DES Collaboration 2021, Phys. Rev. D 105, 023520

[19] The DES Collaboration 2022, arXiv:2207.05766

[20] The Planck Collaboration 2020, A&A 641, A6

[21] Refsdal, S. 1964, MNRAS, 128, 307

[22] Scodeggio, M., Guzzo, L., Garilli, B., et al. 2018, A&A, 609, A84

[23] Treu, T., Agnello, A., Baumer, M.A., 2018, MNRAS, 481, 1041

[24] Vicente, J. de, Sánchez, E. & Sevilla-Noarbe, I., 2016, MNRAS, 459, 3078

[25] Vernet, J., Decker, H., D'Odorico, S. et al. 2011, A&A, 536A, 105

Highlights of Spanish Astrophysics XI, Proceedings of the XV Scientific Meeting of the Spanish Astronomical Society held on September 4–9, 2022, in La Laguna, Spain. M. Manteiga, L. Bellot, P. Benavidez, A. de Lorenzo-Cáceres, M. A. Fuente, M. J. Martínez, M. Vázquez- Acosta, C. Dafonte (eds.), 2023

Are active galaxies different at large-scale than their non-active twin galaxies?.

del Moral-Castro, I.[1,2], Ramos Almeida, C.[1,2], and García-Lorenzo, B.[1,2]

[1] Instituto de Astrofísica de Canarias, C/ Vía Láctea, s/n, 38205, La Laguna, Tenerife, Spain
[2] Departamento de Astrofísica, Universidad de La Laguna, 38206, La Laguna, Tenerife, Spain

Abstract

In this contribution, we will show our results from a sample of 20 pairs of nearby seemingly isolated twin galaxies differing in nuclear activity. Firstly, we present a comparison of the parameter of the spin (λ_R), measured in a region dominated by the galaxy disc. This parameter allows us to assess the rotational support of a galaxy taking advantage of IFU data. Secondly, we will also present our most recent results on the stellar content of the sample. For this, we used full spectral fitting of the optical spectra recovering the star formation history (SFH) of our galaxies. The idea that every massive galaxy goes through a few short active phases during its life is becoming popular. In this scenario, we should not expect to find large-scale differences between the twins either in dynamics or stellar population properties over longer-timescales than the current AGN episode. However, the results presented here indicate that some galaxies are more likely to go through active phases than others, at least in the redshift ($0.005 < z < 0.03$) and mass ranges ($10^{10} < M\odot < 10^{11}$ M$\odot$) considered in this work.

1 Introduction

Active galaxies are these showing strong emission coming from their nuclei. In the case of normal galaxies the nuclear emission has a stellar origin, but in active galactic nuclei (AGN) the emission is produced by accretion of matter into a super-massive black hole (SMBH) (see [13, 1] for reviews). Although only a small percentage of galaxies in the nearby Universe currently show nuclear activity ($< 10\%$ according to [16]), it is thought that all massive galaxies might experience episodes of activity for at least some part of their evolution. In fact, AGN are considered as key ingredients to the evolution of galaxies. Therefore, unveiling the mechanisms that trigger AGN is crucial for our understanding of the formation and evolution of galaxies (see [9] for a review). While major mergers are often associated with the triggering of powerful AGN, less luminous AGN would be driven by secular processes, like disc instabilities or bars. Over the last few years, several observational studies have tried

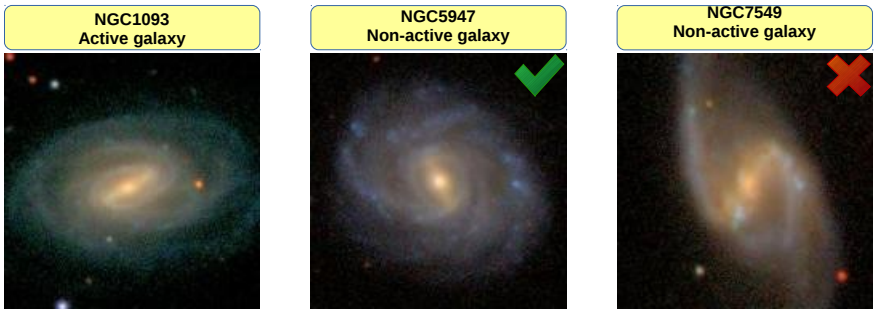

Figure 1: Color-composite SDSS images of an active galaxy (left panel) and two possible non-active twin candidates (middle and right panels, respectively), according to our numerical criteria. The green (red) tick (cross) identifies the selected (discarded) NGC1093 twin candidate according to our visual criteria. Each image has a field of view of 90"×90". North is up and east to the left.

to identify AGN triggering mechanisms in the local Universe (e.g. [11, 12]). Despite these efforts, the main drivers for AGN triggering in isolated galaxies still remain unclear.

The aim of this work is to try to shed some light on this topic by focusing on isolated nearby spiral galaxies. Unlike previous works, which have usually identified a sample of active galaxies and compared with the general population of galaxies (e.g. [16, 10]), we built a sample of pairs of galaxies differing only in nuclear activity (twin galaxies) and performed one to one comparisons. Following this approach, we can identify differences in the kinematics and stellar populations that might be connected to nuclear activity.

2 Sample

We use data from the third Data Release of the CALIFA survey [15]. It provides data cubes for ∼600 galaxies in the Local Universe (0.005<z<0.03). Details on the observational strategy, data quality, data reduction and statistical properties of the CALIFA survey can be found in [14, 17, 8, 15].

We select isolated active galaxies (see [3] for isolation criteria). For each AGN we then selected a control sample of non-active galaxies with similar galaxy properties. Additionally, we visually inspected the SDSS images of each active galaxy and its corresponding twin candidates to select the most similar one (best twin hereafter) and discard only those that clearly have different appearances (see Fig. 1 for an example). After doing this we end up with five AGN with two or more non-active twins. In these cases, we always identified the best twin but we did not discard the others. Furthermore, five non-active galaxies are selected as twins of two different AGN. In total we have 20 pairs of isolated twin galaxies differing in nuclear activity.

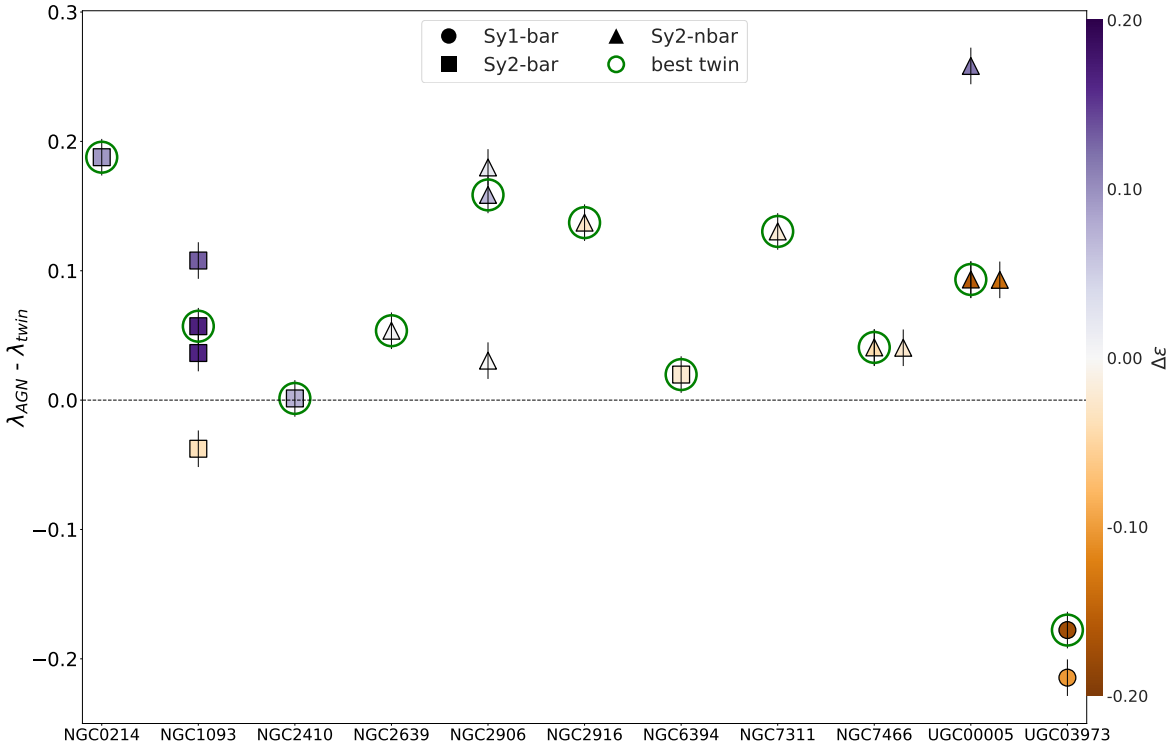

Figure 2: Differences in stellar λ_R between the pairs of twin galaxies. The best twin of each AGN is indicated with a green circle. Each column corresponds to an active galaxy and each symbol to the difference in λ_R with each of its twins. The colour code indicates the difference in ellipticity ($\epsilon_{AGN} - \epsilon_{twin}$). Error bars correspond to propagation of the individual uncertainties. Figure taken from [6]

3 Results

Firtsly, we present a comparison of λ_R measured in the disc-dominated region. We found that active galaxies show higher values of λ_R than their corresponding non-active twins (80% of the pairs; see Fig. 2). Considering only the unbarred pairs, we found that 100% of the active galaxies show larger λ_R than their twins. These results indicate, for the first time, that active galaxies present larger rotational support in the disc than non-active galaxies. We suggest that they could be explained by a more efficient angular momentum transfer from the inflowing gas to the disc baryonic matter in the case of the active galaxies. This inflow of gas could have been induced by disc or bar instabilities, although we cannot rule out the effect of minor mergers, which might not be detectable in the shallow SDSS images.

Secondly, we also characterised the stellar population properties of the sample of pairs [7]. For this, we used full spectral fitting of the optical spectra recovering the star formation history (SFH) of our galaxies. We computed average ages and metallicities, but we also

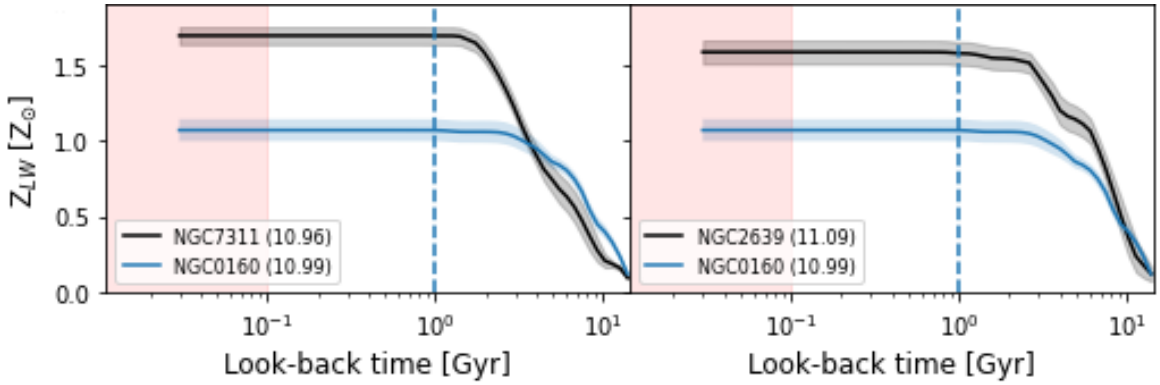

Figure 3: Evolution of the stellar metallicity as a function of look-back time for the bulge-dominated region of two pairs of twin galaxies. The galaxies stellar masses are shown between parentheses on each panel. The metallicity profiles corresponding to AGN are always represented by black lines. Red areas indicate the tentative lifetime of the current episode of nuclear activity and blue dashed lines correspond to the last Gyr.

analysed different stellar sub-populations according to their ages (i.e. young, intermediate and old). Additionally, we stacked the spectra of three different regions within the galaxies (bulge-dominated, disc-dominated and total), and we characterised the chemical enrichment histories of the pairs of galaxies (see Fig. 3). We found that AGN show a higher tendency to have older stellar populations and are more metal rich than their non-active twins in the bulge-dominated region, indicating that active galaxies have a different chemical enrichment history. Our results suggest that the differences in metallicity would not be predominantly associated with the current active phase but they are prior to it.

4 Conclusions

The idea that every massive galaxy goes through a few short active phases during its life is becoming popular. If all galaxies go through active phases, considering that the lifetime of these active phases are estimated to be a tiny fraction of that of galaxies, we should not expect to find large-scale differences between the twins either in dynamics or in stellar population properties over longer-timescales than the current AGN episode. Different active phases in both the active and non-active twins should dilute them. However, the results presented here support the idea that some galaxies are more likely to go through active phases than others, at least in the redshift ($0.005 < z < 0.03$) and mass ranges ($10^{10} < M\odot < 10^{11}$ M$\odot$) considered.

References

[1] Alexander, D. M. and Hickox, R. C., 2012, NAR, 56, 4

[2] Baraffe, I., Chabrier, G., Gallardo, J. 2009, ApJ, 2009, 702, 27

[3] Barrera-Ballesteros, J. K., Falcón-Barroso, J., 2014, A&A, 568, A70

[4] Chabrier, G., & Baraffe, I. 2007, ApJ, 661, L81

[5] del Moral-Castro, I. and García-Lorenzo, B., et. al., 2019, MNRAS, 485, 3

[6] del Moral-Castro, I. and García-Lorenzo, B., et. al., 2020, A&A, 639, L9

[7] del Moral-Castro, I., et. al. in prep

[8] García-Benito, R. and Zibetti, S., 2015, A&A, 576, A135

[9] Kormendy, J. and Ho, L. C., 2013, ARAA, 51

[10] Lacerda, E., Sánchez, S. F., 2020, MNRAS, 492, 3

[11] Marquez, I. and Masegosa, J., 2003, et. al., A&A, 409

[12] Marquez, I. and Masegosa, J., et. al., 2004, A&A, 416

[13] Osterbrock, Donald E. and Ferland, Gary J., 2006, CA: University Science Books

[14] Sánchez, S. F., Kennicutt, R., Gil de Paz, A., et. al., 2012, A&A, 538, A8

[15] Sánchez, S. F., García-Benito, R., et. al., 2016, A&A, 594, A36

[16] Schawinski, Kevin and Treister, Ezequiel, et.al., 2011, ApJL, 727, 2

[17] Walcher, C.J., Wisotzki, L., et. al., 2014, A&A, 569, A1

Highlights of Spanish Astrophysics XI, Proceedings of the XV Scientific Meeting of the Spanish Astronomical Society held on September 4–9, 2022, in La Laguna, Spain. M. Manteiga, L. Bellot, P. Benavidez, A. de Lorenzo-Cáceres, M. A. Fuente, M. J. Martínez, M. Vázquez- Acosta, C. Dafonte (eds.), 2023

Cluster dwarfs galaxies and the [α/Fe]-mass relation.

Romero-Gómez, J.[1,2], **Reynier F. Peletier**[3], **and J. A. L. Aguerri**[1,2]

[1]Instituto de Astrofísica de Canarias, Calle Vía Láctea S/N, La Laguna, Tenerife, Spain
[2]Universidad de La Laguna Avda. Astrofísico Fco. Sánchez, E-38205 La Laguna, Tenerife, Spain
[3]Kapteyn Institute, University of Groningen, Landleven 12, 9747, AD, Groningen, The Netherlands

Abstract

Using spectral data from the SAMI Integral Field Spectrograph and full spectral fitting techniques, we obtain and study the stellar population properties of a sample of dwarf galaxies in the Fornax Cluster. Our analysis focuses on the relation of stellar populations properties with the environment and internal properties of dwarfs.
We covered the stellar mass range from 10^4 to $10^{12} M_\odot$ by adding massive galaxies from the ATLAS^{3D} project and satellite galaxies of the Milky Way. Using the whole sample we find that the mass–metallicity relation is not linear and that the [α/Fe]-stellar mass relation shows a U-shape, with a minimum in [α/Fe] for masses between $10^9 - 10^{10} M_\odot$.
In addition to the [α/Fe]-stellar mass relation, we find that the [α/Fe] of dwarfs also relates with clustercentric distance in nearby clusters and in the the Milky Way. This shows that when the faintest galaxies fall to the environment a rapid burst of star formation is induced, leading to high [α/Fe] values. Then different quenching mechanisms blow the gas content away. More massive galaxies are barely affected by the environment, maintaining their gas and producing several bursts of star formation, thus, regulating their stellar populations by internal processes, leading to [α/Fe] increasing with mass.

1 Introduction

The Local Group used to be our main source of knowledge of dwarf galaxies, but with the newest instruments and telescopes our knowledge of dwarf galaxies is constantly being updating. Dwarf galaxies come in different types such as star-forming and quiescent dwarf galaxies, and each of them is subdivided into high and low surface brightness objects. In this work, we will focus only on the 'classical' low surface brightness dwarfs, mainly on the quiescent dwarf ellipticals (dEs)[2].

Physical mechanisms acting in high density environments like ram-pressure stripping [11] or strangulation [14] can remove the gas from galaxies and stop their star formation [15], thus, changing the morphology of the galaxies and transforming star-forming to quiescent

galaxies. Apart from an external process, low-mass galaxies are also sensitive to an internal process that can quench or trigger star formation [12]. Studying the stellar populations, and their relation with internal and external properties of the galaxies, is a way to find out which one of these is more relevant. In clusters of galaxies, dwarf ellipticals are usually old and metal-poor [20], and have solar-like abundance ratio $[\alpha/Fe]$ [10, 27], although, in the core of a cluster, such as Coma, they could also be slightly more α-enhanced than in the outskirts [19]. Massive stars, which are the progenitors of SN Type II, live very short lives, and produce mostly α-elements, like C, N, O, Mg etc. On the other hand SN Type Ia comes from binaries with at least one white dwarf, and the material produced by these systems is richer in iron than in α-elements. Thus, the [α/Fe] parameter is a useful parameter to measure how fast star formation proceeded [26]. For giant galaxies there is a strong relation between $[\alpha/Fe]$ and mass [22, 17], which is thought to be due to a much faster enrichment in the more massive galaxies. For dwarfs less massive than $\sim 10^9 M_\odot$, it is unknown what the situation is, and if the relation from the massive galaxies can be extended to the low mass regime.

2 Data and analysis

From the Fornax Cluster Catalogue [9] and the Fornax Deep Survey catalogue[25] galaxies with absolute magnitudes in the r-band fainter than -19 mag were selected for spectroscopic observations. Between 2015 and 2018 a total sample of 118 galaxies was observed using the Multi-Object Integral-Field Spectrograph called SAMI [7]. For more details of the spectroscopic observations and target selection see [18]. From the primary targets the kinematic analysis could be performed for 38 dwarfs [18], which constitute our main sample. The sample contains four objects associated with the Fornax A group, and also late-type dwarf irregulars and spirals, as classified by [24], that will not be part of our main analysis.

To analyse the spectra we used the full spectral fitting algorithm pPXF ([6, 5]). Each galaxy spectrum is fitted with a combination of template spectra from a stellar model library, and the properties are obtained as a combination of the model properties. For more details on how to work with pPXF we refer to [5]. For each galaxy we integrated the spectra inside the aperture of SAMI and using the models of the Vazdekis/MILES library [21, 23] we study the stellar population properties. In order to estimate the errors, after the first fit of the stellar population properties we applied a Monte-Carlo (MC) method to retrieve the uncertainties of each parameter. Finally, the age, metallicity and [α/Fe] parameters are the mean values of the distribution and the errors are the standard deviation.

3 Results

In order to compare our results we re-analysed the spectra of massive early-type galaxies from the ATLAS^{3D} Project [3] using the same methodology described in Section 2. These galaxies are located in the Virgo region of the sky, and as for our SAMI-Fornax dwarfs, we used the integrated spectra. We labeled them as cluster members if the local mean surface density of galaxies is higher than $\log(\Sigma_{10}) > 0.6$ Mpc^{-2} [4].

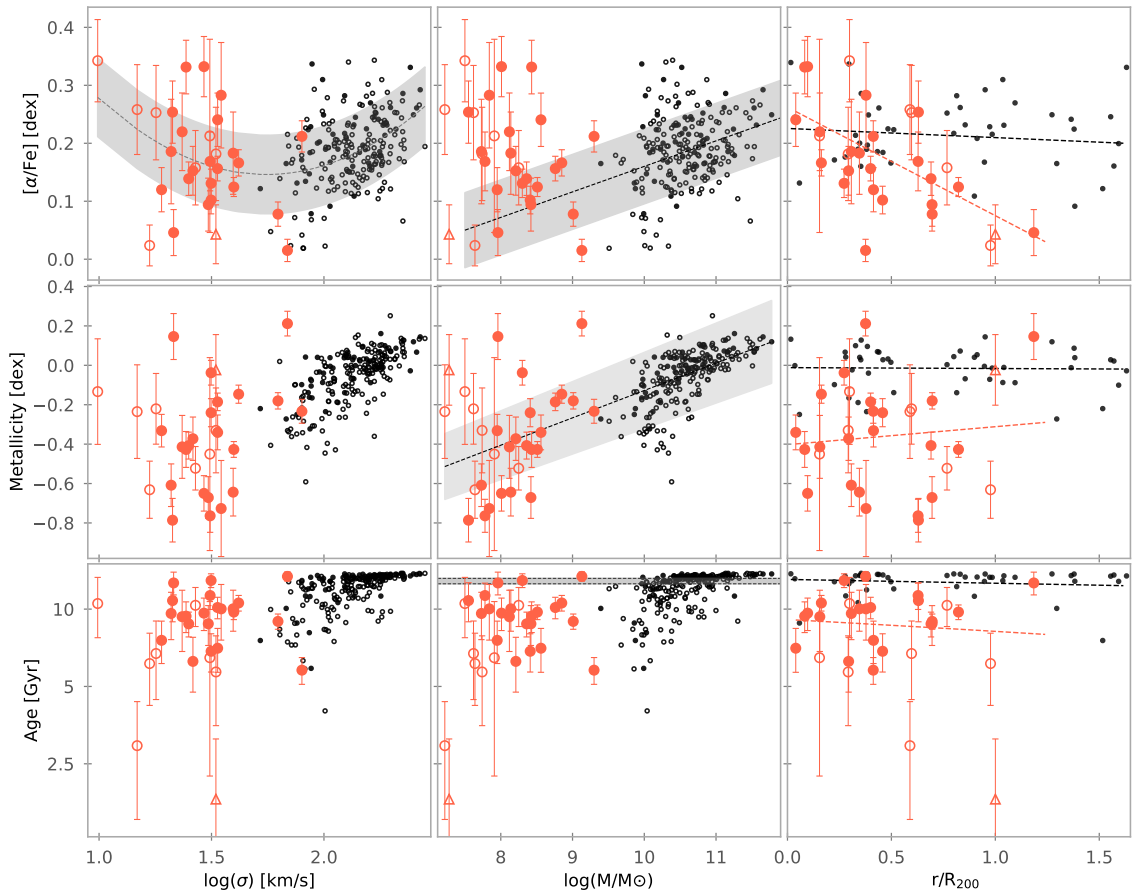

Figure 1: Stellar population properties as a function of the logarithmic velocity dispersion, the stellar mass and the cluster-centric distance, in the left, middle and right column, respectively. The rows show, from top to bottom, the $[\alpha/Fe]$, metallicity and age. For our dwarfs, red circles are for those in the main Fornax cluster and triangles for the ones in the Fornax A group, and the symbols are filled if the S/N is higher than 15. For ATLAS^{3D} we used black-filled circles for cluster galaxies and non-filled black circles for the rest. The black dashed line and grey shaded area on the top left represent a second-degree polynomial fit to all the data, making a U-shape. In the top-center we present the linear fit [α/Fe]-log(M/$M_{\odot}$) taking into account only the galaxies from ATLAS^{3D} project. Since stellar mass and velocity dispersion are tightly related, it is clear that this U-shape can also be applied to the [α/Fe]-log(M/$M_{\odot}$) relation. In the middle center the black dashed line and grey shadow represent the metallicity-mass linear relation for both samples. On every panel of the right column we show with a red or black dashed line the respective linear fit between the stellar population property and the distance to the center of the cluster.

In general our dwarfs show intermediate-old and metal-poor populations, while the massive galaxies are older with solar-like metallicities. Both samples follow the a linear metallicity-

mass relation (central panel of Fig. 1), and do not exhibit any kind of trend with the cluster-centric distance for the age nor the metallicity.

For the [α/Fe] both samples range between 0.0 and 0.4 dex, which are the limits of the α-enhancement grid of the MILES models. The massive galaxies follow a linear relation between [α/Fe] and stellar mass, or velocity dispersion, while the dwarfs are disperse above this linear relation. To fit both samples at the same time we used a second-degree polynomial, conforming a U-shape that can be seen in the top left panel of Fig. 1. When looking at the environment the massive galaxies do not show any trend between [α/Fe] and the cluster-centric distance. However the dwarf galaxies show a strong relation with the distance, where more α-enhanced galaxies are closer to the center.

To further analyse our results we include in our comparison the results of [19] for dwarfs in the Coma cluster. This sample fills the small velocity dispersion gap between our SAMI-Fornax dwarfs and ATLAS^{3D} galaxies. Also, to extend the the range in velocity dispersion in the low end, we include dwarf galaxies within our Local Group that are Milky Way satellites. For this sample we looked for abundances of individual stars in the literature and use as galaxy property the mean value of all its available stars and the standard deviation as the error. It is common to use [Fe/H] abundance as an approximation of the metallicity, and [Mg/Fe] for the overall α-enhancement [22, 23].

Figure 2 shows the compilation of [α/Fe] values for different types of galaxies and environment. On the top left-hand side panel we present how the metallicity-mass linear relation from Fig. 1 does not agree with the metallicity-mass relation of the Local Group [13]. To fit all the samples at the same time we need a second-degree polynomial. On the bottom left we show that the U-shape can be easily extended to the less massive galaxies of the Local Group. On the right side of Fig. 2 we show the [α/Fe] as a function of the distance to the center of the galaxy cluster, or the Milky Way for the Local Group objects. As in our dwarfs in Fornax, those of the Coma cluster and the Local Group also present a trend with the distance, placing the more α-enhanced galaxies at the center of the environment. For the dwarfs in the Virgo cluster the relation is almost flat, possibly because Virgo is a less relaxed cluster than Coma and Fornax.

4 Conclusions

After comparing the stellar population properties of our SAMI-Fornax dwarfs with more massive galaxies we conclude that the usually found [α/Fe]-log(σ) linear relation for massive galaxies, does not fit our dwarf galaxies. Instead a second degree polynomial is more fitting for the whole sample, conforming a U-shape where solar-like abundances are for galaxies of 10^9-10^{10} $M_\odot$ and then α-enhancement values increase for both massive and less massive galaxies. We confirmed the extension of this relation for less massive dwarfs by comparing with abundances of Local Group galaxies. When looking at the environment the α-enhancement show a trend with the projected distance to the Fornax cluster, where more enhanced dwarfs are closer to the centre. This relation is persistent in dwarfs in other environments like like Coma, or the Local Group, but to a lesser degree in Virgo. This is because the Virgo Cluster

is not fully relaxed and the relation of abundance ratio with clustercentric distance is not fully in place yet.

We can explain both the mass-metallicity and the mass-α-enhancement relations using a plausible combination of internal properties, like the mass of the galaxy, and environmental factors, like ram pressure, that can affect galaxies of different mass in different ways.

References

[1] Bidaran, B., La Barbera, F., Pasquali, A., et al. 2022, MNRAS, 515, 4622

[2] Binggeli, B., Sandage, A., & Tammann, G. A. 1988, A&A, 26, 509

[3] Cappellari, M., Emsellem, E., Krajnović, D., et al. 2011, MNRAS, 413, 813

[4] Cappellari, M., Emsellem, E., Krajnović, D., et al. 2011, MNRAS, 416, 1680

[5] Cappellari, M. 2017, MNRAS, 466, 798

[6] Cappellari, M. & Emsellem, E. 2004, PASP, 116, 138

[7] Croom, S. M., Lawrence, J. S., Bland-Hawthorn, J., et al. 2012, MNRAS, 421, 872

[8] Eftekhari, F. S., Peletier, R. F., Scott, N., et al. 2022, MNRAS, 517, 4714

[9] Ferguson, H. C. 1989, AJ, 98, 367

[10] Geha, M., Guhathakurta, P., & van der Marel, R. P. 2003, AJ, 126, 1794

[11] Gunn, J. E. & Gott, J. R. 1972, ApJ, 176, 1

[12] Haines, C. P., Gargiulo, A., La Barbera, F., et al. 2007, MNRAS, 381, 7

[13] Kirby, E. N., Cohen, J. G., Guhathakurta, P., et al. 2013, ApJ, 779, 102

[14] Larson, R. B., Tinsley, B. M., & Caldwell, C. N. 1980, ApJ, 237, 692

[15] Lisker, T. 2009, Astronomische Nachrichten, 330, 1043

[16] Liu, Y., Peng, E. W., Blakeslee, J., et al. 2016, ApJ, 818, 179

[17] McDermid, R. M., Alatalo, K., Blitz, L., et al. 2015, MNRAS, 448, 348

[18] Scott, N., Eftekhari, F. S., Peletier, R. F., et al. 2020, MNRAS, 497, 1571

[19] Smith, R. J., Lucey, J. R., Hudson, M. J., et al. 2009, MNRAS, 392, 1265

[20] Sybilska, A., Lisker, T., Kuntschner, H., et al. 2017, MNRAS, 470, 815

[21] Sánchez-Blázquez, P., Peletier, R. F., Jiménez-Vicente, J., et al. 2006, MNRAS, 371, 703

[22] Trager, S. C., Faber, S. M., Worthey, G., et al. 2000, AJ, 120, 16

[23] Vazdekis, A., Coelho, P., Cassisi, S., et al. 2015, MNRAS, 449, 1177

[24] Venhola, A., Peletier, R., Laurikainen, E., et al. 2019, A&A, 625, A143

[25] Venhola, A., Peletier, R., Laurikainen, E., et al. 2018, A&A, 620, A165

[26] Worthey, G., Faber, S. M., & Gonzalez, J. J. 1992, ApJ, 398, 69

[27] Şen, Ş., Peletier, R. F., Boselli, A., et al. 2018, MNRAS, 475, 3453

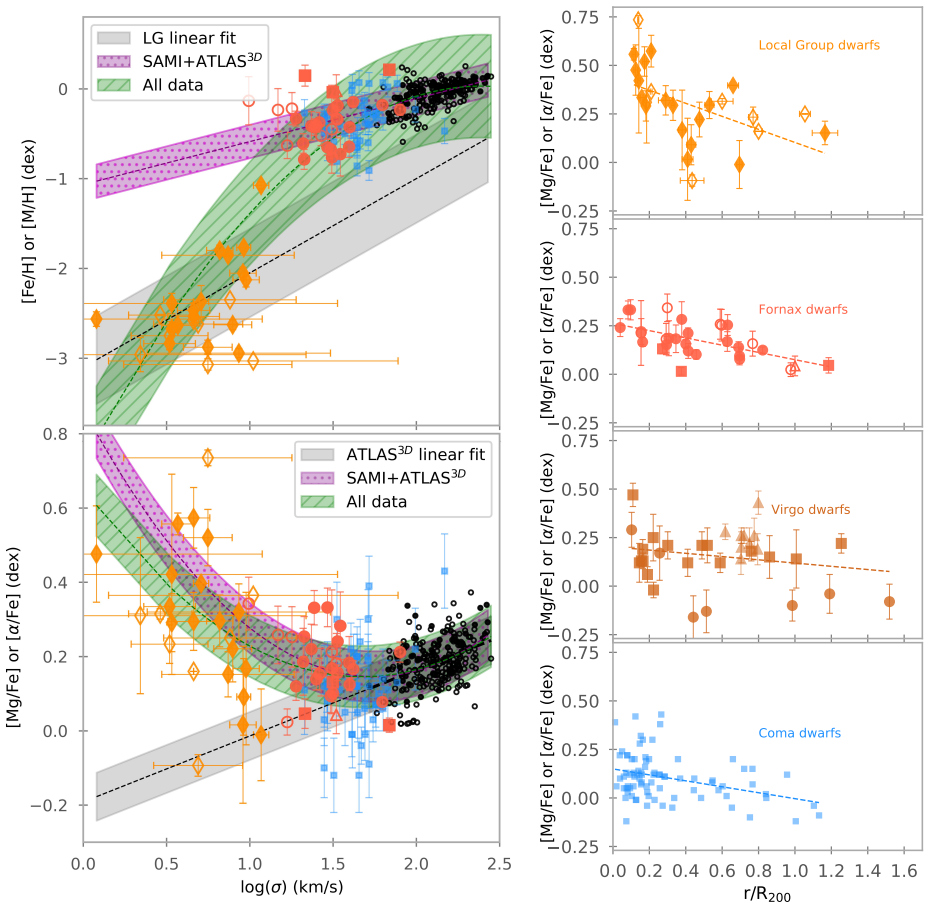

Figure 2: On the top and bottom of the left hand-side panels we show the relation between metallicity and [α/Fe] abundance ratio and stellar velocity dispersion, respectively. We also include a sample of dwarfs in the Coma cluster [19] and measurements of Local Group dwarfs from different works in the literature. Symbols for our SAMI-Fornax dwarfs and ATLAS^{3D} galaxies are the same as in Fig. 1. Light blue squares are for Coma's dwarfs, the orange diamonds are for Local Group dwarfs and the empty orange diamonds are for those objects with 3 or fewer stars. On the top, the purple dashed line and shadow are the linear fit to metallicity-log(σ) for SAMI-Fornax and ATLAS^{3D} samples, the black dashed line and gray shadow is a linear fit the the Local Group objects and the green dashed line and shadow is a second-degree polynomial fit to metallicity-log(σ) for all the objects in the figure. In the bottom, with a black dashed line and grey shadow is the linear relation [α/Fe]-log(σ) only for ATLAS^{3D} galaxies. Purple dashed line and shadow represent the U-shape fit for our SAMI-Fornax and ATLAS^{3D} data, similar to that of Fig. 1, and the green dashed line and shadow represent a second-degree fit to all the data visible in the plot. On the right panels we show the [α/Fe] abundance as a function of the cluster-centric distance for the different environments analysed here. For the dwarfs in Virgo we used the results of [20] (brown squares), [1] (brown triangles) and [16] (brown circles). On every panel there is also a dashed line that represent the linear fit between [α/Fe] and the cluster-centric distance.

Highlights of Spanish Astrophysics XI, Proceedings of the XV Scientific Meeting of the Spanish Astronomical Society held on September 4–9, 2022, in La Laguna, Spain. M. Manteiga, L. Bellot, P. Benavidez, A. de Lorenzo-Cáceres, M. A. Fuente, M. J. Martínez, M. Vázquez- Acosta, C. Dafonte (eds.), 2023

How common are outflows in low luminosity AGNs?.

Hermosa Muñoz, L.[1], **Cazzoli, S.**[1], **Márquez, I.**[1], **Masegosa, J.**[1], **and Agís-González, B.**[1]

[1] Instituto de Astrofísica de Andalucía - CSIC. Glorieta de la Astronomía s/n, 18008, Granada (Spain)

Abstract

Outflows play a major role in the evolution of galaxies and are said to be ubiquitous within the Active Galactic Nuclei (AGNs) population. However, we are far from having a complete picture of their properties, specially considering their impact on the evolution of Low-Ionisation Nuclear Emission-line Regions (LINERs). Although resolved kinematic information has proven to be crucial for the fully characterisation of these phenomena, imaging techniques can be really useful for the systematic search of outflow candidates. We have obtained narrow-band optical Hα images with ALFOSC/NOT and retrieved soft-X ray and narrow-band Halpha images from Chandra and HST archives, respectively, for a total of 70 LINERs. We classified the ionised gas morphologies based on the extension and overall shape of the Hα emission. We find that the soft X-ray and ionised gas emission coincide in the great majority of LINERs (60%), as previously seen for Seyferts [1], suggesting a common origin for both emissions. Our results show that approximately one third of the targets present extended, filamentary emission with a distinguishable bubble-shaped morphology. When combining imaging and spectroscopic data from the current literature we find that outflows are present in 48% of the nearby LINERs.

1 Introduction

Feedback processes driven by outflows have been detected in a large variety of systems, mostly related to star-forming processes or active galactic nuclei (AGNs) [7]. Many works focused on analysing the impact that outflows may have in the evolution of the galaxies through the study of their main properties, such as their kinematics, energetics, etc. (see [16, 17] for a review). The exploration of outflows has generally targeted the most powerful events, as they are detected more easily and, thus, their global properties can be better characterised. The power of the outflow has been suggested to scale with the luminosity of the AGN in active systems [5]. Nevertheless, the presence of outflows in the low luminosity end of the AGN family is largely unstudied, except for a few works on Low-Ionisation Nuclear Emission-line Regions (LINERs) [3, 9]. LINERs [8, 13] are the most numerous AGNs in the local Universe,

up to a 60% [11]. Although they are intrinsically faint, their relative proximity makes them in principle ideal targets to study AGN physics and, particularly, to search for outflows.

We aimed to explore the presence of outflows in LINERs through a systematic search using imaging, a technique already proven to be useful for detecting outflow-like morphologies, even at the lowest AGN luminosities [14, 15]. The inital sample was selected from [6, 3], and included the results from previous similar works [14, 15].

We have produced the largest atlas up-to-date of ionised gas images for LINERs. In total, our sample consists on 70 nearby LINERs (z<0.025), with an average luminosity of $L_{bol} \sim 10^{41.8}\,erg\,s^{-1}$. We gathered data from the Hubble Space Telescope (HST) archive for 38 targets, and we observed the remaining 32 with the Alhambra Faint Object Spectrograph and Camera (ALFOSC) at the Nordic Optical Telescope (NOT) during several observing campaigns. We obtained three individual exposures per target using both broad-band and narrow-band filters (see Tables C.2 and C.3 in [10] for more details), the latter centered around the expected observed wavelength of Hα at the redshift of our targets. Additionally, we obtained Chandra soft X-ray data for 52 LINERs, in order to compare the origin of both X-rays and ionised gas emissions, and test whether they originate in the same region of the AGN as it is the case for more luminous systems [1, 2].

2 Methodology

The data gathered from the HST archival were already fully reduced. We reduced the ALFOSC/NOT imaging data as standard using IRAF, and then we applied a dedicated background subtraction of the images to ensure a proper sky determination (see Sect. 3 in [10] for details). In both datasets, to obtain exclusively the Hα emission from the galaxy, we applied a similar technique as in [14], eliminating the continuum from the narrow-band images. The broad-band images were scaled and subtracted from the narrow-band images to obtain our final continuum free, pure Hα images.

As for the Chandra soft X-ray images (0.3-2 KeV), they were reduced using the software CIAO v4.13.

We classified the Hα emission in four different categories, as defined in [14]: Core-halo, when the emission is diffuse or unresolved around the nucleus; Disc-halo (or disky), when the emission is concentrated along the disc, spiral arms or nuclear rings; Bubble-like (or outflow), when the emission showed a bubble-like, biconical or filamentary structure; and Dusty, when there was a dust lane covering the nuclear region. We added an additional category, Unclear, whenever we could not clearly include the ionised gas morphology of a galaxy into one of the previous classes. We classified the Hα images considering the emission above the 3σ level from the background. Figure 1 shows an example of the different morphologies that we found per each category; all the images can be found in Appendix B of [10].

Given that imaging alone is not sufficient for claiming the detection of an outflow, we searched in the literature for previous kinematical information for all the galaxies. We found the requested information for 60 out of the 70 targets (86%), the majority coming from the long-slit spectroscopic works from [3, 9]. We compared the morphological classification from the

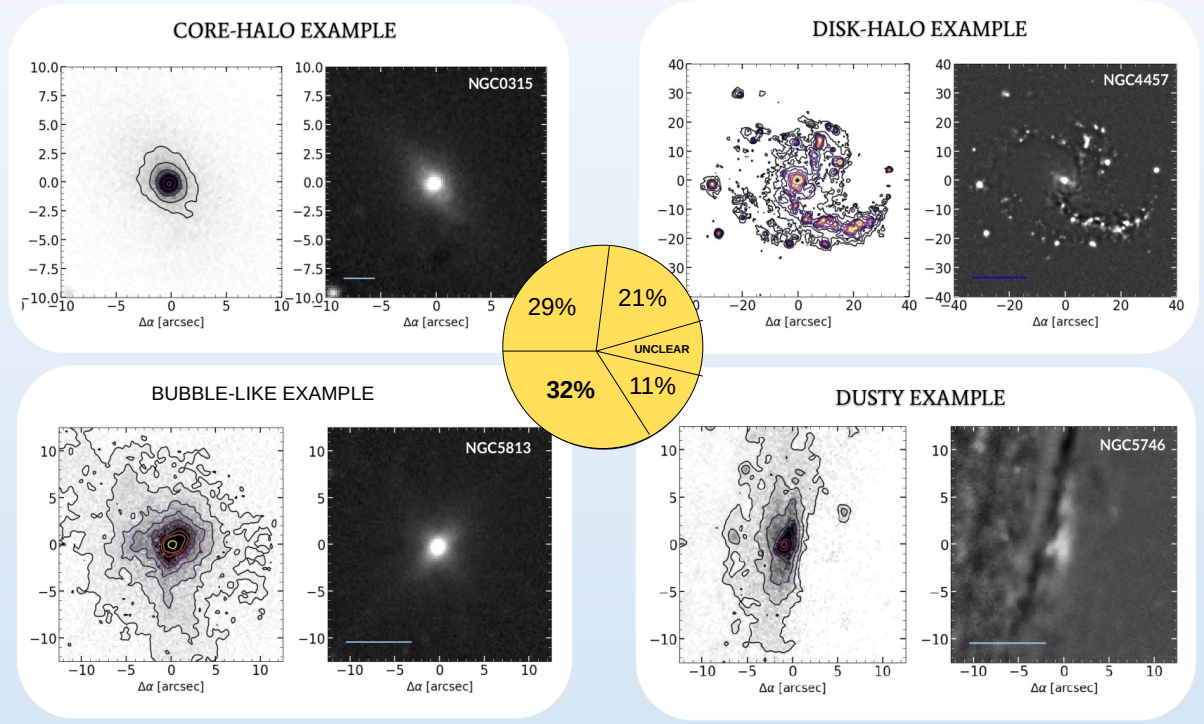

Figure 1: Examples of each morphological class including the percentages of detection per each category. In each panel, the left figure are the Hα images, overimposed by the contours of the emission (levels above 3σ). The right figures are sharp-divided images [12], which highlight non-symmetrical structures. The blue line indicates the 1 kpc scale.

imaging data with the kinematical signatures coming from different sources to further discuss the possible presence of outflows in our LINERs.

3 Results and discussion

As indicated in Fig. 1, we identified a total of 20 LINERs with Core-halo (∼29%), 15 with Disky (∼21%), 8 with Dusty (∼11%), and 22 with Bubble-like morphologies (∼32%). Finally, 7% of the sample was classified as Unclear. The morphological classes in which we found more LINERs is Bubble-ĺike, which are our candidates for hosting outflows. We did not detect any correlation of the classification of the ionised gas with the morphological type of the host.

If we consider the sample of the 60 LINERs for which there is kinematical information from the literature, for 29 (i.e. 48%) there is a reported detection of an outflow or an inflow. This percentage would indicate that approximately 1 out of every 2 LINERs in the local Universe host an outflow. The Hα emission of the galaxies with kinematically detected outflows were classified in all the different classes that we defined (see Sect. 2). In Fig. 2 we show the comparison of the morphological classification with respect to the percentage of kinematically

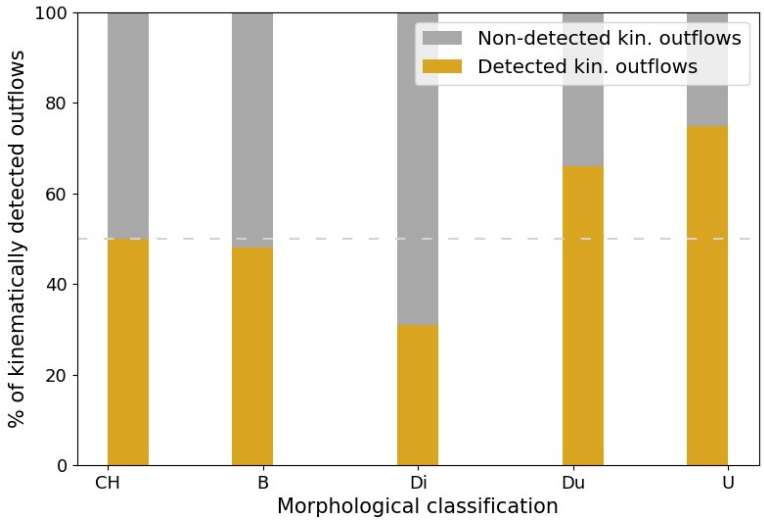

Figure 2: Comparison of the morphological classification of the objects with respect to the percentage of kinematically detected outflows, as obtained from the literature (see Sect. 3). The x-axis from left to right indicates the classes Core-halo, Bubble, Disky, Dusty and Unclear. The orange bars indicate the percentages of kinematical detections; the dashed grey line marks 50% of detection.

detected outflows. For the categories in which we have more than 10 objects (i.e. Core-halo, Bubble-like and Disky) there is a probability of 43% to find an outflow, irrespectively from the morphological distribution of the ionised gas. A lower percentage of kinematic outflows in Disky morphologies could be due to the outflow orientation and the inclination of the disk, which may challenge a possible detection, especially since outflows are expected to be fainter and more compact at the lower accretion rates of our objects [5]. We could also missidentify filamentary structures produced by interactions with Bubble-like morphologies that would not be associated with kinematic outflows.

Finally, when comparing the soft X-ray data with the Hα morphologies, we detected a correlation of both emissions for 60% of the sample. This suggests that the ionised gas and the soft X-ray emissions are correlated, as previously found for Seyferts [1], and already suggested by [14] to also occur in LINERs. We did not find any correlation about the existence of an outflow and a coincidence with the X-ray emission.

4 Conclusions

In this work, we have obtained imaging data for 70 nearby LINERs to study their ionised gas morphologies as traced by Hα. We classified them in four different categories depending on the overall shape: Core-halo, Disky, Bubble-like and Dusty (see Sect. 2). We found that the category with the largest percentage of targets is Bubble-like ($\sim$32%).

In order to confirm if the detected ionised gas emission was caused by an outflow, we searched

for kinematical information in the literature for all the targets. We found data for 60 objects, from which 29 (48%) had a reported kinematical detection of an outflow or an inflow. This results imply that the detection rate of outflows in LINERs in the local Universe is approximately 1 out of every 2 objects. As there is no kinematical information for all our targets, these percentages may slightly vary. For better understanding the physical processes in these outflows, we are exploring the kinematics of the ionised gas for our best candidates using integral field spectroscopic data (see [4]).

Finally, we detected a correlation between the soft X-ray emission and the ionised gas for 60% of the LINERs. Such a co-spatiality points towards a common origin for both emissions in LINERs, as already found in Seyferts (see [1, 2]).

Acknowledgments

We acknowledge financial support from the Spanish Ministerio de Ciencia, Innovación y Universidades (MCIU) under the grants AYA2016-76682-C3, PID2019-106027GB-C41 and BES-2017-082471, and from the State Agency for Research of the Spanish MCIU through the 'Centre of Excellence Severo Ochoa' award to the Instituto de Astrofísica de Andalucía (SEV-2017-0709).

References

[1] Bianchi, S., Guainazzi, M., & Chiaberge, M. 2006, A&A, 448, 499

[2] Bianchi, S., Guainazzi, M. et al. 2019, MNRAS, 485,416

[3] Cazzoli, S., Márquez, I. et al. 2018, MNRAS, 480, 1

[4] Cazzoli, S., Hermosa Muñoz, L. et al. 2022, A&A, 664, A135

[5] Fluetsch, A., Maiolino, R. et al. 2019, MNRAS, 483, 4586

[6] González-Martín, O., Masegosa, J. et al. 2009, A&A, 506, 1107

[7] Harrison, C.M., Costa, T. et al. 2018, Nature Astronomy, 2, 198

[8] Heckman, T.M. 1980, A&A, 500, 187

[9] Hermosa Muñoz, L., Cazzoli, S. et al. 2020, A&A, 635, A50

[10] Hermosa Muñoz, L., Márquez, I. et al. 2022, A&A, 660, A133

[11] Ho, L.C., 2008, ARA&A, 46, 457

[12] Márquez, I. & Moles, M. 1996, A&AS, 120,1

[13] Márquez, I., Masegosa, J. et al. 2017, Frontiers in Astronomy and Space Sciences, 4, 34

[14] Masegosa, J., Márquez, I. et al. 2011, A&A, 527, A23

[15] Pogge, R.W., Maoz, D. et al. 2000, ApJ, 532, 323

[16] Veilleux, S., Cecil, G. et al. 2005 ARA&A, 43, 769

[17] Veilleux, S., Maiolino, R.. et al. 2020 A&ARv, 258, 2

Highlights of Spanish Astrophysics XI, Proceedings of the XV Scientific Meeting of the Spanish Astronomical Society held on September 4–9, 2022, in La Laguna, Spain. M. Manteiga, L. Bellot, P. Benavidez, A. de Lorenzo-Cáceres, M. A. Fuente, M. J. Martínez, M. Vázquez- Acosta, C. Dafonte (eds.), 2023

MEGADES: MEGARA Galaxy Disc Evolution Survey.

Chamorro-Cazorla, M.[1,2], Gil de Paz, A.[1,2], Castillo-Morales, Á.[1,2], Gallego, J.[1,2], Carrasco, E.[3], Iglesias-Páramo, J.[4], García-Vargas; M.L.[5], Pascual, S.[1,2], Cardiel, N.[1,2], Catalán-Torrecilla, C.[1,2], Zamorano, J.[1,2], Sánchez-Blázquez, P.[1,2], Pérez-Calpena, A.[5], Gómez-Álvarez, P.[5], and Jiménez-Vicente, J.[6,7]

[1] Departamento de Física de la Tierra y Astrofísica, Fac. CC. Físicas, Universidad Complutense de Madrid, Plaza de las Ciencias, 1, Madrid, E-28040, Spain
[2] Instituto de Física de Partículas y del Cosmos, IPARCOS-UCM, Fac. CC. Físicas, Universidad Complutense de Madrid, Plaza de las Ciencias 1, Madrid, E-28040, Spain
[3] Instituto Nacional de Astrofísica, Óptica y Electrónica, Luis Enrique Erro No.1, C.P. 72840, Tonantzintla, Puebla, Mexico
[4] Instituto de Astrofísica de Andalucía-CSIC, Glorieta de la Astronomía s/n, 18008, Granada, Spain
[5] FRACTAL S.L.N.E.. C/ Tulipán 2, p13, 1A. E-28231, Las Rozas de Madrid, Spain
[6] Departamento de Física Teórica y del Cosmos, Universidad de Granada, Campus de Fuentenueva, 18071, Granada, Spain
[7] Instituto Carlos I de Física Teórica y Computacional, Universidad de Granada, 18071, Granada, Spain

Abstract

The main interest of the science team for the exploitation of the MEGARA instrument at the 10.4m Gran Telescopio Canarias (GTC hereafter) is devoted to the study of nearby galaxies. The focus lies on researching the history of star formation, and the chemical and kinematical properties of disc systems. We refer to this project as MEGADES: the MEGARA galaxy disc evolution survey. The initial goal of MEGADES is to provide a detailed study of the inner regions of nearby disc galaxies in terms of their spectrophotometric and chemical evolution, and to provide a dynamical characterisation by distinguishing the contribution of in situ and ex situ processes to the history of star formation and effective chemical enrichment of these regions. In addition, the dynamical analysis of these inner regions naturally includes the identification and characterisation of galactic winds that might be present in these regions. At a later stage, we will extend this study farther out in galactocentric distance. The first stage of this project encompasses the analysis of the central regions of 43 nearby galaxies observed with the MEGARA integral field unit for $\sim$ 114 hours, including both guaranteed time and open time observations.

1 Introduction

Given the wide variety of processes and variables that affect the evolution of galaxies and, therefore, their appearance and properties throughout their history, it is clear that understanding the mechanisms that may have influenced the galaxy to reach the state in which we can observe it today requires the collection of as much information as possible. Fortunately, different processes have a different impact in the spectro-photometric, chemical and dynamical evolution of the stars and gas in galaxies.

In an effort to improve our understanding of the universe, with the advent of CCDs in the last 1990s, the idea of large surveys of galaxies became popular. The aim of these surveys has been to provide as much observational information as possible in the observational field in which they are designed. Initially, these surveys mainly relied on photometric observations and long-slit spectroscopy. However, in recent years, the development of instruments with observational capabilities based on Integral Field Spectroscopy (IFS) has represented a technical breakthrough that has led to a better understanding of the mechanisms involved in the evolution of galaxies.

One of the latest advances in astronomical instrumentation is MEGARA (*Multi-Espectrógrafo en GTC de Alta Resolución para Astronomía*). This instrument, capable of observing in both Integral Field Spectroscopy (IFS) and Multi-Object spectroscopy (MOS) modes, has a combination of spatial and spectral resolution unprecedented in this type of device. The fundamental nature of the open questions on galaxy evolution together with the availability of MEGARA@GTC led us to pursue MEGADES (MEgara GAlaxy Discs Evolution Survey), the scientific legacy project associated with the exploitation of the MEGARA instrument Guaranteed Time in the Large Compact Bundle (LCB) Integral Field Unit (IFU) mode.

2 Survey

2.1 MEGADES goals

The long-term objective of MEGADES is to understand the impact of secular processes on disc evolution. Our primary goal is to test whether gas infall is one of the main mechanisms in the evolution of galaxies, and whether it drives the inside-out formation of discs. Therefore, we will test the model predictions for this scenario against our MEGADES observations by analysing the secular and external causes of the differences, that is, nuclear activity, stellar migration, minor mergers, intense star formation, and so on. We will use MEGARA high spatial and spectral resolution 2D spectroscopy to analyse the kinematic properties of the stellar component in order to detect different structures such as bars or inner discs in the central regions of MEGADES galaxies. We will also analyse line indices sensitive to age and metallicity [1], and for the detected HII regions, the gas emission line spectrum, from which we will produce diagnostic diagrams and determine chemical abundances. Finally, we will study the presence and frequency of GWs in the MEGADES sample, both in its warm and cold phases. We will examine the kinematic properties and the shape of the Hα emission line to distinguish different kinematic components to study the warm phase, and we will use the

NaI D absorption doublet to analyse the cold phase.

With this first data release, we will be able to perform all these studies in the central regions of the galaxies in the sample and then place them in context with analyses of the outer emission disc when these observations become available. We will study the stellar populations that make up the bulges of the MEGADES galaxies together with their kinematical properties. With this information, we will be able to determine whether classical bulges dominate the galaxies in our sample or if there are more galaxies with pseudo-bulges [2]. We will also study the possible presence of outflows associated with nuclear starbursts and AGN, considering the existence of different kinematic components in the neutral or warm phase, and the differences that may exist between the two phases. In addition to all of this, we will be able to generate different diagnostic diagrams with the information contained in the different lines we will study.

2.2 MEGADES sample

The original MEGADES sample was extracted from the Spitzer survey of stellar structure in galaxies (S4G) sample [3]). The S4G was designed as a volume- ($d < 40$ Mpc, $|b| > 30°$), magnitude- ($m_{B,corr} < 15.5$ mag), and diameter-limited ($D25 > 1'$) survey. The use of the MEGARA IFU to carry out all observations makes a diameter-limited sample a reasonable idea, as has been the case for the CALIFA sample [4] or PHANGS-MUSE [5].

In addition to the limitations of the S4G sample, we imposed further constraints to fit the sample to our scientific goals. We wished to avoid dwarf systems and elliptical galaxies because in most cases, they are not supported by rotation. We also removed galaxies with inclinations higher than 70° to be able to analyse the metallicity and have the possibility of deriving velocity ellipsoids.

Taking into account all the previous considerations, and because it is not practical to observe the entire S4G sample (2331 galaxies) because of the required telescope time, we must consider further selection criteria in our sample: We limited the diameter to a range in which on the lower side, we removed the smallest galaxies, and on the upper side, we limited the diameter to approximately the field of view of the MEGARA MOS ($2.5' < D25 < 4'$)[1]. We also limited the declination ($Dec(J2000) > -20°$). Summarising all the above selection criteria, the galaxies in our sample are selected by distance $d < 40$ Mpc ($z \sim 0.0092$), galactic latitude $|b| > 30°$, declination $Dec(J2000) > -20°$, apparent magnitude $m_{B,corr} < 15.5$ mag, apparent diameter $2.5' < D25 < 4'$ and inclination $i < 70°$.

This contribution includes a random subsample of 30 out of the 215 galaxies that meet the selection criteria of the MEGADES-S4G sample. However, to enrich our sample, we added 13 galaxies from the CALIFA sample (Calar Alto Legacy Integral Field Area Survey) that show signs of containing interstellar NaI D and are candidates for hosting galactic winds in their neutral phase because their $EW_{ISM-NaID} > 1.5$ Å. The CALIFA survey, with SDSS DR7[2] [6] as the parent sample, is limited in diameter ($45'' < D25 < 80''$), redshift ($0.005 < z < 0.03$),

[1]Note that as part of the outer-disc extension of MEGADES we plan to obtain MOS spectra of HII regions over the whole galaxies extension.

[2]Sloan Digital Sky Survey Data Release 7

galactic latitude above 20°, and declination above +7°.

3 Data release I

3.1 Observations

We release the reduced observations of all galaxies in the sample with all available setups. We observed the central regions of the MEGADES galaxies using three different VPHs, VPH480-LR (LR-B), VPH570-LR (LR-V), and VPH675-LR (LR-R). This produces a combined spectrum covering the spectral range from 4350 to 7288 Åwith a spectral resolution of R $\sim$ 6000. This range includes spectral features such as Hβ, [OIII]λ5007, NaI D, Hα, [NII]λ6584, [SII]λ6717 and [SII]λ6731, as well as absorption features needed for the stellar populations analysis [1]. For the 13 CALIFA galaxies, we only have LR-V and LR-R observations. They suffice for studying the possible presence of outflows in the neutral (NaI D) and the warm (Hα) components. Figure 1 shows an RGB image of the galaxy NGC 3982 created from the LR-B, LR-V and LR-R observations.

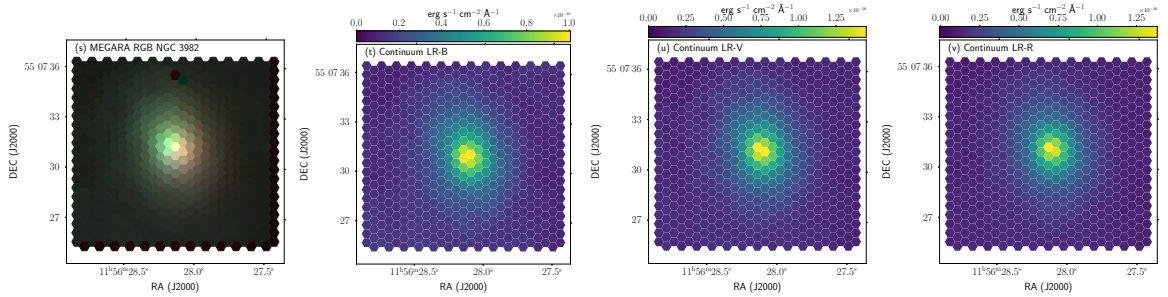

Figure 1: Left subfigure shows a continuum RGB image of NGC 3982 obtained from the MEGARA observations performed with LR-B, LR-V and LR-R (shown in the three following subfigures, respectively).

3.2 Stellar kinematics

We have performed an analysis of the stellar kinematics in the galaxies of the entire sample using the pPXF software based on observations made with the VPH LR-V (5165.57 Å-6176.18 Å). This analysis has been performed on the observations with a Voronoi binning so that all analysed regions reach a signal-to-noise ratio of 10. Figure 2 shows the stellar kinematic analyses performed on NGC 0023. Among the results obtained from this analysis we have velocity, velocity dispersion, skewness (h3) and kurtosis (h4) maps of the stellar component of all the galaxies in the sample.

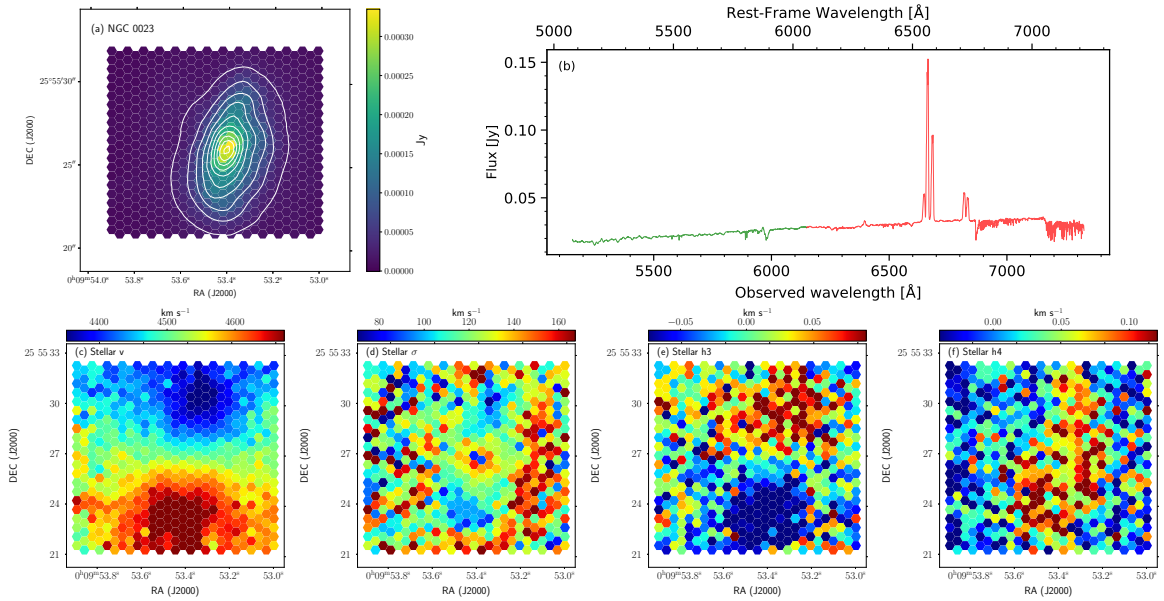

Figure 2: Subfigure (a) shows a continuum image of NGC 0023 obtained with the LR-V VPH (5165 Å- 6150 Å) with the isophotes of the PanSTARRS r-band image overplotted in white. Subfigure (b) shows the integrated spectrum of the separate observations made at different wavelengths. In subfigures (c), (d), (e) and (f) we show the stellar velocity, velocity dispersion, asymmetry and kurtosis maps, respectively, for each galaxy.

3.3 Spectral lines

We have carried out measurements on the emission lines of the ionised gas such as Hβ, [OIII]λ5007, Hα, [NII]λ6584, [SII]λ6717 and [SII]λ6731, and measurements on the neutral gas using the sodium doublet lines NaI D. All lines with a signal to noise ratio measured at the peak of the line higher than 3 were analysed individually using Gauss- Hermite models, except for NaI D, for which we used an an- chored double-Gaussian model. We also fitted the continuum emission around the lines using the information available on both sides of the line. For this task, we made use of one of the tools developed for the analysis of MEGARA observations, the *analyze_rss* megaratool. In Figure 3 we show maps of some of the properties measured for the lines mentioned above for the Hα and [NII]λ6584 lines using observations of NGC 0023.

4 Conclusions

We present the MEGADES survey together with the observations ready for scientific use. We carried out the first studies on the data from the inner regions of the galaxies in the MEGADES sample. We performed an analysis of the stellar kinematics in the galaxies of the entire sample using the pPXF software based on observations made with the VPH LR-

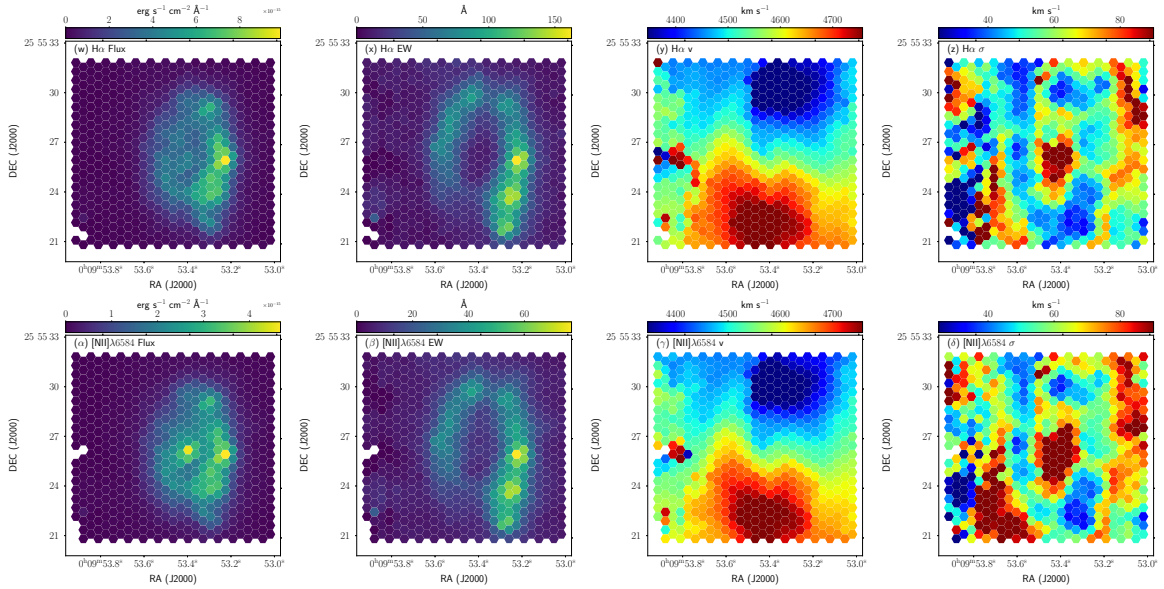

Figure 3: In the top panels, from left to right respectively, we show our measurements of flux, equivalent width, velocity and velocity dispersion from the Hα line in NGC 0023. In the bottom panels we show the same properties measured on the [NII]λ6584 line.

V (5165.6 Å- 6176.2 Å). We present all maps of the kinematic components, that is, radial velocity, velocity dispersion, skewness, and kurtosis. We also carried out measurements on the emission lines of the ionised gas such as Hβ, [OIII]λ5007, Hα, [NII]λ6584, [SII]λ6717, and [SII]λ6731, and measurements on the neutral gas using the sodium doublet lines NaI D. We also present some of the features measured on these lines in maps.

All the observations together with the results of the analyses carried out in this work are available to the community on the MEGADES website (https://www.megades.es). To access the public data, one can log in with the username "public" and the password "6BRLukU55E".

References

[1] Chamorro-Cazorla, M., Gil de Paz, A., Castillo-Morales, A., et al. 2022, A&A 657, A95

[2] Kormendy, J. & Kennicutt, Robert C., J. 2004, ARA&A 42(1), 603

[3] Sheth, K., Regan, M., Hinz, J. L., et al. 2010, PASP 122(898), 1397

[4] Sánchez, S. F., Kennicutt, R. C., Gil de Paz, A., et al. 2012, A&A 538, A8

[5] Emsellem, E., Schinnerer, E., Santoro, et al. 2022, A&A 659, A191

[6] Abazajian, K. N., Adelman-McCarthy, J. K., Agüeros, M. A., et al. 2009, ApJS 182(2), 543

Highlights of Spanish Astrophysics XI, Proceedings of the XV Scientific Meeting of the Spanish Astronomical Society held on September 4–9, 2022, in La Laguna, Spain. M. Manteiga, L. Bellot, P. Benavidez, A. de Lorenzo-Cáceres, M. A. Fuente, M. J. Martínez, M. Vázquez- Acosta, C. Dafonte (eds.), 2023

New molecular size estimation in local LIRGs at high-spatial resolution with ALMA.

Bellocchi, E.[1], Pereira-Santaella, M.[1], Colina, L.[1], Labiano, A.[1,2], Sánchez-García, M.[1,3], Alonso-Herrero, A.[1], Arribas, S.[1], and García-Burillo, S.[3]

[1] Centro de Astrobiología, (CSIC-INTA), Astrophysics Department, Madrid, Spain
[2] Telespazio UK, for the European Space Agency (ESA), ESAC, Villanueva de la Cañada, Madrid, Spain
[3] Observatorio Astronómico Nacional (OAN-IGN)-Observatorio de Madrid, Alfonso XII, 3, 28014 Madrid, Spain

Abstract

We present the first study that provides detailed measurements of the size (i.e., effective radius) of the molecular gas traced by CO(2-1) in a sample of 21 LIRG systems at low-z. To this aim, we used high-resolution ALMA data, which allow us to reach sub kpc spatial resolution scale (<100 pc). The sample encompasses a wide variety of morphological types, suggesting different dynamical phases (isolated spiral galaxies, interacting galaxies, and ongoing and post-coalescence mergers). We performed a comprehensive study of the molecular, stellar, and ionized gas distributions and their relative sizes. Comparison samples of local galaxies and high-z systems have also been included in order to place the low-z LIRGs in a general context.

1 Introduction

The characterization of the distribution of all the ionized, molecular and stellar tracers is key to understanding how the different phases of the interstellar medium (ISM) evolve in size across the cosmic time, studying several types of galaxies, at low- and at high-z. Low-z LIRGs offer a unique opportunity to study extreme star-formation (SF) events at high linear resolution and signal-to-noise ratio (S/N), and compare them with those observed locally (spiral galaxies, early-type galaxies (ETGs), and ULIRGs) and at high-z. In particular, this enables us to compare the size of the host galaxy (stellar component; [1]) with that derived for the ongoing star formation (ionized gas; [2]) as well as the size of the regions where stars are forming (molecular gas) in a local sample of LIRGs and compare them with those derived for local spiral galaxies, ETGs, and ULIRGs as well as high-z star-forming galaxies (SFGs) and sub-millimeter galaxies (SMGs). With the advent of high-resolution instruments such as the Atacama Large Millimeter/Submillimeter Array (ALMA), we are now able to study the

molecular emission in local galaxies at spatial resolutions similar to that covered by typical giant molecular clouds (<100 pc).

2 Sample and observations

The volume-limited sample consists of 21 local LIRGs (24 individual galaxies) at z≤0.02 for which we obtained ALMA data. The sample has been drawn from the IRAS Revised Bright Galaxy Sample (RBGS, [3]) with distance D≤100 Mpc. Our LIRGs were previously observed in the optical band using VIMOS/VLT by [4] and ten of them have also been analyzed in the near-IR using SINFONI/VLT data by [5]. We obtained the CO(2–1) line and the continuum at 247 GHz (∼1.3 mm) emission of a sample of individual local LIRGs observed with ALMA using Band 6 (see Fig. 1) from the projects 2017.1.00255.S (PI: Pereira Santaella, M.), 2015.1.00714.S (PI: Kazimers, S.), 2013.1.00271.S and 2013.1.00243.S (PI: Colina, L.) and 2017.1.00395.S (PI: Díaz-Santos, T.). The synthesized beam full width at half maximum (FWHM) of the sample ranges between ∼0.2″ and 0.4″. The field of view (FoV) imaged by a single pointing has a diameter ranging between ∼5 and 8 kpc.

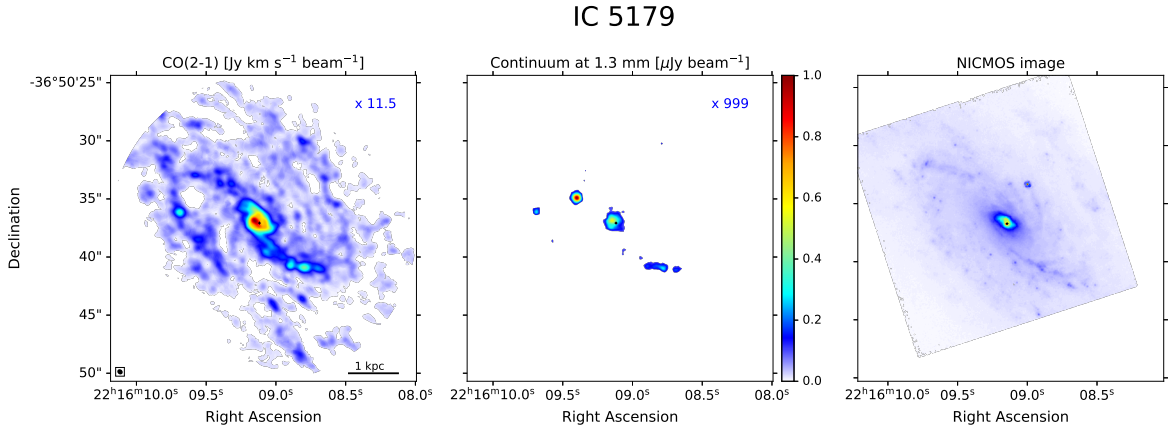

Figure 1: *From left to right:* CO(2–1) and 1.3 mm continuum maps obtained with ALMA, complemented by *HST*/NICMOS image when available. The cross symbol in the three panels represents the stellar peak emission identified using the *HST*/NICMOS image. The beam size and the physical scale in kpc are also shown in the left panel.

3 Data analysis

We generated CO(2–1) and 1.3 mm continuum maps for the whole sample, selecting the emission above 5σ for both maps. To derive the size of a system we consider the curve-of-growth method as a robust way to derive the R_{eff}. We considered an equivalent circular aperture as a good approximation of the (major) elliptical aperture. We select the center of the (circular) aperture, choosing the peak emission observed in the near-IR using *HST/NICMOS* F160W (λ_c = 1.60 μm, FWHM = 0.34 μm) images (see Fig. 1, right panel). When the *HST* images are not available, the peak emission in the continuum map at 1.3 mm is used. The CO(2–1)

and 1.3 mm continuum sizes presented in this work are observed (not corrected for the beam). The intrinsic CO and 1.3 mm continuum sizes are also resolved (larger than the beam) and are (on average) smaller than the observed size by $\leq$1% and $\leq$4%, respectively.

4 LIRGs versus low-z ETGs, spiral galaxies, and ULIRGs

4.1 SFR *versus* R_{CO}

LIRGs are completely decoupled from spiral galaxies and ETGs in the SFR-R_{CO} diagram (see Fig. 2, left panel). While spiral galaxies are extended systems with a CO(2–1) radius of about 2 to 10 kpc, LIRGs have radii of about a factor $\leq$6 smaller. Moreover, the sizes of LIRGs cover a range similar to that covered by the sizes of ETGs, while their SFR is a factor 60 higher than for ETGs.

The large discrepancy in the molecular size between spiral galaxies and local LIRGs seems to be in agreement with what is discussed in [6]: these authors found that galaxies that are more compact in the molecular gas than in stars tend to show signs of interaction (the presence of a bar can also affect the emission distribution). The work by [7] seems to support the aforementioned result: these authors derived still more compact molecular size for their sources with respect to our LIRGs. Their sources are more extreme in terms of SFR ($\sim$340 $M_\odot$ yr^{-1}) and even show a more disturbed morphology. Their molecular size is a factor 2 more compact than that of our LIRGs.

4.2 Stellar mass *versus* R_{CO}

In the stellar mass–R_{CO} diagram (Fig. 2, right panel), LIRGs cover a mass range similar to that of low-z samples of spiral galaxies and ETGs, with values in the 10^{10}-10^{11} $M_\odot$ range. Compared with different types of low-z galaxies, LIRGs are characterized by being located in galaxy hosts with intermediate stellar mass ($\sim5\times10^{10}$ $M_\odot$), forming stars at rates a factor of $\geq$10 above spiral galaxies, and with compact CO sizes ($R_{CO}\sim$0.7 kpc) similar to those of ETGs ($R_{CO}\sim$1 kpc).

4.3 Stellar mass–size plane

A different trend from that derived for the stellar mass and molecular size components is derived for our sample when the stellar size is considered (Fig. 3, left panel). As before, local spiral galaxies (i.e., MS SFGs from [8]) and ETGs are included in the diagram. LIRGs share similar stellar mass and stellar size with ETGs, while they are more compact (by a factor $\sim$5) and more massive (by a factor $\leq$2) than local MS SFGs. From [9], we know that the distributions of molecular gas and stellar disk in galaxies follow each other closely in nearby disk galaxies ($R_{star}\sim R_{CO}$), while the stellar size is larger than the molecular size for ETGs and for our LIRGs by a factor of $\leq$3.

According to evolutionary scenarios, many works support the idea that (U)LIRGs can transform gas-rich spiral galaxies into intermediate-(stellar)mass (10^{10}-10^{11} $M_\odot$) elliptical

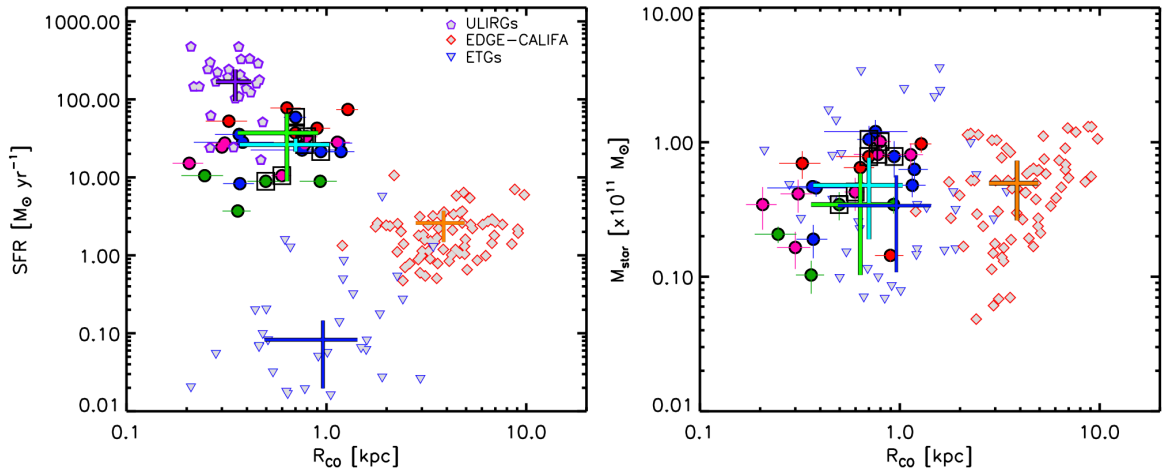

Figure 2: Distribution of LIRGs and other low-z galaxy samples in the SFR–R_{CO} (left) and M_{star}–R_{CO} (right) planes. Our LIRGs are shown using green, magenta and red circles. The median value of each sample is shown according to the following color code: purple for ULIRGs, light green for interacting and merger LIRGs, light blue for disky LIRGs, orange for spiral galaxies, and dark blue for ETGs.

galaxies through merger events ([10]). The kinematic study of local (U)LIRGs ([1]) highlights that these systems fill the gap between rotation-dominated spiral galaxies and dispersion-dominated ETGs in the v/σ–σ plane. Following our present results, most of the LIRGs share similar properties with ETGs while only a few overlap with the region covered by spiral galaxies.

4.4 Stellar hosts in LIRGs *versus* high-z SFGs

A large variety of high-z systems (i.e., MS SFGS, [11], [12], [13], [14], [15], [16], [17], [18] and SMGs, [19], [20], [21], [22], [23]) were selected using different criteria (i.e., stellar mass, optical radius, or IR luminosity) and observational techniques also covering a broad range of redshifts ($1 \leq z \leq 6$) and galaxy properties. Therefore, they represent the rich diversity of galaxies found during the first half of the history of the Universe. The vast majority of high-z galaxies have masses in the $\sim 10^{10}$-2×10^{11} $M_{\odot}$ mass range, but their sizes cover a much wider range, which reflects the large variety of systems considered at high-z (Fig. 3, right panel).

The comparison with MS SFGs indicates that low-z LIRGs have stellar sizes and masses similar to those of K-band-selected SFGs at redshifts 3-4 ([11]). However, LIRGs appear (on average) slightly smaller in size (factor 1.3) than the MS SFGs at $z \sim 1$-2 (e.g., [13], [17], [18]) while their masses (average of 5.6×10^{10} $M_{\odot}$) are within the wide range of stellar masses (from 4.3 to 20.0×10^{10} $M_{\odot}$) covered by the hosts of the MS SFGs. These results indicate that LIRGs, which represent the bursty above-MS SFGs at low-z, appear to be similar to the bulk population of MS SFGs at intermediate redshifts (z∼1-4) in terms of the stellar mass

and size of their hosts.

All the low-z LIRGs, as well as a large fraction of the high-z galaxies, appear in the stellar mass–size diagram (Fig. 3, right panel) in between the relations of early- and late-type galaxies at $z \sim 1.75$ (typical redshift value for the majority of the high-z systems considered in this work), as derived from the *3D-HST* and *CANDELS* surveys ([24] and references therein). As observed in local LIRGs, distant SMG populations also show a mixture of dynamical phases, hosting merger-driven starbursts ([25]) as well as ordered rotating disks ([19]). This could indicate that many of the high-z galaxies could be in a transitory phase related to tidally perturbed disks or galaxies involved in interactions and mergers, such as low-z LIRGs. Deciphering whether or not this transitory phase represents the evolution from extended disks to compact spheroids requires spatially resolved kinematical information traced by the molecular and ionized ISM.

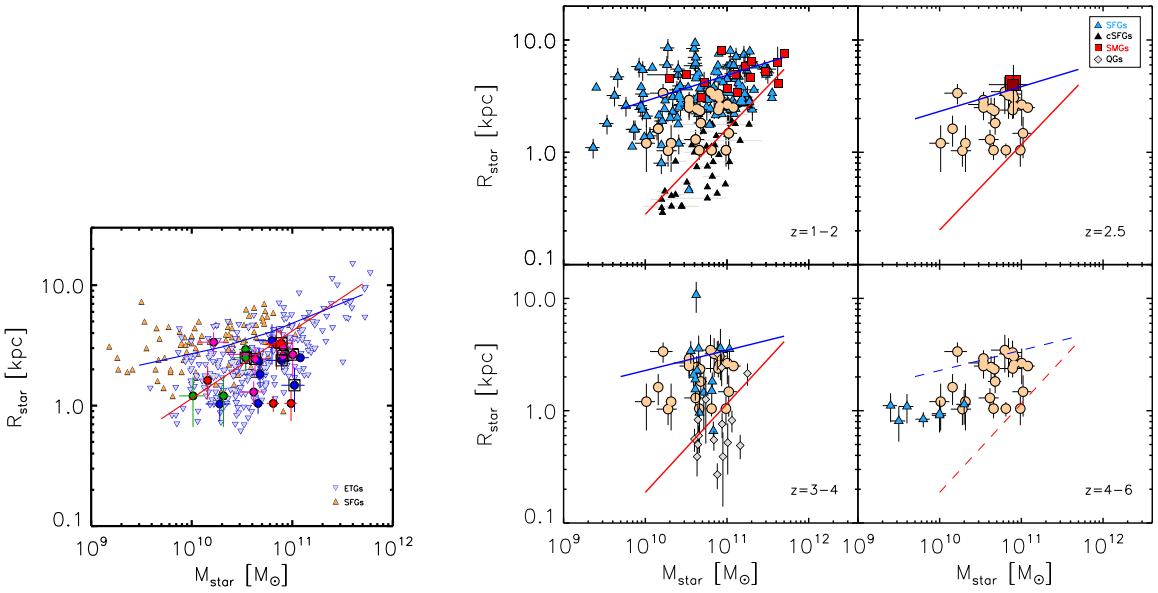

Figure 3: *Left:* Mass–size distribution for our LIRGs including ETGs and local spiral galaxies (i.e., MS SFGs; [8]). LIRGs are identified following the color code used in previous figures. The blue and red slopes represent the mass–size relations derived by [26] for late- and early-type local galaxies, respectively. *Right:* Mass–size distribution for our LIRGs and high-z systems. LIRGs from this work are shown using light orange circles. High-z SFG and SMG data are taken from the following works: SMGs from [19], [20], [21], and [22] and SFGs from [11], [12], [13], [14], [15], [16], [17], and [18]. The blue and red lines in each redshift range represent the mass–size relations for late- and early-type galaxies, respectively, at $z\sim$1.75, 2.25, and 2.75 derived from the *3D-HST+CANDELS* surveys ([24]). At z=4-6, the mass–size relation for late- and early-type galaxies has not yet been derived, and so the dashed blue and red lines still show the behavior considered at z=3-4.

Acknowledgments

This research was supported from the Comunidad de Madrid through the Atracción de Talento grant 2017-T1/TIC-5213. This research has been partially funded by the Spanish State Research Agency (AEI) Project MDM-2017-0737 Unidad de Excelencia 'María de Maeztu'- Centro de Astrobiología (INTA-CSIC). EB also acknowledges financial support from the María Zambrano program of the Spanish Ministerio de Universidades funded by the Next Generation European Union and partly supported by the grant RTI2018-096188-B- I00 funded by MCIN/AEI/10.13039/501100011033.

References

[1] Bellocchi, E., Arribas, S., & Colina, L. 2016, A&A, 591, A85

[2] Arribas, S., Colina, L., Alonso-Herrero, A., et al., 2012, A&A, 541, 20

[3] Sanders, D. B., Mazzarella, J. M., Kim, D. C., Surace, J. A., & Soifer, B. T. 2003, AJ, 126, 1607

[4] Arribas, S., Colina, L., Monreal-Ibero, A., et al., 2008, A&A, 479, 687

[5] Crespo Gómez, A., Piqueras López, J., Arribas, S., et al. 2021, A&A, 650, A149

[6] Bolatto, A. D., Wong, T., Utomo, D., et al. 2017, ApJ, 846, 159

[7] Pereira-Santaella, M., Colina, L., García-Burillo, S., et al. 2021, A&A, 651, A42

[8] Leroy, A. K., Schinnerer, E., Hughes, A., et al. 2021, ApJS, 257, 43

[9] Leroy, A. K., Walter, F., Sandstrom, K., et al. 2013, AJ, 146, 19

[10] Cappellari, M., McDermid, R. M., Alatalo, K., et al. 2013a, MNRAS, 432, 1862

[11] Straatman, C. M. S., Labbé, I., Spitler, L. R., et al. 2015, ApJ, 808, L29

[12] Tadaki, K.-I., Genzel, R., Kodama, T., et al. 2017, ApJ, 834, 135

[13] Förster Schreiber, N. M., Renzini, A., Mancini, C., et al. 2018, ApJS, 238, 21

[14] Puglisi, A., Daddi, E., Liu, D., et al. 2019, ApJ, 877, L23

[15] Cheng, C., Ibar, E., Smail, I., et al. 2020, MNRAS, 499, 5241

[16] Kaasinen, M., Walter, F., Novak, M., et al. 2020, ApJ, 899, 37

[17] Valentino, F., Daddi, E., Puglisi, A., et al. 2020, A&A, 641, A155

[18] Puglisi, A., Daddi, E., Valentino, F., et al. 2021, MNRAS, 508, 5217

[19] Hodge, J. A., Swinbank, A. M., Simpson, J. M., et al. 2016, ApJ, 833, 103

[20] Chen, C.-C., Hodge, J. A., Smail, I., et al. 2017, ApJ, 846, 108

[21] Calistro Rivera, G., Hodge, J. A., Smail, I., et al. 2018, ApJ, 863, 56

[22] Lang, P., Schinnerer, E., Smail, I., et al. 2019, ApJ, 879, 54

[23] Chen, C.-C., Harrison, C. M., Smail, I., et al. 2020, A&A, 635, A119

[24] van der Wel, A., Franx, M., van Dokkum, P. G., et al. 2014, ApJ, 788, 28

[25] Aguirre, P., Baker, A. J., Menanteau, F., Lutz, D., & Tacconi, L. J. 2013, ApJ, 768, 164

[26] Shen, S., Mo, H. J., White, S. D. M., et al. 2003, MNRAS, 343, 978

Highlights of Spanish Astrophysics XI, Proceedings of the XV Scientific Meeting of the Spanish Astronomical Society held on September 4–9, 2022, in La Laguna, Spain. M. Manteiga, L. Bellot, P. Benavidez, A. de Lorenzo-Cáceres, M. A. Fuente, M. J. Martínez, M. Vázquez- Acosta, C. Dafonte (eds.), 2023

Put a ring on it: the origin of star-forming rings in S0 galaxies.

Tous, J. L.[1], **Perea, J.**[2], **Solanes, J. M.**[1], **and Domínguez-Sánchez, H.**[3]

[1] Departament de Física Quàntica i Astrofísica i Institut de Ciències del Cosmos (ICCUB), Universitat de Barcelona. Martí i Franquès 1, 08028 Barcelona, Spain
[2] Instituto de Astrofísica de Andalucía (IAA-CSIC). Glorieta de la Astronomía s/n, 18008 Granada, Spain
[3] Instituto de Ciencias del Espacio (ICE-CSIC), Campus UAB. Can Magrans s/n, 08193 Barcelona, Spain

Abstract

The examination of the spatially resolved IFS maps in a sample of more than 500 lenticular (S0) galaxies drawn from the MaNGA survey has unveiled the existence of transient inner annular structures ($\langle R \rangle \sim 1\,R_{\rm e}$) betraying ongoing star formation in a good number of these objects. Activity gradients in these galaxies have been measured through a novel methodology based on the principal component analysis of their optical spectra averaged over bins of galactocentric radius. We find that the sign of these gradients is closely linked to the presence of rings in the spectral maps, which are specially conspicuous in the equivalent width of Hα-emission, EW(Hα), with a fractional abundance —22–37% depending on the strictness of ring identification— larger than that inferred from optical imaging. While the numbers of S0s with globally positive, negative, and flat activity gradients are comparable, star-forming rings are found almost exclusively in objects with a positive slope for which quenching proceeds inside-out, in good agreement with predictions from cosmological simulations studying S0 buildup. The assessment of these structures and the properties of the galaxies harboring them also indicates that the frequency of such rings increases with the mass of their hosts, that they feed mainly on the gas from the disks, that are more short-lived in galaxies with ongoing star formation, and that the local environment does not play a relevant role in their formation. From the present analysis, we conclude that the presence of rings in the EW of the Hα emission line is a common phenomenon among fully formed S0s, possibly associated with annular disk resonances driven by weakly disruptive mergers preferentially involving the more massive representatives of these galaxies and their smaller and closer satellites.

My poster in zenodo.org can be found here

Highlights of Spanish Astrophysics XI, Proceedings of the XV Scientific Meeting of the Spanish Astronomical Society held on September 4–9, 2022, in La Laguna, Spain. M. Manteiga, L. Bellot, P. Benavidez, A. de Lorenzo-Cáceres, M. A. Fuente, M. J. Martínez, M. Vázquez- Acosta, C. Dafonte (eds.), 2023

Stellar Populations in type Ia supernova host galaxies at intermediate-high redshift: Star formation and metallicity enrichment histories.

Millán-Irigoyen, I.[1], del Valle-Espinosa, M. G.[2], Fernández-Aranda, R.[3], Galbany, L.[4,5], Gomes, J.M.[6], and Mollá, M.[1]

[1] Dpto. de Investigación Básica, CIEMAT, Avda. Complutense 40, E-28040 Madrid, Spain
[2] Institute for Astronomy, The University of Edinburgh, Royal Observatory, Blackford Hill, Edinburgh, EH9 3HJ, UK
[3] Institute of Astrophysics - FORTH & Dept. of Physics ,University of Crete, 70 013 Heraklion, Greece
[4] Institute of Space Sciences (ICE, CSIC), Campus UAB, Carrer de Can Magrans, s/n, E-08193 Barcelona, Spain
[5] Institut d'Estudis Espacials de Catalunya (IEEC), E-08034 Barcelona, Spain
[6] Instituto de Astrofísica e Ciências do Espaço, Universidade do Porto, CAUP, Rua das Estrelas, 4150-762 Porto, Portugal

Abstract

We describe our project to study galaxies hosting type Ia supernova (SN Ia) at different redshifts. We present optical spectroscopy of 6 galaxies at redshift $z \sim 0.45$ observed with Gran Telescopio de Canarias. They are joined to a set of SN Ia host galaxies at intermediate-high redshift, taken from SDSS and COSMOS surveys. After some selection cuts, in terms of signal-to-noise and other criteria, our final sample consists of 680 galaxies in the range $0.04 < z < 1$ of redshift. We perform an inverse stellar population synthesis with the code FADO to estimate the star formation histories. We simultaneously obtain their stellar mass, and their mean stellar age and metallicity. We then look for possible correlations of the Hubble diagram residuals and of the supernova light curve features (luminosity, color and strength) on these stellar parameters. We find that the Hubble diagram residuals show a correlation with the weighted by mass stellar metallicity (in logarithmic scale) with a slope of -0.061 $\mathrm{mag\,dex^{-1}}$. This result supports our previous findings obtained with gas oxygen abundances for local and SDSS galaxies. This is also similar to the value found in other works from the literature. Our result is in agreement with others, but it is obtained with more precision and a better significance due to the higher number of objects and wider range of redshift of our sample.

1 Introduction

Type Ia supernova (SN Ia) have been used as standard candles from the mid 1990s to measure the evolution of the Universe with sufficient precision and at distances large enough to detect an accelerated rate of expansion of the Universe, in the High-z Supernova project [25] and the Supernova Cosmology Project [22].

The SN Ia brightness can be standardized, to use their light-curves and their apparent peak magnitude (m) to estimate distances to their host galaxies. Assuming an universal absolute peak magnitude (M), their distance modulus ($\mu = m - M$) can be represented as a function of the redshift (z) of their host galaxy, in the well known Hubble diagram (HD). However, SNe Ia are not natural standard candles but *standardizable* by means of a relationship between their peak brightness m, and the width of their light-curves (parametrized by $x1$, s, or Δm_{15}), and their color (c or $E(B-V)$) at the peak [23, 24, 32].

This standardization technique is mainly trained with SNe Ia of galaxies of the Local Universe, with typically around Solar abundances and stellar ages. In fact, there are theoretical models that predict that the metallicity of the progenitor system would affects the luminosity of the SN Ia: [30] showed that the excess of neutrons in the explosion of a white dwarf is a direct function of the metallicity of the progenitor star, and that this excess is what controls the ratio between radioactive (as ^{56}Ni, which defines the brightness of the explosion) to non-radioactive (elements of the group of iron) abundances.

There have been a large number of works for the last two decades studying possible correlations between parameters of the SN Ia and the characteristics of the explosion [7, 12, 21] The majority of them showed that SN Ia in massive host galaxies are brighter than less massive ones, after LC shape and color corrections. Considering the mass-metallicity relation [8], it migth to indicate a correlation between the magnitudes of SNe Ia and the metallicity of their host galaxies: the most metallic galaxies would have the brightest SNe Ia with a difference of $\sim$ 0.10 mag dex^{-1} with the less metallic ones.

The direct dependence of SNe Ia luminosities on metallicity was early studied by [6] and [7], who estimated the oxygen abundance using emission lines in star-forming galaxies, and the absorption stellar features in early-type galaxies respectively. In both cases, they found a trend between magnitudes of SNe Ia and the stellar population metallicity of their host galaxies.

We started a project to compute the possible effect of the metallicity of each SNe Ia in its brightness. For that we try to estimate the stellar metallicity of their hosting galaxies or the Oxygen abundance of their interstellar medium, to look for possible correlations between the SNe Ia brightness and those estimates of metallicity, trying to have a redshift range as wide as possible and a number of objects as high as possible. This is the final step of the project [17, 18, 19]. We reanalyse the previous works at intermediate redshift and extend it to higher redshift, up to $z \approx 1$.

First, we present the sample and the selection criteria in Section 2. Then, in Section 3 we present the analysis code FADO [10] that we use to obtain information of the stellar populations. Our results are presented in Section 4. Our conclusions are given in Section 5.

2 Observational data

We compiled spectra of SN Ia host galaxies from 3 different sources focusing on different redshift ranges.

- The low-intermediate redshift SN Ia sample is provided by the SDSS-II/SNe in their Data Release [26]. It is made of 1066 SNe Ia confirmed either spectroscopically (352 spec-Ia) or photometrically, identified based on a Bayesian LC fitting, using the spectroscopic redshift of their host galaxy (714 photo-Ia, [26]), and with publicly available host galaxy spectra in the 16th data release of the SDSS [1]. The sample is similar to the one presented in [19] and [5], where we have now performed aperture corrections to several host galaxy parameters.

- The intermediate redshift sample is made of 6 selected galaxies from the sample Union2.1 [29] at redshift $z \approx 0.45$ that were observed with GTC/OSIRIS [4] in long-slit mode, between November 2014 and January 2015 under the GTC57-14B programme (PI:Moreno-Raya). We set the width of the slit to 0.8 arcsec and used the R1000R grating, which provides spectral coverage in the range from 5100 to 10000 Å, with a resolving power of $R \sim 1100$.

  The data were reduced using the standard packages available for the bias subtraction, flat field correction and cosmic ray rejection and wavelength and flux calibration using the same procedure as in [18] from IRAF software [31]. Moreover, we have corrected the spectra for extinction effect, using the DEREDDEN task together with the tabulated values for the galactic extinction map available in [27].

- The high-z sample of SNe Ia ($0.5 \leq z \leq 1.0$) was taken from the Supernova Legacy Survey[1] (SNLS, [11, 2]). SNLS targeted four regions of $1^\circ \times 1^\circ$ in the sky, named from D1 to D4. The SNLS D2 region overlapped with the COSMOS extragalactic survey [28] footprint[2]. COSMOS consisted of a multi-wavelength imaging and spectroscopy of a region of the sky of $2^\circ \times 2^\circ$ centered at the J2000 coordinates (RA,Dec)=(+150.1191, +2.2058), using a multitude of telescopes. In particular, for our study we took spectra from the COSMOS sub-surveys *Magellan* [33] and *zCOSMOS*, [14].

  We crossmatched the coordinates of SN and the galaxy, with a selection criteria (i) a physical projected distance of 50 kpc between the SN position and the center of the galaxy, and (ii) a redshift relative error of 10%. We found that 44 matches (39 from zCOSMOS and 5 from Magellan) that meet both criteria, 3 of them being galaxies repeated in both surveys. We made a visual inspection with Hubble Space Telescope (HST) I-band images to make sure that the galaxy was the real host of the SN. A total of 28 galaxy-SN pairs was finally considered for further analysis.

The complete sample consists of 1087 galaxies (1053 from SDSS, 6 from GTC-OSIRIS and 28 from COSMOS) with available spectra. From them, we keep 803 galaxies (769 from

[1] https://www.cadc-ccda.hia-iha.nrc-cnrc.gc.ca/en/cfht/cfhtls.html
[2] https://irsa.ipac.caltech.edu/data/COSMOS/tables/spectra/

SDSS, 6 from GTC and 28 from COSMOS) that have spectra with $S/N > 3$. Additionally, we perform some cuts based on the SN Ia light-curve properties: the light-curve stretch in the range $-3 < x1 < 3$ and color in the range $-0.3 < c < 0.3$. We choose these ranges of $x1$ and c to match the training data of the SALT2 [11] empirical SNe Ia model, that was trained in those ranges of stretch and color. The final sample consists in 680 galaxies: 654 from SDSS, 6 from GTC and 20 from COSMOS, for which we have the complete information necessary for our analysis.

3 Analysis

Once selected the spectra of the 680 galaxies[3], we proceed to their analysis using the code FADO [10]. Fado tries to find the best fitting combination of stellar spectra using a basis of Simple Stellar Populations (SSPs). SSPs are sets of stars of the same age and metallicity whose spectra are calculated as the sum of spectra of individual stars that form them. In this work we use as *basis* the set of SSP calculated with the HR-PopStar code from [15]. For this work, we have developed a special set of models, that uses the spectral library of normal from [20], which has a shorter wavelength range than the original HR-pyPopStar, from 2500 Å to 10000 Å, but a wider range in metallicities, $0.0001 < Z < 0.05$.

Since we are working with non-local galaxies, it is necessary to take into account the age of the Universe in each redshift. These galaxies could not have stellar populations older than that age of the Universe corresponding to their redshift. Thus, the stellar populations older than this value can not exist nor contribute to the spectra.

4 Results

First, we have looked for two classical relations between the characteristics of the galaxy: mass-metallicity and age-mass relation. Concerning mass-metallicity relation, we find a similar relation than [8] and [9]. We have a similar relation to both authors, but with more dispersion, because we find a larger number of galaxies with low metallicity than them. In the case of age-mass relation, shown in Fig. 1a, we find younger stellar populations than [8]. We suggest that this difference is caused by the difference in the SSP basis used in the analysis, because the SSPs used in both works are different, HR-pyPopStar being specially tuned for the young SSPs models.

Then, we have computed the Hubble diagram of the SN using the calibration of [26] and the Hubble residuals (HR) using the cosmological distance modulus from the cosmological parameters from the same work, using a standard flat Λ CDM cosmology. From the whole sample of 680 galaxies, we have selected 664 for which $|HR| < 1.0$ mag to analyse the HR results and their dependence on the logarithm of stellar metallicity and current mass. We find correlations in both cases with slopes -0.061 mag dex^{-1} and -0.06 mag dex^{-1}, respectively. We show in Fig. 1b) the correlation of HR with the mean stellar metallicity in logarithmic

[3]The used spectra are in https://github.com/HOSTFLOWS

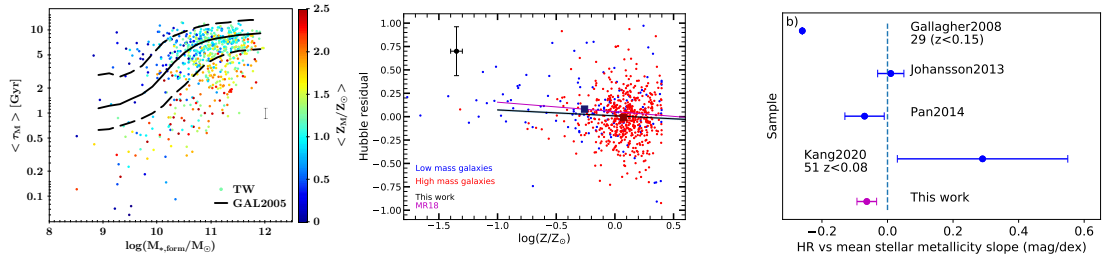

Figure 1: a) Stellar Mass-Age relation compared with [8] results; b) Hubble residuals *vs* the logarithm of the mean stellar metallicity weighted by mass, with the correlation found, the comparison with [19] and the blue and red squares that represent the mean HR of the low mass and the high mass bins respectively; and c) comparison of our results with the ones from [7, 12, 21, 13].

scale.

Finally, we have compared with other work of the literature that have measured the mean metallicity of the stellar population [7, 12, 21, 13] in Fig. 1c). Our results are similar to [21], but with smaller error and with the highest significance of all the works.

5 Conclusions

We have done a study of hosting SN Ia galaxies spectra for a redshift range of $0.1 < z < 1.0$. After analyzing with the FADO code, we have estimated the SFHs, $\langle Z_M \rangle$, $\langle Z_L \rangle$, $\langle \tau_M \rangle$, $\langle \tau_L \rangle$, v_{sys}, σ_{star}, $M_{\rm formed}$ and $M_{\rm present}$. We present our results in [16] where more details may be found.

The two most important conclusions we find are: 1) The HR-pyPopStar models give younger stellar populations when using with FADO compared with previous models; and 2) The residuals of the Hubble diagram, HR, shows a clear dependence with the stellar metallicity, weigthed by mass, when is represented in logarithmic scale, with a slope of $-0.059\,{\rm mag\,dex^{-1}}$. This results is similar to others from the literature [7, 12, 21, 13] but we have the highest significance compared with all of them.

Acknowledgments

Based on observations made with the Gran Telescopio Canarias (GTC), installed at the Spanish Observatorio del Roque de los Muchachos of the Instituto de Astrofísica de Canarias, in the island of La Palma.

This research has made use of the HST-COSMOS database, operated at CeSAM/LAM, Marseille, France.

References

[1] Ahumada R., Prieto C. A., Almeida A., et al., 2020, ApJS, 249, 3.

[2] Betoule M., Kessler R., Guy J., Mosher J., et al., 2014, A&A, 568, A22.

[3] Bruzual G., Charlot S., 2003, MNRAS, 344, 1000.

[4] Cepa J., 2010, ASSP, 14, 15.

[5] Galbany L., Smith M., Duarte Puertas S., et al., 2022, A&A, 659, A89.

[6] Gallagher J. S., Garnavich P. M., Berlind P., et al., 2005, ApJ, 634, 210.

[7] Gallagher J. S., Garnavich P. M., Caldwell N., et al., 2008, ApJ, 685, 752.

[8] Gallazzi A., Charlot S., Brinchmann J., White S. D. M., Tremonti C. A., 2005, MNRAS, 362, 4

[9] González Delgado R. M., Cid Fernandes R., García-Benito R., et al., 2014, ApJL, 791, L16.

[10] Gomes J. M., Papaderos P., 2017, A&A, 603, A63.

[11] Guy J., Sullivan M., Conley A., et al., 2010, A&A, 523, A7.

[12] Johansson J., Thomas D., Pforr J., et al., 2013, MNRAS, 435, 1680.

[13] Kang Y., Lee Y.-W., Kim Y.-L., Chung C., Ree C. H., 2020, ApJ, 889, 8.

[14] Lilly S. J., Le Fèvre O., Renzini A., et al., 2007, ApJS, 172, 70.

[15] Millán-Irigoyen I., Mollá M., Cerviño M., et al., 2021, MNRAS, 506, 4781.

[16] Millán-Irigoyen, I., del Valle-Espinosa, M. G., Fernández-Aranda, R., et al. 2022, MNRAS, 517, 3312.

[17] Moreno-Raya M. E., Mollá M., López-Sánchez Á. R., Galbany L., et al., 2016, ApJL, 818, L19.

[18] Moreno-Raya M. E., López-Sánchez Á. R., Mollá M., et al., 2016, MNRAS, 462, 1281.

[19] Moreno-Raya M. E., Galbany L., López-Sánchez Á. R., et al., 2018, MNRAS, 476, 307.

[20] Munari U., Sordo R., Castelli F., Zwitter T., 2005, A&A, 442, 1127.

[21] Pan Y.-C., Sullivan M., Maguire K., et al., 2014, MNRAS, 438, 1391.

[22] Perlmutter S., Aldering G., Goldhaber G., et al., 1999, ApJ, 517, 565.

[23] Phillips M. M., 1993, ApJL, 413, L105.

[24] Riess A. G., Press W. H., Kirshner R. P., 1996, ApJ, 473, 88.

[25] Riess A. G., Filippenko A. V., Challis P., et al., 1998, AJ, 116, 1009.

[26] Sako M., Bassett B., Becker A. C., et al., 2018, PASP, 130, 064002.

[27] Schlegel D. J., Finkbeiner D. P., Davis M., 1998, ApJ, 500, 525.

[28] Scoville N., Aussel H., Brusa M., et al., 2007, ApJS, 172, 1.

[29] Suzuki N., Rubin D., Lidman C., et al., 2012, ApJ, 746, 85.

[30] Timmes F. X., Brown E. F., Truran J. W., 2003, ApJL, 590, L83.

[31] Tody D., 1993, ASPC, 52, 173

[32] Tripp R., 1998, A&A, 331, 815

[33] Trump J. R., Impey C. D., Elvis M., et al., 2009, ApJ, 696, 1195.

Highlights of Spanish Astrophysics XI, Proceedings of the XV Scientific Meeting of the Spanish Astronomical Society held on September 4–9, 2022, in La Laguna, Spain. M. Manteiga, L. Bellot, P. Benavidez, A. de Lorenzo-Cáceres, M. A. Fuente, M. J. Martínez, M. Vázquez- Acosta, C. Dafonte (eds.), 2023

Stellar population studies in the incoming J-PAS survey.

Díaz-García, L.A.[1], **González Delgado, R.M.**[1], **Martínez-Solaeche, G.**[1], **Rodríguez-Martín, J.E.**[1], **García-Benito, R.**[1], **and Pérez, E.**[1]

[1] Instituto de Astrofísica de Andalucía (IAA-CSIC), P.O. Box 3004, 18080 Granada, Spain

Abstract

Our main goal is to determine the stellar population properties of galaxies from the Javalambre Physics of the Accelerating Universe Astrophysical Survey (J-PAS) in order to perform various galaxy evolution studies up to $z \sim 1$. In our galaxy evolution group at the Instituto de Astrofísica de Andalucía (IAA), we have tested and developed our proper SED-fitting and Artificial Neural Network (ANN) codes to constrain a wide set of stellar population parameters (e.g. age, metallicity, extinction, stellar mass, equivalent widths, etc.) by making use of a preliminary data release referred as mini-JPAS. We obtained consistent results from the ANN and SED-fitting analysis of J-PAS-like galaxies in order to constrain their stellar population properties. In addition, we demonstrated that these results are conducive to exploring the cosmic evolution of the star formation rate (SFR) density, the star formation main sequence, the role of environment for quenching galaxies, the radial variation of the stellar content properties of galaxies in clusters, and the evolution of the luminosity and stellar mass functions since intermediate redshift.

1 Introduction

The state-of-the-art multi-filter surveys (e.g. [13, 14, 1, 3]) present promising advantages over standard spectroscopy for galaxy surveys. For instance, there is not a preliminary selection of galaxies, which is only limited by the depth of the survey that is in turn typically deeper than spectroscopic studies with similar telescopes and observational times. In this regard, the photometric calibration of the spectral energy distribution (SED) of galaxies is typically performed for each individual band, which diminishes the annoying systematic colour terms. In addition, multi-band imaging open the possibility of performing pixel-by-pixel studies of galaxies whose apparent sizes are larger than the point spread function (PSF) of the system. Therefore, these surveys bring us the opportunity to study the stellar content of large samples of galaxies in an alternative way. In fact, during the last years there is an increasing number of studies setting constraints over the stellar content properties of galaxies using this kind of data up to intermediate redshift (see e.g. [5, 6, 7] and references therein). Consequently,

these studies offer complementary and very valuable results to the ones obtained by standard spectroscopic data.

The Javalambre Physics of the Accelerating Universe Astrophysical Survey (J-PAS, see [1]) is an ongoing large-scale photometric survey planning to observe 8500 deg^2 of the sky making use of the 2.55m Javalambre Survey Telescope (JST) at the Observatorio Astrofísico de Javalambre (OAJ). J-PAS is an unprecedented multi-filter survey with a unique photometric system that will allow us to observe a huge amount of galaxies since $z \sim 1$ with an equivalent resolving power of $R \sim 60$ in the optical range. This photometric system comprises 54 narrow-band filters with a full width at half maximum of $FWHM \sim$ 145 Å (equally spaced every 100 Å), one broad band ($FWHM \sim$ 495 Å) and one high-pass filter extending to the UV and near-infrared ends of the optical range, which results in an effective optical range of 3500–9300 Å (further details in [1] and [2]). Prior to the installation of the main camera, since J-PAS is an ongoing survey, there is a first data release dubbed mini-JPAS [2]. This previous survey imaged a stripe of 1 deg^2 in the AEGIS field with the J-PAS photometric system and the JPAS-Pathfinder camera installed in the JST. The mini-JPAS survey is being used by the J-PAS collaboration for testing the potential of the J-PAS survey and the performance of the telescope optical system, as well as performing a first scientific exploitation of the data. As detailed in [2] and [8], the primary mini-JPAS photometric catalogue includes more than 15k galaxies at $z \leq 1$ and is 99 % complete at $r = 23.6$ and $r = 22.7$ for point-like and extended sources, respectively. Owing to the mini-JPAS configuration, the typical error for the photometric redshifts (hereafter photo-z) of galaxies is $\sigma_{\rm NMAD} = 0.013$ with an outlier rate of $\eta = 0.39$ at $r < 23$ [10]. It is also of note that $\sim 5\,200$ galaxies per deg^{-2} are expected to present an accuracy of $\sigma_{\rm NMAD} = 0.003$ and $\eta = 0.05$.

We aim at exploring the stellar population properties of galaxies in the mini-JPAS survey with the ultimate goal of preparing all the techniques and methodologies for the incoming J-PAS survey to carry out galaxy evolution and formation studies. In the following, we outline part of the stellar population results and work that we are conducting in our galaxy evolution group at the IAA.

2 Determination of the properties of mini-JPAS galaxies

The methodologies that we developed for determining the stellar population properties of the mini-JPAS galaxies are based on SED-fitting codes for the stellar continuum [4, 8] and on Artificial Neural Networks (ANNs) for measuring and detecting emission lines in galaxies [11]. In our group, we are using two SED-fitting codes: an updated version of the MUlti-Filter FITting code for stellar population diagnostics (MUFFIT, [4]) and another one using Bayesian statistics (BaySeAGal, de Amorim et al., in prep). One of the differences between both codes lies in the star formation historiy (SFH) assumed. MUFFIT is based on non-parametric composite stellar population models (mixtures of two simple stellar population models or SSPs) and BaySeAGal adopts a parametric SFH (the so-called delayed-τ model). In addition, MUFFIT includes the full redshift probability distribution function (zPDF) from [10] for each of the mini-JPAS galaxies, whereas BaySeAGal assumes a unique photo-z value, which corresponds to the maximum of the zPDF from [10]. From the SED-fitting analysis, we

obtain luminosities (all bands), stellar mass, rest-frame colours, age, metallicity, extinction, etc., along with uncertainties and correlations for each galaxy in mini-JPAS (more details in [8]).

Thanks to the width and configuration of the narrow band filters, J-PAS will be a very competitive survey to identify and characterise emission line galaxies. For this purpose, [11] developed a methodology based on ANN algorithms to detect and measure the equivalent width (EW) of Hα, Hβ, [NII], and [OIII] lines up to $z = 0.35$. Moreover, another ANN was developed to classify mini-JPAS galaxies as emission line or quiescent galaxies. These ANNs were trained with synthetic photometry, which was obtained by convolving galaxy spectra from SDSS, CALIFA, and MaNGA with the J-PAS photometric system (further details in [11]).

3 Stellar population studies in mini-JPAS

Using our SED-fitting results, we performed a first study about the stellar content of mini-JPAS galaxies in [8]. The aim of this study was to check the reliability and consistency of the results to identify and characterise galaxy populations since $z \sim 1$ with real data. After correcting for extinction and following the method detailed in [5], we found consistent results pointing out that galaxies exhibit a bimodal distribution of colours in rest-frame colour diagrams, which is tightly related to their stellar content, with a precision equivalent to that obtained for spectroscopic surveys of similar signal-to-noise ratio (S/N). As a reference and for mini-JPAS galaxies with $S/N > 10$, we expect to constrain the stellar population properties of stellar mass and mass-weighted age with a precision of 0.07 ± 0.03 dex and 0.16 ± 0.07 dex, respectively [8]. Furthermore, we are able to constrain the cosmic evolution of the star formation rate density, $\rho_\star$, by the mini-JPAS galaxies at $0.05 \leq z \leq 0.15$ via fossil record methods and our SED-fitting results (see left panel in Fig. 1). All this in good agreement with previous work including spectroscopic data.

Making use of the results obtained from BaySeAGal and the complete and mass-sensitive catalogue of galaxy groups in the J-PAS collaboration (Maturi et al., in prep.), in [9] we studied the role of environment in galaxy evolution up to $z \sim 1$. At increasing stellar mass, the fraction of red and quiescent galaxies also increases, but it is always higher in groups than in the field. Our results point out that the quenching fraction excess (QFE), or the excess of quiescent galaxies in groups with respect to the field, ranges from < 10 % to 60% at stellar masses of 10^{10} and $10^{11.5}$ $M_\odot$, respectively. A similar result was found for transition galaxies or galaxies quenching their star formation but in a more modest way. The fraction of field star-forming galaxies that are quenched per unit of time (or galaxy quenching rate, R_i) also depends on redshift (see right panel in Fig. 1 and [9]).

Through the ANN methodology introduced in Sect. 2, we studied the emission line galaxies (ELGs) in mini-JPAS up to $z = 0.35$ in [12], which is the limit to which the Hα line can be observed with the J-PAS filter system. Thanks to this method, we are able to measure the equivalent widths of the Hα, Hβ, [OIII], and [NII] emission lines, as well as the ionization mechanism via BTP and WHAN diagrams. According to these criteria, we identify ~ 1800

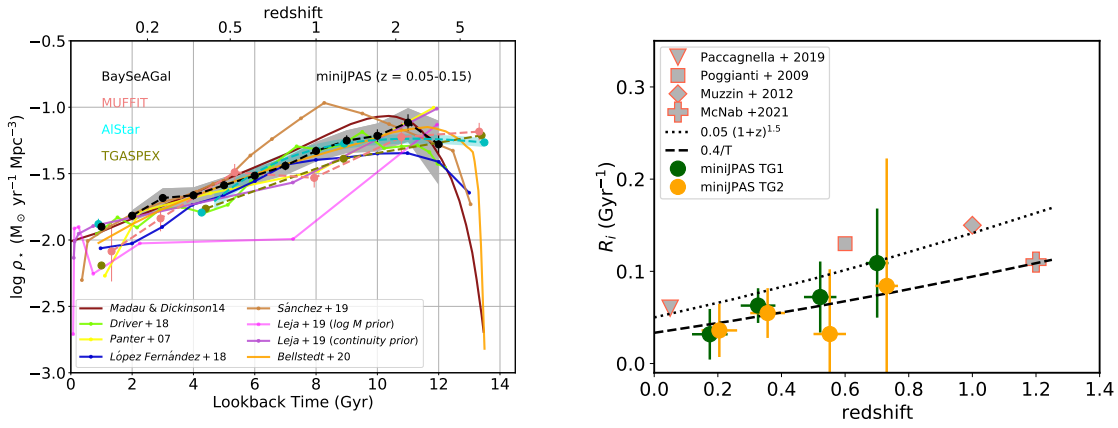

Figure 1: *Left panel*, cosmic evolution of the star formation rate density obtained from mini-JPAS galaxies at $0.05 \leq z \leq 0.15$ with MUFFIT and BaySeAGal (coral and black dots, respectively). *Right panel*, evolution with redshift of the rate of group galaxy quenching for mini-JPAS galaxy groups for two definitions of transition galaxies (green and orange dots). Figures from [8] and [9], respectively.

ELGs up to $z = 0.35$ in mini-JPAS, which are classified as star-forming (SF), active galactic nucleus (Seyfert), and quiescent galaxies (see left panel in Fig. 2). In addition, the SFRs obtained from Hα and Hβ along with the stellar mass obtained via SED-fitting are in agreement with previous studies exploring the star formation main sequence and the cosmic evolution of the SFR density (see right panel in Fig. 2, further details in [12]).

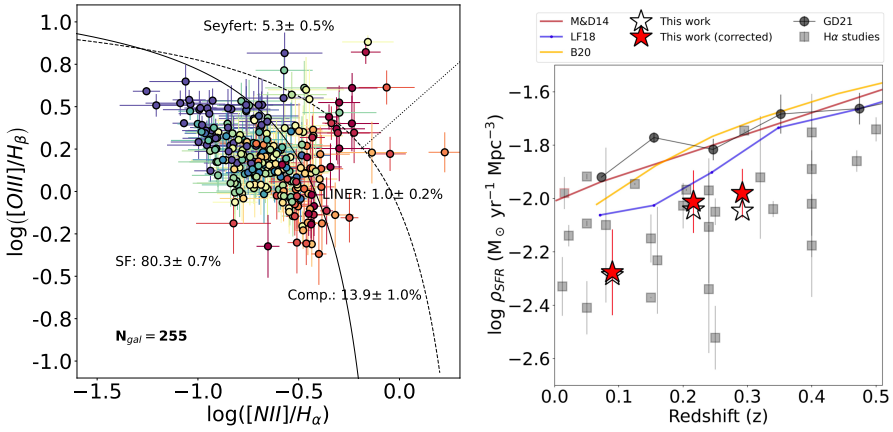

Figure 2: *Left panel*, BPT diagram obtained with the ANNs developed in our group for mini-JPAS galaxies at $z \leq 0.35$ and errors lower than 0.2 dex. Redder colours illustrate more massive galaxies. *Right panel*, evolution with redshift of the star formation rate density obtained from the Hα luminosity using the ANNs (star-shaped markers). Figures from [12].

In a complementary manner, we successfully checked the capability and potential of mini-

JPAS to characterise the stellar population properties of galaxies in clusters (see [15]). In particular, we determined the variation of the stellar population properties of galaxies as a function of the cluster-centric radius in the most massive mini-JPAS galaxy cluster: the mJPC2470-1771 case ($R_{200} \sim 1300$ kpc, $M_{200} \sim 3 \times 10^{14}$ $M_{\odot}$, and $z = 0.29$). For this aim, we used the SED-fitting and ANN results obtained in [8, 12]. In general, the fraction of red galaxies increases in the inner parts of mJPC2470-1771. More precisely, the number of red and blue galaxies within the $0.5 \times R_{200}$ region is roughly the same. We also found that the redder, more metallic and massive galaxies tend to be inside the central part of the cluster, closer to the brightest galaxy of the cluster. On the other hand, blue, less metallic and less massive galaxies are mainly located at distances larger than $0.5 \times R_{200}$ (see Fig. 3). These results suggest that quenching mechanisms are more efficient shutting down the star formation and start at earlier epochs in the inner parts of galaxy clusters.

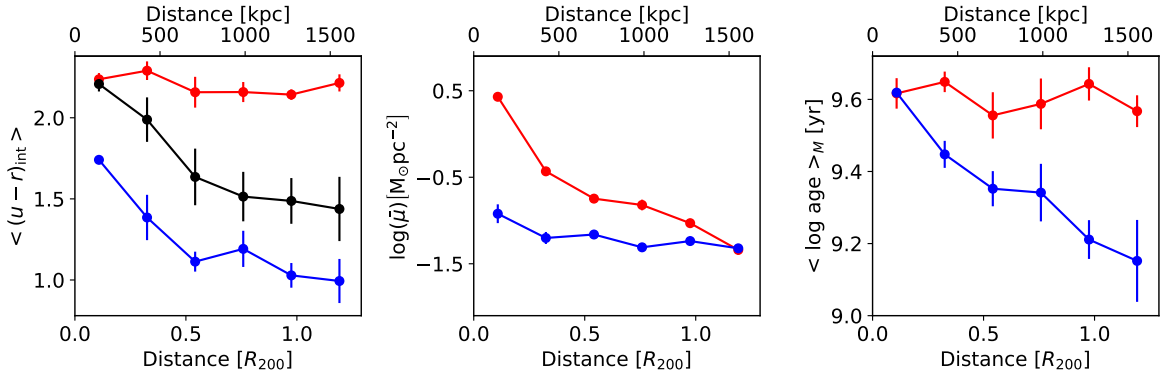

Figure 3: Stellar population properties as a function of the cluster-centric radius in the mini-JPAS galaxy cluster mJPC2470-1771. *From left to right*, $(u - r)$ rest-frame colour corrected for extinction, stellar mass surface density, and mass-weighted age for star-forming and quiescent galaxies (blue and red lines, respectively). Figure from [15].

From the scratch, we developed a statistical methodology to determine the evolution of the parametric stellar mass and luminosity functions of mini-JPAS galaxies up to $z \sim 0.7$ (Díaz-García et al., in prep.). This method is based on a Monte Carlo Markov Chain (MCMC) method involving the probability distribution functions obtained from MUFFIT and will account for all the uncertainties and correlations involved in the analysis, spectral-type, photo-z uncertainties, galaxy-star classification, etc. As a preliminary result, the cosmic evolution of the stellar mass and B-band luminosity densities obtained from the MUFFIT analysis is in good qualitative agreement with previous work in deeper surveys (see Fig. 4).

As a conclusion, we developed a set of methodologies and techniques that have proven to provide reliable stellar population properties of galaxies only using J-PAS-like data. Nowadays, we are ready to perform very promising stellar population studies with the incoming J-PAS survey involving stellar population properties, environment, and emission lines that can be used to carry out galaxy evolution and formation studies in a reliable way up to $z \sim 1$.

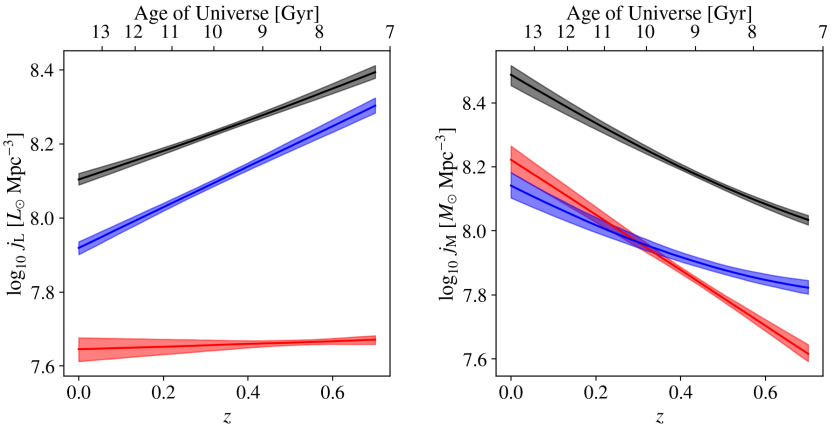

Figure 4: Cosmic evolution of the B-band luminosity and stellar mass densities for quiescent and star-forming mini-JPAS galaxies (red and blue solid lines, respectively). The solid black line illustrates the values for the full galaxy sample.

Acknowledgments

The authors acknowledge financial support from the State Agency for Research of the Spanish MCIU through the "Center of Excellence Severo Ochoa" award to the Instituto de Astrofísica de Andalucía (SEV-2017-0709) and to the PID2019-109067-GB100.

References

[1] Benitez, N., Dupke, R., Moles, M., et al. 2014, ArXiv e-prints, [arXiv:1403.5237]

[2] Bonoli, S., Marín-Franch, A., Varela, J., et al. 2020, A&A, 653, A31

[3] Cenarro, A.J., Moles, M., Cristóbal-Hornillos, D., et al. 2019, A&A, 622, A176

[4] Díaz-García, L.A., Cenarro, A.J., López-Sanjuan, C., et al. 2015, A&A, 582, A14

[5] Díaz-García, L.A., Cenarro, A.J., López-Sanjuan, C., et al. 2019a, A&A, 631, A156

[6] Díaz-García, L.A., Cenarro, A.J., López-Sanjuan, C., et al. 2019b, A&A, 631, A157

[7] Díaz-García, L.A., Cenarro, A.J., López-Sanjuan, C., et al. 2019c, A&A, 631, A158

[8] González Delgado, R.M., Díaz-García, L.A., de Amorim, A., et al. 2021, A&A, 649, A79

[9] González Delgado, R.M., Rodríguez-Martín, J.E., Díaz-García, L.A., et al. 2022, A&A, 666, A84

[10] Hernán-Caballero, A., Varela, J., López-Sanjuan, C., et al. 2021, A&A, 654, A101

[11] Martínez-Solaeche, G., González Delgado, R.M., García-Benito, R., et al. 2021, A&A, 647, A158

[12] Martínez-Solaeche, G., González Delgado, R.M., García-Benito, R., et al. 2022, A&A, 661, A99

[13] Moles, M., Benítez, N., Aguerri, J. A. L., et al. 2008, AJ, 136, 1325

[14] Pérez-González, P. G., Cava, A., Barro, G., et al. 2013, ApJ, 762, 4

[15] Rodríguez-Martín, J.E., González Delgado, R.M., Martínez-Solaeche, G., et al. 2022, A&A, 666, A160

Highlights of Spanish Astrophysics XI, Proceedings of the XV Scientific Meeting of the Spanish Astronomical Society held on September 4–9, 2022, in La Laguna, Spain. M. Manteiga, L. Bellot, P. Benavidez, A. de Lorenzo-Cáceres, M. A. Fuente, M. J. Martínez, M. Vázquez- Acosta, C. Dafonte (eds.), 2023

The extreme relic galaxy NGC 1277 is dark matter deficient.

Comerón, S.[1,2], Cappellari, M.[3], Buitrago, F.[4], Garduño, L. E.[5], Zaragoza-Cardiel, J.[5,6], Zinchenko, I. A.[7,8], Lara-López, M. A.[9,10], Ferré-Mateu, A.[2,1], and Dib, S.[11]

[1] Departamento de Astrofísica, Universidad de La Laguna, E-38200, La Laguna, Tenerife, Spain
[2] Instituto de Astrofísica de Canarias E-38205, La Laguna, Tenerife, Spain
[3] Sub-Department of Astrophysics, Department of Physics, University of Oxford, Denys Wilkinson Building, Keble Road, Oxford OX1 3RH, UK
[4] Departamento de Física Teórica, Atómica y Óptica, Universidad de Valladolid, E-47011 Valladolid, Spain
[5] Instituto Nacional de Astrofísica, Óptica y Electrónica (INAOE), Luis Enrique Erro No. 1, Tonantzintla, Puebla, CP 72840, México
[6] Consejo Nacional de Ciencia y Tecnología, Av. Insurgentes Sur 1582, 03940 México City, México
[7] Faculty of Physics, Ludwig-Maximilians-Universität, Scheinerstr. 1, 81679 Munich, Germany
[8] Main Astronomical Observatory, National Academy of Sciences of Ukraine, 27 Akademika Zabolotnoho St, 03680, Kyiv, Ukraine
[9] Departamento de Física de la Tierra y Astrofísica, Universidad Complutense de Madrid, E-28040 Madrid, Spain
[10] Instituto de Física de Partículas y del Cosmos IPARCOS, Fac. de Ciencias Físicas, Universidad Complutense de Madrid, E-28040 Madrid, Spain
[11] Max Planck Institute for Astronomy, Königstuhl 17, 69117, Heidelberg, Germany

Abstract

Relic galaxies are extremely compact early-type objects that have failed to accrete an extended envelope of stars. We observed the relic galaxy NGC 1277 with the integral field George and Cynthia Mitchel spectrograph (GCMS). The observations also include the regular early-type galaxy NGC 1278, which is used for comparison. We obtained resolved kinematics of both targets and performed a Jeans modelling to determine their dark matter content and distribution. We find that, whereas NGC 1278 has a dark matter fraction compatible with the expectations from models, NGC 1277 displays a negligible dark matter fraction within the radius of 6 kpc (five effective radii) from which we recovered stellar kinematics. We propose that the fact that NGC 1277 is dark matter deficient might explain its relic status. This is because for a galaxy lacking an extended dark matter halo, dynamical friction is greatly reduced, resulting in a small efficiency at accreting satellites.

1 Introduction

The current paradigm for the formation of early-type galaxies (ETGs) is that they are the result of two distinct successive phases of formation (see [16]). First, a dense core is quickly formed. Afterwards, an extended envelope is slowly accreted as smaller objects are cannibalised. In doing so, the size of the ETG increases by a factor of roughly four (e.g., [2]).

A minute fraction of ETGs skip the second evolutionary phase and are left as the passively-evolved remains of the compact ETGs at a redshift $z \sim 2$. These objects, called relic galaxies, are extremely interesting because they allow us to directly study the properties of the early ETGs without suffering from envelope contamination. NGC 1277, discovered by [18], is the cleanest relic galaxy known to date. It is located in the dense environment of the Perseus Cluster, at an estimated distance of 65 Mpc [1].

Here, we study the kinematics of NGC 1277 obtained from deep integral field data. To do so, we used the Jeans Anisotropic Modelling (`JAM`) code [4, 6]. The dataset covers the nearby regular ETG NGC 1278 that we used to obtain a direct comparison between the properties of a relic galaxy and those of an ETG that has undergone the full two-phase evolution.

2 The data

The data were obtained with the George and Cynthia Mitchel spectrograph (GCMS) at the 2.7 m Harlan J. Smith telescope. The fibres of the instrument are $4\farcs16$ in diameter and cover a field of view of $100'' \times 100''$. Through a dithering scheme we obtained a large filling factor and an equivalent exposure time of 2.5 hours per position. We performed our analysis using the spectral range 4400 Å − 6650 Å. The data have a radial coverage of 6 kpc for NGC 1277 (about five effective radii) and 12 kpc for NGC 1278 (about three effective radii).

In order to mitigate the effects of the low angular resolution of the GCMS, we comple-

mented our dataset with kinematics of the innermost $1\farcs6 \times 1\farcs6$ of NGC 1277 obtained by [20] using NIFS, an adaptive-optics-assisted (AO-assisted) integral field spectrograph.

3 Galaxy resolved kinematics and MGE modelling

To obtain resolved stellar kinematics, we fitted the spectra from the GCMS fibres using `pPXF` [8, 7]. For each fibre, we computed the velocity corrected for the mean recession velocity of the galaxy, V, and the velocity dispersion, σ. We calculated $V_{\rm rms} \equiv \sqrt{V^2 + \sigma^2}$, as it is a necessary input for the dynamical modelling (Sect. 4). We selected for further processing the fibres with a good signal-to-noise ratio (S/N > 7 per spectra pixel) and where the error in $V_{\rm rms}$ is smaller than $65\,{\rm km\,s^{-1}}$.

The main goal of the Jeans modelling is to characterise the dark matter halo of the target galaxies. To disentangle the dark matter dynamical effects from those of the baryonic component, baryonic mass distribution models were required. We created them using the code by [3] in order to compute a multi-Gaussian expansion (`MGE`) of baryonic mass maps derived from *HST* colour maps. We assumed mass-to-light ratios based on colours following the recipes from [17, 10] and a Salpeter initial mass function (IMF).

4 Jeans modelling

`JAM` was used to produce Jeans models of the target galaxies. For dark matter haloes we assumed a Navarro-Frenk-White profile with a characteristic radius $r_{\rm s} = 100\,{\rm kpc}$. The Jeans models were fitted to the $V_{\rm rms}$ maps using the Adaptive Metropolis algorithm code `adamet` [5]. The fitted parameters were:

- The deprojected axial ratio of the flattest `MGE`, $q_{\star\,{\rm min}}$. This is equivalent to fitting the inclination of the galaxy.
- The shape of the velocity ellipsoid, which was parametrised by either β_z or β_r, depending on the alignment of the ellipsoid (cylindrical or spherical, respectively).
- The mismatch parameter α, which is a multiplying factor of the mass map that accounts for differences between the actual IMF of the object and the assumed Salpeter IMF.
- The central black hole mass, $M_{\rm BH}$.
- The dark matter fraction within 6 kpc, $f_{\rm DM}(6\,{\rm kpc})$,

For NGC 1277 we fitted $M_{\rm BH}$ using the AO-assisted NIFS kinematics. The resulting mass was fixed in the fit of the more extended GCMS data. Because NGC 1277 is disc-dominated, we assumed it to have a cylindrically-aligned velocity ellipsoid. Since NGC 1278 is a slow rotator, we assumed that its ellipsoid is spherically-aligned. The inferred posterior probability distribution functions of the model parameters are shown in Figs. 1 and 2.

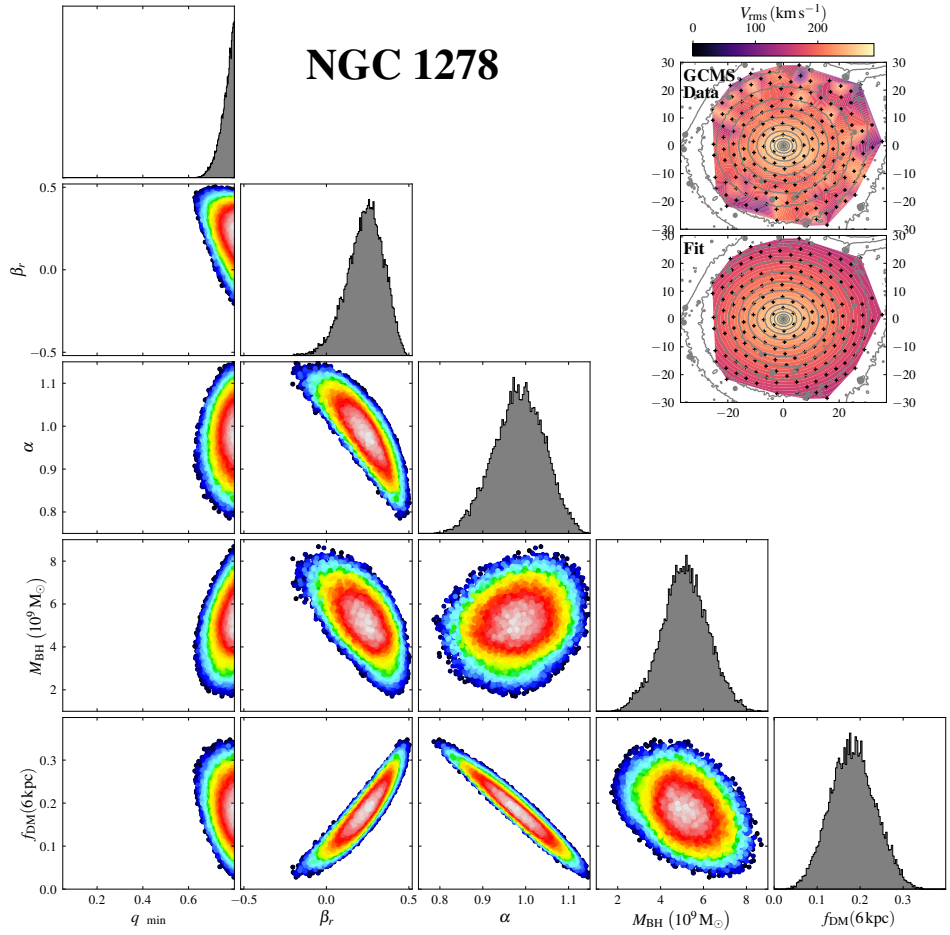

Figure 1: Result of the Jeans modelling to the GCMS-based $V_{\rm rms}$ map of NGC 1278. The panels show the probability distribution of the fitted parameters marginalised over either two parameters (contour plots), or one parameter (histograms). In the contour plots, white shades indicate the maximum likelihood and blue shades correspond to a three-sigma confidence level. The upper-right panels show the observed and the fitted $V_{\rm rms}$ maps. The grey contours correspond to surface brightness contours separated by 0.5 mag arcsec^{-2} intervals, and the black + signs indicate the position of the centre of the GCMS fibres.

5 Discussion

As a sanity test, we checked that the fitted central black hole mass for NGC 1277 is compatible with that obtained by previous authors [11, 20, 14]. We thus confirm that the central black hole in NGC 1277 is over-massive according to several scaling relations, but not quite as much as postulated by [19], who found $M_{\rm BH} > 10^{10}\,{\rm M}_\odot$.

The large mismatch parameter value of $\alpha \approx 1.2$ indicates that NGC 1277 has a bottom-heavy IMF, confirming the results by [15, 12]. On the other hand, NGC 1278 has a smaller

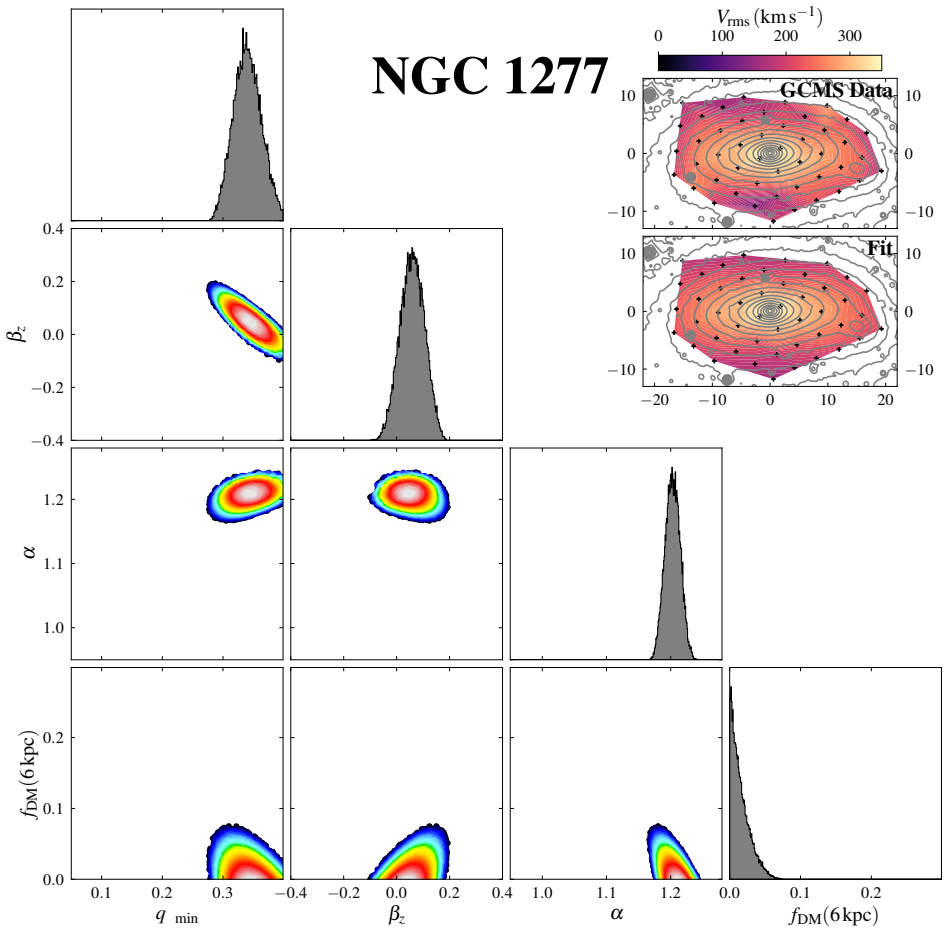

Figure 2: Same as Fig. 1, but this time for NGC 1277. Here the black hole mass was fixed to $M_{\rm BH} = 4.58 \times 10^9\,{\rm M}_\odot$, as obtained from the AO-assisted kinematics measured by [20].

α, indicating an IMF in line with that of regular ETGs.

The most striking result of the fits is that NGC 1277 has a negligible fraction of dark matter within 6 kpc. Combining the stellar-mass-to-halo relation from [13] with the dark matter halo shape parametrisation from [9], we found that this result is in a strong tension with the expected fraction $f_{\rm DM}(6\,{\rm kpc}) \approx 0.1$. On the other hand, the measured dark matter halo in NGC 1278 is fully compatible with the expectations.

How is it possible that one of the densest known galaxies has formed within an under-dense dark matter halo? The parsimony aesthetical criterion suggests that the two peculiarities of the galaxy (the relic status and the lack of detectable dark matter) are related. We propose that there is a causation between the lack of dark matter and the failure to accrete a stellar envelope. Indeed, the smaller the density of the dark matter halo, the lesser the effect of dynamical friction. Hence, small galaxies approaching NGC 1277 are not dragged inwards as efficiently as in a galaxy with a regular dark matter halo, resulting in little envelope growth.

To test the plausibility of the above scenario we need to find a viable formation mechanism to explain a compact giant galaxy with little dark matter. In a study by [21] one such galaxy is found within the $1.2 \times 10^6\,\mathrm{Mpc}^3$ volume of the Illustris simulation. It is very suggestive that this number is close to the observed density of relics (three in $5 \times 10^6\,\mathrm{Mpc}^3$; [12]).

Acknowledgments

SC and MALL acknowledge support from the Ramón y Cajal programme funded by the Spanish Government (references RYC2020-030480-I and RYC2020-029354-I). SC acknowledges funding from the State Research Agency (AEI-MCINN) of the Spanish Ministry of Science and Innovation under the grants "The structure and evolution of galaxies and their central regions" with reference PID2019-105602GB-I00/10.13039/501100011033, and "Thick discs, relics of the infancy of galaxies" with reference PID2020-113213GA-I00. AFM has received support from the Severo Ochoa Excellence scheme (CEX2019-000920-S) and grant PID2019-107427GB-C32 from the MCIU. MALL acknowledges support from the Spanish grant PID2021-123417OB-I00.

References

[1] Beasley, M. A., Trujillo, I., Leaman, R., & Montes, M. 2018, Nature, 555, 483

[2] Buitrago, F., Trujillo, I., Conselice, C. J., et al. 2008, ApJ, 687, L61

[3] Cappellari, M. 2002, MNRAS, 333, 400

[4] Cappellari, M. 2008, MNRAS, 390, 71

[5] Cappellari, M., Scott, N., Alatalo, K., et al. 2013b, MNRAS, 432, 1709

[6] Cappellari, M. 2020, MNRAS, 494, 4819

[7] Cappellari, M. 2022, arXiv e-prints, arXiv:2208.14974

[8] Cappellari, M. & Emsellem, E. 2004, PASP, 116, 138

[9] Child, H. L., Habib, S., Heitmann, K., et al. 2018, ApJ, 859, 55

[10] Cimatti, A., Cassata, P., Pozzetti, L., et al. 2008, A&A, 482, 21

[11] Emsellem, E. 2013, MNRAS, 433, 1862

[12] Ferré-Mateu, A., Trujillo, I., Martín-Navarro, I., et al. 2017, MNRAS, 467, 1929

[13] Girelli, G., Pozzetti, L., Bolzonella, M., et al. 2020, A&A, 634, A135

[14] Krajnović, D., Cappellari, M., McDermid, R. M., et al. 2018, MNRAS, 477, 3030

[15] Martín-Navarro, I., La Barbera, F., Vazdekis, A., et al. 2015, MNRAS, 451, 1081

[16] Naab, T., Johansson, P. H., & Ostriker, J. P. 2009, ApJ, 699, L178

[17] Roediger, J. C. & Courteau, S. 2015, MNRAS, 452, 3209

[18] Trujillo, I., Ferré-Mateu, A., Balcells, M., Vazdekis, A., & Sánchez-Blázquez, P. 2014, ApJ, 780, L20

[19] van den Bosch, R. C. E., Gebhardt, K., Gültekin, K., et al. 2012, Nature, 491, 729

[20] Walsh, J. L., van den Bosch, R. C. E., Gebhardt, K., et al. 2016, ApJ, 817, 2

[21] Yu, H., Ratra, B., & Wang, F.-Y. 2018, arXiv e-prints, arXiv:1809.05938

Highlights of Spanish Astrophysics XI, Proceedings of the XV Scientific Meeting of the Spanish Astronomical Society held on September 4–9, 2022, in La Laguna, Spain. M. Manteiga, L. Bellot, P. Benavidez, A. de Lorenzo-Cáceres, M. A. Fuente, M. J. Martínez, M. Vázquez- Acosta, C. Dafonte (eds.), 2023

The interplay of internal and external processes in the buildup of disk galaxies: thick disks in AURIGA simulations.

Pinna, F.[1], **Walo-Martín, D.**[2,3], **and Grand, R. J. J.**[2,3]

[1] Max Planck Institute for Astronomy, Koenigstuhl 17, D-69117 Heidelberg, Germanyemail: pinna@mpia.de
[2]Instituto de Astrofísica de Canarias, Calle Vía Láctea s/n, E-38205 La Laguna, Tenerife, Spain
[3]Departamento de Astrofísica, Universidad de La Laguna, Av. del Astrofísico Francisco Sánchez s/n, E-38206, La Laguna, Tenerife, Spain

Abstract

Recent integral-field spectroscopy observations have revealed that thick- and thin-disk star-formation histories are regulated by the interplay of internal and external processes. We analyze stellar-population properties of 24 spiral galaxies from the AURIGA zoom-in cosmological simulations, to offer a more in-depth interpretation of observable properties. We extracted edge-on maps of stellar age, metallicity and [Mg/Fe] abundance, and star-formation and chemical-evolution histories of thin and thick disks. These show signs of the interplay between internal chemical enrichment and gas and star accretion. Thick disks show particularly complex stellar populations, including an in-situ component, formed from both enriched and more pristine accreted gas, and a significant fraction of ex-situ stars.

1 Introduction

The spatially resolved stellar-population analysis of massive galactic disks allows us to draw the spatial and temporal distribution of star formation during the mass assembly of disk-dominated galaxies. Properties of thick disks, old, metal poor and enhanced in α elements, trace mostly the early stages of galaxy formation, while younger metal-rich thin disks tell us about later evolutionary phases [7, 14]. While it is clear that thin disks form mostly in situ with their massive star formation being fuelled by gas accretion, there is no common agreement on how thick disks form. Three main formation scenarios were proposed to explain thick-disk properties: their stars may have formed in situ, at high redshift, from turbulent gas [2], in satellites that were later directly accreted [1], or in a preexisting thinner disk which was later dynamically heated [3].

Observational studies of thick disks are generally based on edge-on galaxies, where fainter thick disks can be morphologically decomposed from the bright thin disks [5]. Spectroscopic

studies have revealed some variety in thick-disk properties, pointing towards one or another formation scenario [6, 9, 14]. On the other hand, detailed star-formation and chemical-evolution histories of thick disks, extracted from deep integral-field spectroscopic MUSE observations, have recently unveiled a combination of in-situ and ex-situ stellar populations. Thick disks would result from complex scenarios with different mechanisms at play [10, 11, 12]. Here we probe these combined scenarios using numerical simulations.

2 Simulations, sample selection and data analysis

The AURIGA project [8] includes zoom-in magneto-hydrodynamical cosmological simulations of 30 Milky Way-mass late-type galaxies, with stellar masses between 10^{10} and $\sim 10^{11}\,\mathrm{M}_{\odot}$. These were obtained by re-simulating 30 relatively isolated haloes from the parent largest-volume Dark Matter Only EAGLE simulation [13]. The galaxy formation model, including star formation, stellar and black-hole feedback and magnetic fields, led to realistic galaxies matching a large variety of properties found in observed galaxies (e.g. morphologies and properties of structures such as spiral arms or bars, galaxy sizes and masses, kinematic and chemical properties). The initial conditions to be used in the re-simulations, and in particular the initial distribution of dark-matter particles, were taken from the haloes in the parent simulation. Then, each dark-matter particle was substituted by a pair of a dark-matter particle and a gas cell. AURIGA simulations offer different resolution levels [8], and we use "level 4" in this work, corresponding to typical masses of high-resolution dark-matter and baryonic-mass particles of $\sim 3 \times 10^5\,\mathrm{M}_{\odot}$ and $\sim 5 \times 10^4\,\mathrm{M}_{\odot}$, respectively. The physical gravitational softening length for stellar and high-resolution dark-matter particles was set to 369 pc at redshift $z < 1$.

From the original sample of 30 galaxies, we selected a sample of 24 with a clear disk structure and no strong distortions due to mergers. We projected the galaxies in an edge-on view, to allow a similar analysis to what is usually done in integral-field spectroscopy observations. We performed a Voronoi binning to ensure a similar number of star particles in each spatial bin and we used for the analysis a region of radius the optical radius R_{opt} of the galaxy [8] and of height $2 \times h_{scale}$, where h_{scale} is the standard deviation of the vertical positions of stars at R_{opt}. For each galaxy, we fitted vertical luminosity-density profiles, extracted in four radial bins, with two components associated with the thin and the thick disks, each one represented by a hyperbolic secant square function. The fits gave us the average height, for each galaxy, at which the light of the thick disk starts to dominate. This allows us to define the thick and the thin disks in a purely geometrical way, using the same definition that is usually adopted in edge-on external galaxies [4, 6, 10, 11, 12]. We show in Fig. 1 mock images, of a size of 50 kpc×20 kpc, of the 24 galaxies in our sample. We indicate with orange dashed horizontal lines the height above (below) which the thick disk starts to dominate. The region between these lines is dominated by the thin disk. For one galaxy, Au1, we obtained a good fit only when using one disk component instead of two, indicating that this galaxy does not have a clear double-disk structure.

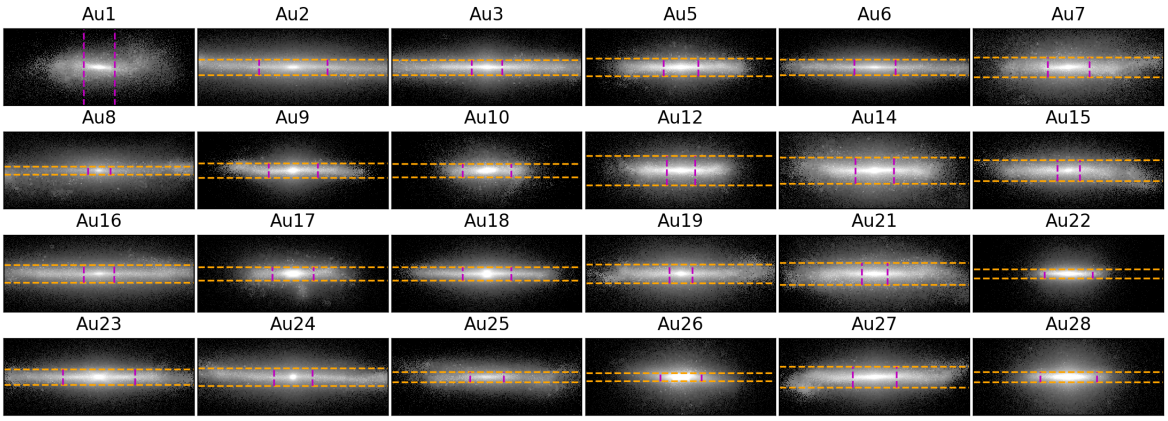

Figure 1: Mock V-band edge-on images of our selected sample of 24 Milky Way-like galaxies from AURIGA simulations. The region showed here has a 50 kpc×20 kpc size. The two orange dashed horizontal lines indicate where the light of the thin-disk component dominates over the thick disk (between the two lines), and where the thick disk dominates (above and below that region). The region between the two vertical magenta dashed lines is dominated by a central component (a bar in barred galaxies and a classical bulge in non-barred galaxies).

3 Results and discussion

Stellar populations. We mapped the stellar populations of the 24 galaxies. In the thick-disk regions, we found a variety of ages, with average values respectively between 5 and 9 Gyr. Average total metallicities ([M/H]) are between -0.2 and 0.1 dex, and [Mg/Fe] abundances between 0.12 and 0.17. A sharp change in the stellar-population parameters corresponds to the transition between the thick- and thin-disk dominated regions (Pinna et al., in prep.). In Fig. 2, we summarize and compare the stellar-population properties of thick and thin disks. Each point indicates the average age, [M/H] or [Mg/Fe] (respectively in the left, middle and right panels) calculated in the thick- and the thin-disk dominated regions. Thick disks are in all cases older, more metal-poor and more [Mg/Fe] enhanced than thin disks. We have color coded each point according to the total stellar mass of the galaxy. While a general trend of the thick- and thin-disk properties with galaxy stellar mass is not clear, galaxies with the lowest masses show smaller differences between the properties of the thin and the thick disks (points closer to the one-to-one line).

We extracted the star-formation histories of the thin and thick disks, in terms of the mass fraction of stars of a specific age, averaging the age distribution in the regions dominated by each one of them [10, 11, 12]. We color coded age bins according to their average metallicity and [Mg/Fe] abundance, to interpret these plots in terms of chemical evolution. Star-formation histories of the full sample can be found in Pinna et al. (in prep.), while we describe an example later in this section.

In-situ and ex-situ components. To assess the ex-situ formation scenario of thick disks, we tracked star particles during the simulations, and classified them as in situ or ex situ. We

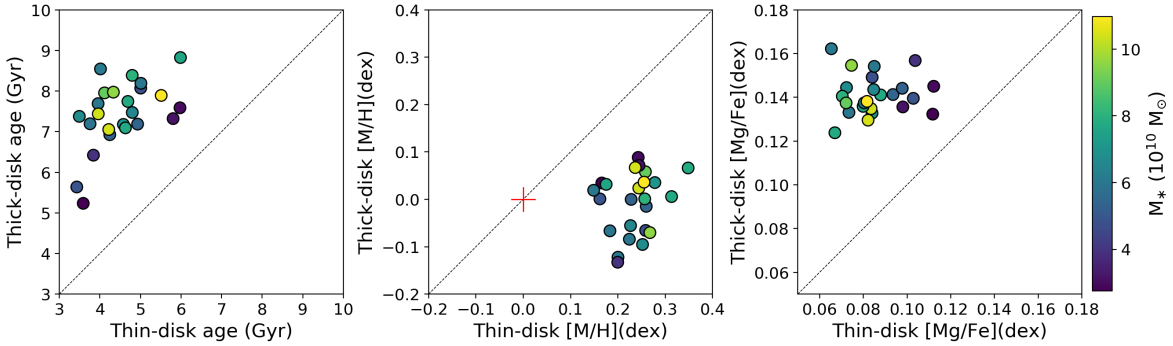

Figure 2: Thick-disk versus thin-disk stellar-population properties. From left to right: age, [M/H] and [Mg/Fe] abundance. Points are color coded according to the total stellar mass of the galaxy. The one-to-one line is indicated as black dashed, in each panel. A red "+" symbol indicates solar metallicity in the middle panel.

mapped the fraction of accreted stars for the full galaxy sample, and found that they are mostly located in the thick-disk dominated region (see Pinna et al., in prep.). Thick disks host a fraction of accreted stars between 5 and 65% of their mass, depending on the specific galaxy. The accreted mass is less than 50% in most cases, and thick disks are therefore mostly formed in situ with a strong contribution from satellites.

A representative galaxy: Au5. We show here one specific galaxy as an example, Au5, representative of our sample. Au5 is a barred spiral galaxy of stellar mass $\sim 7 \times 10^{10} M_{\odot}$. Stellar-population maps of Au5 are shown in Fig. 3, and show an old, metal-poor and [Mg/Fe]-enhanced thick disk and a young, very metal-rich and poorly [Mg/Fe]-enhanced thin disk. We show in Fig. 4 (left panels) the star-formation history of the thick disk in Au5, color coded by [M/H] (top panels) and [Mg/Fe] (bottom panels). At the oldest ages (until about 12 Gyr ago), we see a global increase in the star-formation rate (or the mass fraction in each age bin, evolving across time from right to left in each panel), and a later decrease at young ages (from about 7 Gyr ago to now), with numerous star-formation bursts across the galaxy life. The colors display a global chemical enrichment, transitioning from metal-poor values and a strong [Mg/Fe] enhancement at the oldest ages, to slightly subsolar metallicities and slightly supersolar [Mg/Fe] values at very recent times. However, on top of this global trend, both [M/H] and [Mg/Fe] respectively drop or rise back to previous values, on different occasions across the thick-disk evolution. Similar features are found in most galaxies of our sample.

In order to understand the origin of these [M/H] and [Mg/Fe] oscillations, which often correspond to star-formation bursts, we decomposed the star-formation histories into in-situ and ex-situ components, and revealed that the oscillations in the chemical abundances are driven by the combination of these two components. In Au5 (Fig. 4, middle and right panels), a satellite contributed ∼35% of the thick-disk mass. This satellite had its own chemical evolution (right panels), and an enhanced chemical enrichment during the star-formation burst at the final stage of the merger (at ages of about 7 Gyr; note that these higher metallicities are still much lower than the thin-disk values). The in-situ component

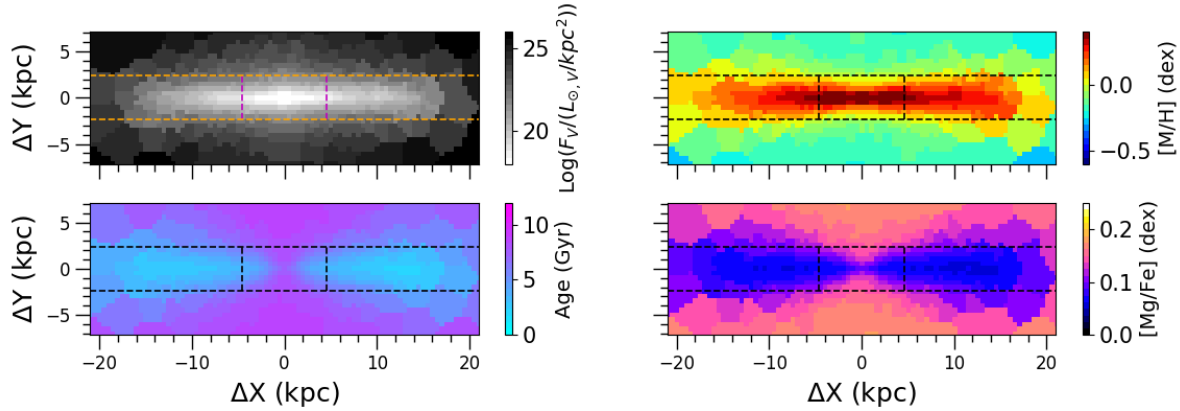

Figure 3: Maps of the galaxy Au5 covering a central region of size $2R_{opt} \times 4h_{scale}$. Logarithmic luminosity density (top-left panel), age (bottom-left panel), [M/H] (top-right panel), and [Mg/Fe] abundance (bottom-right panel). Dashed horizontal lines indicate the distance from the midplane at which the thick disk starts to dominate. The region between the dashed vertical lines is dominated by the bar.

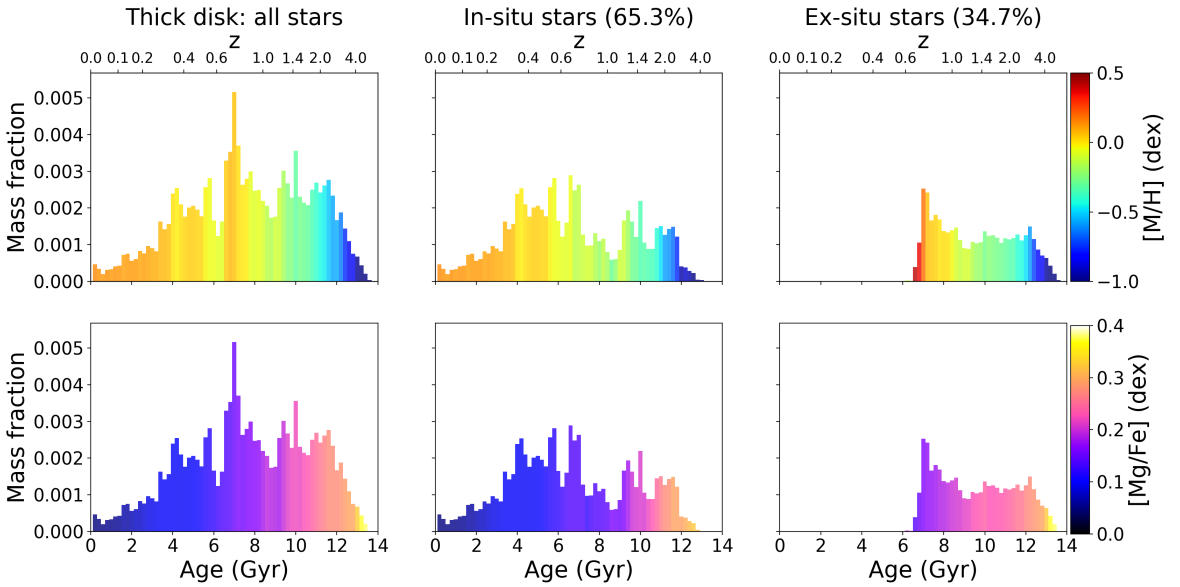

Figure 4: Star-formation history of the thick disk in Au5, color-coded by [M/H] (top panels) and [Mg/Fe] abundance (bottom panels). Left panels include all stars, while middle and right panels include only stars formed respectively in situ or ex situ. The corresponding mass fraction (over the total thick-disk mass) is indicated on top of each column.

(middle panels) is characterized by several star-formation bursts with lower metallicity values (and higher [Mg/Fe]) than immediately younger and older ages. These drops in metallicity are driven by the accretion of gas, mostly coming from the satellite.

4 Conclusions

We analyze the properties of thick and thin disks in a sample of 24 spiral galaxies from AURIGA simulations. Thick and thin disks were defined geometrically in an edge-on projection, according to the regions where their light dominates. Similarly to what was previously found in most observations [4, 7, 9, 10, 12], thick disks are older, more metal poor and [Mg/Fe] enhanced than thin disks. We investigated the fraction of in-situ and ex-situ particles and their contribution in the star-formation histories of thick disks. These results show that although most of the thick-disk mass was formed in situ, but with an important contribution of gas accreted at the time of frequent mergers, they host a significant fraction of accreted stars (in some cases, even most of their mass). Thin disks, as expected from previous observations [7, 10], host a very low mass fraction of accreted stars, and the bulk of their mass was formed at recent times thanks to a large amount of accreted gas.

Star-formation histories of thick and thin disks, and thus of disk galaxies, result from the interplay of internal and external processes: the internal chemical enrichment is challenged by the accretion of more pristine gas and more metal-poor stars.

References

[1] Abadi, M. G., Navarro, J. F., Steinmetz, M., et al., 2003, ApJ, 597, 21.

[2] Brook, C. B., Kawata, D., Gibson, B. K., et al., 2004, ApJ, 612, 894.

[3] Di Matteo, P., Lehnert, M. D., Qu, Y., et al., 2011, A&A, 525, L3.

[4] Comerón, S., Salo, H., Janz, J., et al. 2015, A&A, 584, A34.

[5] Comerón, S., Salo, H., Knapen, J. H. 2018, A&A, 610, A5.

[6] Comerón, S., Salo, H., Knapen, J. H., et al., 2019, A&A, 623, A89.

[7] Gallart, C., Bernard, E. J., Brook, C. B., et al. 2019, Nature Astronomy, 3, 932.

[8] Grand, R. J. J., Gómez, F. A., Marinacci, F., et al. 2017, MNRAS, 467, 179.

[9] Kasparova, A. V., Katkov, I. Y., Chilingarian, I. V., et al. 2016, MNRAS, 460, L89.

[10] Martig, M., Pinna, F., Falcón-Barroso, J., et al. 2021, MNRAS, 508, 2458.

[11] Pinna, F., Falcón-Barroso, J., Martig, M., et al. 2019, A&A, 623, A19.

[12] Pinna, F., Falcón-Barroso, J., Martig, M., et al. 2019, A&A, 625, A95.

[13] Schaye, J., Crain, R. A., Bower, R. G., et al. 2015, MNRAS, 446, 521

[14] Yoachim, P., & Dalcanton, J. J. 2008, ApJ, 683, 707.

Highlights of Spanish Astrophysics XI, Proceedings of the XV Scientific Meeting of the Spanish Astronomical Society held on September 4–9, 2022, in La Laguna, Spain. M. Manteiga, L. Bellot, P. Benavidez, A. de Lorenzo-Cáceres, M. A. Fuente, M. J. Martínez, M. Vázquez- Acosta, C. Dafonte (eds.), 2023

The separated star formation main sequence of bulges and discs. New clues for the galaxy mass assembly.

Méndez-Abreu, J[1,2], de Lorenzo-Cáceres, A.[1,2], and Sanchez, S. F.[3]

[1] Departamento de Astrofísica, Universidad de La Laguna, 38205, La Laguna, Tenerife, Spain
[2] Instituto de Astrofísica de Canarias, 38200, La Laguna, Tenerife, Spain
[3] Instituto de Astronomía, Universidad Nacional Autónoma de México, A.P. 70-264, 04510 México, D.F., México

Abstract

Disc galaxies are complex systems shaped by different stellar structures such as bulges, discs, and bars. Every galaxy structure keeps a unique memory of their past evolution, thus, understanding the mass assembly of disc galaxies can only be achieved by analysing separately all these independent footprints of past evolution. In this work, we have analysed the separated star formation main sequence (SFMS) of bulges and discs in the CALIFA sample. To this aim, we use the C2D algorithm to separate the spectra of bulges and discs using the information provided by the CALIFA integral field survey. We find that the star formation in galaxies mainly occurs in the disc component and not in bulges. Remarkably, once we only account for the disc mass, even the discs of early-type galaxies are compatible with the SFMS defined by star forming galaxies at z $\sim$ 0. Moreover, we find a strong mass depedence in the SFMS. For the bulges, only the low-mass bulges in late-type spirals ($\log M_{\star,\mathrm{b}}/M_{\odot} < 9$) are compatible with the SFMS of z $\sim$ 0 star-forming galaxies. The fraction of discs compatible with the SFMS is also a function of the disc (or total) stellar mass. Our results remark the importance of separating the spectral properties of different galaxy structures to provide a whole picture of the galaxy mass assembly throughout cosmic time.

1 Introduction

A powerful tool to study the evolution of the star formation rate (SFR) in galaxies is provided by scaling relations such as the star formation main sequence (hereafter, SFMS), a tight relation between a galaxy's SFR and its total stellar mass ($M_{\star}$; [1]). This relationship exists out to high redshifts, increasing its normalization to higher values at earlier epochs such that SFRs at a fixed stellar mass are higher by a factor of ~ 20 at $z \sim 2$ [5, 26]. The position of the

galaxies with respect to the SFMS, at any given epoch, gives us information about whether the SFR is enhanced or suppressed relative to the mean for their stellar mass. Despite the large amount of literature in the topic, most of the works on the properties of the SFMS have been limited to studies of star-forming galaxies. Nevertheless, it is known that ETGs remain well below the SFMS [23], with various processes invoked as responsible for the differences in SFR with respect to star forming galaxies. These include: i) internal structure (such as bars and bulges; [31]), cold gas fraction [25], interaction with other galaxies [30] and the presence of an AGN [10, 27].

Observationally, it has become increasingly clear that a general scenario to understand the trigger and shut-down of star-formation in galaxies must include a description on how this happens for their different stellar structures, in particular for their main components: bulges and discs. The difficulties inherent to identify, and separate, these structures have hindered most of our advance in this topic to photometry-based studies. They generally use standard photometric decomposition techniques applied to broad-band galaxy images [22, 21, 8, 6]. On the other hand, even after the revolution introduced by integral-field spectrographs, spectroscopic studies have been mostly limited to radial analysis of galaxies [12], or in the best cases to define regions where the light of each component (bulge and disc) dominates over the others using segmentation maps [9, 3, 7]. Fortunately, the necessity to understand the stellar population properties and mass growth of galactic structures have led to some methodological advances: i) spectro-photometric techniques, understood as an extension of standard photometric decomposition techniques to the case of IFS data (BUDDI, [14]; C2D, [18]); ii) kinematic decomposition of the spectra into galaxy components [4], and iii) orbital decomposition into dynamically different structures using Schwarzchild modelling [32].

In this work, we explore for the first time the SFR vs. $M_\star$ relation of ETGs separated into their bulge and disc components. To this aim, we use the new algorithm C2D [17] designed to perform spectro-photometric decompositions of galaxy structures using integral field spectroscopy (IFS), in combination with Pipe3D [29], a taylor-made pipeline to retrieve the stellar populations and ionised-gas properties from IFS.

2 The CALIFA sample

A detailed description of the galaxy sample used in this study can be found in [16]. As a brief reminder, we have studied a sample of 129 galaxies drawn from the CALIFA data release 3 (DR3; [28]. The galaxy sample was selected as unbarred following the photometric decomposition analysis of the SDSS imaging presented in [20]. From this work we found that 58 galaxies were well described by a Sérsic bulge and a single exponential disc, 40 galaxies required a broken disc profile in addition to the Sérsic bulge, and 31 are early-type galaxies fitted with a two component model (Sérsic+single exponential) even if their fit is statistically indistinguisable from a single component (pure Sérsic) model (see [19],for details). The spectro-photometric decomposition of our sample into separated bulge and disc datacubes was performed using C2D [18]. The stellar population analysis shown in this paper was performed using the Pipe3D pipeline. This software has been thoroughly applied to

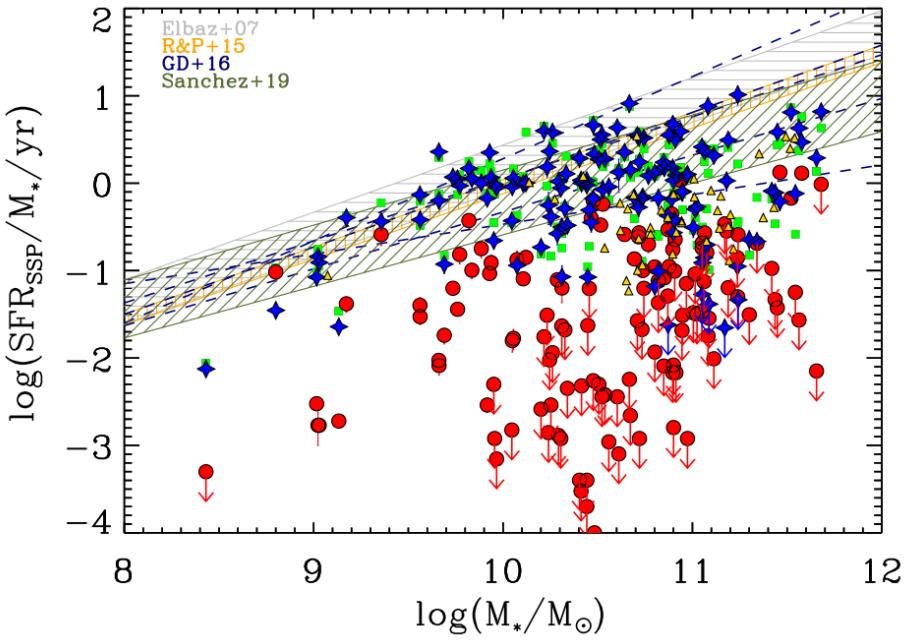

Figure 1: Star formation rate (SFR) vs. galaxy stellar mass. The values for bulges and discs are shown with red circles and blue stars, respectively. Green squares represent measurements of the same galaxies, but considering the galaxy as a whole. Yellow triangles display the control sample of elliptical galaxies. The best fit to the SFMS from Elbaz et al. (2007, Grey), Renzini & Peng (2015, Orange), González Delgado et al. (2016, Navy), Sánchez et al. (2019, Green). Downward arrows mark where the measured SFR is an upper limit (see text for details).

CALIFA data and provides, among others, luminosity/mass weighted ages and metallicities, star formation histories, and intensity maps of strong emission lines for both components [29].

3 The separated SFMS of bulges and discs

Figs. 1 and 2 show the relation between the SFR of our bulges and discs and both the stellar mass of the host galaxy and the stellar mass of each component, respectively. In order to provide a complete picture for our whole sample, we computed the SFR using the analysis of the stellar populations and the recipe given in [13]. We refer the readers to [17] for a detailed description of the process applied to this dataset, and for a discussion on the difference with SFR derived from ionised gas emission lines. The star formation main sequence (SFMS) derived from previous studies in the literature is also shown for comparison, as well as the location of the control sample of ellipticals and the position of the galaxies in the sample if they are considered as a whole.

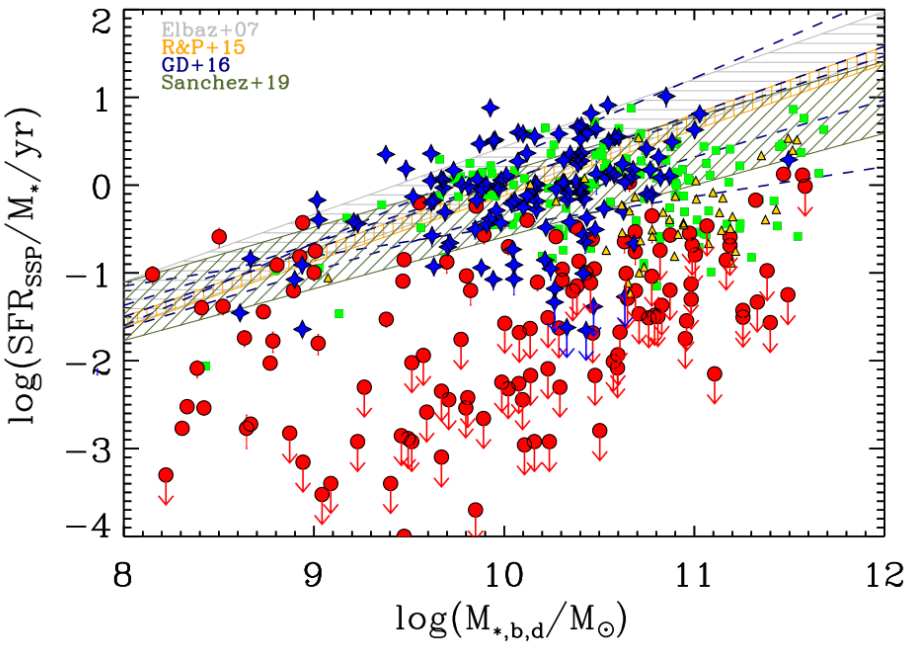

Figure 2: Same as Fig. 1, but using the stellar mass of each component.

The comparison of our bulges and discs with the SFMS derived for star forming galaxies at $z \sim 0$ shows clearly how, independently on which stellar mass is used, most of the discs are compatible with the SFMS whereas most of the bulges lie below this relation, i.e., they are mostly in the region of the diagram occupied by retired galaxies [2]. We find a similar result in [17] using only early type galaxies, and this was also found in [3] for CALIFA galaxies. In particular, we find that, when considering each component stellar mass, 16 (12%) bulges and 99 (77%) discs are compatible (within 1σ) with the SFMS defined in [26]. The fraction of bulges compatible with the SFMS is strongly dependent with the bulge mass. We do not find any bulges compatible with the SFMS in the high mass bin ($\log M_\star/M_\odot > 10.5$), but they reach 38% for bulges with $\log M_\star/M_\odot < 9$. Therefore low-mass bulges are more subject to show recent star formation. The trend is similar for discs even if less dramatic. About 72% of the high-mass discs ($\log M_\star/M_\odot > 10$) lie in the SFMS and this number rises to 91% when considering those with $\log M_\star/M_\odot < 10$. When considering the galaxies as a whole and applying the same analysis, we find that 67% of the galaxies are compatible with the SFMS. Galaxies also show a decline in their fraction of galaxies located in the SFMS with global stellar mass. This is such that 91%, 73%, and 37% of galaxies with masses $9 < \log M_\star/M_\odot < 10$%, $10 < \log M_\star/M_\odot < 11$, and $11 < \log M_\star/M_\odot < 12$ are in the SFMS, respectively. We also computed these fractions as a function of the bulge mass finding that 88%, 59%, and 31% of the galaxies with bulge masses $9 < \log M_\star/M_\odot < 10$, $10 < \log M_\star/M_\odot < 11$, and $11 < \log M_\star/M_\odot < 12$ lie in the SFMS, respectively. Finally, we compare the fraction of bulges and elliptical galaxies that are compatible with the SFMS. We find that, in the mass range where both sample are representative ($10 < \log M_\star/M_\odot < 11.5$), elliptical galaxies are

more prone to star formation (16% in the SFMS) than bulges (3%). Our results are in good agreement with those presented in Lang et al. (2014). Using a separation between star forming galaxies (SFG) and retired galaxies (RG) based on a threshold on their specific SFR (sSFR), they found a strong increase in the fraction of retired galaxies with global galaxy mass and bulge mass, changing from $\sim 10\%$ at $\log M_\star/M_\odot = 10$ to 50% at $\log M_\star/M_\odot = 11.3$. Despite in this work we used the location (or not) of a galaxy with respect to the SFMS to identify SFGs (RGs), the quantitative agreement is remarkable.

Acknowledgments

JMA acknowledges the support of the Viera y Clavijo Senior program funded by ACIISI and ULL. JMA and AdLC acknowledge support from Spanish Ministerio de Ciencia, Innovación y Universidades through grant PID2021-128131NB-I00.

References

[1] Brinchmann, J., Charlot, S., White, S. D. M., et al. 2004, MNRAS, 351, 1151

[2] Cano-Díaz, M., Sánchez, S. F., Zibetti, S., et al. 2016, ApJl, 821, L26

[3] Catalán-Torrecilla, C., Gil de Paz, A., Castillo-Morales, A., et al. 2017, ApJ, 848, 87

[4] Coccato, L., Fabricius, M. H., Saglia, R. P., et al. 2018, MNRAS, 477, 1958

[5] Daddi, E., Dickinson, M., Morrison, G., et al. 2007, ApJ, 670, 156

[6] de Lorenzo-Cáceres, A., Méndez-Abreu, J., Thorne, B., et al. 2020, MNRAS, 494, 1826

[7] de Lorenzo-Cáceres, A., Sánchez-Blázquez, P., Méndez-Abreu, J., et al. 2019b, MNRAS, 484, 5296

[8] de Lorenzo-Cáceres, A., Méndez-Abreu, J., Thorne, B., et al. 2019a, MNRAS, 484, 665

[9] de Lorenzo-Cáceres, A., Falcón-Barroso, J., & Vazdekis, A. 2013, MNRAS, 431, 2397

[10] Ellison, S. L., Teimoorinia, H., Rosario, D. J., et al. 2016, MNRAS, 458, L34

[11] Elbaz, D., Daddi, E., Le Borgne, D., et al. 2007, A&A, 468, 33

[12] González Delgado, R. M., García-Benito, R., Pérez, E., et al. 2015, A&A, 581, A103

[13] González Delgado, R. M., Cid Fernandes, R., Pérez, E., et al. 2016, A&A, 590, A44

[14] Johnston, E. J., Häußler, B., Aragón-Salamanca, A., et al. 2017, MNRAS, 465, 2317

[15] Lang, P., Wuyts, S., Somerville, R. S., et al. 2014, ApJ, 788, 11

[16] Méndez-Abreu, J., de Lorenzo-Cáceres, A., & Sánchez, S. F. 2021, MNRAS, 504, 3058

[17] Méndez-Abreu, J., Sánchez, S. F., & de Lorenzo-Cáceres, A. 2019b, MNRAS, 488, L80

[18] Méndez-Abreu, J., Sánchez, S. F., & de Lorenzo-Cáceres, A. 2019a, MNRAS, 484, 4298

[19] Méndez-Abreu, J., Aguerri, J. A. L., Falcón-Barroso, J., et al. 2018, MNRAS, 474, 1307

[20] Méndez-Abreu, J., Ruiz-Lara, T., Sánchez-Menguiano, L., et al. 2017, A&A,a 598, A32

[21] Méndez-Abreu, J., Debattista, V. P., Corsini, E. M., et al. 2014, A&A, 572, A25

[22] Méndez-Abreu, J., Aguerri, J. A. L., Corsini, E. M., et al. 2008, A&A, 478, 353

[23] Noeske, K. G., Weiner, B. J., Faber, S. M., et al. 2007, ApJl, 660, L43

[24] Renzini, A. & Peng, Y. 2015, ApJl, 801, L29

[25] Saintonge, A., Tacconi, L. J., Fabello, S., et al. 2012, ApJ, 758, 73

[26] Sánchez, S. F., Avila-Reese, V., Rodríguez-Puebla, A., et al. 2019, MNRAS, 482, 1557

[27] Sánchez, S. F., Avila-Reese, V., Hernandez-Toledo, H., et al. 2018, RMA&A, 54, 217

[28] Sánchez, S. F., García-Benito, R., Zibetti, S., et al. 2016, A&A, 594, A36

[29] Sánchez, S. F., Pérez, E., Sánchez-Blázquez, P., et al. 2016, RMA&A, 52, 21

[30] Willett, K. W., Schawinski, K., Simmons, B. D., et al. 2015, MNRAS, 449, 820

[31] Wuyts, S., Förster Schreiber, N. M., van der Wel, A., et al. 2011, ApJ, 742, 96

[32] Zhu, L., van de Ven, G., Leaman, R., et al. 2020, MNRAS, 496, 1579

Highlights of Spanish Astrophysics XI, Proceedings of the XV Scientific Meeting of the Spanish Astronomical Society held on September 4–9, 2022, in La Laguna, Spain. M. Manteiga, L. Bellot, P. Benavidez, A. de Lorenzo-Cáceres, M. A. Fuente, M. J. Martínez, M. Vázquez- Acosta, C. Dafonte (eds.), 2023

X-ray spectral properties of nearby AGN using clumpy torus model.

Koushika VP[1], Corral A[1], Carrera FJ[1], Laloux B[2], and Akylas A[2], and Georgakakis A[2]

[1] Instituto de Física de Cantabria (CSIC- Universidad de Cantabria), Santander, Spain
[2] National Observatory of Athens, Athens, Greece

Abstract

We have used a sample of 50 nearby ($z \leq 0.06$) obscured and unobscured AGN (about half of each) with NuSTAR hard X-ray spectra to explore the capabilities of clumpy torus models that represent the wide variety of X-ray spectral properties shown by AGN. We have used UXCLUMPY, which allows self-consistent multi-wavelength analyses. We have found that good individual spectral fits can be obtained with that model for all sources, including Compton Thick sources. We were looking for the smallest set of model parameters, that fit reasonably well with all our sources. We found that 23 such model parameter combinations span the sample, and additionally, they can be grouped into only four basic spectral shapes. We will extend this approach to an expanded sample and use the resulting maximally spanning sets of model parameter combinations to simulate AGN observations with *Athena*, to develop a method for automatically determining redshifts from their X-ray spectra.

1 Introduction

The compact centers of some galaxies accrete matter and emit enormous amounts of radiation at all wavelengths. These are called active galactic nuclei (AGN) [20]. They are persistent sources across all redshifts of the observable Universe[4][11][24]. It is essential to understand these enigmatic objects to answer important questions about the environment of the early Universe, the growth of SMBH[1] [5], and the evolution of galaxies.[15] [17]

AGN models theorize the presence of a torus-shaped dusty region that encloses the central supermassive black hole (SMBH) and the accretion disk[16]. The material related to the torus would be responsible for the obscuration [8] seen along the lines of sight to many AGN, if not most. Several studies have pointed out from observational evidence that the nature of this obscuring structure is clumpy.[18][19]

X-rays are produced at regions close to the SMBH through thermal and non-thermal processes [21]. Thanks to their high penetrating power, X-rays could be used to probe the central

regions. Also, a part of the intrinsic UV/optical continuum radiation from the accretion disk gets reprocessed into X-rays by the geometric features present near the accretion disk[12]. This leaves an imprint on the X-ray continuum spectra with the characteristic emission lines. Thus, X-rays can not only be used to study the properties of the central SMBH but also to understand the anatomy of the AGNs and the physical processes in the inner regions that characterize a particular source[6]. One of the fundamental properties required to characterize the AGN is redshift (z). The redshift of an object not only tells us how far away it is but also its age and, in turn, its nature. This helps us understand the stages of evolution in the AGN life cycle.[10]

Our ultimate aim is to extract redshift information entirely from the X-ray spectrum of the AGN. A characteristic feature in the reflection X-ray spectrum of the AGN is the Fe K-α line [9]. It is produced when the continuum emission is reprocessed by the circumnuclear material. Thus, this line gives an important diagnosis of the nature of the AGN's surroundings[7] [13]. The redshift of the AGN can be found by identifying the energy at which this Fe Kα line is present in the X-ray spectrum. Previous studies have attempted to do this characterization by employing a fitting method directly on the observed spectra and filtering techniques on simulated data [3][22][23].

In this work, we present preliminary results, representative AGN spectral shapes from the nearby AGN population. These will then be used for simulations in particular for *Athena*/WFI surveys which will be used for testing and optimizing our redshift extraction algorithm. Representative AGN spectral shapes are obtained using NuSTAR data from a nearby AGN population and a recent, up-to-date clumpy torus model. The data and the model are explained in section 2. Methodology, results, and conclusions are presented in Section 3, Section 4, and Section 5 respectively.

2 Sample data and model

2.1 Data

Our sample consists of 50 Seyfert objects, of which 29 are Seyfert Type-I and 21 are Seyfert Type-II. Out of 21 Type-II sources, 7 are Compton thick (CT; neutral hydrogen column density, $N_H \geq 1.5 \times 10^{24} cm^{-2}$) and 14 are Non-CT. The important obscuration features, the Fe Kα line, and the Compton edge occur in the hard X-ray energy range. The Nuclear Spectroscopic Telescope Array, NuSTAR [14] operates between 3 and 79 keV and fits the criteria. NuSTAR data for our sample were extracted with the standard NuSTAR pipeline. The sample can be accessed in the link https://doi.org/10.5281/zenodo.7390156

2.2 Model

We have employed a recent and up-to-date clumpy torus model UXCLUMPY [2]. The model assumes a central X-ray source surrounded by an inner ring of Compton thick clouds and an outer ring of diffuse, Compton thin clouds. The model is self-consistent and reproduces the X-ray and IR spectra of nearby AGN. The model parameters are explained in Table 1

Table 1: UXCLUMPY Model Parameters

Parameter	Description	Range	Bins in the Table model
NH (N_H)	Total LOS column density [cm^{-2}]	$10^{20} - 10^{26}$	41 bins
PhoIndex (Γ)	Photon index	1-3	11 bins
Ecut (E_{cut})	Energy cut-off [keV]	60-400	60, 100, 140, 200, 400
TORsigma (σ)	Vertical cloud dispersion	0-84°	0°, 7°, 28°, 84°
CTKcover (C)	Covering fraction of inner CT ring	0-0.6	0, 0.25, 0.3, 0.45, 0.6
Theta_inc (θ_{inc})	Viewing angle	0-90°	0°, 60°, 90°

3 Methodology

In a holistic approach, data from the NuSTAR FPMA module and Xspec model *atable{uxclumpy-cutoff.fits} + atable{uxclumpy-cutoff-omni.fits} *const* were used. The *const* parameter defines the fraction of the total intrinsic component that is scattered. All the parameter values were fixed from the values of the parameter combinations from the UXCLUMPY table model.

1. Each of the sources is fitted with parameter combinations allowing only *normalization* and *const* parameters to vary
2. For each fit, χ^2 statistic and degrees of freedom (dof) are noted
3. For each parameter combination, global χ^2/dof [1] - contribution of χ^2/dof from each source fit is calculated
4. The parameter combinations are then arranged in a table in the increasing order of the global χ^2/dof
5. When the individual $\chi^2/dof \leq 1.5$ for a fit, the particular parameter combination is said to have spanned that object
6. Starting from the parameter combination with the least global χ^2/dof in the rearranged table, a new one is included only if it adds to the spanned list a new object

4 Results and Discussions

Following the method established earlier, we obtained 23 models in Table 2 that span the entire sample.

[1] Global χ^2/dof is a measure of how well a parameter contribution fits all the objects of the sample set. This includes both $\chi^2/dof \leq 1.5$ for objects that it fits well and χ^2/dof for the objects that it does not. For example, this quantity tells the parameter combination 1 in the table in addition to fitting very well 26 objects, it has fitted fairly-well other objects in comparison to the parameter combination 2

Table 2: 23 Models that are required to span the sample set

	N_H	Γ	E_{cut}	σ	C	θ_{inc}	$const_{avg}$	global χ^2/dof	Number of Objects spanned			
	$10^{22}cm^{-2}$			deg		deg			Total	Sy1	Non CT	CT
1	1.78	1.8	100	84	0	60	0.04	3.47	26	19	7	0
2	1.26	1.8	100	84	0	60	0.04	3.48	28	21	7	0
3	1.26	1.8	100	84	0.25	90	0.04	3.51	29	22	7	0
4	1.26	1.8	100	28	0	60	0.04	3.52	27	20	7	0
5	2.51	2	400	84	0.25	90	0.05	3.56	25	18	7	0
6	3.55	1.8	200	7	0	90	0.08	3.59	23	16	7	0
7	3.55	1.8	140	84	0	90	0.02	3.91	17	10	7	0
8	1.26	2	140	84	0.3	60	0.09	4.10	21	15	6	0
9	0.891	2	140	84	0.25	0	0.09	4.35	20	14	6	0
10	7.08	1.8	140	7	0.25	90	0.08	4.38	10	4	5	1
11	1.26	2	100	84	0.25	0	0.08	4.43	18	12	6	0
12	7.08	1.8	200	7	0	90	0.07	4.53	9	3	5	1
13	10	1.8	400	7	0.25	90	0.06	6.01	7	1	4	2
14	10	1.8	140	28	0	0	0.06	7.28	8	1	5	2
15	14.1	1.6	100	7	0.25	90	0.05	10.28	5	0	3	2
16	14.1	1.4	60	7	0	60	0.06	13.63	5	0	3	2
17	28.2	1.8	400	7	0.25	60	0.07	16.23	5	0	3	2
18	891	1.6	60	0	0.3	60	0.02	18.00	1	0	0	1
19	891	2	200	28	0	0	0.01	20.60	2	0	0	2
20	56.2	1.8	200	0	0.25	60	0.04	25.77	2	0	1	1
21	79.4	1.8	100	7	0	60	0.01	26.43	2	0	1	1
22	79.4	1.6	60	7	0	90	0.01	29.53	3	0	2	1
23	224	1.8	60	28	0	60	0.05	33.01	3	0	0	3

An example fit is shown in Figure 1 for an object NGC 424. The number of models required to span each category of objects is presented in Table 3. From the Table, it is clear that only a few different parameter combinations are required to span/represent the unabsorbed and the mildly absorbed population of sources. Also, only the first 11 parameter combinations are required to span $\sim$ 74 % of the sample which includes 100 % of Type-I and 57 % of the Type-II sources.

On the other hand, heavily absorbed sources practically require one combination each. This is attributed to the fact that as absorption increases, the underlying continuum power law diminishes and the signatures of the interesting complex absorbing material become more and more prominent.

Interestingly, these 23 parameter combinations can be grouped into 4 different groups based on the spectral shape they produce. The shape groups are represented in Figure 1. The groups clearly show the influence that the amount of absorption has in determining the

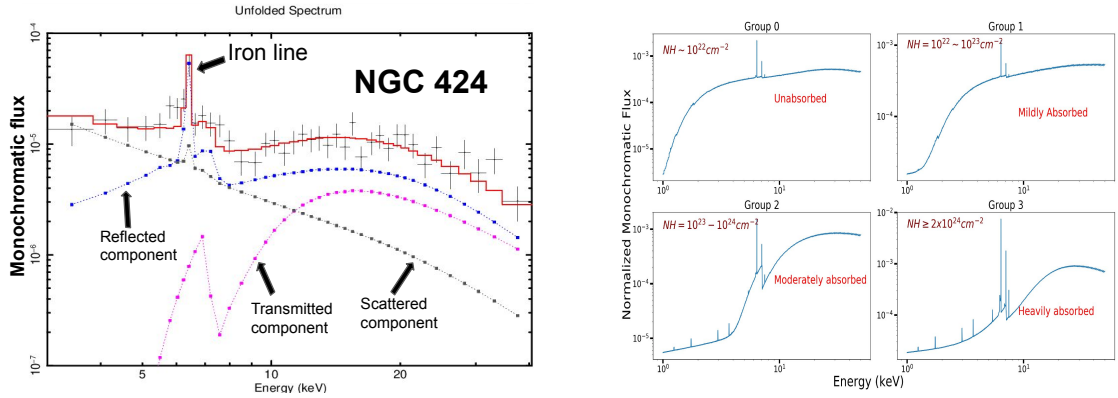

Figure 1: *Left:* Showing the model components of one fit. *Right:* Spectral shape groups into which the 23 parameter combinations can be grouped

Table 3: Models required to span each AGN type

Source Type	Number of Sources	Number of Parameter combinations required to span [a]
Sy1	29	9
Non CT Sy2	14	8
CT Sy2	7	7

[a]Few parameter combinations are common in spanning Sy1s and Non CT Sy2s.

spectral shape of an object.

5 Conclusions and Future work

Using a representative sample, we obtained 23 representative AGN spectra. Type-I and mildly absorbed Type-II sources prefer similar spectral shapes. Moderately and heavily absorbed Type-II sources prefer to be more unique.

It is also noticed that parameter combinations with low to medium absorption span a range of objects simultaneously and prefer having a higher torus spread. On the other hand, as absorption increases, the parameter combinations span fewer and fewer objects at a time. This is because, as the universally mildly absorbed power-law is attenuated, the interesting physics of the complex absorbing material emerges, revealing each source to be unique.

This methodology will be applied to an expanded sample and the resulting maximally spanning sets of model parameter combinations will be used to simulate AGN observations with Athena. These simulations will then be used to test and develop our automated method to extract spectroscopic redshifts from X-ray AGN spectra.

Acknowledgments

Activities partially funded by project RTI2018-096686-B-C21 funded by MCIN/AEI/10.13039/501100011033 and by "ERDF A way of making Europe" and by the Agencia Estatal de Investigación, Unidad de Excelencia María de Maeztu, ref. MDM-2017-0765.

References

[1] Brandt WN, Alexander DM. 2015, Astron Astrophys Rev, 23(1):1

[2] Buchner J, Brightman M, Nandra K, Nikutta R, Bauer FE. 2019, A&A, 629:A16

[3] Castelló-Mor N, Barcons X, Ballo L., 2011, Advances in Space Research, 48(7):1304–10

[4] Ceraj L, Smolčić V, Delvecchio I, Novak M, Zamorani G, et al, 2018, A&A, 620:A192

[5] Civano F, Cappelluti N, Hickox R, Canning R, Aird J, et al, 2019, Bulletin of the AAS, 51(3):

[6] Corral A, Della Ceca R, Caccianiga A, Severgnini P, Brunner H, et al., 2011, A&A. 530:A42

[7] Wilkins DR, Fabian AC. 2011, MNRAS, 414(2):1269–77

[8] Elitzur M., 2006, New Astronomy Reviews, 50(9–10):728–31

[9] Fabian, A. C., Iwasawa, K., Reynolds, C. S., Young, A. J. PASP, 2000, 112, 1145

[10] Fanidakis N, Baugh CM, Benson AJ, Bower RG, Cole S, et al. 2012, MNRAS, 419(4):2797–2820

[11] Fiore F, Puccetti S, Grazian A, Menci N, Shankar F, et al, 2012, A&A, 537:A16

[12] Haardt F. and Maraschi L., 1993, ApJ, 413:507

[13] Ghosh R, Laha S. 2021. ApJ. 908(2):198

[14] Harrison, F. A., Craig, W. W., Christensen, F. E., et al. 2013, ApJ, 770, 103

[15] Heckman TM, Best PN, 2014, Annu. Rev. Astron. Astrophys, 52(1):589–660

[16] Krolik JH, Begelman MC, 1988, ApJ, 329:702

[17] Lanzuisi G, Delvecchio I, Berta S, Brusa M, Comastri A, et al. 2017, A&A, 602:A123

[18] Markowitz AG, Krumpe M, Nikutta R. 2014, MNRAS, 439(2):1403–58

[19] Nenkova M, Ivezić Ž, Elitzur M. 2002. ApJ. 570(1):L9

[20] Netzer H, 2013, Cambridge University Press, 353 pp.

[21] Padovani P, 2017, Front. Astron. Space Sci. 4:35

[22] Sicilian D, Civano F, Cappelluti N, Buchner J, Peca A, 2022, ApJ, 936(1):39

[23] Simmonds C, Buchner J, Salvato M, Hsu L-T, Bauer FE, 2018, A&A, 618:A66

[24] Wang F, Yang J, Fan X, Hennawi JF, Barth AJ, et al, 2021, ApJL, 907(1):L1

Highlights of Spanish Astrophysics XI, Proceedings of the XV Scientific Meeting of the Spanish Astronomical Society held on September 4–9, 2022, in La Laguna, Spain. M. Manteiga, L. Bellot, P. Benavidez, A. de Lorenzo-Cáceres, M. A. Fuente, M. J. Martínez, M. Vázquez- Acosta, C. Dafonte (eds.), 2023

Chemical evolution of local galaxies.

Artemi Camps-Fariña[1,2], Patricia Sánchez Blázquez[1], and Sebastián F. Sánchez[2]

[1] Departamento de Física de la Tierra y Astrofísica, Facultad de Ciencias Físicas, Universidad Complutense de Madrid, 28040, Madrid
[2]Instituto de Astronomía, Universidad Nacional Autónoma de México, CP 04510, Mexico City, Mexico

Abstract

We show the results of a study using the spectral synthesis technique study to measure the chemical evolution of local galaxies. The main parameters measured are the chemical enrichment history (ChEH) and the evolution of the stellar mass-metallicity relation (MZR) over cosmic time. We find that the more massive galaxies became enriched first and the lower-mass galaxies did so later, producing a change in the MZR that becomes shallower in time. The mass dependence of the MZR becomes less relevant for later morphological types, to the extent that it inverts for Sd/Irr galaxies, suggesting that morphology is at least as important a factor as mass in the chemical evolution. We also find that the average metallicity gradient is currently negative for all mass bins but for low-mass galaxies it used to be positive before switching to the current negative average value. Some galaxies show decreases in their ChEHs, which we find correlate with the presence of an AGN and the sSFR. Finally, by comparing the expected yields of the star-forming histories to the measured ChEHs using a chemical evolution model we can estimate the history of pristine gas accretion over the lifetime of the galaxies. The inflow histories show that for a galaxy to still be forming stars in the present time it requires a steady flow of pristine gas which dilutes its chemical content, meaning the primary parameter that shapes the star-forming main sequence is access to gas accretion.

My poster is available at https://zenodo.org/record/7017730

Highlights of Spanish Astrophysics XI, Proceedings of the XV Scientific Meeting of the Spanish Astronomical Society held on September 4–9, 2022, in La Laguna, Spain. M. Manteiga, L. Bellot, P. Benavidez, A. de Lorenzo-Cáceres, M. A. Fuente, M. J. Martínez, M. Vázquez- Acosta, C. Dafonte (eds.), 2023

Databases and web-based software tools for HR-pyPopStar models and MEGASTAR library.

Mollá M.[1], García-Vargas, M.L.[2], Carrasco-Licea, E.[3], Mújica Álvarez E.[2], and Millán-Irigoyen, I.[1]

[1] Departamento de Investigación Básica, CIEMAT, Avda. Complutense 40. E-28040 Madrid, Spain
[2] FRACTAL S.L.N.E., Calle Tulipán 2, portal 13, 1A, E-28231 Las Rozas de Madrid, (Spain)
[3] Instituto Nacional de Astrofísica, Óptica y Electrónica, INAOE, Calle Luis Enrique Erro 1, C.P. 72840 Santa María Tonantzintla, Puebla, (Mexico)

Abstract

MEGASTAR is a stellar spectral atlas for MEGARA (Multi Espectrógrafo en GTC de Alta Resolución para Astronomía). MEGARA is an optical (3650 – 9750 Å), fiber-fed, medium-high spectral resolution (R = 6000, 12000, 20000) instrument in operation on the GTC 10.4m telescope. The scientific exploitation of MEGARA demanded a stellar-spectra library to interpret galaxy data and to estimate the contribution of the stellar populations. MEGASTAR atlas is focused on the highest resolution setups, HR-R and HR-I, and already has almost 1000 stars (twice spectra) thanks to the filler-type OpenTime obtained up to now in 7 semesters. We have developed a web-based tool and a database that allow working in the project (for MEGASTAR team) and making the observations and products available to the scientific community. HR-pyPopStar model provides a complete set of high resolution Spectral Energy Distributions (SED) of Single Stellar Populations. The model uses the most recent high wavelength-resolution theoretical atmosphere libraries for main sequence, post-AGB/planetary nebulae and Wolf-Rayet stars. The SEDs are given for more than a hundred ages ranging from 0.1 Myr to 13.8 Gyr, four values of metallicity (Z = 0.004, 0.008, 0.02 and 0.05), and four different IMFs. We have developed a public web-based software tools and a database to manage HR-pyPopStar models and to make this available to the users community.

My poster is available at https://zenodo.org/record/6989174#.Y1b5CIJBxmE

Highlights of Spanish Astrophysics XI, Proceedings of the XV Scientific Meeting of the Spanish Astronomical Society held on September 4–9, 2022, in La Laguna, Spain. M. Manteiga, L. Bellot, P. Benavidez, A. de Lorenzo-Cáceres, M. A. Fuente, M. J. Martínez, M. Vázquez- Acosta, C. Dafonte (eds.), 2023

Finding the limits of galaxies up to $z = 1$.

F. Buitrago[1,2], and I. Trujillo[3,4]

[1] Departamento de Física Teórica, Atómica y Óptica, Universidad de Valladolid, 47011 Valladolid, Spain
[2] Instituto de Astrofísica e Ciências do Espaço, Universidade de Lisboa, OAL, Tapada da Ajuda, PT1349-018 Lisbon, Portugal
[3] Instituto de Astrofísica de Canarias, Vía Láctea $s\backslash n$, 38200 La Laguna, Tenerife, Spain [4] Departamento de Astrofísica, Universidad de La Laguna, E-38205, La Laguna, Tenerife, Spain

Abstract

The superb depth of present ultradeep observations and next generation synoptic surveys allow us to reach sudden decrements of the galaxy surface brightness in their outer parts. These truncations are intimately linked with the expected location of the cold gas density threshold for star formation. The unexpected existence of these limits in the galaxy light has led some authors to propose these truncations as the long-sought physically-motivated proxy for galaxy sizes, as opposed to traditional effective radii. We have analysed all the HST CANDELS fields (best trade-off between depth and spatial resolution) to follow the evolution of these galaxy borders in massive disk galaxies up to $z = 1$. By determining galaxy colors and mass profiles, we show that Milky Way analogs (galaxies with stellar mass$\sim 5\times10^{10}$ $M_\odot$) grow in size by a factor of 2 in the last 8 Gyr, while at the same time decreasing their stellar density at these limit positions by an order of magnitude. We plan to apply our techniques to the forthcoming data from the Euclid satellite, that will cover one third of the sky down to 29.5 mag/arcsec^2 (3 magnitudes deeper than SDSS and with HST spatial resolution!). Therefore we have developed Machine Learning techniques that will derive the most accurate galaxy size-mass relation for millions of galaxies in the future, and going one step beyond, as these computational methods also help the astronomer to determine the existence of any galaxy stellar haloes and galaxy tidal tails.

My poster is available at https://zenodo.org/record/7037734#.Y71pLtLMJhE

Highlights of Spanish Astrophysics XI, Proceedings of the XV Scientific Meeting of the Spanish Astronomical Society held on September 4–9, 2022, in La Laguna, Spain. M. Manteiga, L. Bellot, P. Benavidez, A. de Lorenzo-Cáceres, M. A. Fuente, M. J. Martínez, M. Vázquez- Acosta, C. Dafonte (eds.), 2023

GTC data exploitation in the search for the first galaxies.

Cabello, C.[1,2], Gallego, J.[1,2], Cardiel, N.[1,2], Pascual, S.[1,2], Guzmán, R.[3], Herrero, A.[4,5], Manrique, A.[6], Marín-Franch, A.[7], Mas-Hesse, J.M.[8], Rodríguez-Espinosa, J.M.[4,5], Salvador-Solé, E.[6], and Eikenberry, S.[9]

[1] Universidad Complutense de Madrid (UCM)
[2] Instituto de Física de Particulas y del Cosmos (UCM-IPARCOS)
[3] University of Florida (UF)
[4] Instituto de Astrofísica de Canarias (IAC)
[5] Universidad de La Laguna (ULL)
[6] Institut de Ciències del Cosmos (UB-IEEC)
[7] Centro de Estudios de Física del Cosmos de Aragón (CEFCA)
[8] Centro de Astrobiología (CSIC-INTA)
[9] The College of Optics and Photonics (CREOL)

Abstract

Detecting the first galaxies of the Universe has always been a goal in extragalactic astronomy because the study of these sources provides important constraints on cosmic reionization. In Cabello et al. 2022, we exploited the capabilities of the 10.4 m Gran Telescopio Canarias (GTC) to carry out the narrow-band (NB) Lyα survey at the highest redshift ever. The NB filter (FWHM = 11nm, $\lambda_c = 1257$ nm) targets the Lyα line of $z = 9.34$ galaxies and it was specially designed by the ALBA team to be used on the near-IR camera CIRCE@GTC for this work. After 18.3 hours of exposure time, we obtained an NB image of ~ 6.7 arcmin^2 within the Extended Groth Strip (EGS) field. No robust LAE candidates were found down to an emission-line flux of 2.9×10^{-16} erg s^{-1} cm^{-2}, which allowed us to derive an exclusion zone of the Lyα luminosity function that agrees well with the previous observational constraints at $z \sim 9$. The current NB surveys at very high redshift probe only the most luminous rare sources, but wider and deeper observations are needed to address the scientific challenge of detecting galaxies at the cosmic dawn. In this context, the study of the early Universe is one of the main scientific cases of the upcoming facilities such as the JWST or the ELT, which will allow us to reach fainter magnitudes and detections at higher redshifts.

My poster is available at https://zenodo.org/record/7015519#.Y1arRuxBw3l

Highlights of Spanish Astrophysics XI, Proceedings of the XV Scientific Meeting of the Spanish Astronomical Society held on September 4–9, 2022, in La Laguna, Spain. M. Manteiga, L. Bellot, P. Benavidez, A. de Lorenzo-Cáceres, M. A. Fuente, M. J. Martínez, M. Vázquez- Acosta, C. Dafonte (eds.), 2023

Gravitational waves or X-ray counterpart ? No need to choose.

Mignon-Risse, R.[1], **Varniere, P.**[2,3], **and Casse, F.**[2]

[1] Université Paris Cité, CNRS, CNES, Astroparticule et Cosmologie, F-75013 Paris, France
[2] Université Paris Cité, CNRS, Astroparticule et Cosmologie, F-75013 Paris, France
[3] Universitté Paris-Saclay, Universitté Paris Citté, CEA, CNRS, AIM, 91191, Gif-sur-Yvette, France

Abstract

Binary black holes emit gravitational waves (GWs) as they inspiral towards coalescence. Searches for electromagnetic counterparts to GWs rely on looking for common sources producing both waves. Here, we take a different approach: we investigate the impact of radiation zone effects including retardation effects associated with GWs onto the outer circumbinary disk around stellar-mass black holes, using general relativistic hydrodynamical simulations and a general relativistic ray-tracing code. We show that radiation zone effects leave an imprint onto the disk, leading to quasi-periodic patterns in the X-ray lightcurve.

My poster is available at https://zenodo.org/record/7257054##.Y6l-K-zMIfF

Highlights of Spanish Astrophysics XI, Proceedings of the XV Scientific Meeting of the Spanish Astronomical Society held on September 4–9, 2022, in La Laguna, Spain. M. Manteiga, L. Bellot, P. Benavidez, A. de Lorenzo-Cáceres, M. A. Fuente, M. J. Martínez, M. Vázquez- Acosta, C. Dafonte (eds.), 2023

Machine learning classification of the ISM in NGC 300.

Asier Castrillo[1,2]**, and Yago Ascasibar**[1,2]

[1] Departamento de Física Teórica, Universidad Autónoma de Madrid, 28049 Madrid (Spain)
[2] esearch Center of Advanced Fundamental Physics (CIAFF-UAM), Universidad Autónoma de Madrid, 28049 Madrid (Spain)

Abstract

In this work, we present a machine learning clustering algorithm for the classification of the interstellar medium (ISM) main components (HII regions, supernova remnants and diffuse ionize regions). We study the ISM components of the NGC 300 galaxy from MUSE integral field spectroscopy observations. These observations give us an ISM spatial resolution of a few parsec scales. We apply an unsupervised Bayesian Gaussian Mixture Model algorithm to a data set of spaxel-by-spaxel main strong emission lines. Our method allows an automatic and unbiased detection of the main components of the ISM combining the spatial and spectral information. We compare our catalog with previous studies and measure the main properties of the ISM components.

My poster is available at https://zenodo.org/record/7044152#.Y3NQ-77MIXU

Highlights of Spanish Astrophysics XI, Proceedings of the XV Scientific Meeting of the Spanish Astronomical Society held on September 4–9, 2022, in La Laguna, Spain. M. Manteiga, L. Bellot, P. Benavidez, A. de Lorenzo-Cáceres, M. A. Fuente, M. J. Martínez, M. Vázquez- Acosta, C. Dafonte (eds.), 2023

Measurement of radial velocities and velocity dispersions in Python using MEGARA data.

S. Zamora[1,2], Ángeles I. Díaz[1,2], D. Mayya[3]

[1] Departamento de Física Teórica, Universidad Autónoma de Madrid (UAM), Spain
[2]Centro de Investigación Avanzada en Física Fundamental (CIAFF), Spain
[3]Instituto de Astrofísica, Óptica y Electrónica, 72840 Puebla, México

Abstract

Cross-correlation techniques have been applied since 1974 (see Simkin, S.M.: A&A, 31, 129) in order to calculate objects' redshift and velocity dispersions from the center and the width of the cross-correlation peak respectively. In 1979, Tonry and Davis (ApJ 84, 1511) developed a correlation analysis based in the Fourier Method. It provides a determination of a cross correlation function operationally straightforward and with an internal error measure of the correlation peak. In this work, we have adapted this method to implement it in very high spectral resolution data at red wavelengths and have written a Python package that can be used to perform the calculations automatically. We present an example of the correlation function using observations from the MEGARA instrument attached to the 10.4-m GTC. We have used the HR-I setup (VPH863-HR grating) that covers a wavelength range between 8380 and 8882 angstroms and provides a velocity dispersion limit around 14.6 km/s (FWHM). The algorithms developed in this work will be published soon and will be available in the standard Python distribution channels.

My poster is available at https://zenodo.org/record/7043332#.Y1pXvOxBxJU

Highlights of Spanish Astrophysics XI, Proceedings of the XV Scientific Meeting of the Spanish Astronomical Society held on September 4–9, 2022, in La Laguna, Spain. M. Manteiga, L. Bellot, P. Benavidez, A. de Lorenzo-Cáceres, M. A. Fuente, M. J. Martínez, M. Vázquez- Acosta, C. Dafonte (eds.), 2023

Measuring chemical abundances in AGN from infrared nebular lines: HII-CHI-Mistry-IR for AGN.

Pérez-Díaz, B.[1], Pérez-Montero, E.[1], Fernández-Ontiveros, J. A.[2], and Vílchez, J. M.[1]

[1] Instituto de Astrofísica de Andalucía (IAA-CSIC), Glorieta de la Astronomía s/n, 18008 Granada, Spain
[2] Centro de Estudios de Física del Cosmos de Aragón (CEFCA), Unidad Asociada al CSIC, Plaza San Juan 1, E–44001 Teruel, Spain

Abstract

Future and on-going infrared and radio observatories such as JWST, METIS or ALMA will increase the amount of rest-frame IR spectroscopic data for galaxies by several orders of magnitude. While studies of the chemical composition of the ISM based on optical observations have been widely spread over decades for Star-forming Galaxies (SFG) and, more recently, for Active Galactic Nuclei (AGN), similar studies need to be performed using IR data. This regime can be especially useful in the case of AGN given that it is less affected by temperature and dust extinction, traces higher ionic species and can also provide robust estimations of the chemical abundance ratio N/O. We present a new tool based on a bayesian-like methodology (HII-CHI-Mistry-IR) to estimate chemical abundances from IR emission lines in AGN. We use a sample of 58 AGN with IR spectroscopic data retrieved from the literature, composed of 43 Seyferts, 8 ULIRGs, 4 LIRGs and 3 LINERs, to probe the validity of our method. The estimations of the chemical abundances based on IR lines in our sample are later compared with the corresponding abundances derived from the optical emission lines in the same objects. This tool takes advantage of photoionization models, characterized by the chemical abundance ratios O/H and N/O and the ionization parameter U, to compare their predicted emission-line fluxes with a set of observed values. We report mainly solar and also subsolar abundances for O/H in the nuclear region for our sample of AGN, whereas N/O clusters around solar values. We find a discrepancy between the chemical abundances derived from IR and optical emission lines. This discrepancy, also reported by previous studies of the composition of the ISM in AGN from IR observations, is independent from the gas density or the incident radiation field to the gas, and it is likely associated with dust obscuration and/or temperature stratification within the gas nebula.

My poster is available at https://zenodo.org/record/7042846#.Y_YE-oDMJuQ

Highlights of Spanish Astrophysics XI, Proceedings of the XV Scientific Meeting of the Spanish Astronomical Society held on September 4–9, 2022, in La Laguna, Spain. M. Manteiga, L. Bellot, P. Benavidez, A. de Lorenzo-Cáceres, M. A. Fuente, M. J. Martínez, M. Vázquez- Acosta, C. Dafonte (eds.), 2023

Molecular gas in star-forming galaxies of the intermediate redshift cluster Zw Cl0024.

M. Sánchez-Portal[1,2], A. Bongiovanni[1,2], J. Cepa[3,4,3], A. M. Pérez García[5,2], C. P. Padilla-Torres[6,3,4,2], J. I. González-Serrano[7,2], I. Pintos-Castro[8,2], R. Pérez-Martínez[2,9], I. Cruz-González[10], A. Negrete[10], Z. Beyoro-Amado[11,12], and M. Pović[12,13]

[1] Institut de Radioastronomie Millimétrique (IRAM), Granada, Spain
[2] Asociación ASPID, Tenerife, Spain
[3] Instituto de Astrofísica de Canarias (IAC), La Laguna, Tenerife, Spain
[4] Departamento de Astrofísica, Universidad de La Laguna (ULL), Tenerife, Spain
[5] Centro de Astrobiología (CSIC/INTA), Villanueva de la Cañada, Madrid, Spain
[6] Fundación Galileo Galilei-INAF, Breña Baja, Tenerife, Spain
[7] Instituto de Física de Cantabria (CSIC-Universidad de Cantabria), Santander, Spain
[8] Centro de Estudios de Física del Cosmos de Aragón (CEFCA), Teruel, Spain
[9] ISDEFE for ESAC/ESA, Villanueva de la Cañada, Madrid, Spain
[10] Instituto de Astronomía, Universidad Nacional Autónoma de México, Mexico
[11] Kotebe Metropolitan University, Addis Ababa, Ethiopia
[12] Ethiopian Space Science and Technology Institute ESSTI/EORC, Addis Ababa, Ethiopia
[13] Instituto de Astrofísica de Andalucía (IAA), Granada, Spain

Abstract

We present preliminary results from a survey of cold gas in an intermediate-redshift cluster, Zw Cl0024.1+1652 at z = 0.395, using the EMIR receiver at the IRAM-30m telescope, Pico Veleta observatory, Spain. We observed the CO(1-0) and CO(2-1) transitions in a sample of seven star-forming galaxies drawn out of the GLACE catalogue of Hα+[NII] emission-line galaxies. These galaxies have been chosen to be bright in the far-IR and to span a wide range of local densities/cluster-centric distances. We have derived the $L'_{\rm CO}$ luminosity (tracing the amount of cold gas available for star formation) and combined these data with the total IR luminosity $L_{\rm TIR}$ values (tracing the star formation rate, SFR) derived by our team, and with additional CO and FIR data from literature to study how the amount of cold gas in an intermediate-redshift cluster relates to the SFR and cluster-centric distance. The results suggest that, at a given SFR, the reservoir of cold gas is smaller in cluster galaxies. Furthermore, there are also hints that the amount of cold gas increases with the cluster-centric distance, hence pointing to an environmental dependency.

My poster is available at https://zenodo.org/record/7051415#.Y7_uGezMKek

Highlights of Spanish Astrophysics XI, Proceedings of the XV Scientific Meeting of the Spanish Astronomical Society held on September 4–9, 2022, in La Laguna, Spain. M. Manteiga, L. Bellot, P. Benavidez, A. de Lorenzo-Cáceres, M. A. Fuente, M. J. Martínez, M. Vázquez- Acosta, C. Dafonte (eds.), 2023

Multi-wavelength characterisation of activity in nearby S0 galaxies.

Jiménez-Palau, C.[1], **Tous, J.L.**[1,2], **Solanes, J.M.** [1,2] **del Olmo, A.** [3], **and Perea, J.D.**[3]

[1] Institut de Ciències del Cosmos (ICCUB), Universitat de Barcelona
[2] Departament de Física Quàntica i Astrofísica, Universitat de Barcelona
[3] Departamento de Astronomía Extragaláctica, Instituto de Astrofísica de Andalucía (IAA-CSIC)

Abstract

We provide a comprehensive characterization of the activity of present-day S0s throughout both the broad-band PC1–PC2 spectral classifier and the conventional narrow-line BPT/WHAN ones, contrasting the different types of activity classes they define, and present an alternative diagram that exploits the concordance between WHAN and PCA demarcations. The analysis is extended to the mid-infrared, radio and X-ray wavelengths by cross-matching our core sample with data from the WISE, FIRST, XMM–Newton, and Chandra surveys. This has allowed us to carry out a thorough comparison of the most important activity diagnostics in the literature over different wavebands, discuss their similarities and differences, and explore the connections between them and with parameters related to star formation and black hole accretion. We find evidence that the bulk of nebular emission from radio and X-ray detected S0–Seyfert and LINER systems is not driven by star birth, while the dominant ionising radiation for a number of LINERs might come from post-AGB stars. These and other outcomes from the present work should be transferable to other morphologies.

My poster is available at https://zenodo.org/record/7043218#.Y4cynuzMLt1

Highlights of Spanish Astrophysics XI, Proceedings of the XV Scientific Meeting of the Spanish Astronomical Society held on September 4–9, 2022, in La Laguna, Spain. M. Manteiga, L. Bellot, P. Benavidez, A. de Lorenzo-Cáceres, M. A. Fuente, M. J. Martínez, M. Vázquez- Acosta, C. Dafonte (eds.), 2023

On the growth of diffuse light from simulations of galaxy clusters.

Betelehem Bilata-Woldeyes[1], Jaime Perea[1], and José María Solanes[2]

[1] Instituto de Astrofísica de Andalucía (IAA-CSIC)
[2] Institut de Ciències del Cosmos (ICCUB), Universitat de Barcelona

Abstract

Deep surface photometry reveals the presence in a good number of galaxy clusters, as well as in their smaller counterparts, galaxy groups, of an extended, diffuse luminous component that fills the space between galaxies. This intracluster light (ICL) is believed to originate from the disruption of the outermost regions of the galaxies that make up these systems.
Our aim in this work is to make use of controlled numerical simulations of pre-virialized clusters to study the formation of the diffuse ICL, and investigate its potential to describe the assembly history of such systems of galaxies.
We are currently using our simulations to track the growth of the ICL over cosmic time, tracing its evolution across clusters spanning a range of masses and galaxy memberships. Here, we present our first results, where we analyzed the relationship of ICL formation with the mass and size of the brightest galaxy in the cluster and its dependence on both the merger fraction and the efficiency of interactions.

My poster is available at https://zenodo.org/record/7031730#.YwyawNVBzJU

Highlights of Spanish Astrophysics XI, Proceedings of the XV Scientific Meeting of the Spanish Astronomical Society held on September 4–9, 2022, in La Laguna, Spain. M. Manteiga, L. Bellot, P. Benavidez, A. de Lorenzo-Cáceres, M. A. Fuente, M. J. Martínez, M. Vázquez- Acosta, C. Dafonte (eds.), 2023

Photometric Classification of QSOs with Machine Learning Techniques.

Néstor Sánchez, Benjamín Arroquia-Cuadros, Vicent Gómez, Pere Blay, and Vicent Martínez-Badenes

Universidad Internacional de Valencia (VIU), Valencia, Spain

Abstract

With the advent of wide-area photometric surveys and the large amount of available data, the use of machine learning techniques is becoming more and more frequent to classify stars, galaxies and QSOs. In this work we investigate the performance of random forest in classifying QSOs using photometry of the 20 contiguous, equal-width, non-overlapping, medium-bands filters of the ALHAMBRA Survey. We systematically analyse the effects of the main free parameters on the final classification results and the advantages and limitations of using ALHAMBRA photometry in comparison to other surveys like Sloan (SDSS). The best performance is obtained when using colours from the ALHAMBRA survey.

My poster is available at https://zenodo.org/record/7041705#.YxD2htVByvw

Highlights of Spanish Astrophysics XI, Proceedings of the XV Scientific Meeting of the Spanish Astronomical Society held on September 4–9, 2022, in La Laguna, Spain. M. Manteiga, L. Bellot, P. Benavidez, A. de Lorenzo-Cáceres, M. A. Fuente, M. J. Martínez, M. Vázquez- Acosta, C. Dafonte (eds.), 2023

Physical properties of circumnuclear ionising clusters.

S. Zamora[1,2], **Ángeles I. Díaz**[1,2]

[1] Departamento de Física Teórica, Universidad Autónoma de Madrid (UAM), Spain
[2]Centro de Investigación Avanzada en Física Fundamental (CIAFF), Spain

Abstract

Nuclear rings are generally formed when gas is accumulated in orbital resonances, due to a non-axisymmetric gravitational potential related to a barred structure. However, NGC 7742 does not exhibit this latter feature, thus being an ideal candidate for a minor merger event. In this work, we analyze 89 HII regions of the nuclear ring, from MUSE integral-field spectroscopy data. We have studied their metal content using sulfur as tracer in order to find patterns in chemical composition. From R-I colors and H beta equivalent width values and using PopStar models, we estimate ages and percentages of red super giant stars. In addition, we have measured calcium triplet (CaT) equivalent widths and we can estimate the luminosity class of the stars in these clumps producing this feature. Finally, we expect to test if this is compatible with the idea of all regions having formed at the same time and if a minor merger event is consistent with observations.

My poster is available at https://zenodo.org/record/7043323#.Y1pXWexBxJU

Highlights of Spanish Astrophysics XI, Proceedings of the XV Scientific Meeting of the Spanish Astronomical Society held on September 4–9, 2022, in La Laguna, Spain. M. Manteiga, L. Bellot, P. Benavidez, A. de Lorenzo-Cáceres, M. A. Fuente, M. J. Martínez, M. Vázquez- Acosta, C. Dafonte (eds.), 2023

Positive feedback, quenching and sequential super star cluster (SSC) formation in NGC 4945.

Bellocchi, E.[1], **Martín-Pintado, J.**[1], **Rico-Villas, F.**[1], **Martín, S.**[2,3] **and Jiménez-Sierra, I.**[1]

[1] Centro de Astrobiología, (CSIC-INTA), Astrophysics Department, Madrid, Spain
[2] European Southern Observatory, Alonso de Córdova, 3107, Vitacura, Santiago, 763-0355, Chile
[3] Joint ALMA Observatory, Alonso de Córdova, 3107, Vitacura, Santiago, 763-0355, Chile

Abstract

We have used ALMA imaging (resolutions 0.1″-0.4″) of ground and vibrationally excited lines of HCN and HC_3N toward the nucleus of NGC 4945 to trace the protostellar phase in Super Star Clusters (proto-SSC). Out of the 14 identified SSCs, we find that 8 are in the proto-SSC phase showing vibrational HCN emission with 5 of them also showing vibrational HC_3N emission. We estimate proto-SSC ages of 5-9.7$\times10^4$ yr. The more evolved ones, with only HCN emission, are close to reach the Zero Age Main Sequence (ZAMS; ages $\geq10^5$ yr). The excitation of the parental cloud seems to be related to the SSC evolutionary stage, with high ($\sim$65 K) and low ($\sim$25 K) rotational temperatures for the youngest proto and ZAMS SSCs, respectively. Heating by the HII regions in the SSC ZAMS phase seems to be rather local. The youngest proto-SSCs are located at the edges of the molecular outflow, indicating SSC formation by positive feedback in the shocked regions. The proto-SSCs in NGC 4945 seem to be more evolved than in the starburst galaxy NGC 253. We propose that sequential SSC formation can explain the spatial distribution and different ages of the SSCs in both galaxies.

My poster is available at https://zenodo.org/record/7015155#.Y4H9DSHMLYI

Highlights of Spanish Astrophysics XI, Proceedings of the XV Scientific Meeting of the Spanish Astronomical Society held on September 4–9, 2022, in La Laguna, Spain. M. Manteiga, L. Bellot, P. Benavidez, A. de Lorenzo-Cáceres, M. A. Fuente, M. J. Martínez, M. Vázquez- Acosta, C. Dafonte (eds.), 2023

Put a ring on it: the origin of star-forming rings in S0 galaxies.

Tous, J. L.[1], **Perea, J.**[2], **Solanes, J. M.**[1], **and Domínguez-Sánchez, H.**[3]

[1] Departament de Física Quàntica i Astrofísica i Institut de Ciències del Cosmos (ICCUB), Universitat de Barcelona. Martí i Franquès 1, 08028 Barcelona, Spain
[2] Instituto de Astrofísica de Andalucía (IAA-CSIC). Glorieta de la Astronomía s/n, 18008 Granada, Spain
[3] Instituto de Ciencias del Espacio (ICE-CSIC), Campus UAB. Can Magrans s/n, 08193 Barcelona, Spain

Abstract

The examination of the spatially resolved IFS maps in a sample of more than 500 lenticular (S0) galaxies drawn from the MaNGA survey has unveiled the existence of transient inner annular structures ($\langle R \rangle \sim 1\,R_{\rm e}$) betraying ongoing star formation in a good number of these objects. Activity gradients in these galaxies have been measured through a novel methodology based on the principal component analysis of their optical spectra averaged over bins of galactocentric radius. We find that the sign of these gradients is closely linked to the presence of rings in the spectral maps, which are specially conspicuous in the equivalent width of Hα-emission, EW(Hα), with a fractional abundance —22–37% depending on the strictness of ring identification— larger than that inferred from optical imaging. While the numbers of S0s with globally positive, negative, and flat activity gradients are comparable, star-forming rings are found almost exclusively in objects with a positive slope for which quenching proceeds inside-out, in good agreement with predictions from cosmological simulations studying S0 buildup. The assessment of these structures and the properties of the galaxies harboring them also indicates that the frequency of such rings increases with the mass of their hosts, that they feed mainly on the gas from the disks, that are more short-lived in galaxies with ongoing star formation, and that the local environment does not play a relevant role in their formation. From the present analysis, we conclude that the presence of rings in the EW of the Hα emission line is a common phenomenon among fully formed S0s, possibly associated with annular disk resonances driven by weakly disruptive mergers preferentially involving the more massive representatives of these galaxies and their smaller and closer satellites.

My poster is available at https://zenodo.org/record/7043398#.Y24MEtLMJhE

Highlights of Spanish Astrophysics XI, Proceedings of the XV Scientific Meeting of the Spanish Astronomical Society held on September 4–9, 2022, in La Laguna, Spain. M. Manteiga, L. Bellot, P. Benavidez, A. de Lorenzo-Cáceres, M. A. Fuente, M. J. Martínez, M. Vázquez- Acosta, C. Dafonte (eds.), 2023

Reconstructing the optical spectral variability of gamma-ray blazars.

Otero-Santos, J.[1,2], Acosta-Pulido, J. A.[1,2], Becerra González, J.[1,2], Luashvili, A.[3], Castro Segura, N.4, González-Martín, O.[5], Raiteri, C. M.[6], and Carnerero, M. I.[6]

[1] Instituto de Astrofísica de Canarias (IAC), E-38200 La Laguna, Tenerife, Spain
[2] Universidad de La Laguna (ULL), Departamento de Astrofísica, E-38206 La Laguna, Tenerife, Spain
[3] Laboratoire Univers et Théories, Observatoire de Paris, Université PSL, CNRS, Université de Paris, 92190, Meudon, France
[4] School of Physics & Astronomy, University of Southampton, Highfield, Southampton, SO17, 1BJ, UK
[5] Instituto de Radioastronomía y Astrofísica (IRyA-UNAM), 3-72 (Xangari), 8701, Morelia, México
[6] INAF-Osservatorio Astrofisico di Torino, via Osservatorio 20, 10025, Pino Torinese, Italia

Abstract

Blazars are a subclass of active galactic nuclei (AGNs) with a relativistically boosted jet pointing towards the Earth. They are one of the most violent and variable objects in the Universe, showing extreme variability across the entire electromagnetic spectrum. The jet generally dominates the optical emission of these sources. However, other components such as the stellar emission from the host galaxy or the accretion disk may contribute significantly to this emission. Disentangling the different contributions to the optical emission of these sources is challenging due to the high dominance of the jet, but is crucial to study and understand the variability detected in these objects. In this work we will present the results of the spectral variability analysis performed in a sample of gamma-ray blazars monitored by the Steward Observatory from 2008 to 2018. We make use of the non-negative matrix factorization (NMF), a statistical tool of dimensionality reduction to decompose the spectra of each source in the minimum number of components required to explain its spectral variability. We propose an approach based on a meaningful association of each component with the different expected emitting regions in the AGN, namely the jet, broad line region, accretion disk and stellar population. Using this decomposition we study the contribution of each component, and its corresponding physical association, to the flux evolution and the overall variability of the AGN, together with a possible interpretation of the different variability signatures observed in each blazar. This study has been published in MNRAS: 10.1093/mnras/stac475.

My poster is available at https://zenodo.org/record/7047405#.Y34WCS3FTUp

Highlights of Spanish Astrophysics XI, Proceedings of the XV Scientific Meeting of the Spanish Astronomical Society held on September 4–9, 2022, in La Laguna, Spain. M. Manteiga, L. Bellot, P. Benavidez, A. de Lorenzo-Cáceres, M. A. Fuente, M. J. Martínez, M. Vázquez- Acosta, C. Dafonte (eds.), 2023

Resolving the ionised outflows in GATOS Seyfert galaxies with GTC/MEGARA.

L. Peralta de Arriba[1], A. Alonso-Herrero[1], M. Villar-Martín[2], S. García-Burillo[3], I. García-Bernete[4], B. García-Lorenzo[5,6], D. J. Rosario[7], E. Bellocchi[8,9], E. K. S. Hicks[10], Á. Labiano[11], and N. A. Levenson[12]

Affiliations are listed at the next page

Abstract

Active galactic nuclei (AGNs) play a crucial role in galaxy evolution, as their feedback has been proposed to shape some galaxy properties (for instance, the galaxy luminosity functions). Ionised outflows and their feedback effects have been routinely studied in powerful AGNs, but are less explored for Seyfert galaxies. The abundance of the latter in the local universe gives us the opportunity to investigate the phenomenon with more physical detail. In particular, optical integral-field unit (IFU) observations (covering the most prominent nebular lines: [O III], Hβ, [O I], Hα, [N II] and [S II]) of nearby Seyfert galaxies are ideal to identify ionised outflows and derive their properties. IFU observations also provide spatially-resolved information about the main ionisation mechanisms, including, AGN, shocks, and/or star formation, in the nuclear and circumnuclear regions. In this contribution, we present GTC/MEGARA results obtained for six nearby Seyfert galaxies belonging to the Galactic Activity, Torus, and Outflow Survey (GATOS).

My poster is available at https://zenodo.org/record/7048958

Highlights of Spanish Astrophysics XI, Proceedings of the XV Scientific Meeting of the Spanish Astronomical Society held on September 4–9, 2022, in La Laguna, Spain. M. Manteiga, L. Bellot, P. Benavidez, A. de Lorenzo-Cáceres, M. A. Fuente, M. J. Martínez, M. Vázquez- Acosta, C. Dafonte (eds.), 2023

Star Formation Histories and chemical enrichment using Neural Networks.

Enrique Galceran[1], Paricia Sánchez-Blázquez[1], and The PHANGS team

[1] Departamento de Física de la Tierra y Astrofísica & IPARCOS-UCM (Instituto de Física de Partículas y del Cosmos de la UCM)

Abstract

We present spatially resolved Star Formation Histories and metallicity evolution on nearby galaxies. We use Convolutional Neural Networks with a combination of MUSE optical spectroscopy and HST photometry in the UV range. Combined with the high-resolution CO emission information, this analysis will allow inferring the timescales for star formation and cloud destruction in different galaxy environments, providing clues about the dominant mechanisms of stellar feedback.

The Convolutional Neural Network has been trained with simulated spectra, generated based on observational data from the PHANGS catalogue. One of the main challenges of this work resides in the degeneracy in the resulting spectra as a result of combinations of Star Formation History and Metallicity. To break this degeneracy, Ultraviolet photometric observations from HST are added to the neural network's input. This additional information allows the Convolutional Neural Network to improve the prediction and distinguish between different Star Formation Histories and Metallicities. The outputs are weighted favouring younger star formation, as these are the star formation histories we are interested in using further on.

My poster is available at https://zenodo.org/record/7047433#.Y8Ery-zMLCV

Highlights of Spanish Astrophysics XI, Proceedings of the XV Scientific Meeting of the Spanish Astronomical Society held on September 4–9, 2022, in La Laguna, Spain. M. Manteiga, L. Bellot, P. Benavidez, A. de Lorenzo-Cáceres, M. A. Fuente, M. J. Martínez, M. Vázquez- Acosta, C. Dafonte (eds.), 2023

Temporal resolution of transient sources with LST-1: application to BL Lacertae.

A. Aguasca-Cabot[1], P. Bordas[1], and M. Ribó[1] for the CTA LST Project

[1] Departament de Física Quàntica i Astrofísica, Institut de Ciències del Cosmos (ICCUB), Universitat de Barcelona (IEEC-UB)

Abstract

The capability of LST-1 to probe the rapid variability emission of fast gamma-ray flares produced by BL Lacertae is studied. We use a dedicated algorithm developed for very-high-energy transient sources to retrieve the minimum time-binning of the light curve considering the detection of the source above a given statistical significance level. Our results show that the LST-1 can achieve a temporal resolution shorter than one minute with a statistical significance of at least 3σ for bright flares as the one produced by BL Lacertae in August 2021.

My poster is available at https://doi.org/10.5281/zenodo.7042520

Highlights of Spanish Astrophysics XI, Proceedings of the XV Scientific Meeting of the Spanish Astronomical Society held on September 4–9, 2022, in La Laguna, Spain. M. Manteiga, L. Bellot, P. Benavidez, A. de Lorenzo-Cáceres, M. A. Fuente, M. J. Martínez, M. Vázquez- Acosta, C. Dafonte (eds.), 2023

The OTELO Survey.

Padilla-Torres, Carmen P.[1,2,3,4]**; Cepa Nogué, Jordi**[2,3,4]**; Cedrés, Bernabé** [2,3,4]**;, and OTELO team***

[1]Fundación Galileo Galilei, Rambla José Ana Fdez.Pérez, Breña Baja C.P. 38264, Santa Cruz de Tenerife, Spain. [2] Instituto de Astrofísica de Canarias, c/ Vía Láctea s/n, C.P. 38200 San Cristobal de La Laguna, Santa Cruz de Tenerife, Spain. [3]Universidad de La Laguna, San Cristobal de La Laguna, Santa Cruz de Tenerife, Spain. [4]Asociación Astrofísica para la Promoción de la Investigación, Instrumentación y su Desarrollo, ASPID, E-38205 La Laguna, Tenerife, Spain * multiple intitutions

Abstract

OTELO is an ultradeep, 2D-spectroscopic (R∼700) blind survey, defined on a window of 210Å, centred at 9175Å, targeting a region of the Extended Groth Field that is embedded in the Deep field 3 of the Canada-France-Hawaii Telescope Legacy Survey (CFHTLS). Is the deepest pointing of GALEX in imaging and spectroscopy. Such Pseudo-spectra(PS) were obtained using the red Tunable Filter (RTF) of the OSIRIS instrument at GTC. OTELO detects emission lines with a limiting flux of 5×10^{-19} erg/s/cm^2 and observed equivalent widths (EW)≥5Å. Besides, OTELO is targeting low mass galaxies, down to $M_* \sim 10^6 M_\odot$. As reference, the MUSE Hubble Ultra Deep Field barely reach down to $M_* \sim 10^8 M_\odot$ in few cases, and only at redshifts below 0.4, and none at redshifts above ~ 0.7. However, OTELO detects the bulk of emitters around $10^8 - 10^9 M_\odot$ even at redshifts as high as 1.4, reaching down to $10^7 M_\odot$ at redshift 0.4. Then, OTELO reaches stellar masses one order of magnitude lower than MUSE Hubble Ultra Deep Field. We were able to generate a catalogue of 60[OII] emitters at $< z >= 1.43$. The 93% of those have masses in the range of $10^8 < M_*/M_\odot < 10^9$, classified as late-type galaxies. From [OII] emitters we generated the Luminosity Function, sampling it down to ~ 1 dex lower than in previous works. Taking into account the results obtained for the lines H_α, H_β and [OII], we were able to study the star formation rate, star formation rate density, and number density and the evolution of those parameters between $z \sim 0.4$ and 1.43. We obtained a robust estimate of the specific star formation rate stellar mass relation based on the lowest mass sample published so far. We also determine a flat trend of the star formation rate density and number density with redshift.

My poster is available at https://zenodo.org/record/7033260#.Y8RTHuzP10t

Highlights of Spanish Astrophysics XI, Proceedings of the XV Scientific Meeting of the Spanish Astronomical Society held on September 4–9, 2022, in La Laguna, Spain. M. Manteiga, L. Bellot, P. Benavidez, A. de Lorenzo-Cáceres, M. A. Fuente, M. J. Martínez, M. Vázquez- Acosta, C. Dafonte (eds.), 2023

The demographics of dynamically-formed binary black holes in star clusters.

Daniel Marín Pina[1]

[1] Departament de Física Quàntica i Astrofísica, Institut de Ciències del Cosmos, Universitat de Barcelona, Martí i Franquès 1, E-08028 Barcelona, Spain

Abstract

Dynamical binaries are formed from unbound objects by multiple-body interactions in the centre of star clusters. These binaries release energy by shrinking their orbital radius via encounters with single objects, which prevents the core collapse of globular clusters. This process is one of most important pathways for the formation of black hole mergers and the production of gravitational waves.

If we take their formation rate, the maximum binding energy and its increase rate due to binary-single encounters, we should expect many binaries, increasing with lower cluster masses. Instead, in N-body simulations we find that there is only one dynamical binary at any given moment in a cluster. This discrepancy can be explained by binary-binary encounters, which are very effective at disrupting binaries. Such interactions may cause mergers with characteristic observables (i.e. orbital eccentricity) so neglecting them may have led us to wrongly predict the distribution of gravitational wave observables.

Improving our understanding of these observables will open up new probes for studying star clusters.

My poster is available at https://zenodo.org/record/7046551#.Y29zzdLMKV4

Highlights of Spanish Astrophysics XI, Proceedings of the XV Scientific Meeting of the Spanish Astronomical Society held on September 4–9, 2022, in La Laguna, Spain. M. Manteiga, L. Bellot, P. Benavidez, A. de Lorenzo-Cáceres, M. A. Fuente, M. J. Martínez, M. Vázquez- Acosta, C. Dafonte (eds.), 2023

Uncovering hundreds of extreme emission line galaxies with J-PLUS: beyond Green Peas and Blueberry galaxies.

Lumbreras-Calle, A.[1], López-Sanjuan, C.[1], Sobral, D.[2], Fernández-Ontiveros, J. A.[1], Víchez, J. M.[3], Hernán-Caballero, A.[1], and Akhlaghi, M[1]

[1] Centro de Estudios de Física del Cosmos de Aragón (CEFCA). Teruel (Spain)
[2] Lancaster University (United Kingdom)
[3] Instituto de Astrofísica de Andalucía (IAA). Granada (Spain)

Abstract

Extreme emission line galaxies (EELGs) constitute a population of unique systems undergoing very intense events of star formation, which are very rare in the local Universe. They nevertheless hold clues into the limits of star formation processes and can be considered analogs of the first galaxies in the Universe, given the physical properties they share.
To find EELGs, we have used the unprecedented dataset of the second data release of the J-PLUS survey, with 2000 square degrees of the northern sky observed from the Observatorio Astronómico de Javalambre (Teruel) with a set of narrow, medium and broad-band filters. We select as emitters objects with excess of flux in mediumband filters, and remove contaminants using WISE and J-PLUS photometry.
We have found 466 EELGs selected by their [OIII]5007 emission, with 410 of them previously unclassified as such. The derived [OIII]/Hα ratios show a wide range, more similar to previous simulations of reionization-era galaxies than Green Peas or Blueberries. The strong [OIII] and high [OIII]/[OII] ratios can be considered proxies for high ionization parameter and potential Lyman continuum leakage. Thanks to the use of mediumband filters, the volume density of the EELGs in this work is more than one order of magnitude higher than previous broadband-selected samples, and similar to magnitude-limited spectroscopic surveys. Additionally, we find 310 extreme Hα emitters at z$\sim$0.3, out of which 271 are newly discovered.
Finally, we have obtained longslit spectroscopic data for a subsample these EELGs. Preliminary analysis of the spectra show the accuracy of the sample selection, and the low metallicity and strong ionizing spectrum of the sources.

My poster is available at https://zenodo.org/record/7048043#.Y8RNftLMJH4

Highlights of Spanish Astrophysics XI, Proceedings of the XV Scientific Meeting of the Spanish Astronomical Society held on September 4–9, 2022, in La Laguna, Spain. M. Manteiga, L. Bellot, P. Benavidez, A. de Lorenzo-Cáceres, M. A. Fuente, M. J. Martínez, M. Vázquez- Acosta, C. Dafonte (eds.), 2023

What can we learn from constraining Extreme-Emission Line Galaxies models with large samples of local analogs?.

Enrique Pérez-Montero[1], Ricardo Amorín[2,3], José M. Vílchez[1], Jorge Sánchez Almeida[4,5], Rubén García-Benito[1], and Carolina Kehrig[1]

[1] Instituto de Astrofísica de Andalucía. CSIC. Apartado de correos 3004. 18080, Granada, Spain
[2]Instituto de Investigación Multidisciplinar en Ciencia y Tecnología, Universidad de La Serena, Raul Bitrán 1305, La Serena, Chile
[3]Departamento de Astronomía, Universidad de La Serena, Av. Juan Cisternas 1200 Norte, La Serena, Chile
[4]Instituto de Astrofísica de Canarias. C/ Vía Lactea s/n. La Laguna, Tenerife, Spain
[5] Departamento de Astrofísica, Universidad de La Laguna, Tenerife, Spain

Abstract

Extreme Emission Line Galaxies (EELGs) are characterized by their compact sizes and very high equivalent widths of certain optical emission lines (e.g. EW([OIII]) > 500Å), indicative of very high specific star formation rates, similar to those detected in the reionization epoch galaxies. Many of them also present certain high-excitation emission-lines, such as HeII at λ 4686Å, indicative of a very hard incident stellar radiation.
We compiled from the Sloan Digital Sky Survey (SDSS) the largest (around 2000) sample of EELGs using an automatic algorithm and we studied their physical properties and chemical abundances from the direct method. This allowed us to study the fundamental relations followed by this type of galaxies (e.g MZR, O/H vs N/O). This observational feedback can be used to constrain photoionization models from which we can provide model-based solutions to derive the properties of the high-redshift galaxies using only their available observed strong emission-lines.
Among the model-based solutions that benefit from this constrains and can be subsequently applied to high-redshift EELGs it is the HII-CHI-MISTRY code. We show that this code can be adapted to give specific solutions to derive e.g. chemical abundances and to interpret the softness diagram involving the nebular HeII emission. The latter can be used to quantify the hardness of ionizing incident spectral energy distribution and the fraction of leaking photons.

My poster is available at https://zenodo.org/record/7034458#.Y1oq8i8l03U

Highlights of Spanish Astrophysics XI, Proceedings of the XV Scientific Meeting of the Spanish Astronomical Society held on September 4–9, 2022, in La Laguna, Spain. M. Manteiga, L. Bellot, P. Benavidez, A. de Lorenzo-Cáceres, M. A. Fuente, M. J. Martínez, M. Vázquez- Acosta, C. Dafonte (eds.), 2023

ΩMEGA: the Ωrigin of the Morphological Evolution of GAlaxies.

Luca Costantin[1], Pablo Pérez-González[1], Jesús Vega-Ferrero[2], and Marc Huertas-Company[2,3,4]

[1] Centro de Astrobiología (CAB/CSIC-INTA), Ctra. de Ajalvir km 4, Torrejón de Ardoz, E-28850, Madrid, Spain
[2] Instituto de Astrofísica de Canarias, 38200, La Laguna, Tenerife, Spain
[3] Departamento de Astrofísica, Universidad de La Laguna, 38205, La Laguna, Tenerife, Spain
[4] LERMA, Observatoire de Paris, CNRS, PSL, Université de Paris, France

Abstract

How do galaxies shape their morphology through time? How many details of galaxies at cosmic noon are we going to unveil? This contribution aims at presenting the expected performance of JWST imaging observations in constraining the evolution of galaxies and the origin of the Hubble sequence. In particular, I describe NIRCam mock observations of high-redshift galaxies ($3 < z < 6$) from the TNG50 cosmological simulation, discussing their parametric and non-parametric morphology.

To date, most of the available JWST simulations on the market are based on semi-analytic models and use smooth morphologies (mainly Sérsic profiles) to describe the galaxy light distribution. Providing the need for a more realistic description of the diversified structures of high-redshift galaxies, I describe the creation of synthetic images of about 25,000 galaxies from the suite of TNG50 galaxies tailored for JWST observations at multiple wavelengths. These noiseless images were processed with the mirage simulator to mimic the observational strategy (e.g., noise, dithering pattern, etc.) of the Cosmic Evolution Early Release Science survey (CEERS), one of the thirteen Early Release Science (ERS) programs approved worldwide. For each galaxy, I present the parametric and non-parametric morphology, comparing the expected performances of NIRCam in characterizing the galaxies' features at different redshift and wavelengths.

This analysis provides a fundamental bench test for the forthcoming ERS programs, granting the community realistic mock observations and a catalog of high-redshift galaxies to compare with the first data releases and investigate the best strategy for future observations.

My poster is available at https://zenodo.org/record/7034766#.Y62J2y1aZpQ

Highlights of Spanish Astrophysics XI, Proceedings of the XV Scientific Meeting of the Spanish Astronomical Society held on September 4–9, 2022, in La Laguna, Spain. M. Manteiga, L. Bellot, P. Benavidez, A. de Lorenzo-Cáceres, M. A. Fuente, M. J. Martínez, M. Vázquez- Acosta, C. Dafonte (eds.), 2023

Can matter enter voids? Inflows in underdense regions.

Vallés-Pérez, D.[1], Planelles, S.[1,2], and Quilis, V.[1,2]

[1] Departament d'Astronomia i Astrofísica, Universitat de València. Burjassot (València), E-46100, Spain
[2] Observatori Astronòmic, Universitat de València. Paterna (València), E-46980, Spain

Abstract

In this contribution, we report results from the analysis of a cosmological simulation specially designed to accurately resolve low-density regions, such as cosmic voids. Contrary to the common expectation, we find that some voids experience significant mass inflows over cosmic history. On average, 10% of the mass of voids in the sample at $z \sim 0$ is inflown from overdense regions, reaching values beyond 35% for a significant fraction of voids. More than half of the mass entering the voids lingers on periods of time up to 10 Gyr well inside them, reaching inner regions. This would imply that part of the gas lying inside voids at a given time proceeds from overdense regions (e.g., clusters or filaments), where it could have been preprocessed. These results could potentially challenge the scenario of galaxy formation in voids, since they dissent from the idea of them being pristine environments.

1 Introduction

Cosmic voids are underdense regions which fill up most of the volume in the Universe. They emerge in regions comprising negative primordial density fluctuations, and subsequently expand as the matter (dark matter [DM], gas and galaxies) around them collapses and forms walls, filaments, and clusters. Therefore, their dynamics are governed by outflows, which have been found both in simulations [11, 6], observations [4] and analytical models of isolated voids [1]. However, in a complex, non-linear, cosmological environment, it is in principle possible to expect that some matter that unbinds from dense structures (e.g., in galaxy cluster mergers [3]) ends up penetrating in and circulating through underdense regions.

Whether there are relevant inflows to voids or there are not is an important question to address, since voids are assumed to be pristine regions (i.e., uncontaminated by material coming from the outside). This implies important consequences for the galaxy formation scenario in these environments [10]. Within this context, the aim of the work reported in this contribution is to check whether there are any relevant inflows through the boundaries of cosmic voids. For this aim, we make use of a Λ cold dark matter (ΛCDM) cosmological

simulation of a moderately large volume, which is specially designed to describe matter in and around cosmic voids.

This contribution is organised as follows. In Sec. 2, we cover the numerical aspects of this work, including the simulation details, the void identification scheme and the method used to estimate gas mass fluxes. In Section 3 we present our results, and in Section 4 we summarise and discuss our conclusions. While this is a short contribution, we refer the interested reader to [13], where we presented a complete description of this work.

2 Numerical details

Here, we provide the basic details about the numerical aspects concerning this work, while a more complete description can be found in [13].

2.1 The simulation

We have analysed the results of a cosmological, DM+hydrodynamics simulation of a periodic, cubic domain of comoving side length $L = 100\,h^{-1}$Mpc, carried on with `MASCLET` [8]. The simulation is well suited to describe the gaseous component in low-density regions such as cosmic voids, thanks to the Eulerian hydrodynamics and the Adaptive Mesh Refinement (AMR) scheme in `MASCLET`.

The initial conditions are set up at $z_{\rm ini} = 100$, with a procedure aimed to sample the regions which will evolve into voids at low redshift with enhanced resolution (see [9]). The simulation is then evolved with AMR, dynamically refining underdense regions and the structures emerging within them. Several gas cooling processes, a phenomenological treatment of star formation, supernova feedback and metal enrichment are also accounted for in the simulation, although this is not the main focus of this work.

2.2 The void finding strategy

To identify our sample of cosmic voids in the simulated domain, we have defined voids as the largest possible ellipsoids around underdense, peculiarly expanding regions, possibly limited by steep density gradients. In practical terms, our void finding algorithm is based on the one of [9], but imposing a smooth, ellipsoidal shape, in contrast to the complex, arbitrarily-shaped voids (i.e., non-convex, non-simply connected) of the original finder. In this sense, our ellipsoidal voids are more conservatively defined than the arbirarily-shaped ones, since by definition our algorithm looks for the largest possible ellipsoids inside the complex-shaped voids. Having a smooth shape is crucial for the reliability of the pseudo-Lagrangian estimation of gas mass fluxes (see Section 2.3).

Once the sample of cosmic voids is identified at each snapshot of the simulation (at each fix redshift), the evolutionary history of each void is traced by connecting, between each pair of snapshots, the voids which maximise their *volume retention*, defined as $VR = V_{A\cap B}/\sqrt{V_A V_B}$, where A (B) refers to the void in the first (second) iteration of the pair.

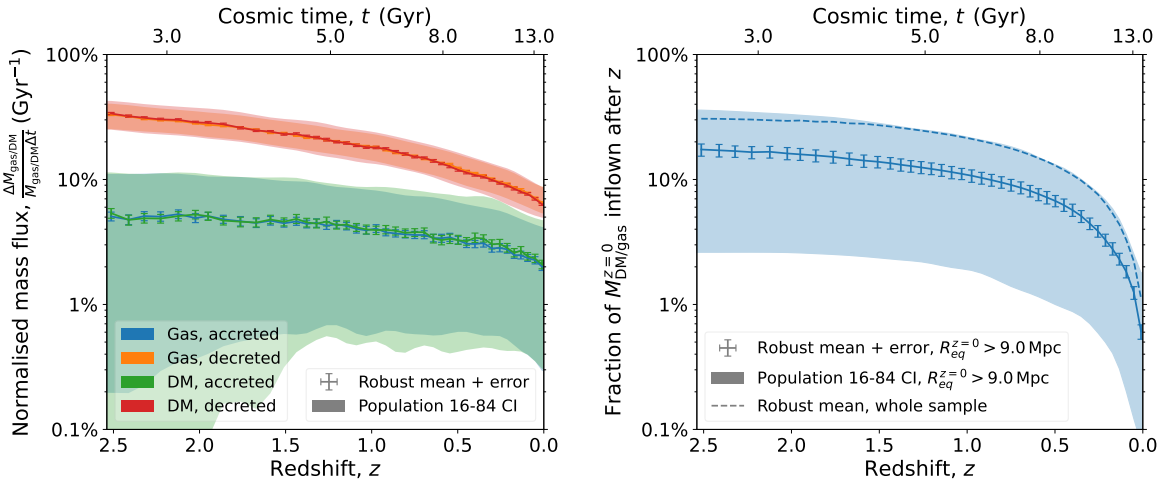

Figure 1: Evolution of the inflow and outflow rates in the void sample. *Left panel:* evolution of the normalised mass fluxes (of gas and DM; inflown and outflown; according to the legend in the bottom left corner) as a function of redshift (lower axis) or cosmic time (upper axis). Lines refer to the robust mean, and shaded regions correspond to $(16-84)$ confidence intervals (CIs) over the population. *Right panel:* Fraction of the gas mass having been inflown after a given redshift z. The solid line corresponds to the robust mean of this quantity over the subsample of voids with $R^{z=0}_{\rm eq} > 9\,{\rm Mpc}$, while the dashed line corresponds to the whole sample. The shaded region correspond to the $(16-84)$ CI for the former case. Figure from [13], ©AAS. Reproduced with permission.

2.3 The pseudo-Lagrangian estimation of gas mass fluxes

In order to estimate the fluxes of gas through the boundary of a void, given that Eulerian gas is not directly traceable, we use a simple pseudo-Lagrangian approach, which was also previously applied in the context of accretion flows onto galaxy clusters [12]. At each fix-time snapshot, we consider all volume elements (i.e., gas cells) of the simulation as pseudo-Lagrangian fluid elements, and we advect them using an explicit, first-order step. We use that information for assessing the flux of gas mass towards/from the (instantaneously fix) ellipsoidal boundary of the void at a given time[1]. We thoroughly discuss the validity of this approach in [13].

3 Results

Figure 1 presents a summary of our results over the void sample. In the left-hand side panel, we present the evolution of the integrated gas and DM mass fluxes, both for inflows and for outflows, normalised to the mass of the corresponding component (gas or DM) within the

[1]It is worth emphasizing that: (i) we are not properly integrating the motion of the pseudo-Lagrangian fluid elements, but only estimating the fluxes at a given, fix time; and (ii) our measured fluxes are not produced by the change of the volume of the void between a pair of snapshots, but to matter actively approaching/moving away from the void.

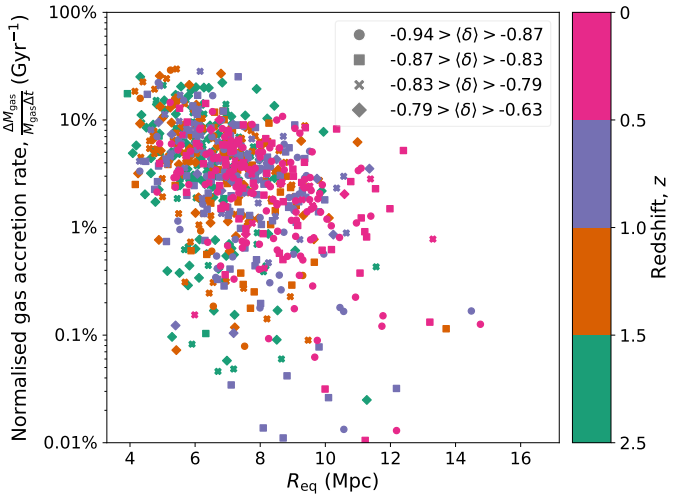

Figure 2: Normalized gas inflow rate (gas inflow per gigayear in units of the void's gas mass; vertical axis) versus the size of the void (equivalent radius; horizontal axis). The gas inflow rates are computed on four redshift intervals, shown in the colour scale. Different markers split the sample in different mean overdensity within the void according to the legend. Figure from [13], ©AAS. Reproduced with permission.

void at the given moment. This quantity is to be read as the fraction of the mass of the given component being inflown/outflown per unit time. Naturally, the flow of gas through void boundaries is dominated by outflows. However, inflows are also present in our sample in a statistical sense, with mean values $1/6 - 1/3$ those of the outflows. The average magnitude of the inflows evolves from $\sim 5\%\,\mathrm{Gyr}^{-1}$ at $z \simeq 2.5$ to $\sim 2\%\,\mathrm{Gyr}^{-1}$, with remarkably large scatter. This implies that, while many of the voids do not undergo significant inflows, some others suffer inflows considerably stronger than the mean.

The right-hand side panel of Fig. 1 presents the anticummulative inflown gas mass fraction, that is to say, the fraction of the gas mass of a void at redshift $z = 0$ that has been inflown since a given redshift z. The solid line (robust mean [2]) and the shaded region ($16-84$ percentiles) correspond to the subsample of large voids (equivalent radius at $z = 0$ $R_{\mathrm{eq}}^{z=0} > 9\,\mathrm{Mpc}$). This shows that around 10% of the current gas mass of the typical large void at $z = 0$ has been dynamically inflown since $z = 1$ (reaching beyond 20% since $z = 2.5$).

Looking at the whole population of voids, Fig. 2 displays the gas inflow rates (normalised to the gas mass within the void; vertical axis) in relation to size of the void (horizontal axis). Here, we have considered four broad redshift bins to compute the inflow rates, which are encoded in the figure by the colour. The plot shows that, at any cosmic epoch, there are voids having relevant inflow rates (higher than a few percents per Gyr). While small voids show the highest inflow rates (since they are more susceptible to external influences), large voids with large inflow rates do also exist.

4 Summary and conclusions

The results that we present in the contribution challenge the usual picture of voids as pristine environments due to their purely outflowing velocity field and, therefore, could potentially impact the scenario of galaxy formation and evolution in these environments. We find that, if voids are to be defined as the largest possible ellipsoidal regions around peculiarly expanding density minima, possibly limited by steep density gradients, then it is not possible to guarantee the absence of inflows. Material circulating within the void, coming from the outside, may be able to bring chemically and thermodynamically preprocessed gas, which could be subsequently accreted by void galaxies. A more complete presentation of our results can be found in [13].

While in this work we show the presence of inflows onto our sample of cosmic voids, it is worth emphasizing a few caveats and future directions. First, there are many different strategies to define a void, with remarkable differences in the resulting objects (see, for example, [5]). Therefore, future work should be directed to compare with other void definitions and identification strategies. Secondly, future cosmological simulations, capable of forming realistic galaxies both inside and outside voids, could be used to assess the impact of this effect on galaxies residing within voids, if any.

Acknowledgments

This work has been supported by the Spanish Agencia Estatal de Investigación (AEI, grant PID2019-107427GB-C33) and by the Generalitat Valenciana (grant PROMETEO/2019/071). D.V. acknowledges partial support from Universitat de València through an Atracció de Talent fellowship. Simulations have been carried out using the supercomputer Lluís Vives at the Servei d'Informàtica of the Universitat de València.

References

[1] Baushev, A.N., 2021, MNRAS, 504:1, L56

[2] Beaton, A.E. & Tukey, J.W., 1974, Technometrics, 16, 147

[3] Behroozi, P.S., Loeb, A. & Wechsler, R.H., 2013, JCAP, 06, 019

[4] Bothun, G.D., Geller, M.J., Kurtz, M.J., Huchra, J.P. & Schild, R.E., 1992, ApJ, 395, 347

[5] Colberg, J.M., Pearce, F., Foster, C., et al., 2008, MNRAS, 387:2, 933

[6] Padilla, N.D., Ceccarelli, L. & Lambas, D.G., 2005, MNRAS, 363:3, 977

[7] Patiri, S.G., Betancort-Rijo, J. & Prada, F., 2012, A&A, 541, L4

[8] Quilis, V., 2004, MNRAS, 352:4, 1426

[9] Ricciardelli, E., Quilis, V. & Planelles, S., 2013, MNRAS, 434:2, 1992

[10] Ricciardelli, E., Cava, A., Varela, J. & Quilis, V., 2014, MNRAS, 445:4, 4045

[11] van de Weygaert, R., & van Kampen, E., 1993, MNRAS, 263:2, 481

[12] Vallés-Pérez, D., Planelles, S. & Quilis, V., 2020, MNRAS, 499:2, 2303

[13] Vallés-Pérez, D., Quilis, V. & Planelles, S., 2021, ApJL, 920, L2

Highlights of Spanish Astrophysics XI, Proceedings of the XV Scientific Meeting of the Spanish Astronomical Society held on September 4–9, 2022, in La Laguna, Spain. M. Manteiga, L. Bellot, P. Benavidez, A. de Lorenzo-Cáceres, M. A. Fuente, M. J. Martínez, M. Vázquez- Acosta, C. Dafonte (eds.), 2023

Constraining VHE and optical emission from Fast Radio Bursts with the MAGIC telescopes.

Jiménez Martínez, I.[1] **for the MAGIC Collaboration**

[1] Centro de Investigaciones Energéticas Medioambientales y Tecnológicas (CIEMAT)

Abstract

Fast Radio Bursts (FRBs) are radio transients characterized by bright radio pulses of millisecond duration. Most of them show dispersion measures (DMs) consistent with extragalactic progenitors, something that has been confirmed with multiple high-resolution localizations and associations. Even if multiple theories have been proposed to explain the origin of FRBs, magnetars are currently the prime progenitor candidates: this is supported by the successful association of a FRBs source with the galactic magnetar SGR 1935+2154, which proves that at least some of them are originated in this kind of source. These sources are well known emitters of fast, bright, non-thermal emission. Flares have been associated with both fast optical and high-energy gamma-ray emission. MAGIC, a system of two 17 m diameter imaging atmospheric Cherenkov telescopes located in the island of La Palma, is technically well suited to constrain their multi-wavelength emission. MAGIC started observing FRBs back in 2016 in both the very-high-energy (VHE, E $>$ 100 GeV) and optical bands, coordinating with radio instruments. This is a report on the status of several joint campaigns between MAGIC and other observatories to constrain both the optical and VHE gamma-ray emission simultaneous to FRBs.

1 Introduction

1.1 Fast Radio Bursts

Fast Radio Bursts (FRBs) are a kind of astrophysical transient that consists on fast, bright radio flashes. They were first discovered with the Parkes Radio Telescope in Australia in 2007 [5]. Since then, over 600 FRB sources have been detected, displaying a wide range of characteristics. So far, 24 of them exhibit a repeating behaviour but others do not, which may suggest different emission mechanisms. At least 2 of the repeaters also display periodic states of activity: FRB 20121102A [9] and FRB 20180916B [1], with periods of 157 [8] and 16.35 [2] days respectively. For this kind of FRB sources (repeaters), young magnetars are the prime candidates (and perhaps also for non-repeating ones). This is supported by the detection of FRBs coming from the galactic magnetar SGR 1935+2154, which was the first known FRB

emitter associated to a known source within our galaxy. In case of the non-repeaters, more cataclysmic scenarios have been proposed like merging of neutron stars [11].

Most FRB emitters have been identified to come from outside of our galaxy by studying their dispersion measures (DMs): depending on from where and from how far away the FRB was produced with respect to Earth, the pulse gets more dispersed by the free electrons in our galaxy (different column depths) the farther away the source is, which has a direct effect on the delay of the pulse observed in different frequencies. Given that there is a maximum dispersion measure in any given direction within our galaxy (that can be explained by the models of free galactic electrons), if a significantly greater dispersion is observed, then we are looking at an extragalactic event. This is one of the main reasons why these events remain a mystery: most of them come from cosmological distances and yet we observe them with such a great brightness that the energy involved in their production must be huge. Another reason is that they have only been detected in radio and very few of them simultaneous to other wavelengths. Nevertheless, several multi-wavelength campaigns are being proposed for these targets.

1.2 The potential of MAGIC telescopes in detecting FRBs counterparts

The MAGIC telescopes are 2 IACTs located in Roque de los Muchachos, in La Palma, Spain. They have 17 m diameter reflectors composed of tessellated mirrors and are sensitive to gamma-rays between 25 GeV and 30 TeV.

1.2.1 MAGIC's potential to detect fast VHE bursts

In 2020 two bursts were detected almost simultaneously in radio and X-rays for the galactic magnetar SGR 1935+2154 [7].

Magnetars show very diverse transient activity with short, large and giant flares. For the moment there is no link between short flares and high energy (HE) emission, but giant flares (GFs) have been detected by Fermi-LAT ($E > 1$ GeV). This proves that these sources have the energy budget to emit in HE. If there is an even higher energy present, MAGIC could not only detect the flare, but thanks to its higher collection area it would be more sensitive than Fermi-LAT over very-short timescales ($\sim$minutes).

1.2.2 MAGIC's potential to detect fast optical bursts

Current magnetar models support the possibility of observing optical bursts. In fact, ultra-fast optical emission was detected some years ago and it may be associated with a SGR [10]. MAGIC has a special setup called Central Pixel in the central pixel of each camera that works as a fast optical photometer [3]

1.2.3 FRB 121102

It was the first repeating source of FRBs. It was observed by MAGIC in 2017 in both VHE and optical and by Arecibo in radio [6]. Five radio bursts were detected simultaneous to MAGIC observations. No counterpart was found for any of the pulses, but the emission was constrained in both VHE and optical. A bright 12ms optical flash occurred 4.3 s before one FRB but it was consistent with irreducible background (2.2σ). Still MAGIC was able to provide the strongest upper limits by then.

2 Sources

Since then, we focus on these known repeaters:

SGR 1935+2154: This soft gamma repeater (SGR) is the first FRB emitter associated to a known source. It is located within our galaxy (9.0±2.5 kpc), which has allowed it to be detected in both radio and X-rays.

FRB 20200120E: It is the closest known extragalactic source of FRBs, it is a repeater and it is located in a globular cluster of M81. The fact that it is located in a globular cluster challenges the current models that support that FRBs originate from young magnetars. Instead, in [4], authors propose that this FRB source is a highly magnetized neutron star, formed by accretion-induced collapse of a white dwarf or by a merger of compact stars in a binary system.

FRB 20180916B: This FRBs source is a repeater, and it is the first one observed to have periodic episodes of activity with repeating bursts over 4 days every 16.35±0.18 days.

3 Observations

Because of the nature of this transient (it is observed in radio) we exclusively focus on strictly simultaneous multi-wavelength coverage with both radio (for galactic and extragalactic sources) and X-rays (only for the galactic SGR due to extinction).

SGR 1935+2154: We have performed several campaigns totaling 43.5h of observation time, but no burst has been detected simultaneous to our observations so far, so we keep pursuing active states via ToO requests.

FRB 20200120E: We have performed a deep campaign of 17h simultaneous to 3 large radio antennas (in 3 different frequencies), but no FRBs were detected.

FRB 20180916B: We performed a short campaign of 2.4h together with radio, soft and hard X-rays and a FRB was detected simultaneous to our observations. Unfortunately, no burst was detected in X-rays, optical nor VHE; but we are providing differential and integral upper limits on the persistent VHE emission, integral VHE upper limits within the 10ms window surrounding the TOA, optical light curves covering 200ms around the TOA with an integration window of 2ms and optical upper limits.

4 Summary and discussion

The versatility of MAGIC allows it to act as a "triple threat": It can operate as a VHE telescope for bursts and persistent emission and as a fast optical telescope for optical bursts, all at the same time. Even with the bad luck of recent years (COVID and a volcano eruption in the island of La Palma) we have been able to gather a very significant amount of strictly simultaneous multi-wavelength data on several FRB repeaters, although the number of simultaneous bursts is still very limited. Unlike other major observatories, the time investment on this project is relatively minor compared with other MAGIC proposals, while its discovery potential is enormous. We will continue triggering multi-wavelength campaigns of these close-by repeaters with MAGIC (in the optical and VHE), radio antennas and X-ray satellites, hoping for a positive detection and a high-impact result.

References

[1] Andersen, B. C., Bandura, K., Bhardwaj, M., Boubel, P., Boyce, M. M., Boyle, P. J., ... and CHIME/FRB Collaboration. (2019). The Astrophysical Journal Letters, 885(1), L24.

[2] The CHIME/FRB Collaboration. Nature, 2020, vol. 582, no 7812, p. 351-355.

[3] Hassan, T., Hoang, J., López, M., Barrio, J. A., Cortina, J., Fidalgo, D., ... and Will, M. (2017). arXiv preprint arXiv:1708.07698.

[4] Kirsten, F., Marcote, B., Nimmo, K., Hessels, J. W. T., Bhardwaj, M., Tendulkar, S. P., ... and Vlemmings, W. (2022). Nature, 602(7898), 585-589.

[5] Lorimer, D. R., Bailes, M., McLaughlin, M. A., Narkevic, D. J., and Crawford, F. (2007). Science, 318(5851), 777-780.

[6] MAGIC Collaboration, Acciari, V. A., Ansoldi, S., Antonelli, L. A., Arbet Engels, A., Arcaro, C., ... and Zarić, D. (2018). Monthly Notices of the Royal Astronomical Society, 481(2), 2479-2486.

[7] Mereghetti, S., Savchenko, V., Ferrigno, C., Götz, D., Rigoselli, M., Tiengo, A., ... and Ubertini, P. (2020). The Astrophysical Journal Letters, 898(2), L29.

[8] Rajwade, K. M., Mickaliger, M. B., Stappers, B. W., Morello, V., Agarwal, D., Bassa, C. G., ... and Lorimer, D. R. (2020). Monthly Notices of the Royal Astronomical Society, 495(4), 3551-3558.

[9] Spitler, L. G., Cordes, J. M., Hessels, J. W. T., Lorimer, D. R., McLaughlin, M. A., Chatterjee, S., ... and Fehrmann, H. (2014). The Astrophysical Journal, 790(2), 101.

[10] Stefanescu, A., Kanbach, G., Słowikowska, A., Greiner, J., McBreen, S., and Sala, G. (2009, May). In AIP Conference Proceedings (Vol. 1133, No. 1, pp. 491-496). American Institute of Physics.

[11] Yamasaki, S., Totani, T., and Kiuchi, K. (2018). Publications of the Astronomical Society of Japan, 70(3), 39.

Highlights of Spanish Astrophysics XI, Proceedings of the XV Scientific Meeting of the Spanish Astronomical Society held on September 4–9, 2022, in La Laguna, Spain. M. Manteiga, L. Bellot, P. Benavidez, A. de Lorenzo-Cáceres, M. A. Fuente, M. J. Martínez, M. Vázquez- Acosta, C. Dafonte (eds.), 2023

Cosmology with the Rubin Observatory from the Dark Energy Science Collaboration.

Sevilla-Noarbe, I[1], and on behalf of the Dark Energy Science Collaboration

[1] Centro de Investigaciones Energéticas Medioambientales y Tecnológicas (CIEMAT), Madrid, Spain

Abstract

In this contribution, we briefly present the current status of the Rubin Observatory with a focus on the activities of the DESC: the Dark Energy Science Collaboration. This group has been developing a large body of preparatory work towards maximizing the scientific output of the Legacy Survey of Space and Time (LSST) for cosmology, including dark energy and dark matter research. We will highlight some of the projects performed, including work on precursor data, development of highly detailed simulations, and sophisticated software for testing and analysis.

1 The Vera C. Rubin Observatory and the LSST

The Vera C. Rubin Observatory is a new astronomical facility being built (as of January 2023) at Cerro Pachón, in Chile. It includes the Simonyi Survey telescope, whose primary mirror has an 8.4 meter diameter and a 9.6 square degree field of view and six optical-near infrared filters (*ugrizy*).

Once construction and commissioning are complete, by mid-2024 as of current schedule, the Rubin Observatory will conduct the 10-year Legacy Survey of Space and Time (LSST), a uniform photometric survey across half of the celestial sphere up to $r \sim 27.5$, using around 800 visits per pointing. In terms of raw data volume, this amounts to nearly 20 TB/night, with hundreds of petabytes accumulated by the end of the survey, in the 2030s. The data will be publicly released in catalogs, in a cadence to be determined, after a 2 year proprietary period. However, transient alerts will be public immediately through 'broker´ systems, less than a minute after shutter closure.

Commissioning is planned to start in late 2023. Currently, a 1.2 m telescope (AuxTel) is being operated with LSST software for testing, and eventually calibration purposes. Survey strategy is being finalized after several rounds of iterations. The LSST camera (LSSTCam) is set to be shipped to the summit in the coming weeks.

1.1 The LSST science topics

The LSST science revolves around four topics [5]:

- Cosmology and fundamental physics: which includes the exploration of the dark sector of fundamental physics, the mass of the sum of the different neutrino species and the nature of gravity. This will be done using a variety of approaches available to photometric surveys, such as the measurement of supernovae of type Ia, the combination of weak lensing and large scale structure, the study of galaxy cluster counts, the study of strong lensing systems, and various studies related to nearby dwarf systems and stellar streams.
- Milky Way structure and formation: including its evolutionary history and tests against small scale predictions of cosmology; spatial maps of stellar characteristics; reaching deep into the halo ($\sim$ 100 kpc), to map billions of main sequence stars and estimate their metallicities photometrically; detect and measure tidal stream properties and origin; find new and old satellite galaxies.
- Exploration of the transient sky: variable stars, e.g., creating an RR-Lyr census up to $\sim$ 400 kpc; a thorough search of supernovae of all types; filling the variability phase space; finding new rare, transient types; follow-up of targets of opportunity.
- Cataloging the Solar System: such as potentially hazardous asteroids; NEOs; and in general making an inventory of the Solar System.

2 The Dark Energy Science Collaboration

LSST science is mainly being developed through a federation of self-organized science collaborations. Their function is to prepare for data analysis, advise Rubin personnel in terms of the science goals, engage and train the scientific community, fundraise, develop inclusion practices, and provide software development.

In particular, the Dark Energy Science Collaboration aims at exploring the physics of the dark Universe, namely the nature of dark matter and dark energy. The core aspect of the DESC approach is firstly to have a tenfold increase in the dark energy figure of merit of Stage II experiments, according to the definitions of the Dark Energy Task Force [3] (Figure 1), but also focus on accuracy, by closing in on the systematic error budget. DESC will combine information from large scale structure and weak lensing, plus cluster count information, and in parallel incorporate supernovae and strong lensing cosmological constraints, while being open to new probes as they are developed in the coming years.

In addition, from the start, the DESC wants to focus on a collaborative approach that fosters an inclusive environment, as a core part of its way of functioning. On the other hand, DESC's procedures are being developed ensuring a continuous learning process based on experiences from previous Stage III collaborations, technically, scientifically and in terms of collaboration environment.

2.1 Technical challenges for the DESC

Following from previous experience, the DESC has been able to identify several technical aspects in which it will have to focus. The following list provides some non-exhaustive examples:

- Uniform coadded catalogs for weak lensing science will be a necessity, possibly creating new types of coadds to avoid PSF inhomogeneities. This is an intense are of research currently.
- Value added data will be needed beyond regular Rubin pipeline outputs, in particular for photometric redshifts whose systematic errors will have to be exquisitely calibrated.
- Supernovae cosmology will have to rely on photometric classifications (Ia) and on millimag level photometry using highest standards in calibration.
- Large scale structure wide area systematics have been proven (Stage III) to be thoroughly tested through several approaches.
- A new systematic source for cosmology surveys appears significantly in this dataset: blending effects (on object detection, for LSS, and photo-z, among others).

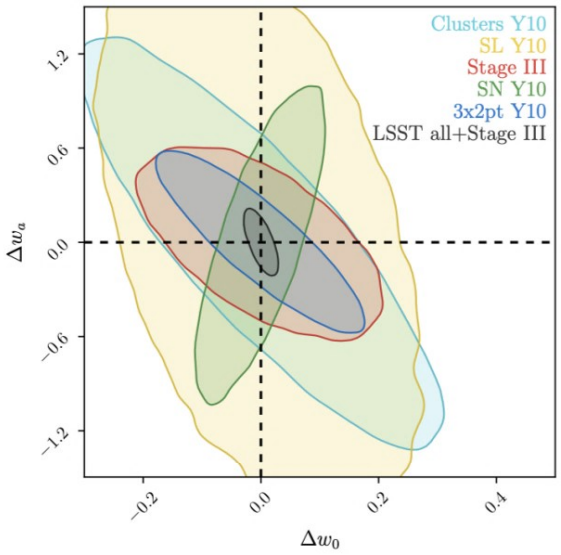

Figure 1: The forecast for dark energy constraints in $w_0 - w_a$ space (the DETF Figure of Merit) for DESC [2] using 10 years worth of data. Contours are 68% confidence intervals.

2.2 Selected DESC achievements to date

The author's biased selection of results from DESC. A full list can be found at this link:

- Simulations. A 300 square degree N-body simulation of objects with realistic colors and spatial correlations was created [1]. This included injections of supernovae and AGN light curves. The LSST observations were simulated with proper cadences, creation of images based on this cosmological simulation, and detection of sources using Rubin pipelines. The catalog testing and validation framework is described in [9] and [7]. This simulated catalog is used, among other things, to study for example optimization strategies for the tomographic binning of the combined large scale structure and weak lensing (3x2pt) measurements, as shown in [12]. A different set of simulations was used for the PLAsTiCC challenge [6] to understand the best approaches for supernova classification in the LSST area (analysis of results in [4]).
- Data Challenge 2. Various analyses groups developed and tested their science pipelines over these simulations with interesting results. An example is the realistic and rigorous analysis performed in [11] of the Difference Image Analysis pipeline of Rubin using these detailed simulations with realistic cadences and injected astrophysical transients.
- Precursor data analysis. Analyzing data from the Hyper Suprime Camera DR1 for large scale structure combined with weak lensing analyses for the first time in this data set in power spectra, as a test run for the high level DESC pipelines such as TXPipe [10] and Firecrown. Also using these pipelines to compare the cosmic shear outputs of precursor datasets [8].

Acknowledgments

DESC acknowledges ongoing support from the IN2P3 (France), the STFC (United Kingdom), and the DOE, NSF, and LSST Corporation (United States). DESC uses resources of the IN2P3 Computing Center (CC-IN2P3–Lyon/Villeurbanne - France) funded by the Centre National de la Recherche Scientifique; the National Energy Research Scientific Computing Center, a DOE Office of Science User Facility supported under Contract No. DE-AC02-05CH11231; STFC DiRAC HPC Facilities, funded by UK BEIS National E-infrastructure capital grants; and the UK particle physics grid, supported by the GridPP Collaboration. This work was performed in part under DOE Contract DE-AC02-76SF00515.

References

[1] The Dark Energy Science Collaboration 2021, ApJS, 253, 31

[2] Mandelbaum, R., Eifler, T., Hložek, R. et al. arXiv:1809.018669

[3] The Dark Energy Task Force arXiv:astro-ph/0609591

[4] Hložek, R., Ponder, K., Malz, A., et al. arXiv:2012.12392

[5] Ivezić,Ž., Kahn, S., Tyson, A., et al. 2019, ApJ, 873, 111

[6] Kessler, R., Narayan, G., Avelino, A. et al. PASP 2019, 131, 094501

[7] Kovacs, E., Mao, Y.-Y., Aguena, M. et al. 2021 The Open Journal of Astrophysics, 5, 1

[8] Longley, E.P., Chang, C., Walter, C., et al. arXiv:2208.07179

[9] Mao, Y-Y., Kovacs, E., Heitmann, K. et al. ApJS, 234, 36

[10] Prat, J., Zuntz, J., Omori, Y. et al. arXiv:2212.09345

[11] Sánchez, B., Kessler, R., Scolnic, D., et al. 2022, ApJ, 934, 96

[12] Zuntz, J., Lanusse, F., Malz, A. et al. 2021 The Open Journal of Astrophysics, 4, 1

Highlights of Spanish Astrophysics XI, Proceedings of the XV Scientific Meeting of the Spanish Astronomical Society held on September 4–9, 2022, in La Laguna, Spain. M. Manteiga, L. Bellot, P. Benavidez, A. de Lorenzo-Cáceres, M. A. Fuente, M. J. Martínez, M. Vázquez- Acosta, C. Dafonte (eds.), 2023

Testing the homogeneity of Type Ia Supernovae in the Near-infrared for accurate distance estimations.

Müller-Bravo T. E.[1,2], Galbany L.[1,2], Karamehmetoglu E.[3], Stritzinger M.[3], Burns C.[4], Phan K.[3,2], Iáñez-Ferres A.[1], Anderson J.[5], Ashall C.[6], Baron E.[7,8,9], Hoeflich P.[10], Hsiao E.[10], de Jaeger T.[6], Kumar S.[10], Lu J.[10], Phillips M.[11], Shahbandeh M.[10], Suntzeff N.[12], and Uddin S.[12,13]

[1] Institute of Space Sciences (ICE, CSIC), Campus UAB, Carrer de Can Magrans, s/n, E-08193 Barcelona, Spain
[2]Institut d'Estudis Espacials de Catalunya (IEEC), E-08034 Barcelona, Spain
[3]Department of Physics and Astronomy, Aarhus University, Ny Munkegade 120, DK-8000 Aarhus C, Denmark
[4]Observatories of the Carnegie Institution for Science, 813 Santa Barbara St., Pasadena, CA 91101, USA
[5]European Southern Observatory, Alonso de Córdova 3107, Casilla 19, Santiago, Chile
[6]Institute for Astronomy, University of Hawai'i, 2680 Woodlawn Drive, Honolulu, HI 96822, USA
[7]Department of Physics & Astronomy, University of Oklahoma, Norman, OK 73019 USA
[8]Department of Physics & Astronomy, George Washington University, Washington, DC USA
[9]Hamburger Sternwarte, Hamburg, Germany
[10]Department of Physics, Florida State University, 77 Chieftan Way, Tallahassee, FL 32306, USA
[11]Carnegie Observatories, Las Campanas Observatory, Casilla 601, La Serena, Chile
[12]George P. and Cynthia Woods Mitchell Institute for Fundamental Physics and Astronomy, Texas A&M University, Department of Physics and Astronomy, College Station, TX 77843, USA
[13]Centre for Space Studies, American Public University System, 111 W. Congress Street, Charles Town, WV 25414, USA

Abstract

Since the discovery of the accelerating expansion of the Universe more than two decades ago, Type Ia Supernovae (SNe Ia) have been extensively used as standardisable candles in the optical. However, SNe Ia have shown to be more homogeneous in the near-infrared (NIR), where the effect of dust extinction is also attenuated. In this work, we explore the possibility of using a low number of NIR observations for accurate distance estimations, given the homogeneity at these wavelengths. We found that one epoch in J and/or H band, plus good gr-band coverage, gives an accurate estimation of peak magnitudes in the J and H bands. The use of a single NIR epoch only introduces a small additional scatter for epochs around the time of B-band peak magnitude. These results provide confidence for our FLOWS project that is aimed at using SNe Ia with public ZTF optical light curves and few NIR epochs to map out the peculiar velocity field of the local Universe. This will allow us to determine the distribution of dark matter in our own supercluster, Laniakea, and to test the standard cosmological model by measuring the growth rate of structures, parameterised by fD, and the Hubble-Lemaître constant, H_0.

1 Introduction

The expansion rate of the Universe, parameterised by the Hubble-Lemaître parameter, H(z), varies across cosmic time. In the last few years, there has been tremendous effort to measure the local value, known as the Hubble-Lemaître constant (H_0), with extremely high precision ($< 2\%$ uncertainty;[37]). Recent results have further increased the discrepancy in the value of H_0 between the local distance ladder ($H_0 = 73.04 \pm 1.04\,\mathrm{km\,s^{-1}\,Mpc^{-1}}$, baseline with systematics; [37]) and the cosmic microwave background (CMB; $H_0 = 67.4 \pm 0.5\,\mathrm{km\,s^{-1}\,Mpc^{-1}}$;[34]) measurements, colloquially known as the 'Hubble tension', to 5σ (however, see [15, 22, 24] for some alternative local measurements). This discrepancy possibly hints towards new physics beyond the standard cosmological model, or alternatively, unaccounted systematic effects (see [11] for a recent review on the Hubble tension).

In the local Universe, the recession velocities measured from galaxies are affected by a combination of the expansion of the Universe and the gravitational pull of other adjacent galaxies. The measurement of these peculiar velocities is critical for two main reason. First, cosmological analyses with Type Ia Supernovae (SNe Ia) rely on discerning the contribution of peculiar velocities to isolate the cosmological redshift. Secondly, peculiar velocities can be used to inferred the matter-density distribution in the local Universe ([29]), including our own supercluster, Laniakea (e.g. [43]). The latter provides a direct measurement of the growth-rate of structure, which can be compared to estimates from the early Universe (e.g. [27]).

Current measurements of peculiar velocities often rely on methods such as the Fundamental-Plane and Tully-Fisher relations (e.g. [44]), which provide distances with relatively large uncertainties (with an rms of $\sim 20 - 30\%$ per galaxy) and only reach out to $z \sim 0.05$, standing

in the way of the study of the peculiar velocities at further distances. Therefore, there is a lack of higher-precision methods that can also extend to further redshifts for the estimation of distances in the local Universe.

Since the discovery of the accelerating expansion of the Universe more than two decades ago ([36, 30]), SNe Ia have been extensively used as cosmological distance indicators. In the optical, their light curves can be standardised through empirical relations between their peak brightness, stretch (e.g. [38, 35, 31]), and colour ([42]). In addition, SNe Ia are brighter in the optical (where detectors are larger as well), compared to other wavelengths, making them easier to observe. Therefore, cosmological analyses with SNe Ia (e.g. [4, 39, 1]) commonly focus on optical wavelengths and rely on light-curve fitters, such as SALT2 ([18, 19]), for the estimation of their light-curve parameters. Moreover, SNe Ia in the optical have recently been used to estimate the growth-rate of structures (e.g. [5, 40]).

SNe Ia were first proposed as distance indicators in the near-infrared (NIR) around four decades ago ([12, 13], but also see [28]), where they seem to be true 'standard candles' (as opposed to 'standardisable candles' in the optical). In other words, an estimation of the NIR peak magnitudes is all that is needed to measure distances. The NIR light curves of SNe Ia present lower intrinsic dispersion than the optical light curves and have the advantage of being less affected by dust extinction, which makes them exceptional for measuring cosmological distances (e.g. [25, 46, 14, 3, 32, 45, 16, 23]). Moreover, the NIR light curves of SNe Ia have already been used to constrain H_0 to a few percent (e.g. [8, 10]).

The low intrinsic dispersion of SNe Ia in the NIR raises the the possibility of using them to achieve accurate cosmography by measuring peculiar velocities of local galaxies, reaching out to $z \sim 0.1$ or even beyond. However, the sample of SNe Ia observed in the NIR is currently low due to several factors: low NIR detector sensitivity in the past; SNe Ia are fainter at these wavelengths, where the sky brightness dramatically decreases the contrast for the (SN) observations, thus needing to integrate for longer; and the number of facilities with NIR instruments (compared to optical ones) is low. However, by taking advantage of the exceptional homogeneity of the SNe Ia in the NIR, we can possibly reconstruct their light curves with just a few photometric data points (e.g. [25]), increasing the total number of observed objects.

Given the large stream of optical photometry publicly provided by the Zwicky Transient Facility (ZTF; [17]), which works as a precursor and testing ground for LSST, hundreds to thousands of SNe Ia are being followed-up with high-cadence (average of 2 days) *gr*-bands photometry. Thus, ZTF can provide the optical data coverage while NIR photometry can be obtained with other facilities. This work aims to test how accurately we can retrieve NIR peak magnitudes with well-covered optical light curves and few NIR epochs for distance estimations. Our results will give assurance to use SNe Ia with public ZTF *gr*-band light curves with sparse data in the NIR to reconstruct the cosmography of our local supercluster, measure the growth-rate of structure and H_0, and test ΛCDM and alternative cosmological models. In the future, this can be extended to use optical data from the Rubin Observatory Legacy Survey of Space and Time (LSST) and NIR data from telescopes such as the Roman Space Telescope and James Webb Space Telescope.

2 Data and method

We use the Carnegie Supernova Project (CSP; [20]) sample as it is one of the most comprehensive samples of SNe Ia with extensive *uBgVriYJH* (optical to NIR) coverage and well-understood magnitude systems to date. The data from CSP-I consists of three data releases (DRs) described in [9](DR1), [41](DR2) and [26](DR3), while the data from CSP-II are described in [33] and [21]. CSP-II does not have a public DR to date, but one is in progress (Suntzeff et al., in prep.). We include all the 134 SNe Ia from CSP-I and 202 from CSP-II (the cosmology sub-sample from [33]). Thus, the CSP sample we use consists of a total of 336 SNe Ia.

As CSP observations have used different filters and telescopes throughout the different campaigns, we apply S-corrections ([41]) to work in a single magnitude system, simplifying the handling of data. This is specifically useful for those CSP-I SNe with multiple V, Y, or J bands, and for combining SNe from CSP-I and CSP-II.

To fit the SNe Ia, we use SNooPy ([6]) with the *max_model* model, as we require measurements of the peak magnitudes in J and H ($J_{\max}$ and $H_{\max}$, respectively). The resulting fits provide the following output parameters: $T_{\max}$, s_{BV}, and $x_{\max}$, where $T_{\max}$ is the time of B-band peak magnitude, s_{BV} is the 'colour stretch' parameter as defined in [7] and $x_{\max}$ represents the peak magnitude in x-band, for each of the observed filters. We note that the multi-colour light-curve templates (optical to NIR) are driven by the values of $T_{\max}$ and s_{BV}. All magnitudes presented are in the CSP natural system and the reported uncertainties from SNooPy fits are statistical uncertainties only.

As not all CSP SNe are useful for the purpose of this work, we proceeded to apply some cuts to the initial sample. We only used SNe Ia labelled as 'normal' according to [26] and [2]. We then proceed to remove any SN without g, r, J, or H bands, as these are strictly required for our analysis: g and r being the bands used by ZTF while J and H being the NIR bands commonly available. The Y band is not included as catalogues of standard stars for this band are not available for the whole sky, which are needed for the calibration. The next cut requires the SN to have coverage of the optical peak as the estimation of $T_{\max}$ is fundamental when fitting the light curves of SNe Ia. For this, we need to have one or more photometric points at least two days before and two days after $T_{\max}$ in B, g, V, or r bands, providing an accurate estimation of the location of the peak. Finally, we require at least one photometric point before and after the time of $J_{\max}$ and $H_{\max}$, as precise measurements of these are needed.

3 Simulations

Given that we want to replicate what real observations would be (i.e. optical bands well covered with few NIR data points), the simulations consist of taking the complete gr-band light curves, plus n epochs of coeval J- and ″band photometric points, for $n = 1, 2$, and 3. We note that we are sampling from the available photometry (henceforth referred to as 'simulations' in this paper). Combinations without repetition of the JH-band photometry are

used for this The resulting simulations are then fit, using SNooPy and the output parameters saved for a later comparison.

Assuming that SNe Ia are standard candles in the NIR, peak NIR magnitudes can be directly used to estimate distances without further corrections (e.g. from stretch or colour). Thus, our main interest is to see how well we can measure $J_{\rm max}$ and $H_{\rm max}$ using just a few NIR photometric points. However, the retrieved peak magnitudes highly depend on the time of the observations with respect to $T_{\rm max}$. We therefore define three different metrics to understand what type of observations are best at obtaining accurate $J_{\rm max}$ and $H_{\rm max}$ measurements:(i) time of the closest J/H epoch with respect to $T_{\rm max}$; (ii) mean time of the J/H epochs with respect to $T_{\rm max}$; and (iii) difference between the earliest and latest (i.e. range) J/H epochs. Note that in the case of the simulations with only one epoch ($n = 1$), metrics (i) and (ii) are the same, while (iii) is not calculated. Also note that these metrics are defined in the restframe, i.e. epochs are corrected for time dilation using the SN redshift.

In Figure 1, we show $J_{\rm max}$ residuals between the simulations and the reference sample (using all bands) as a function of metric (i), for simulations with *grJH* bands and $n = 1$. From this comparison, we see that the scatter in the residuals tends to be smaller around $T_{\rm max}$, with the smallest scatter before $T_{\rm max}$, and increases at later epochs. In general, the scatter is smaller for the H band (not shown in the figure) compared to the J band. This is consistent with what has been found in other works (e.g. [**?**]). Additionally, we note that offsets in $J_{\rm max}$ and $H_{\rm max}$ tend to be larger where the NIR light-curve templates have a larger gradient or slope.

As we are aiming to reduce the scatter, ideally, we would need data around $T_{\rm max}$. Unfortunately, as it is hard to obtain photometric data at specific epochs due to different constraints (weather, time, allocation, etc.), we have to look for a time window with a large-enough range. We noticed that a time range between -5 to 15 days with respect to $T_{\rm max}$ possess a relatively low scatter in $J_{\rm max}$ and $H_{\rm max}$. The weighted mean (Δ) and weighted standard deviation (σ) of the residuals in this time window are $\Delta = 0.004\,$mag and $\sigma = 0.047\,$mag, and $\Delta = -0.006\,$mag and $\sigma = 0.053\,$mag, for $J_{\rm max}$ and $H_{\rm max}$, respectively.

4 Near-infrared distances

The final step in this work is to calculate the precision in the distance estimations from the simulations. Assuming that SNe Ia are standard candles in the NIR, the peak apparent magnitude is the only parameter necessary to calculate distances and its uncertainty is directly propagated to the measured distance:

$$\mu = m_{\rm max} - M, \tag{1}$$

where μ is the distance modulus, $m_{\rm max}$ is the peak apparent magnitude in a NIR band (e.g. $J_{\rm max}$ or $H_{\rm max}$) and M is the peak absolute magnitude in that same band. To calculate distances, a cosmological model needs to be fitted. For simplicity, we assume a flat ΛCDM cosmology and fix the value of M ($M_J = M_H = -18.5\,$mag), fitting only H_0 and the intrinsic

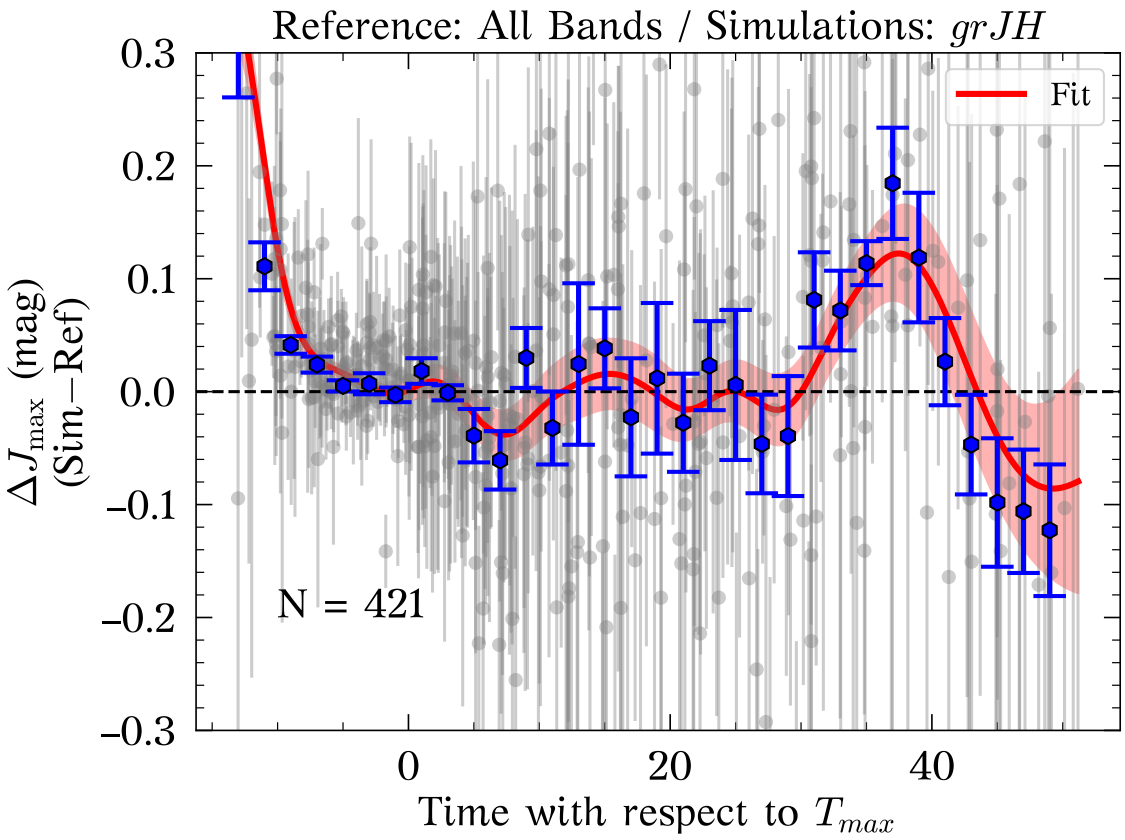

Figure 1: $J_{\rm max}$ residuals, between simulations with coeval coeval J-band epoch and reference value. The weighted mean and uncertainty on the weighted mean in bins of two days are shown in blue. A "correction snake" and its uncertainty are calculated by fitting the residuals with Gaussian Process (red line and shaded region), while N is the total number of simulations.

dispersion of SNe Ia ($\sigma_{\rm int}$). Only SNe at $z > 0.01$ are used as the contribution from peculiar velocities is relatively small at these redshifts. This reduces our reference sample to 36 objects. The resulting Hubble diagram in J band is shown in Figure 2 (red circles). The Hubble residuals have an rms of 0.166 mag, while $\sigma_{\rm int} = 0.14$ mag was obtained.

Using the simulations with phase between −5 days and 15 days, where a low scatter in $J_{\rm max}$ was found (see the previous section), an rms of 0.180 mag is obtained. Although the simulations have larger scatter than the reference sample, the difference is relatively small (0.014 mag). In the case of the H band, the reference sample and the simulations have Hubble residuals rms of 0.149 mag and 0.147 mag, respectively. The rms values are very similar, being slightly smaller for the simulations (a negligible difference of 0.002 mag).

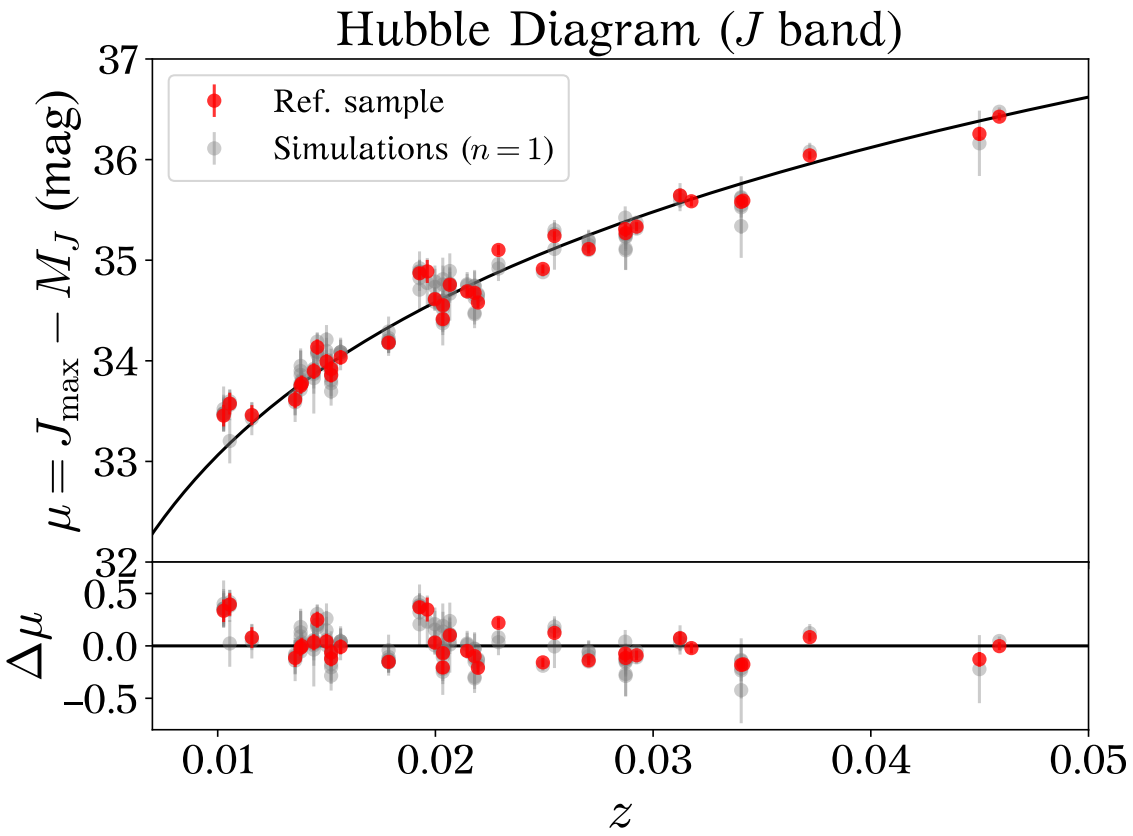

Figure 2: Hubble diagram in J-band. Only SNe Ia with $z > 0.01$ were used as the contribution from peculiar velocities is relatively small at these redshifts. The reference sample was used to fit H_0 and the intrinsic dispersion ($\sigma_{\rm int}$), keeping the peak absolute magnitude in J band ($M_J = -18.5$ mag) fixed. The rms for the reference sample (red) and the simulations with $n = 1$ (grey) are 0.166 mag and 0.180 mag, respectively.

Acknowledgments

TEMB acknowledges financial support from the Spanish Ministerio de Ciencia e Innovación (MCIN), the Agencia Estatal de Investigación (AEI) 10.13039/501100011033 under the PID2020-115253GA-I00 HOSTFLOWS project, from Centro Superior de Investigaciones Científicas (CSIC) under the PIE project 20215AT016 and the I-LINK 2021 LINKA20409, and the program Unidad de Excelencia María de Maeztu CEX2020-001058-M.

References

[1] Abbott, T., Allam, S., Andersen, P. 2019 ApJ, 872L, 30A

[2] Ashall, C., Lu, J., Burns, C. 2020 ApJ, 895L, 3A

[3] Barone-Nugent, R., Lidman, C., Wyithe, J. 2012 MNRAS, 425, 1007B
[4] Betoule, M., Kessler, R., Guy, J. 2014 A&A, 568A, 22B
[5] Boruah, S., Hudson, M., Lavaux, G. 2020 MNRAS., 498, 2703B
[6] Burns, C., Stritzinger, M., Phillips, M. 2011 AJ, 141, 19B
[7] Burns, C., Stritzinger, M., Phillips, M. 2014 ApJ, 789, 32B
[8] Burns, C., Parent, E., Phillips, M. 2018 ApJ, 869, 56B
[9] Contreras, C., Hamuy, M., Phillips, M. 2010 AJ, 139, 519C
[10] Dhawan, S., Jha, S., Leibundgut, B. 2018 A&A, 609A, 72D
[11] Di Valentino, E., Mena, O., Pan, S. 2021 CQGra, 38o3001D
[12] Elias, J., Frogel, J., Hackwell, J. 1981 ApJ, 251L, 13E
[13] Elias, J., Matthews, K., Neugebauer, G. 1985 ApJ, 296, 379E
[14] Freedman, W., Burns, C., Phillips, M. 2009 ApJ, 704, 1036F
[15] Freedman, W., Madore, B., Hatt, D. 2019, ApJ, 882, 34F
[16] Friedman, A., Wood-Vasey, W., Marion, G. 2015 ApJS, 220, 9F
[17] Graham, M., Kulkarni, S., Bellm, E. 2019 PASP, 131g8001G
[18] Guy, J., Astier, P., Nobili, S. 2005 A&A, 443, 781G
[19] Guy, J., Astier, P., Baumont, S. 2007 A&A, 466, 11G
[20] Hamuy, M., Folatelli, G., Morrell, N. 2006 PASP, 118, 2H
[21] Hsiao, E., Phillips, M., Marion, G. 2019 PASP, 131a4002H
[22] Huang, C., Riess, A., Yuan, W. 2020 ApJ, 889, 5H
[23] Johansson, J., Cenko, S., Fox, O. 2021 ApJ, 923, 237J
[24] Khetan, N., Izzo, L., Branchesi, M. 2021 A&A, 647A, 72K
[25] Krisciunas, K., Phillips, M., Suntzeff, N. 2004 ApJ, 602L, 81K
[26] Krisciunas, K., Contreras, C., Burns, C. 2017 AJ, 154, 211K
[27] Linder, E. 2005 PhRvD, 72d3529L
[28] Meikle, W. 2000 MNRAS, 314, 782M
[29] Peebles, P. 1976 ApJ, 205, 318P
[30] Perlmutter, S., Aldering, G., Goldhaber, G. 1999 ApJ, 517, 565P
[31] Phillips, M. 1993ApJ, 413L., 105P
[32] Phillips, M. 2012 PASA, 29, 434P
[33] Phillips, M., Contreras, C., Hsiao, E. 2019 PASP, 131a4001P
[34] Planck Collaboration 2020, A&A, 641A, 6P
[35] Pskovskii, I. 1977 SvA, 21, 675P
[36] Riess, A., Filippenko, A., Challis, P. 1998 AJ, 116, 1009R

[37] Riess, A., Casertano, S., Yuan, W. 2021, ApJ, 908L, 6R

[38] Rust, B. 1974 PhDT, 7R

[39] Scolnic, D., Jones, D., Rest, A. 2018 ApJ, 859, 101S

[40] Stahl, B., de Jaeger, T., Boruah, S. 2021 MNRAS, 505, 2349S

[41] Stritzinger, M., Phillips, M., Boldt, L. 2011 AJ, 142, 156S

[42] Tripp, R. 1998 A&A, 331, 815T

[43] Tully, R., Courtois, H., Hoffman, Y. 2014 Natur., 513, 71T

[44] Tully, R., Courtois, H., Sorce, J. 2016 AJ, 152, 50T

[45] Weyant, A., Wood-Vasey, W., Allen, L. 2014 ApJ, 784, 105W

[46] Wood-Vasey, W., Friedman, A., Bloom, J. 2008 ApJ, 689, 377W

Highlights of Spanish Astrophysics XI, Proceedings of the XV Scientific Meeting of the Spanish Astronomical Society held on September 4–9, 2022, in La Laguna, Spain. M. Manteiga, L. Bellot, P. Benavidez, A. de Lorenzo-Cáceres, M. A. Fuente, M. J. Martínez, M. Vázquez- Acosta, C. Dafonte (eds.), 2023

Transient and multi-messenger astrophysics with the Cherenkov Telescope Array.

López-Oramas, A.[1] **for the CTA Consortium**

[1] Instituto de Astrofísica de Canarias and Departamento de Astrofísica, Universidad de La Laguna, La Laguna, Spain

Abstract

The Cherenkov Telescope Array (CTA) will be the next generation ground-based very-high-energy (VHE) gamma-ray observatory. The first of the Large Size Telescopes (LST1), is already under commissioning at Roque de los Muchachos observatory, in La Palma. The unprecedented sensitivity at short timescales of CTA will make of this observatory the leading instrument for the discovery of new transient events of both Galactic and extragalactic origin in the VHE regime. It will unveil the physics of the most extreme objects in the Universe and their interaction with the surrounding environment. The recent discoveries of the first gamma-ray bursts (GRBs) at VHE, the connection between gravitational waves and short GRBs and the association of an extragalactic neutrino with a flaring blazar, have opened new lines of research in multi-messenger and transient astrophysics. The detections of these different cosmic messengers have shown the importance of coordinated campaigns. CTA will perform follow-up observations of these events and open a new window for time-domain astrophysics at VHE. The Transient program is one of the Key Science Projects of CTA. This program includes a wide range of sources in a multi-messenger and multi-wavelength context, ranging from GRBs, to gravitational waves, energetic neutrinos, core-collapse supernovae and Galactic transients (such as microquasars, pulsar wind nebulae or novae). In this contribution, I will present the results of the exploration of the capabilities of CTA to detect new transient astrophysical phenomena at VHE.

1 Introduction

Very-high-energy (VHE, E> 100 GeV) transient astrophysics has proven to be a powerful tool to study extreme astrophysical processes, at the crossroads of multi-messenger and time-domain astronomy. Thanks to the development of the last generation of Imaging Atmospheric Cherenkov Telescopes (IACTs), more than 250 sources of VHE gamma rays have been discovered, many of them of transient nature.

The Cherenkov Telescope Array (CTA) is the next-generation ground-based observatory for gamma-ray astronomy at very-high energies. It will count with two arrays located in two sites: CTA-North at Observatorio Roque de los Muchachos (ORM) in La Palma (Spain);

and CTA-South, placed near Paranal Observatory (Chile). It will count with telescopes of three different sizes (Large Size Telescopes, LSTs; Medium Size Telescopes, MSTs; Small Size Telescopes, SSTs), that will cover the energy range between 20 GeV and 300 TeV [1]. The improved sensitivity (x5-10), energy and angular resolution (by a factor 2) and energy coverage (four decades) with respect to current generation of IACTs, will make of CTA the best instrument to study the VHE gamma-ray Universe.

Specially interesting for the transient and multi-messenger case, is the unprecedent sensitivity at short timescales (see Fig. 1), which will allow for the discovery of new sources, perhaps even of new types. This short-time sensitivity is closely connected to the presence of LSTs in CTA, which allow for fast slewing (with the goal of only 20 sec to point anywhere in the sky) and low energy threshold (of only 20 GeV).

In this contribution, we summarize the work of the Transients Science Working Group (SWG) of CTA Consortium, focused on exploiting the capabilities of future CTA to discover and detect new transient sources in a multi-messenger context [2, 3], as one of nine Key Science Projects of the CTA observatory [1]. In these proceedings, we will concentrate on the topics of neutrinos, gamma-ray bursts (GRBs), gravitational waves (GWs) and Galactic transients, specifically microquasars and flares from pulsar-wind nebulae (PWNe).

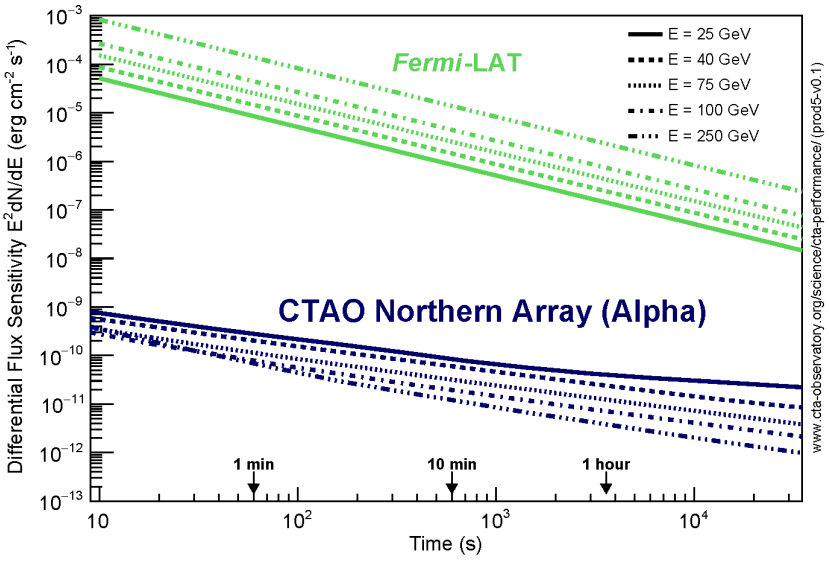

Figure 1: Differential flux sensitivity of CTAO-North as function of observation, compared to *Fermi*-LAT.

2 VHE transient phenomena as seen by CTA

2.1 Neutrinos

CTA will aim at the detection of the VHE counterpart of neutrino sources. Two source populations are considered: transient, based on neutrino source alerts (blazars); and steady, refereing to nu-clusters exceeding IceCube sensitivity (following the star formation rate evolution). The results of the simulations are:

- Flaring sources: the simulations consider the model of the neutrino flare of the blazar TXS 0506+056 during 2014-2015, assuming the same duration. During neutrino flares from blazars CTA will detect a counterpart for about one third of the cases after only 10 mins of observations.
- Steady sources: this scenario considers that the diffuse neutrino flux is due to steady neutrino sources. The resulting simulations show that CTA-North will be able to detect all sources down to the density of 10^{-9} Mpc^{-3} in 30 min (considering they are always visible to CTA), given that they could be observed at low to mid zenith angles (20°-40°),.

Considering these results, we can conclude that CTA will detect both flaring and steady sources of neutrino counterparts. For a more detailed overview check [5].

2.2 GRBs

The search for VHE emission from GRBs supposed a major challenge for IACTs from both the technical and the scientific point of view for more than a decade. The discovery of GRB 190114C [14] and GRB 180720B [10] finally proved that GRBs are indeed sources of VHE gamma rays. IACTs aim not only at detecting the afterglow, but also the prompt emission.

Regarding the afterglow component (prompt simulations are on-going), to test the detectability prospects and rates with CTA, the GRB task force has simulated 1000 bright GRBs detected by Swift with the population synthesis code POSyTIVE [9]. Considering visibility constraints, duty cycle, detection delays and assuming detection if 90% of trials are successful, we conclude that about 10% of the visible population will be detected by CTA, with a rate of about ∼2 detected GRB per year.

2.3 GWs

The detection of GW170817 with LIGO-Virgo [13] provided the first evidence of binary neutron star (BNS) mergers as progenitors for short GRBs (sGRBs).

Our goal is to perform follow-up of GW alerts to search for a putative VHE counterpart. For understanding the chances of CTA to detect these events, the GW task force of the Transients SWG has performed simulations of BNs mergers accompanied by sGRBs, making use of the GWCOSMoS database [18, 19]. Fig. 2, shows the percentage of detectable GRBs,

both on-axis and off-axis, given an exposure time as a function of the delay from the onset [20]. We can conclude that CTA will be sensitive enough to detect more than 90% of on-axis sGRBs with time delays up to 10 min, while about 50% of off-axis GRBs will be detected within a few hours assuming the same time delay. For a more detailed information, check [20]

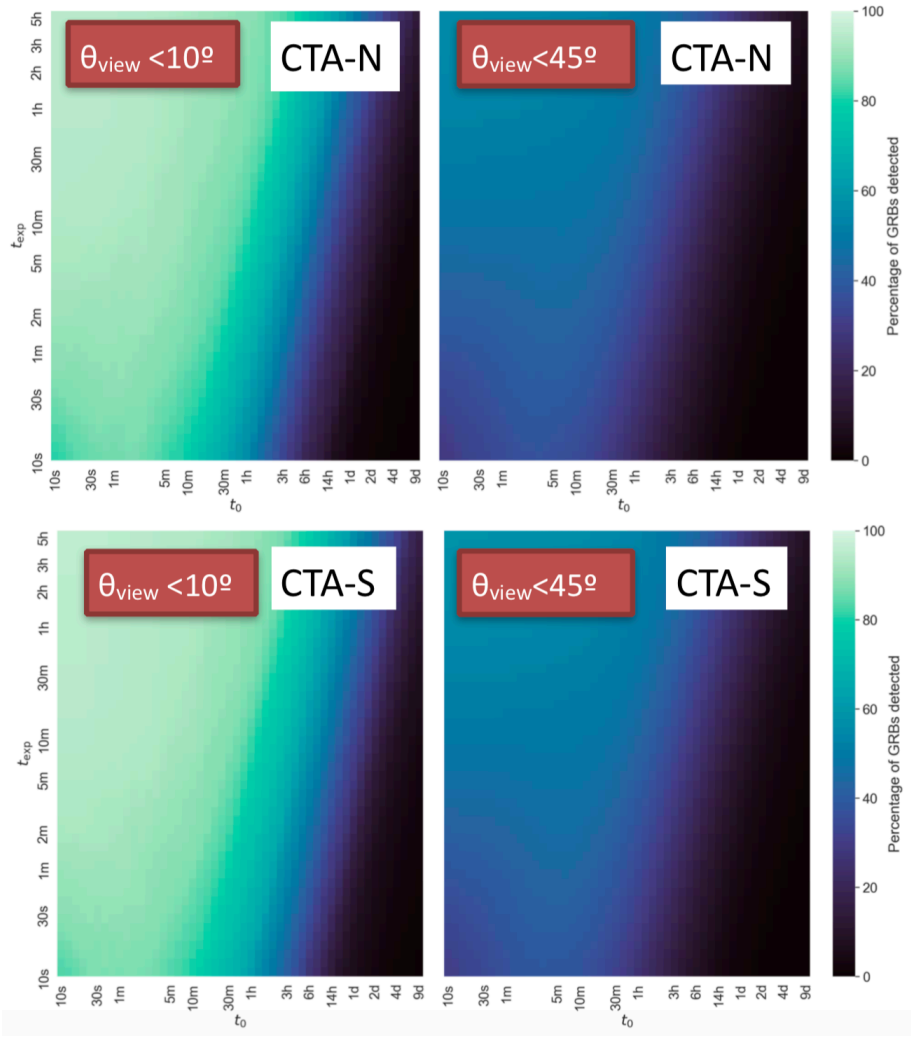

Figure 2: Percentage of detected GRBs as a funcion of the exposure time versus the time delay, both for on-axis (left) and off-axis (right) sGRBs for both CTA arrays. Figure adapted from [20].

2.4 Galactic transients

The topic of Galactic transients cover all those sources in the Milky Way that show unexpected flaring emission, ranging from microquasars, to novae, PWNe or magnetars, among others (see [4] and references therein). In this contribution, we focus on the chances to detect emission from two sources of interest: the microquasar Cygnus X-1 and Crab Nebula (flares). In both cases, the simulations are performed only for CTA-North array, due to visibility constraints.

- Cygnus X-1: this microquasar, composed of a massive O star and a black hole, showed a hint of transient emission at 4.9σ in an 80-min observation by [16]. Persistent emission has been reported in *Fermi*-LAT after 7.5yr of data [22]. For the CTA-North simulations in the energy range 100 GeV–1 TeV, the Galactic transients task force simulated both the transient and persistent component. For the transient emission, the MAGIC hint [16] was extrapolated. In the case of persistent emission, we used the lepto-hadronic model by [12], assuming 50 h of observations. Our results led to the detection of both transient (at 44σ) and persistent emission (39σ) from the microquasar Cyg X-1.
- Flaring emission from the Crab Nebula: the Crab Nebula is the standard candle for VHE astronomy. However, it shows flaring emission in the MeV band [21, 8] with timescales of hours. In order to discover this flares at VHE for the first time, we tested the capacity both of the full CTA-North array and a subarray of 4 LSTs, to detect flares of different intensities [17, 4]. There are good prospects for detection for CTA and especially LSTs, leading for a detection in the low energy range in < 5h.

For a more detailed analysis of the different Galactic transient cases to be studied by CTA, check [4].

3 Towards CTA

The first LST (LST1) of CTA-North was inaugurated in 2018 and it is finalizing its commissioning phase at ORM. LST1 is already producing scientific data and performing follow-up of transient events [7]. LST1 has already detected its first transient source of Galactic origin: the recurrent symbiotic nova RS Ophiuchi [6], results that are compatible with those reported by [15, 11]. The construction of the three remaining LSTs has already started and its finalization is planned for end of 2025. The first step to discover new transient sources with unprecedented sensitivity with the future CTA observatory is already taken.

Acknowledgments

This work was conducted in the context of the CTA Consortium, and it made use of the CTA instrument response functions provided by the CTA Consortium and Observatory. This research is the result of the work of the Transients Science Working Group of CTA Consortium. We gratefully acknowledge financial support from the agencies and organizations listed here. This research made use

of ctools, a community-developed analysis package for Imaging Air Cherenkov Telescope data based on GammaLib, a community-developed toolbox for the scientific analysis of astronomical gamma-ray data; and gammapy, a community-developed core Python package for TeV gamma-ray astronomy.

References

[1] CTA Consortium, Acharya, B. S., Agudo, I. et al. 2018, arXiv 1709.07997

[2] CTA Consortium, Bošnjak, Ž, Brown, A. M. et al., 2021, arXiv:2106.03621

[3] CTA Consortium, Carosi, A., López-Oramas, A. et al., 2021, Proceedings of ICRC 2021, 395, id 736, arXiv:2108.04317

[4] CTA Consortium, López-Oramas, A., Bulgarelli A. et al. 2021, Proceedings of ICRC 2021, 395, id 784, arXiv:2108.03911

[5] CTA Consortium, Sergijenko, O., Brown, A. et al., 2021, Proceedings of ICRC 2021, 395, id 975, arXiv:2108.05217

[6] CTA-LST Project, Bernardos Martin, M. SEA 2022, Poster ID7

[7] CTA-LST Project, Carosi, A., López-Oramas, A. et al., 2021, Proceedings of ICRC 2021, 395, id 838, arXiv:2108.04309 LST Collaboration

[8] Fermi-LAT, Abdo A. et al. 20211, Science, 331, 739

[9] Ghirlanda, G. and Salvaterra, R. and Ghisellini, G. et al. 2015, MNRAS, 448, 2514-2524

[10] H.E.S.S. Collaboration, Abdalla, H. & et al., 2019, Nature, 575, 464

[11] H.E.S.S. Collaboration, Abdalla, H. & et al., 2022, Science, 376, 77-80

[12] Kantzas, D., Markoff, S. et al., 2021, MNRAS, 500, Issue 2, 2112-2126

[13] LIGO Scientific Collaboration and Virgo Collaboration, Abbott et al., 2017, Phys. Rev. Lett. 119, 161101

[14] MAGIC Collaboration, Acciari, V. A. & et al., 2019, Nature, 575, 455

[15] MAGIC Collaboration, Acciari, V. A. & et al. 2022, Nature Astronomy, 6, 689-697

[16] MAGIC Collaboration, Albert, J. et al., 2007, ApJL, 665, L51–L54

[17] Mestre E., de Oña Wilhelmi, E., 2020, MNRAS, 492, 708

[18] Patricelli, B., Razzano, M., Cella, G. et al. 2016, JCAP, 11, 056P

[19] Patricelli, B., Stamerra, A., Razzano, M. et al. 2016, JCAP, 5, 056

[20] Patricelli, B., Carosi A., Nava, L. et al. 2021, Proceedings of ICRC 2021, 395, id 998, 5, 056

[21] Tavani M., Bulgarelli, A., Vittorini V. et al. 2011, Science, 331, 736

[22] Zanin R. et al., 2016, A&A, 596, A55

Highlights of Spanish Astrophysics XI, Proceedings of the XV Scientific Meeting of the Spanish Astronomical Society held on September 4–9, 2022, in La Laguna, Spain. M. Manteiga, L. Bellot, P. Benavidez, A. de Lorenzo-Cáceres, M. A. Fuente, M. J. Martínez, M. Vázquez- Acosta, C. Dafonte (eds.), 2023

Absorption spectroscopy of GRB 160410A: The first complete study of the ISM of a short GRB.

Agüí Fernández, J. F.[1] **et al**

[1] Instituto de Astrofísica de Andalucía, Glorieta de la Astronomía s/n, 18008 Granada, Spain

Abstract

Short gamma-ray bursts (sGRBs) are produced on the coalescence of two compact objects such as two neutron stars. These cataclismic events release a large amount of energy in gravitational waves during the coalescence event to a single compact object. We present the results of the study of GRB 160410A that, at $z = 1.7177$, is one of the farthest SGRBs ever detected. The GRB afterglow emission was first detected by Swift/BAT and observed with the X-shooter spectrograph at VLT starting just $\sim$ 8 minutes after the GRB. This is one of the best spectra ever obtained on the GRB afterglow emission of a sGRB. It allow us to perform for the first time a chemical study of the circumburst medium of a sGRB. The spectrum shows low-ionization features common to long GRBs (lGRB), however, high-ionization features are missing. We detect the broad absorption line corresponding to Lyman-alpha feature with a measured value for the column density compatible with a Damped Lyman-alpha Absorption (DLA) region. We find no evidence for dust depletion. The measured metallicity, [Fe/H] = -2.5 $\pm$ 0.2, is low as compared to lGRB-DLA systems. Late observations with OSIRIS/GTC failed to detect an underlying galaxy at the GRB location down to r $>$ 27 mag. The GRB ligh-curve is better described by a double-broken power-law and a spectral energy distribution consistent with no extinction. GRB 160410A is in contrast with our findings for GRB 201221D, a softer sGRB that shows only Fe II and Mg II features at $z = 1.045$ with line strength consistent with the mean value measured for lGRB environments. The host galaxy is a well detected massive galaxy with low star formation rate.

My poster is available at https://doi.org/10.5281/zenodo.7048964

Highlights of Spanish Astrophysics XI, Proceedings of the XV Scientific Meeting of the Spanish Astronomical Society held on September 4–9, 2022, in La Laguna, Spain. M. Manteiga, L. Bellot, P. Benavidez, A. de Lorenzo-Cáceres, M. A. Fuente, M. J. Martínez, M. Vázquez- Acosta, C. Dafonte (eds.), 2023

About the multiplicity of M dwarfs.

Cifuentes, C.[1], Caballero, J. A.[1], Cortés-Contreras, M.[1], Montes, D.[2], Béjar, V. J. S.[3,4], Zapatero Osorio, M. R.[5], Ribas, I.[6,7], Reiners, A.[8], Quirrenbach, A.[9], Amado, P. J.[10], and Seifert, W.[9]

[1] Centro de Astrobiología (CAB), CSIC-INTA, ESAC Campus, Camino bajo del castillo s/n, 28692 Villanueva de la Cañada, Madrid, Spain
[2] Departamento de Física de la Tierra y Astrofísica & IPARCOS-UCM (Instituto de Física de Partículas y del Cosmos de la UCM), Facultad de Ciencias Físicas, Universidad Complutense de Madrid, 28040 Madrid, Spain
[3] Instituto de Astrofísica de Canarias (IAC), Calle Vía Láctea, s/n, 38205 San Cristóbal de La Laguna, Tenerife, Spain
[4] Departamento de Astrofísica, Universidad de La Laguna, 38206 La Laguna, Tenerife, Spain
[5] Centro de Astrobiología (CAB), CSIC-INTA, Carretera de Ajalvir km 4, 28850 Torrejón de Ardoz, Madrid, Spain
[6] Institut de Ciéncies de l'Espai (CSIC-IEEC), Can Magrans s/n, Campus UAB, 08193 Bellaterra, Barcelona, Spain
[7] Institut d'Estudis Espacials de Catalunya (IEEC), 08034 Barcelona, Spain
[8] Institut für Astrophysik, Georg-August-Universität, Friedrich-Hund-Platz 1, D-37077 Göttingen, Germany
[9] Landessternwarte, Zentrum für Astronomie der Universtät Heidelberg, Königstuhl 12, D-69117 Heidelberg, Germany
[10] Instituto de Astrofísica de Andalucía (IAA-CSIC), Glorieta de la Astronomía s/n, 18008 Granada, Spain

Abstract

Stellar multiplicity is a common consequence of the stellar formation process. Low-mass stars are the prime constituent of the nearby stellar population, with late-type accounting for the majority of the hydrogen-fusing objects in the Solar neighborhood. The CARMENES input catalogue of M dwarfs (Carmencita) is a comprehensive and homogeneous sample of M dwarfs, with more than 2200 well-characterised main sequence stars, and therefore constitutes a solid basis for the investigation of the multiplicity of these stars. We search for physical companions at all physical separations, from close-orbiting spectroscopic binaries to very wide common proper motion pairs, up to 200 000 au apart from each other. For this, we make extensive use of the latest data from *Gaia* DR3 together with published measurements from the literature. We find that the multiplicity rate in these stars can be as high as 40%, given that candidate systems hinted by *Gaia* are eventually resolved.

1 Introduction

Stellar multiplicity is a common outcome of the stellar formation process [1, 2, 3], with the frequency of multiple systems increasing with the primary stellar mass [4, 5]. In the case of M dwarfs, early studies estimated in 33–42 % the fraction of them that are part of a multiple system [6, 7]. More specifically, the multiplicity rate of M dwarfs has been estimated to approximate to 30 and 20 per cent for a stellar (M dwarf) and substellar (brown dwarf) companion, respectively [8]. Recent estimates suggest that the observed multiplicity of M dwarfs is 26–27 %, or even lower [9, 10, 11, 12]. Although intrinsically small and faint ($\mathcal{M} < 0.62\,\mathcal{M}_\odot$, $\mathcal{L} < 0.076\,\mathcal{L}_\odot$, [13]), M dwarfs represent the majority of the stars in the Universe (e.g. [14, 15]).

Stars in binary systems offer the opportunity to directly measure fundamental parameters, such as masses and radii. Important applications of wide pairs include the calibration of metallicities of M dwarfs [16], the age-metallicity and age-magnetic activity relation [17, 18], and even studies of dark matter in the Milky Way [19]. All in all, multiple systems can help in the important topic of how stars form and develop, and can ultimately serve as pieces in the puzzle of the Galactic constitution. Learning about multiplicity is also interesting in the field of exoplanet searches. For instance, all-sky surveys such as *TESS* or *Kepler* may draw conclusions about planet occurrence, based on the systematic observation of brightness-limited samples of M dwarfs, without taking into consideration the effect of many unresolved binaries disguised as single objects [20].

In this work we present a descriptive study of the multiplicity of M dwarfs, in a volume-limited sample of more than 2200 stars (classified M0.0 V to M9.5 V), from 0.3 au to 206 000 au.

2 Methodology

The sample of our study is Carmencita, the CARMENES input catalogue [21]. Carmencita contains 2216 late-K and M dwarfs, which were intentionally chosen to be independent of multiplicity, age, or metallicity. For every star in this volume-limited sample, we looked for physical companions covering all ranges of separation: from compact object companions, only resolved employing dedicated techniques (e.g., lucky imaging, adaptive optics, speckle interferometry), to wider pairs that can be resolved using the *Gaia* astrometric solution, and in some cases other all-sky surveys.

For the analysis of multiplicity we made extensive use of the third data release of *Gaia* astrometry and photometry (DR3) [22], numerous public all-sky surveys from the ground and space, the Washington Double Star Catalog (WDS) [23], and Virtual Observatory tools such as the Aladin interactive sky atlas [24], the Tool for OPerations on Catalogues And Tables (TOPCAT) [25], and the Virtual Observatory Spectral energy distribution Analyzer (VOSA) [26]. To ensure the correct description of the systems, we eye-inspected individually each one of the systems found, with a special attention to the existing literature and the past characterisations.

We carried out a blind search of equidistant and comoving companions to all the stars in

Carmencita, up to physical separations of 10^5 au, and for the first time, also considering the potential unresolved binaries at very close separations, by using several statistical indicators and data products in *Gaia* DR3. We compiled photometry in *Gaia* DR3, The Two Micron All Sky Survey (2MASS) [27], and the Wide-field Infrared Survey Explorer (AllWISE) [28].

3 Results

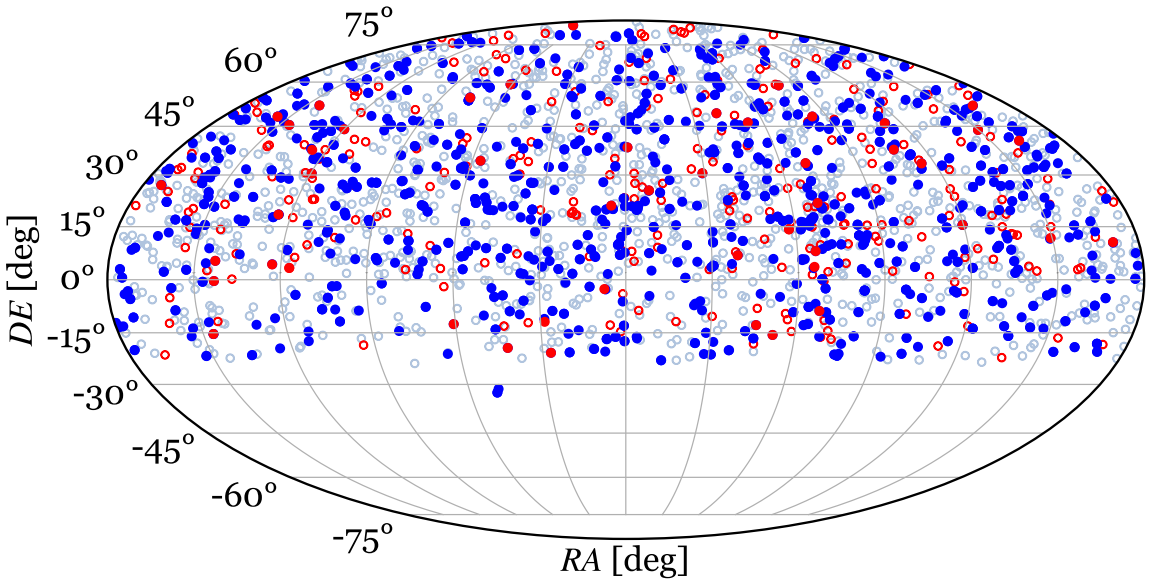

Figure 1: Location in the Mollweide-projection sky of all the stars in the sample of M dwarfs, including their companions, in equatorial coordinates. The coloured circles show single stars (empty grey), stars that belong to a multiple system (filled darker blue), and candidates to unresolved binarity for bona fide singles (empty red) and widely separated components of multiple systems (filled red).

We found that approximately 38% of the M dwarfs in the sample belong to an identified multiple system with a companion of *any* mass (Fig. 1). Under this broad definition of multiplicity, the number of single, binaries, triples, quadruples, and quintuples systems for every 100 M dwarfs in all the range of subtypes (from M0.0 V to M9.5 V) represented as S:B:T:Q:Q, is 62.3:40.1:13.3:2.8:0.8:0.2. On the other hand, the classical definition of multiplicity requires that the M dwarf is the primary component (i.e., the most massive) of the system. We calculated the multiplicity fraction (MF) and the stellar companion fraction (SCF), accounting for observational biases, finding that:

- The MF and SCF both decrease as a function of spectral type, as expected.
- For M dwarfs in which multiplicity is confirmed, the MF and SCF are 29.0% and 35.1%, respectively.

- Binaries outnumber by far the higher order systems: For every 100 M dwarfs with a companion, the ratio S:B:T:Q4:Q5 is 70.9:23.4:4.6:0.6:0.1.

- The MF becomes 40.4% if the unresolved binary candidates are also confirmed.

In the process of identifying multiplicity in our stars, we discovered several pairs with an astrometry compatible with physical parity, but that were not found either in the WDS catalog or in the literature. Some of them are isolated pairs (i.e. binaries), whereas some are components of known systems.

Several statistical indicators in *Gaia* DR3 can be used to find probable cases of non-resolved multiplicity, this is, of double or possibly higher order multiples, in stars previously thought to be single. In a small sample of 16 of these cases, which additionally show notable radial velocity standard deviations as measured by *Gaia*, we performed a systematic search for spectroscopic binaries using medium resolution ($R = 46\,000$) spectra with the high-resolution FIbre-fed Echelle Spectrograph (FIES) at the 2.56m Nordic Optical Telescope (NOT). We discovered that 13 of them are spectroscopic binaries of several types, including two clear triple-lined triples, two are high rotators (so the multiplicity could not be identified properly), and one is single.

With this, to the known physically bound systems reported in the literature, we add 48 newly discovered pairs, and propose 300 candidates to very compact binaries, to date unresolved, except for the few for which we were able to characterise spectroscopically.

When possible, we determined descriptive parameters of the multiplicity (angular and physical separation, positional angle, binding energies, orbital periods), fundamental parameters of the components (luminosities, masses, radii, effective temperatures, surface gravities), compile astrometry (positions, proper motions, parallaxes, radial velocities), photometry in up to 10 passbands, and *Gaia* statistical indicators. Additionally, we give an individual description of the components, including their candidacy for unresolved binarity.

In the cumulative distribution of physical separations, changes of slope are apparent and measurable, and we could fit them to two distinct power laws following the general form of Öpik's law. This observational evidence has been motivated in the literature by the existence of at least two different formation mechanisms. We deem the scarcity of multiple systems at very close and very wide separations to an observational effect (because of the amount of unresolved pairs), and to a real configuration (because of the smaller binding energies are more likely disrupted by gravity), respectively.

4 Conclusions

In this work we perform a systematic, complete study and description of multiplicity for all separations: from very compact systems in close-in orbits, to wide and very wide pairs, some of them in very fragile configurations placed in the limit of dynamical stability.

We computed the classically defined multiplicity fraction and the stellar companion fraction in different un-biased samples. The multiplicity fractions derived are in agreement with

similar studies published in the last three decades. This work, however, estimates that the actual multiplicity fraction of M dwarfs could be as high as ∼40% if the unresolved systems hinted by *Gaia* are, indeed, real. In this regard, we have demonstrated using spectroscopic scrutiny in a small subsample of these that, in fact, many single stars are indeed compact systems of two or three stars. If all the candidates to unresolved multiples were confirmed, the global multiplicity fraction of M dwarfs could increase by approximately 11 %.

Finally, we provide homogeneous observational data for the investigation of the different formation mechanisms of close and wide binaries in stars of small mass. The study of multiplicity can serve in a myriad of topics of astrophysical interest, including an empirical test for models of stellar formation, to prove the hypothesis of whether all stars form in multiple systems.

References

[1] Duquennoy, A., & Mayor, M. (1991), Astronomy and Astrophysics, 248, 485.

[2] Tokovinin, A. (2008), Monthly Notices of the Royal Astronomical Society, 389, 925.

[3] Duchêne, G., & Kraus, A. (2013), Annual Review of Astronomy and Astrophysics, 51, 269.

[4] Lada, C. J. (2006), The Astrophysical Journal 640, L63.

[5] Parker, R. J., & Meyer, M. R. (2014), Monthly Notices of the Royal Astronomical Society, 442, 3722.

[6] Fischer, D. A., & Marcy, G. W. (1992), The Astrophysical Journal, 396, 178.

[7] Reid, I. N., & Gizis, J. E. (1997), The Astronomical Journal, 113, 2246.

[8] Chabrier, G. (2003), The Astrophysical Journal Letters, 586, L133.

[9] Delfosse, X., Beuzit, J.-L., Marchal, L., Bonfils, X., et al. (2004), ASP Conference Series, 318, 166.

[10] Ward-Duong, K., Patience, J., De Rosa, R. J., Bulger, J., et al. (2015), Monthly Notices of the Royal Astronomical Society, 449, 2618.

[11] Cortés-Contreras, M., Béjar, V. J. S., Caballero, J. A., Gauza, B., Montes, et al. (2017), Astronomy and Astrophysics, 597, A47.

[12] Winters, J. G., Henry, T. J., Jao, W.-C., Subasavage, J. P., Chatelain, J. P., et al. (2019), The Astronomical Journal, 157, 216.

[13] Cifuentes, C., Caballero, J. A., Cortés-Contreras, M., Montes, D., Abellán, F. J., et al. (2020), Astronomy and Astrophysics, 642, A115.

[14] Winters, J. G., Henry, T. J., Lurie, J. C., Hambly, N. C., Jao, W.-C., et al.(2015), The Astronomical Journal, 149, 5.

[15] Reylé, C., Jardine, K., Fouqué, P., Caballero, J. A., Smart, R. L., & Sozzetti, A. (2021), Astronomy and Astrophysics, 650, A201.

[16] Montes, D., González-Peinado, R., Tabernero, H. M., Caballero, J. A. et al. (2018), Monthly Notices of the Royal Astronomical Society, 479, 1332.

[17] Rebassa-Mansergas, A., Anguiano, B., García-Berro, E., Freeman, K. C., Cojocaru, et al. (2016), Monthly Notices of the Royal Astronomical Society, 463, 1137.

[18] Chanamé, J., & Ramírez, I. (2012), The Astrophysical Journal, 746, 102.

[19] Yoo, J., Chanamé, J., & Gould, A. (2004), The Astrophysical Journal, 601, 311.

[20] Lillo-Box, J., Barrado, D., & Bouy, H. (2012), Astronomy and Astrophysics, 546, A10.

[21] Alonso-Floriano, F. J., Morales, J. C., Caballero, J. A., Montes, D., et al. (2015), Astronomy and Astrophysics, 577, A128.

[22] Gaia Collaboration, Vallenari, A., Brown, A. G. A., Prusti, T., et al. (2022), arXiv e-prints, arXiv:2208.00211.

[23] Mason, B. D., Wycoff, G. L., Hartkopf, W. I., Douglass, G. G., & Worley, C. E. (2001), The Astronomical Journal, 122, 3466.

[24] Bonnarel, F., Fernique, P., Bienaymé, O., Egret, D., et al. (2000), Astronomy and Astrophysics Supplement, 143, 33.

[25] Taylor, M. B. (2005), Astronomical Data Analysis Software and Systems XIV, 347, 29.

[26] Bayo, A., Rodrigo, C., Barrado Y Navascués, D., Solano, E., et al. (2008), Astronomy and Astrophysics, 492, 277.

[27] Skrutskie, M. F., Cutri, R. M., Stiening, R., Weinberg, M. D., et al. (2006), The Astronomical Journal, 131, 1163.

[28] Cutri, R. M., Wright, E. L., Conrow, T., Fowler, J. W., et al. (2021), VizieR Online Data Catalog, II/328.

Highlights of Spanish Astrophysics XI, Proceedings of the XV Scientific Meeting of the Spanish Astronomical Society held on September 4–9, 2022, in La Laguna, Spain. M. Manteiga, L. Bellot, P. Benavidez, A. de Lorenzo-Cáceres, M. A. Fuente, M. J. Martínez, M. Vázquez- Acosta, C. Dafonte (eds.), 2023

Characterization of intermediate mass young stars from spectral energy distributions and Gaia EDR3.

Guzmán-Díaz, J.[1,2]

[1] Centro de Astrobiología (CSIC-INTA), ESA-ESAC Campus, 28692, Villanueva de la Cañada, Madrid, Spain
[2] Universidad Autónoma de Madrid, Campus de Cantoblanco, 28049 Madrid, Spain

Abstract

Herbig Ae/Be objects (HAeBes) are young, intermediate-mass stars surrounded by protoplanetary disks. From the point of view of star and planet formation, these objects have crucial characteristics. First, their stellar parameters, such as mass or temperature, are between those belonging to the low-mass and high-mass regimes. Second, the presence of bright and large protoplanetary disks makes these stars excellent laboratories to learn how planets form. However, the relatively small amount of known HAeBes sharply contrasts with the large number of their low-mass counterparts. Furthermore, HAeBes have usually been studied on the basis of small samples scattered on the sky, and their stellar and circumstellar parameters have been derived using heterogeneous methodologies.
In this contribution I will show the work carried out by Guzmán-Díaz et al. (2021), who provided a homogeneous characterization of a sample of 209 HAeBes from their spectral energy distributions (SEDs) and Gaia EDR3 parallaxes. Using the online tool Virtual Observatory SED Analyzer (VOSA), multi-wavelength photometry of our objects was collected, and the stellar parameters were derived by fitting the optical SEDs with the best Kuruzc models. In addition, the infrared SEDs were classified according to two schemes, and the mass accretion rates, protoplanetary disks masses, and the sizes of dust inner cavities were uniformly estimated. Such a large amount of data allowed us to perform a statistical analysis searching for correlations between the stellar and circumstellar parameters. A major result is that the disk dissipation mechanism in B-type and A-type Herbig stars is most probably different. With the advent of new techniques and more powerful instrumentation, the number of known HAeBes is increasing. A homogeneous stellar and circumstellar characterization, such as the one presented here, will allow us to better understand the formation and evolution of Herbig Ae/Be stars.

1 Introduction

Herbig Ae/Be stars (HAeBes) are pre-main sequence, intermediate-mass objects that are surrounded by a circumstellar or protoplanetary disk. Their stellar masses range between 2 and 10 $M_{\odot}$. Such objects are the link between T Tauri stars, the low-mass counterparts of

HAeBes, and massive young stellar objects (MYSOs). Knowledge of the physical parameters (e.g., temperature or mass) of HAeBes will allow us to better understand the stellar evolution and to bridge the formation of low-mass objects with that of the more massive ones. HAeBes are also of interest in the field of planetary formation because they have bright and large protoplanetary disks. In contrast, this study is difficult for higher-mass stars because they evolve more rapidly from the embedded phase to the main sequence stage. However, only one candidate planet has been detected so far in the HAeBe star AB Aur (see [7, 30]), being PDS 70, a T Tauri star, the only pre-sequence object in which the presence of planets has been confirmed [15, 19]. Works such as those of [14] or [18], which have been carried out a study relating the stellar abundances observed in HAeBes to the possible presence of planets, in addition to others that have extended the known catalog of HAeBes [26, 27], may pave the way in the search for planets in this type of stars.

HAeBes have spectral types ranging from early B-types to late F-types. Nevertheless, these stars can be grouped into two groups: Herbig Ae stars (HAes), with stellar masses less than or equal to 4 $M_{\odot}$, and Herbig Be stars (HBes), with stellar masses larger than 4 $M_{\odot}$. One of the main differences between both groups is the accretion mechanism that takes place in them. In HAes, accretion is dominated by the magnetic field, as in T Tauri stars. The disk is truncated by the magnetic field and the ionized material from the disk flows along the magnetic field lines to the star, causing shocks on the stellar surface. This mechanism is called "magnetospheric accretion" (MA). In contrast, in HBes, these models are not able to explain the large accretion rates observed in this group of stars. Other mechanisms have been proposed in HBes, one of which is known as "boundary layer", where the star accretes material directly from the disk (see [22] or [28] for more information on accretion mechanisms in HAeBes).

In the next two sections I will discuss in a brief way the evolution of protoplanetary disks and their classification from the spectral energy distributions (SEDs), as well as the work carried out by [13], where a homogeneous characterization of a large sample of HAeBes has been performed from the SEDs and the Gaia EDR3 data [10].

2 Protoplanetary disks

The formation of protoplanetary disks is a common process that occurs as a consequence of the conservation of angular momentum at a stage almost immediately after the collapse of a molecular core. They can be observed directly from the (sub-)millimeter emission of the dust grains (see, e.g., [2]), or from the scattered light by such grains in the near-infrared (near-IR) range [11]. Telescopes as ALMA or VLT allow us to take high resolution images, being able to appreciate how the dust grains are distributed, and identifying structures such as rings, spirals or cavities. Protoplanetary disks are also possible to detect in an indirect way, either from the gas emission lines (one of the most used to trace the gas are those of the carbon monoxide molecule, see [16]), or from the excess in the IR observed in the SEDs [13]. Regarding the latter, the SED of HD 139614 can be seen in Fig. 1 as an example.

The disk lifetime is around 2-3 Myr for T Tauri stars, although this can range from 1 to 10

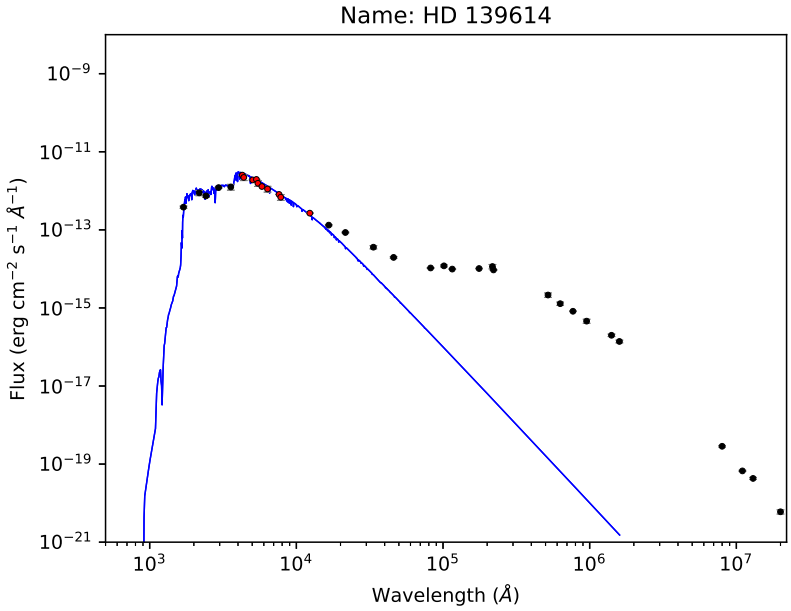

Figure 1: SED of HD 139614. The solid blue line corresponds to the best photospheric model that fits the optical photometry (red dots). On the other hand, black dots refer to the disk emission.

Myr (see [29]). In the case of more massive stars, the disks dissipate faster than in solar-type stars [29]. In their initial state, the disks are dominated by viscous evolution. Material from the inner part of the disk is accreted by the star whereas the outer part spreads as angular momentum is transported outward. At some point, the disk material starts to disperse from inside to outside by different mechanisms [9] that will dominate against the viscous evolution, and which are mentioned next: i) grain growth, which causes the decrease of small particles in the innermost regions; ii) ultraviolet and X-ray photoevaporative winds; iii) the presence of companions that sweep the material into their orbits. As a consequence of these processes, an inner cavity is formed. Protoplanetary disks with such cavities are known as transitional disks, which can be inferred from the SEDs. As an example, Fig. 2 shows the SED of HD 199603, where the presence of a cavity is deduced as there is no emission from the disk below 10 μm. Finally, the remnant of the transitional disks are called debris disks. These disks have low luminosities, with lack of gas and they contain large bodies.

The shapes of the SEDs can provide some hints on the evolution of protoplanetary disks. In particular, I will discuss two schemes used to classify the SEDs. The first one was proposed by [23], where the SEDs are classified into two groups: Group I and group II, which differ mainly in the mid-IR emission. The authors found that in group II SEDs the continuum from the IR to the submillimeter region could be only fit by a power-law component, whereas in group I SEDs an additional blackbody component had to be added. Such a classification has been related to the morphology of the protoplanetary disks, where group I and group

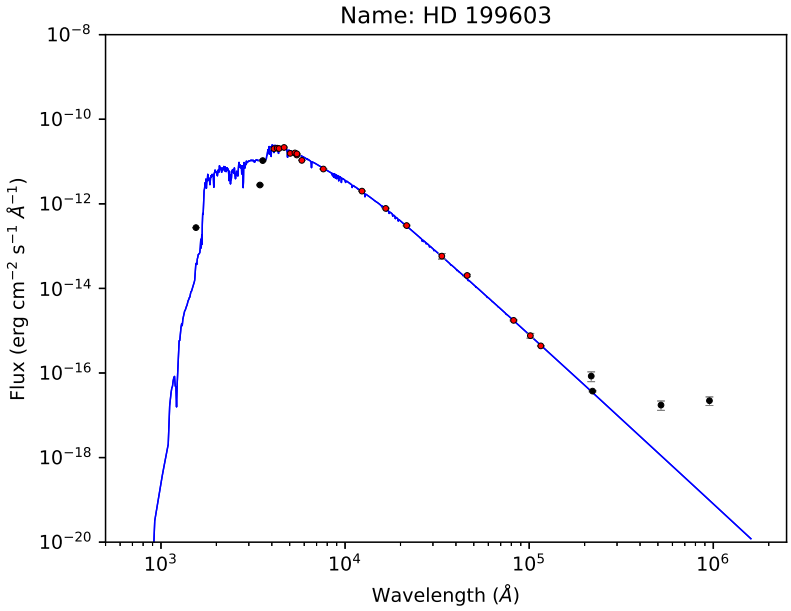

Figure 2: SED of HD 199603. The effect of a cavity can be observed as there is no emission in the near-IR range.

II sources are associated with "flared" and "flattened" disks, respectively. An evolutionary path from group I to group II disks has traditionally been proposed due to the grain growth and the settling of such grains in the midplane of the disk [1]. Nevertheless, a more complex scenario has arisen because recent high-resolution images have revealed that most of the disks belonging to group I show cavities (see, e.g., [11, 17]).

The second scheme is based on the wavelength at which the IR excess observed in SEDs begins (see [13, 21]). In this scheme the SEDs are also classified into two groups, one in which the excess starts at J or H bands (e.g., Fig. 1), and another in which such excess starts at K band or at longer wavelengths (e.g., Fig. 2). This type of classification is directly related to the size of the inner dust cavities.

3 Homogeneous characterization of HAeBes

This section is devoted to briefly describe the research carried out in our work [13]. One of the main reasons that motivated this study lay in the fact that, before the launch of Gaia, HAeBes were studied in small samples scattered on the sky, which contrasted with the hundreds of known T Tauri stars at that time. Furthermore, their stellar and circumstellar parameters were derived using different techniques. Therefore, departing from the sample presented in [25], we have homogeneously characterized a sample of 209 bonafide HAeBes from their SEDs and their Gaia EDR3 parallaxes [20]. The stellar parameters were estimated using the

online tool VOSA (Virtual Observatory SED Analyzer) [3]. VOSA allows us to compare the optical observed SEDs, built from the catalogs available in such a tool, with the synthetic photometry from the photospheric theoretical models. The effective temperatures, visual extinctions, stellar luminosities and radii were obtained from the best-fitting Kurucz model [6], whereas stellar masses and ages were estimated from the PARSEC V2.1s evolutionary tracks and isochrones of [5].

The IR SED were classified according to the two schemes shown in Section 2. Firstly, the ratio between the near-IR and the mid-IR luminosity, and the non-color-corrected IRAS color were used in order to classify them into Meeus groups I and II (see the procedure following [1] and [24]). Secondly, the SEDs fits with VOSA were helpful with the classification into JHK groups, showing at which photometric point the IR excess starts or, equivalently, when the best Kurucz model obtained no longer fits the observed SED.

We also provide in our work circumstellar parameters such as mass accretion rates, disk masses and sizes of the inner dust cavities. The accretion rates were estimated from the correlations between the stellar luminosity and accretion luminosity quantified in [28], which depend on the stellar mass. The disk masses were calculated from the continuum (sub-)millimeter fluxes, assuming that the emission at this wavelength range is optically thin and the gas-to-dust ratio is equal to 100 [4]. However, several studies point out that the disk masses derived from this method could be underestimated. Thus, we used as well an alternative procedure to infer this parameter based on knowledge of the mass accretion rate and stellar age (see, e.g, [8, 21]). Finally, the sizes of the dust inner cavities have been known from the SEDs, depending on the wavelength at which the IR excess starts.

All stellar and circumstellar parameters of our 209 HAeBes are collected in an online archive called HArchiBe. This also includes the figures of the SEDs and a tool for visualizing the position of the objects on the sky. Recently, 109 new HAeBes have been added to this archive, which have been discovered and characterized by [26, 27].

Afterwards, we performed a statistical study relating the stellar and circumstellar parameters with both SED classifications, in order to find some hints on the evolution of protoplanetary disks. One of the major results we have obtained is described as follows. We found that the main mechanism driving the dissipation of the disks in HBes is probably photoevaporation, although other processes can not be ruled out, such as the presence of planets. Figure 3 shows two evidence that support this idea. In the top panel, the size of the inner dust cavities and the stellar mass are represent on the y- and x-axis, respectively. The blue dashed line indicates the critical radius. This parameter denotes the distance at which a cavity starts to open due to photoevaporation [12]. It can be observed that there are more HBes with sizes of the inner dust cavities above this line. On the other hand, the stellar age vs. the stellar mass is plotted in the bottom panel. The blue dashed line indicates in this case the disk lifetime if the photoevaporation is considered as the main mechanism involved in disk dissipation [12]. As you can see, most HBes have stellar ages below this line, whereas HAes are older, pointing out that there must be another mechanism governing the disk dissipation for the latter.

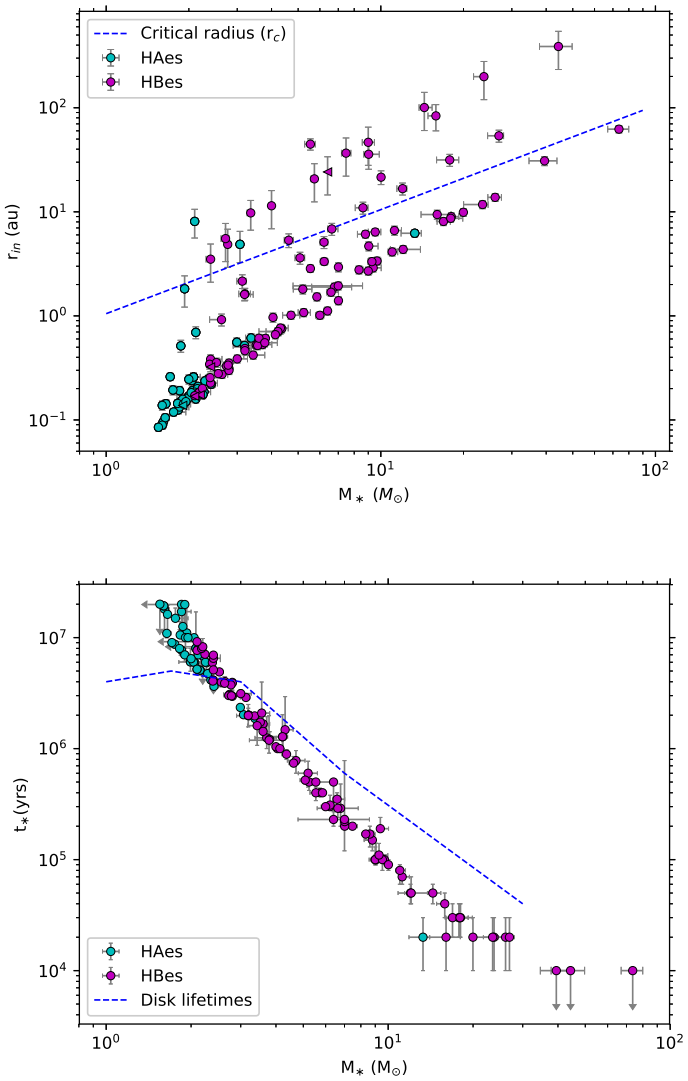

Figure 3: **Top panel:** Inner disk cavities as a function of the stellar mass for HAes and HBes. The dashed blue line represents the critical radius above which the stars are consistent with the photoevaporation scenario. Upper limits are indicated by arrows. **Bottom panel:** Stellar age vs. stellar mass for HAes and HBes. The dashed blue line represents the disk lifetime below which the stars are consistent with the photoevaporation scenario. Upper limits are indicated by arrows.

Acknowledgments

Acknowledgement to I. Mendigutía, B. Montesinos, R.D. Oudmaijer, M. Vioque, C. Rodrigo, E. Solano, G. Meeus and P. Marcos-Arenal for their participation and help in the work presented in this

document.

References

[1] Acke, B., van den Ancker, M. E., Dullemond, C. P., van Boekel, R., & Waters, L. B. F. M. 2004, A&A, 422, 62

[2] Andrews, S. M., Huang, J., Pérez, L. M., et al. 2018, The Messenger, 174, 19

[3] Bayo, A., Rodrigo, C., Barrado Y Navascués, D., et al. 2008, A&A, 492, 2

[4] Beckwith, S. V. W., Sargent, A. I., Chini, R. S., & Guesten, R. 1990, AJ, 99, 924

[5] Bressan, A., Marigo, P., Girardi, L., et al. 2012, MNRAS, 427, 127

[6] Castelli, F., Gratton, R. G., & Kurucz, R. L. 1997, A&A, 318, 841

[7] Currie, T., Lawson, K., Schneider, G., et al. 2022, Nature Astronomy, 6, 751

[8] Dong, R., Najita, J. R., & Brittain, S. 2018, ApJ, 862, 103

[9] Espaillat, C., Muzerolle, J., Najita, J., et al. 2014, in Protostars and Planets VI, ed. H. Beuther, R. S. Klessen, C. P. Dullemond, & T. Henning, 497

[10] Gaia Collaboration, Vallenari, A., Brown, A. G. A., et al. 2022, arXiv e-prints, arXiv:2208.00211

[11] Garufi, A., Meeus, G., Benisty, M., et al. 2017, A&A, 603, A21

[12] Gorti, U., Dullemond, C. P., & Hollenbach, D. 2009, ApJ, 705, 1237

[13] Guzmán-Díaz, J., Mendigutía, I., Montesinos, B., et al. 2021, A&A, 650, A182

[14] Guzman-Diaz, J., Montesinos, B., Mendigutia, I., et al. 2022, arXiv e-prints arXiv:2212.14022

[15] Haffert, S. Y., Bohn, A. J., de Boer, J., et al. 2019, Nature Astronomy, 3, 749

[16] Hein Bertelsen, R. P., Kamp, I., Goto, M., et al. 2014, A&A, 561, A102

[17] Honda, M., Maaskant, K., Okamoto, Y. K., et al. 2015, ApJ, 804, 143

[18] Kama, M., Folsom, C. P., & Pinilla, P. 2015, A&A, 582, L10

[19] Keppler, M., Benisty, M., Müller, A., et al. 2018, A&A, 617, A44

[20] Lindegren L. et al., 2021, A&A, 649, A2

[21] Mendigutía, I., Mora, A., Montesinos, B., et al. 2012, A&A, 543, A59

[22] Mendigutía, I. 2020, Galaxies, 8, 39

[23] Meeus, G., Waters, L. B. F. M., Bouwman, J., et al. 2001, A&A, 365, 476

[24] van Boekel, R., Waters, L. B. F. M., Dominik, C., et al. 2003, A&A, 400, L21

[25] Vioque, M., Oudmaijer, R. D., Baines, D., Mendigutía, I., & Pérez-Martínez, R. 2018, A&A, 620, A128

[26] Vioque, M., Oudmaijer, R. D., Schreiner, M., et al. 2020, A&A, 638, A2

[27] Vioque, M., Oudmaijer, R. D., Wichittanakom, C., et al. 2022, ApJ, 930, 39

[28] Wichittanakom, C., Oudmaijer, R. D., Fairlamb, J. R., et al. 2020, MNRAS, 493, 234

[29] Williams J. P., Cieza L. A., 2011, ARA&A, 49, 67

[30] Zhou, Y., Sanghi, A., Bowler, B. P., et al. 2022, ApJ, 934, L13

Highlights of Spanish Astrophysics XI, Proceedings of the XV Scientific Meeting of the Spanish Astronomical Society held on September 4–9, 2022, in La Laguna, Spain. M. Manteiga, L. Bellot, P. Benavidez, A. de Lorenzo-Cáceres, M. A. Fuente, M. J. Martínez, M. Vázquez- Acosta, C. Dafonte (eds.), 2023

Continuum and line emission of the symbiotic binary R Aqr.

Gómez-Garrido, M.[1], Bujarrabal, V [2], Alcolea, J.[1], and Castro-Carrizo, A.[3]

[1] Observatorio Astronómico Nacional (OAN-IGN), C/ Alfonso XII, 3, 28014 Madrid, Spain
[2] Observatorio Astronómico Nacional (OAN-IGN), Apartado 112, 28803 Alcalá de Henares, Spain
[3] Institut de Radioastronomie Millimétrique, 300 rue de Piscine, 38406 Saint Martin d'Hères, France

Abstract

Symbiotic stellar systems (SSs) are interacting binaries consisting of two close components: an asymptotic giant branch (AGB) star and a white dwarf (WD). As a result of the mass loss of the AGB star, SSs are surrounded by a circumstellar environment whose shape and dynamics are affected by the presence of the hot companion. The study of SSs is key to understanding different phenomena, such as jets, non-spherical planetary nebulae, and Type Ia supernovae. R Aqr is one of the best-studied SSs. The orbit shows a period of ~ 42 years with a stellar separation between 10 and 60 mas. Although R Aqr shows molecular emission in some species, due to the photodissociation by the WD, this is rarely detected in SSs. We present high- and medium-resolution ALMA observations of the continuum and line emission exploring both extended and inner regions of this SS system for a total of three ALMA bands (6, 7, and 9). Continuum emission helps to locate the position of the AGB in the system. In addition, the jets and the mass transfer from the AGB to the WD are mapped by the continuum. Some of the studied lines are CO, SiO, SO, and $H30_{\alpha}$. We describe a new scenario for the molecular emission in R Aqr explaining the brightness distributions shown by the different lines.

1 Introduction

Symbiotic stellar systems (SSs) are interacting binaries composed by an evolved star and a compact object. In the particular case of the D-type symbiotics, which show intense continuum dust emission, the systems are formed by two close components: the primary, an asymptotic giant branch (AGB) and the secondary, a white dwarf (WD) [5]. The material ejected by the AGB component falls to the WD forming an accretion disk around the secondary component. The jets observed in SSs emerge from the central region of these accretion disks. The study of the symbiotic binaries can be a fundamental to understanding the morphology found in planetary nebulae. By observing, modeling, and studying the molecular gas and dust in these objects, we can learn more about the non-spherical structures that appear in the final stage of Sun-like stars.

Due to the intense ultraviolet (UV) emission from the hot component, most of the molecules are photodissociated. As a result, only CO, SiO and H_2O are detected in some SSs, such as R Aqr and CH Cyg [1]. R Aqr is the best-studied symbiotic stellar system. The inner region of the nebula is dominated by a precessing jet (see [9] and [4]). The primary component of this system is a Mira-type

variable with a pulsation period of 388 days, and the secondary is a white dwarf. A size of 15 mas for the primary component is estimated from measurements of R Aqr in the Infrared range [7]. The distance to R Aqr from Gaia parallax is 320 pc, while the distance derived from VLBI observation of SiO masers is 218 pc [6]. The origin of this difference is unknown, but these discrepancies are also found in distances calculated from Gaia parallaxes for other objects with nebulous structures. We assume an intermediate value for the distance adopting 265 pc in our calculations. New orbital parameters have been derived recently (see the contribution by Alcolea *et al.* in these proceedings). The white dwarf describes an elliptical orbit with a period of 42.4 yr. The major semi-axis is 57 mas with an inclination angle of 110 deg, which means that the white dwarf is moving almost in the right ascension (R.A) direction. We have studied the molecular line and continuum emissions of R Aqr and the spatial distribution of the material in this symbiotic system.

2 ALMA observations

We observed R Aqr using the Atacama Large Millimeter/sub-millimeter Array (ALMA). We have used three ALMA bands, namely 6, 7, and 9, corresponding to 1.3, 0.9, and 0.45 mm, and angular resolutions between 20 and 250 mas. Thanks to the high spatial resolution provided by the extended ALMA configurations, we can probe the inner region of R Aqr. The observations of Band 6 were carried out using the extended and compact configuration of ALMA. In this case, both data sets are mixed to achieve a higher signal-to-noise ratio (S/N). To study the main molecular lines, such as CO and SiO, in detail, high spectral units of the correlator were connected. Moderate spectral resolution units were also used simultaneously to derive the continuum emission with good S/N.

The position of both components of R Aqr varies in time because of proper motion and their orbital movements. Since the observations at the different frequencies were performed on different dates, we center all our *uv*-tables to the centroid of the continuum emission at each frequency to present our data in the same reference framework. As a result, our final maps are expected to be referenced to the AGB position for all observations.

Note that to better study the line emission, the continuum distribution was subtracted and it can affect the brightness distribution observed in the line maps in a complex way. We also study the continuum emission of R Aqr. Since the high- and low-resolution continuum maps at 0.9 mm were studied by [2] in detail, we focus on the analysis of the observation at 1.3 and 0.45 mm.

3 Continuum and H30α maps

Fig. 1(a) shows the low spatial resolution image of the continuum emission of R Aqr at 1.3 mm, where we can see the large-scale emission of the jet. Fig. 1(b) shows the high resolution continuum maps at 1.3 and 0.45 mm, bands 6 and 9 respectively. The high-resolution maps let us study the inner region of R Aqr where the formation of the jet is taking place. In Fig. 1(b) we can see the emergence of the jet, which connects to the large-scale jet shown by Fig. 1(a). We can also see how the continuum emission at 1.3 mm extends from the central position, where is located the Mira component, to the position of the white dwarf. This suggests a physical connection between both components as previously seen in the continuum data at 0.9 mm (see [2]). However, the angular resolution is not enough to separate the

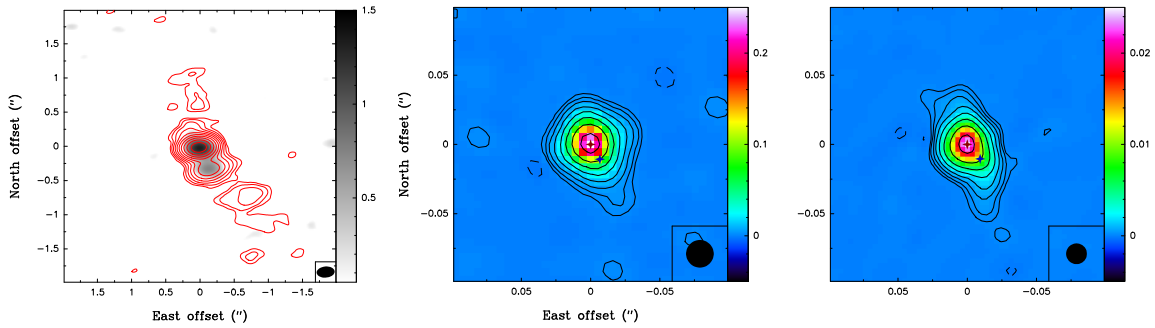

(a) (b)

Figure 1: (*a*): Red contours: low-resolution map of continuum at 1.3 mm towards R Aqr. The contour level spacing is logarithmic with a jump of factor 2. The first positive contour is 0.07 mJybeam^{-1}. The brightness distribution of H30α integrated over all velocities is shown in greyscale. In the inset we can see the beam, with a size of 264×163 mas and P.A. of 95 deg. (*b*):High-resolution continuum maps at 1.3 and 0.45 mm towards R Aqr. The contour level spacing is logarithmic, with a jump of factor two. The first positive contours are 0.15 and 1.5 mJybeam^{-1} respectively. The observations are centered on the continuum centroid, the position of the Mira component (red cross); the predicted position for the WD is also indicated (blue cross). See the beams in the insets, with a size of 15×15 and 20×20 mas respectively.

emission of the radio photo-sphere, jet, and other components. We also studied the emission of H30α. Fig. 1(a) shows the low-resolution emission of this recombination line, which extends in the direction nort-east to south-west. Note that the brightness distribution corresponds to the intensity integrated over the complete velocity range. We find that the distribution of H30α and the continuum show similar structures. This was also found in the Hα in the visual spectral region by [8]. The differences between the continuum and H30α can be caused by the lower sensitivity of the recombination line map. We can estimate the spectral index of the compact component, although this value is highly uncertain due to the intense flux variability of the AGB in time. We obtain a value of 2.2, which is compatible with the emission of dust emitting as a black body. The extended component in Fig. 1(b) is more difficult to understand because in that region the emission of the jet, white dwarf and material falling to the hot companion are all mixed up.

4 Molecular line maps

Many molecular species, such as CO, SiO, SO, and H_2O are detected in R Aqr. Figs. 2 and 3 show the emission of ^{12}CO J=2–1 and ^{28}SiO v=0 J=16–15 as an example of the molecular emission found in this SS. The emission of CO is the most intense and extended. We find a typical size for the emission of CO of 800×200 mas. This means that the CO molecules survive at distances larger than the orbital size. The emission of CO was modeled using hydrodynamical calculations (see [3]). This model predicts the spiral structures around this binary system as a result of the interaction between

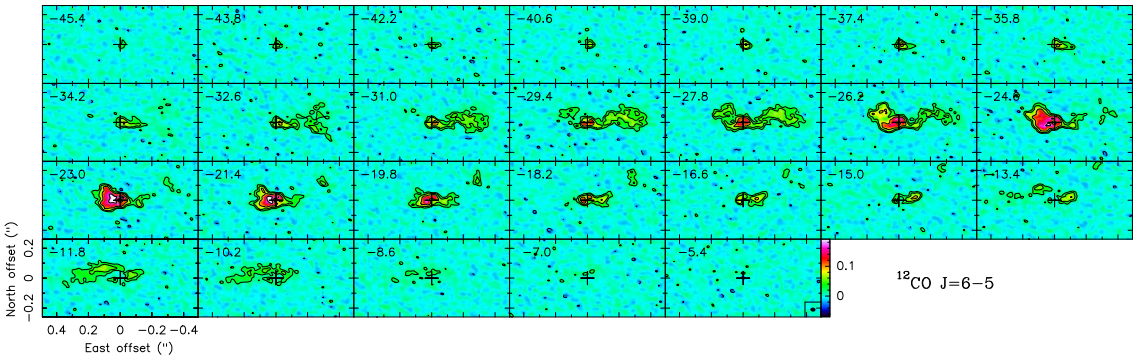

Figure 2: ALMA maps per velocity channel of ^{12}CO J=6–5 emission in R Aqr. Local standard of rest (LSR) velocities are indicated in the upper left corners. The contours are logarithmic, with a jump of factor two and a first level of 2 mJybeam^{-1}. The dashed contours represent negative values. The beam is shown in the inset in the last panel.

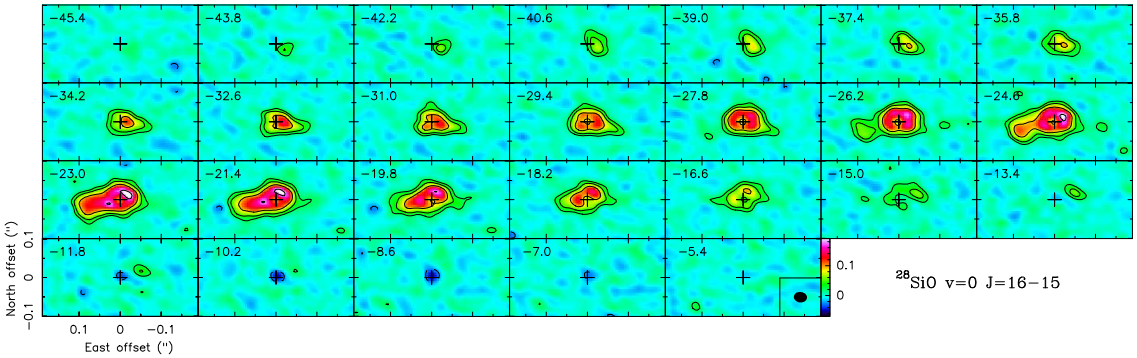

Figure 3: Same as Fig. 2 but for ^{28}SiO v=0 J=16–15 using a first level of 2 mJybeam^{-1}.

the two stellar components.

The SiO molecule shows emission beyond the orbital size in the R.A. direction, but it is not more extended than CO. Note that its extent to the south-east is similar to that seen in CO (see Fig. 4), and therefore, the emissions of both molecules probably come from the same region. We find absorption at positive velocities in many rotational transitions of this molecule and its isotopic substitution ^{29}SiO. We identify this absorption with falling material ejected previously by the AGB component. Note that the extended component of the SiO and CO tends to be confined in the orbital plane, which is in the R.A. direction approximately. We suppose that the molecules out of this region are photodissociated by the UV radiation from the WD.

In the cases of the less abundant molecules, the emission is also more compact. Fig. 4 shows the central velocities maps of several molecular species, which are representative of the shapes shown by the different molecular lines: ^{12}CO J=6–5, ^{28}SiO v=0 J=16–15, SO $^3\Sigma$ v=0 16_{16}–15_{15}, H_2O v_3=1 $5_{7,2}$–$6_{6,1}$, and SiO v=9 J=17–16. Note that the brightness distributions of CO and SiO show a ring-like structure in the central region, while for the less abundant molecules we can distinguish several shapes of brightness distributions: ”peanut”-like, compact and compact-offset. The brightness

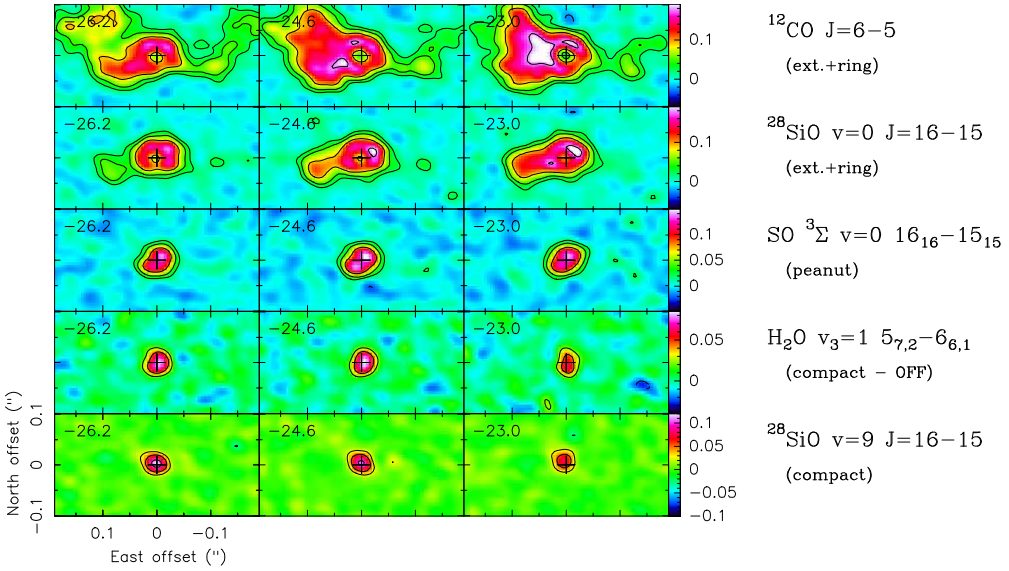

Figure 4: Same as Fig. 2 but for the central velocities ALMA maps of the ^{12}CO J=6–5, ^{28}SiO v=0 J=16–15, SO $^3\Sigma$ v=0, 16_{16}–15_{15}, H_2O v_3=1 $5_{7,2}$–$6_{6,1}$, and SiO v=9 J=17–16 lines.

distributions of the less abundant molecules are more compact, showing emission only in the central region, and in many cases, only inside the orbital region. This behavior means that is very difficult to find little abundant molecules at large distances from the AGB envelope where they are formed. These molecules are photo-dissociated by the WD and only survive in the densest and best-shielded regions close to the AGB.

Gravitational interactions between the WD and the material ejected by the AGB result in a complex dynamical scenario. Therefore, modeling the extended emission shown by the most abundant molecules is very hard. We focus on modeling the compact emission seen in the central region. We model the emission of the ^{28}SiO v=0 J=16–15 line, which is taken as reference, using a radiative transfer model. For the calculations, we take into account two different components: a relatively hot expanding envelope and cool layers falling back onto to the AGB. The resulting map is shown in Fig. 5. We obtain similar theoretical brightness distribution and intensities than the observed per velocity channel for the ^{28}SiO v=0 J=16–15 line. Thanks to the introduction of the falling material we also obtain good results for the absorption feature seen on the positive velocities.

The variety of brightness distribution shown by the different lines can be partially explained by the continuum subtraction. This effect is more important in optically thick molecules, such as CO and SiO, which show a well defined hole in the maps of their central velocity channels. For optically thiner molecules, such as SO and H_2O, the subtraction of the continuum distribution is less noticeable in the final maps.

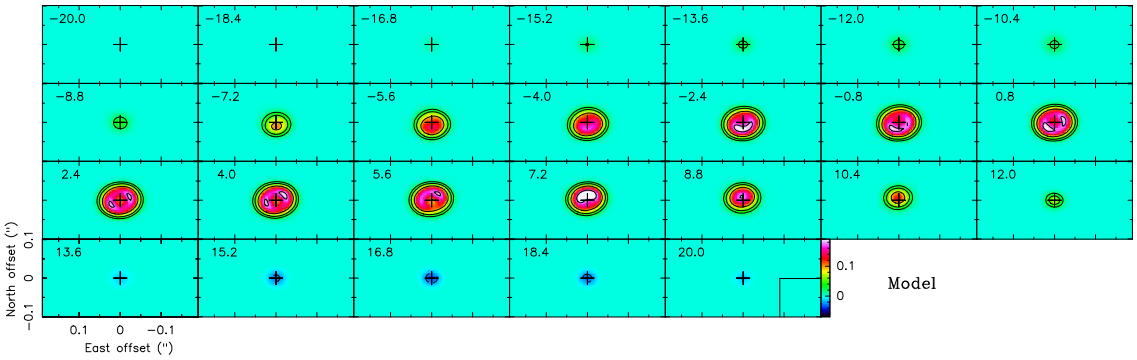

Figure 5: Same as Fig. 2 but for synthetic maps per velocity channel and using a first level of 3 mJybeam^{-1}.

Acknowledgments

Authors acknowledge the support of the Spanish Ministry of Science and Innovation through the Agencia Estatal de Investigación research grant PID2019-105203GB-C21 (EVENTs / Nebulae Web project).

References

[1] Bujarrabal, V., Mikołajewska, J., Alcolea, J., and Quintana-Lacaci, G. 2010, A&A, 516A, 19B

[2] Bujarrabal, V., Alcolea, J., Mikołajewska, J., *et al.* 2018, A&A, 616, L3

[3] Bujarrabal, V., Agúndez, M., Gómez-Garrido, M., *et al.* 2021, A&A 651, A4

[4] Melnikov, S., Stute, M., & Eislöffel, J. 2018, A&A, 612, A77

[5] Mikołajewska, J. 2012, Balt. Astron. 21, 5

[6] Min, C., Matsumoto, N., Kim, M. K., *et al.* 2014, PASJ, 66, 38

[7] Ragland, S., Le Coroller, H., Pluzhnik, E., *et al.* 2008, ApJ, 679, 746R

[8] Schmid, H. M., Bazzon, A., Milli, J., *et al.* 2017, A&A, 602, A53

[9] Solf, J., & Ulrich, H. 1985, A&A, 148, 274

Highlights of Spanish Astrophysics XI, Proceedings of the XV Scientific Meeting of the Spanish Astronomical Society held on September 4–9, 2022, in La Laguna, Spain. M. Manteiga, L. Bellot, P. Benavidez, A. de Lorenzo-Cáceres, M. A. Fuente, M. J. Martínez, M. Vázquez- Acosta, C. Dafonte (eds.), 2023

Determining density and gravity of intermediate-mass stars with Convolutional Neural Networks.

Suárez, J.C.[1], **García Hernández, A.**[1], **Maestre, R.**[1], **Barceló Forteza, S.**[1], **and Mirouh, G.M.**[1]

[1] Dpt. Física Teórica y del Cosmos, Universidad de Granada, Campus de Fuentenueva s/n, 18071 Granada, Spain

Abstract

In this work we used a convolutional neural network to determine the mean density and surface gravity of stars from 1.5 to 3 times more massive than the Sun. These physical quantities are key to better understand their structure as well as the physical processes occurring during their evolution. Relying on asteroseismic models we deployed and trained a CNN to detect patterns in the oscillation frequencies. The mean density and surface gravity estimates obtained accurately matched our set of benchmark observations. This method will allow us to analyse massively thousands of A-F stars observed by past, present and future space missions such as CoRoT, Kepler/K2, TESS, and the upcoming PLATO mission.

1 Introduction

In the last decades, the characterisation of the internal structure and evolution of intermediate-mass stars has significantly improved thanks to asteroseismology. More specifically, pattern recognition has been key to significantly constrain models representative of these stars, and thereby to better understand the physics taking place in their interiors. Such patterns have been found in the oscillation spectrum, which allow us to avoid identifying from hundreds to thousands of individual pulsation modes, which is, today, far from being achieved.

For intermediate-mass stars, frequency patterns are not easy to detect. Some theoretical works predicted its existence (e.g. [13, 10, 8]), as well as a scaling relation with the stellar mean density ([15], [14]). Thanks to the ultra-precise photometric lightcurves from the CoRoT ([1]) space mission, quasi-periodic patterns were clearly found in the oscillation spectra of δ Scuti stars (e.g. [6]) and the scaling relation with the mean density was empirically confirmed (see e.g. [5, 7]). This opened the door to multi-variable correlation analyses [9, 3], the study of other patterns, like the rotational splitting [12], to perform certain mode identification in young stars [4], or constrain the age of open clusters [11], to name a few examples.

Statistics- and/or Fourier-based techniques for pattern recognition often yield ambiguous results for intermediate-mass stars. This is because of the small number of frequencies exhibited by these objects on the one side, and the nature of the modes, on the other side, which pulsate around the fundamental radial mode, i.e. far from the asymptotic regime in which solar-like oscillations show clear patterns. Here we tried to overcome those problems using machine learning techniques.

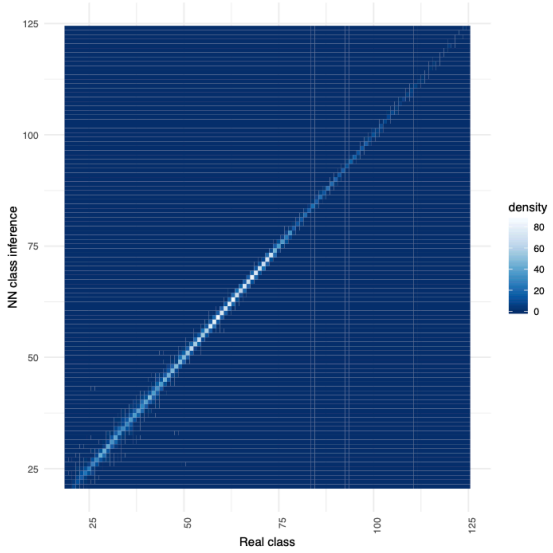

Figure 1: $\Delta\nu$ confusion matrix for the control sample (97% of accuracy for top-1 ranked probabilities).

2 The CNN

To avoid systematic errors due to human criteria, we trained a convolutional neural network (CNN) to identify the large separation, $\Delta\nu$. This pattern is built upon the frequency difference of modes such as

$$\Delta\nu = \nu_{n,\ell} - \nu_{n-1,\ell}. \tag{1}$$

Among intermediate-mass stars, we focused here on a specific type of pulsating stars, the δ Scuti stars, which mainly pulsate with pressure modes (p modes), for which $\Delta\nu$ have been determined with techniques such as the autocorrelation function (AC), the histogram of frequency differences (HDF) and the discrete Fourier transform (DFT).

We built a CNN whose NN are composed by staked layers with convolution, max pooling, and batch normalisation with dropout, all of them combined then into a dense layer with a *Softmax* activation function that normalises the output into a probability distribution that represents a categorical distribution. Each convolution layer of the CNN is fed with a three-dimensional vector composed by the AC, HDF and DFT.

To train the CNN we constructed a dataset composed by 500k asteroseismic models (equilibrium and oscillation frequencies) meant to be representative of δ Scuti stars. To do so, we computed the models varying the mass, metallicity and initial rotation velocity sufficiently dense to reduce uncertainty (and minimise possible selection bias) in the ranges known for these stars. Following [6, 15], for each model we computed the oscillation frequencies in a range covering radial orders from $n = 2$ to $n = 8$, from which the 30 highest-amplitude modes are kept. The amplitude was simulated assuming a visibility law uniquely based on the photometric cancellation effect (up to $\ell = 3$), where the mode visibility decrease for increasing ℓ in the form $A_\ell \sim \ell^{-1/2}$.

From the models dataset we randomly extracted 50k models to be used as our control sample. The CNN provides a probability over the partition class C of mesh p in the interval in which the large separation is expected for δ Scuti stars, i.e. $[0, 100]\,\mu$Hz. The internal accuracy of the machine is tested over 50k models previously extracted from the training dataset[1]. This was done by evaluating the top-k categorical accuracy rate, meaning the success when the target class is within the k predictions ranked by probability. For the control sample, an accuracy of 97% is reached for top-1 probabilities (see Fig. 1).

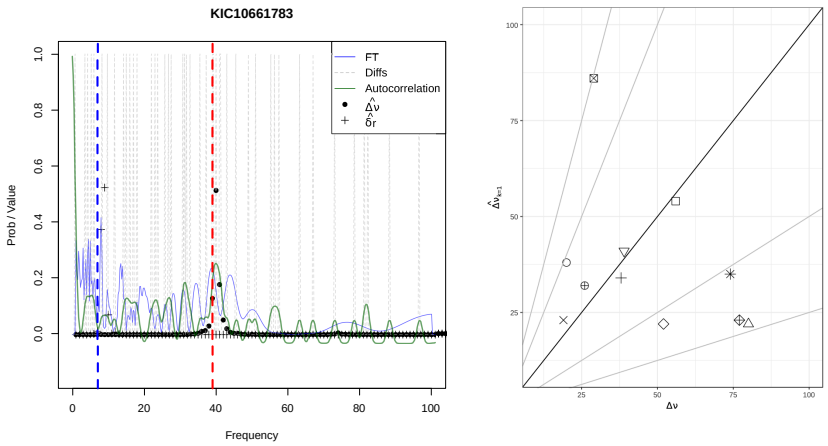

Figure 2: Left: CNN inferences for KIC 10661783 (black dots represent the probability density as a function of the frequency bucket in $\Delta\nu$), together with DFT, AC and HFD predictions. Vertical red line represents the independently observed value. Blue dashed line represents the rotational splitting frequency estimate (for illustrative purpose). Right: comparison between $\Delta\nu$ inferred by the CNN for the benchmark sample of δ Scuti stars in eclipsing binary systems, with those obtained with other methods ([7]). Each symbol represent a different star of the sample. Lines show the 1:1, 0.5:2, and 0.33:3 match relations.

[1]These models were randomly selected assuming uniform distribution along the models grid, which ensures there is no selection bias.

3 The results.

In order to validate the usefulness of the CNN, we applied it to real stars for which we previously had confident values of the large separation and mean density independently: our benchmark sample composed of 17 eclipsing binary systems with a δ Scuti star component (see details in [5, 7]). The confusion matrix shown for these observed stars is shown in Figure 2.

Note that for about 56% of the stars the CNN precisely found (within 1-5% of error) the correct value of the large separation (1:1 line) using top-1 inferences. This implies a RMSE of 28.09 muHz for the complete set of stars. Even more interesting is the fact the for the rest of objects, the results were not randomly distributed in the diagram, but around multiples and submultiples of the 1:1 relation. This implies that the CNN is properly finding $\Delta\nu$ in all the cases, but is not able to *decide* whether is the actual $\Delta\nu$ value or a multiple/submultiple. When these multiples were considered the RMSE of the match significantly decreased to 4.80 muHz.

In other words, the CNN is properly finding $\Delta\nu$ in all the cases, but is not able to *decide* whether is the actual $\Delta\nu$ value or a multiple/submultiple. This problem comes from the lack of information about the visibility of the modes, which, in the range of the observed frequencies, may be prone to display submultiple/multiple instead the actual $\Delta\nu$.

Once inferred robust values for the large separation, it is straightforward to get the mean density [5] and surface gravity [9] of the stars. In addition, the uncertainty coming from the angle of inclination of the stars can be neglected since they stars belong to eclipsing binary systems. For field stars, this might be an important indeed, since the visibility of the modes depend on the angle of inclination, and thereby affecting the number of modes that contribute to the large separation pattern.

4 Discussion and conclusions

The promising results obtained in this work need to be confirmed by the analysis of other stars. The next steps of this investigation are: (1) to apply the CNN to large samples of stars observed by space missions in order to determine their mean density and surface gravity; (2) compare our results with other determinations of $\Delta\nu$ in the literature; (3) include additional information to the analysis that may help us to automatically eliminate the degeneracy with multiples/submultiples of the large separation, like luminosities from Gaia mission, corrections for gravity darkening effects [2] or constraints from other seismic indices like $\nu_{\max}$ [3].

Acknowledgments

JCS, AGH, RM, SBF, and GM acknowledge support by University of Granada and by Spanish public funds for research under project "Contribution of the UGR to the PLATO2.0 space mission. Phases C / D-1", funded by MCNI/AEI/PID2019-107061GB-C64. AGH also acknowledges support from

"FEDER/Junta de Andalucía-Consejería de Economía y Conocimiento" under project E-FQM-041-UGR18 by Universidad de Granada.

References

[1] Baglin, A., Auvergne, M., Barge, P., et al. 2006, in ESA Special Publication, Vol. 1306, ESA Special Publication, ed. M. Fridlund, A. Baglin, J. Lochard, & L. Conroy, 33

[2] Barceló Forteza, S., Moya, A., Barrado, D., et al. 2020, Astronomy and Astrophysics, 638, A59

[3] Barceló Forteza, S., Roca Cortés, T., & García, R. A. 2018, Astronomy and Astrophysics, 614, A46

[4] Bedding, T. R., Murphy, S. J., Hey, D. R., et al. 2020, Nature, 581, 147

[5] García Hernández, A., Martín-Ruiz, S., Monteiro, M. J. P. F. G., et al. 2015, The Astrophysical Journal Letters, 811, L29

[6] García Hernández, A., Moya, A., Michel, E., et al. 2009, Astronomy & Astrophysics, 506, 79

[7] Hernández, A. G., Suárez, J. C., Moya, A., et al. 2017, Monthly Notices of the Royal Astronomical Society: Letters, 471, L140

[8] Mirouh, G. M., Angelou, G. C., Reese, D. R., & Costa, G. 2019, Monthly Notices of the Royal Astronomical Society: Letters, 483, L28

[9] Moya, A., Suárez, J. C., García Hernández, A., & Mendoza, M. A. 2017, Monthly Notices of the Royal Astronomical Society, 000, 1

[10] Ouazzani, R.-M., Roxburgh, I. W., & Dupret, M.-A. 2015, Astronomy & Astrophysics, 579, A116

[11] Pamos Ortega, D., García Hernández, A., Suárez, J. C., et al. 2022, Monthly Notices of the Royal Astronomical Society, 513, 374

[12] Ramón-Ballesta, A., García Hernández, A., Suárez, J. C., et al. 2021, Monthly Notices of the Royal Astronomical Society, 505, 6217

[13] Reese, D., Lignières, F., & Rieutord, M. 2008, Astronomy & Astrophysics, 481, 449

[14] Rodríguez-Martín, J. E., García Hernández, A., Suárez, J. C., & Rodón, J. R. 2020, Monthly Notices of the Royal Astronomical Society, 498, 1700

[15] Suárez, J. C., Hernández, A. G., Moya, A., et al. 2014, Astronomy & Astrophysics, 563, 11

Highlights of Spanish Astrophysics XI, Proceedings of the XV Scientific Meeting of the Spanish Astronomical Society held on September 4–9, 2022, in La Laguna, Spain. M. Manteiga, L. Bellot, P. Benavidez, A. de Lorenzo-Cáceres, M. A. Fuente, M. J. Martínez, M. Vázquez- Acosta, C. Dafonte (eds.), 2023

Determining the orbital parameters of binary systems with an AGB primary. The case of the R Aqr symbiotic system.

Alcolea, J.[1], Mikołajewska, J.[2], Gómez-Garrido, M.[1], Bujarrabal, V.[1], Iłkiewicz, K.[2], Castro-Carrizo, A.[3], Desmurs, J.-F.[1], Santander-García, M.[1], and Bachiller, R.[1]

[1] Observatorio Astronómico Nacional (IGN, Spain)
[2] Centrum Astronomiczne im. Mikołaja Kopernika (PAN, Poland)
[3] Institute de Radioastronomie Millimétrique (France)

Abstract

Binary stars including an AGB star hold the clues for understanding important phenomena in stellar evolution, such as common-envelope events, the formation of SN-Ia, and the origin of aspherical pPNe/PNe. Hydro-dynamical codes simulating the companion's influence on the primary mass loss exist, but we still lack information on the orbital parameters of systems where these models can be tested. The best case where this can be pursued is R Aqr. Here, we present the results of the first-ever determination of the whole set of orbital parameters of the system purely based on observational data. The results agree very well with the observational characteristics of the nebula around the system. Reasonable values for the stellar masses agree with distances from period- and diameter-luminosity relationships for Mira variables, but not with those from VLBI observations of SiO masers or GAIA.

1 AGB binaries and the case of R Aqr

Binary systems are interesting astrophysical laboratories as they are responsible for several extreme physical phenomena. In addition, when the system is spatially resolved and we know the velocity curve for at least one star, we can derive the (otherwise elusive) individual masses of the member stars. Binary stars including an Asymptotic Giant Branch (AGB) primary are particularly interesting since the presence of a compact companion can induce a mass transfer process that can severely affect the evolution of both members. AGB stars lose mass at such high rates (up to 10^{-5} $M_\odot\,yr^{-1}$) that this process is ultimately responsible for the evolution of the star into a white dwarf (WD). This wind forms a circumstellar envelope (CSE), rich in molecular gas and dust particles, around the AGB star, which will turn into a planetary nebula (PN) in the forthcoming post-AGB phases. The standard theory predicts that AGB CSEs should be roughly spherical. However, this may not be the case for AGB

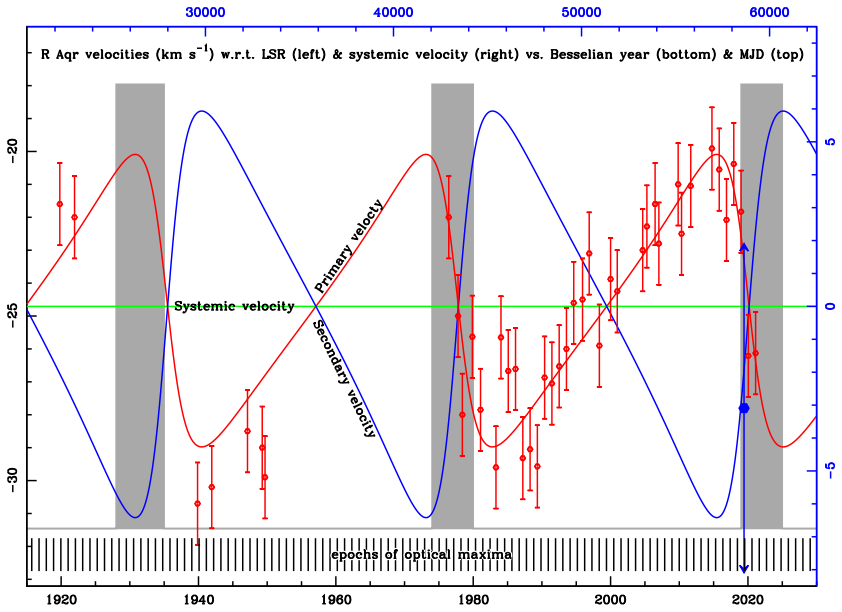

Figure 1: The updated velocity curve of the primary, the Mira variable R Aqr-A, based on the data presented by [7], but including new values from SiO maser observations up to mid-2021. Data are averaged for each pulsation period (black lines at the bottom show the dates for R Aqr optical maxima according to AAVSO). Red dots show the observed values (with $\pm 1.25\,\mathrm{km\,s^{-1}}$ error bars), while the red and green lines show the fitting to the data and the systemic velocity of the centre of masses. The blue line displays the prediction for the companion velocity for a mass ratio of 1.4. The blue dot (and error bar) shows de velocity derived for the companion R Aqr-B for 2019.4 from the H30α line. The dark areas mark the occurrence of eclipses in the system.

binaries, where the presence of the companion breaks the spherical symmetry: the launching of bipolar jets by these companions (powered by mass accretion from the primary) is the most plausible explanation for the formation of axis-symmetric PNe via their interaction with the AGB wind (see e.g. [5]). This hypothesis is supported by the presence of spiral density waves in the CSEs of many AGBs [6], which can be easily explained as a result of the gravitational pull of the companion on the AGB star, and the focusing of the mass-loss on the orbital plane. These spiral-like features are not only seen in AGB CSEs but also in some PNe (e.g. NGC 7027, NGC 3132), and the transition objects in between them (e.g. the pre-PNe CRL 2688), strengthen the evolutive relationship between these three kinds of sources.

Although hydrodynamical models for binary systems with an AGB mass-losing primary reproduce the observations (e.g. [11]), an independent measurement of the orbital parameters is mandatory to establish the connection between the companions and the arising of these spiral density waves, which is the best support for the binary/aspherical-PNe link hypothesis. So far, there is only one case in which the spiral imprint is detected and we can find about the orbital parameters of the system: the symbiotic star R Aqr.

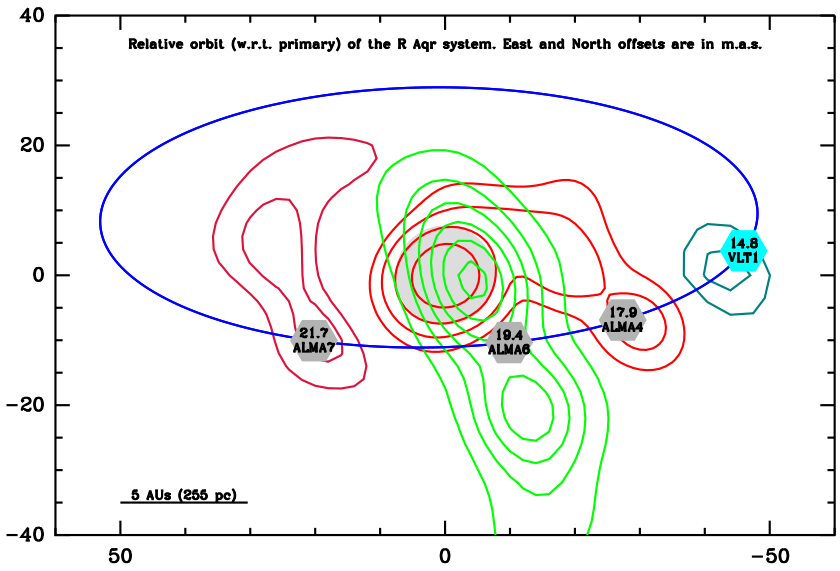

Figure 2: Relative positions of the WD secondary w.r.t. the Mira primary for the four observed epochs. We include the VLT results by [15] (2014.8, teal green contours), and ALMA 0.8 mm continuum by [3] (2017.9 red contours). For 2019.4, the secondary is assumed to be at the centre of the jet seen in H30α (green contours). For 2021.7, we assume that the secondary is at the southernmost end of the 0.8 mm continuum after removing the contribution of the primary (dark red contours). Both 2019.4 and 2021.7 positions are from unpublished ALMA observations. The position of the primary is always at the origin of the coordinates. East and North offsets are in mas. The grey disk at the centre shows the size of the primary ($\sim$17 mas). The relative orbit in the plane of the sky resulting from the fitting is shown by the blue ellipse: the system rotates clockwise. Predictions for the epochs of the observations are marked by hexagons. Scale in AUs for a distance of 255 pc is also indicated.

R Aqr is a symbiotic system consisting of a primary AGB star (R Aqr-A) and a WD secondary (R Aqr-B). Located 220–385 pc away [14, 2], it is one of the closest interacting binaries. As a result of mass accretion, the companion launches a bipolar precessing jet that illuminates an arc-minute-wide point-symmetric nebula [12] (supporting the link between aspherical PNe and binary stars). ALMA CO mapping has revealed the strong shaping of the CSE by the companion, with the detection of a two-arm spiral in molecular gas [3, 4]. In addition to the composite stellar spectrum [13], the occurrence of eclipses [16] and the regular variations of the velocity of the primary [9] support the binary nature of the system, also suggesting an orbital period of $\sim$40–44 a. Based on these results [10, 7] performed the first attempts to derive the orbital parameters of the system. However, these calculations were based on a wrong identification of the secondary [10] and some assumptions on the orientation of the orbit; it was not till 2014–17 that the two components were finally resolved through VLT [15] and Cycle-4 ALMA observations [3]. In this contribution, we present the first determination of the full set of orbital parameters for the R Aqr-AB system purely based on observational data, which include an updated dataset for the radial velocity of the primary,

and additional Cycle-6 and -7 ALMA observations of the relative position of the two stars.

2 The new/updated observational data and their fitting

One of the problems inherent to the determination of the orbital parameters in systems involving a Mira star is that the expected variations in the radial velocity are smaller than those due to its regular pulsations [9]. This problem can be partially overcome by using radial velocities derived from the SiO maser emission, which is so common in O-rich Mira stars. Due to pumping constraints, these emissions come from regions at a few stellar radii, where the pulsation effects are not so strong. In addition, maser amplification favours the detection of regions close to the plane of the sky [1], where Doppler shifts due to radial movements are largely suppressed. In this work, we have used the radial velocity curve compiled by [7] but updated with newer SiO observations up to May 2021, including those from the new Yebes monitoring of SiO masers in evolved stars. To further minimize the possible effects of the stellar pulsation, velocity data have been averaged for each pulsation period (following AAVSO database results for optical variability period and epochs of maxima). After this binning, we adopted the midpoint between the maximum and minimum velocity observed in SiO maser emission as the radial velocity for the primary for the corresponding pulsation period. The results are shown in Fig. 1.

For the first time, we have combined the velocity curve of the primary, with data for the relative position between the two components for several epochs. In addition to the published data by [15, 3], we have also included new Cycle-6 and -7 ALMA maps for epochs 2019.4 and 2021.7 respectively, both with spatial resolutions of about 20 mas (see Fig. 2). In 2019.4, the system was observed very closely to its inferior conjunction: we could not separate the 1.3 mm continuum emission of the secondary from the much stronger primary (as we did for the 2017.9 observation [3]). However, we have identified the position of the secondary as the mid-point of the two-sided jet structure seen in H30α (see the contribution by Gomez-Garrido *et al.* in these proceedings). In 2021.7, due to the larger separation of the stars, the secondary has been identified at the base of the elongated structure (the jet) seen in the 0.8 mm continuum image after the removal of the primary's contribution.

The combined velocity and relative position data are fitted for the determination of the orbital parameters of the system. We have used the code BINARY by Donald H. Gudehus [8]. The resulting set of parameters is shown in Table 1. The predictions for the primary's velocity curve and relative position of the stars based on these orbital parameters are also shown in Figs.1 and 2. A short movie of the configuration of the system in the orbital plane can be seen in this YouTube link. For a distance of 255 pc (see next section), the separation between the stars varies between 8 and 21 AUs, the periastron occurring very close to the inferior conjunction. The inclination of the orbit agrees very well with that of the ring seen in the optical nebula at much larger scales [12], supporting our results and that the ring is also due to interactions in the system.

Table 1: Campbell's elements for the R Aqr system derived from the fitting

Parameter name	Symbol	Value	Error	Units
Revolution period	P	42.4	$\pm$0.2	a
Periastron epoch	T	2019.9	$\pm$0.1	BSY
Eccentricity	e	0.45	$\pm$0.01	
Position angle of ascending node	Ω	91.4	$\pm$0.7	deg.
Inclination	i	110.7	$\pm$1.0	deg.
Angle of line of nodes to periastron	ω	84.8	$\pm$2.5	deg.
Major semi-axis	a	57	$\pm$8	mas

3 Implications on the distance to R Aqr

The fitting of the new data provides values for all the orbital parameters without requiring any assumptions. However, we need the distance to the system to estimate the masses. Inversely, if we can provide some guesses on the masses of the stars, we can determine the distance. These dependencies are very steep as the system's total mass is proportional to the distance to the third power. A plot of the system's total mass, as well as for individual stars, as a function of the assumed value for the distance to R Aqr is displayed in Fig 3. Other properties of the Mira primary, such as elemental/isotopic abundances and the pulsation period suggest a mass of $\sim 1\,M_\odot$, in agreement with the values obtained from the orbital parameters for the distances based on general properties of Mira variables (period-luminosity and diameter-luminosity relationships). On the contrary, for the distances derived from trigonometric parallaxes by VLBI observations of SiO masers and GAIA, we obtain masses for the Mira that are either too low or too high, respectively. We, therefore, conclude that, unless the presence of the companion strongly modifies the basic stellar properties of the primary, the most likely distance to the system is 255 pc, resulting in a total mass of $2.7\pm0.1\,M_\odot$, a mass ratio of 1.4, and individual masses of 1.0 ± 0.2 and 0.7 ± 0.2 $M_\odot$ for the Mira and WD, respectively. We also conclude that the most likely explanation for the wrong distance estimation by the parallax methods is the size of the primary and the orbital motion around the barycentre, which are both larger than the parallaxes determined.

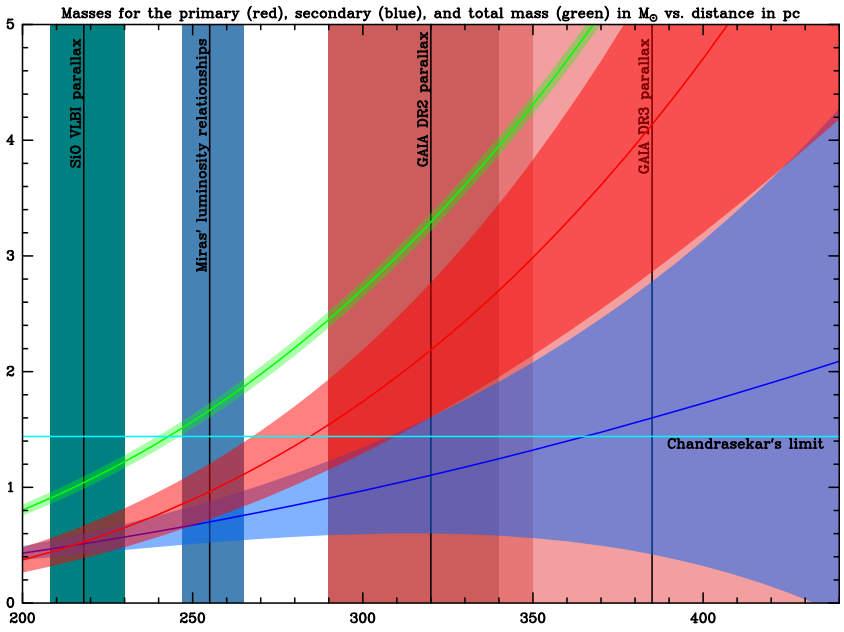

Figure 3: Masses and confidence intervals (in $M_{\odot}$) for the primary (red), secondary (blue), and total mass (green) as a function of the distance to R Aqr (in pc). The vertical black lines and coloured areas show the values and confidence intervals for the distance estimated using different methods. In teal green, the distance by VLBI parallax of SiO masers by [14]; in steel blue, that from pulsation-period and diameter versus luminosity relationships for Mira variables; and in dark/light red, values from GAIA DR2/DR3. Both VLBI and GAIA distances result in masses either too low or too high. The most reasonable values are those given by the Miras' luminosity relationships; see Sect. 3.

Acknowledgments

Authors acknowledge the support of the Spanish Ministry of Science and Innovation through the AEI research grant PID2019-105203GB-C21 (EVENTs / Nebulae Web project).

References

[1] Alcolea, J., 2004, 7th EVN Symp., 169A

[2] Bailer-Jones, C.A.L., Rybizki, J., Fouesneau, M., *et al.*, 2021, AJ 161, 147B

[3] Bujarrabal, V., Alcolea, J., Mikołajewska, J., *et al.*, 2018, A&A 616L, 3B

[4] Bujarrabal, V., Agúndez, M., Gómez-Garrido, M., *et al.*, 2021, A&A 651A, 4B

[5] De Marco, O., Akashi, M., Akras, S., *et al.*, 2022, NatAs 6, 1421D

[6] Decin, L., Montargès, M., Richards, A.M.S., *et al.*, 2020, Sci 369, 1497D

[7] Gromadzki, M., & Mikołajewska, J., 2009, A&A 495A, 931G

[8] Gudehus, D.H., 2001, BAAS 33, 850G

[9] Hinkle, K.H., Wilson, T.D., Scharlach, W.W.G, & Fekel, F.C., 1989, AJ 98, 182H

[10] Hollis, J.M., Pedelty, J.A., & Lyon, R.G., 1997, ApJ 482L, 85H

[11] Kim, H. & Taam, R.E., 2012, ApJ 759L, 22K

[12] Liimets, T., Corradi, R.L.M., Jones, D., *et al.*, 2018, A&A 612A, 118L

[13] Merrill, P.W., 1935, ApJ, 81, 312M

[14] Min, C., Matsumoto, N., Kim, M.K., *et al.*, 2014, PASJ 66, 38M

[15] Schmid, H.M., Bazzon, A., Milli, J, *et al.*, 2017, A&A 602A, 53S

[16] Willson, L.A., Garnavich, P., & Mattei, J.A. 1981, IBVS 1961, 1W

Highlights of Spanish Astrophysics XI, Proceedings of the XV Scientific Meeting of the Spanish Astronomical Society held on September 4–9, 2022, in La Laguna, Spain. M. Manteiga, L. Bellot, P. Benavidez, A. de Lorenzo-Cáceres, M. A. Fuente, M. J. Martínez, M. Vázquez- Acosta, C. Dafonte (eds.), 2023

High-precision Mg abundances in the metal-rich Galactic disc: chemodynamical relations and comparison with chemical evolution models.

Santos-Peral, P.[1,2], Palla, M.[3,4,5], Recio-Blanco, A.[2], Kordopatis, G.[2], and and Fernández-Alvar, E.[2]

[1] Departamento de Física de la Tierra y Astrofísica, Universidad Complutense de Madrid, 28040 Madrid, Spain
[2] Université Côte d'Azur, Observatoire de la Côte d'Azur, CNRS, Laboratoire Lagrange, Bd de l'Observatoire, CS 34229, 06304 Nice cedex 4, France
[3] INAF – Osservatorio Astronomico di Trieste, Via G.B. Tiepolo 11, 34131 Trieste, Italy
[4] Dipartimento di Fisica, Sezione di Astronomia, Università di Trieste, Via G.B. Tiepolo 11, 34131 Trieste, Italy
[5] Sterrenkundig Observatorium, Ghent University, Krijgslaan 281 - S9, 9000 Gent, Belgium

Abstract

The [Mg/Fe] abundance ratios are a fundamental fossil signature in Galactic archaeology for tracing the chemical evolution of disc stellar populations. High-precision chemical abundances, accurate stellar ages, distances, and dynamical data, together with their direct comparison with theoretical models, are crucial to infer the Milky Way formation history. We derived new more precise [Mg/Fe] abundances from the AMBRE:HARPS dataset, and estimated ages and dynamical properties using *Gaia* DR2 data. The data are compared with detailed chemical evolution models for the Milky Way, exploring different formation scenarios for the Galactic disc (i.e. the delayed two-infall and the parallel models). Our data favour the rapid formation of an early disc that settled in the inner regions, followed by the accretion of external metal-poor gas. The bulk of the data are well reproduced by the parallel and two-infall scenarios, but both scenarios have problems in explaining the most metal-rich and metal-poor tails of the low-α stars, which can be explained in light of radial migration from the inner and outer disc regions, respectively.

1 Introduction

This proceeding is a brief summary of the main results already published in the works from [1] and [2], we refer the reader to them for further detailed information.

The formation of the Galactic disc is still not well understood and in particular the origin and existence of a thin–thick disc bimodality is a matter of debate. The thick disc is often

reported to be [α/Fe]-enhanced relative to the thin disc, suggesting distinct chemical evolution histories, where the thick disc stellar population could have been formed on a short timescale before the epoch of the thin disc formation. In particular, magnesium is often used as an α-elements tracer. In a previous analysis ([3]), we showed a significant improvement in the precision of [Mg/Fe] abundance estimates by carrying out an optimisation of the spectral normalisation procedure, in particular for the metal-rich population ([M/H] $>$ 0), showing a decreasing trend in the [Mg/Fe] abundance even at supersolar metallicites, partly solving the apparent discrepancies between the observed flat trend in the metal-rich disc (e.g. [4]), and the steeper slope predicted by chemical evolution models (e.g. [5]).

In this project, we use these new [Mg/Fe] abundance measurements in order to study their impact on the observed chemodynamical features, and therefore on the interpretation of the Galactic disc evolution.

2 Data & Models

On the observational side, we considered the AMBRE:HARPS stellar sample ($R \sim 115\,000$, described in [6]), that corresponds to a total of 1066 stars in the solar neighbourhood, compiled from the analysed samples of [3] and [1]. The stellar [Mg/Fe] abundances were derived by the spectrum synthesis algorithm GAUGUIN, following the described methodology in [3], where the spectral normalisation procedure was optimised for different stellar types with a significant improvement in precision. In addition, we estimated the orbital parameters with the *Gaia* DR2 astrometric positions and proper motions, and we also estimate the age for a subsample of main sequence turn-off (MSTO) stars using an isochrone fitting method (see [1] for details). Figure 1 illustrates the chemical distinction in the [Mg/Fe]-[M/H] plane for the stellar subsample with reliable age estimates, classifying the stars into high- and low-α population, commonly referred as the thick and the thin disc respectively.

On the theoretical side, we adopted two different chemical evolution scenarios to explain the chemical history of the solar annulus, assuming a 2 kpc ring centred at R = 8 kpc, also including prescriptions for stellar radial migration (see [2] for details):

1. Delayed two-infall model: MW forms by two sequential infall episodes. The first infall give rise to the high-α sequence, whereas the second (delayed and slower) infall forms the low-α stars. The second infall is delayed by 3.25 Gyr (see e.g. [5] [7]).

2. Parallel model ([8]): two separate infall episodes. Both evolve independently from different gas reservoirs, the infall episode forging high-α stars happens on shorter timescales than the one forming low-α ones.

In Figs 2 we show the predicted chemical evolution by the two proposed scenarios over the full observational dataset. Both models predict well the bulk of the stellar distribution in the [Mg/Fe] versus [M/H] plane. However, it can be seen that the two models do not explain the low-α, low-metallicity ([M/H] $\leq$ -0.6 dex) data or the high-metallicity tail (above [M/H] $\sim$ 0.2 dex) of the low-α sequence.

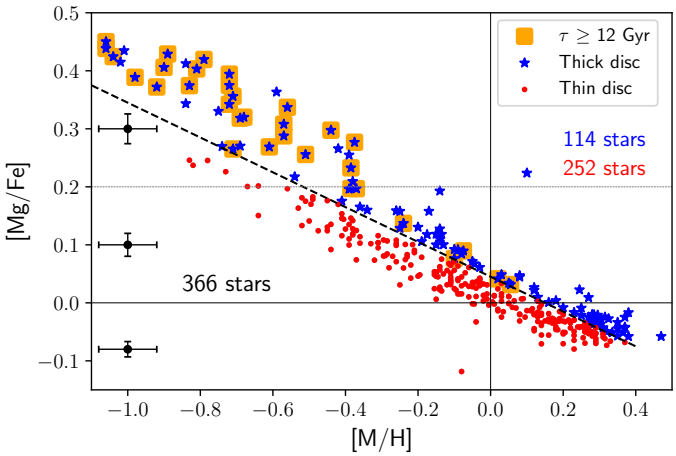

Figure 1: [Mg/Fe] vs. [M/H] for the stars with reliable age estimates. The stars with ages older than 12 Gyr are highlighted with orange squares. The black dashed line defines the thin(red circles)–thick(blue stars) disc chemical separation. The mean estimated errors are represented on the left-hand side for three different intervals in [Mg/Fe].

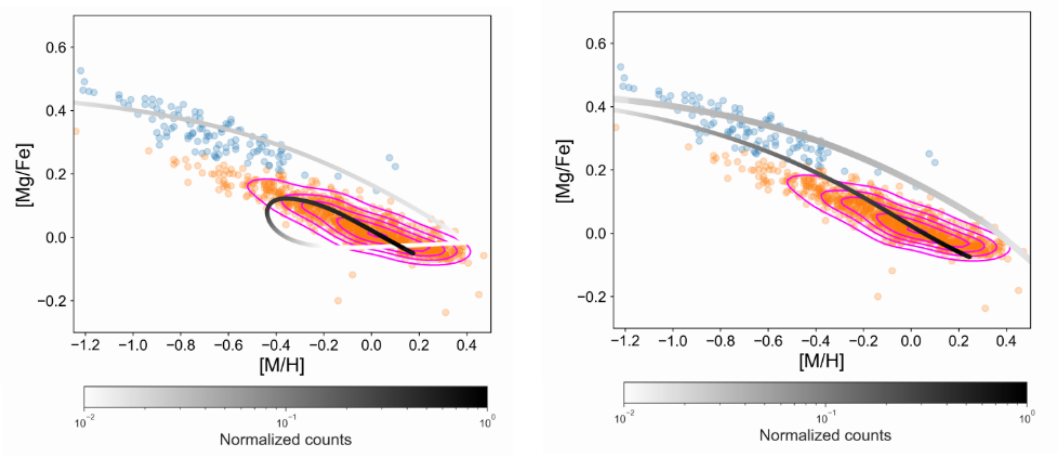

Figure 2: [Mg/Fe] versus [M/H] abundance diagram for the delayed two-infall (left panel) and the parallel (right panel) model scenarios of chemical evolution with [9] yields. The colour bar indicates the predicted stellar number counts. The light-blue points are the observed high-α stars, whereas the orange points are the observed low-α stars. The magenta contour lines enclose the observed density distribution of stars.

3 Temporal evolution in the [Mg/Fe]-[M/H] plane

We explored the distribution of [Mg/Fe] and [M/H] in the Galactic disc as a function of the Galactocentric position, and analysed the disc evolution with time.

Figure 3 illustrates the [Mg/Fe] abundance ratios relative to [M/H] for our MSTO stars,

in different age intervals and Galactic disc locations, assuming the guiding radius (R_g) as their true position in the Galaxy (top row: inner Galactic disc $R_g \leq 7.5$ kpc; bottom row: outer disc $R_g > 7.5$ kpc). We observe that the oldest stellar population ($\tau \geq 12$ Gyr) at every radius is located in what has been classically called the thick disc, that is, an α-enhanced population. During this early epoch, we observe rapid chemical enrichment, reaching solar metallicities. Interestingly, 11-12 Gyr ago, a second chemical sequence appears in the outer regions of the Galactic disc, populating the metal-poor low-[Mg/Fe] tail and starting at [M/H] $\sim$ -0.8 dex and [Mg/Fe] $\sim$ 0.2 dex. This corresponds to the population that has classically been referred to as the thin disc or low-α population, highlighted in the figure by red points. The average R_g of this second chemical sequence seems to be significantly larger than the Galactic disc extension at that time ($R_g < 8.5$ kpc), reaching the outer parts up to $R_g \sim 11$ kpc. Furthermore, those stars are shown to be significantly more metal-poor ([M/H] $\leq$ -0.4 dex) with respect to the coexisting stellar population in the inner parts of the disc (top row). They also show lower [Mg/Fe] abundances than the older disc population in the outer parts (lower left panel), although presenting a similar metallicity distribution. This implies a chemical discontinuity in the disc around 11 Gyr ago, suggesting that the new sequence might have followed a different chemical evolution pathway from that followed by the previously formed component, possibly triggered by accretion of metal-poor external gas.

During the last 10 Gyr evolution (see [1]), we observe that the Galactic disc seems to have experienced a slower and more continuous chemical evolution towards more metal-rich and lower [Mg/Fe] regimes, without any remarkable star formation episode.

We performed a direct comparison with models to draw a more robust interpretation of our observational results:

Impact of inner and outer disc on the solar neighbourhood

The difficulties encountered by both the chemical evolution scenarios in predicting low-α, low metallicity and metal-rich stars (see Fig. 2) point towards a context where these stars were born at different Galactic locations from the solar vicinity. In this context, we did not consider the parallel scenario but rather the one-infall model that traces the formation of low-α sequence only.

In Fig. 4, we show the results of two-infall and one-infall models for outer (R_g >9 kpc) and inner (R_g <7 kpc) regions of the disc.

First, reproducing the outer Galactic regions (left-column panels), we need to adopt larger proportion of pristine gas during the second infall episode, reaching lower metallicities, to recover a good agreement with the two-infall model (top-left panel). On the other hand, the one-infall model for outer radii (bottom-left panel) naturally reproduce the tail of the low-α abundance trend for most of the data with large R_g (yellow crosses).

Secondly, regarding the inner parts of the Galaxy (right-column panels), the chemical tracks obtained with the two-infall model for inner radii (top-right panel) better reproduces the bulk of the metal-rich stars when a pre-enrichment (e.g. formation of the thick disc, Galactic halo, Galactic bar, previous merger event) in the second gas accretion episode is

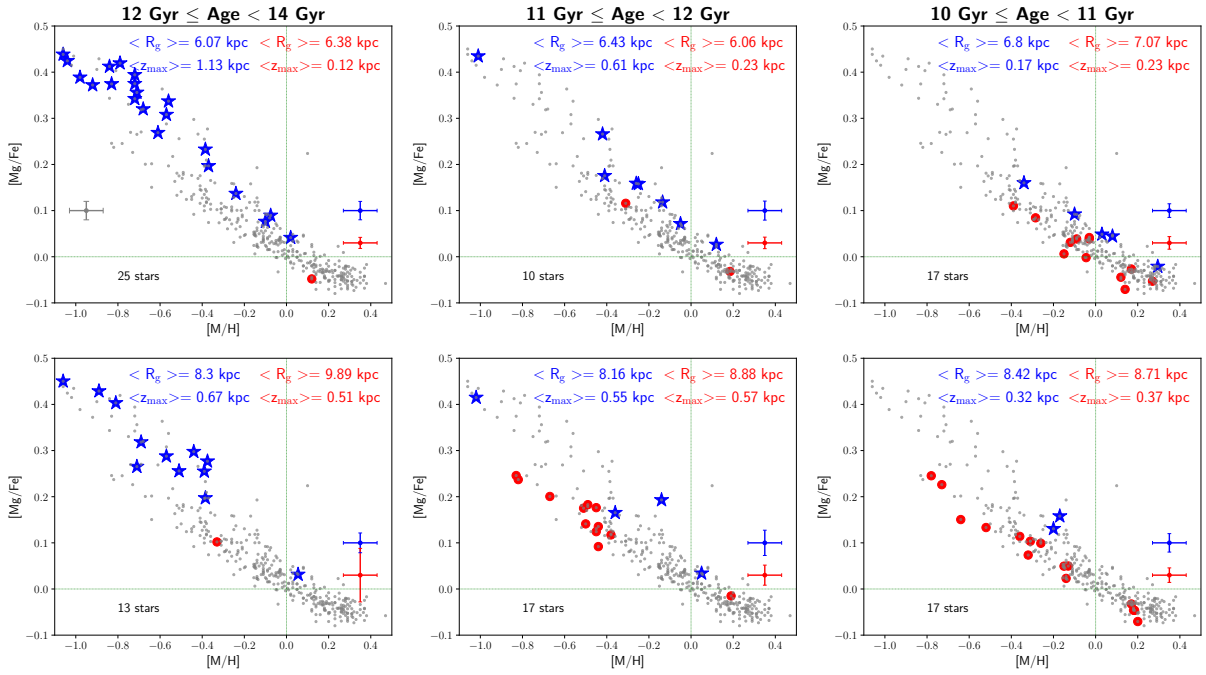

Figure 3: Distribution of the selected sample in the ([M/H], [Mg/Fe]) plane at different ages and locations in the Galaxy (R_g). Two chemical sequences appear for ages younger than $\sim$ 11-12 Gyr, corresponding to the classical thick (blue stars) and thin (red circles) disc components. Each panel corresponds to a bin in the (age, R_g) space, dividing the Galactic disc into two regions: inner ($R_g \leq 7.5$ kpc; top row) and outer ($R_g > 7.5$ kpc; bottom row). The blue and red crosses in the bottom-right corner of each panel represent the mean estimated errors in [Mg/Fe] and [M/H] for the thick and thin disc population, respectively, at that particular radius and time. The average R_g and z_{max} for each population are given at the top of each panel. The whole MSTO sample is shown by the dotted grey points.

considered, enabling a larger rise in the [α/Fe] abundances. Contrary, we note that the one-infall model (bottom-right panel) has similar problems to the two-infall model without infall pre-enrichment, predicting lower [Mg/Fe] abundances for a given metallicity.

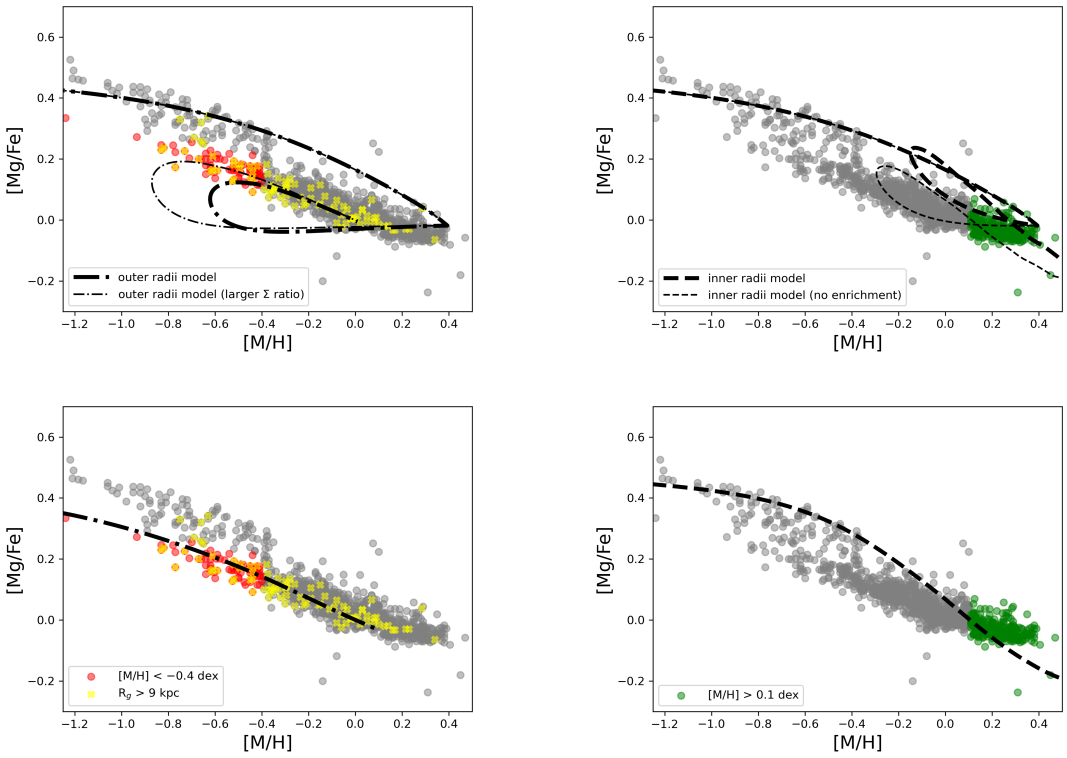

Figure 4: Mg/Fe] versus [M/H] abundance diagram for the delayed two-infall (upper panels) and the one-infall (lower panels) models for outer (R =12 kpc, dash-dotted lines, left panels) and inner Galactocentric radii (R =4 kpc, dashed lines, right panels). The red points are the observed low-α, low metallicity stars ([M/H]<-0.4 dex), whereas the yellow crosses indicate the stars with guiding radius (R_g) larger than 9 kpc and the green points indicate the observed stars with [M/H]>0.1 dex.

References

[1] Santos-Peral, P., Recio-Blanco, A., Kordopatis, G., Fernández-Alvar, E., & de Laverny, P. 2021, A&A, 653, A85

[2] Palla, M., Santos-Peral, P., Recio-Blanco, A., & Matteucci, F. 2022, A&A, 663, A125

[3] Santos-Peral, P., Recio-Blanco, A., de Laverny, P., Fernández-Alvar, E., & Ordenovic, C. 2020, A&A, 639, A140

[4] Hayden, M. R., Recio-Blanco, A., de Laverny, P., Mikolaitis, Š., & Worley, C. C. 2017, A&A, 608, L1

[5] Palla, M., Matteucci, F., Calura, F., & Longo, F. 2020b, ApJ, 889, 4

[6] De Pascale, M., Worley, C. C., de Laverny, P., et al. 2014, A&A, 570, A68

[7] Spitoni, E., Verma, K., Silva Aguirre, V., et al. 2021, A&A, 647, A73

[8] Grisoni, V., Spitoni, E., Matteucci, F., et al. 2017, MNRAS, 472, 3637

[9] François, P., Matteucci, F., Cayrel, R., et al. 2004, A&A, 421, 613

Highlights of Spanish Astrophysics XI, Proceedings of the XV Scientific Meeting of the Spanish Astronomical Society held on September 4–9, 2022, in La Laguna, Spain. M. Manteiga, L. Bellot, P. Benavidez, A. de Lorenzo-Cáceres, M. A. Fuente, M. J. Martínez, M. Vázquez- Acosta, C. Dafonte (eds.), 2023

Linking the dust and chemical evolution in Taurus and Perseus: new collisional rates for HCN, HNC, and their C, N, and H isotopologues.

Navarro-Almaida, D.[1], T. Bop, C.[2], Lique, F.[2], Esplugues, G.[3], Rodriguez-Baras, M.[3], Kramer, C.[4], E. Romero, C.[5], Fuente, A.[3], Caselli, P.[6], Riviére-Marichalar, P.[3], and Mroczkowski, T.[7]

[1] Département d'Astrophysique (DAp), CEA, Orme des Merisiers, 91191 Gif sur Yvette, Paris-Saclay, France
[2] University Rennes, CNRS, Institut de Physique de Rennes (IPR) - UMR 6251, 35000 Rennes, France
[3] Observatorio Astronómico Nacional (OAN), Alfonso XII, 3, 28014, Madrid, Spain
[4] Institut de Radioastronomie Millimétrique (IRAM), 300 Rue de la Piscine, 38406 Saint Martin d'Hères, France
[5] Center for Astrophysics, Harvard and Smithsonian, 60 Garden Street, Cambridge, MA 02143, USA
[6] Centre for Astrochemical Studies, Max Planck Institute for Extraterrestrial Physics, Giessenbachstrasse 1, 85748 Garching, Germany
[7] European Southern Observatory (ESO), Karl-Schwarzschild-Strasse 2, D-85741 Garching, Germany

Abstract

Despite their use as molecular probes and chemical clocks, the collisional rates of some of the C, N, and H isotopologues of HCN and HNC were, until now, absent. Here, we provide new collisional coefficients for these molecules and perform an up-to-date gas and dust chemical characterization of two different star-forming regions, TMC 1-C and NGC 1333-C7. With millimeter observations we derived their column densities, the C and N isotopic ratios, the isomeric ratios, and the deuterium fraction. Continuum data at 3 mm and 850 μm allowed us to compute the emissivity spectral index and look for grain growth, an evolutionary tracer. We found that gas temperature, deuterium fraction, and spectral index are complementary evolutionary tracers.

1 Introduction

The two isomers of the H-C-N system, hydrogen cyanide (HCN) and hydrogen isocyanide (HNC), are ubiquitous in the interstellar medium (ISM) and have been used to study its

physical and chemical properties [1, 2]. However, notorious cases show that the HCN/HNC chemistry is not fully understood yet (see, e.g., [3]).

Understanding isotopic abundance ratios is a major goal in modern astrochemistry. Rarer isotopologues are often used to determine physical conditions and as a proxy of the most abundant isotopologues as they do not usually suffer from opacity problems. A great limitation of this approach is the absence of collisional coefficients for the rarer isotopologues, forcing the assumption of isotopic ratios and leading to uncertainties [4]. The environment plays a crucial role in isotopic fractionation. Indeed, the abundance of molecules with deuterium is enhanced in the low-temperature gas prevailing in dense cores, becoming a diagnostic tool to determine the evolutionary stage of dense cores [5]. However, dating using deuterated molecules is limited by the absence of collisional rates for some of these species. Aiming to a better understanding of the chemistry and evolution of star-forming regions, we present collisional coefficients for the C, N, and H isotopologues of HCN and HNC.

Chemistry is not the only tool used to study the evolution of stellar objects, it can also be inferred by dust emission. In dense regions, grains are covered by icy mantles that make grains sticky, favoring grain coagulation, producing a different dust size distribution, and changing dust emissivity [6]. This change in dust emissivity is measured through the dust emissivity spectral index. In this work, we combine spectroscopic observations, dust continuum emission, and new collisional coefficients for the C, N, and H isotopologues of HCN and HNC to explore the chemical and physical evolution of the pre-stellar and protostellar envelopes during the first stages of the star formation process.

2 Collisional coefficients

Rate coefficients induced by collision with H_2 of the isotopologues of HCN and HNC, namely DCN, D^{13}CN, H^{13}CN, HC^{15}N, DNC, DN^{13}C, HN^{13}C and H^{15}NC, are missing in the literature. Using the MOLSCAT computer code [7], we calculated state-to-state inelastic cross sections of these molecules induced by collision with p-H_2. Variations of up to 50% in collisional rates have been found, having an impact of up to 30% in the brightness temperatures estimated using RADEX [8]. These new coefficients would therefore introduce an increase up to $\sim 30\%$ in the molecular hydrogen number density derived using these molecules.

3 Case study: TMC 1-C and NGC 1333

In this section we assess the impact of these new collisional coefficients in astrochemical modeling. We used the emission spectra of the $J = 1 \rightarrow 0$ rotational transitions of HCN, HNC, and their ^{13}C, ^{15}N, and D isotopologues towards positions in TMC 1-C and NGC 1333-C7 (Figure 1 and Table 1), observed with the Yebes 40m telescope.

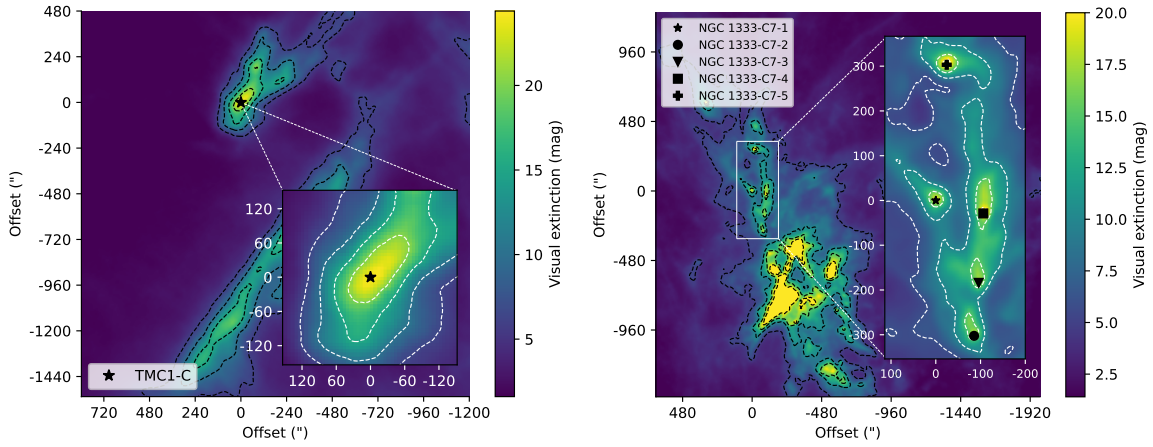

Figure 1: Visual extinction map of TMC 1-C (left) and NGC 1333-C7 (right)

Table 1: Target positions, spectral classes, and radii.

Source	RA (2000)	Dec (2000)	Class
TMC 1-C	04:41:37.58	26:00:31.10	Starless core
NGC 1333-C7-1	03:29:25.57	31:28:14.83	Class 0
NGC 1333-C7-2	03:29:19.05	31:23:14.45	Class I
NGC 1333-C7-3	03:29:18.29	31:25:08.34	Starless core[1]
NGC 1333-C7-4	03:29:17.38	31:27:46.09	Class 0
NGC 1333-C7-5	03:29:23.95	31:33:18.15	Class 0

3.1 Molecular column densities

From the line emission we derived the column densities of the species using the new collisional coefficients and the RADEX [8] radiative transfer code. In all positions belonging to NGC 1333-C7, the gas temperature is assumed to be $\sim$ 15 K, similar to the dust temperature derived from the *Herschel* space telescope maps of [9]. For TMC 1-C, we adopted $T_{\rm kin} = 8$ K following the calculations of [10, 5]. The density was assumed to be $n_{\rm H} = 4 \times 10^5$ cm^{-3}, a reasonable value for our sample [5, 11]. Our collisional rates do not consider hyperfine splitting, so in the case this splitting is present, the column density was obtained reproducing the integrated flux of the weakest hyperfine component observed. Then, the total column density is scaled using the relative intensities of the hyperfine components from the CDMS catalogue.

[1]NGC1333-C7-3 class is uncertain as it was classified as starless core by default since it did not fit the criteria of any other class.

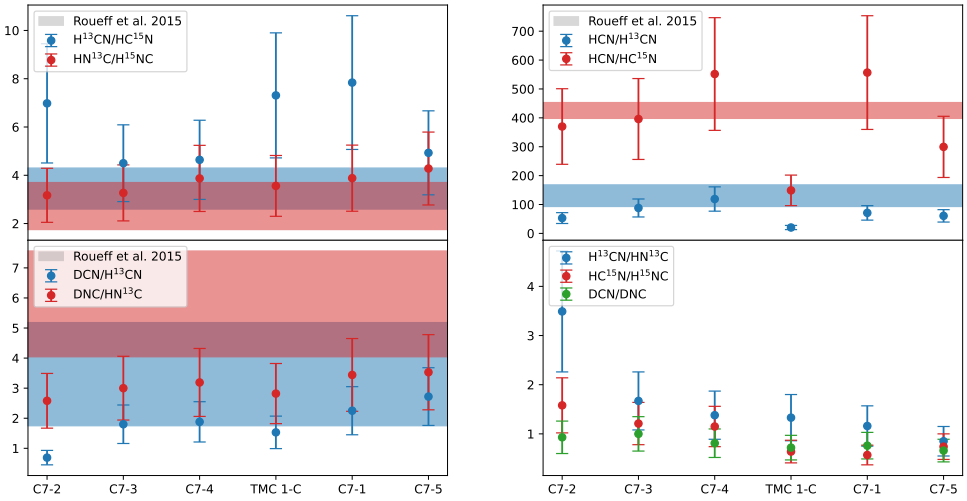

Figure 2: Blue, red, and green dots represent the different observed molecular ratios across the positions analyzed in this paper. The horizontal bands span from the minimum to the maximum values for the ratios obtained in the models of [4]. The sources are ordered by decreasing dust temperature.

3.2 Isotopic and isomeric ratios

Figure 2 shows the resulting column density ratios. We found a differentiated behavior between the two isomers. The isotopic ratios involving HNC, the $HN^{13}C/H^{15}NC$ and $DNC/HN^{13}C$ present uniform values across the sample. However, we detected variations in those of HCN, in particular $DCN/H^{13}CN$, $H^{13}CN/HN^{13}C$, and $HC^{15}N/H^{15}NC$ ratios show systematic changes with core evolution. The $H^{13}CN/HN^{13}C$ ratio we computed across our sample shows a trend that can be interpreted as a progressive increase in the average gas temperature from the coldest core starless cores NGC1333-C7-5 and TMC 1-C to the Class I source NGC1333-C7-2 [2]. This interpretation is consistent with the decreasing deuterium fraction $DCN/H^{13}CN$, as deuteration in the gas phase is less efficient in warmer gas. The $H^{13}CN/HN^{13}C$ ratio therefore becomes an evolutionary tracer of our sample, from the colder, less evolved members, to the warmer and more evolved members.

3.3 Continuum emission, grain growth, and evolution

The freeze out of molecules during the evolution of prestellar cores and ice growth are linked to grain coagulation, changing the emission properties of the grains, measured by the dust emissivity spectral index β. Here we examine the behavior of β using 3 mm MUSTANG-2 images and Herschel data at 850 μm. Assuming a modified blackbody model:

$$\beta_{0.85mm-3mm} = \frac{\log\left(\tau_{3\mathrm{mm}}/\tau_{0.85\mathrm{mm}}\right)}{\log\left(\nu_{3\mathrm{mm}}/\nu_{0.85\mathrm{mm}}\right)}, \qquad I_\nu = B_\nu(T_d)\tau_\nu, \tag{1}$$

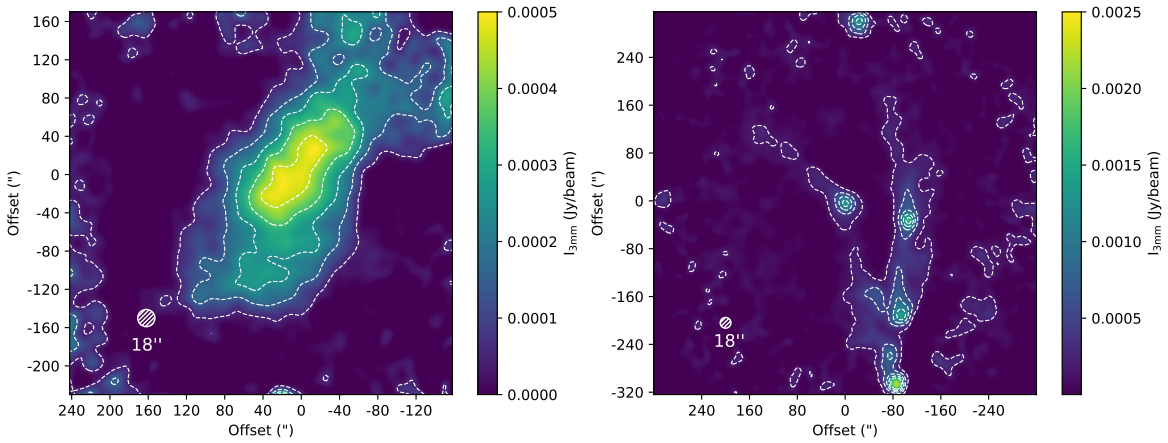

Figure 3: *Left panel:* Flux at 3 mm in the TMC 1-C prestellar core. *Right panel:* Flux at 3 mm in the NGC 1333-C7 sector.

and combining the information of the extinction maps in Figure 1, the dust temperature data [9], and the 3 mm continuum flux maps in Figure 3, we obtain the dust optical depth at 850 μm and 3 mm, and the dust emissivity spectral index $\beta_{0.85mm-3mm}$ (see Table 2). Our results show that the Class I object NGC1333-C7-2 presents the lower spectral index, $\beta_{0.85mm-3mm} \sim 1.1 - 1.3$, consistent with the presence of large grains in its protostellar disk. The spectral index of the Class 0 members of the sample is found to be higher, in the range $1.6 - 1.7$ and, finally, of around ~ 2 for the prestellar core TMC 1-C. We conclude that the value of β at millimeter wavelengths is useful to discern starless cores and Class 0 objects from Class I protostars, pointing to the existence of grain growth in the Class I protostellar disks. This is coherent with the chemical information obtained from the HCN and HNC molecules about temperature and deuterium fraction, as more evolved sources are warmer, exhibit less deuterium fractionation, and show lower spectral indexes, a sign of grain growth (Figure 4).

4 Summary and conclusions

We performed a chemical study of two different star-forming regions with updated collisional rates to investigate their chemical and evolutionary characteristics:

- We presented new collisional coefficients of HCN, HNC, and their C, N, and H isotopologues. We computed the $^{13}C/^{12}C$ and $^{15}N/^{14}N$ isotopic ratios, deuterium fractions, and isomeric ratios, showing good agreement with current chemical models [4]. The ratios between the two isomers show different variability across our sample, suggesting a different origin of their emission. The $H^{13}CN/HN^{13}C$ ratio is found to be a proxy of the temperature. The deuterium fraction of HCN is an evolutionary tracer past the prestellar phase since it decreases as heating from the nascent star increases the gas and dust temperature.

Table 2: Continuum 3 mm flux, optical depth at 850 μm and 3 mm, and the spectral index.

Position	$\tau_{3\mathrm{mm}} \times 10^4$ (18″)	$\tau_{850\mu\mathrm{m}} \times 10^3$ (18″)	$\beta_{0.85mm-3mm}$ (18″)
TMC 1-C	0.82 ± 0.02	1.43 ± 0.14	2.09 ± 0.08
NGC1333-C7-1	1.35 ± 0.04	1.26 ± 0.13	1.63 ± 0.09
NGC1333-C7-2	1.85 ± 0.03	1.15 ± 0.12	1.34 ± 0.08
NGC1333-C7-3	1.26 ± 0.04	1.09 ± 0.11	1.56 ± 0.09
NGC1333-C7-4	1.65 ± 0.04	1.64 ± 0.16	1.68 ± 0.09
NGC1333-C7-5	1.54 ± 0.05	1.57 ± 0.16	1.70 ± 0.09

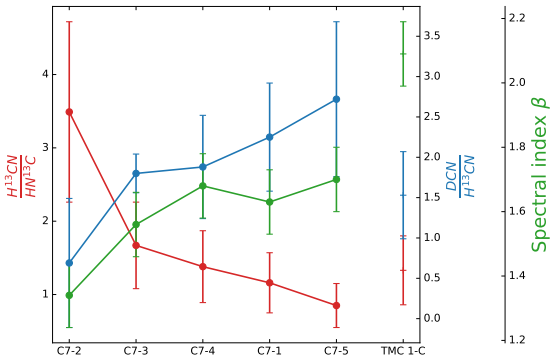

Figure 4: Values of the $H^{13}CN/HN^{13}C$ (red) and $DCN/H^{13}CN$ (blue) ratios, and the spectral index (green) across the sources of our sample.

- We analyzed the continuum emission of our sample to estimate the spectral index. The dust spectral index is found to be $\beta_{0.85mm-3mm} = 1.34$ for the most evolved member of our sample, and rises up to $\beta_{0.85mm-3mm} = 2.09$ in TMC 1-C, a prestellar core. We find a tentative correlation between the spectral index and the HCN deuterium fraction. This is consistent with the presence of grain growth in evolved objects past the prestellar phase as the dust and gas temperatures increase, thus reducing the HCN deuterium fraction.

References

[1] Aalto, S., Garcia-Burillo, S., Muller, S., et al. 2012, A&A, 537, A44

[2] Hacar, A., Bosman, A. D., & van Dishoeck, E. F. 2020, A&A, 635, A4

[3] Hily-Blant, P., Walmsley, M., Pineau Des Forêts, G., & Flower, D. 2010, A&A, 513, A41

[4] Roueff, E., Loison, J. C., & Hickson, K.M. 2015, A&A, 576, A99

[5] Navarro-Almaida, D., Fuente, A., Majumdar, L., et al. 2021, A&A, 653, A15

[6] Ormel, C. W., Paszun, D., Dominik, C., & Tielens, A. G. G. M. 2009, A&A, 502, 845

[7] Hutson, J. & Green, S. 1994, Collaborative computational project

[8] van der Tak, F. F. S., Black, J. H., Schöier, F. L., Jansen, D. J., & van Dishoeck, E. F. 2007, A&A, 468, 627

[9] Zari, E., Lombardi, M., Alves, J., Lada, C. J., & Bouy, H. 2016, A&A, 587, A106

[10] Navarro-Almaida, D., Le Gal, R., Fuente, A., et al. 2020, A&A, 637, A39

[11] Rodríguez-Baras, M., Fuente, A., Riviére-Marichalar, P., et al. 2021, A&A, 648, A120

[12] Milam, S.N., Savage, C., Brewster, M.A., Ziurys, L.M.,& Wyckoff, S. 2005, ApJ, 634, 1126

[13] Colzi, L., Sipilä, O., Roueff, E., et al. 2013, A&A, 560, A3

[14] Caselli, P., Walmsley, C. M., Tafalla, M., Dore, L., & Myers, P. C. 1999, ApJ, 523, L165

[15] Tafalla, M., Santiago-García, J., Myers, P. C., et al. 2006, A&A, 455, 577

Highlights of Spanish Astrophysics XI, Proceedings of the XV Scientific Meeting of the Spanish Astronomical Society held on September 4–9, 2022, in La Laguna, Spain. M. Manteiga, L. Bellot, P. Benavidez, A. de Lorenzo-Cáceres, M. A. Fuente, M. J. Martínez, M. Vázquez- Acosta, C. Dafonte (eds.), 2023

Monitoring the evolution of maser emission from water fountain stars.

Gómez, J.F.[1], Imai, H.[2,3], Uscanga, L.[4], Suárez, O.[5], Cala, R.[1], Miranda, L.F.[1], and Tafoya, D.[6], and Orosz, G.[7]

[1] Instituto de Astrofísica de Andalucía, CSIC, Glorieta de la Astronomía s/n, 18008 Granada, Spain
[2] Amanogawa Galaxy Astronomy Research Center, Graduate School of Science and Engineering, Kagoshima University, 1-21-35 Korimoto, Kagoshima, Kagoshima 890-0065, Japan
[3] Center for General Education, Institute for Comprehensive Education, Kagoshima University, 1-21-30 Korimoto, Kagoshima, Kagoshima 890-0065, Japan
[4] Departamento de Astronomía, Universidad de Guanajuato, A.P. 144, 36000 Guanajuato, Gto., Mexico
[5] Laboratore Lagrange, Observatoire de la Côte d'Azur, Université Côte d'Azur, CNRS, Bd de l'Observatoire, CEDEX 4, F-06304 Nice, France
[6] Department of Space, Earth and Environment, Chalmers University of Technology, Onsala Space Observatory, 439 92 Onsala, Sweden
[7] Joint Institute for VLBI ERIC, Oude Hoogeveensedijk 4, 7991 PD Dwingeloo, The Netherlands

Abstract

Water Fountains (WFs) are objects in a transitional phase from the asymptotic giant branch to early planetary nebulae (PNe) of stars $M < 8\,M_{\odot}$, which show high-velocity collimated jets traced by water masers. Here we present some results from an ongoing monitoring of maser emission 14 WFs, carried out with the Nobeyama and Effelsberg radio telescopes, as well as with the Australia Telescope Compact Array. The water masers trace very different kinematical and spatial distribution depending on the source, with accelerating, decelerating, or kinematically stable mass-loss. In the case of the nascent PN IRAS 15103-5754, the masers have quickly evolved in less than 10 years, from tracing a collimated jet to a circumstellar toroid. These different patterns might be related to the particular evolutionary stage of each source, or to the properties of central binary stars. We expect that the analysis of our full monitoring data will provide important clues to explain the diversity of patterns in WFs.

1 Introduction

During the final stages of evolution of low and intermediate-mass stars ($M < 8\,M_{\odot}$), there occur dramatic changes in morphology, so that the spherical symmetry that is present during most of the stellar lifetime turns into the plethora of shapes seen in planetary nebulae (PNe). It is now widely accepted that the non-spherical shapes of PNe are the result of interactions in a binary/multiple stellar system [3].

This contribution focus on a particular category of evolved objects, which host water maser emission with high velocities, tracing winds that reach velocities > 250 km s^{-1} [12], significantly larger than the expansion velocities of circumstellar envelopes in Asymptotic Giant Branch (AGB) stars, 10–30 km s^{-1} [4, 14]. Given these characteristics, these objects are collectively called "water fountains" (WF). Radio interferometric observations of masers in WFs reveal that they trace collimated jets with kinematic ages < 100 yr. This means that these events are short-lived. It is still to be determined whether WF events are episodic and could happen during relatively long periods of times (e.g., the whole post-AGB phase), or they are restricted to a particular limited phase of the evolution of these stars. Fortunately, given that the kinematic ages of WF jets are comparable to the human lifetimes, significant changes are expected to happen over just a few years. Therefore, some questions can be solved by carrying out a long-term monitoring of their water maser emission.

2 Monitoring projects of the maser emission from water fountains

We are currently monitoring the maser emission of 14 WFs, collecting data from different observational projects. In project FLASHING (Finest Legacy Acquisitions of SiO- and H_2O-maser Ignitions by Nobeyama Generation) we are using the Nobeyama 45 m antenna to simultaneously observe SiO and H_2O masers in WFs with declination $> -32°$ [10]. We have also used the Effelsberg 100 m radio telescope to specifically monitor the water masers in IRAS 18113-2503 during three years. These single-dish data allow us to track velocity variations in the maser spectra, including acceleration/deceleration of the ejections, or the appearance of new mass-loss events.

These observations have been complemented with interferometer monitoring observations of maser emission with the Australia Telescope Compact Array (ATCA), to obtain information on possible variations of the spatial distribution of the maser emission. In the particular case of IRAS 15103-5754, we have collected interferometer data from 2011 to 2022.

3 Preliminary results

FLASHING has provided some interesting results that have already been published elsewhere, such as the detection of SiO masers in IRAS 16552-3050 [1] (the second WF known to have this type of emission after W43A [9]), or the detection of new high-velocity ejections in IRAS 18286-0959 [10]. We have also confirmed IRAS 18043-2116 as the WF with the largest velocity

spread in its water masers to date [15]. The data analysis of the whole data set does not show a consistent behavior in the kinematic and morphological variations of masers in WFs, but a variety of patterns, whose origin is still to be determined.

An interesting case is that of W43A, the only WF that has been proposed to be still in the AGB phase [9]. The FLASHING spectra indicate that the water maser components are accelerating [8]. Since this water maser emission is found at the locations where the jet is shocking against the circumstellar envelope [13], this acceleration indicates that this shock is accelerating the gas entrained by the jet.

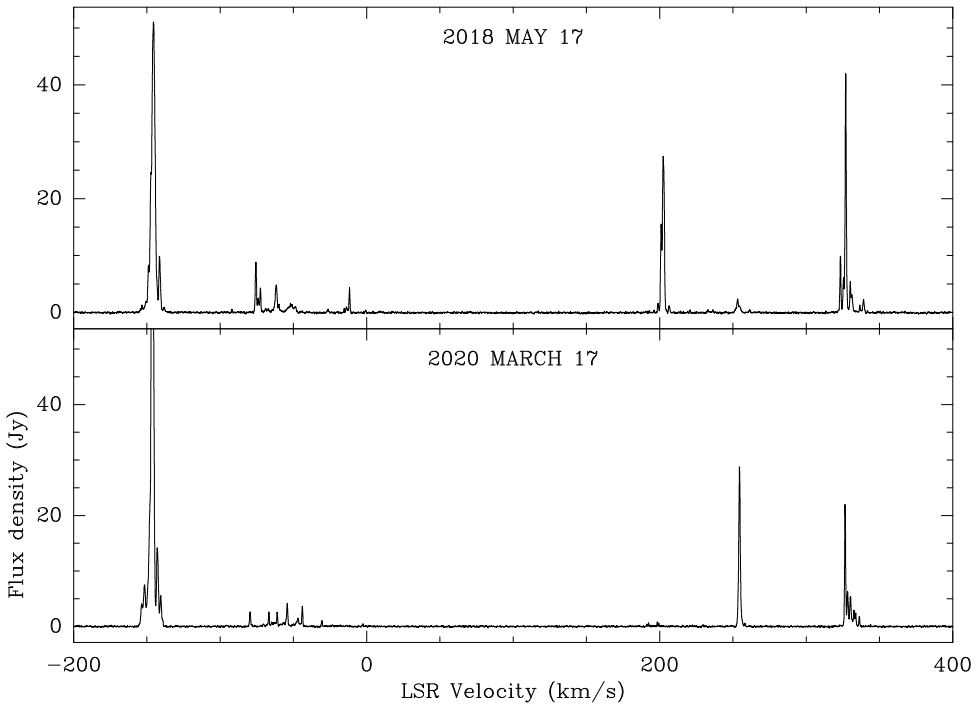

Figure 1: Water maser spectra of IRAS 18113-2503 taken on 2018 May 17 and 2020 March 17, with the Effelsberg 100m radio telescope.

The opposite kinematic trend (deceleration) was proposed for the post-AGB star IRAS 18113-2503 by [12] from high resolution water maser observations taken with the Very Long Baseline Array. These authors detected three nested bipolar ejections, with lower velocities for those farther away from the central source. This was interpreted as episodic ejections with similar initial velocities that were decelerated as they move along a dense circumstellar envelope. The estimated interval between these ejections (12 years) was linked to the period of a possible binary companion to the central star. The estimated deceleration of the water maser components under this model (2 km s^{-1} per month) should be easily seen in a single-dish monitoring. Moreover, a new ejection should already been produced, since the most recent one was already 12 years old by the time of the VLBA observations (epoch 2015). However, our monitoring with Effelsberg shows water maser spectra with relatively stable kinematics. In Fig. 1 we show two spectra taken almost two years apart. Apart from an

obvious flux variability, the velocities of the spectral components do not show any significant drift. This velocity stability is more clearly seen in Fig. 2, where we show the temporal variation of the velocities in the most redshifted components. A deceleration should have been seen as a drift to the left from bottom to top. The stable velocities suggest that the ejections are moving freely against a low-density medium, and their injection velocities increase with time.

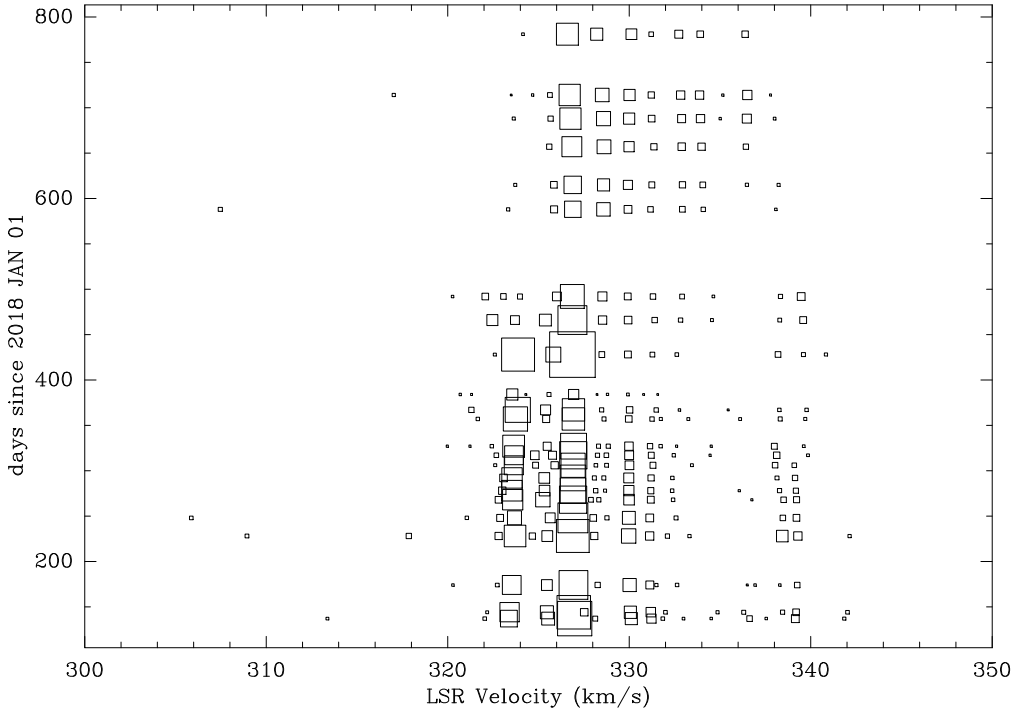

Figure 2: Temporal variation of the velocity of the most redshifted water maser components in IRAS 18113-2503. Each component is marked with a square, whose size is proportional to flux density

While maser deceleration has not been confirmed in IRAS 18113-2503, there is some hints that it could be occurring in IRAS 18286-0959 [10]. However, further data from FLASHING will be needed to confirm this.

The WF that seems to be more evolved is IRAS 15103-5754, which has been suggested to be a nascent PN [6, 7]. It is, in fact, the only known WF that has already started photoionization of its envelope. Our interferometric observations showed its water masers to be tracing a high velocity jet, also aligned with the infrared nebula, until 2014, but the position angle of the maser distribution significantly changed after that [7, 5], departing from the jet axis. More recent observations (March 2019, Fig. 3) shows that this source is no longer a WF, since all its water maser components are of low velocity (< 20 km s^{-1} from the systemic velocity), and their distribution is nearly perpendicular to the collimated jet, which was traced by the water masers in 2011 [7]. Actually, the maser distribution in 2019 in oriented in a similar direction as the toroid of molecular gas (traced by $C^{18}O$ and HCO^+) seen

with ALMA [6]. All this seems to indicate that physical conditions for maser pumping are rapidly evolving in this source, and water masers are changing from tracing a high-velocity jet, as seen in other AGB and post-AGB WFs, to a low-velocity toroid, as in the water masers observed in young PNe [2, 11].

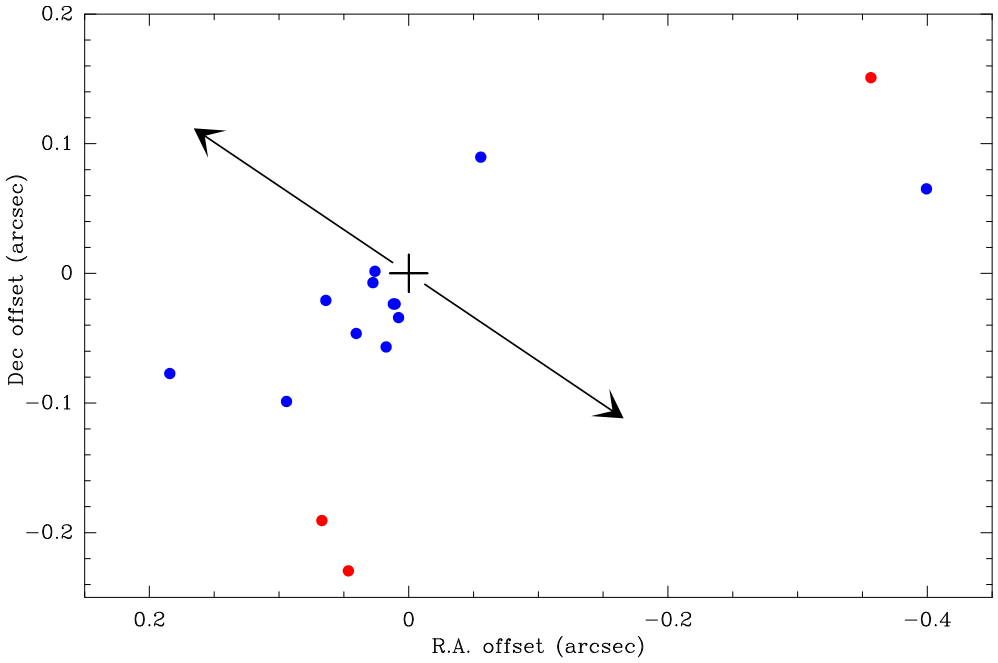

Figure 3: Distribution of water masers in IRAS 15103-5754, as observed with ATCA in March 2019. Blue and red filled circles mark the position of the spectral maser components that are blue- and redshifted with respect to the systemic velocity, respectively. The cross at offset [0,0] marks of the peak of radio continuum emission, coinciding with the location of the central star. The arrows show the direction of the jet, as traced by the water masers in 2011 [7].

4 Final remarks

Our monitoring shows very different patterns in the kinematics and spatial distribution of water masers in WFs. It is difficult at this point to explain the reason behind each particular pattern. It is tempting to think of the evolutionary stage of the source as the main explanation. In this framework, masers could be tracing accelerating gas in outflows during early stages (AGB), stable or decelerating outflowing gas in the post-AGB phase, and dramatically changing to trace toroids with low velocities as the star becomes a PN. Obviously the data presented here refer to only a few WF, and no solid evolutionary trend is possible at this point. Moreover, there are other possible parameters that could be key to explain the kinematical patters, such as the initial mass of the central star, or the mass and orbital period of a putative binary companion. The data from our ongoing monitoring of WFs could certainly

provide further clues on the behavior of masers in these objects.

Acknowledgments

Part of the data shown in this contribution were taken with the 100 m telescope of the MPIfR (Max-Planck-Institut für Radioastronomie) at Effelsberg, and with the Australia Telescope Compact Array, part of the Australia Telescope National Facility (grid.421683.a), which is funded by the Australian Government for operation as a National Facility managed by CSIRO. The research leading to these results has received funding from the European Union's Horizon 2020 research and innovation programme under grant agreement No 730562 [RadioNet]. JFG, RC, and LFM acknowledge financial support from grants PID2020-114461GB-I00 and CEX2021-001131-S, funded by MCIN/AEI /10.13039/501100011033. RC is also supported by the predoctoral grant PRE2018-085518, funded by MCIN/AEI/ 10.13039/501100011033 and by ESF Investing in your Future. LU acknowledges support from the University of Guanajuato (Mexico) grant ID CIIC 164/2022. This work is also partially supported by grant P20-00880, funded by the Economic Transformation, Industry, Knowledge and Universities Council of the Regional Government of Andalusia and the European Regional Development Fund from the European Union.

References

[1] Amada, K., Imai, H., Hamae, Y., et al. 2022, AJ, 163, 85

[2] de Gregorio-Monsalvo, I., Gómez, Y., Anglada, G., et al. 2004, ApJ, 601, 921

[3] García-Segura, G., Villaver, E., Langer, N., et al. 2014, ApJ, 783, 74

[4] Goldman, S. R., van Loon, J. T., Zijlstra, A. A., et al. 2017, MNRAS, 465, 403

[5] Gómez, J. F., Miranda, L. F., Uscanga, L., et al. 2018, in IAU Symp 336, Astrophysical Masers: Unlocking the Mysteries of the Universe, 377

[6] Gómez, J. F., Niccolini, G., Suárez, O., et al. 2018, MNRAS, 480, 4991

[7] Gómez, J. F., Suárez, O., Bendjoya, P., et al. 2015, ApJ, 799, 186

[8] Imai, H., Amada, K., Gómez, J. F., et al. 2022, in IAU Symp 370, Winds of stars and exoplanets, in press

[9] Imai, H., Obara, K., Diamond, P. J., et al. 2002, Nature, 417, 829

[10] Imai, H., Uno, Y., Maeyama, D., et al. 2020, PASJ, 72, 58

[11] Miranda, L. F., Gómez, Y., Anglada, G., et al. 2001, Nature, 414, 284

[12] Orosz, G., Gómez, J. F., Imai, H., et al. 2019, MNRAS, 482, L40

[13] Tafoya, D., Imai, H., Gómez, J. F., et al. 2020, ApJ, 890, L14

[14] te Lintel Hekkert, P., Caswell, J. L., Habing, H. J., et al. 1991, A&SS, 90, 327

[15] Uscanga, L., Imai, H., Gómez, J. F., et al. 2023, ApJ, submitted

Highlights of Spanish Astrophysics XI, Proceedings of the XV Scientific Meeting of the Spanish Astronomical Society held on September 4–9, 2022, in La Laguna, Spain. M. Manteiga, L. Bellot, P. Benavidez, A. de Lorenzo-Cáceres, M. A. Fuente, M. J. Martínez, M. Vázquez- Acosta, C. Dafonte (eds.), 2023

Post-red-giant-branch Planetary Nebulae.

Jones, D.[1,2], Hillwig, T.C.[3], and and Reindl, N.[4]

[1] Instituto de Astrofísica de Canarias, E-38205 La Laguna, Tenerife, Spain
[2] Departamento de Astrofísica, Universidad de La Laguna, E-38206 La Laguna, Tenerife, Spain
[3] Department of Physics and Astronomy, Valparaiso University, Valparaiso, IN 46383, USA
[4] Institute for Physics and Astronomy, University of Potsdam, Karl-Liebknecht-Str. 24/25, D-14476 Potsdam, Germany

Abstract

Common envelope events have been associated with the formation of a planetary nebulae since its proposition more than forty five years ago. However, until recently there have been doubts as to whether a common envelope while the donor is ascending the red giant branch, rather than the subsequent asymptotic red giant branch, would result in a planetary nebula. There is now strong theoretical and observational evidence to suggest that some planetary nebulae are, indeed, the products of common envelope phases which occurred while the nebular progenitor was on the red giant branch. The characterisation of these systems is challenging but has the potential to reveal much about the common envelope – a critical evolutionary phase in the formation of a plethora of interesting astrophysical phenomena.

1 Introduction

The common envelope (CE) phase is perhaps the most poorly understood aspect of close-binary evolution [9], in spite of its critical nature for the formation of a number of important phenomena – ranging from type Ia supernovae (irrespective of their formation channel) through to merging binary black holes recently observed in gravitational waves. A CE is formed following run-away unstable mass transfer in a close binary and ultimately leads to dramatic in-spiral of the binary, sometimes to merger, and the ejection of the donor's envelope (partial ejection in the case of a merger). Planetary nebulae (PNe) have long been seen as important probes of the CE, being identified by Paczyński (one of the first to outline the CE scenario) as the critical proof of its existence [16]. They are of particular interest because post-CE PNe are the immediate after-products of the CE (where the central stars have yet to have time to relax/evolve), and the only systems where the ejected envelope is still observable[1] (as the PN itself).

[1]The envelopes surrounding (Luminous) Red Novae represent the partial ejection of the evolution as the stars merged prior to complete ejection [14].

Until recently, it was thought that observable PNe would only be formed following CE events occurring when the donor was on the asymptotic giant branch (AGB), or close to the very tip of the red giant branch (RGB). Otherwise, the post-RGB post-CE remnants were expected to evolve too slowly or to too low a maximum temperature in order to ionise the ejected material before it dissipated into the surrounding interstellar medium [8]. Updated simulations by Hall et al. have since shown that most CE events on the RGB should, in fact, lead to observable PNe, revising the minimum mass limit for the post-RGB central star down to around 0.25 $M_{\odot}$ (c.f. the previous estimate of >0.4 $M_{\odot}$). This is particularly interesting in understanding the population of PNe as a whole given that at least 20% of all PNe are found to be the products of a CE phase [11] and the majority of post-CE binaries are post-RGB [17]. As such, a number of recent studies have focussed on the search for and characterisation of post-RGB central stars of PNe, and their implications for our understanding of the CE. In this proceedings, I present a review of this recent work and its future prospects.

2 Candidates

Roughly eight strong candidate post-RGB central stars have thus far been identified (see table 1). Although the central stars are orders of magnitude more luminous than their low-mass (M-type) companions, these systems are generally double-lined to the high levels of irradiation leading to the formation of spectroscopically detectable emission lines on the day face of the companions. Similarly, even when they are not eclipsing, the central star systems present strong photometric variability due to the differing projection of the irradiated face of the companion as a function of orbital phase. Here, we will discuss further the properties of each of these candidates as determined by detailed modelling of light and radial velocity curves, and/or through non-local thermal equilibrium (NLTE) modelling of the spectrum of the hot post-RGB component.

Table 1: Candidate post-RGB central stars of PNe

PN	RA	Dec	Period	Reference
Abell 46	18:31:18.3	+26:56:12.9	0.472 d	[1]
ESO 330-9	16:02:18.1	−41:26:49.5	0.296 d	[7]
HaTr 4	16:45:00.2	−51:12:21.1	1.738 d	[6]
HaTr 7	17:54:09.5	−60:49:57.7	0.322 d	[7]
HaWe 13	19:31:07.2	−03:42:31.5	–	[4, 15]
Hf 2-2	18:32:30.8	−28:43:20.0	0.399 d	[6]
Ou 5	21:14:20.0	+43:41:36.0	0.364 d	[13]
PN G283.7−05.1	09:58:32.3	−61:26:40.0	0.246 d	[12]

2.1 Abell 46

Simultaneous light and radial velocity curve modelling of the HW Vir-type central star of Abell 46 derives a mass of 0.51 ± 0.05 $M_\odot$ with a luminosity of $\log L \sim 2.2$ [1]. While the derived mass is a little on the high side for a post-RGB central star, the uncertainties do clearly encompass post-RGB masses (see figure 1). The low luminosity on the other hand is entirely consistent with a post-RGB remnant. Furthermore, the nebula has been found to have a very large abundance discrepancy factor, a property speculatively linked with post-RGB evolution [10]. Interestingly, the surface gravity and temperature implied by the light and radial velocity curve modelling are consistent with a post-RGB evolutionary track for a much lower mass than that derived by the modelling (see figure 2). An NLTE modelling of the central star spectrum could better constrain the effective temperature and surface gravity, placing stronger constraints on the possible post-RGB nature of Abell 46.

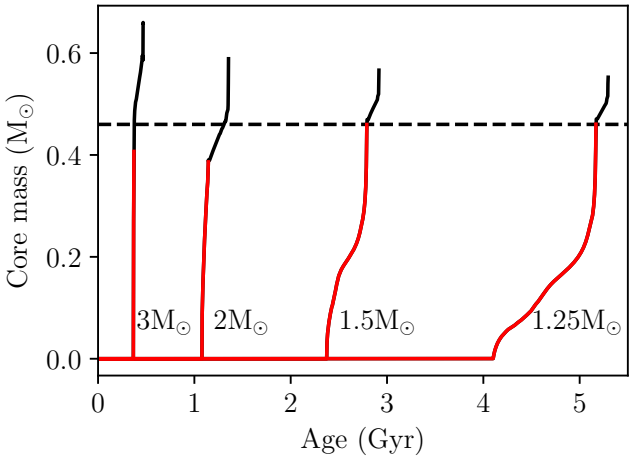

Figure 1: The core mass evolution of stars for a range of initial masses. The evolution to the tip of the RGB is shown in red with the subsequent AGB evolution in black. This demonstrates that the maximum mass for the post-RGB central star is approximately 0.46 $M_\odot$.

2.2 ESO 330-9

NLTE modelling of the spectrum of the central star of ESO 330-9 gives a surface gravity and effective temperature consistent with post-RGB evolutionary tracks (see figure 2). Furthermore, an excellent fit to the light and radial velocity curves of the binary could be found constraining the parameters of the primary to match those derived from the NLTE modelling [7]. The light curve itself is not eclipsing so this is perhaps not a stringent test of the system parameters but, nonetheless, ESO 330-9 is an excellent candidate post-RGB central star.

2.3 HaTr 4

Multi-band modelling of the eclipsing light curve of HaTr 4 results in a range of radii and temperatures consistent with post-RGB evolution [6]. Unfortunately, without radial velocities to properly constrain the mass or NLTE spectral modelling, it is difficult to assess the true nature of the central star.

2.4 HaTr 7

NLTE modelling of the spectrum of the central star of HaTr 7 gives parameters which lie between post-RGB and post-AGB tracks on the Kiel diagram (figure 2). Just as for ESO 330-9, an excellent fit to the non-eclipsing light curve and radial velocity curves could be found with parameters which match those predicted by the NLTE modelling [7].

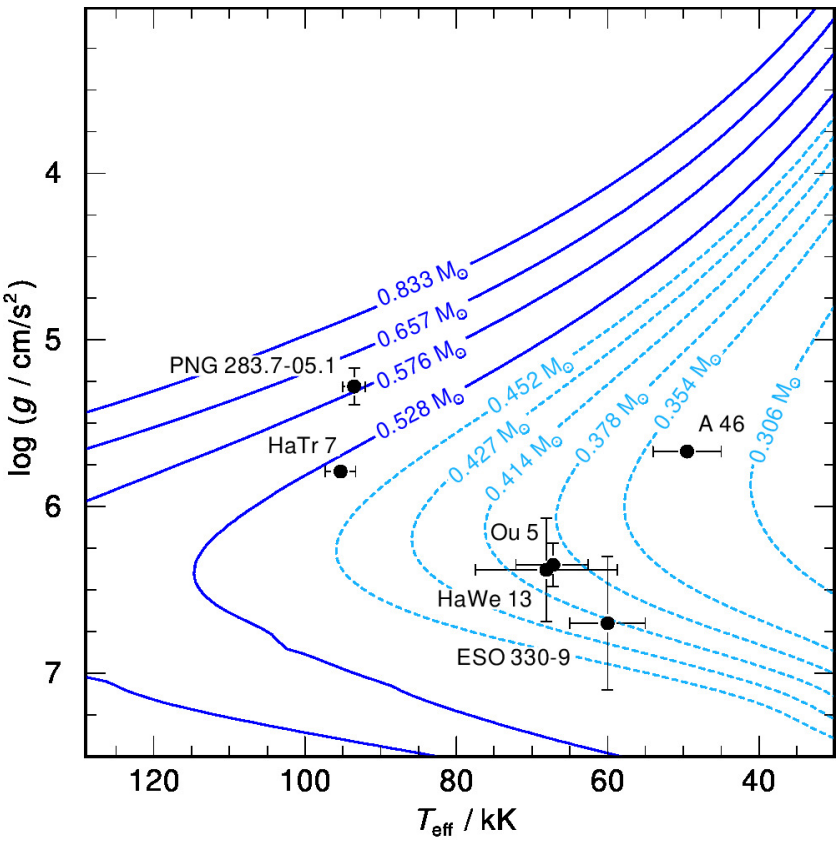

Figure 2: A Kiel diagram showing the properties of the five strongest candidate post-RGB stars for which effective temperatures and surface gravities have been measured (either spectroscopically or via combined light and radial velocity curve modelling. Figure reproduced from [13].

2.5 HaWe 13

The central star of HaWe 13 was identified as being under-luminous based on its gravity distance, while the nebula presents a morphology consistent with being the product of a CE phase [4]. However, no study has as yet definitively revealed the binary nature of the central star.

2.6 Hf 2-2

Just as for HaTr 4, modelling of multi-band non-eclipsing light curves indicates a low luminosity central star. A single spectrum of the central star was also taken allowing the mass ratio to also be constrained, indicating a low-mass primary [6].

2.7 Ou 5

Simultaneous light and radial velocity curve modelling of the eclipsing binary (HW Vir-type) at the heart of Ou 5 derives a mass of 0.50 ± 0.06 $M_\odot$ with a luminosity of $\log L \sim 2.1$ [13] – very similar to the parameters derived for Abell 46. Just as for Abell 46, the implied surface gravity and temperature lie on a post-RGB evolutionary track for a much lower mass than that derived from the light and radial velocity curve modelling (figure 2).

2.8 PN G283.7−05.1

Simultaneous light and radial velocity curve modelling of the eclipsing binary (HW Vir-type) in PN G283.7−05.1 leads to a definitively post-RGB mass determination of 0.34 ± 0.05 $M_\odot$, however the implied luminosity is extremely high for a post-RGB star – $\log L \sim 3.5$ [12]. Similarly, the surface gravity and temperature of the model central star reside in a distinctly post-AGB region of the Kiel diagram (figure 2). Nonetheless, comparison of the spectra, used to derive the radial velocities of the system, with NLTE models indicates that the surface gravity and temperature from the light and radial velocity curve modelling are indeed consistent with the observed spectroscopy.

3 Conclusions

Theoretical studies indicate that post-RGB masses greater than approximately 0.25 $M_\odot$ should lead to observable PNe [5]. Furthermore, comparison of the orbital period distribution of naked post-CE binaries (i.e. those that are now too old to reside inside a visible PNe) – a significant fraction of which are post-RGB [17] – and the orbital period distribution of post-CE central stars of PNe indicates that the two are consistent with being drawn from the same population [2]. As such, there is little reason to believe that the currently known sample of post-CE central stars (now roughly 100) contains a number of post-RGB systems. However, as yet, no definitively post-RGB central star of a PN has been identified, although a handful of excellent candidates have been found. If the strongest of the candidates are indeed

post-RGB then this reveals important information about the CE – in particular, given the apparent discrepancy between masses derived by from radial velocities and those based on their loci in the Kiel diagram (Abell 46, Ou 5, PN G283.7−05.1), that post-RGB evolutionary tracks may not be entirely representative of post-CE evolution. Any difference between post-CE models and reality can provide an invaluable window into the CE process. Additionally, RGB CEs have been speculatively linked to the extreme abundance discrepancies in observed in some PNe. As such, continued attempts to discover and characterise post-RGB central stars may be key not only in constraining the importance of this formation pathway among PNe but also in constraining the CE and its relation to other long-standing astrophysical questions.

Acknowledgments

D.J. acknowledges support from the Erasmus+ programme of the European Union under grant number 2020-1-CZ01-KA203-078200.

References

[1] Afşar, M., & Ibanoğlu, C., 2008, MNRAS, 391, 802

[2] Boffin, H.M.J., & Jones, D., 2019, The Importance of Binaries in the Formation and Evolution of Planetary Nebulae (Springer Nature)

[3] Brown, A.J., Jones, D., Boffin, H.M.J., & Van Winckel, H., 2019, MNRAS, 482, 4951

[4] Frew, D.J., Parker, Q.A., & Bojičić, I.S., 2016, MNRAS, 455, 1459

[5] Hall, P.D., Tout, C.A., Izzard, R.G, & Keller, D., 2013, MNRAS, 435, 2048

[6] Hillwig, T.C., Bond, H.E., Frew, D.J., et al., 2016, AJ, 152, 34

[7] Hillwig, T.C., Frew, D.J., Reindl, N., et al., 2017, AJ, 153, 24

[8] Iben, I. Jr., & Tutukov, A.V., 1993, ApJ, 418, 343

[9] Ivanova, N., Justham, S., Chen, X., et al., 2013, A&ARv, 21, 59

[10] Jones, D., Wesson, R., García-Rojas, J., et al., 2016, MNRAS, 455, 3263

[11] Jones, D., & Boffin, H.M.J., 2017, Nat. Astron., 1, 0117

[12] Jones, D., Boffin, H.M.J., Hibbert, J., et al., 2020, A&A, 642, 108

[13] Jones, D., Munday, J., Corradi, R.L.M., et al., 2022, MNRAS, 510, 3102

[14] Kamiński, T., Steffen, W., Bujarrabal, V., et al. 2021, A&A, 646, 1

[15] Napiwotzki, R., 1999, A&A, 350, 101

[16] Paczyński, B., 1976, IAUS, 73, 75

[17] Rebassa-Mansergas, A., Nebot Gómez-Morán, A., Schreiber, M.R., et al., 2011, MNRAS, 413, 1121

Highlights of Spanish Astrophysics XI, Proceedings of the XV Scientific Meeting of the Spanish Astronomical Society held on September 4–9, 2022, in La Laguna, Spain. M. Manteiga, L. Bellot, P. Benavidez, A. de Lorenzo-Cáceres, M. A. Fuente, M. J. Martínez, M. Vázquez- Acosta, C. Dafonte (eds.), 2023

Spectral evolution and calcium white dwarfs in J-PLUS.

López-Sanjuan, C.[1], Tremblay, P.-E.[2], Ederoclite, A.[1], Vázquez Ramió, H.[1], Varela, J.[1], Spinoso, D.[3,4], Carrasco, J. M.[5], Gentile Fusillo, N. P.[6], Gänsicke, B. T.[2], Marín-Franch, A.[1], Cenarro, A. J.[1], and J-PLUS collaboration

[1] Centro de Estudios de Física del Cosmos de Aragón (CEFCA), Unidad Asociada al CSIC, Plaza San Juan 1, 44001 Teruel, Spain; clsj@cefca.es
[2] Department of Physics, University of Warwick, Coventry, CV4 7AL, UK
[3] Department of Astronomy, Tsinghua University, Beijing 100084, China
[4] Centro de Estudios de Física del Cosmos de Aragón (CEFCA), Plaza San Juan 1, 44001 Teruel, Spain
[5] Institut de Ciències del Cosmos, Universitat de Barcelona (IEEC-UB), Martí i Franquès 1, 08028 Barcelona, Spain
[6] European Southern Observatory, Karl Schwarzschild Straße 2, Garching D-85748, Germany

Abstract

We complement the *Gaia*-based catalogue of white dwarfs with the optical photometry from the Javalambre Photometric Local Universe Survey (J-PLUS) DR2, covering 2 176 deg^2 with 12 passbands (*ugriz* + 7 medium bands). We define a common sample of 5 926 white dwarfs with $r < 19.5$ mag and derive their effective temperature ($T_{\rm eff}$), surface gravity, mass (M), and atmospheric composition (H- *versus* He-dominated). We also estimate the presence of polluting metals with the $J0395$ filter in J-PLUS, sensitive to the calcium H+K absorption. Using this information, we analyse the spectral evolution and the change in the fraction of metal-polluted white dwarfs with effective temperature. Finally, we expand our analysis to the eleven white dwarfs in the miniJPAS area, covered with the 56 medium-band passbands of 14 nm designed for the Javalambre Physics of the Accelerating Universe Astrophysical Survey (J-PAS).

1 Introduction

White dwarfs are the degenerate remnant of stars with masses lower than $8 - 10\ M_\odot$ and the endpoint of the stellar evolution for more than 97% of stars [16, 10]. This makes them an essential tool to disentangle the star formation history of the Milky Way, the late phases of stellar evolution and to understand the physics of condensed matter.

Decades of spectroscopic analysis revealed a diversity of white dwarf atmospheric compositions [30, 36], with sources presenting hydrogen lines (DA type), HeII lines (DO), HeI lines (DB), metal lines (DZ), and featureless spectra (DC) among others. White dwarfs can be selected from the general stellar population using their location in the Hertzsprung-Russell (H-R) diagram, typically ten magnitudes fainter than main sequence stars of the same effective temperature. Thanks to *Gaia* parallaxes and photometry, the efficient use of the H-R diagram to define the white dwarf population became feasible, with more than 350 000 candidates discovered so far [14]. It also permits the definition of high-confidence volume-limited white dwarf samples [15, 17, 18, 27, 12].

We complimented the most recent *Gaia*-based catalogue of white dwarfs [14] with the photometric information from the Javalambre Photometric Local Universe Survey (J-PLUS; [6]) second data release (DR2) to study the spectral evolution of white dwarfs and the presence of polluting metals. In addition, we explore the capabilities of the future Javalambre Physics of the Accelerating Universe Astrophysical Survey (J-PAS; [2]) with the miniJPAS [4] dataset.

2 J-PLUS and miniJPAS

Both J-PLUS and miniJPAS were carried out at the Observatorio Astrofísico de Javalambre (OAJ, [5]), located at the Pico del Buitre in the Sierra de Javalambre, Teruel (Spain). The data for J-PLUS were acquired using the 83 cm Javalambre Auxiliary Survey Telescope (JAST80) and T80Cam, a panoramic camera of 9.2k × 9.2k pixels that provides a 2 deg^2 field of view (FoV) with a pixel scale of 0.55 arcsec pix^{-1} [25]. The data for miniJPAS were acquired with the 2.5m Javalambre Survey Telescope (JST250) and the JPAS-Pathfinder (JPF) camera, which was the first scientific instrument installed at the JST250 before the arrival of the JPCam [26]. The JPF is a single 9200 × 9200 CCD located at the centre of the JST250 FoV with a scale of 0.23 arcsec pixel^{-1}, providing an effective FoV of 0.27 deg^2.

The J-PLUS photometric system is composed of five SDSS-like (*ugriz*) and seven medium band filters located in key stellar features, such as the 4 000 Å break (*J*0378, *J*0395, *J*0410, and *J*0430), the Mg *b* triplet (*J*0515), Hα at rest-frame (*J*0660), or the calcium triplet (*J*0861). The J-PAS filter system [24] comprises 54 filters with a full width at half maximum (FWHM) of 145 Å that are spaced every ≈ 100 Å from 3 800 Å to 9 100 Å. They are complemented with two broader filters at the blue and red end of the optical range, with an effective wavelength of 3 479 Å (*u*, FWHM = 509 Å) and 9 316 Å (*J*1007, FWHM = 635 Å), respectively.

The J-PLUS DR2 comprises 1 088 pointings (2 176 deg^2) observed, reduced, and calibrated in all survey bands [21]. The limiting magnitudes (5σ, 3 arcsec aperture) of the DR2 are ∼ 22 mag in *g* and *r* passbands and ∼ 21 mag in the other ten bands. The median point spread function (PSF) FWHM in the DR2 *r*-band images is 1.1 arcsec. Objects near the borders of the images, close to bright stars, or affected by optical artefacts were masked from the initial 2 176 deg^2, providing a high-quality area of 1 941 deg^2. The DR2 is publicly available on the J-PLUS website.

The miniJPAS observations comprise four JPF pointings in the Extended Groth Strip

area along a strip aligned at 45 deg with respect to North at (RA, Dec) = (215, +53) deg, amounting to a total area of ~ 1 deg^2 [4]. The depth achieved is fainter than 22 mag for filters bluewards of 7 500 $\mathring{A}$ and ~ 22 mag for longer wavelengths. The images and catalogues are publicly available on the J-PAS website.

3 Results

We define a common sample of 5 926 white dwarfs with $r < 19.5$ mag and derive their effective temperature ($T_{\rm eff}$), surface gravity, parallax, mass (M), and atmospheric composition (H-*versus* He-dominated) by comparison with theoretical models for pure-H atmospheres ([32, 33]; H-dominated) and mixed atmospheres with H/He $= 10^{-5}$ ([7, 8]; He-dominated). The mass-radius relation in [11] for thick (H-atmospheres) and thin (He-atmospheres) hydrogen layers was assumed in the modelling. The obtained likelihood is weighted with the prior information from the parallax observed in *Gaia* DR3. Moreover, a self-consistent prior in the fraction of white dwarfs with He-dominated atmospheres ($f_{\rm He}$) was derived with a hierarchical Bayesian model. The technical details of the procedure are presented in [22]. The derived atmospherical parameters are publicly available in the J-PLUS database[1] and ViZieR.

As a second layer in the analysis, the equivalent width in the filter $J0395$ was used as a proxy for the presence of polluting metals in the white dwarfs' atmosphere via the CaII H+K absorption. The equivalent width was estimated by comparing the expected flux in the $J0395$ filter from the fitting to the other eleven J-PLUS passbands with the observed flux.

We find that

- The fraction of white dwarfs with He-dominated atmospheres ($f_{\rm He}$) has a minimum of $8 \pm 2\%$ at $T_{\rm eff} > 20\,000$ K. Then, $f_{\rm He}$ increases by $21 \pm 3\%$ between $T_{\rm eff} \sim 20\,000$ K and $T_{\rm eff} \sim 5\,000$ K [22]. This is in good agreement with previous results [31, 13, 28, 3, 1, 27, 9].

- The mass distribution at $d < 100$ pc for H-dominated white dwarfs agrees with previous work, presenting a dominant $M = 0.59\,M_{\odot}$ peak and an excess at $M \sim 0.8\,M_{\odot}$. This high-mass excess has been reported in several studies [19, 20, 29, 34, 17, 18, 35]. Interestingly, the high-mass excess is absent in the He-dominated distribution, which presents a single peak [22].

- The fraction of white dwarfs with calcium H+K absorption increases from nearly zero at $T_{\rm eff} \sim 14\,000$ K to 15% at $T_{\rm eff} \sim 6\,000$ K. This trend reflects the dependence of the calcium absorption intensity on both the temperature and the Ca/He abundance.

- We defined a sample of 39 white dwarfs with a high probability ($> 99\%$) of having polluting metals. Of them, 20 sources are already classified as DZs in the literature, and we confirmed 6 more as DZs with new OSIRIS/GTC spectroscopy.

[1] Table jplus.WhiteDwarf

The medium bands from J-PLUS complement the *Gaia* data to derive atmospheric compositions and spot the presence of polluting metals. This analysis will be improved thanks to J-PAS, which with 56 medium bands of 14 nm spaced by 10 nm to cover the optical range will provide low-resolution ($R \sim 50$) data down to $r = 21.5$ mag.

We used the miniJPAS data as a pathfinder, and analysed the eleven confirmed white dwarfs in the field [23]. We find that the effective temperature determination has a typical relative error of 2%, whereas the estimation of a precise surface gravity demands parallax information from *Gaia*. Regarding the atmospheric composition, the J-PAS filter system is able to correctly classify H- and He-dominated atmosphere white dwarfs, at least in the temperature range covered by the miniJPAS white dwarf sample, $7\,000 < T_{\rm eff} < 22\,000$ K. We also show that the presence of polluting metals can be revealed by the calcium, as traced by the $J0390$ and $J0400$ passbands. Furthermore, the miniJPAS low-resolution information is able to disentangle between white dwarfs with $T_{\rm eff} > 7\,000$ K and extragalactic QSOs with similar broad-band colours.

Acknowledgments

We dedicate this work to the memory of our six IAC colleagues and friends who met with a fatal accident in Piedra de los Cochinos, Tenerife, in February 2007, with special thanks to Maurizio Panniello, whose teachings of python were so important. Based on observations made with the JAST80 and T80Cam camera for J-PLUS and the JST250 telescope and PathFinder camera for the miniJPAS project at the Observatorio Astrofísico de Javalambre (OAJ), in Teruel, owned, managed, and operated by the Centro de Estudios de Física del Cosmos de Aragón (CEFCA). We acknowledge the OAJ Data Processing and Archiving Unit (UPAD) for reducing and calibrating the OAJ data used in this work. Funding for OAJ, UPAD, and CEFCA has been provided by the Governments of Spain and Aragón through the Fondo de Inversiones de Teruel; the Aragonese Government through the Research Groups E96, E103, E16_17R, and E16_20R; the Spanish Ministry of Science, Innovation and Universities (MCIU/AEI/FEDER, UE) with grant PGC2018-097585-B-C21; the Spanish Ministry of Economy and Competitiveness (MINECO/FEDER, UE) under AYA2015-66211-C2-1-P, AYA2015-66211-C2-2, AYA2012-30789, and ICTS-2009-14; and European FEDER funding (FCDD10-4E-867, FCDD13-4E-2685). Funding for the J-PAS Project has been provided by the Governments of Spain and Aragón through the Fondo de Inversiones de Teruel, European FEDER funding and the Spanish Ministry of Science, Innovation and Universities, and by the Brazilian agencies FDNCT, FINEP, FAPESP, FAPERJ and by the National Observatory of Brazil. Additional funding was also provided by the Tartu Observatory and by the J-PAS Chinese Astronomical Consortium.

References

[1] Bédard, A., Bergeron, P., Brassard, P., & Fontaine, G. 2020, ApJ, 901, 93

[2] Benítez, N., Dupke, R., Moles, M., et al. 2014, ArXiv e-prints [arXiv:1403.5237]

[3] Blouin, S., Dufour, P., Thibeault, C., & Allard, N. F. 2019, ApJ, 878, 63

[4] Bonoli, S., Marín-Franch, A., Varela, J., et al. 2021, A&A, 653, A31

[5] Cenarro, A. J., Moles, M., Marín-Franch, A., et al. 2014, in Observatory Operations: Strategies, Processes, and Systems V, Proc. SPIE, 9149, 91491I

[6] Cenarro, A. J., Moles, M., Cristóbal-Hornillos, D., et al. 2019, A&A, 622, A176

[7] Cukanovaite, E., Tremblay, P. E., Freytag, B., Ludwig, H. G., & Bergeron, P. 2018, MNRAS, 481, 1522

[8] Cukanovaite, E., Tremblay, P. E., Freytag, B., et al. 2019, MNRAS, 490, 1010

[9] Cunningham, T., Tremblay, P.-E., Gentile Fusillo, N. P., Hollands, M., & Cukanovaite, E. 2020, MNRAS, 492, 3540

[10] Doherty, C. L., Gil-Pons, P., Siess, L., Lattanzio, J. C., & Lau, H. H. B. 2015, MNRAS, 446, 2599

[11] Fontaine, G., Brassard, P., & Bergeron, P. 2001, PASP, 113, 409

[12] Gaia Collaboration (Smart, R. L., et al.) 2021b, A&A, 649, A6

[13] Genest-Beaulieu, C., & Bergeron, P. 2019, ApJ, 882, 106

[14] Gentile Fusillo, N. P., Tremblay, P. E., Cukanovaite, E., et al. 2021, MNRAS, 508, 3877

[15] Hollands, M. A., Tremblay, P. E., Gänsicke, B. T., Gentile-Fusillo, N. P., & Toonen, S. 2018, MNRAS, 480, 3942

[16] Ibeling, D., & Heger, A. 2013, ApJ, 765, L43

[17] Jiménez-Esteban, F. M., Torres, S., Rebassa-Mansergas, A., et al. 2018, MNRAS, 480, 4505

[18] Kilic, M., Bergeron, P., Kosakowski, A., et al. 2020, ApJ, 898, 84

[19] Liebert, J., Bergeron, P., & Holberg, J. B. 2005, ApJS, 156, 47

[20] Limoges, M. M., Bergeron, P., & Lépine, S. 2015, ApJS, 219, 19

[21] López-Sanjuan, C., Yuan, H., Vázquez Ramió, H., et al. 2021, A&A, 654, A61

[22] López-Sanjuan, C., Tremblay, P. E., Ederoclite, A., et al. 2022a, A&A, 658, A79

[23] López-Sanjuan, C., Tremblay, P. E., Ederoclite, A., et al.2022b, A&A 665, A151

[24] Marín-Franch, A., Chueca, S., Moles, M., et al. 2012, in Modern Technologies in Space- and Ground-based Telescopes and Instrumentation II, eds. R. Navarro, C. R. Cunningham, & E. Prieto, SPIE Conf. Ser., 8450, 84503S

[25] Marín-Franch, A., Taylor, K., Cenarro, J., Cristóbal-Hornillos, D., & Moles, M. 2015, in IAU General Assembly, 29, 2257381

[26] Marín-Franch, A., Taylor, K., Santoro, F. G., et al. 2017, in Highlights on Spanish Astrophysics IX, eds. S. Arribas, A. Alonso-Herrero, F. Figueras, C. Hernández-Monteagudo, A. Sánchez-Lavega, & S. Pérez-Hoyos, 670

[27] McCleery, J., Tremblay, P.-E., Gentile Fusillo, N. P., et al. 2020, MNRAS, 499, 1890

[28] Ourique, G., Romero, A. D., Kepler, S. O., Koester, D., & Amaral, L. A. 2019, MNRAS, 482, 649

[29] Rebassa-Mansergas, A., Rybicka, M., Liu, X. W., Han, Z., & García-Berro, E. 2015, MNRAS, 452, 1637

[30] Sion, E. M., Greenstein, J. L., Landstreet, J. D., et al. 1983, ApJ, 269, 253

[31] Tremblay, P. E., & Bergeron, P. 2008, ApJ, 672, 1144

[32] Tremblay, P. E., Bergeron, P., & Gianninas, A. 2011, ApJ, 730, 128

[33] Tremblay, P. E., Ludwig, H. G., Steffen, M., & Freytag, B. 2013, A&A, 559, A104

[34] Tremblay, P. E., Cummings, J., Kalirai, J. S., et al. 2016, MNRAS, 461, 2100

[35] Tremblay, P. E., Cukanovaite, E., Gentile Fusillo, N. P., Cunningham, T., & Hollands, M. A. 2019, MNRAS, 482, 5222

[36] Wesemael, F., Greenstein, J. L., Liebert, J., et al. 1993, PASP, 105, 761

Highlights of Spanish Astrophysics XI, Proceedings of the XV Scientific Meeting of the Spanish Astronomical Society held on September 4–9, 2022, in La Laguna, Spain. M. Manteiga, L. Bellot, P. Benavidez, A. de Lorenzo-Cáceres, M. A. Fuente, M. J. Martínez, M. Vázquez- Acosta, C. Dafonte (eds.), 2023

Strong lithium lines in red supergiants at different metallicities.

Negueruela, I.[1], Alonso-Santiago, J.[2], Dorda, R.[3,4] and Patrick, L. R.[1]

[1]Departamento de Física Aplicada, Facultad de Ciencias, Universidad de Alicante, Carretera de San Vicente s/n, E03690, San Vicente del Raspeig, Spain email: ignacio.negueruela@ua.es
[2] INAF–Osservatorio Astrofisico di Catania, via S. Sofia 78, 95123 Catania, Italy
[3] Instituto de Astrofísica de Canarias, Vía Láctea s/n, E38200, La Laguna, Tenerife, Spain
[4] Escuela de Arquitectura, Universidad Europea de Canarias, Tenerife, Spain

Abstract

Lithium (Li) is a fragile material, easily destroyed in stellar interiors. Within our current understanding of stellar evolution for stars more massive than $\sim 6 M_{\odot}$, Li should be depleted in the atmospheres of all such stars well before the time when they reach the He core burning phase. Despite this prediction, we find a high fraction of red supergiants (RSGs), i.e. He-core burning massive stars with convective envelopes, displaying moderate to strong Li I 6708Å doublet lines. Based on a large sample of Perseus arm RSGs, about one third of Milky Way supergiants contain measurable amounts of lithium. For the Magellanic Cloud, relatively small samples point in very different directions. In the LMC, the fraction is at least as high as that of the Milky Way. Contrarily, in the SMC, the fraction seems to be much smaller. These observational results may hint at either a Li production mechanism in RSGs or the widespread engulfment of substellar companions. Further characterisation work is ongoing, while theoretical studies into this matter are urgently needed.

1 Introduction

The light elements lithium, beryllium, and boron are important for our understanding of stellar structure because of their frailty. They are easily destroyed in stellar interiors by fusion reactions at relatively low temperatures, and thus inform us about the existence of material transport in stars. Among them, the most important isotope of lithium (^{7}Li) is the heaviest nucleus created during primordial nucleosynthesis. In the Milky Way, low-metallicity stars consistently display Li abundances around $A(\mathrm{Li}) = 2.2$ (e.g. [3]), significantly lower than predictions based on models of Big Bang nucleosynthesis. Stars with higher metallicity (Z) show higher values, around $A(\mathrm{Li}) = 3.2$, suggesting that a production mechanism exists in the present-day Universe (see [22], for a comprehensive review of light elements).

At temperatures slightly above $T = 2\times10^6$K, ^{7}Li easily captures a proton and disintegrates into two He nuclei. Therefore we expect Li to be depleted in stars with convective envelopes, unless they are very young (e.g. [14]). Intermediate-mass stars with radiative envelopes keep their original Li abundance in a thin outer layer until they leave the main sequence. Observations of clusters containing stars with masses $\lesssim 2$M$_\odot$ show how Li is severely depleted as the star evolves, because of dilution (as the star becomes larger) and destruction in the stellar interior (e.g. [2]). More massive stars are expected to behave similarly, although Li lines cannot seen in stars with $T_{\rm eff} > 8\,500$ K ([15]). A few studies of low-luminosity supergiants [17] and stars in moderately young clusters [18] did not hint at significant differences with respect to less massive stars with radiative envelopes.

Despite this, very high Li abundances are seen in massive AGB stars, very luminous giants of late-M type, believed to represent the last phase in the life of stars with initial masses ≈ 4–9 M$_\odot$. Evolved AGB stars, understood to be close to the end of the thermal-pulse phase, show high Rb abundances and a very wide range of A(Li). In the Magellanic Clouds, the brightest of such objects display $-7 \lesssim M_{\rm bol} \lesssim -6$ [12], and are believed to be stars of ≈ 7M$_\odot$. Other similar objects, assumed to be in a slightly earlier phase, have been found to display very high A(Li) > 3, while not showing high abundances of s-process elements [13]. Current models predict strong Li production at the start of the thermal-pulse phase, when Hot Bottom Burning is activated, as the base of the envelope of the star reaches $T \gtrsim 4 \times 10^7$ K, and the Cameron-Fowler mechanism [7] can proceed: enhanced production of beryllium (^{7}Be) will occur at the base of the envelope and convection during the third dredge-up will move it to regions of lower T in the outer layers, where it may decay into lithium [19].

The behaviour of Li in massive stars has not been studied in depth. Lyubimkov et al. [16] observed a sample of Galactic F and G-type supergiants, determining stellar parameters and Li abundances. They found that stars with initial masses $\lesssim 6$ M$_\odot$ may show a wide range of Li abundances, going from non-detectable to the same value as main-sequence stars, a spread that they interpret as a consequence of different initial rotations – suggesting that stars with very low rotation may keep most of their original surface Li until the first dredge-up, and a reduced abundance A(Li)$\lesssim 1.3$ after it has happened. Conversely, they barely detect any lithium in any star with estimated mass $\gtrsim 6$ M$_\odot$, a fact that they explain resorting to stellar models that include the effect of rotation (e.g. [4]; [10]). These models predict that, even for relatively low initial rotational velocities, Li is depleted below detectability by the end of the main sequence, due to rotational mixing. Even in models without rotation, a precipitous drop in Li abundances happens during the B-type giant phase for stars of 7 to 15 M$_\odot$. The validity of these models finds some support in limited observations of the behaviour of Be, another light element [21]. Nevertheless, recent observations of red supergiants in some Milky Way open clusters have shown a non-negligible fraction of objects with strong Li lines [20, 11], in open contradiction with models and previous results. In an attempt to check if this behaviour extends to higher masses, we have observed larger samples of RSGs at different metallicities.

2 Observations

As a first step, we conducted an exploratory survey with the robotic 80 cm Telescopi Joan Oró at the Montsec Observatory. We used the ARES spectrograph with the Red VPH, which provides a resolving power $R \approx 10\,000$ over the 630 to 673 nm range. Observations, taken between December 2019 and June 2020, targeted a small sample of RSGs from the Perseus arm. Since these spectra indicated that a sizeable fraction of the RSGs present Li lines, we proceeded to observe large samples of stars.

A sample of Perseus arm RSGs was observed with the high-resolution FIbre-fed Echelle Spectrograph (FIES) attached to the 2.56 m Nordic Optical Telescope (NOT; La Palma, Spain) during a run on 2020, October 2 – 5. FIES is a cross-dispersed high-resolution echelle spectrograph that covers the 370 – 830 nm range. We used the large aperture, which provides a resolving power $R \approx 25\,000$. The spectra were homogeneously reduced using the FIEStool software in advanced mode. We observed > 50 RSGs, distributed over the Northern sky, most of them from the Cassiopeia region of the Perseus Arm. When combined with over 20 RSGs from the region of Per OB1 in [5], observed with the same instrument, this results in a sample of over 70 Perseus Arm RSGs. Sample spectra in the region of the Li I doublet are shown in Fig. 1.

Samples of RSGs at different metallicities were obtained by observing RSGs in Magellanic Cloud clusters. These objects were observed with *X-shooter*, mounted on the VLT UT3 (Melipal). Most of the observations used the UVB arm with an $1.3''$ slit ($R \approx 4\,000$) and the VIS arm with a $0.9''$ slit ($R \approx 9\,000$). Observations were obtained in service mode between 2020 October 13 and December 29. The targets observed were selected to belong to open clusters of different ages, in order to cover a wide range of masses.

3 Results

Analysis of the spectra obtained is ongoing, in order to provide a full characterisation of all the target stars that will serve as a context for the detection of Li lines. Meanwhile, visual inspection can inform us about the basic properties of the stars.

Among the Perseus Arm sample, we find a high fraction of stars with Li lines. About 25% of the stars of all spectral types (stars observed fall mainly in the K5 – M4 range, typical of Milky Way RSGs – see [9]) display strong Li lines. A few others have weak Li lines that appear blended with neighbouring weak metallic features. This result is in agreement with a recent report by [11], based on a smaller sample.

Our RSG sample in the Perseus Arm consists mostly of field stars, which cannot be assigned ages, and thus masses, to compare to evolutionary tracks. To address this issue, all our targets in the Magellanic Clouds are members of open clusters, which can provide an evolutionary context for them. Our Magellanic samples are smaller than that from the Milky Way, but likely large enough to be statistically representative. The LMC sample includes one of the most well-populated RSG clusters, NGC 2100, which is likely younger than 20 Ma, and a range of clusters extending to the well studied NGC 1755 (60 Ma), which is believed

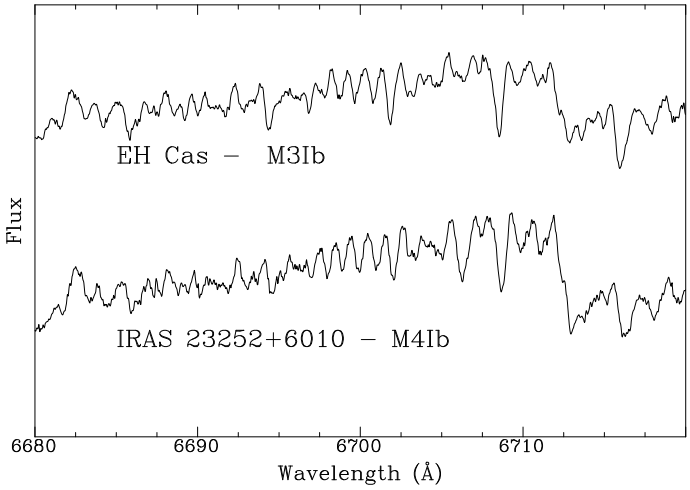

Figure 1: FIES spectra of two Perseus-arm RSGs of similar spectral type around the region where the Li I 6708 Å doublet is expected. A broad and deep Li line is seen in the spectrum of IRAS 23252+6010.

to contain RSGs of $\sim 7\,M_{\odot}$. In total, we have observed 21 RSGs. Stars with Li lines are found in all clusters, except in NGC 1818, where only 3 could be observed and one turns out to have an early (G) spectral type. In total, about 40% of the stars observed have lithium. Given the small sample size, this value is consistent with that found in the Milky Way.

In the SMC, the number of large young open clusters is much smaller than in the LMC, and we could not find many suitable targets. As a consequence, our clusters cover a wider range in ages, reaching NGC 256, where the RSGs are expected to have $\sim 6\,M_{\odot}$. Among 17 stars observed, there is only one with a moderately strong Li line, in Bruck 71. Two stars in NGC 241/2 may have weak Li present. Although the sample is small, this result very strongly suggests a different behaviour from that seen at higher Z.

4 Discussion

We find strong Li lines in a substantial fraction of RSGs in the Milky Way and the LMC. This detection is unanticipated, not only because current models for massive stars do not predict it, but also because red giants of similar spectral types do not present Li lines. Only a very small fraction of K-type giants display detectable lithium (see [24] for a comparable survey of low-mass red giants in older clusters). The lithium that we detect is unlikely to be primordial material preserved in the outer atmosphere. Irrespectively of model predictions for the atmospheric abundances of massive stars, preservation of primordial Li would require a complete absence of rotational mixing and extremely weak mass loss, both unlikely for

normal stars of $\gtrsim 8\,M_\odot$.

The possibility of a production mechanism cannot be ruled out. In massive AGB stars, the Cameron-Fowler mechanism is believed to occur during the He-shell burning phase, as it relies on the penetration of the convective envelope below the H-burning shell during third dredge-up for the transport of recently created ^{7}Be to the outer regions, where it may decay to ^{7}Li that will not be destroyed because of the lower temperatures in these external layers. Some other mechanism should be at work in a true RSG, which is expected to be a He-core burning star (some lower mass stars are morphologically classified as K-type low-luminosity supergiants even if they are giants in the physical sense; a true RSG is an object classified as a supergiant that will explode as a supernova). There is an open debate at present about the possibility of a new mechanism creating Li in low mass giants (e.g. [26, 8]) and thus a different mechanism operating in massive stars is not a precluded possibility.

A second, more exotic possibility to explain the presence of Li in the atmospheres is the engulfment of substellar companions as the stars expand when crossing the Hertzsprung gap. Engulfment of giant planets has been proposed as an explanation for the existence of some Li-rich giants [1], although not considered for massive stars. However, recent observations have unveiled the presence of low-mass brown-dwarfs around early-B stars [23], making such a scenario at least worth considering. As only direct imaging can be used to search for substellar objects around hot stars, all the detections correspond to brown dwarfs orbiting their parent system at very large distances, too large to permit engulfment. Nevertheless, the existence of other brown dwarfs or giant planets at lower distances is not ruled out. Simulations suggest that a solar-type star would have its Li abundance considerably enhanced by the engulfment of a low-mass brown dwarf (e.g. [6]), but the effect on a massive star has not been studied. Recent observations suggest that some giant planets might be Li-rich [25], but the much higher fraction of RSGs with Li as compared to solar-mass giants would require some other ingredient for this mechanism to be viable.

In summary, the detection of Li in a high fraction of RSGs is extremely surprising under the light of our current stellar models. Further theoretical developments are certainly needed to provide an understanding of this phenomenon.

Acknowledgments

Partially based on observations collected at the European Organisation for Astronomical Research in the Southern Hemisphere under ESO programme 106.212J.001 and on observations made with the Nordic Optical Telescope, operated by the Nordic Optical Telescope Scientific Association at the Observatorio del Roque de los Muchachos (La Palma, Spain) of the Instituto de Astrofísica de Canarias. We thank the director of the Montsec Observatory for DDT time on the TJO. This research is partially supported by the Spanish Government Ministerio de Ciencia e Innovación and Agencia Estatal de Investigación (MCIN/AEI/10.13039/501100011033/FEDER, UE) through grants PGC2018-093741-B-C21/C22 and PID2021-122397NB-C22, and by the Generalitat Valenciana under grant PROMETEO/2019/041.

References

[1] Aguilera-Gómez, C., Chanamé, J., Pinsonneault, M. H., et al. 2016, ApJ, 829, 127

[2] Anthony-Twarog, B. J., Deliyannis, C. P., & Twarog, B. A. 2021, AJ, 161, 159

[3] Bensby, T. & Lind, K. 2018, A&A, 615, A151

[4] Brott, I., de Mink, S. E., Cantiello, M., et al. 2011,A&A, 530, A115

[5] de Burgos, A., Simon-Díaz, S., Lennon, D. J., et al. 2020,A&A, 643, A116

[6] Cabezón, R. M., Abia, C., Domínguez, I., et al. 2022, `arXiv:2210.17363`

[7] Cameron, A. G. W., & Fowler, W. A. 1971, ApJ, 164, 111

[8] Chanamé J., Pinsonneault M. H., Aguilera-Gómez C., Zinn J. C., 2022, ApJ, 933, 58

[9] Dorda, R., Negueruela, I., & González-Fernández, C. 2018, MNRAS, 475, 2003

[10] Ekström, S., Georgy, C., Eggenberger, P., et al. 2012,A&A, 537, A146

[11] Fanelli, C., Origlia, L., Mucciarelli, A., et al. 2022, ApJ, 931, 61

[12] García-Hernández, D. A., García-Lario, P., Plez, B., et al. 2007,A&A, 462, 711

[13] García-Hernández, D. A., Zamora, O., Yagüe, A., et al. 2013,A&A, 555, L3

[14] Jeffries, R. D. 2006, in Chemical Abundances and Mixing in Stars in the Milky Way and its Satellites, p163

[15] Lyubimkov, L. S. 2016, Astrophysics, 59, 411

[16] Lyubimkov, L. S., Lambert, D. L., Kaminsky, B. M., et al. 2012, MNRAS, 427, 11

[17] Luck, R. E. 1977, ApJ, 218, 752

[18] Luck, R. E. 1994, *ApJS*, 91, 309

[19] Mazzitelli, I., D'Antona, F., & Ventura, P. 1999,A&A, 348, 846

[20] Negueruela, I., Alonso-Santiago, J., Tabernero, H. M., et al. 2020, *MemSAIt*, 91, 114

[21] Proffitt, C. R., Lennon, D. J., Langer, N., et al. 2016, ApJ, 824, 3

[22] Randich S., & Magrini L., 2021, *FrASS*, 8, 6

[23] Squicciarini, V., Gratton, R., Janson, M., et al. 2022, A&A, 664, A9

[24] Sun, Q., Deliyannis, C. P., Twarog, B. A., et al. 2022, MNRAS, 513, 5387

[25] Tabernero, H. M., Zapatero Osorio, M. R., Allart, R., et al. 2021, A&A, 646, A158

[26] Zhang, J., Shi, J.-R., Yan, H.-L., et al. 2021, ApJL, 919, L3

Highlights of Spanish Astrophysics XI, Proceedings of the XV Scientific Meeting of the Spanish Astronomical Society held on September 4–9, 2022, in La Laguna, Spain. M. Manteiga, L. Bellot, P. Benavidez, A. de Lorenzo-Cáceres, M. A. Fuente, M. J. Martínez, M. Vázquez- Acosta, C. Dafonte (eds.), 2023

Substructure in molecular outflow bullets from protostars.

Blázquez-Calero, G.[1], Osorio M.[1], Anglada G.[1], Gómez J.F.[1], Diaz-Rodriguez A.K.[2], and Fuller G.[1,2,3]

[1] Instituto de Astrofísica de Andalucía, CSIC, Glorieta de la Astronomía s/n, 18008 Granada, Spain
[2] UK ALMA Regional Centre Node, Jodrell Bank Centre for Astrophysics, Department of Physics and Astronomy, The University of Manchester, Oxford Road, Manchester M13 9PL, UK
[3] I. Physikalisches Institut, University of Cologne, Zülpicher Str. 77, D-50937 Köln, Germany

Abstract

Some protostellar molecular outflows are associated with the so-called extremely high velocity molecular bullets, discrete clumps of gas ejected from the close environment of the protostar, travelling at velocities of >100 km/s. We carried out ALMA observations that resolve the morphology and kinematics of one of these molecular bullets. We present model results that account for the main observed features of the source.

.

1 Introduction

Outflows are an ubiquitous ingredient of the star formation process. Moreover, they are not a mere by-product of the protostar evolution, but they play an important role in the assembly of stars, can alter the properties of the protoplanetary disks and, consequently, they might be able to have an impact also on the planet formation process [12]. Outflows from young stellar objects usually present two different components. A highly-collimated and partially ionized component (the jet), which is traveling at extremely high velocities (∼100 km/s), and a fairly collimated (and usually bipolar) component (the molecular outflow) with velocities of the order of 10 km/s. Jets are originated from the proximity of the star (likely from its accretion disk) and frequently observed at optical, infrared and radio wavelengths [7, 2, 21]. Jets are thought to be powerful enough to entrain ambient gas and produce the usually more massive molecular outflows ubiquitously observed in low-excitation transitions of CO and other molecular species at mm wavelengths [22, 16, 5, 18].

Nonetheless, for some young sources, the outflow also has a low excitation molecular component traveling at extremely high velocities of ∼100 km/s. In these cases, we see that this

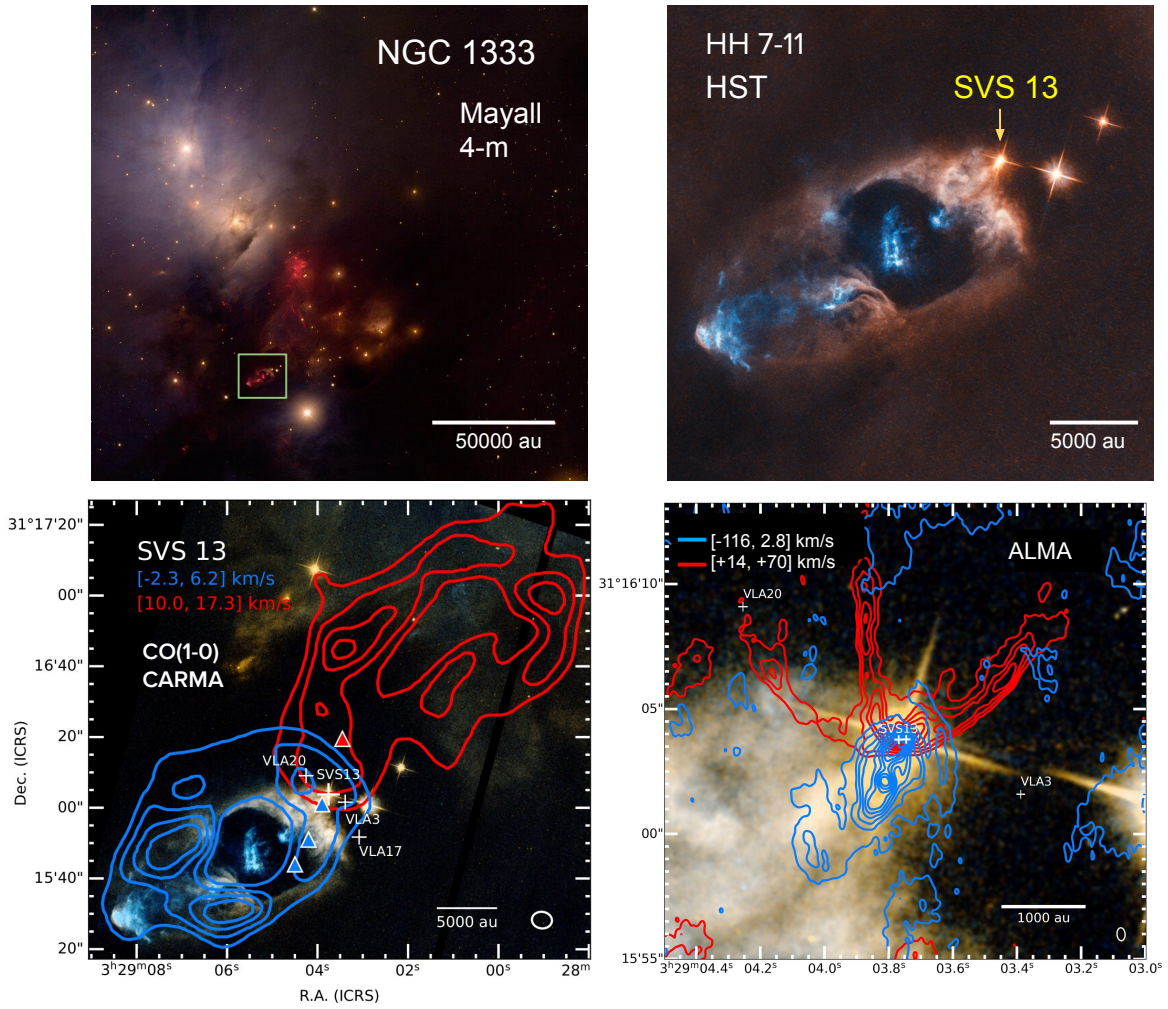

Figure 1: Top left: Optical (B, V, I, Hα) image of the NGC 1333 star-forming region obtained with the Mayall 4-m telescope at Kitt Peak (credits: T.A. Rector/University of Alaska Anchorage, H. Schweiker/WIYN and NOIRLab/NSF/AURA). Top right: HST image (F606W filter) showing a close-up of the HH7-11 objects (from the Hubble Legacy Archive). Bottom left: CARMA CO(1-0) map of the blue-shifted and red-shifted lobes of the large-scale bipolar molecular outflow [20, 24], overlaid on the HST image. The triangles mark the location of the molecular bullets [6, 9]. Bottom right: ALMA CO(3-2) map (with a resolution of $0.520'' \times 0.324''$) of the blue-shifted and red-shifted integrated emission in a region close to the SVS 13 protostars. The image shows the arc-shaped walls of the outflow lobes, as well as the blue-shifted bullet closest to SVS 13 [8]. All velocities are with respect to the LSR. The systemic LSR velocity is $\sim +8.5$ km/s [11].

component appears not as a continous jet but as a collection of roughly aligned discrete clumps called molecular bullets [3]. The observed bullets present typical separations corresponding

to time intervals of ∼50 to ∼1000 yr, and their masses are about 10^{-4} $M_\odot$ (several orders of magnitude smaller than the masses of standard molecular outflows) [13, 19, 17, 23, 14, 28, 25].

Although several interpretations have been proposed for the extremely high velocity bullets [3, 4, 27], their true nature remains unclear. We obtained high angular and spectral resolution ALMA observations of one of these bullets associated to SVS 13 showing its substructure that can help to understand its nature [8].

2 The SVS13 outflow

Figure 1 shows and overview of the NGC 1333 region and the outflows associated with the SVS 13 at optical and millimeter wavelengths. Figure 2 shows our ALMA images of the molecular bullet closest to SVS 13.

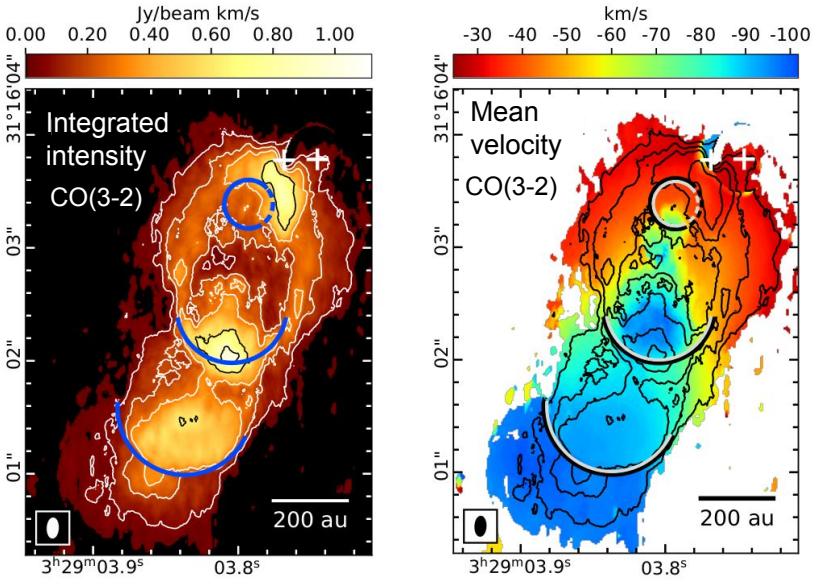

Figure 2: Left: Image of the velocity-integrated intensity (zeroth-order moment) of the molecular bullet closest to SVS 13, obtained from ALMA CO(J=3-2) observations [8]. Right: Image of the mean velocity field (first-order moment), in color scale, overlaid on the integrated intensity (in contours). The velocities are line-of-sight velocities relative to the systemic velocity of the ambient cloud (+8.5 km/s; [11]). A clear global velocity gradient is seen along the major axis of the bullet. The images have been corrected by the decrease in sensitivity due to the primary beam response. The positions of the two protostars of the SVS 13 binary [1], near the top right corner of the images, are indicated by plus signs. The H_2 arcuate features imaged by [15] are plotted as arcs. The synthesized beam ($0.163'' \times 0.084''$, PA = 4.2°) is plotted as an ellipse in the bottom left corner of the images.

3 Modelization of the molecular bullet

Figure 3 shows a comparison of our model results (based on [10, 26]) and the ALMA observations of the blue-shifted bullet closest to SVS 13.

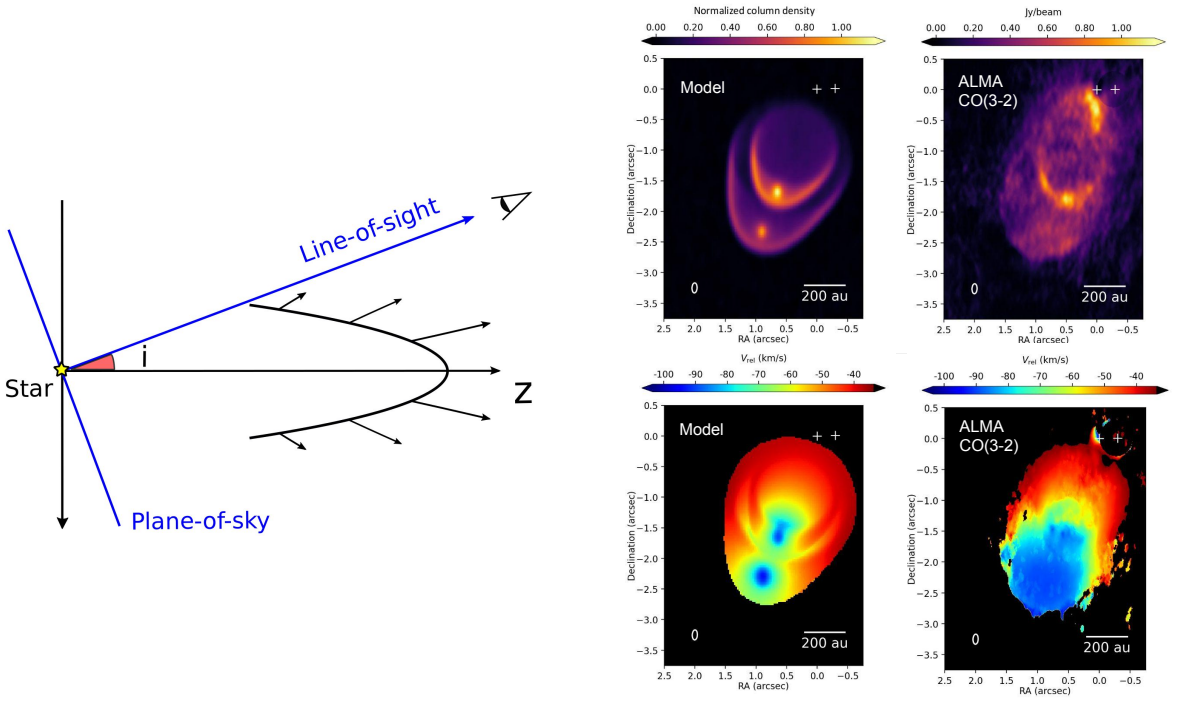

Figure 3: Left: Geometrical scheme of a bowshock observed at an inclination angle i. Right: Comparison of the model results (central column) and the ALMA observations (right column) for the northern region of the observed bullet (see Fig. 2). The model assumes a sequence of two bowshocks driven by SVS 13 and a inclination angle $i = 20°$. The top panels show the normalized column density of the model (left) and the observed integrated intensity. The bottom panels show the mean velocity relative to the ambient cloud. The offsets are relative to the position of the eastern component of the SVS 13 protobinary (from [8]).

Acknowledgments

G.A., G.B.-C., G.F., J.F.G, M.O., and A.K.D.-R acknowledge financial support from grants PID2020-114461GB-I00 and CEX2021-001131-S, funded by MCIN/AEI/ 10.13039/501100011033. This work has received financial support from Junta de Andalucía (Spain) grant P20-00880 (FEDER, EU). G.B-C acknowledges support from grant PRE2018-086111, funded by MCIN/AEI/ 10.13039/501100011033 and by 'ESF Investing in your future'. This work makes use of the following ALMA data: ADS/JAO.ALMA#2015.1.01229.S, ADS/JAO.ALMA#2016.1.01305.S. ALMA is a partnership of ESO (representing its member states), NSF (USA) and NINS (Japan), together with NRC (Canada) and

NSC and ASIAA (Taiwan) and KASI (Republic of Korea), in cooperation with the Republic of Chile. The Joint ALMA Observatory is operated by ESO, AUI/NRAO and NAOJ. This publication use images based on observations made with the NASA/ESA Hubble Space Telescope, and obtained from the Hubble Legacy Archive, which is a collaboration between the Space Telescope Science Institute (STScI/NASA), the Space Telescope European Coordinating Facility (ST-ECF/ESA) and the Canadian Astronomy Data Centre (CADC/NRC/CSA).

References

[1] Anglada, G., Rodríguez, L. F., Torrelles J. M. 2000, ApJL, 542, L123.

[2] Anglada, G., Rodríguez, L. F., Carrasco-González C. 2018, A&ARv, 26, 3.

[3] Bachiller, R., Cernicharo, J., Martin-Pintado, J., Tafalla, M., Lazareff, B. 1990, A&A, 231, 174

[4] Bachiller, R., Martin-Pintado, J., Fuente, A. 1991, A&A, 243, L21

[5] Bachiller, R. 1996, ARA&A, 34, 111.

[6] Bachiller, R., Gueth F., Guilloteau S., Tafalla M., Dutrey A. 2000, A&A, 362, L33

[7] Bally, J. 2016, ARA&A, 54, 491.

[8] Blázquez-Calero, G. et al. 2023, in preparation

[9] Chen, X., Arce, H. G., Zhang, Q., Launhardt, R., Henning, T. 2016, ApJ, 824, 72.

[10] Masson, C. R., Chernin, L. M. 1993, ApJ, 414, 230.

[11] Diaz-Rodriguez, A. K., Anglada, G., Blázquez-Calero, G. et al. 2022, ApJ, 930, 91.

[12] Frank, A., Ray, T. P., Cabrit, S. et al. 2014, prpl.conf, 451.

[13] Hatchell, J., Fuller, G. A., Ladd, E. F. 1999, A&A, 346, 278.

[14] Hirano, N., Ho, P. P. T., Liu, S.-Y. et al. 2010, ApJ, 717, 58.

[15] Hodapp, K. W., Chini, R. 2014, ApJ, 794, 169.

[16] Lada, C. J. 1985, ARA&A, 23, 267.

[17] Lee, C.-F., Hsu, M.-C., Sahai, R. 2009, ApJ, 696, 1630.

[18] Lee, C.-F. 2020, A&ARv, 28, 1.

[19] Lefloch, B., Cernicharo, J., Reipurth, B., Pardo, J. R., Neri, R. 2007, ApJ, 658, 498.

[20] Plunkett, A. L., Arce, H. G., Corder, S. A., et al. 2013, ApJ, 774, 22.

[21] Ray, T. P., Ferreira, J. 2021, NewAR, 93, 101615.

[22] Rodriguez, L. F., Carral, P., Ho, P. T. P., Moran, J. M. 1982, ApJ, 260, 635.

[23] Santiago-García, J., Tafalla, M., Johnstone, D., Bachiller, R. 2009, A&A, 495, 169.

[24] Stephens, I. W., Dunham, M. M., Myers, P. C. et al. 2017, ApJ, 846, 16.

[25] de A. Schutzer, A., Rivera-Ortiz, P. R., Lefloch, B. et al. 2022, A&A, 662, A104.

[26] Tabone, B., Raga, A., Cabrit, S., Pineau des Forêts, G. 2018, A&A, 614, A119.

[27] Tafalla, M., Su, Y.-N., Shang, H., et al., 2017, A&A, 597, A119.

[28] Tychoniec, Ł., Hull, C. L. H., Kristensen, L. E. et al. 2019, A&A, 632, A101.

Highlights of Spanish Astrophysics XI, Proceedings of the XV Scientific Meeting of the Spanish Astronomical Society held on September 4–9, 2022, in La Laguna, Spain. M. Manteiga, L. Bellot, P. Benavidez, A. de Lorenzo-Cáceres, M. A. Fuente, M. J. Martínez, M. Vázquez- Acosta, C. Dafonte (eds.), 2023

The SOFIA Massive (SOMA) Star Formation Survey and the open-source python package sedcreator.

Rubén Fedriani[1] **and Jonathan C. Tan**[1,2]

[1] Chalmers University of Technology (Sweden)
[2] University of Virginia (USA)

Abstract

Massive stars have dramatic impacts throughout the universe at different scales and are one of the reasons you are reading this abstract today. But their birth, deep within dusty molecular clouds, is literally shrouded in uncertainty. The formation of massive protostars is still an open question and there is still a lot to be understood. Theories range from Core Accretion, i.e., a scaled-up version of low-mass star formation, to Competitive Accretion at the crowed centres of forming star clusters, to Stellar Collisions. The SOMA survey aims at understanding the basic formation mechanisms governing massive stellar birth through multi-wavelength observations but also through radiative transfer (RT) modelling of their spectral energy distributions (SEDs).

Here I present the current status of the SOFIA Massive (SOMA) Star Formation Survey for which more than 40 sources have been observed in the mid-infrared with SOFIA/FORCAST and that have been combined with Spitzer and Herschel observations. These data were used to construct SEDs and to fit a grid of RT models. To do this, we used the open-source python package sedcreator which is also presented to the community. This package includes a number of convenient tools to measure fluxes on any astronomical image and to fit to a set of models. We find evidence that relatively massive protostars can form across a range of clump mass surface density environments, which contradicts some models for the required conditions of massive star formation. However, we see a trend that to form the most massive protostars, i.e., $m_* > 25\,M_\odot$, the mass surface density ($\Sigma_{\rm cl}$) needs to be $> 1\,{\rm g\,cm^{-2}}$. Our favoured explanation for this result is the Turbulent Core Accretion model prediction that the star formation efficiency of a core due to internal protostellar feedback is higher in higher $\Sigma_{\rm cl}$ environments.

1 Introduction

Massive stars are fundamental in driving the evolution of galaxies. Their strong radiation, winds, and supernovae impact their surrounding environments, including protoplanetary disks around lower-mass stars that are forming in the same protocluster. In spite of their importance, there are many open questions about the origins of massive stars, including the basic nature of their formation mechanism, e.g., whether it is a scaled-up version of the standard core accretion theory [1] or whether it requires a more chaotic, competitive accretion in the centre of a dense protocluster of low-mass protostars [2, 3].

The *SOFIA* Massive (SOMA) Star Formation Survey (PI: Tan) aims to characterise a sample of > 50 high- and intermediate-mass protostars over a range of evolutionary stages and environments with their ~ 10 to $40\,\mu$m emission observed with the *SOFIA*-Faint Object infraRed CAmera for the *SOFIA* Telescope (FORCAST) instrument [4]. These SOFIA observations have been complemented with Spitzer and Herschel archival data to have a wavelength coverage from ~ 3 to $\sim 500\,\mu$m. In Paper I of the survey [5], the first eight sources were presented, which were mostly massive protostars. In Paper II [6], seven additional high luminous sources were presented, corresponding to some of the most massive protostars in the survey. In Paper III [7], 14 intermediate-mass sources were presented and analysed. Here in Paper IV in the series [8], we present 10 regions that harbour a total of 11 sources, selected based on the nature of their environment, i.e., appearing to be relatively *isolated* in $37\,\mu$m imaging.

2 Methods

We have introduced a number of new and updated analysis methods to analyse efficiently the SOMA sources. The main update is the release of `sedcreator`, which is an open-source python package hosted in GitHub (https://github.com/fedriani/sedcreator) and the documentation can be accessed at this URL https://sedcreator.readthedocs.io/. The main two sets of tools of `sedcreator` are encapsulated into *SedFluxer* and *SedFitter*. *SedFluxer* helps one construct an SED by providing tools to measure fluxes on a given image. *SedFitter* fits an SED with massive star formation radiation transfer model grid by [9].

Figure 1: Logo for sedcreator python package.

3 Main results

We used sedcreator/SedFluxer to measure the fluxes at wavelengths 3.6, 4.5, 5.8, and $8.0\,\mu$m from Spitzer/IRAC; at 7.7, 19.7, and 31.5, and $37.1\,\mu$m from SOFIA/FORCAST; and at 70,

160, 250, 350, and 500 μm from Herschel /PACS and SPIRE. We note that not all bands were available for all sources. We then used sedcreator/SedFitter to fit the measured fluxes to the [9] model grid. In this section, we highlight the main findings.

The 11 *isolated* protostars analysed in this work span a wide range in bolometric luminosity, i.e., $\sim 10^2 - 10^5\,L_\odot$. Fitting the SEDs with the RT models, we obtain protostellar masses ranging from $m_* \sim 3 - 50\,M_\odot$, which are accreting at rates of $\dot{m}_{\rm disk} \sim 10^{-5} - 10^{-3}\,M_\odot\,{\rm yr}^{-1}$ from cores with initial masses $M_c \sim 20 - 430\,M_\odot$ and in clump environments with mass surface densities ranging $\Sigma_{\rm cl} \sim 0.3 - 1.7\,{\rm g\,cm}^{-2}$. The SOMA IV sub-sample complements the full SOMA sample and adds some of the most massive protostars in the survey. Figure 2 left panel summarises the three main physical parameters in the SED fit, i.e., core mass, mass surface density of the clump, and protostellar mass ($M_{\rm c} - \Sigma_{\rm cl} - m_*$) for all SOMA sources analysed so far. Figure 2 right panel shows the values of m_* versus $\Sigma_{\rm cl}$ for the SOMA survey sample to date. One can see how the most massive protostars, i.e., with $m_* > 25\,M_\odot$, tend to be concentrated in the higher $\Sigma_{\rm cl}$ region of parameter space. The fiducial condition for massive star formation from [10] is that one needs $\Sigma_{\rm cl} \sim 1\,{\rm g\,cm}^{-2}$ to form stars with $> 10\,M_\odot$ (red line). The prediction is that massive protostars should only be found on the right of this line, i.e., which defines a minimum $\Sigma_{\rm cl}$ for high-mass star formation. We see that the SOMA results are inconsistent with this, i.e., there are numerous massive protostars that appear to be forming in conditions with $\Sigma_{\rm cl} \ll 1\,{\rm g\,cm}^{-2}$.

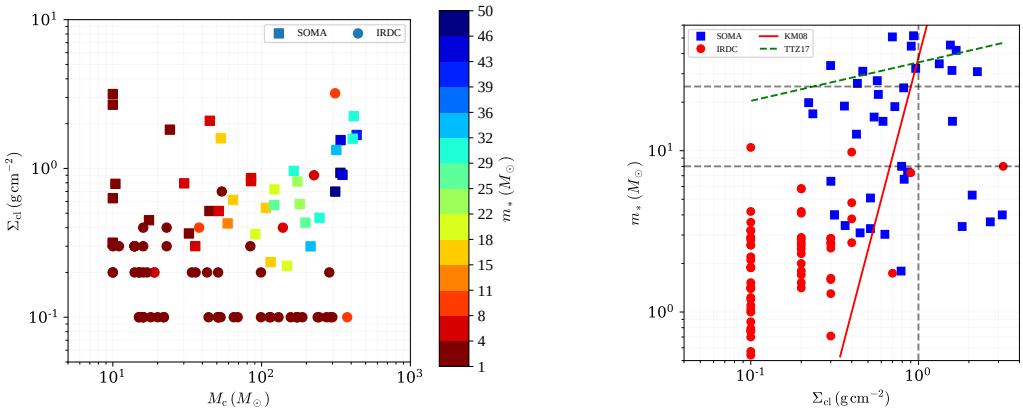

Figure 2: Left: Mass surface density of the clump environment ($\Sigma_{\rm cl}$) versus initial mass of the core ($M_{\rm c}$) for the full SOMA sample to date and the IRDC samples. Each data point is the average of good model fits. Each point is also colour coded with current mass of the protostar (m_*). Right: m_* versus $\Sigma_{\rm cl}$ for the 40 SOMA sources of Papers I to IV and IRDC sources. The red solid line shows the fiducial prediction of [10] for the minimum $\Sigma_{\rm cl}$ needed to form a star of given mass m_*. The green dashed line is results for the final stellar mass formed from 100 $M_\odot$ prestellar cores as a function of $\Sigma_{\rm cl}$ [11].

References

[1] McKee, C. F. & Tan, J. C. 2003, ApJ, 585, 850. doi:10.1086/346149

[2] Bonnell, I. A., Bate, M. R., & Zinnecker, H. 1998, MNRAS, 298, 93. doi:10.1046/j.1365-8711.1998.01590.x

[3] Grudić, M. Y., Guszejnov, D., Offner, S. S. R., et al. 2022, MNRAS, 512, 216. doi:10.1093/mnras/stac526

[4] Herter, T. L., Adams, J. D., Gull, G. E., et al. 2018, Journal of Astronomical Instrumentation, 7, 1840005-451. doi:10.1142/S2251171718400056

[5] De Buizer, J. M., Liu, M., Tan, J. C., et al. 2017, ApJ, 843, 33. doi:10.3847/1538-4357/aa74c8

[6] Liu, M., Tan, J. C., De Buizer, J. M., et al. 2019, ApJ, 874, 16. doi:10.3847/1538-4357/ab07b7

[7] Liu, M., Tan, J. C., De Buizer, J. M., et al. 2020, ApJ, 904, 75. doi:10.3847/1538-4357/abbefb

[8] Fedriani, R., Tan, J. C., Telkamp, Z., et al. 2023, ApJ, 942, 7. doi:10.3847/1538-4357/aca4cf

[9] Zhang, Y. & Tan, J. C. 2018, ApJ, 853, 18. doi:10.3847/1538-4357/aaa24a

[10] Krumholz, M. R. & McKee, C. F. 2008, Nature, 451, 1082. doi:10.1038/nature06620

[11] Tanaka, K. E. I., Tan, J. C., & Zhang, Y. 2017, ApJ, 835, 32. doi:10.3847/1538-4357/835/1/32

Highlights of Spanish Astrophysics XI, Proceedings of the XV Scientific Meeting of the Spanish Astronomical Society held on September 4–9, 2022, in La Laguna, Spain. M. Manteiga, L. Bellot, P. Benavidez, A. de Lorenzo-Cáceres, M. A. Fuente, M. J. Martínez, M. Vázquez- Acosta, C. Dafonte (eds.), 2023

The blue supergiant 2MASS J20395358+4222505, a Rosetta stone in the realm of massive stars.

Herrero, A.[1,2], **Berlanas, S. R.**[3,4], **Maíz Apellániz, J.**[5], **and Comerón, F.**[6]

[1]Instituto de Astrofísica de Canarias, 38200, La Laguna, Tenerife, Spain
[2]Departamento de Astrofísica, Universidad de La Laguna, 38205, La Laguna, Tenerife, Spain
[3]Departamento de Física Aplicada, Facultad de Ciencias II, Universidad de Alicante,Spain
[4]Astrophysics Group, Keele University, Keele ST5 5BG, Staffordshire, UK
[5]Centro de Astrobiología (CAB), CSIC-INTA, Campus ESAC, E-28 692 Villanueva de la Cañada, Madrid, Spain
[6]European Southern Observatory, Karl Schwarzschild Str. 2, 85748, Garching, Germany

Abstract

2MASS J20395358+4222505 is a highly extincted (Av= 9.6 mag) early B-supergiant located in the nearest massive star forming region, Cyg-X, in the outskirts of the massive star association Cyg OB2. A mass of M= 46 $M_{\odot}$ and a luminosity of $\log(L/L_{\odot})$= 5.7 make it one of the most massive and luminous stars in the Milky Way. Interestingly, the star seems to be in a transition stage, in the way to become one of the few (half a dozen) early-type hypergiants in the Galaxy. Moreover, the star is orbiting an unknown companion, with a semi-amplitude of the radial velocity curve of ∼100 km/s. We especulate about the possibility that the unseen companion is a compact object, a back hole of ∼18 $M_{\odot}$, or a fast rotating main sequence star of that mass.

1 Introduction

Since its discovery by [11], the massive star population of the Cyg OB2 association has been subject to numerous studies. In particular, there have been a number of census in the region, like, f.e., those by [16, 10, 4]. The initial list of the first authors contained 11 candidate members, whereas the lists presented by the last authors contain 102 OB stars, plus 61 new OB candidates. [1] carried out a spectroscopic survey of those candidates. They confirmed 11 new O-type stars and 31 B-type stars earlier than B3.

The analysis of [1] included an estimation of extinction, from which the peculiarities of one of the object classified as a B0 I star were evident: the star had an estimated extinction $A_v \approx 11$, from which the luminosity could also be estimated, adopting the observed NOMAD magnitude in the B-band (B= 15.9, [17]), a standard extinction law and a bolometric correction appropriated for the spectral type. Together with the distance to Cyg OB2 determined

Table 1: Main stellar parameters for 2MASS J20395358+4222505. The gravity includes the centrifugal correction and $\epsilon = \frac{N(He)}{N(H)+N(He)}$ is the helium abundance with respect to hydrogen, by number. The whole set of values is given for the adopted distance, together with the statistical errors of the analysis. Full details of the analysis can be found in [6]

V sini ($\mathrm{km\,s^{-1}}$)	$T_{\rm eff}$(K) (K)	log g (dex cgs)	ϵ	$\mathrm{V_\infty}$ ($\mathrm{km\,s^{-1}}$)	R ($\mathrm{R_\odot}$)	M ($\mathrm{M_\odot}$)	$\mathrm{M_{bol}}$ (mag)	$\dot{M}\times10^6$ ($\mathrm{M_\odot\ a^{-1}}$)
110	24 000	2.88	0.12	1500	41.2	46.5	-9.52	2.40
±25	±500	±0.15	±0.04	±200	±4.0	±15.0	±0.10	$^{+0.20}_{-0.30}$

by [2] (1.76 kpc), this results in an estimated luminosity $\log L/L_\odot \approx 6.6$, which would place 2MASS J20395358+4222505 among the most luminous stars in the Galaxy.

2 2MASS J20395358+4222505: a very luminous blue supergiant

Because of the peculiar characteristics of 2MASS J20395358+4222505, we decided to have a look at the object. During the commisioning of the MEGARA spectrograph attached to the Gran Telescopio Canarias ([5]) we obtained R= 6000 spectra with the LR-U and LR-B gratings, and R= 20 000 spectra with the HR-R grating, thus covering a spectral range from 3655 to 5200 Å and from 6405 to 6797 Å. We note that the LR-U and LR-B spectra were further degraded to R= 3000 to increase the Signal-to-Noise ratio.

The observations were analyzed in [6] by means of FASTWIND ([15, 13, 14]), an atmosphere code that calculates the emergent stellar spectrum in spherical geometry with mass-loss and NLTE conditions. Their results (see Tab. 1) confirmed that 2MASS J20395358+4222505 is a massive hot B-supergiant. It is very luminous, but not as extremely luminous as the first estimations (its luminosity is "only" $\log L/L_\odot = 5.71\pm0.04$, if the adopted distance from [2] is correct).

The luminosity however is somewhat uncertain, and can be a bit lower or clearly higher. This uncertainty comes from the uncertainty in the distance. The projected position of the star in the sky lies not far from the core of the Cyg OB2 association, but actually a bit further out to the North-East. Extinction indicates that the star cannot be closer than 1.5 kpc, whereas the work by [12] makes very unprobable that the star is beyond 2.3 kpc from the Sun. The adopted distance (the distance to Cyg OB2, as determined by [2]) lies in between and in addition the proper motion of 2MASS J20395358+4222505 is consistent with that of the stars in Cyg OB2. However, there is no direct evidence of its membership, and the Gaia parallaxes have a large error. Therefore, although probable, we cannot be completely sure that 2MASS J20395358+4222505 belongs to the Cyg OB2 association.

What makes 2MASS J20395358+4222505 a very interesting object to study in relation to its parameters is that it has a very large wind terminal velocity for its spectral type (see Tab. 1) combined with a large mass-loss rate (which by the way results in a spectacular H_α emission

profile). This places the star between the normal B-supergiants and the hot hypergiants, from which only a handful are known in the Milky Way. Therefore, the star seems to be in a transition stage (see Fig. 1) whose study can shade new light on the structure of this kind of stars. But surprisingly, there were more findings that made 2MASS J20395358+4222505 even more interesting.

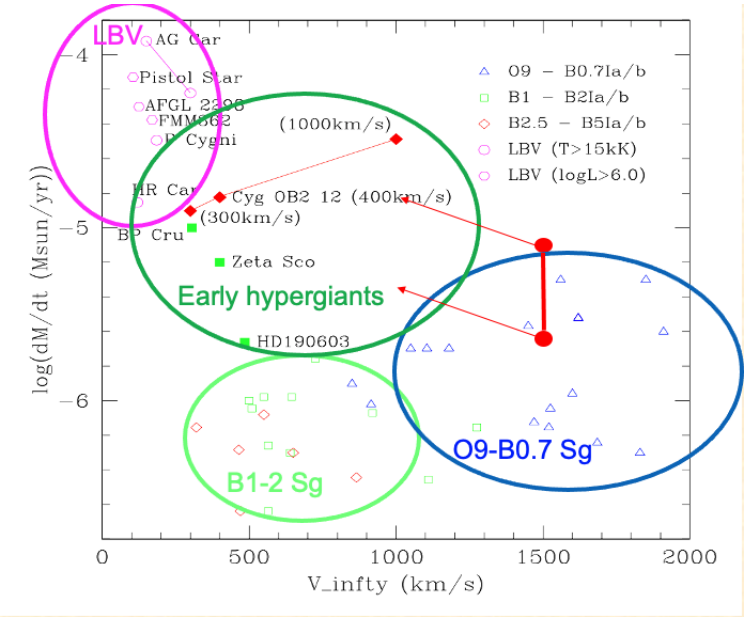

Figure 1: (adapted from [3]) Terminal wind velocity versus mass loss rate for different groups of massive hot stars. The two red points indicate the position of 2MASS J20395358+4222505 in this diagram (taking the distance uncertainty into account) whereas the two arrows indicate the direction in which the terminal velocity is expected to evolve (according to the $T_{\rm eff}$ vs. ($V_\infty/V_{\rm escape}$) diagram in [9] (see their Fig. 12)

.

3 Is 2MASS J20395358+4222505 a binary?

During the commissioning of the MEGARA spectrograph we took spectra with the LR-B, LR-U and HR-R gratings. But because of the needs of the commissioning tasks, these observations couldn't be taken consecutively. The observations with the LR-B grating were carried out on the night of August 29, 2017, whereas those with the LR-U and HR-R gratings were taken the night after, with some time difference. The surprise came when later inspecting the data: while the HR-R and LR-U observations gave radial velocities of -10 and +15 $\rm km\,s^{-1}$(with a large uncertainty of $\pm$20 $\rm km\,s^{-1}$), the spectrum taken the day before with the LR-B grating showed a radial velocity of 68$\pm$23 $\rm km\,s^{-1}$. We can see those variations in Fig. 2. Interestingly, the lightcurve of 2MASS J20395358+4222505 obtained by the TESS satellite shows two small dips, separated by 13.25 days. Although at this stage the possible

binarity of 2MASS J20395358+4222505 was still based on circumstancial evidence, it was a clear possibility.

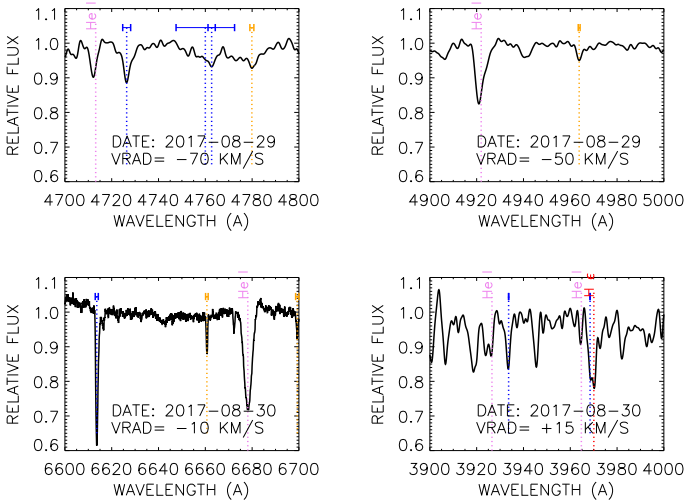

Figure 2: Radial velocity variations in the MEGARA observations of 2MASS J20395358+4222505. Top: observations with the LR-B grating on August 29, 2017; Bottom: observations with the HR-R (left) and LR-U (right) gratings. We have marked the stellar spectral lines and interstellar features (bars indicate their widths; orange features are usually weaker than blue ones)

4 The nature of the binary 2MASS J20395358+4222505

We have obtained new observations of 2MASS J20395358+4222505, but now with more spectrographs: MEGARA@GTC, FIES@NOT and CARMENES@3.6m. Fig. 3 shows three spectra obtained in different nights, where we can easily see the radial velocity variations spanning nearly 200 $\mathrm{km\,s^{-1}}$.

In addition to the three spectra shown in Fig. 3 we have 12 additional spectra taken at different nights from which we can determine the radial velocity. We have used those spectra to estimate a possible period and velocity amplitude from the radial velocity curve using the rvfit procedure in idl (see [7]). We obtained a best-fitting period of 12.4 days and a value of the semi-amplitude of the radial velocity curve of 95 $\mathrm{km\,s^{-1}}$. Thus we confirm that 2MASS J20395358+4222505 is a binary, whose present primary is a massive early B-supergiant orbiting at high velocity around the center of mass of the system.

The confirmation of the binarity of 2MASS J20395358+4222505 is the most important

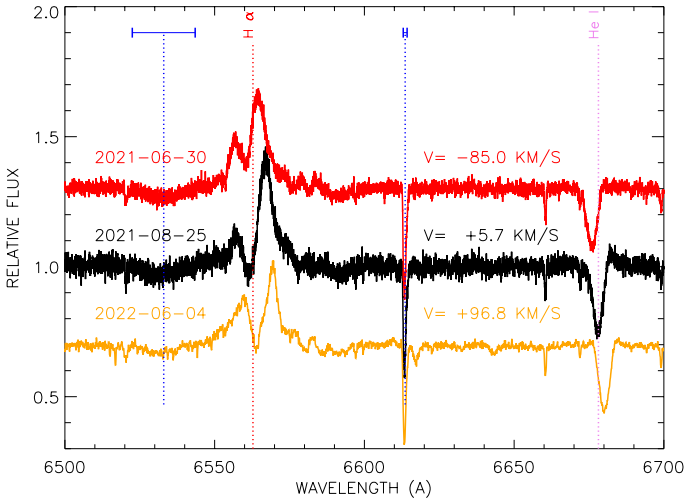

Figure 3: Spectra of the H_α region obtained in three different nights with CARMENES@3.6m (upper two spectra) and MEGARA@GTC (bottom spectrum). We have marked the H_α and HeI 6678 lines, as well as the interstellar line at 6613.62 Å and the interstellar band centered at 6533 Å

.

firm result of the present work. However, with due caution, we can especulate about the nature of the companion. From the radial velocity curve, and assuming an spherical orbit, an inclination of the orbital plane of 90 degrees, a period of 13 days (intermediate between the dips separation in the TESS lightcurve and that obtained with rvfit) and a semiamplitude of the radial velocity curve of 100 $\mathrm{km\,s^{-1}}$, we obtain a mass function of 1.35 $M_\odot$, implying a secondary mass of $\sim$18 $M_\odot$.

What could be the nature of such a companion? If still in the main sequence, it should be an O9V star with $T_{\rm eff}\sim$ 33 000 K, and an absolute visual magnitude of $M_v \sim -4.0$. That would imply a difference of Δm$\sim$ 3.3 mag. with the primary. Simulations indicate that we should see such a star in high quality spectra, like those presented in Fig. 3. If correct, that would imply that the companion should be a compact object and, with the estimated mass, a massive stellar black hole. However, there are several problems with this interpretation: (a) the O9V star could be hidden in the spectrum due to a large rotational velocity (if the orbital and rotational velocities are synchronized, the secondary should rotate at about 250 $\mathrm{km\,s^{-1}}$); and (b) we see neither X-rays nor ellipsoidal variations in the light curve, which would be expected in a system with a supergiant filling its Roche lobe (as the parameters of the system indicate) close to a black hole.

Therefore we conclude that the binary nature of 2MASS J20395358+4222505 has been

confirmed. But the nature of the companion, key to characterize the system and its past and future evolution, is still open.

References

[1] Berlanas, S.R., Herrero, A., Comerón, F. et al., 2018, A&A, 612, A50

[2] Berlanas, S.R., Wright, N., Herrero, A., et al., 2019, MNRAS, 484, 18

[3] Clark, J.S., Najarro, F., Negueruela, I. et al., 2012, A&A, 541, A145

[4] Comerón, F., & Pasquali, A. 2012, A&A, 543, A101

[5] Gil de Paz, A., Carrasco, E., Gallego, J., et al., 2018, Proc. SPIE, 10702, p.1070217

[6] Herrero, A., Berlanas, S.R., Gil de Paz, A. et al., 2022, MNRAS, 511, 3113

[7] Iglesias-Marzoa, R., López-Morales, M., Arévalo Morales, M.J., 2015, PASP, 127, 567

[8] Maíz Apellániz, J., Evans, C.J., Barbá, R.H. et al., 2014, A&A, 564, A63

[9] Markova, N. & Puls, J. 2008, A&A478, 823

[10] Massey, P. & Thomson, A.B. 1991, AJ 101, 1048

[11] Münch, L. & Morgan, W. W., 1953, ApJ, 118, 161

[12] Pantaleoni González, M., Maíz Apellániz, J., Barbá, R.H. & Reed, B.C., 2021, MNRAS, 504, 2968

[13] Puls J., Urbaneja M. A., Venero R., Repolust T., Springmann U., Jokuthy A., Mokiem M. R., 2005, A&A, 435, 669

[14] Rivero-González, J.G., Puls, J. & Najarro, F., 2011, A&A, 536, A58

[15] Santolaya-Rey, A.E., Puls, J., Herrero, A., 1997, A&A, 323, 488

[16] Schulte, D.H., 1958, ApJ, 128, 41

[17] Zacharias, N., Monet, D.G., Levine, S.E. et al. , 2004, AAS 205, 4815

Highlights of Spanish Astrophysics XI, Proceedings of the XV Scientific Meeting of the Spanish Astronomical Society held on September 4–9, 2022, in La Laguna, Spain. M. Manteiga, L. Bellot, P. Benavidez, A. de Lorenzo-Cáceres, M. A. Fuente, M. J. Martínez, M. Vázquez- Acosta, C. Dafonte (eds.), 2023

The interaction of a planetary nebula with the ISM.

Manchado, A.[1,2,3] **Villaver, E.**[4]**, García-Segura, G.**[5]**, and Bianchi, L.**[6]

[1] Instituto de Astrofísica de Canarias, Vía Láctea S/N, E-38200 La Laguna, Tenerife, Spain
[2] Departmento de Astrofísica, Universidad de La Laguna (ULL), E-38206 La Laguna, Tenerife, Spain
[3] Consejo Superior de Investigaciones Científicas, Spain
[4] Centro de Astrobiología (CAB, CSIC-INTA), ESAC Campus Camino Bajo del Castillo, s/n, Villanueva de la Cañada, 28692, Madrid, Spain
[5] Instituto de Astronomía-UNAM, Apartado postal 877, Ensenada, 22800 Baja California, México
[6] Department of Physics and Astronomy, Johns Hopkins University,Baltimore, MD 21218, USA

Abstract

NGC 7293, the Helix nebula, represents one of the rare instances in which theoretical predictions of stellar evolution can be accurately tested against observations since the precise parallax distance and the velocity and proper motion of the star are well known. We present numerical simulations of the formation of the Helix PN that are fully constrained by the (inferred) progenitor stellar mass, stellar evolution history, and star-interstellar medium (ISM) interaction. We have followed the evolution of the star from the early Asymptotic Giant Branch (AGB) phase to the PN stage and modeled the density and kinematical evolution of the expanding shells considering the observed relative motion of the star. In the simulations, multiple bow-shock structures are formed by fragmentation of the shock front where the direct interaction of the stellar wind with the ISM takes place.

1 Introduction

NGC 7293 (a.k.a The Helix, PN G036.1−57.1) is one of the planetary nebula (PN) with a very good determination of its distance; 202 pc from Gaia DR3 [4]. The central star has a mass of 0.60±0.02 $M_{\odot}$[1] and a high temperature $T_{eff} = 104\,000$ K [5] implying that the star+nebula system is in a rather evolved stage. The *Galaxy Evolution Explorer* (*GALEX*; [8]) wide field-of-view (26 arcminutes) revealed for the first time striking morphological features in the form of extended bow-shocks beyond the nebular halo ([2]).

2 Numerical simulations

The numerical simulations have been performed with the fluid solver ZEUS-3D ([10]), developed by M. L. Norman and the Laboratory for Computational Astrophysics. The computations have been carried out on a 2D spherical polar grid with the angular coordinate ranging from 0° to 180° and a physical radial extension of 3 pc. They have been run at a resolution of 1600 × 1440 zones in the radial and angular coordinates of the grid respectively (or equivalently ∼ 388 au × 0.125°). Our boundary conditions are the AGB stellar wind of a 1.5 $M_{\odot}$star and a ISM density of $n_{\rm ISM}$= 0.06 cm^3, and a relative velocity respect to its ambient medium of 40 $km\,s^{-1}$. For the post-AGB stage and PN evolution we follow the stellar wind according to the prescription given in [12] by using the post-AGB evolutionary sequence given by [14] for a hydrogen burner with solar metallicity for the assumed stellar mass.

Note that the wind velocities of the central stars of PNe are several orders of magnitude higher than those experienced during the AGB phase. For the wind temperature on the AGB we used the effective temperature of the star. During the PN stage we consider the dynamics induced by the photoionization of the gas by using the approximation implemented by [3] to derive the location of the ionization front. Radiative cooling follows the cooling curves of [11] and [6] for gas temperatures above 10^4 K and according to [7] for temperatures between 10^2 and 10^4 K. The unperturbed gas is treated adiabatically. Finally, the photoionized gas is always kept at 10^4 K, so no cooling curve is applied inside the photoionized region unless there is a shock. The simulations start at the early-AGB phase, before the onset of the first thermal pulse, and continue for 20 000 years into the PN stage [1]. The stellar time for which we run the simulations is 8.3×10^5 yr.

To model the interaction process it is fundamental to know the velocity of the object with respect of its environment, relative to its external ISM. Fortunately, the available observations of the Helix allow a good determination of the space velocity of the star. Using a radial velocity of -15 $km\,s^{-1}$for the nebula, the parallax distance of 202 pc [4] and the proper motion measurement of Gaia DR3 we determined a relative velocity of NGC 7293 with respect to its ambient medium of 37.5 $km\,s^{-1}$. The Helix star belongs to the kinematic population of the thin disk in the Galaxy and as such this velocity is consistent with the range observed for this population 10-40 $km\,s^{-1}$[7]. For the simulations we have thus set the relative velocity of of NGC 7293 with respect to its ambient medium to 40 $km\,s^{-1}$.

3 RESULTS

In Figure 1., (right panel) we show the result of the numerical simulation after 819000 yr in the AGB, and 1000 yr, after the onset of the photoionization. In the left panel we show the *GALEX* FUV filter image, which at a distance of 202 pc has a FOV of 4.23 pc. It is remarkable that both figures show bow shock structures in the direction of the movement, and that the actual size in parsec is quite similar. We conclude that the morphology of the

[1]The zero age of the PN is set at the time when the star's effective temperature reaches 10 000 K

Helix can be explained by the evolution of a 1.5 $M_{\odot}$star interacting with an ISM with a relative velocity of 40 $\mathrm{km\,s^{-1}}$. apparent multiple bow-shocks.

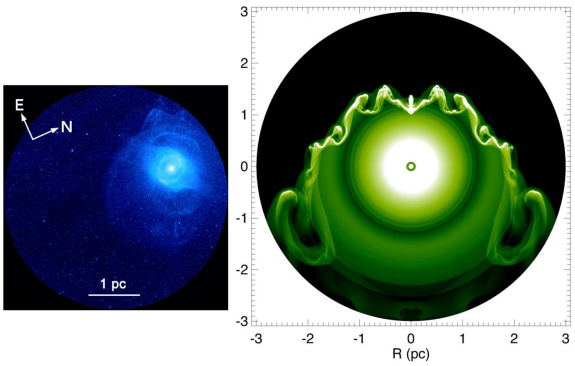

Figure 1: Left, *GALEX* FUV image of NGC 7293. At a distance of 202 pc, the FOV is 4.23 pc. Right, density map from our simulations, the snapshot corresponds to a ∼1 000 yr old PN. The morphology of the UV features is reproduced by the simulations; more important, the physical scale of the predicted structures matches the observations.

Acknowledgments

A. M. acknowledge support from the ACIISI, Gobierno de Canarias and the European Regional Development Fund (ERDF) under grant with reference PROID2020010051 as well as from the State Research Agency (AEI) of the Spanish Ministry of Science and Innovation (MICINN) under grant PID2020-115758GB-I00.

References

[1] Benedict, G. F., McArthur, B. E., Napiwotzki, R., et al. 2009, AJ, 138, 1969

[2] Bianchi, L., Manchado, A., Forster, K. 2012, IAU Symp. 283 , p. 308

[3] Garcia-Segura, G., & Franco, J. 1996, ApJ, 469, 171

[4] González-Santamaría, I., Manteiga, M., Manchado, A., et al. 2021, A&A, 656, A51. doi:10.1051/0004-6361/202141916

[5] Guerrero, M. A., & De Marco, O. 2013, A&A, 553, A126

[6] Dalgarno, A., & McCray, R. A. 1972, ARAA, 10, 375

[7] MacDonald, J. & Bailey, M. E. 1981, MNRAS, 197, 995

[8] Martin, D. C., Fanson, J., Schiminovich, D., et al. 2005, ApJ Letters, 619, L1

[9] Martin, D. C., et al. 2007, Nature, 448, 780

[10] Stone, J. M., Mihalas, D., & Norman, M. L. 1992, ApJS, 80, 819

[11] Raymond, J. C., & Smith, B. W. 1977, ApJS, 35, 419

[12] Villaver, E., García-Segura, & Manchado, A. 2002a, ApJ, 571, 880

[13] Villaver, E., García-Segura, G., & Manchado, A. 2003, ApJ Letters, 585, L49

[14] Vassiliadis, E., & Wood, P. R. 1994, ApJS, 92, 125

Highlights of Spanish Astrophysics XI, Proceedings of the XV Scientific Meeting of the Spanish Astronomical Society held on September 4–9, 2022, in La Laguna, Spain. M. Manteiga, L. Bellot, P. Benavidez, A. de Lorenzo-Cáceres, M. A. Fuente, M. J. Martínez, M. Vázquez- Acosta, C. Dafonte (eds.), 2023

The planetary nebula NGC 6153 through the eyes of MUSE.

Gómez-Llanos, V.[1,2], García-Rojas, J.[1,2], Morisset, C.[3], Jones, D.[1,2], Monteiro, H.[4], Wesson, R.[5], Boffin, H. M. J.[6], Corradi, R. L. M. [2,7], Pérez-Toledo, F.[7], and Rodríguez-Gil, P.[1,2]

[1] Instituto de Astrofísica de Canarias, E-38205 La Laguna, Tenerife, Spain
[2] Departamento de Astrofísica, Universidad de La Laguna, E-38206 La Laguna, Tenerife, Spain
[3] Instituto de Astronomía, UNAM, Apdo. postal 106, C.P. 22800 Ensenada, Baja California, México
[4] Instituto de Física e Química, Universidade Federal de Itajubá, Av. BPS 1303-Pinheirinho, 37500-903, Itajubá, Brazil
[5] School of Physics and Astronomy, Cardiff University, Queen's Buildings, The Parade, Cardiff CF24 3AA, UK
[6] European Southern Observatory, Karl-Schwarzschild-Str. 2, D-85738 Garching bei München, Germany
[7] Gran Telescopio CANARIAS S.A., c/ Cuesta de San José s/n, Breña Baja, E-38712 Santa Cruz de Tenerife, Spain

Abstract

In this contribution, we present the results of a study on the high abundance discrepancy factor (ADF $\sim$ 10) planetary nebula (PN) NGC 6153 with MUSE. We have constructed flux maps for dozens of emission lines, that allowed us to build spatially resolved maps of extinction, electron temperature (T_e), electron density (n_e), and ionic abundances. We have simultaneously constructed ADF maps for O^+ and O^{2+} and found that they centrally peak in this PN, with a remarkable spatial coincidence with the low T_e found from recombination line diagnostics. This finding strongly supports the hypothesis that two distinct gas phases co-exist: one cold and metal-rich, and a second warm and with "normal" metal content. We show that to build T_e([N II]) and ionic abundance maps of low-ionization species for these objects, recombination contribution to the auroral [N II] and [O II] lines must be properly evaluated and corrected.

1 Introduction

Since [16] first reported it, the abundance discrepancy problem, i. e., the long standing difference between the chemical abundances computed for a given metal ion from recombination lines (RLs) or collisionally excited lines (CELs) has cast doubt on the chemical

abundances determinations in both planetary nebulae (PNe) and H II regions. The RL/CEL ratio, the so-called abundance discrepancy factor (ADF) can show extreme values (up to 700) in some PNe. Some scenarios have been proposed to explain this problem (see [4] and references therein). However, for PNe there are several observational evidences pointing to the presence of two gas components with different chemical composition (and possibly kinematics) ([2, 6, 15, 11, 3, 9, 12, 13]). This bi-abundance scenario (first proposed by [14]) consists of a "normal" chemical composition gas with a relatively warm electron temperature (T_e ~10,000 K) that emits mainly the metal CELs and the H and He RLs , and an H-poor gas with a much lower temperature (~1,000 K) and higher density whose emission is dominated by metals RLs.

NGC 6153 is a southern PN with strong emission of metal RLs, thus making it a good object to address the abundance discrepancy problem ([8, 10, 15, 17, 7, 13]). The chemical composition of this PN has been extensively studied by different authors who hypothesised on the presence of two plasma components based on deep multi-wavelength spectroscopic data ([8]) or on integral field spectroscopy ([15]). Very recently, making use of a very high-resolution spectra and position-velocity maps, [13] reached a similar conclusion with the addition of finding also differences in the kinematics of the gas between the two components. From the theoretical side, empirical, one-dimensional, and 3D photoionization models have been constructed for this object considering a chemically inhomogeneous gas, successfully fitting both the RLs and CELs ([8, 10, 17, 7]) and hence, strengthening the bi-abundance scenario for this object.

The analysis of 2D spectroscopic data of PNe with large ADFs have revealed that extreme care should be taken when constructing physical conditions and ionic abundance maps, especially for low ionization species (see [5]). In this work we present some of the preliminary results we have obtained from the analysis of very deep MUSE data of NGC 6153.

2 Observations

NGC 6153 was observed with the Multi Unit Spectroscopic Explorer (MUSE) integral-field spectrograph ([1]) on the Very Large Telescope (VLT), in seeing-limited mode, on the night of 6 to 7 July 2016. We used the extended mode of MUSE (WFM-NOAO-E), which covers the wavelength range $460 - -930$ nm with an effective spectral resolution that increases from $\mathcal{R} \sim 1600$ at the bluest wavelengths to $\mathcal{R} \sim 3500$ at the reddest wavelengths. The on-target exposure time was 2320 s divided in several long and short exposures. The observing conditions, observation techniques and reduction process have been described by [5].

3 Electron temperature maps

From the MUSE observations of NGC 6153, we have constructed flux maps and their uncertainties for more than 60 emission lines following the same methodology as described by [5]. We then built spatially resolved maps of extinction, electron temperature (T_e), electron density (n_e), and ionic abundances. The T_e and n_e maps were obtained using different line ratios

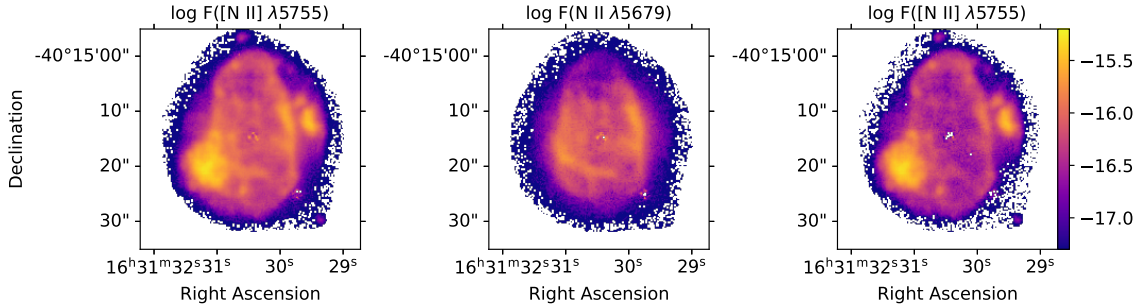

Figure 1: Left panel: spatial distribution of the auroral [N II] λ5755 emission line in the PN NGC 6153 prior to applying the recombination contribution. Middle panel: spatial distribution of the N II λ5679 RL. Right panel: same as left panel but after applying the recombination contribution correction, considering a constant $n_e = 10^4\,cm^{-3}$ and $T_e = 2,000\,K$ for the recombination emission.

as diagnostics (e.g., [N II] λ5755/λ6548[1] and [S III] λ6312/λ9069 for T_e, and [S II] λ6731/λ6716 and [Cl III] λ5538/λ5518 for n_e). However, the diagnostics based on second-row elements such as O and N can have an important contribution from recombination to the low metastable levels, like [N II] λ5755 and [O II] $\lambda\lambda$7320, 7730, that if not corrected, will lead to an overestimate of the temperature. This may be especially important for spatially resolved observations of PNe with high ADF, where in extreme cases, the [N II] λ5755 emission can be dominated by recombination (see Fig. 7 in [5]).

In this work, we present the recombination contribution to [N II] λ5755 in the PN NGC 6153 (ADF$\sim$10 [8, 15]). In the left panel of Fig. 1 we show the spatially resolved emission of [N II] λ5755. To estimate its recombination contribution we use Eq. 1 presented by [5], which is based on the emission of N II λ5679 (middle panel of Fig. 1) and the recombination emissivities of $j_{5755}(T_e, n_e)$ and $j_{5679}(T_e, n_e)$. [13] presents an estimate of the electron temperature and density of the recombination emitting region in NGC 6153, giving an average value of $n_e = 10^4\,cm^{-3}$ and $T_e = 2,000\,K$. We use these values for the recombination emissivities. The corrected [N II] λ5755 emission map is presented in the right panel of Fig. 1, which shows the main emission in two bright knots and on the edges of the nebula's main shell, while the uncorrected flux also shows a bright emission at inner regions of the nebula. To emphasize the importance of this correction, in Fig. 2 we show the [N II] λ5755/λ6548 temperature distribution map with and without applying the correction on the top right and left panels of Fig. 2, respectively. Notice the considerably higher temperatures in the inner parts of the nebula that are predicted without the correction. We also explore the effect of increasing the temperature of the recombination emitting region to 4,000 K and 6,000 K (bottom left and bottom right panels of Fig. 2), which results in a decrease on the temperature in the inner parts of the nebula.

We tried to compute T_e and n_e from metal RL diagnostics in order to break the degeneracies found by [5] when trying to fully characterize the H-poor component. However, the

[1]Hereafter all wavelengths will be in Å.

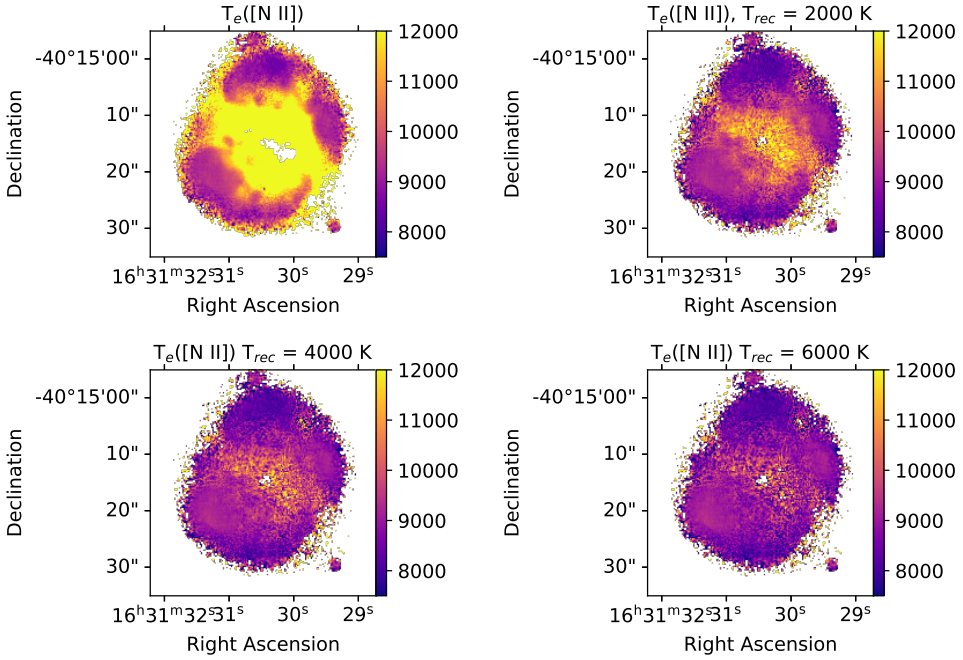

Figure 2: Electron temperature map computed from the T_e-sensitive [N II] $\lambda\lambda$5755/6548 line ratio. In the top left panel we show the map with no recombination correction to the [N II] λ5755 auroral line; in the top right, bottom left, and bottom right panels we show the maps constructed with the recombination correction, considering a constant $n_e = 10^4\,\mathrm{cm}^{-3}$ and $T_e = 2,000\,\mathrm{K}$, $4,000\,\mathrm{K}$, and $6,000\,\mathrm{K}$, respectively, for the recombination emission.

most sensitive O II and N II RLs are either out of the wavelength range covered by MUSE or the maps constructed were too noisy to reach any conclusion. As already pointed out, [13] could estimate the physical conditions of the H-poor component of the gas where most of the metals recombination emission comes. These values can be used to qualitatively estimate the influence of the cold region on abundance determinations and to determine the oxygen mass ratio between the cold and the warm regions (Gómez-Llanos et al. in prep.)

4 The abundance discrepancy maps

Once we computed the ionic abundances from CELs and RLs, we constructed the abundance discrepancy factor maps for O^+ and O^{2+} following the methodology described by [5]. [15] constructed the ADF(O^{2+}) map for NGC 6153, but only sampled a small area of the nebula. [13] made a study on the variation of the ADF over a position-velocity map, finding the highest values at positions close to the central star. These authors also find that the ADF was close to the unity in the diffuse emission beyond the receding side of the main shell of the nebula. As far as we know, this is the first time that the ADF is mapped for the whole nebula.

On the other hand, we have constructed the H I RL temperature diagnostic from the ratio of the Paschen jump to the H I P9 λ9229 line, following the same methodology described by [5]. This temperature diagnostic can provide hints on the influence of the cold gas on the computation of the global physical conditions in the nebula (Gómez-Llanos et al. in prep.).

In Fig. 3 we present the spatial distribution of log[ADF(O^+)] (left panel) and log[ADF(O^{2+})] (central panel). In both maps, the ADF peak is clear in the central parts of the nebula, although the ADF variation in these central zones is not as extreme as that in the three high-ADF PNe presented in [5]. This is an expected behaviour if we take into account the lower ADF value in the integrated spectrum of NGC 6153. In the right panel of Fig. 3, we illustrate the spatial distribution of the T_e obtained from the H I Paschen jump. The spatial coincidence between the high values of the ADF(O^{2+}) and the low T_e's in this map is remarkable. This behavior strongly supports the hypothesis of the presence of a cold, metal-rich gas phase embedded in a warm gas phase with"normal" metal content. The full analysis of the NGC 6153 MUSE data set will be presented in a forthcoming paper (Gómez-Llanos et al., in prep.).

Acknowledgements

This paper is based on observations made with ESO Telescopes at the Paranal Observatory under program ID 097.D-0241. VG-LL and JG-R acknowledge financial support from the Canarian Agency for Research, Innovation and Information Society (ACIISI), of the Canary Islands Government, and the European Regional Development Fund (ERDF), under grant with reference ProID2021010074. JG-R acknowledges support from an Advanced Fellowship under the Severo Ochoa excellence program CEX2019-000920-S. DJ acknowledges support from the Erasmus+ program of the European Union under grant number 2020–1–CZ01–KA203–078200. VG-LL, JG-R, DJ, and RC acknowledge support under grant P/308614 financed by funds transferred from the Spanish Ministerio de Ciencia,

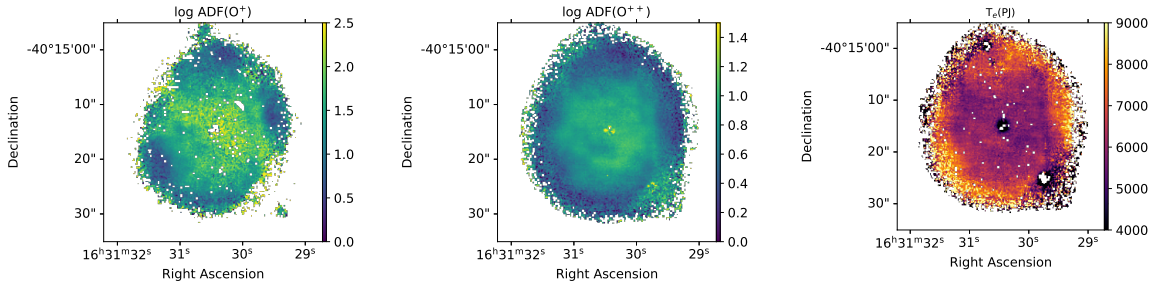

Figure 3: Spatial distributions of log[ADF(O^+)] (left panel) and log[ADF(O^{2+})] (central panel). In the right panel we show the T_e map obtained from the Paschen jump relative to H I P9 λ9229 line.

Innovación y Universidades, charged to the General State Budgets and with funds transferred from the General Budgets of the Autonomous Community of the Canary Islands by the MCIU. CM acknowledges support from grant UNAM / PAPIIT –IN101220. PR-G acknowledges support from the Consejería de Economía, Conocimiento y Empleo del Gobierno de Canarias and the European Regional Development Fund (ERDF) under grant with reference ProID2021010132 and ProID2020010104.

References

[1] Bacon, R., et al. 2010, Proceedings of the SPIE, 7735, 773508

[2] Barker, T. 1982, ApJ, 253, 167

[3] García-Rojas, J. et al. 2016, ApJL, 824, 27

[4] García-Rojas, J. et al. 2019, arXiv e-prints, arXiv:1904.06763

[5] García-Rojas, J., et al. 2022, MNRAS, 510, 5444

[6] Garnett, D. R., & Dinerstein, H. L. 2001, ApJ, 558, 145

[7] Gómez-Llanos, V. & Morisset, C. 2020, MNRAS, 497, 3363

[8] Liu, X. -W., et al. 2000, MNRAS, 312, 585

[9] Peña, M. et al. 2017, MNRAS, 472, 1182

[10] Péquignot D., et al. 2002, Revista Mexicana Astronomia y Astrofisica Conference Series, 12, 142

[11] Richer, M. G. et al. 2013, ApJ, 773, 133

[12] Richer, M. G. et al. 2017, AJ, 153, 140

[13] Richer, M. G., et al. 2022, AJ, 164, 243

[14] Torres-Peimbert, S. et al. 1990, A&A, 233, 540

[15] Tsamis Y. G., et al. 2008, MNRAS, 386, 22

[16] Wyse, A. B. 1942, ApJ, 95, 356

[17] Yuan, H. B., et al. 2011, MNRAS, 411, 1035

Highlights of Spanish Astrophysics XI, Proceedings of the XV Scientific Meeting of the Spanish Astronomical Society held on September 4–9, 2022, in La Laguna, Spain. M. Manteiga, L. Bellot, P. Benavidez, A. de Lorenzo-Cáceres, M. A. Fuente, M. J. Martínez, M. Vázquez- Acosta, C. Dafonte (eds.), 2023

The power of XP Gaia spectrophotometry and Self-Organizing Maps to analyze the evolutionary state and physical properties of Milky Way stars.

Lara Pallas-Quintela[1], Daniel Garabato[1], Minia Manteiga[1], and Carlos Dafonte[1]

[1] CIGUS-CITIC, University of A Coruña

Abstract

The Gaia space telescope is able to gather a vast amount of data from each of the sources it explores. Among them, are the Blue and Red Photometer (BP/RP) spectra, also known as XP spectra. Most of those sources (and their physical properties) are easy to identify, but for some others, it is necessary to perform a deeper study on them. More precisely, at the Outlier Analysis (OA) working package, led by the University of A Coruña, it was created an artificial intelligence algorithm able to determine the spectral type of those atypical objects, which is followed by a template-matching procedure.

In this work, it is introduced a method to extract representative sources to be used as templates from a Hertzsprung–Russell diagrams according to the evolutionary stage of the stars of which it is composed. Therefore, we will be able to make a more refined star-classification for the following Gaia's Data Release.

1 Introduction

On June 13^{th}, the Gaia Space Mission made available to the scientific community its third data release, also known as Gaia DR3 or GDR3. GDR3 made a huge difference with respect to the previous ones by being the first time that spectra gathered from the telescope were published. Among the data products, are BP and RP spectra, which are a low-resolution type of spectra that, nevertheless, are very powerful for extracting the properties of the sources they represent. The Outlier Analysis (OA) working package [4], is in charge of using artificial intelligence (AI) algorithms to group similar BP/RP spectra which are considered to be atypical or outliers, and finally try to find its representative spectral type. Such task is performed following an unsupervised learning process using Self-Organizing Maps (SOM)[3].

Since it is being used an unsupervised AI algorithm, if we want to set the spectral type of each neuron in the trained map, it is important to have a well-characterized subset of sources which are representative of the objects Gaia gathers, also known as templates. In the current work, we are introducing how important is this task and how it is possible to extract templates for stars from Hertzsprung–Russell (HR) diagrams. Before diving into the

template extraction method, it will be made a brief introduction of SOM Maps and the results achieved at OA in DR3.

2 Self-Organizing Maps

The machine learning algorithm implemented at OA is a neural network-based technique which aims to group a set of data in a multidimensional grid (typically 2D) preserving the topological order of the input elements, that is, similar input spectra will be grouped in similar output neurons, the well-known Self-Organizing Maps [3]. It was in GDR3 when the first OA results were published by processing 56 million sources. Such outcomes can be graphically manipulated through the GUASOM platform [1]. In Figure 1 are shown the neurons which matched any of the reference templates, making a classification according to the evolutionary state of the stars.

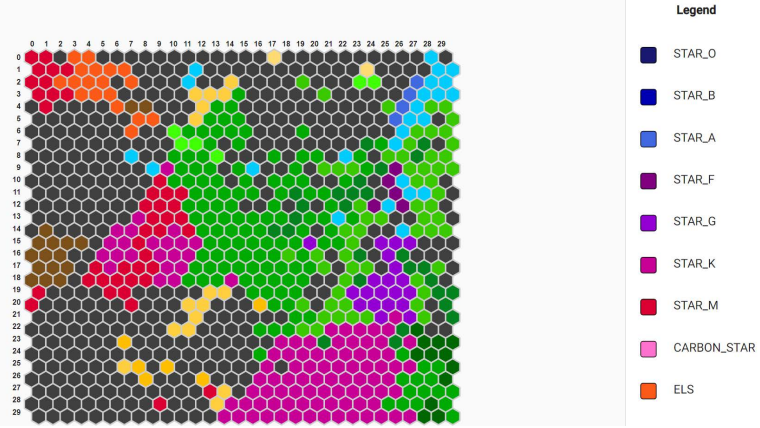

Figure 1: Result SOM Map from OA. Available at the GUASOM platform

2.1 The importance of selecting representative templates

Since the AI model is trained following an unsupervised classification algorithm, the training dataset does not contain any tagging information about the sources being used. This means that the model is just generated by the similarity of the processed signals. Nonetheless, at OA we want to tag the neurons for their sources to be characterized according to their spectral type. For such, it is necessary to follow a neuron-tagging process once the model is trained.

Among the statistics obtained from the training process, it is computed the "prototype" of each neuron, which is a spectrum representing the average of every BP/RP spectra contained in such neuron. For performing the neuron-tagging process, it is checked which template is more similar to the prototype of the neuron and, afterwards, it is assigned to the neuron the spectral type of such template.

To make the classification as meaningful as possible, it is important that the templates are as representative as possible of the data OA deals with. In order to go on refining the

neuron-tagging process, it was developed a method to extract templates from an HR diagram, that will be introduced in the following section.

3 Template extraction from HR diagrams

In order to achieve a finer star-classification for OA in DR4, we are developing a method to extract template sources from the fiducial line (line traced on highly populated areas across M_g) of a low-extinction HR diagram based on the ones introduced in [2] for DR2. We built our own based on DR3 sources and, in addition to the conditions stated in [2], we set a residual threshold value for extinction of $a_g < 0.003$, getting an HR diagram composed of 16.7 million low-extinction stars. The distribution of such stars is shown in Figure 2.

3.1 Method followed for extracting templates from HR diagrams

Once the general idea was explained, it is time to dive into the method followed, which is summarized in the following four steps:

1. **Dividing the HR diagram into 3 different areas**. The sources under the diagram are divided into *white dwarfs*, *giants* and *main sequence*. Even though white dwarfs were already differentiated from the other stars at OA in DR3, it is also interesting to differentiate between giants and main sequence stars, since, it is also interesting to analyse the feasibility of using XP spectra to differentiate stars according to their evolutionary stages, not necessarily relying on their magnitude and colour values. As shown in Figure 3, for the same spectral type (in this case, G stars), depending on their stage, even though both spectra are quite similar, it is possible to find differences between them, corroborating such differentiations according to the evolutionary stages of the stars.

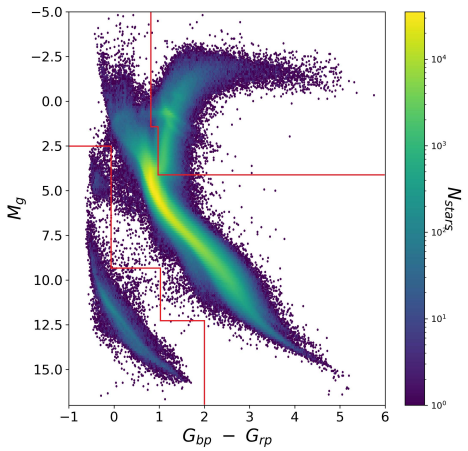

Figure 2: HR diagram used for the template selection, divided in the three main areas.

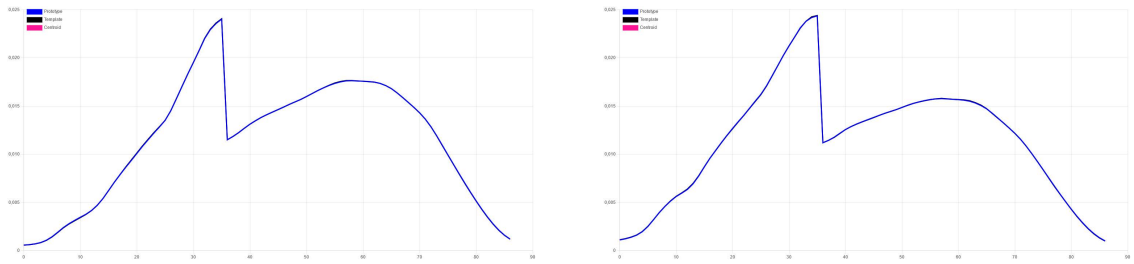

(a) Main sequence G star (b) Giant G star

Figure 3: Comparison of the BP/RP spectra of two G stars, one from main sequence (left) and the other one from the giants branch (right).

2. **Building the fiducial line**. The fiducial line represents the most populated regions of each of the previously defined areas in terms of magnitude. Even though this procedure worked really well for both the main sequence and giant branch areas, we were still unable to do so for white dwarfs. In the latter case, for white dwarfs located at very close points in the HR diagrams, we can find major differences among spectra for not to be able to group them in the same spectral type in a reliable way.

   To carry be able to create the fiducial lines, the main sequence and the giants area is divided in small regions in terms of magnitude to find its most populated point. Afterwards, such points were interpolated to create a mathematical representation of the most populated regions, as shown in the following Figure:

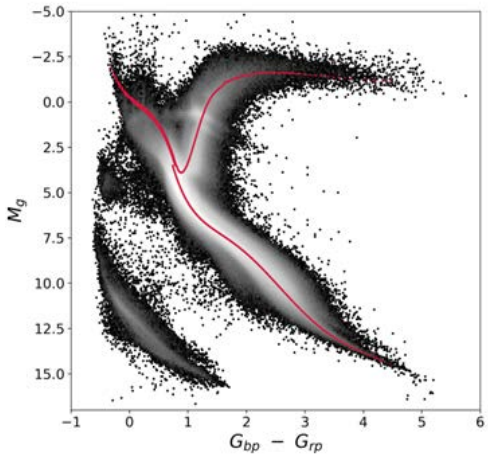

Figure 4: Fiducial lines for *main sequence* and *giant branch* stars.

3. **Selecting templates under the fiducial line**. In this step, there were selected the candidate sources to be used as templates for tagging a SOM Map. For such, biased

spectra were removed and, to simplify the list of templates, we only picked some samples of the ones which were very similar among them, since, as it was previously stated, we only use spectra both for training and labelling the neurons. In this way, we make sure that our templates are built from really representative sample of the stars we are dealing with.

4. **Assigning a spectral type to every template**. Finally, it is assigned a spectral type to each of the templates. Following [5], it was made a colour-Teff transformation and, afterwards, a Teff-spectral type transformation using the tables at [6]. In both cases, it was necessary to take into account if they were main sequence or giant branch stars.

4 Conclusions

With the method explained in this paper, we were able to create a simple and reliable method for extracting templates from an HR diagram following a MK classification. With regard to the next Gaia release, it will be possible for OA to offer to the scientific community a more detailed version of what we did for GDR3.

As it was previously mentioned, this is a reliable algorithm since we are picking spectra from highly populated areas. That is, there is a good sample of stars in the same region with very similar spectra. As a consequence, it is possible to obtain a subset of well-characterized objects that can be used not only for the template-matching procedure followed at OA, but also to explore specific properties that can characterize each type of spectra.

Acknowledgments

We wanted to acknowledge “Xunta de Galicia” for the scholarship granted to the PhD researcher Lara Pallas, with code ED481A 2021/296, for developing her PhD Thesis.

References

[1] Álvarez, M., Dafonte, C. et al., 2022, Neural Comput & Applic, 34, 14

[2] Babusiaux, B. et al., 2018, A&A, 616, 29

[3] Dafonte, C., Garabato, D. et al., 2018, Sensors, 18, 16

[4] Delchambre, L., Bailer-Jones, C.A.L. et al., 2022, A&A, 36

[5] Mucciarelli, A. and Bellazzini, M., 2020, A&A, 616, 29

[6] University of South Iowa, Spectral type characteristics

Highlights of Spanish Astrophysics XI, Proceedings of the XV Scientific Meeting of the Spanish Astronomical Society held on September 4–9, 2022, in La Laguna, Spain. M. Manteiga, L. Bellot, P. Benavidez, A. de Lorenzo-Cáceres, M. A. Fuente, M. J. Martínez, M. Vázquez- Acosta, C. Dafonte (eds.), 2023

The role of turbulence in the chemical evolution of the interstellar medium.

Beitia-Antero, L.[1,2] **and Fuente, A.**[1]

[1] Observatorio Astronómico Nacional, Instituto Geográfico Nacional
[2] Departamento de Física de la Tierra y Astrofísica, Facultad de CC. Matemáticas, Universidad Complutense de Madrid

Abstract

Turbulence is ubiquitous in the interstellar medium (ISM) and can introduce large variations in the density field of molecular clouds. However, the vast majority of chemical models for the ISM can only assume a constant gas density based on line-of-sight averaged observations. In order to assess the impact of these variations of the gas density in the chemical evolution of the ISM, we are conducting a series of magnetohydrodynamical (MHD) numerical simulations of different phases of the ISM with `Athena++`; the resulting three-dimensional distributions of gas are then used to compute the chemical evolution of the system using the code `Nautilus`. In this contribution, we present the first results of our study focused on the chemistry of a molecular cloud filament.

1 Introduction

Observational studies of the chemistry of the interstellar medium (ISM) rely on state-of-the-art chemical codes that, provided a given number of input parameters such as gas and dust temperatures, hydrogen particle number, visual extinction, cosmic ray ionisation rate, the intensity of the local ultraviolet radiation field, and the dust to gas ratio, compute the expected chemical abundances $n_{\rm X}/n_{\rm H}$ of a set of molecules X (CO, HCO^+, N_2H^+, etc.) based on a huge amount of chemical reactions [6, 8]. However, sometimes the predictions made by the models do not match the observations, and it is in fact very complicated to fit all the molecular species to the same chemical model [3]. Appart from the limitations imposed by the observing facilities, the cause of this mismatch between observations and predictions may rely on the chemical networks, input parameters and underlying approximations. The chemical reactions involved in the chemical networks are being revised in laboratories in order to improve the accuracy of the binding energies, although so far only rough estimates have been set with large uncertainties [7]. Therefore, as a complement to laboratory experiments, it seems reasonable to explore to what extent the input parameters might explain the deviations of the predictions from the expectations. In this work, we have focused on two key elements

that drastically affect the predicted abundances: the hydrogen number density and the dust-to-gas ratio.

resulting chemical model and its predictions has been shown, for instance, by [3]. On the other hand, several recent numerical studies have shown that the dust-to-gas ratio is not constant due to turbulent motions of the gas and the decoupling of dust grains as a result of their net charge and their interaction with the ambient magnetic field; these variations of the dust-to-gas ratio are present in all regimes of the ISM, from the diffuse ionised envelopes of molecular clouds [1] to their cool interiors [5] (see Fig. 1).

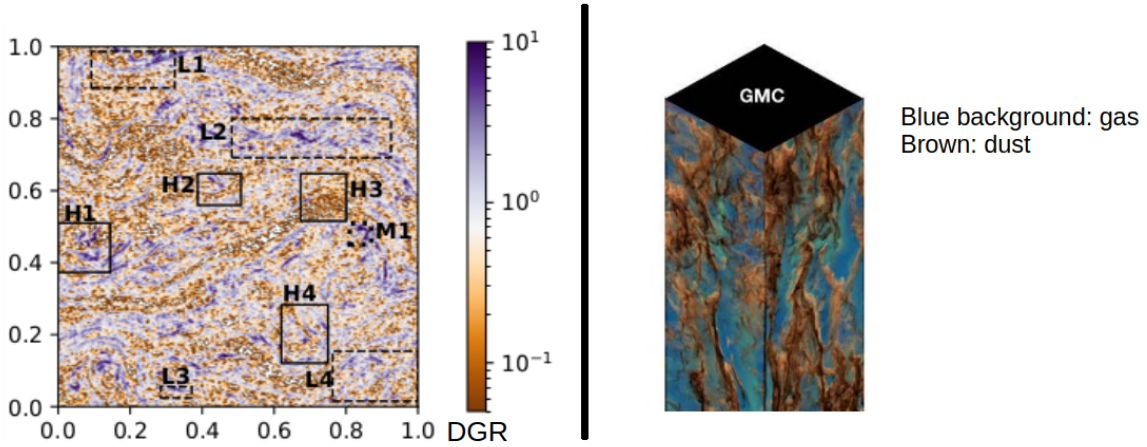

Figure 1: Examples of variations of the dust-to-gas ratio in simulations of the ISM. *Left*: dust-to-gas ratio map for a 2D simulation of a molecular cloud envelope [1]. *Right*: dust (brown) and gas (blue) distribution on a 3D simulation of a giant molecular cloud [5].

In consequence, we want to explore two possible reasons for the mismatch between observations and predictions of chemical models: small-scale density variations caused by turbulence at scales not resolved by telescopes, and variations of the dust-to-gas ratio that affect the abundances of solid-phase formed species. In this contribution we present our results for the first part, the one centred on the effects of turbulence on the predicted chemical abundances. The effects of the variations of the dust-to-gas ratio are going to be assessed in future publications.

2 Chemistry and MHD simulations

In order to recreate the turbulent state of a molecular cloud, we run a simulation with the `Athena++` code [9] in three dimensions under the assumption of isothermal, ideal MHD with periodic boundary conditions and at a resolution of 256^3. We assume a molecular hydrogen particle density $n_{\mathrm{H_2}} = 2.57 \times 10^4$ cm^{-3} with a magnetic field parallel to the x-axis and a strength of $B_0 = 40$ μG. We take a medium initially at rest to which we continuously inject turbulence until the energy injection rate equals the dissipation rate, a point at which we as-

sume we reproduce the steady state of a trans-sonic molecular filament (which is compatible with the interior of a molecular cloud before collapse, see [4]). Although this simulation is dimensionless, for the discussion we always consider a nominal length for our box of 0.05 pc, which is small enough to contain from two to three beams of IRAM 30 m telescope at frequencies between 80 GHz and 200 GHz.

As a consequence of turbulence, we obtain large deviations of the initial gas density of $n_{H_2} = 2.57 \times 10^4$ cm^{-3}, by a factor of up to two orders of magnitude (see Fig 2); regions with high and low gas density share their sheet-like morphology and are extended along the mean magnetic field direction (x-axis). If we take these hydrogen densities and assume a constant gas and dust temperature of $T = 12$ K, a visual extinction $A_V = 4$ mag and a cosmic ray ionisation rate of $\zeta = 5 \times 10^{-17}$ s^{-1}, and retrieve the predicted chemical abundances of the commonly studied molecules with the `Nautilus` code [8] at an age of 10^6 yr (see Fig. 2), we see that turbulence is bound to produce notable differences in the observed abundances of some species, especially CO.

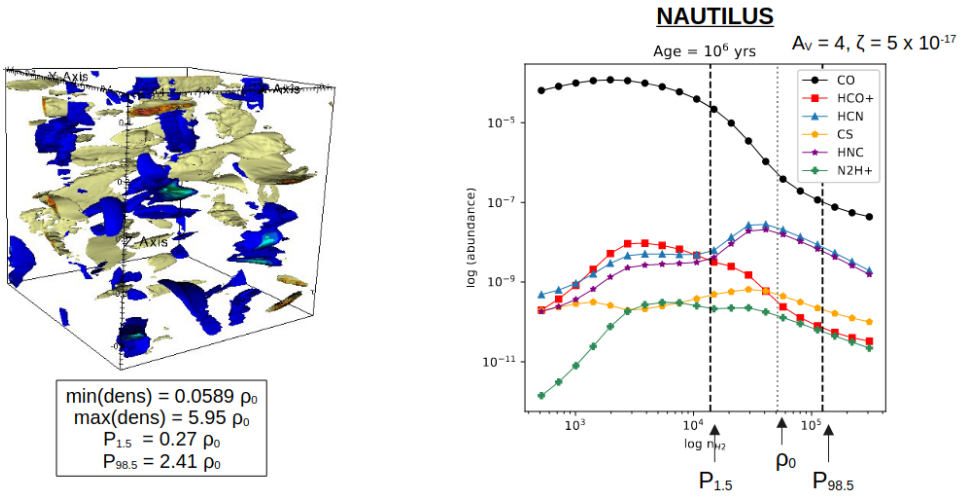

Figure 2: *Left*: gas structures present in the steady state simulation. Low-density structures are those below the 1.5 % of the density distribution and are coded in yellow. High-density structures are selected based on the 98.5 % threshold and are coded in blue. *Right*: chemical abundances predicted by `Nautilus` in the density range of the steady state simulation. The vertical dotted line corresponds to the initial density, while the dashed lines correspond to the 1.5 % and 98.5 % density percentiles used in the left panel.

3 Observational expectations

Using the chemical network shown in Fig. 2, we have estimated for each simulation cell the expected abundance of the considered molecules using a linear interpolation in log-space density bins. With that, we have used the MHD cubes that provide the gas velocity field and gas distribution, together with the molecule distribution, and have applied the radiative

transfer code RADMC-3D [2] to obtain the spectra of rotational transitions. In Fig. 3 we show the molecular hydrogen column density map projected onto one of the faces of the 3D cube (xy plane, with the magnetic field parallel to the x-axis and, therefore, perpendicular to the line of sight) together with the predicted integrated intensity maps for ^{13}CO ($1 \rightarrow 0$) and CS ($2 \rightarrow 1$). Note that the range of integrated intensities is much wider for ^{13}CO ($1 \rightarrow 0$) (of the order of 0.4 K km s^{-1}) than for CS ($2 \rightarrow 1$) (of the order of 0.2 K km s^{-1}).

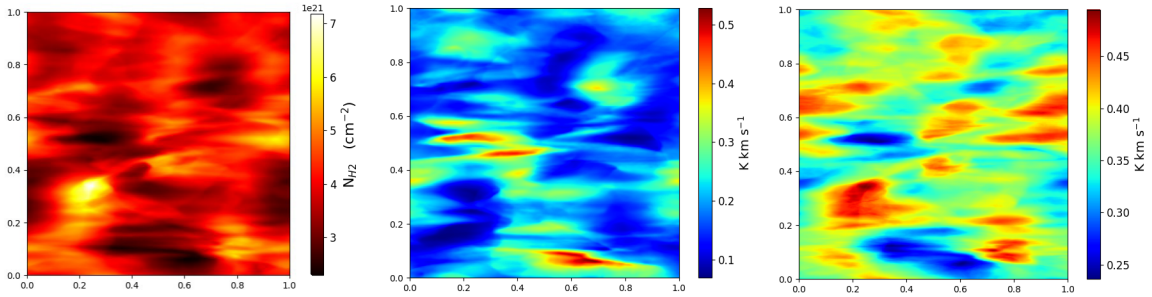

Figure 3: Molecular hydrogen column density (left) for the xy face of the cube, and the RADMC-3D predicted moment-zero maps for ^{13}CO ($1 \rightarrow 0$) (middle panel) and CS ($2 \rightarrow 1$) (right panel).

When trying to fit a chemical model to observations, a common assumption is to consider that the hydrogen density along the line of sight is constant, *i.e.* that the gas distribution is uniform. In order to quantify the effects of this assumption, we have post-processed with RADMC-3D a cube with uniform molecular hydrogen density and chemical abundances, and have computed the ratio between the turbulent case shown in Fig. 3 and the uniform ones. The results are shown in Fig. 4 in the form of relative integrated intensity maps and histograms of relative integrated intensities. In general, we see that the expectations raised in the view of the chemical network shown in Fig. 2 are in agreement with the results: turbulence produces large variations in the local abundance of ^{13}CO ($1 \rightarrow 0$), and can produce integrated intensities six times higher than when assuming a uniform gas distribution along the line of sight. On the other hand, other molecules are less sensitive to turbulence and the variations introduced are of the order of $10 - -20\%$, as is the case for CS ($2 \rightarrow 1$).

4 Summary and conclusions

In this contribution, we have presented the preliminary results of our study on the effects of turbulence on the chemistry of molecular clouds. Assuming a hydrogen particle density of $n_{\mathrm{H_2}} = 2.57 \times 10^4$ cm^{-3} and a magnetic field of $B_0 = 40$ μG, we have run an ideal MHD 3D turbulent box simulation with `Athena++` until we reproduce a steady-state molecular filament before collapse. Later, we have post-processed this simulation with the chemical code `Nautilus` in order to derive a cube of chemical abundances that has been used to estimate the molecular emission with RADMC-3D. We have compared the results of this post-processed turbulent simulation with the case where the gas density and the chemical

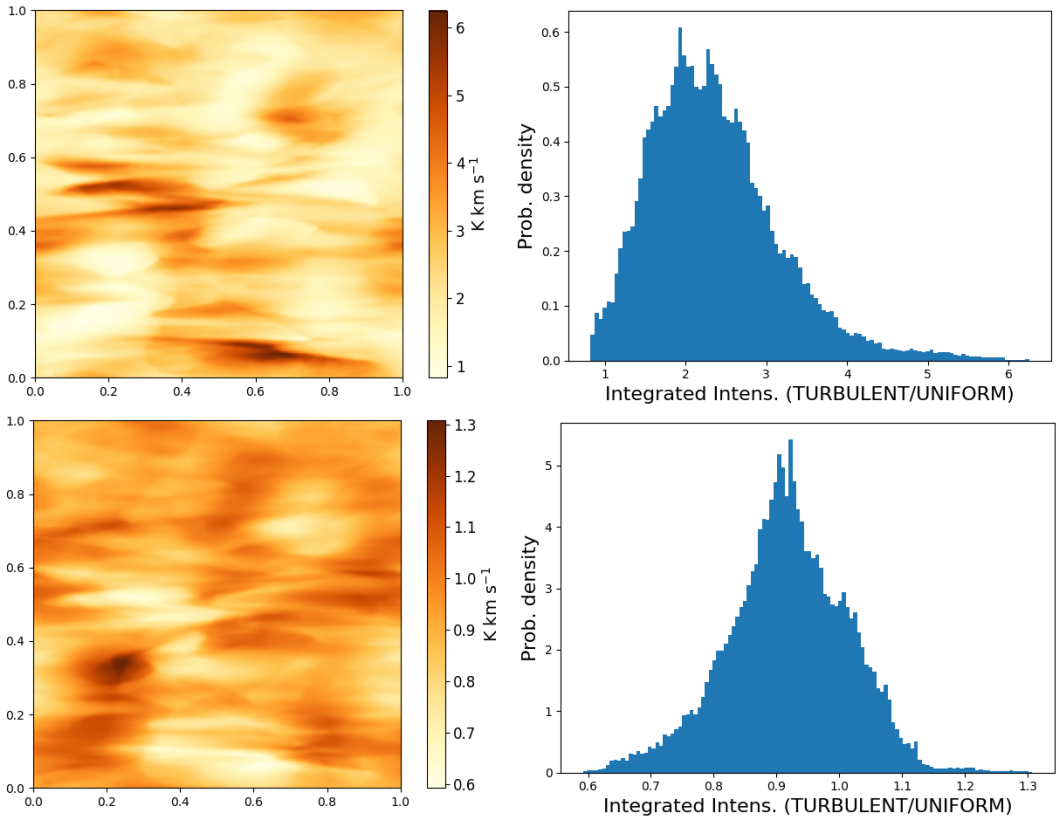

Figure 4: Relative integrated intensity maps and associated histograms for ^{13}CO ($1 \rightarrow 0$) (upper row) and CS ($2 \rightarrow 1$) (lower row). Note the significant differences between both molecules.

abundance are uniform along the line of sight. The results of this preliminary study can be summarised as follows:

- Turbulence can generate important density fluctuations – in this case from 0.05 to 6 times the mean value. Inside this range of densities, the chemical abundance of some elements present critical variations (especially CO).

- These density fluctuations are translated into variations in the moment-zero maps, which are especially important for ^{13}CO ($1 \rightarrow 0$) where the integrated intensities can be up to a factor of 6 higher than for the uniform case. Other molecules, such as CS ($2 \rightarrow 1$), are less affected by turbulence, although the difference in integrated intensities are of the order of a $10 - -20\%$.

Acknowledgments

L. B.-A. acknowledges the receipt of a Margarita Salas postdoctoral fellowship from Universidad Complutense de Madrid, funded by 'Ministerio de Universidades' with NextGeneration EU Funds. A.F. thanks the Spanish MICIN for funding support from PID2019-106235GB-I00

References

[1] Beitia-Antero, L., Gómez de Castro, A.I., Vallejo, J.C., 2021, ApJ, 908, 112

[2] Dullemond, F., et al. 2012, Astrophysics Source Code Library, record ascl:1202.015

[3] Fuente, A., et al. 2023 A&A, 670, 114

[4] Hacar, A., et al. 2022, arXiv:2203.09562

[5] Hopkins, P.F. et al. 2022, MNRAS, 517, 1491

[6] Le Petit, F., Nehmé, C., Le Bourlot, J., Roueff, E. 2006, ApJS, 164, 506

[7] Perrero, J. et al. 2022 ApJ, 938, 158

[8] Ruaud, M., Wakelam, V., Hersant, F., 2016, MNRAS, 459, 3756

[9] Stone, J.M., Tomida, K., White, C.J., Felker, K.G. 2020, ApJS, 249, 4

Highlights of Spanish Astrophysics XI, Proceedings of the XV Scientific Meeting of the Spanish Astronomical Society held on September 4–9, 2022, in La Laguna, Spain. M. Manteiga, L. Bellot, P. Benavidez, A. de Lorenzo-Cáceres, M. A. Fuente, M. J. Martínez, M. Vázquez- Acosta, C. Dafonte (eds.), 2023

A Validation Method for Exoplanet Transit Candidates with Auto-Regressive Models.

J. Pascual-Granado[1]

[1] Instituto de Astrofísica de Andalucía (CSIC)

Abstract

Ultra-precise observations from space missions such as CoRoT, Kepler/K2 or TESS can be contrasted with data from ground-based surveys such as CARMENES or HARPS to validate extra-solar planets detection through spectroscopy or using different photometric bands to discard false positives. Though several thousands of exoplanets have already been confirmed the number of candidates is orders of magnitude higher. Since it is not possible to allocate time from ground-based surveys to perform the follow-up of all the candidates, an automatic validation procedure is required which is robust enough to confirm the detections. I introduce here a new validation method for exoplanet transit candidates based on modeling the data as auto-regressive processes. These can fit either stellar pulsations, stellar activity or any intrinsic variability so they are very suitable to model out of transit light variations. This procedure does not require any a priori from the star or planet such as period, depth, duration or shape of the signal. It neither does require any colors, spectroscopic observations or any informed assumptions, only one light curve with several transits is required.
Here I show that transits can be validated with no necessity of follow-up observations in many cases and false positives can be reliably identified with auto-regressive models.

My poster is available at https://zenodo.org/record/7044837

Highlights of Spanish Astrophysics XI, Proceedings of the XV Scientific Meeting of the Spanish Astronomical Society held on September 4–9, 2022, in La Laguna, Spain. M. Manteiga, L. Bellot, P. Benavidez, A. de Lorenzo-Cáceres, M. A. Fuente, M. J. Martínez, M. Vázquez- Acosta, C. Dafonte (eds.), 2023

Accretion disc winds from X-ray transients.

Guayente Panizo-Espinar[1,2], Montserrat Armas Padilla[1,2], and Teodoro Muñoz-Darias[1,2]

[1] Instituto de Astrofísica de Canarias
[2] Universidad de La Laguna

Abstract

Low-mass X-ray binaries (LMXB) are stellar systems where a neutron star or a black hole accretes mass from a low-mass ($\lesssim 1 M_\odot$) donor star. A subclass, so-called X-ray transients, spend most of their lives in a dim, quiescent state. However, these systems go into sporadic, powerful outbursts produced by one of the most energetic process in the Universe: accretion. The accretion flow has been found to be strongly coupled to the presence of outflows (radio-jets, hot X-ray winds and the recently discovered cold, optical winds), which is a fundamental characteristic of their outbursts. Thus, the study of these winds can provide us with crucial information about accretion processes in the Universe. In this poster, we briefly review the state-of-the-art of the field and present the case of one LMXB transient that has recently shown signatures of accretion disc winds in its optical spectra, MAXI J1348–630. We discuss the properties of the outflow and its impact on the accretion process.

My poster is available at https://zenodo.org/record/7034414#.Y2pA3-zP1LA

Highlights of Spanish Astrophysics XI, Proceedings of the XV Scientific Meeting of the Spanish Astronomical Society held on September 4–9, 2022, in La Laguna, Spain. M. Manteiga, L. Bellot, P. Benavidez, A. de Lorenzo-Cáceres, M. A. Fuente, M. J. Martínez, M. Vázquez- Acosta, C. Dafonte (eds.), 2023

Analysis of chromospheric flux-flux relationships of M Dwarfs using visible and near-infrared CARMENES spectra.

Labarga, F.[1], Montes, D.[1], Duque-Arribas, C.[1], Lopez-Gallifa, A.[1,2], Caballero, J.A.[2], Jeffers, S.V.[3], Reiners, A.[4], Ribas, I.[5], Quirrenbach, A.[6], and Amado, P.J.[7]

[1] Departamento de Física de la Tierra y Astrofísica & IPARCOS-UCM (Instituto de Física de Partículas y del Cosmos de la UCM), Facultad de Ciencias Físicas, Universidad Complutense de Madrid, Spain
[2] Centro de Astrobiología, Villanueva de la Cañada, Madrid, Spain
[3] Max Planck Institute for Solar System Research, Göttingen, Germany
[4] Institut für Astrophysik, Georg-August-Universität, Göttingen, Germany
[5] Institut de Ciències de l'Espai & IEEC-CSIC, Barcelona, Spain
[6] Zentrum für Astronomie der Universität Heidelberg, Heidelberg, Germany
[7] Instituto de Astrofísica de Andalucía (IAA, CSIC), Granada, Spain

Abstract

Exploiting the huge amount of data provided by the CARMENES survey, this work aims to study the chromospheric activity of M dwarfs based on a sub-sample (active RV-loud M dwarfs) of CARMENES GTO sample. Using the spectral subtraction technique and calibrations of the continuum-flux near the line of interest, the available information on the chromospheric activity flux is extracted. Most of the chromospheric indicators included in the spectral range of the spectrograph, ranging from visible (VIS) - including the Na I (D_1,D_2) He I D_3, and Hα lines - to near-infrared (NIR) - that include the Ca II IRT, He I λ10830 Å, Paschenα and Paschenβ lines - are used. For the implementation of the spectral subtraction technique, a PYTHON code iSTARMOD based on a previous FORTRAN one, formerly used by the research group, is used. The synthetic spectra for effective temperatures in the range [2400, 7000] K, allow through the calibrations a comparison of the flux-flux relationships with previous works performed for F, G and K dwarfs. The studies of flux-flux relationships of lines formed at different chromosphere layers seek for a better understanding of the magnetic activity of M-type dwarf stars and try to determine the number of different chromospheric emitters populations, deduced from the non-universality of these relationships for Ca II IRT lines.

My poster is available at https://doi.org/10.5281/zenodo.7668217

Highlights of Spanish Astrophysics XI, Proceedings of the XV Scientific Meeting of the Spanish Astronomical Society held on September 4–9, 2022, in La Laguna, Spain. M. Manteiga, L. Bellot, P. Benavidez, A. de Lorenzo-Cáceres, M. A. Fuente, M. J. Martínez, M. Vázquez- Acosta, C. Dafonte (eds.), 2023

CHIPS: Chemistry in outflows of Post-AGB stars.

Velilla-Prieto, L.[1], Alcolea, J.[2], Bujarrabal, V.[3], Castro-Carrizo, A.[4], Olofsson, H.[5], Vlemmings, W.[5], Khouri, T.[5], and Agúndez, M.[1]

[1] Instituto de Física Fundamental (IFF), CSIC, Serrano 123, 28006, Madrid (Spain)
[2] Observatorio Astronómico Nacional (OAN-IGN), Alfonso XII 3, 28014, Madrid (Spain)
[3] Observatorio Astronómico Nacional (OAN-IGN), Apartado 112, 28803, Alcalá de Henares, Madrid (Spain)
[4] Institut de Radioastronomie Millimétrique, 300 Rue de la Piscine, 38406, St-Martin d'Héres (France)
[5] Dept. of Space, Earth, and Environment, Chalmers University of Technology, Onsala Space Observatory, 439 92 Onsala (Sweden)

Abstract

Low and intermediate-mass (LIm) evolved stars are major contributors to the enrichment and growth of the chemical complexity of the Universe. Substantial outflows of dust and gas are injected into the interstellar medium during the last stages of LIm stellar evolution, from the Asymptotic Giant Branch (AGB) and beyond. Post-AGBs experience different processes leading to important changes in their molecular content due to the ocurrence of shocks and an enhanced photo-chemistry as they evolve towards the planetary nebulae (PNe) stage. This complex chemistry, which in certain cases resemble that of young stellar objects, is poorly characterized. Our aim is to investigate the molecular content and the chemical evolution of the circumstellar envelopes from the AGB to the PNe stage, making use of (sub)-mm wavelength observations with radio telescopes and chemical kinetics models. We are carrying out different observational projects towards OH231.8+4.2, V Hya, and KJPN 8, among others. Recent observations with the IRAM-30 m telescope towards KJPN 8 allowed us to detect lines of typical molecular young PNe content: CO, CN, HCO^+, HCN, HNC, CS, and isotopologues. Preliminary results on the isotopic ratios ($^{17}O/^{18}O \gtrsim 6$ and $^{12}C/^{13}C \gtrsim 2$) add more constraints to the origin of this puzzling bipolar nebulae, which is still under debate.

My poster is available at https://zenodo.org/record/7048922#.Y8Ew4uzMJz8

Highlights of Spanish Astrophysics XI, Proceedings of the XV Scientific Meeting of the Spanish Astronomical Society held on September 4–9, 2022, in La Laguna, Spain. M. Manteiga, L. Bellot, P. Benavidez, A. de Lorenzo-Cáceres, M. A. Fuente, M. J. Martínez, M. Vázquez- Acosta, C. Dafonte (eds.), 2023

Gaia-based comparative study of protoplanetary disk frequencies in young stellar clusters.

Mendigutía, I.[1], **Solano, E.**[1,2], **Vioque, M.**[3,4], **Balaguer-Nuñez, L.**[5], **Ribas, A.**[6], **Huélamo, N.**[1], **and Rodrigo, C.**[1,2]

[1] Centro de Astrobiología (CAB), CSIC-INTA, Camino Bajo del Castillo s/n, 28692 Villanueva de la Cañada, Madrid, Spain
[2] Spanish Virtual Observatory, Spain
[3] Joint ALMA Observatory, Alonso de Córdova 3107, Vitacura, Santiago 763-0355, Chile
[4] National Radio Astronomy Observatory, 520 Edgemont Road, Charlottesville, VA 22903, USA
[5] Institut de Ciències del Cosmos, Universitat de Barcelona (IEEC-UB), Martí i Franquès 1, 08028 Barcelona, Spain
[6] European Southern Observatory (ESO), Alonso de Córdova 3107, Vitacura, Casilla 19001, Santiago de Chile, Chile

Abstract

This poster presents the results of a recent work (Mendigutía et al. 2022, A&A, 664, A66), where we have compared protoplanetary disk frequencies inferred from 2 widely different regions corresponding to 2 pc and 20 pc from the centers of a representative sample of young stellar clusters. Gaia EDR3 parallaxes and proper motions, along with a best suited tool (Clusterix), were used for membership determination. Near-infrared color-color diagrams served to identify disk sources. Our results cover the largest fields ever probed when dealing with disk fractions for all clusters analysed. Although the density of member stars decreases outside the clusters' centers, the absolute number of members is significantly larger in the peripheries, implying that the complete characterization of young clusters requires to probe wide fields. In turn, our comparative study does not support a previous hypothesis proposing that disk fractions should be significantly larger considering extended regions. On the contrary, disk frequencies inferred from the 2 pc- and 20 pc- regions are typically equal within 10%. The resulting database is stored in a Virtual Observatory-compliant archive, constituting a benchmark for future detailed studies of young clusters.

My poster is available at https://zenodo.org/record/7023372#.Y5LK4tLMKUl

Highlights of Spanish Astrophysics XI, Proceedings of the XV Scientific Meeting of the Spanish Astronomical Society held on September 4–9, 2022, in La Laguna, Spain. M. Manteiga, L. Bellot, P. Benavidez, A. de Lorenzo-Cáceres, M. A. Fuente, M. J. Martínez, M. Vázquez- Acosta, C. Dafonte (eds.), 2023

Identification of ultracool dwarfs in J-PLUS DR2 using Virtual Observatory tools and machine learning techniques.

P. Mas-Buitrago[1,2], E. Solano[1,2], and A. González-Marcos[3]

[1] Centro de Astrobiología (CAB), CSIC-INTA, Camino Bajo del Castillo s/n, 28692, Villanueva de la Cañada, Madrid, Spain
[2] Spanish Virtual Observatory
[3] Departamento de Ingeniería Mecánica, Universidad de la Rioja, c/ San José de Calasanz 31, 26004 Logroño, La Rioja, Spain

Abstract

We present the search for ultracool dwarfs (UCDs, spectral types later than M7 V) performed across the entire Javalambre Photometric Local Universe Survey (J-PLUS) second data release (2 176 deg^2) following a Virtual Observatory methodology. We also explored the ability to reproduce this search with a purely machine learning (ML)-based methodology that relies solely on J-PLUS photometry. We followed three different approaches based on parallaxes, proper motions, and colours, respectively, using the VOSA tool to estimate the effective temperatures. For the ML methodology, we built a two-step method based on principal component analysis and support vector machine algorithms. We identified a total of 7 827 new candidate UCDs, which represents an increase of about 135 % in the number of UCDs reported in the sky coverage of the J-PLUS second data release. With the ML approach, we obtained a recall score of 92 % and 91 % in the 20×20 deg^2 regions used for testing and blind testing, respectively. We consolidated the proposed search methodology for UCDs, which will be used in deeper and larger upcoming surveys such as J-PAS and Euclid. We concluded that the ML methodology is more efficient in the sense that it allows for a larger number of true negatives to be discarded prior to analysis with VOSA, although it is more photometrically restrictive.

My poster is available at https://zenodo.org/record/7018654#.Y4dCxdLMJFF

Highlights of Spanish Astrophysics XI, Proceedings of the XV Scientific Meeting of the Spanish Astronomical Society held on September 4–9, 2022, in La Laguna, Spain. M. Manteiga, L. Bellot, P. Benavidez, A. de Lorenzo-Cáceres, M. A. Fuente, M. J. Martínez, M. Vázquez- Acosta, C. Dafonte (eds.), 2023

Is there also a planet-metallicity correlation for young stars with protoplanetary disks?.

Guzmán-Díaz, J.[1,2], **Montesinos, B.**[1], **and Mendigutía, I.**[1]

[1] Centro de Astrobiología (CSIC-INTA), ESA-ESAC Campus, 28692, Villanueva de la Cañada, Madrid, Spain
[2] Universidad Autónoma de Madrid, Campus de Cantoblanco, 28049 Madrid, Spain

Abstract

Metallicity is a stellar parameter that plays a fundamental role in planet formation. The well known planet-metallicity correlation for FGK stars tells us that the higher the metallicity of a star, the higher the likelihood that it harbors exoplanets. On the other hand, the situation in A-type stars is far from clear. Because of their higher rotational velocities and luminosities, the number of exoplanets discovered in these stars from the radial velocity and transit methods is actually very low, which makes a statistical study unfeasible. One way to potentially circumvent this problem is through the study of optically-visible intermediate-mass young objects surrounded by protoplanetary disks, so called "Herbig Ae/Be" stars. Although the detection of young planets embedded in protoplanetary disks is still a challenging task, the shape of the infrared spectral energy distributions reflects the properties of the disks and thus the potential presence of planets. Under this view, Kama et al. (2015, A&A 582, L10) hypothesized that the presence or absence of a Jupiter-like size exoplanet could explain the relation between the stellar metallicity and the shape of the spectral energy distributions that they found in a few Herbig Ae/Be stars.

In this poster, we expand the work carried out by Kama et al. (2015) by considering a significantly larger sample of stars. The spectra of 67 Herbig Ae/Be stars have been collected and their metallicities estimated by comparing them with Kurucz synthetic models. We confirm that there is indeed a correlation between the stellar metallicity and a specific shape of the spectral energy distributions suggestive of the presence of planets. This result may represent a major step forward in the field of planet formation and the evolution of protoplanetary disks.

My poster is available at https://zenodo.org/record/7024797#.Y5nDOXbMJEY

Highlights of Spanish Astrophysics XI, Proceedings of the XV Scientific Meeting of the Spanish Astronomical Society held on September 4–9, 2022, in La Laguna, Spain. M. Manteiga, L. Bellot, P. Benavidez, A. de Lorenzo-Cáceres, M. A. Fuente, M. J. Martínez, M. Vázquez- Acosta, C. Dafonte (eds.), 2023

J-PLUS: Estimating the Galactic halo density profile using Blue Horizontal Branch stars selected from multifilter data.

Domínguez-Fernández, A. J.[1,2], **López-Sanjuan, C.**[3], **Vázquez Ramió, H.**[3], **and J-PLUS collaboration**[1]

[1] Centro de Estudios de Física del Cosmos de Aragón, Plaza San Juan 1, 44001 Teruel, Spain
[2] Departamento de Física de la Tierra y Astrofísica, Facultad de Ciencias Físicas, Universidad Complutense de Madrid, 28040 Madrid, Spain
[3] Centro de Estudios de Física del Cosmos de Aragón, Unidad Asociada al CSIC, Plaza San Juan 1, 44001 Teruel, Spain

Abstract

To study the Galactic halo we need to rely on intrinsically bright and fair distance indicators. Blue Horizontal Branch (BHB) stars accomplish these requirements but traditionally suffer from high levels of contamination from Blue Stragglers stars in photometric samples. Surveys like Pristine and SkyMapper have demonstrated that colors combining a broad- and a narrow-band filter with central wavelength bluewards 4,000Å allow them to build high completeness and purity samples of BHB stars. In this context, the Javalambre Photometric Local Universe Survey (J-PLUS), with a broad- and two custom narrow-band filters (among its 12) having central wavelengths shorter than 4,000Å, has released more than 2,000 sq. deg in 2020. In this contribution, we review the latest attempts to study the density profile of the halo, discuss our work in which we used three methods to select BHB stars from J-PLUS DR2, present our estimation of the halo profile, and forecast the expectations for J-PAS and its 56 narrow-band filter system.

My poster is available at https://zenodo.org/record/7025724#.Y2jJ1C1Dl-U

Highlights of Spanish Astrophysics XI, Proceedings of the XV Scientific Meeting of the Spanish Astronomical Society held on September 4–9, 2022, in La Laguna, Spain. M. Manteiga, L. Bellot, P. Benavidez, A. de Lorenzo-Cáceres, M. A. Fuente, M. J. Martínez, M. Vázquez- Acosta, C. Dafonte (eds.), 2023

Keplerian disks and outflows around binary post-AGB stars.

Gallardo Cava, I.[1], Bujarrabal, V.[1], Alcolea, J.[1], Gómez-Garrido, M.[1], Castro-Carrizo, A.[2], Van Winckel, H.[3], and Santander-García, M.[1]

[1] Observatorio Astronómico Nacional (OAN-IGN), Alfonso XII 3, 28014, Madrid, Spain
[2] Institut de Radioastronomie Millimétrique (IRAM), 300 rue de la Piscine, 38406 Saint-Martin-d'Hères, France
[3] Instituut voor Sterrenkunde, KU Leuven, Celestijnenlaan 200B, 3001 Leuven, Belgium

Abstract

There is a class of binary post-AGB stars that systematically shows evidence of the presence of disks. All of them present a remarkable NIR excess and the narrow CO line profiles characteristic of rotating disks. Their spectral energy distributions (SEDs) reveal the presence of hot dust close to the stellar system, and interferometric IR data have confirmed its disk-like shape. These disks must be stable structures because their IR spectra reveal the presence of highly processed grains. Observations of CO through single-dish and interferometric observations confirm the presence of another structure surrounding the disk with expansion velocity.

This contribution explores the existence of two subclasses of nebulae around binary post-AGB stars: the disk- and the outflow-dominates sources. Our interferometric maps (in the ^{12}CO and ^{13}CO $J = 2-1$ lines) and our models confirm this bimodal distribution. The disk-dominated sources, such as AC Herculis, contain $\sim 90\%$ of the material of the nebula located in the rotating disk. On the contrary, the outflow-dominated sources, such as 89 Herculis, contain $\sim 70\%$ of the nebular material located in the massive outflows, which are mostly composed of cold gas.

The existence of these different subclasses does not support an evolutionary path between them, since the post-AGB phase is believed to be fast compared to the evolution of this type of nebulae (around 10^4 a). Therefore, the existence of both the disk- and outflow-dominated sources could be due to a different initial configuration of the stellar system.

Our deep single-dish radio molecular survey (~ 600 hours of telescope time) in the 1.3, 2, 3, 7, and 13 mm bands confirm the low molecular content in this kind of sources. This fact is significant in those sources where the disk is the dominant component of the nebula. Additionally, we classify the Red Rectangle, AI Canis Minoris, IRAS 20056+1834, and R Scuti as O-rich, while 89 Herculis presents a C-rich environment.

My poster is available at https://zenodo.org/record/6984936

Highlights of Spanish Astrophysics XI, Proceedings of the XV Scientific Meeting of the Spanish Astronomical Society held on September 4–9, 2022, in La Laguna, Spain. M. Manteiga, L. Bellot, P. Benavidez, A. de Lorenzo-Cáceres, M. A. Fuente, M. J. Martínez, M. Vázquez- Acosta, C. Dafonte (eds.), 2023

MEGASTAR: The MEGARA-GTC stellar spectral library.

Mollá M.[1], García-Vargas, M.L.[2], Millán-Irigoyen, I. [1], Cardiel, N. [3,4], Carrasco-Licea, E. [5], Gil de Paz, A. [3,4], Berlanas, S.R.[6,7], and Gómez-Ávarez, P.[2]

[1] Departamento de Investigación Básica, CIEMAT, Avda. Complutense 40. E-28040 Madrid, Spain
[2] FRACTAL S.L.N.E., Calle Tulipán 2, portal 13, 1A, E-28231 Las Rozas de Madrid, Spain
[3] Dpto. de Física de la Tierra y Astrofísica, Fac. CC. Físicas, Universidad Complutense de Madrid, Plaza de las Ciencias, 1, E-28040 Madrid, Spain
[4] Instituto de Física de Partículas y del Cosmos, IPARCOS, Fac. CC. Físicas, Universidad Complutense de Madrid, Plaza de las Ciencias 1, E-28040 Madrid, Spain
[5] Instituto Nacional de Astrofísica, Óptica y Electrónica, INAOE, Calle Luis Enrique Erro 1, C.P. 72840 Santa María Tonantzintla, Puebla, Mexico
[6] Departamento de Física Aplicada, Universidad de Alicante, 03690 San Vicente del Raspeig, Alicante, Spain. [7] Astrophysics Group, Keele University, Keele ST5 5BG, Staffordshire, UK

Abstract

We are observing a large sample of stars with MEGARA on GTC through a filler-type OpenTime program obtained in 7 semesters up to now. We summarize our advances done with MEGASTAR, the stellar spectral library we are observing with MEGARA at R=20000 in two setups HR-R around Hα and HR-I around CaT. We described our project in García Vargas et al. (2020, MNRAS, 493, 871). We published our first data release in Carrasco et al. (2021, MNRAS, 501, 3568). In our third piece of work (Mollá et al. 2022, MNRAS, submitted) we have determined the stellar parameters (effective temperature, surface gravity and metallicity) of a subsample of the DR1 stars with spectral types later than B2, and we have measured some stellar indices, also giving the first set of MegaPopStar evolutionary synthesis models. Next papers will be devoted to the second data release and to the physical parameters determination of the hot stars.

My poster is available at https://zenodo.org/record/6991175#.Y1bgxoJBxmE

Highlights of Spanish Astrophysics XI, Proceedings of the XV Scientific Meeting of the Spanish Astronomical Society held on September 4–9, 2022, in La Laguna, Spain. M. Manteiga, L. Bellot, P. Benavidez, A. de Lorenzo-Cáceres, M. A. Fuente, M. J. Martínez, M. Vázquez- Acosta, C. Dafonte (eds.), 2023

Massive stars in Carina from GES, GOSSS & LiLiMaRlin: A new census of OB stars to obtain a reliable distribution of rotational velocities for the O-star population.

S. R. Berlanas[1,2], A. Herrero[3,4], and J. Maíz Apellániz[5]

[1] Dpto. de Física Aplicada, Universidad de Alicante, E-03 690, Alicante, Spain
[2] Astrophysics Group, Keele University, Keele ST5 5BG, Staffordshire, UK
[3] Instituto de Astrofísica de Canarias, E-38200 La Laguna, Tenerife, Spain
[4] Dpto. de Astrofísica, Universidad de La Laguna, E-38205 La Laguna, Tenerife, Spain
[5] Centro de Astrobiología, CSIC-INTA, Campus ESAC, E-28692, Madrid, Spain

Abstract

The Carina Nebula complex consists of several stellar groups, some bound and some not, immersed in the Car OB1 association, a unique region to study Galactic massive stars. Containing a large number of O-stars, it is the most massive star-forming region within 3 kpc of the Sun. Even though the Carina Nebula harbors hundreds of massive stars, there is no systematic spectroscopic analysis of its early-type members.

In this contribution we present results from Berlanas et al. 2022 (submitted) in which we created the most complete to date census of massive stars in the central part of the Carina Nebula, Car OB1. The final census contains a total of 315 stars, being 17 of them in the background and four in the foreground. Of the 294 stellar systems in Car OB1, 74 are of O type, 214 are of non-supergiant B type and 6 are of WR or non-O supergiant (II to Ia) spectral class. We identified 20 spectroscopic binary systems with an O-star primary, of which 6 are reported for the first time, and another 17 with a B-star primary, of which 12 are new detections. We estimate that our sample is around 90% complete for low to moderate extinction O and early B systems. Thanks to this census and high-resolution spectra from GES and the LiLIMaRlin library, we obtained a reliable distribution of rotational velocities for the O-star population in the GES footprint of Carina (Berlanas et al. 2023, in prep). We find a bimodal structure with the low velocity peak at 60 km s^{-1} and a tail of fast rotators above 200 km s^{-1}, similar to previous studies in other regions except for a shorter tail of fast rotators.

My poster is available at https://doi.org/10.5281/zenodo.7046980

Highlights of Spanish Astrophysics XI, Proceedings of the XV Scientific Meeting of the Spanish Astronomical Society held on September 4–9, 2022, in La Laguna, Spain. M. Manteiga, L. Bellot, P. Benavidez, A. de Lorenzo-Cáceres, M. A. Fuente, M. J. Martínez, M. Vázquez- Acosta, C. Dafonte (eds.), 2023

Multi-transitional SHAPEMOL modelling of M1-92: the discovery of a shock excited hot molecular component.

Domínguez-Salamanca, I.[1,2], Alcolea, J.[2], Bujarrabal, V.[2], Santander-García, M.[2], Agúndez, M.[3], Castro Carrizo, A.[4], Desmurs, J.-F.[2], and Sánchez Contreras, C.[5]

[1] Dept. de Física de la Tierra y Astrofísica, Fac. CC. Físicas (UCM)
[2] Observatorio Astrómico Nacional (IGN)
[3] Dept. de Astrofísica Molecular, Instituto de Física Fundamental (CSIC)
[4] Institute de Radioastronomie Millimétrique
[5] Centro de Astrobiología (INTA-CSIC)

Abstract

M1–92 is a well-studied pre-planetary nebula characterized by a bipolar appearance with a high degree of axial symmetry. It consists of a thick equatorial structure dividing the two emptied lobes. The nebula is rich in molecular gas and dust, with a total mass $\sim 1\,M_\odot$, except for two knots in the middle of the lobes where there is ionized gas as a result of shocks, as proved by the detection of optically forbidden lines and vibrationally excited H_2. We present the most complete and detailed modelling of M1–92, using ^{13}CO, $C^{17}O$, and $C^{18}O$ J=2–1 NOEMA maps with $0\farcs7$ resolution, and single-dish data for ^{12}CO J=1–0, J=2–1, J=3–2, J=5–4, J=7–6, and J=9–8, and for ^{13}CO, $C^{17}O$, and $C^{18}O$ J=1–0 and J=2–1 (from IRAM 30m, CSO, and HSO/HIFI). The modelling is performed using `SHAPE+shapemol`, computing the excitation of CO using the LVG approximation and solving the radiative transfer problem via ray tracing. We have derived the nebular structure, the density and temperature distributions of the different molecule-rich components, and the $^{12}C/^{13}C$ and $^{16}O/^{17}O/^{18}O$ ratios. These ratios confirm the hypothesis that the nebula is the result of a 1200 yr old sudden mass-loss event, leading to the premature end of the AGB phase of the central star (probably as a consequence of a common-envelope event).
The fitting of the high-J lines of CO requires a new molecular component that is relatively hot, 700–900 K, in striking contrast with the rest of the molecular gas. There are no maps of these transitions: we suggest that this component could be the molecular counterpart of the shocked knots seen in optical forbidden lines and vibrationally excited H_2.

My poster is available at https://doi.org/10.5281/zenodo.7041389

Highlights of Spanish Astrophysics XI, Proceedings of the XV Scientific Meeting of the Spanish Astronomical Society held on September 4–9, 2022, in La Laguna, Spain. M. Manteiga, L. Bellot, P. Benavidez, A. de Lorenzo-Cáceres, M. A. Fuente, M. J. Martínez, M. Vázquez- Acosta, C. Dafonte (eds.), 2023

OH maser-emitting planetary nebulae.

Roldán A. Cala[1], José F. Gómez[1], and Luis F. Miranda[1]

[1] Instituto de Astrofísica de Andalucía, CSIC, Glorieta de la Astronomía s/n, E-18008 Granada, Spain

Abstract

The expected evolution of the Sun and stars with initial masses up to 8 $M_\odot$, after the asymptotic giant branch phase, will be to form a planetary nebula (PN) ionized by a central star (CS). Searching for extremely young PNe is important to better characterize the onset of this transitional phase. In particular, OH maser-emitting PNe (OHPNe) are considered nascent PNe. In fact, only 6 OHPNe are known to date. Using high-resolution optical spectra on Vy 2-2, the first OHPN identified, we report a kinematical age of $\sim$135 $\pm$ 90 yr (for a distance of 3 $\pm$ 2 kpc) for the very compact ionized central region of this PN. Moreover, our spectra reveal an unexpected C-rich nature for its CS. The ejected circumstellar matter is O-rich, where dense photoionized gas, silicate dust, water ice and OH masers coexist in an environment with C/O $<$ 1. Therefore, Vy 2-2 is a nascent O-rich PN around a C-rich CS. The formation of this kind of dual-chemistry in PNe is not well understood. Also, in order to identify more OHPNe, we processed the unpublished continuum data of the interferometric follow-up of an OH maser line survey that covered 176 deg^2 of the Southern Galactic Plane and the Galactic Center. We then cross-matched the interferometric positions of the OH maser and radio continuum emission, considering the latter as a possible tracer of free-free emission from photoionized gas, which is characteristic of PNe. Out of the 933 OH maser line sources in that survey, we report 8 objects with a positive coincidence between maser and radio continuum emission, 4 of which are bona fide OHPNe, and other 4 are identified as OHPNe candidates for the first time (OH 341.6811+00.2634, IRAS 16372−4808, IRAS 17494−2645 and IRAS 18019−2216). Hence, these results could significantly increase the number of known members of nascent PNe.

My poster is available at https://zenodo.org/record/7051527

Highlights of Spanish Astrophysics XI, Proceedings of the XV Scientific Meeting of the Spanish Astronomical Society held on September 4–9, 2022, in La Laguna, Spain. M. Manteiga, L. Bellot, P. Benavidez, A. de Lorenzo-Cáceres, M. A. Fuente, M. J. Martínez, M. Vázquez- Acosta, C. Dafonte (eds.), 2023

Phase spirals in cosmological simulations of Milky Way sized galaxies.

B. García-Conde[1], S. Roca -Fàbrega[1,2], T. Antoja[3], and P. Ramos[4]

[1] Universidad Complutense de Madrid
[2] Instituto de Astronomía, Universidad Nacional Autónoma de México
[3] Universitat de Barcelona
[4] National Astronomical Observatory of Japan

Abstract

The Gaia DR2 revealed the phase spirals in the Z - Vz plane, whose origin is still under study, but linked to the Sagittarius dwarf galaxy tidal interaction. In our work, we detect phase spirals in the vertical projection Z - Vz of the disc's stellar particles for the first time in the zoom-in cosmological simulation GARROTXA which includes hydrodynamics, and star formation. The detection and characterization of the phase spirals have been carried out with a Fourier decomposition-based technique. Our results indicate that these spiral-like structures in the phase space are present in a wide range of times and locations across the disk and that they become more evident in times close to the satellite pericenters. The phase spirals are better observed in the range of younger-intermediate star populations in cosmological simulations. We state that other mechanisms might appear naturally in our model, such as the physics of gas, the collective effect of multiple perturbers, and a dynamically cold population continuously renovated by the star formation that helps satellites to trigger the observed disk response.

My poster is available at https://zenodo.org/record/7022523#.Y7QECKfML0o

Highlights of Spanish Astrophysics XI, Proceedings of the XV Scientific Meeting of the Spanish Astronomical Society held on September 4–9, 2022, in La Laguna, Spain. M. Manteiga, L. Bellot, P. Benavidez, A. de Lorenzo-Cáceres, M. A. Fuente, M. J. Martínez, M. Vázquez- Acosta, C. Dafonte (eds.), 2023

Photometric calibration of M-dwarf metallicity using Bayesian inference.

C. Duque-Arribas[1], D. Montes[1], H. M. Tabernero[2], J. A. Caballero[3], J. Gorgas[1], and E. Marfil[4]

[1] Departamento de Física de la Tierra y Astrofísica & IPARCOS-UCM (Instituto de Física de Partículas y del Cosmos de la UCM), Facultad de Ciencias Físicas, Universidad Complutense de Madrid, E-28040 Madrid, Spain
[2] Centro de Astrobiología (CSIC-INTA), carretera de Ajalvir km 4, 28850 Torrejón de Ardoz, Spain
[3] Centro de Astrobiología (CSIC-INTA), camino bajo del Castillo s/n, 28691 Villanueva de la Cañada, Madrid, Spain
[4] Instituto de Astrofísica de Canarias (IAC), Universidad de La Laguna, E-38200 La Laguna, Tenerife, Spain

Abstract

Metallicity has remained as a challenging parameter when characterizing M-type dwarf stars due to difficulties in the analysis of their spectra, dominated by molecular features, but it is required in multiple areas of astrophysics, for example to constrain theoretical stellar models or guide exoplanet searches. In order to estimate the metallicity of these cool stars, we have carried out multi-band photometric calibrations for early and intermediate M dwarfs using the precision, accuracy and homogeneity of both astrometry and photometry from Gaia DR3, complemented by near- and mid-IR photometry from 2MASS and CatWISE2020 surveys. These catalogs, combined with a sample of 5453 M dwarfs with additional parameters determined by APOGEE high-resolution spectroscopy, allow us to study the effect of the chemical composition in color-color and color-magnitude diagrams. We train calibrations using Bayesian statistics and Markov Chain Monte Carlo (MCMC) techniques using Stan to derive several photometric calibrations applicable to M dwarfs with metallicities in the range of $-0.45 \leq$ [Fe/H] $\leq +0.45$ and spectral types down to M5.0V, obtaining . Finally, we compare our results with previous photometric studies of metallicity found in the literature for an additional sample of 46 M-dwarf common-proper- motion companions of FGK-type primary stars with well-defined spectroscopic metallicities, finding a great predictive performance.

My poster is available at https://zenodo.org/record/7043212#.Y77OAS8rxqs

Highlights of Spanish Astrophysics XI, Proceedings of the XV Scientific Meeting of the Spanish Astronomical Society held on September 4–9, 2022, in La Laguna, Spain. M. Manteiga, L. Bellot, P. Benavidez, A. de Lorenzo-Cáceres, M. A. Fuente, M. J. Martínez, M. Vázquez- Acosta, C. Dafonte (eds.), 2023

Planetary Nebulae catalogue with Gaia EDR3.

I. González-Santamaría[1,2], M. Manteiga[1,2], A. Manchado[3], A. Ulla[4], and C. Dafonte[1,2]

[1] Universidade da Coruña (UDC)
[2] Centro de Investigación en Tecnologiás de la Información y las Comunicaciones de Coruña (CITIC)
[3] Instituto de Astrofísica de Canarias (IAC)
[4] Universidade de Vigo (UVigo)

Abstract

We have created a new Planetary Nebulae (PNe) catalogue by using astrometric and photometric data from Gaia EDR3. Firstly, we have developed an algorithm that selects the most reliable source from EDR3 to be the Central Star (CS) of each PN, among all sources in the neighbourhood of them. This algorithm considers both the angular distance to PN coordinates and also the Gaia colour (BP-RP) of the sources, and catalogues each CS in three different reliability groups. As a result, we have obtained more than 2000 CSPNe with enough reliability.

Then, from Gaia EDR3 parallaxes, we have derived the distances for most of these objects, and we have selected a subset of CSPNe with most accurate parallax and distance values, obtaining a sample of 405 objects that we call the Golden Astrometric Planetary Nebula (GAPN) sample. Then, we have analysed different properties of these nebulae, as their galactic distribution, nebular size, morphology, expansion velocity or kinematical age. In addition, for a group of them, we have studied the evolutionary state of their CSs, from the star's effective temperatures and luminosities, and by using the evolutionary tracks from Miller-Bertolami (2016). Thus, we have been able to estimate the CSPNe masses and evolutionary ages, that has allowed us to contrast this information with the spectral type of the stars.

Finally, we have also searched for and detected several wide binary stars within GAPN sample, by using EDR3 parallaxes and proper motions. In addition, we have also been able to shed some light on the close binarity in CSPNe.

My poster is available at https://zenodo.org/record/6907446#.YuPFZXZByUk

Highlights of Spanish Astrophysics XI, Proceedings of the XV Scientific Meeting of the Spanish Astronomical Society held on September 4–9, 2022, in La Laguna, Spain. M. Manteiga, L. Bellot, P. Benavidez, A. de Lorenzo-Cáceres, M. A. Fuente, M. J. Martínez, M. Vázquez- Acosta, C. Dafonte (eds.), 2023

Quantitative Spectroscopic Analysis of O stars in the IACOB+OWN project: Massive stars in the Galaxy with GAIA-DR3.

Holgado, G.[1], **and Simón-Díaz, S.**[2,3]

[1] Centro de Astrobiología (CAB), CSIC-INTA, Camino Bajo del Castillo s/n, campus ESAC, E-28692, Villanueva de la Cañada, Madrid, Spain
[2] Instituto de Astrofísica de Canarias, 38200 La Laguna, Tenerife, Spain
[3] Departamento de Astrofísica, Universidad de La Laguna, 38205 La Laguna, Tenerife, Spain

Abstract

Massive stars are luminous beacons that help us to extract information about the star formation history and the chemodynamical evolution of galaxies in the Universe. Our Galaxy is full of massive stars, which expend their short-lived existence within bright star-forming regions, depositing huge amounts of mechanical and radiative energy to the interstellar medium before they explode as energetic supernovae event. They are also the origin of the recently detected phenomena of gravitational waves, with the merger of a pair of their typical end products: black holes or neutron stars.

The IACOB and OWN projects have collected a large database of high-resolution multi-epoch spectra of Galactic O and B-type stars, ∼10000 spectra for more than 1000 OB stars. This unique spectroscopic dataset, once analyzed and interpreted with state-of-the-art tools and techniques will provide a new, global overview of the physical and evolutionary properties of massive stars in their early phases.

In this contribution, I will present the results from the quantitative spectroscopic analysis of ∼300 O stars targeted by the IACOB and OWN surveys (implying the largest sample of O Galactic O stars analyzed homogeneously, using modern automatized tools). I will put special emphasis on highlighting the impact of the GAIA mission in the determination of physical parameters of massive stars, with distance calculation of unprecedented precision for these bright objects. With this, we intend to revisit calibrations of stellar parameters with spectral type and luminosity class, and provide a homogeneous and statistically significant empirical anchor of the physical attributes of Galactic O-type stars.

My poster is available at https://doi.org/10.5281/zenodo.7005255

Highlights of Spanish Astrophysics XI, Proceedings of the XV Scientific Meeting of the Spanish Astronomical Society held on September 4–9, 2022, in La Laguna, Spain. M. Manteiga, L. Bellot, P. Benavidez, A. de Lorenzo-Cáceres, M. A. Fuente, M. J. Martínez, M. Vázquez- Acosta, C. Dafonte (eds.), 2023

Searching for a second occultation in EPIC 204376071.

Roi Alonso[1,2], Hans J. Deeg[1,2], and Saul Rappaport[3]

[1] Instituto de Astrofísica de Canarias, E-38205, La Laguna, Spain
[2] Departamento de Astrofísica, Universidad de La Laguna, E-38200, La Laguna, Spain
[3] Department of Physics, and Kavli Institute for Astrophysics and Space Research, M.I.T., Cambridge, MA 02139, USA

Abstract

EPIC 204376071 is a young (∼10 Myr) M star (estimated mass 0.16 $M_\odot$, and radius 0.63 $R_\odot$), probable member of the Upper Sco association, that exhibited an 80% drop in flux lasting one day, in the course of one campaign of the K2 mission (Rappaport et al. 2019). Different scenarios have been proposed to explain this feature, some of them requiring a periodic behaviour of these events. With only one event observed, it becomes challenging to obtain further observations to investigate further the origin of the abrupt flux drops, and start confirming/rejecting possible scenarios. We have obtained new photometric observations, and analysed archival photometry, with the goal to identify additional flux drops on this star, and get the ephemeris, should these events be periodic. We do not detect any further deep drop in flux, and place stronger constraints on posible periods. With only K2 data, ∼80% of the periods between 70 and 1200 days would have been missed. With the new data, this fraction drops to ∼40%.

My poster is available at https://zenodo.org/record/7054575#.Y2uaKVLP37g

Highlights of Spanish Astrophysics XI, Proceedings of the XV Scientific Meeting of the Spanish Astronomical Society held on September 4–9, 2022, in La Laguna, Spain. M. Manteiga, L. Bellot, P. Benavidez, A. de Lorenzo-Cáceres, M. A. Fuente, M. J. Martínez, M. Vázquez- Acosta, C. Dafonte (eds.), 2023

Searching for open clusters in Gaia DR3 using a parallax-blind approach.

Julio A. Carballo-Bello[1], Karla Peña-Ramírez[2], Felipe Gran[3], and Sebastián Ramírez-Alegría[2]

[1] Instituto de Alta Investigación, Sede Esmeralda, Universidad de Tarapacá, Av. Luis Emilio Recabarren 2477, Iquique, Chile
[2] Centro de Astronomía (CITEVA), Universidad de Antofagasta, Av. Angamos 601, Antofagasta, Chile
[3] University Côte d'Azur, Observatory of the Côte d'Azur, CNRS, Lagrange Laboratory, Observatory Bd, CS 34229, 06304 Nice cedex 4, France

Abstract

Gaia data is providing a unique opportunity to explore the structure of the Milky Way by discovering more and more of one of its best tracers: open clusters. Innovative algorithms, supported by Gaia accurate proper motions, parallaxes, photometry, and radial velocities (whenever available), have identified hundreds of new clusters of stars across the Galactic disk and bulge in only a few years. However, parallax measurements as a key ingredient in those techniques might lead to the possible loss of clusters when individual-associated uncertainties are relatively high. In this work, we will describe our attempts to perform a parallax-blind search of open clusters and show that there is still room for further discoveries thanks to the precious information contained in such an unprecedented database.

My poster is available at https://zenodo.org/record/7039479#.Y8FZYeLMJqw

Highlights of Spanish Astrophysics XI, Proceedings of the XV Scientific Meeting of the Spanish Astronomical Society held on September 4–9, 2022, in La Laguna, Spain. M. Manteiga, L. Bellot, P. Benavidez, A. de Lorenzo-Cáceres, M. A. Fuente, M. J. Martínez, M. Vázquez- Acosta, C. Dafonte (eds.), 2023

Supernova rates and [α/Fe] abundances in Milky Way Galaxy: their variations in time and space.

Mollá M.[1], **Cavichia O.**[2], **Bazán, J.J.**[1], **Castrillo, A.**[3], **Galbany, L.**[4,5], **and Millán-Irigoyen, I.** [1]

[1] Dpto. Investigación Básica, CIEMAT, Avda. Complutense 40, E-28040 Madrid, Spain
[2] Instituto de Física e Química, Universidade Federal de Itajubá, Av. BPS, 1303, 37500-903 Itajubá-MG, Brazil
[3] Dpto. de Física Teórica, Universidad Autónoma de Madrid, E-28049 Madrid, Spain
[4] Instituto de Ciencias del Espacio (ICE, CSIC), Campus UAB, Carrer de Can Magrans, s/n, E-08193 Barcelona, Spain
[5] Institut d'Estudis Espacials de Catalunya (IEEC), E-08034 Barcelona, Spain

Abstract

We present an update of the MulChem chemical evolution model applied to the Milky Way Galaxy (Molla et al. submitted), by using the most recent stellar yields for low and intermediate mass stars and for massive stars. We study the role of the type Ia supernova (SN Ia) rate, using 15 different Delay Time Distribution (DTD) prescriptions, depending on the binary star scenario able to create a SN Ia. Simultaneously, 12 tables of yields of elements produced by different explosion mechanisms for SN Ia are explored. The chemical abundances derived from these 180 models, resulting from the combination of different SN Ia yields and DTDs, are analized. The Solar Region results for [Fe/H] and [α/Fe] *vs.* stellar age and for [α/Fe] *vs.* [Fe/H] (where α-elements are O, Mg, Si, S, and Ca) are compared with an extensive observational dataset coming from the most recent surveys and compiled for this work. A χ^2 technique is used to look for the best model for reproducing the data set. Finally, we analyse the relative abundances [α/Fe] for disc and halo regions of the best model. As in previous works, we find that a significant fraction of type Ia SNe must take place at short delay times in order to reproduce the observations. The large dispersion of data could be explained by a mix of stars located at different spatial regions that moved after their birth. However, a mix of different DTD's or explosion mechanisms is a likely hypothesis in light of comparison models-data.

My poster is available at https://zenodo.org/record/7015711#.Y1bbgIJBxmE

Highlights of Spanish Astrophysics XI, Proceedings of the XV Scientific Meeting of the Spanish Astronomical Society held on September 4–9, 2022, in La Laguna, Spain. M. Manteiga, L. Bellot, P. Benavidez, A. de Lorenzo-Cáceres, M. A. Fuente, M. J. Martínez, M. Vázquez- Acosta, C. Dafonte (eds.), 2023

The GALANTE Photometric Project: First results and the MUDEHaR extension.

Holgado, G.[1], **Maíz Apellániz, J.**[1], **and Alfaro, E.**[2]

[1] Centro de Astrobiología (CAB), CSIC-INTA, Camino Bajo del Castillo s/n, campus ESAC, E-28692, Villanueva de la Cañada, Madrid, Spain
[2] Instituto de Astrofísica de Andalucia, (CSIC), E-18 008 Granada, Spain

Abstract

GALANTE is an optical (3000-9000 Å) photometric survey with seven intermediate/narrow filters that has been covering the northern Galactic Plane and some adjacent regions since 2016 using the Javalambre T80 telescope (P.I.s Emilio J. Alfaro & Jesús Maíz Apellániz). Originally designed to identify the majority of the early-type massive stars within several kpc of the Sun –including extinction characteristics– its data will be also used for a variety of other stellar studies and the generation of a high-resolution map of the Hα emission.
As of early 2022, the observations are almost complete resulting in over 300 astronomical fields, and the first Data Release including 20 fields of 2 deg^2 is now available. The results show a photometric dynamic range comparable to that of Gaia, reaching a 1% accuracy and precision for stars brighter than AB magnitude 17, and the detection of many fainter stars In this contribution, I present results of our test fields and a brief summary of the MUDEHaR project, a multi-epoch photometric survey complementary to GALANTE, proposed as the next long-term survey at the Javalambre facilities.

My poster is available at https://doi.org/10.5281/zenodo.7039330

Highlights of Spanish Astrophysics XI, Proceedings of the XV Scientific Meeting of the Spanish Astronomical Society held on September 4–9, 2022, in La Laguna, Spain. M. Manteiga, L. Bellot, P. Benavidez, A. de Lorenzo-Cáceres, M. A. Fuente, M. J. Martínez, M. Vázquez- Acosta, C. Dafonte (eds.), 2023

The Li-age relation: Calibration with open clusters and associations.

M.L. Gutiérrez Albarrán[1], D. Montes[1], H.M. Tabernero[1,2], J.I. González Hernández[3,4], A. Frasca[5], A.C. Lanzafame[5], R. Smiljanic[6], A.J. Korn[7], S. Randich[8], G. Gilmore[9], et al, and GES Survey Builders[3]

[1] Departamento de Física de la Tierra y Astrofísica and IPARCOS-UCM (Instituto de Física de Partículas y del Cosmos de la UCM), Facultad de Ciencias Físicas, Universidad Complutense de Madrid, E-28040, Madrid, Spain
[2] Centro de Astrobiología (CAB, CSIC-INTA)
[3] Instituto de Astrofísica de Canarias (IAC)
[4] Universidad de la Laguna, Dept. Astrofísica, E-38206 La Laguna, Tenerife
[5] INAF - Osservatorio Astrofisico di Catania
[6] Nicolaus Copernicus Astronomical Center, Polish Academy of Sciences
[7] Department of Physics and Astronomy, Uppsala University
[8] INAF - Osservatorio Astrofisico di Arcetri
[9] Institute of Astronomy, University of Cambridge

Abstract

In this work we used a series of open clusters and associations observed by the *Gaia*-ESO Survey (GES) to study the use of lithium abundances (Li I spectral line at 6708 Å) as an age indicator for pre- and main-sequence FGKM late-type stars. Previous studies of open clusters have shown that lithium depletion is not only strongly age dependent, but also shows a complex pattern with several other parameters, such as rotation, chromospheric activity (Hα) and metallicity. Using the available data from both GES iDR6 and *Gaia* EDR3, we performed a thorough membership analysis and obtained lists of candidate members for 42 open clusters, ranging in age from 1–3 Myr to 4.5 Gyr. We then conducted a comparative study that allowed us to quantify the observable lithium dispersion in each cluster and study the influence of rotation, activity and metallicity in the lithium dispersion of the selected candidates. All this allowed us to calibrate a Li-age relation and create empirical lithium envelopes for key ages in our sample, also constraining the LDB for those clusters in the 15–600 Myr age range.

My poster is available at https://zenodo.org/record/7044661#.Y2158uTMI2z

Highlights of Spanish Astrophysics XI, Proceedings of the XV Scientific Meeting of the Spanish Astronomical Society held on September 4–9, 2022, in La Laguna, Spain. M. Manteiga, L. Bellot, P. Benavidez, A. de Lorenzo-Cáceres, M. A. Fuente, M. J. Martínez, M. Vázquez- Acosta, C. Dafonte (eds.), 2023

The circumstellar medium around five LBV stars through the light of NIKA2 and the Virtual Observatory.

J. R. Rizzo[1,2], C. Bordiu[3], B. López Martí[4], F. M. Jiménez-Esteban[2], R. Martín-López[5], and A. Ritacco[6]

[1] ISDEFE, Spain
[2] Centro de Astrobiología (CAB/CSIC-INTA), Spain
[3] Ossevatorio Astrofisico di Catania, INAF, Italy
[4] Universidad CEU San Pablo, Spain
[5] Robert Bosch España, Spain
[6] Osservatorio Astronomico di Cagliari, INAF, Italy

Abstract

Luminous Blue Variable (LBV) stars are post-main sequence massive objects in a very fast ($10^4\,a$) transitional stage characterized by dense winds and impressive mass eruptions, as they are close to the Eddington limit. LBVs profoundly affect their surroundings, creating ionized and dusty nebulae, some times surrounded by molecular gas. They are great infrared emitters due to their high luminosity and the usually high extinction. They have also been detected at cm-wavelengths, dominated by non-thermal emission. The mm/submm regime, however, has not been much investigated. NIKA2 is a highly sensitive continuum camera installed at the IRAM 30m radio telescope near Pico Veleta, Granada. The camera can provide images at 150 and 260 GHz (2 and 1.15 mm of wavelength, approximately), with a field of view of up to 6.5 arcmin. The operational frequencies of NIKA2 are of great interest in the study of LBVs because it is a range where both thermal and non-thermal process compete in their contribution to the SEDs.

In this work we present the results achieved towards a sample of five galactic LBVs obtained using NIKA2 and a set of information gathered using Virtual Observatory tools and archives. We detected emission from the stars themselves, in their close surroundings, and also outside the IR nebulae. All these components depict very different spectral indexes, pinpointing that diverse mechanisms coexist, such as free-free gas emission, thermal dust and synchrotron radiation. We complemented these findings by building the SEDs of the LBV stars, where the contribution from the extended photosphere is clearly separated from warm black (grey) body emission, and non-thermal flux in some cases.

My poster is available at https://doi.org/10.5281/zenodo.7046127

Highlights of Spanish Astrophysics XI, Proceedings of the XV Scientific Meeting of the Spanish Astronomical Society held on September 4–9, 2022, in La Laguna, Spain. M. Manteiga, L. Bellot, P. Benavidez, A. de Lorenzo-Cáceres, M. A. Fuente, M. J. Martínez, M. Vázquez- Acosta, C. Dafonte (eds.), 2023

The lithium-rotation connection in the M35 open cluster.

D. Cuenda-Muñoz[1], **and D. Barrado**[1]

[1] Centro de Astrobiología (CAB), CSIC-INTA

Abstract

Lithium abundance is an age indicator for G and K stellar types since its surface abundance decreases over time for these spectral types. However, despite all the observational efforts made during the last 30 years, the role of rotation and stellar activity in this process is still unclear. Our purpose is to investigate how lithium depletion is affected by rotation in G and K stars of the M35 open cluster. We take advantage of three previous WIYN/HYDRA spectroscopic studies of Li in M35 G-K stellar types, which provide an initial sample of 251 dwarfs. In addition, we have also taken into account over 160 candidate members observed with the same instrument, collecting a final sample of nearly 400 stars. In order to distinguish between members and non members of the cluster, we have combined the membership probabilities published in 2015 as part of the DANCe program and the results provided by Clusterix 2.0, a Spanish Virtual Observatory tool. Finally, we have measured the LiI 6707.8 $\AA$ equivalent width for the M35 candidates added and we have crossed our sample with several photometric surveys to obtain rotational periods for the members of this cluster. The analysis carried out so far confirms that fast rotators of K spectral type tend to be Li-rich compared with slow rotators of similar effective temperature. This general trend follows the results already observed in the Pleiades for G and K dwarfs.

My poster is available at https://zenodo.org/record/7041728#.Y2ObhSbTX0o

Highlights of Spanish Astrophysics XI, Proceedings of the XV Scientific Meeting of the Spanish Astronomical Society held on September 4–9, 2022, in La Laguna, Spain. M. Manteiga, L. Bellot, P. Benavidez, A. de Lorenzo-Cáceres, M. A. Fuente, M. J. Martínez, M. Vázquez- Acosta, C. Dafonte (eds.), 2023

The variation of the optical SED of RR Lyrae stars with the multi-filter J-VAR survey.

Domínguez-Fernández, A. J.[1,2], Vázquez Ramió, H.[3], López-Sanjuan, C.[3], and J-VAR Team

[1] Centro de Estudios de Física del Cosmos de Aragón, Plaza San Juan 1, 44001 Teruel, Spain
[2] Departamento de Física de la Tierra y Astrofísica, Facultad de Ciencias Físicas, Universidad Complutense de Madrid, 28040 Madrid, Spain
[3] Centro de Estudios de Física del Cosmos de Aragón, Unidad Asociada al CSIC, Plaza San Juan 1, 44001 Teruel, Spain

Abstract

Time domain surveys, whether in the form of wide-field photometric (like LSST) or spectroscopic (SDSS-V) surveys, will expand our knowledge in many aspects of stellar Astrophysics in the next decade. J-VAR constitutes a trade-off between such approximations, having a photometric-based approach but with some (low) spectral resolution around key stellar features thanks to its medium- and narrow-band filters (J0395, J0515, J0660, J0861).
RR Lyrae stars, intimately tracers of old (>10 Gyr) stellar populations, are classical pulsators with periods between around 0.2 to 1.2 d. They pulsate mainly in two modes: the fundamental (RRab/RR0) and the first-overtone (RRc/RR1) modes. Although they are present in all the MW components, their number stands out in the halo. They are very fair distance indicators (following a well-known and tight luminosity-period-metallicity relation).
In this contribution, we explore the capabilities of J-VAR data to analyze how the Spectral Energy Distributions (SEDs) of RR Lyrae stars vary with the phase and what can we learn from it about the physics of these classical pulsators.

My poster is available at https://zenodo.org/record/7025748#.Y2jNJC1Dl-V

Highlights of Spanish Astrophysics XI, Proceedings of the XV Scientific Meeting of the Spanish Astronomical Society held on September 4–9, 2022, in La Laguna, Spain. M. Manteiga, L. Bellot, P. Benavidez, A. de Lorenzo-Cáceres, M. A. Fuente, M. J. Martínez, M. Vázquez- Acosta, C. Dafonte (eds.), 2023

Time-frequency analysis of HD 179436 and HD 179466 using the wavelet transform.

Ramón-Ballesta, A.[1], **Pascual-Granado, J.**[1], **and Garrido, R.**[1]

[1] Instituto de Astrofísica de Andalucía (CSIC), Glorieta de la Astronomía S/N, 18008, Granada, Spain

Abstract

δ Scuti stars are intermediate-mass stars (i.e. between 1.5 and 3 solar masses) pulsators located in the classical Cepheids instability strip, either in their pre-main sequence stage, or already in the main sequence or also moving from the main sequence to the giant branch. Their spectral types range from A to F. Before the era of space telescopes, these stars were thought to have a small number of pulsating frequencies, but with the data coming from space missions like CoRoT, Kepler, TESS, etc., it has been found that there are some δ Scuti stars with hundreds of pulsation frequencies. In the last years, some authors found an amplitude modulation in a few δ Scuti stars but a time-frequency analysis has not yet been performed up to date. In our work we have chosen the wavelet transform as the more appropriate tool to perform such analysis. Unlike the short time Fourier transform, that uses a fixed windows size, the wavelet transform uses short windows at high frequencies and long windows at low frequencies, making it like an adaptive analysis tool. The wavelet analysis relies on the use of a mother wavelet, i.e. a wave-like function of finite energy that can be scaled and shifted in a way that conserves the energy, so it can correlate with the variations on the signal, thus providing a measure of the instantaneous frequencies of the signal. In our work, we analyse the stability of the pulsation frequencies of the δ Scuti stars HD 179436 and HD 179466. The results show that some frequencies are stable, at least within the observation run time, although some others show some kind of variation.

My poster is available at https://zenodo.org/record/7046708#.Y1k7pkhByZg

Highlights of Spanish Astrophysics XI, Proceedings of the XV Scientific Meeting of the Spanish Astronomical Society held on September 4–9, 2022, in La Laguna, Spain. M. Manteiga, L. Bellot, P. Benavidez, A. de Lorenzo-Cáceres, M. A. Fuente, M. J. Martínez, M. Vázquez- Acosta, C. Dafonte (eds.), 2023

VIOMASS: Virtual Observatory Integration Of Madcuba And SLIM Spectra.

J. R. Rizzo[1,2], C. Blanco[2], and J. Martín-Pintado[2]

[1] ISDEFE, Spain
[2] Centro de Astrobiología (CAB/CSIC-INTA), Spain

Abstract

MADCUBA is an astronomical package primarily aimed to reduce and analyze data from many radio astronomical facilities. MADCUBA is not only able to process individual spectra, but also data cubes. In addition, it is able to identify thousands of molecular rotational transitions and radio recombination lines by consulting the most important molecular databases. One of its tasks -SLIM- simulates LTE conditions and makes a semi-automatic fitting of many lines simultaneously.
Under a collaborative effort of Virtual Observatory (VO) and MADCUBA groups, we are implementing new functionalities in MADCUBA to make it VO-compliant. The final objective is to profit the robustness of MADCUBA and the versatility of VO in order to increase visibility of MADCUBA and allow users to enhance results through the interaction with the pleiad of VO tools and available data sets.
In this e-poster we present the scope of the project, changes already implemented and future work. In detail, we show the data model which will be implemented and the options that the user will have to export their work adhering to the VO standards.

My poster is available at https://doi.org/10.5281/zenodo.7046116

Highlights of Spanish Astrophysics XI, Proceedings of the XV Scientific Meeting of the Spanish Astronomical Society held on September 4–9, 2022, in La Laguna, Spain. M. Manteiga, L. Bellot, P. Benavidez, A. de Lorenzo-Cáceres, M. A. Fuente, M. J. Martínez, M. Vázquez- Acosta, C. Dafonte (eds.), 2023

Vela X-1 in depth: a review article on an outstanding object.

Martínez-Núñez, S.[1], Kretschmar, P.[2], El Mellah, I.[3], Fuerst, F.[4], Grinberg, V.[5], Sander, A. A. C[6], van den Eijnden, J.[7], Degenaar, N.[8], Maíz Apellániz, J.[9], Jiménez Esteban, F.[9], Ramos-Lerate, M[10], and Utrilla, E.[11]

[1] IFCA (CSIC-UC), Spain
[2] ESA-ESAC, Spain
[3] IPAG, France
[4] Quasar Science Resources S.L for ESA, ESAC, Spain
[5] ESA-ESTEC, Netherlands
[6] ZHA, Germany
[7] U. Oxford, UK
[8] API, Netherlands
[9] CAB (CSIC-INTA), Spain
[10] Vitrociset Belgium for ESA, ESAC, Spain
[11] Aurora Technology BV for ESA, ESAC, Spain

Abstract

The paper - Revisiting the archetypical wind accretor Vela X-1 in depth. Case study of a well-known X-ray binary and the limits of our knowledge - provided a thoughtful compilation of the knowledge of the Vela X-1 system and its modelling published over decades; added new information derived from public data or catalogues, including an updated distance and spectral classification based on the Gaia EDR3 release; and identified specific avenues of future research that could help to clarify open questions.
This publication triggered a discussion on the editorial board of A&A journal, leading to the creation of a new type of review article on uniquely interesting objects.

Acknowledgements

SMN acknowledgements funded by project RTI2018-096686-B-C21 funded by MCIN/AEI/10.13039/501100011033 and by "ERDF A way of making Europe".

My poster is available at https://zenodo.org/record/7038485#.Y5sH16fMLpg

Highlights of Spanish Astrophysics XI, Proceedings of the XV Scientific Meeting of the Spanish Astronomical Society held on September 4–9, 2022, in La Laguna, Spain. M. Manteiga, L. Bellot, P. Benavidez, A. de Lorenzo-Cáceres, M. A. Fuente, M. J. Martínez, M. Vázquez- Acosta, C. Dafonte (eds.), 2023

What determines the inner sizes of protoplanetary disks?.

Mendigutía, I.[1], Marcos-Arenal, P.[1], Koumpia, E.[2], Oudmaijer, R.D.[2], Vioque, M.[3,4], Guzmán-Díaz, J.[1], Wichittanakom, C.[2,5], de Wit, W.J.[6], Montesinos, B.[1], and Ilee, J.D.[2]

[1] Centro de Astrobiología (CAB), CSIC-INTA, Camino Bajo del Castillo s/n, 28692 Villanueva de la Cañada, Madrid, Spain
[2] School of Physics and Astronomy, EC Stoner Building, University of Leeds, Leeds LS2 9JT, UK
[3] Joint ALMA Observatory, Alonso de Córdova 3107, Vitacura, Santiago 763-0355, Chile
[4] National Radio Astronomy Observatory, 520 Edgemont Road, Charlottesville, VA 22903, USA
[5] Department of Physics, Faculty of Science and Technology, Thammasat University, Rangsit Campus, Pathum Thani 12120, Thailand
[6] European Southern Observatory (ESO), Casilla 19001, Santiago 19, Chile

Abstract

Dust particles do not survive temperatures > 1500 K, for which all protoplanetary disks should be cleared of dust close to the central stars. The size of such inner dust holes should be larger for more luminous (hotter) sources, but have angular scales of milliarcsec even for the closest young stars. Thus, they can be resolved only from near-infrared interferometry. This poster summarises our work in Marcos-Arenal et al. 2021, A&A 652, A68, where we inferred inner disk sizes of young stars based on GRAVITY/ESO-Paranal Interferometer observations. We presented the most complete "size-luminosity diagram" of optically-visible young stars. Although the overall trend relating both parameters is confirmed, there is significant scatter. We tested the three main hypotheses aiming to account for the observed size-luminosity relation and its scatter: the presence or absence of large amounts of inner gas, alternative accretion mechanisms, and the different dust disk properties based on spectral energy distributions. None of these scenarios serve as a general explanation, and the origin of the size-luminosity relation and its scatter remains an open question. Future observations avoiding underlying trends with the distance are proposed, which may help to better understand what determines the inner sizes of protoplanetary disks.

My poster is available at https://zenodo.org/record/7023467#.Y5LzcNLMKUl

Highlights of Spanish Astrophysics XI, Proceedings of the XV Scientific Meeting of the Spanish Astronomical Society held on September 4–9, 2022, in La Laguna, Spain. M. Manteiga, L. Bellot, P. Benavidez, A. de Lorenzo-Cáceres, M. A. Fuente, M. J. Martínez, M. Vázquez- Acosta, C. Dafonte (eds.), 2023

Written in the stars: spectral synthesis on CARMENES GTO M-dwarf spectra.

Marfil, E.[1,2,3,4], Tabernero, H. M.[2], Montes, D.[1], Caballero, J. A.[2], and the CARMENES consortium

[1] Departamento de Física de la Tierra y Astrofísica & IPARCOS-UCM (Instituto de Física de Partículas y del Cosmos de la UCM), Facultad de Ciencias Físicas, Universidad Complutense de Madrid
[2] Centro de Astrobiología (CAB, CSIC-INTA)
[3] Instituto de Astrofísica de Canarias (IAC)

Abstract

We present the results recently published by Marfil et al. (2021, A&A, 656, A162) regarding the determination of the stellar atmospheric parameters ($T_{\rm eff}$, $\log g$, and [Fe/H]) of 343 M dwarfs observed with CARMENES. We employed StePar Syn, a Bayesian spectral synthesis implementation particularly designed to infer the stellar atmospheric parameters of late-type stars following a Markov chain Monte Carlo approach. We made use of the BT-Settl model atmospheres and the radiative transfer code Turbospectrum to compute a grid of synthetic spectra around 75 magnetically insensitive Fe I and Ti I lines plus the TiO γ and ϵ bands. To avoid any potential degeneracy in the parameter space, we imposed Bayesian priors based on the photometric data available for the sample. We find that this methodology is suitable down to M7.0 V, where refractory metals such as Ti are expected to condense in the stellar photospheres. Although our $T_{\rm eff}$ scale is in good agreement with the literature, we report large discrepancies in the [Fe/H] scales, which might arise from the different methodologies and sets of lines considered. However, our [Fe/H] is in agreement with the metallicity distribution of FGK-type stars in the solar neighbourhood and correlates well with the kinematic membership of the targets in the Galactic populations. Lastly, excellent agreement in $T_{\rm eff}$ is found for M dwarfs with interferometric angular diameter measurements, as well as in the [Fe/H] between the components in the wide physical FGK+M and M+M systems included in our sample.

The StePar Syn code (Tabernero et al. 2022, A&A, 657, A66) is available at GitHub: https://github.com/hmtabernero/SteParSyn/.

My poster is available at https://doi.org/10.5281/zenodo.6973999

Highlights of Spanish Astrophysics XI, Proceedings of the XV Scientific Meeting of the Spanish Astronomical Society held on September 4–9, 2022, in La Laguna, Spain. M. Manteiga, L. Bellot, P. Benavidez, A. de Lorenzo-Cáceres, M. A. Fuente, M. J. Martínez, M. Vázquez- Acosta, C. Dafonte (eds.), 2023

A probability distribution for the amplitude of Solar Cycle 25.

Arregui, I.[1,2]

[1] Instituto de Astrofísica de Canarias, Vía Láctea S/N, E-38205 La Laguna, Spain
[2] Departamento de Astrofísica, Universidad de La Laguna, E-38206 La Laguna, Spain

Abstract

We suggest a method to calculate the probability for the maximum amplitude of Solar Cycle 25 using Bayesian inference. We illustrate this approach with the predictions made by one particular phenomenological model that relates the time interval between termination events of preceding cycles with the amplitude of the next cycle. Our results show well-constrained posterior-predictive distributions for the maximum sunspot-number. The impact of uncertainty on sunspot-number and time interval between terminators is quantified. A comparison between past maximum sunspot-number values and posterior-predictive distributions computed using the method enables us to quantify the quality of the inference and of the prediction.

1 Introduction

Solar cycle prediction has been a matter of interest for decades and has led to a vast literature, see for example the recent reviews by [3, 6, 5]. Among the different techniques employed, precursor methods aim at predicting the amplitude of a given cycle based on a measure of solar activity/magnetism in a preceding cycle at a given moment of time.

One example is the empirical relationship between the time interval between termination events and the amplitude of the upcoming solar cycle, recently suggested by [4]. Termination events delimit epochs of toroidal-magnetic-activity-band interaction and mark the limit between 11-year sunspot cycles and the end of 22-year magnetic activity cycles. According to the proposed relationship, widely separated terminators would correspond to low-amplitude sunspot cycles. Conversely, more narrowly separated terminators would lead to large amplitude sunspot-cycles.

A drawback of the statistical method employed by [4] and similar studies is that they do not permit one to make probability statements, nor do they offer straightforward ways to propagate the uncertainty from the observations to the quantities of interest. We propose a method for computing the probability distribution of the maximum amplitude of Solar Cycle 25 using Bayesian inference and illustrate the method using the phenomenological model and data by [4].

2 Method

Given a model $\mathcal{M}$, with parameter vector $\boldsymbol{\theta}$, proposed to explain observed data $\mathcal{D}$, the posterior distribution of the parameters is given by the product of the likelihood function $p(\mathcal{D}|\boldsymbol{\theta},\mathcal{M})$ and the prior distribution $p(\boldsymbol{\theta}|\mathcal{M})$

$$p(\boldsymbol{\theta}|\mathcal{D},\mathcal{M}) = \frac{p(\mathcal{D}|\boldsymbol{\theta},\mathcal{M})\,p(\boldsymbol{\theta}|\mathcal{M})}{p(\mathcal{D}|\mathcal{M})}. \tag{1}$$

The quantity in the denominator is the evidence, or prior predictive distribution

$$p(\mathcal{D}|\mathcal{M}) = \int_{\boldsymbol{\theta}} p(\mathcal{D}|\boldsymbol{\theta},\mathcal{M})\,p(\boldsymbol{\theta}|\mathcal{M})\,d\boldsymbol{\theta}. \tag{2}$$

The evidence is a measure of the quality of the model. It quantifies how well the data $\mathcal{D}$ are predicted by the model $\mathcal{M}$.

Once the inference of the model parameters is performed, a distribution over possible unobserved future data $\widetilde{\mathcal{D}}$, conditional on the observed data and the inferred model, is given by the posterior-predictive distribution

$$p(\widetilde{\mathcal{D}}|\mathcal{D},\mathcal{M}) = \int_{\boldsymbol{\theta}} p(\widetilde{\mathcal{D}}|\boldsymbol{\theta},\mathcal{M})\,p(\boldsymbol{\theta}|\mathcal{D},\mathcal{M})\,d\boldsymbol{\theta}. \tag{3}$$

The first factor in the integrand is the likelihood of the new unobserved data as a function of the parameter vector. The second factor is the posterior inferred from the old observed data.

3 Analysis and results

Following [4], we assume a linear relationship between the maximum sunspot number SSN and the time interval between termination events ΔT, $\mathrm{SSN} = \mathcal{M}(\Delta T|\alpha,\beta) = \alpha\Delta T + \beta$, and infer the posterior density for the slope α and the intercept β of the model, $p(\alpha,\beta|\mathcal{D},\mathcal{M})$, with $\mathcal{D} = d_i = \{\mathrm{SSN}_i, \Delta T_{i-1}\}_{i=2}^{24}$ the (past) observed data in Table 1 by [4].

A particular choice of likelihood function for the special case of a straight-field model, when there are independent errors in both data coordinates, is the following (see e.g., [2])

$$\begin{aligned} p(\mathcal{D}|\mathcal{M},\alpha,\beta) &= (2\pi)^{-N/2}\left(\prod_{i=1}^{N}(\sigma^2_{\mathrm{SSN}_i} + \alpha^2\sigma^2_{\Delta T_{i-1}})^{-1/2}\right) \\ &\times \exp\left\{\sum_{i=1}^{N}\frac{-[d_i - \mathcal{M}(\Delta T_{i-1}|\alpha,\beta)]^2}{2(\sigma^2_{\mathrm{SSN}_i} + \alpha^2\sigma^2_{\Delta T_{i-1}})}\right\}, \end{aligned} \tag{4}$$

with each σ_{SSN} and $\sigma_{\Delta T}$ expressing the uncertainty on sunspot number and time interval between termination events, respectively.

The combination of likelihood function and uniform priors over certain ranges leads to

the posterior distribution. Figure 1 shows an example solution for given fixed values for the uncertainty on the sunspot number and the time-interval between termination events. Well-constrained distributions are obtained for the marginal posteriors of the model parameters α and β (top and middle panels on the left).

Following the definition in Equation 3, the posterior predictive distribution for the future unobserved amplitude of Solar Cycle 25, $\widetilde{\mathcal{D}} = \mathrm{SSN}_{25}$, based on the time interval for the preceding termination event, ΔT_{24}, can then be computed from the inferred posterior and by considering a Gaussian likelihood for the new data as a function of the parameter vector

$$\begin{aligned} p(\mathrm{SSN}_{25}|\mathcal{M},\alpha,\beta) &= \frac{1}{\sqrt{2\pi}}\left((\sigma^2_{\mathrm{SSN}_{25}}+\alpha^2\sigma^2_{\Delta T_{24}})^{-1/2}\right) \\ &\times \exp\left\{\frac{-[\mathrm{SSN}_{25}-\mathcal{M}(\Delta T_{24}|\alpha,\beta)]^2}{2(\sigma^2_{\mathrm{SSN}_{25}}+\alpha^2\sigma^2_{\Delta T_{24}})}\right\}, \end{aligned} \tag{5}$$

with $\sigma_{\mathrm{SSN}_{25}}$ and $\sigma_{\Delta T_{24}}$ expressing the uncertainty we are willing to consider for the future sunspot number and the last time interval between termination events, respectively.

Let us assume the termination event for Solar Cycle 24 occurred in October 2021. This leads to $\Delta T_{24} = 10.72$. The obtained posterior-predictive distribution for the maximum amplitude of Cycle 25 is displayed in the bottom-left panel of Fig. 1 and shows a well-constrained posterior density. The rounded summary of the posterior predictive distribution is $\mathrm{SSN}_{25} = 191^{+11}_{-11}$, with the estimate corresponding to the median and the uncertainties given at the 68% credible interval. The main advantage of having the posterior-predictive distribution is that it is now perfectly possible and straightforward to make probability statements. For instance, according to the result displayed in Fig. 1, the probability that the maximum amplitude of Solar Cycle 25 will fall between $\sim$ 180 and 201 is 68%, the area under the green curve covering that percentage of the full probability mass.

Another advantage of the method is that it propagates uncertainty from the observations to the inferred quantities of interest. The right panels in Fig. 1 show how varying the uncertainty about sunspot number and time interval between termination events influences the resulting posterior-predictive distribution. Uncertainty in the sunspot number affects the dispersion of the probability distribution (top-right panel). Uncertainty on the time interval between termination events affects dispersion and the location parameter of the probability distribution (middle-right panel). Adopting an approximate formula by [1] for the sunspot number error, produces a probability distribution (bottom-right panel) with a larger uncertainty and with a median, $\mathrm{SSN}_{25} = 184^{+25}_{-22}$, that is also displaced with respect to the calculation with fixed sunspot number error.

Because the method provides us with a distribution of probability among different possible sunspot-number values, it becomes possible to quantify the predictive capabilities of the precursor and/or the model. While Solar Cycle 25 is underway, we can do this exercise with past solar cycles and use the method to compute posterior-predictive distributions using the data in Table 1 by [4]. Figure 2 shows that the 95% credible intervals of the computed probability distributions cover the actually observed sunspot number in all except three cases

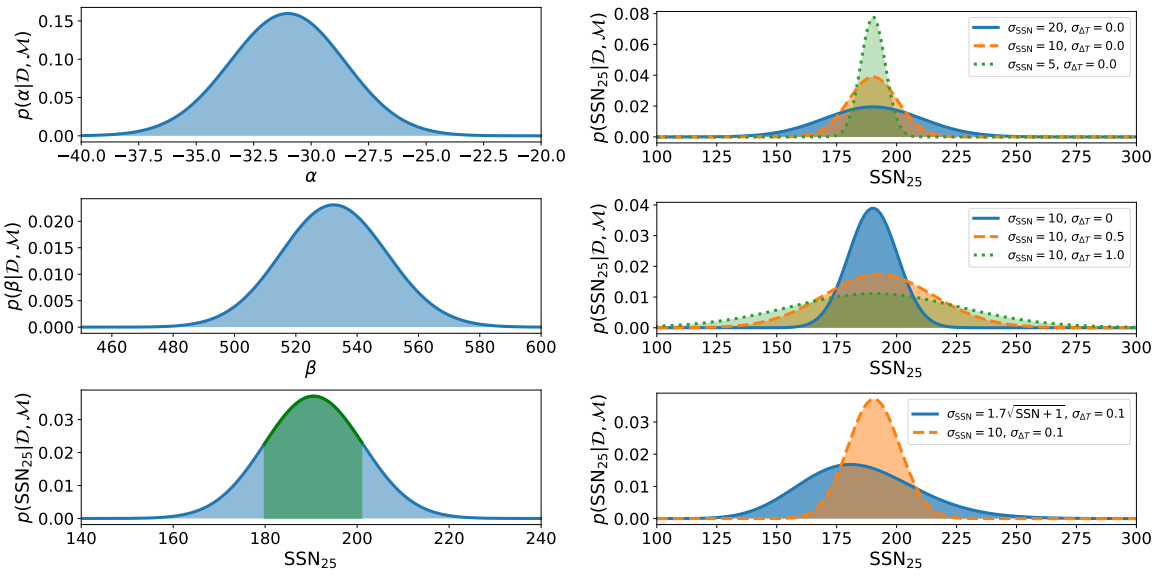

Figure 1: Left: top and middle panels show marginal posterior densities for the slope α and the intercept β of the linear model $\mathcal{M}$ that account for the past sunspot-number data $\mathcal{D}$. The calculations assume $\sigma_{\mathrm{SSN}_i} = 10$ and $\sigma_{\Delta T_{i-1}} = 0.1\,\forall i$. The bottom panel displays the posterior-predictive distribution for the sunspot-number during Solar Cycle 25, based on the posterior from past data and the likelihood of new data. The shaded green area covers 68 % of the mass centred around the median: $\mathrm{SSN}_{25} = 190.6^{+10.6}_{-10.8}$. The calculation assumes $\Delta T_{24} = 10.72$. Right: top panel shows the influence of uncertainty on sunspot-number [σ_{SSN}] on the posterior-predictive distribution for SSN_{25} for the case with no uncertainty on the time interval between termination events: $\sigma_{\Delta T} = 0$. The middle panel shows the influence of uncertainty about the time interval between termination events [$\sigma_{\Delta T}$] on the posterior-predictive distribution for SSN_{25} for the case with $\sigma_{\mathrm{SSN}} = 10$. The bottom panel shows a comparison between posterior-predictive distributions for SSN_{25} computed with a fixed error on sunspot-number and with the approximate formula by [1].

(SC16, SC19, and SC21). The observed values are within the 68% credible interval of the prediction in 12 cases. The median of the prediction is fairly accurate in six cases. The NOAA Space Weather Prediction Center prediction interval is also shown in the figure and falls below the prediction interval for this precursor and model. On the other hand, our estimate is in good agreement with the climatological forecast by Pesnell (2018) which considers that the maximum amplitude of Solar Cycle 25 will be the average of all observed maxima.

4 Summary

In this work we suggest a method for computing predictions for the maximum amplitude of Solar Cycle 25, based on Bayesian inference, and adopting a particular precursor as example application. The relevant quantity is the posterior-predictive distribution of the maximum

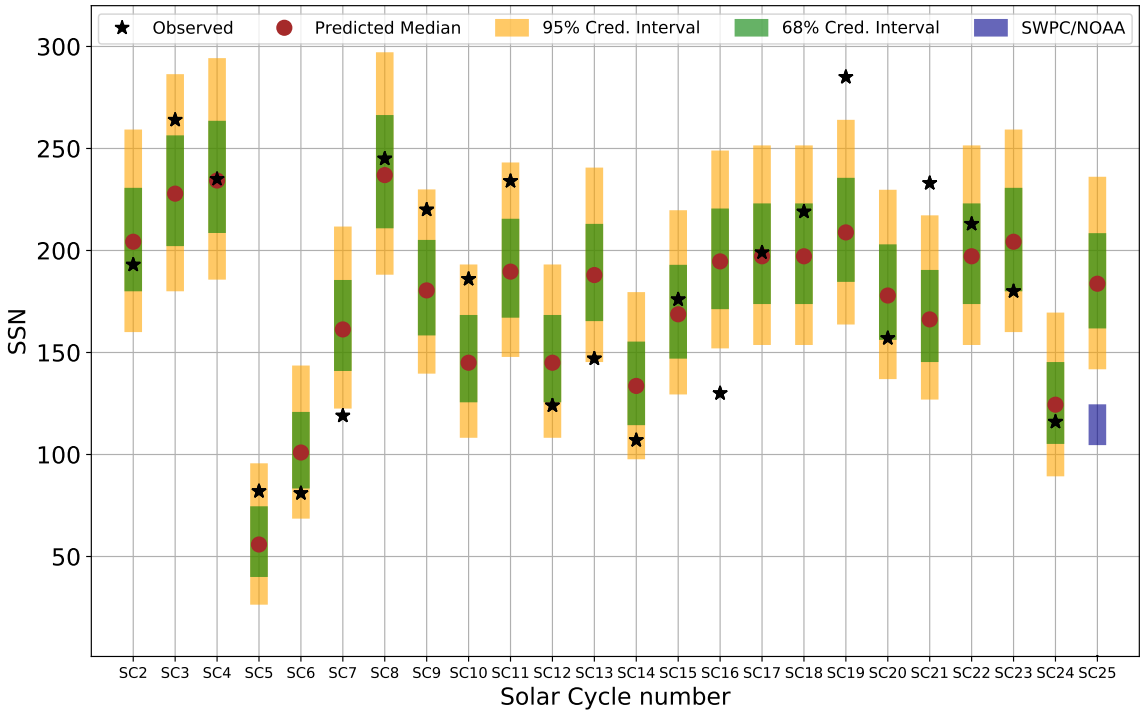

Figure 2: Comparison between observed sunspot-number values for past Solar Cycles 2 to 24 from Table 1 of [4] and posterior-predictive distributions computed using Equation (5) with data on Table 1 of [4]. In all calculations, $\sigma_{\Delta T} = 0.1$ and the approximate formula by [1], $\sigma_{\mathrm{SSN}} = 1.7\sqrt{\mathrm{SSN}+1}$, are employed . For Solar Cycle 25, $\Delta T = 10.72$ is employed. Also shown is the interval between the minimum and maximum peak sunspot-number values currently predicted by the SWPC/NOAA. Colours indicate different credible intervals of the obtained posterior distributions.

sunspot number. It is a probability distribution and results from the combination of a posterior probability distribution, inferred from past data, and a likelihood function for unobserved future data. The useful qualities of the method are the following: it enables to make probability statements about the quantity of interest, the SSN; the inference considers the propagation of uncertainty from observables to inferred quantities; and it is applicable to other predictive methods and alternative models, hence can be used to assess the quality of the predictor and/or the adopted model.

Acknowledgements

This study was motivated by correspondence with Scott W. Mcintosh. I am grateful to Andrés Asensio Ramos, José Manuel Vaquero, and Víctor Manuel Sánchez Carrasco for helpful comments and suggestions. This research was supported by projects PGC2018-102108-B-I00 and PID2021-127487NB-I00 from Ministerio de Ciencia, Innovación y Universidades and FEDER funds.

References

[1] Dudok de Wit, T., Lefèvre, L., & Clette, F. 2016, Solar Phys., 291, 2709

[2] Gregory, P. C. 2005, Bayesian Logical Data Analysis for the Physical Sciences: A Comparative Approach with 'Mathematica' Support (Cambridge University Press)

[3] Hathaway, D. H. 2015, Living Reviews in Solar Physics, 12, 4

[4] McIntosh, S. W., Chapman, S., Leamon, R. J., Egeland, R., & Watkins, N. W. 2020, Solar Phys., 295, 163

[5] Nandy, D. 2021, Solar Physics, 296, 54

[6] Petrovay, K. 2020, Living Reviews in Solar Physics, 17, 2

Highlights of Spanish Astrophysics XI, Proceedings of the XV Scientific Meeting of the Spanish Astronomical Society held on September 4–9, 2022, in La Laguna, Spain. M. Manteiga, L. Bellot, P. Benavidez, A. de Lorenzo-Cáceres, M. A. Fuente, M. J. Martínez, M. Vázquez- Acosta, C. Dafonte (eds.), 2023

Astro+: Design, construction, and scientific exploitation of a large-scale massive star spectroscopic database.

Klaus Rübke[1], Amparo Marco[1], Ignacio Negueruela[2], Artemio Herrero[3,4], Sergio Simon-Diaz[3,4], and Hugo Tabernero[5] and Lee Patrick[2,5,6]

[1] Departamento de Física, Ingeniería de Sistemas y Teoría de la Señal, Universidad de Alicante, Carretera de San Vicente s/n, E03690, San Vicente del Raspeig, Spain e-mail : klaus.rubke@ua.es
[2] Departamento de Física Aplicada, Facultad de Ciencias, Universidad de Alicante, Carretera de San Vicente s/n, E03690, San Vicente del Raspeig, Spain
[3] Instituto de Astrofísica de Canarias, Vía Láctea s/n, E38200, La Laguna, Tenerife, Spain
[4] Universidad de La Laguna, Departamento de Astrofísica, E38206 La Laguna, Tenerife, Spain
[5] Centro de Astrobiología, CSIC-INTA. Campus ESAC. C. bajo del castillo s/n. E-28 692 Villanueva de la Cañada, Madrid, Spain
[6] School of Physical Sciences, The Open University, Walton Hall, Milton Keynes MK7 6AA, UK

Abstract

Massive stars condition the evolution of the interstellar medium by the amount of energy released during their lives and especially by their deaths as supernova explosions. The vast amounts of spectroscopic data for massive stars provided by previous and existing instruments on ground-based and space-based telescopes have already saturated our capability to process them by the use of human routines. As a consequence, there is a pressing need for machine-assisted tools to help handle incoming data. To this end, we present the development of a massive star spectroscopic multiwavelength interactive database designed for scientific research and a fully automatic stellar parameter determination tool. Here we show the preliminary results of the application of these tools to optical spectra of O-type stars.

1 Introduction

Massive stars play a very important role in the evolution and formation of galaxies. They possess strong winds energising their neighbourhood and through their deaths as a supernova explosion, enrich the interstellar medium (ISM) with heavier materials. Having a centralized database of spectra of massive stars is the goal of this research, as it is crucial to have a place where homogenous procedures could study their properties.

In this matter, we present the first multi-wavelength database dedicated to massive star spectra, covering from Xrays to far infrared, Astro+, both for young OB-type and evolved Red Supergiants (RSGs), of K and M spectral types. The purpose of this project is to host as many spectra of massive stars as possible. To this end, we provide to the scientific community, a tool

to upload spectra through a user-friendly interface, so those who would like to contribute to our project can upload spectra to our database via the website **https://astroplus.ua.es/**. We allow either FITS or ASCII formats.

The idea of having a database of massive star spectra, covering everything from young to evolved stars, provides us with a place to study and deeply understand the evolution of these stars and hence of the galaxy that hosts them. The first step in this process is to make a correct identification and characterization of the spectrum before further analysis can lead to the extraction of stellar parameters. To this aim, we have concentrated on creating an automation tool, *HiLineThere*, for the correct identification of the type of star, differentiating whether the spectrum meets the properties corresponding to an OB or RSG star, and then determining stellar parameters depending on the type of star.

2 The Database

We have created a web application which is divided into three main components, the insertion, the search, and finally the analysis, which is running in the background, and it will be explained in more detail in section 3.

The insertion of spectra is achieved via an interactive interface that greatly facilitates the correct upload of the data by any user. This versatile interface allows for uploading either one or many stars simultaneously, depending on their format. The platform accepts a multi-variety of FITS file formats and ASCII data.

More in detail, the upload of a FITS file is divided into four steps:

- The user must provide the minimum mandatory information on the file. This includes the unit in which wavelength is expressed, if the spectrum is either not-normalized, normalized or flux calibrated, and the headers that will be extracted from the FITS file, such as Object Name, Right Ascension (RA), Declination (DEC), Observation Date, Telescope, Instrument and Exposure Time.
- The user must specify how the wavelength should be extracted; for example, if the wavelength is an array embedded in the data or if it must be calculated using CRVAL and CDELT1.
- The user must specify how the flux and the error of the flux, if they exist, should be extracted; for example, if this is a binary data or an array
- Selecting the files to be uploaded to this corresponding configuration.

The upload of an ASCII file is straightforward but requires more preparation. This is due to the fact that a CSV file must be filled. In the file, the user must specify the name of the file where the spectrum is and the star header's mandatory parameters. The first step will ask for the unit of the wavelength if the spectrum is normalized, and the second step is where the header CSV file and the spectrum/s can be uploaded.

During the upload, we have provided the user with the possibility to check and correct any field or configuration, if needed. It is in this part where the uploaded files are standardised in Astro+'s own standard FITS format and are correlated with the GAIA and SIMBAD databases through their respective APIs. The last step to be completed by the user is to send the spectrum with all the parameters checked to the administrator for final review and subsequently transfer it to the final database.

The role of the Astro+ administrator is to check that the spectrum is correctly loaded and configured, e.g. that the wavelength is correct, that the resolution is that of the instrument, or that the different name was correctly acquired from SIMBAD or GAIA, when is actually not in those databases we have provided the option to classify the spectrum as new (not yet catalogued). If any of these items is not correct, the administrator will send back the spectrum for corrections.

After approval, the star will be available in the search engine of our application, where it can be searched either by name, coordinates or a more advanced search by SQL command, where further star parameters will be available.

3 Science/Artificial Inteligence

The possibility and capability to gather stellar spectra in a single repository give us an excellent position to develop tools for analysing the data. Although the idea of having full automation of both spectrum identification/characterisation and stellar parameter extraction sounds quite ambitious, we have created *HiLineThere*, a fully automatic tool for characterisation and parameter determination. This tool considers standard diagnostic methods based on the literature and the working group members' and collaborators' expertise.

HiLineThere is mainly divided into two main routines, characterisation and classification routine, from where we can check the presence or absence of diagnostic lines to identify the type of the star, and the Best Model fitting routine, where the spectrum is compared to a grid of synthetic models by using the χ^2 technique, a simple but effective method to compare line profiles, in which the minimum of the sum of all lines, corresponds to the best fitting model, and the parameters used to generate this stellar spectrum are associated to the observed spectrum.

3.1 Characterisation and classification

This routine is based on iterations, which stop when the parameter $V \sin i$ converges, as explained later in this section. It starts by using a series of characteristic lines for OB-type stars (see Table 3). Using the laboratory centre of each line, we establish a search range of ± 300 [Km/s] in the spectrum, as the radial velocity (RV) is not always corrected, and try to detect the presence of the line by attempting a line profile fit. We are considering in each iteration the standard procedures of renormalising and cleaning, before trying to find inflection points and finally trying to fit a gaussian and a pseudo-voigt profile within this range.

Table 1: Diagnostic lines used by Astro+. Lines used for the determination of RV are marked with X, while the lines used to determine $v \sin i$ are numbered according to priority.

Line	Lambda [Å]	Vrad	Vsini
HALPHA	6562.80		
HBETA	4861.33		
HGAMMA	4340.46		
HDELTA	4101.74		
HEPSILON	3970.07		
HEI4026	4026.19	X	
HEI4387	4387.93	X	
HEI4471	4471.47	X	
HEI4713	4713.16		
HEI4922	4921.93		
HEI5876	5875.62	X	
HEI6678	6678.15		
HEII4200	4199.83		
⋮	⋮	⋮	⋮

Line	Lambda [Å]	Vrad	Vsini
⋮	⋮	⋮	⋮
HEII4541	4541.59	X	4
HEII4686	4685.71		
HEII5411	5411.52	X	3
HEII6527	6527.00		
OIII5592	5592.37	X	1
SIII4128	4128.07		
SIII4131	4130.89		
SIII6347	6347.11		
SIII6371	6371.37		
SIIII4552	4552.00	X	2
SIIV2089	4088.85		
SIIV4116	4116.10		
MGII4481	4481.00	X	5
CII4267	4267.00	X	6

If a line profile is identified, the following checks are performed:

- If it has an equivalent width (EW) greater than 0.4 Å, it is considered as detected.
- It is considered to be absorption or emission based on the sign of EW.
- It is retained as detected if the centre displacement is within the 100 [km/s] limit of the calculated RV, this is explained in the next paragraph (this is not considered in the first iteration).
- It is considered as quality detected if, in addition, the maximum or minimum of the line is greater than 3σ of the flux selected in the range of the line.

As we mentioned, this process iterates three or more times. The first two iterations try to detect lines used to determine the RV of the spectrum using the centre of the detected lines and averaging them to obtain a general value used on the next iteration as input. In the third or higher iteration, the program uses one of the rotational velocity diagnostic lines to determine the projected rotational velocity $V \sin i$.

The method of determining $V \sin i$ follows the theory of [**?**], [**?**], [**?**], [**?**], [**?**], [**?**], [**?**], [**?**] and [**?**], by using the fourier-transformation of the profile of the line to create the power spectrum from which the first zeros of the derivate corresponds to the pure rotational velocity of the star.

As the resolution limits the accuracy on the $V \sin i$ determination, we have set the program to stop when the velocity converges to less than a third of the speed as a function of the

resolution ($\Delta V \sin i < (\frac{c_{light}}{Resolution})/3$), and the determination uses the same line as the previous iteration, as the line used to determine $v \sin i$ may not be the same in the iteration.

After confirming the existence and good quality of the diagnostic lines, another subroutine *isblue* determines if the star is an OB star, an RSG candidate star or an intermediate type star, based on counting the lines found. This counting is done separately for the H, HeI and HeII lines. For example, if a star has no detected HeI or HeII lines, it will be considered as an RSG candidate.

3.2 Best model fitting

If the star is labelled as OB (blue path) or RSG (red path, not discussed in this article), it initiates the last part of the automation. The blue path uses the χ^2 technique ([**?**], [**?**], [**?**] and [**?**]) to find the best model based on a synthetic grid of spectral model generated by the FASTWIND code ([**?**] and [**?**]), obtaining the most critical stellar parameter, such as the effective temperature ($T_{\rm eff}$) and the gravity, expressed in log scale ($\log g$), in a completely automatic way for this type of star.

4 Preliminary results

We have tested the automatic processes by uploading the sample studied in detail by [**?**] and comparing their result with those obtained here; we present preliminary results in Figure 1.

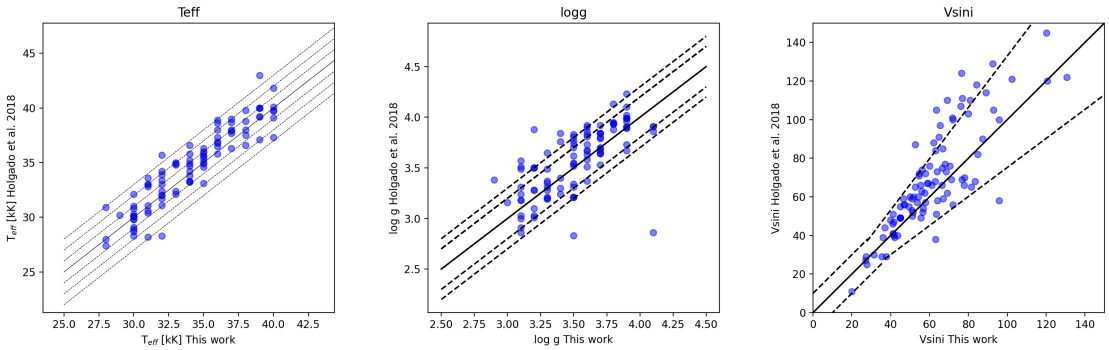

Figure 1: Comparison of stellar parameters obtained by *HiLineThere* in a fully automated analysis with those obtained by [**?**] with a manual range and flux selection analysis for all the stars in their sample. The left figure illustrates the results in temperature; each of the dotted lines represents 1000 [K]. The Center figure illustrates the result of the comparison for gravity; dotted lines represent 0.2 and 0.3 [dex]. Right figure, $V \sin i$ comparison, dotted line represent firstly $\pm$10[km/s] and later the 20% of the value.

We are finding differences within the expected errors, $T_{\rm eff} \sim 1500$[K] , $\log g \sim 0.3$[dex] and $V \sin i \sim 20\%$. It is important to highlight that all these stellar parameters, which include

the $V \sin i$, RV, Temperature and gravity, were obtained entirely in a fully automatic way by using *HiLineThere*.

Acknowledgements

The Generalitat Valenciana partially supports this research under grant PROMETEO/2019/041, and the Spanish Government Ministerio de Ciencia e Innovación and Agencia Estatal de Investigación under grant PGC2018-093741-B-C21/22 (MICIU/AEI/FEDER, UE) and grant PID2021-122397NB-C22 (MCIN/AEI/10.13039/501100011033/FEDER, UE).

Highlights of Spanish Astrophysics XI, Proceedings of the XV Scientific Meeting of the Spanish Astronomical Society held on September 4–9, 2022, in La Laguna, Spain. M. Manteiga, L. Bellot, P. Benavidez, A. de Lorenzo-Cáceres, M. A. Fuente, M. J. Martínez, M. Vázquez- Acosta, C. Dafonte (eds.), 2023

Astrometric Centering of WFPC2/HST images with Deep Learning.

Baena-Gallé, R.[1], Girard, T.M.[2], Casetti-Dinescu, D.I.[2], and Martone, M.[2]

[1] Universidad Internacional de la Rioja. Avenida de la Paz, 137, 26006 Logroño, La Rioja, Spain. https://orcid.org/0000-0001-5214-7408
[2] Physics Dept., Southern Connecticut State University, 501 Crescent Street, New Haven CT 06515, USA

Abstract

Archival WFPC2/HST exposures hold great potential for proper motion studies. Up to now, the astrometric precision of WFPC2 images is limited to $\sim$ 20 mpix as these are the most undersampled images from the various HST optical imagers. We explore deep-learning techniques, specifically, Convolutional Neural Network (CNN) algorithms, to implicitly model the PSF and determine stars centers. The method is tested on HST images and the resulting astrometric precision is compared to that obtained with traditional, state-of-the-art centering algorithms. This approach is data-driven as the behaviour of CNNs is not based on a predefined PSF, rather it is based on estimating the stars' center positions directly from pixel intensity values in the images. We present the description of the CNN architecture, data preprocessing, and learning strategy together with preliminary results from simulated WFPC2 data.

1 Introduction

The study of stars' proper-motions allows us to go deeper into our understanding of how the local universe is evolving. In this respect, the long temporal baseline provided by the Wide Field Planetary Camera 2 (WFPC2), at Hubble Space Telescope (HST), is of high importance ([4], [5], [8]). For example, the Mikulski Archive for Space Telescope includes a rich WFPC2 database of around one hundred globular clusters in the Milky Way and other regions near the Magellanic Clouds. However, performing precision astrometry is essential for this task, taking into account that the average proper motion of regular stars is of the order of milli-arcsec and the pixel resolution of the WF chip is 0.1 arcsec/pixel (0.045 arcsec/pixel for PC).

Traditionally, the problem of estimating stars' proper-motions has been faced by fitting a predefined PSF shape to every star, and using some centering algorithm to estimate its intra-pixel position [6]. Here, we share first results of a new approach based on Deep Learning (DL) methodology that does not make any assumption of the PSF morphology. Specifically,

we train a Convolution Neural Network (CNN) model, in a supervised manner over a set of point-like simulated stars, to measure correlations between pixels. Thus, the way the star light is distributed across the field of view (FOV) provides a measurement of the star's position within the pixel.

2 Classical Centering Algorithms

All classic methods used to date basically differ in the PSF and the centering algorithm to provide star positions at milli-pixel precision. Among those tested in [6] are as follows:

1. 2D elliptical Gaussian and centering routines developed by [11]. This method is fast and works relatively well on bright stars.
2. Effective PSFs (ePSF) built from real observations, which are the ones used in the hst1pass code developed by [1]. This method is especially good at low SNR but it has the tendency to discard sources close to the saturation level.
3. PSFs created with ray tracer Tiny Tim [10] and Dolphot v2.0 package developed by [7]. This algorithm is optimized for point-like sources but is computationally expensive.
4. PSFs computed empirically from real images to take into account the variability accross the field of view (FOV) by means of SExtractor software (PSFex). It uses a set of 636 exposures (160s. at filter F555W) from globular cluster 47 Tucanae. SExtractor is also used to compute centering measurements [3]
5. The image is deconvolved in the Fourier domain prior to the computation of star's centers. An ideal PSF at the instrument diffraction limit is used, as well as a LP Butterworth filter to avoid noise amplification. The resulting image is processed with the method from [11]. Sources with low SNR are usually lost.

In general, it can be stated that the method using a library of ePSFs within the code hst1pass [1] yields the best results, at the cost of discarding sources near the saturation regime. We refer the reader to [6] for further details.

3 Deep Learning Model for Centering

To our knowledge, Deep Learning (DL) has never been used for astrometric estimations in stars' proper-motion studies with HST data. Our approach does not make any assumption of the PSF shape, but it estimates the (x,y) coordinates of the star center by measuring correlations in the pixel intensity values within an aperture around the star.

Our particular CNN model is a VGG [12] with six trainable layers, four of them convolutional layers plus two fully-connected which end in two neurons outputs, each of them to provide an estimate in x- and y-axis, respectively. One max-pool layer is inserted every two

convolutional ones, and all hidden layers are equipped with ReLu non-linearity except the last one which is *linear*, in keeping with the regression nature of this problem. We found that inserting a batch-normalization layer after the fourth convolutional one yields better results and helps stabilize the convergence process in our particular problem. The final architecture is plotted in Fig. 1, subplot a.

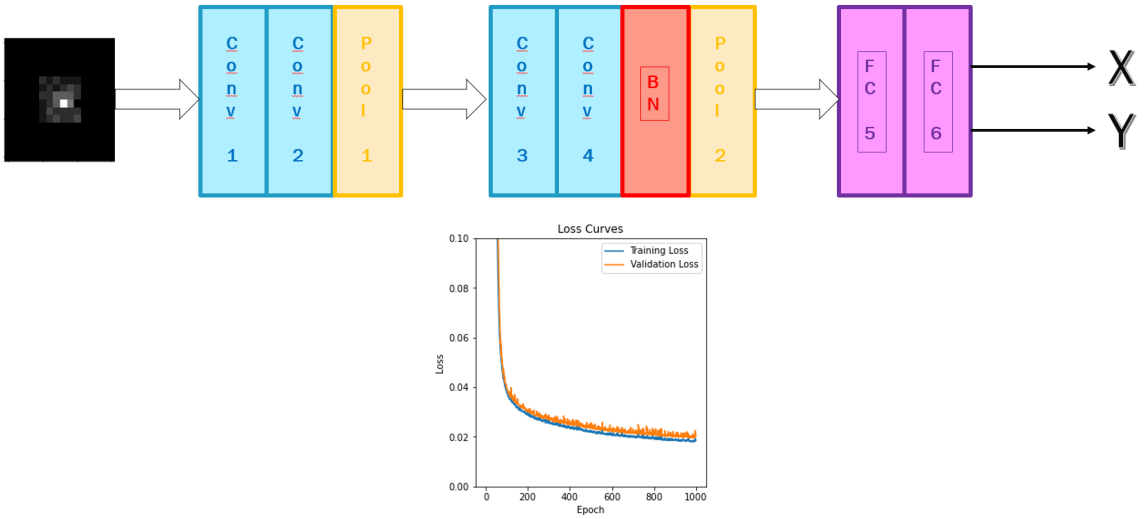

Figure 1: Top: final VGG model. Bottom: loss curves for training and validation dataset.

Due to the finite dimensions of each cutout image of 6×6 pixels around a star, the model is limited in depth. Thus, we cannot add up as many layers as we want, a feature that is generally assumed to increase the level of detail that can be analysed or the number of features that can be extracted from the data. Hence, we opted to modify the number of trainable parameters by increasing the number of kernels at each layer. This allows us to check how the model behaves with respect to the number of parameters in terms of overfitting. This is critical at this stage since our simulations are based on shift-invariant PSFs and isolated sources with no light contamination from nearby sources. Hence, two different VGG models are trained, the first one with $34K$ parameters, and the second one with $214K$. We found that the second one exhibits better results but with some overfitting effect during training. Images are also framed with a zero padding to guarantee a minimum number of layers as the model increases in depth. A typical training process is plotted in Fig. 1, subplot b.

The dataset consists of $\sim$ 4,600 images of individual stars which are divided in $70-10-20\%$ for training, validation and final test. All images are normalized to sum one, independently of the noise level or if the star is saturated. All stars are located over the same image pixel, hence, output positions are also normalized between 0 and 1 so the model is estimating relative shifts within the same pixel. Batch sizes are between 250 and 325 images. We noticed the minimization of the cost function (Mean Absolute Error) benefits of low learning rates (10^{-5}), while epochs had to be increased (between 1,000 and 2,000). The model was designed in Keras/TF and optimized with ADAM using default values.

4 Dataset description and Results

The Deep Learning (DL) model is tested over images of point-like sources which simulate typical observations with the PC and WF chips of the WFPC2 camera. Two different simulation codes were used to generate the data set. The first one, SkyMaker [2], makes use of a user defined PSF model, a list of sky positions, and CCD specifications, which vary depending on the pixel size and the noise level. From a whole image simulation, for instance, a cluster, a set of individual stars can be extracted with known positions. The second one, currently under development and from now on named Simu_WFPC2, is being created specifically for the PC/WF3 chips. The code includes, among other specifications, the variability of the PSF across the chip, vignetting, charge transfer inefficiency effects, CCD columns illuminations due to electron excess, A/D saturation, background, cosmic rays, bias, darks, shot noise, etc... Hence, its simulated images can be considered as more realistic than the ones provided by SkyMaker. At the current stage of this project, we are not making use of the variability of the PSF over the chip. Both simulations were fed with two different PSF models, the ePSFs used by the library in the hst1pass code and the PSFex computed by SExtractor from a real dataset, namely exposures in the field of NGC 104. The former can be considered somehow more realistic than the latter. In all cases, we have a "ground truth" of star positions and magnitudes which allows us to train the model in a supervised way.

Table 1: MEAN RESIDUALS IN (x,y) FOR PC (top) AND WF (bottom)

Simulation + PSF	[11]	[1]	VGG 34K	VGG 214K
Simu_WFPC2 + ePSF	(31.9 , 27.9)	(9.5 , 8.6)	(7.8 , 6.9)	(6.8 , 6.8)
Simu_WFPC2 + PSFex	(15.0 , 12.0)	(47.7 , 43.7)	(6.4 , 6.4)	(5.4 , 5.4)
SkyMaker + ePSF	(36.3 , 32.1)	(8.7 , 8.5)	(9.3 , 8.1)	(7.5 , 6.4)
SkyMaker + PSFex	(17.3 , 13.6)	(48.5 , 41.7)	(8.5 , 7.5)	(6.8 , 6.3)
Simulation + PSF	[11]	[1]	VGG 34K	VGG 214K
Simu_WFPC2 + ePSF	(34.1 , 35.1)	(8.3 , 8.0)	(7.8 , 7.4)	(6.8 , 6.5)
Simu_WFPC2 + PSFex	(12.3 , 13.7)	(13.6 , 14.3)	(6.7 , 6.0)	(5.0 , 5.0)
SkyMaker + ePSF	(41.1 , 44.3)	(9.1 , 9.0)	(8.7 , 8.8)	(7.4 , 7.2)
SkyMaker + PSFex	(13.4 , 15.8)	(20.8 , 16.2)	(8.3 , 7.4)	(5.9 , 5.9)

Table 1 shows mean residuals in both x- and y-axis for PC and WF3 chip achieved by two classic methods [11] and [1], as well as for the DL model with two different numbers of trainable parameters. Outliers above 3σ have been removed. All four methods were applied on the same set of stars and known positions, simulated by SkyMaker and Simu_WFPC2 and making use of ePSF and PSFex. It is shown that the VGG with 214K parameters exhibit slightly better results w.r.t. hst1pass, in particular when ePSF was used to generate the data set. Additionally, DL models are more stable in their results independently of the simulation code and the PSF used to generate the dataset.

Figure 2 plots for all four methods the distribution of x, y-residuals (left panels) and their

dependence with magnitude (middle and right panels). Residuals shown are for the PC chip under the configuration Simu_WFPC2 + ePSF. Similar results are obtained for the WF chip. The hst1pass code has a built-in quality that can be used to reject outlier star images thus producing tighter plots. On the other hand, hst1pass cannot provide results for magnitudes < 15, in contrast with the DL model, which extends this range up to magnitudes < 14.

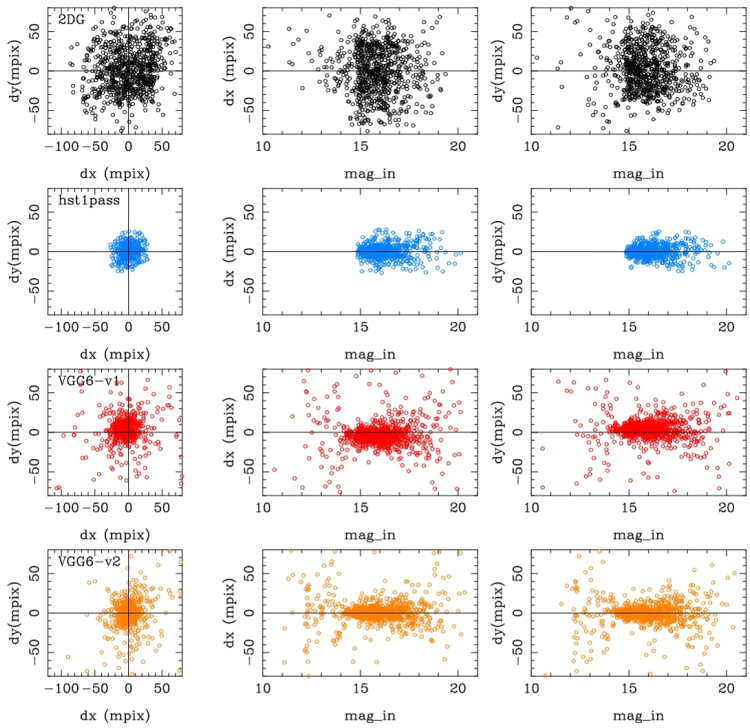

Figure 2: From top to bottom: 2D elliptical Gaussian and centering routine by [11]; ePSFs and hst1pass by [1]; VGG with 34K parameters; VGG with 214K parameters. Leftmost column: residuals distribution w.r.t. (x,y) position. Middle and right columns: residuals in x,y as a function of magnitude. Simulations are with Simu_WFPC2 and using ePSFs. Results are for the PC chip. Similar results are obtained for WF.

5 Conclusions and Future Work

The VGG model introduced in this paper has performed well on simulated HST data, overcoming some challenges of traditional centering methods and performing comparably or slightly better that the state-of-the-art classic algorithm in hst1pass. Our current simulations can still be improved to introduce non-isolated stars and the variation of the PSF across the FOV. This can limit the final performance of the current model, taking into account that we are constrained in the number of convolutional layer, due to the input image size, and the number of trainable parameters, due to the overfitting effect. We have recently

begun testing this methodology on real WFPC2 data. Preliminary results are encouraging.

Finally, we are planning to test a new model on this problem, in particular, ResNets architectures [9]. These architectures involve skipping connections which connects activations of a layer to further layers by skipping some of them in between, thus forming a so-called residual block. ResNets are built by stacking these residual blocks together. Therefore, the final network will fit the residual mapping instead of the features mapping, resulting in training deeper networks avoiding vanishing gradients. Additionally, we will explore the use of larger image sizes by upsampling as well as an automatic choice of the training hyperparameter.

Acknowledgments

RBG was funded by the Universidad Internacional de la Rioja (UNIR) Research Project "ADELA: Aplicaciones de Deep Learning para Astrofísica", no. B0036, and by the Call for Grants for Research Stays Abroad 2021/2022 of UNIR. TG, DC and MM are funded by the NASA Connecticut Space grant 80NSSC20M0129.

References

[1] Anderson, J., & King, I. R. 2000, PASP, 112, 1360

[2] Bertin, E. 2009, Memorie della Società Astronomica Italiana, 80, 422

[3] Bertin, E., & Arnouts, S. 2010, SExtractor: Source Extractor, AstrophysicsSource Code Library, record ascl:1010.064

[4] Casetti-Dinescu, D., Girard, T. M., Jílková, L., van Altena, W. F., Podestá, F. & López, C. 2013, AJ, 146, 33

[5] Casetti-Dinescu, D., Girard, T. M. & Schriefer, M. 2017, MNRAS, 473, 4064

[6] Casetti-Dinescu, D., Girard, T. M., Kozhurina-Platais, V., Platais, I., Anderson, J. & Horch, E. P. 2021, PASP, 133, 064505

[7] Dolphin, A. E. 2000, PASP, 112, 1383

[8] Girard, T. M., van Altena, W. F., Zacharias, N., Vieira, K., Casetti-Dinescu, D., Castillo, D. J., Herrera, D., Lee, Y. S., Beers, T. C., Monet, D. G. & López, C. E. 2011, AJ, 142, 15

[9] K. He, X. Zhang, S. Ren & J. Sun. 2016 Proc. CVPR, pp. 770-778

[10] Krist, J. E., Hook, R. N., & Stoehr, F. 2011, Proc. SPIE, 8127, 81270J

[11] Lee, J.-F., & van Altena, W. F. 1983, AJ, 88, 1683

[12] Simonyan, K. & Zisserman, A. 2015, Proc. ICLR, arXiv preprint arXiv:1409.1556

Highlights of Spanish Astrophysics XI, Proceedings of the XV Scientific Meeting of the Spanish Astronomical Society held on September 4–9, 2022, in La Laguna, Spain. M. Manteiga, L. Bellot, P. Benavidez, A. de Lorenzo-Cáceres, M. A. Fuente, M. J. Martínez, M. Vázquez- Acosta, C. Dafonte (eds.), 2023

Colour corrections from atmospheric transmission with AuxTel for LSST.

Rodríguez Monroy, M.[1], Moniez, M.[1], Dagoret-Campagne, S.[1], Chevalier, J.[1], Neveu, J.[1], Ansari, R.[1], Perdereau, O.[1], and Campagne, J.E.[1]

[1] Laboratoire de Physique des 2 infinis Irène Joliot-Curie (IJCLab), UMR9012 – CNRS, Bât. 100, 15 rue Georges Clémenceau, 91405 Orsay cedex

Abstract

Measuring colours is a crucial task for many of current and future cosmological surveys. Colour calibration is essential to obtain cosmological information from supernovae to photometric redshifts. In the coming years the Legacy Survey of Space and Time will start to carry out a massive survey which will provide data with statistical errors below the systematic uncertainty due to photometric calibration. Therefore, photometric calibration will be one of the main challenges in our way to obtain reliable cosmological measurements. One of the main sources of photometric uncertainty is associated with atmospheric transmission. We propose a method to derive colour corrections based on spectroscopic observations with the Auxiliary Telescope (AuxTel). In this method, we will measure the colour corrections to compensate for the effect of atmospheric transmission by measuring this transmission from spectro-photometric standard stars.

1 Introduction

When carrying out ground-based observations we wish to recover the photometric information (magnitudes, colours, etc) of the observed objects as if they were seen from top of atmosphere (TOA). Another possibility is to obtain this information for a standard atmosphere. In both cases, we need to apply some type of correction in order to obtain the desired photometry.

For a survey such as the Legacy Survey of Space and Time (Rubin-LSST) [1, 3] the colour information of the sources comes from observing their fluxes through broadband filters. In particular, the filters used by Rubin-LSST are *ugrizY*, which cover from 320 nm to 1080 nm. In the right hand side of Figure 1 the filter passbands are represented by the shaded regions with solid contours. The observed flux is the integrated product of the TOA spectral energy distribution (SED) of the source, $F_\nu(\lambda)$, and the filter passband, $S^b_{filter}(\lambda)$. However, the filters are not the only factor that determines the observed magnitude of an object. The optical throughput of the telescope affects the number of photoelectrons converted in the CCD. The throughput is the product of the filter passband with the efficiency of the different mirrors and of the disperser element in the case of spectroscopic observations, the quantum

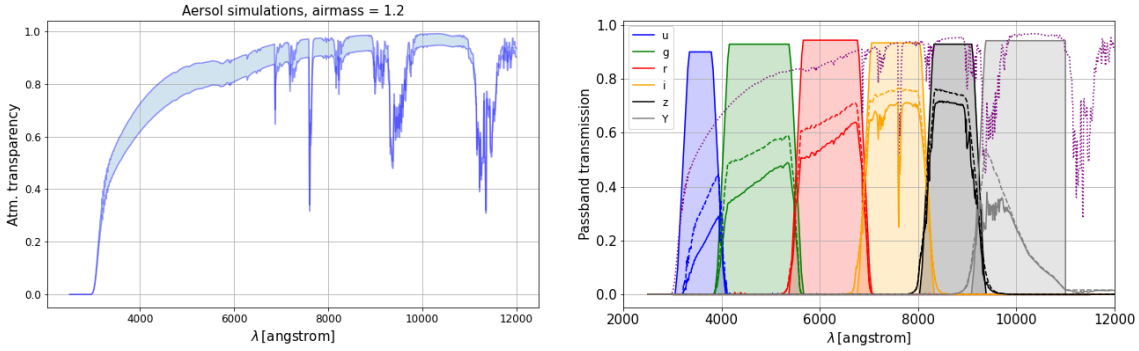

Figure 1: *Left*: simulated atmospheric transparencies obtained using *libRadtran* varying the amount of aerosols from 0.01 to 0.09 for airmass = 1.2, PWV = 3.0 mm, O_3 = 300 DU and no clouds. *Right*: filter passbands (shaded regions with solid contours), atmospheric transparency (dotted line), throughput of the telescope (dashed lines) and effective passbands (solid lines) of LSST telescope.

efficiency of the CCD and the transmission of the refractive elements (lenses, entrance window, etc). The product of all these wavelength dependent factors is $S^b_{inst}(\lambda)$.

Finally, the observed flux is also impacted by the atmospheric conditions. In particular, the concentrations of some of the components of the atmosphere, such as precipitable water vapour (PWV), aerosols or ozone, together with the airmass of observation have different effects on the atmospheric transparency, $S_{atm}(\lambda)$. For example, PWV has more impact on the redder part of the spectrum, inducing several telluric absorption lines, while aerosols are more important on the bluer wavelengths. The atmospheric transparency for different values of the aerosol concentration at an airmass of 1.2 is shown in the left hand side of Figure 1.

Then, the effective passband, $S^b_{obs}(\lambda)$, through which the light of a source goes through is the product of the throughput of the telescope and the atmospheric transparency given by the state of the atmosphere at the moment of observation. This way, the flux (in number of photons) observed through each filter is given by

$$F^b_{obs} \propto \int F_\nu(\lambda) \cdot S^b_{obs}(\lambda) \cdot \frac{d\lambda}{h\lambda}\,, \tag{1}$$

and from it is possible to compute the observed magnitudes, m^b_{obs}. Therefore, the atmosphere affects the magnitudes and thus the colours of the astronomical sources with respect to a reference case (e.g. TOA or a standard atmosphere). In the right hand side of Figure 1 we depict a certain atmospheric transparency (dotted line), the throughput of the LSST telescope (dashed lines) and the effective passbands (solid lines).

In this work, we present the basics of the colour correction method that we propose to employ for the photometry of LSST. This method makes use of the standard spectra observed by AuxTel to derive corrections by comparing with their corresponding TOA observations.

2 An auxiliary telescope for Rubin-LSST: AuxTel

The auxiliary telescope, AuxTel, is a 1.2m telescope equiped with a single CCD and located in Cerro Pachón, Chile, together with the Rubin-LSST's 8.4 m main telescope. Since 2021 AuxTel is taking data twice a month during 3-day long observing runs on average, making it the prototype instrument used for data management commissioning of Rubin-LSST.

AuxTel is equiped with a slitless spectrograph. Slitless spectroscopy has the advantage of not requiring a precise positioning of the source to make it coincident with the slit, thus making this technique much less time consuming. In addition, the absence of slit means that there is no loss light, allowing to perform spectro-photometric observations. On the other hand, this also implies that the subtraction of sky and stellar background must be performed more carefully and that the spectral resolution is limited by the seeing.

In order to obtain the spectra, a especially designed thin phase hologram [5] was installed in AuxTel. It was obtained by recording the interference pattern of two point sources at the zero-order position and at the desired first-order position (see Figure 2). Periodic gratings rely on the assumption that the incident beam is parallel, which is not the case, since the beam is convergent. Moreover, in the geometrical configuration of an imager, each wavelength is focused at different distances from the focal plane. These problems are overcome by the hologram, since it works with a convergent beam and each wavelength is correctly focused near the focal plane, allowing to reach the nominal resolution (R>200 within [342,1100] nm) and to increase the signal-to-noise ratio. Figure 2 showcases the different focus positions as function of wavelength between a normal periodic grating and the hologram. The final mission of the spectrograph is to measure the atmospheric transmission so we can correct one by one the fluxes of the observed objects so we can recover their photometric information as if seen with standard atmospheric conditions.

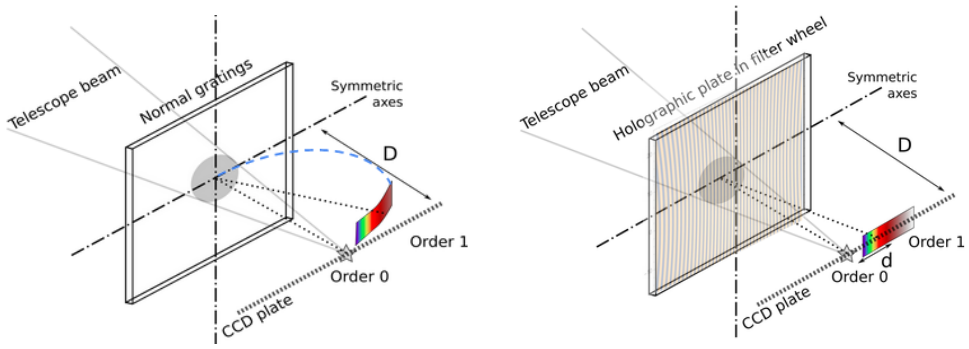

Figure 2: Difference between the focus position for each wavelength obtained with a periodic grating (left) and a holographic optical element (right) [5].

3 A colour correction method for Rubin-LSST

The final goal of the images obtained with a survey such as Rubin-LSST is to infer cosmological information from them. In this regard, there are different ways of working with the images. For example, galaxy clustering and weak-lensing analyses make use of coadded images, obtained by stacking the individual images to reach higher depths. On the other hand, transient object analyses, such as the study of the lightcurves of SNe Ia, use individual images. The differences between cosmological probes imply different photometric calibration requirements. The official Rubin-LSST precision goal is 10 mmag, while for SNe Ia the desirable goal is 1 mmag.

From the point of view of photometric calibration, there are two main sources of systematic uncertainty: the instrumental signature, caused by a plethora of effects (e.g. vignetting, filter transmission variations over time and position, electronic gains, non-linearities, PSF, etc), and the atmospheric absorption. Furthermore, both elements are wavelength dependent. As introduced in Section 1, we can express the effective passband as

$$S^b_{obs}(x, y, alt, az, t, \lambda) = S^b_{inst}(x, y, t, \lambda) \cdot S_{atm}(alt, az, t, \lambda)\,, \tag{2}$$

where the subscript b represents each photometric filter, x, y correspond to the CCD coordinates, t is the time of observation, alt, az are the altitude and azimuth coordinates and λ is the wavelength. In order to correct the impact of both effects on photometry, we need to apply corrections to compensate them within the precision requirements.

The current proposal to obtain such photometric corrections for Rubin-LSST is to use the Forward Global Calibration Method (FGCM) [2]. It assumes that passbands vary over time, so it defines a standard passband that corresponds to standard atmospheric conditions. Then, it computes the correction as the difference between the observed and standard magnitudes.

Here we present the basics of a method proposed as an alternative to FGCM. The main idea behind it is to infer the atmospheric transparency and the amount of different atmospheric components in real time using the spectrograph placed in AuxTel. For this task, we use a set of standard spectra that have been observed from space, such as HST or Gaia standards. The main steps of the method are the following:

- We generate a set of atmospheric simulations using the *libRadtran* software [4] by varying one of the atmospheric parameters while keeping the others fixed. These parameters are PWV, aerosols and ozone. We can also vary the airmass and the cloudiness. Then, for each simulated atmospheric transparency we generate the effective passband multiplying by the telescope's throughput.
- We pass each standard SED through each of the simulated passbands (see Equation 1), obtaining the observed fluxes at different atmospheric conditions. An example of this is shown in the left panel of Figure 3.
- For each simulated flux we compute the observed colours: $u - g$, $g - r$, $r - i$, $i - z$ and $z - Y$. Then, we define Δc_i as the difference of a given colour, c_i, with respect to the colour expected with a standard atmosphere that we fix beforehand. Then, we obtain

the variation of colour, Δc_i, as a function of the atmospheric parameters, enabling us to determine the colour correction that needs to be applied to each object in order to recover the standard photometry. This is shown in the right panel of Figure 3. By doing this, we populate an N-dimensional space with the N observed colours of each SED and the corresponding correction.

- Finally, when observing with LSST we can identify to which hyper-volume element belongs each observed object based on its colours, so we can apply the corresponding colour correction to it.

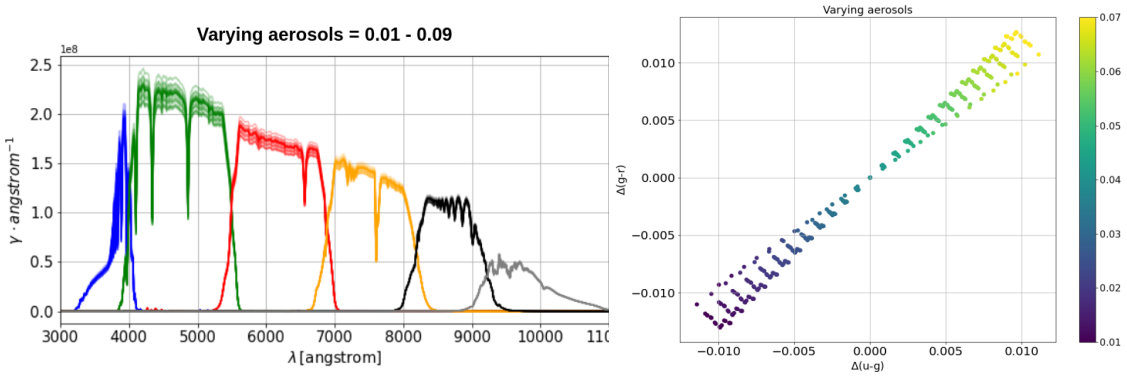

Figure 3: *Left*: standard star flux observed through the different simulated passbands, which take into account the diffente atmospheric transmissions. *Right*: colour evolution of different standards as a function of simulated values of aerosols.

Since LSST uses broadband filters, the shape of the SED plays an important role. For example, high aerosols concentrations have more impact on hotter (i.e. bluer) stars, making them to appear redder. On the other hand, high PWV values have more impact on the redder wavelengths, so colder (i.e. redder) stars appear bluer. For this reason, we consider the spectral type as a variable to populate the N-dimensional parameter space from which we determine the colour corrections.

We have tested our sensitivity to various observing conditions by measuring the equivalent width (EW) of stellar and telluric lines on the spectra of reference stars. While the EW of the stellar lines only depend on stellar and interstellar physics, the EW of the telluric lines depends on the atmosphere. In particular, we evaluate its dependence with the airmass, which traces the O_2 column density. Our preliminary results, presented in Figure 4, show that we are sensitive to variations on the amount of O_2 and H_2O.

4 Summary and prospects

In this contribution we present the basics of a new method proposed to obtain colour corrections for Rubin-LSST using of the spectra obtained with the holographic optical element installed in AuxTel. Our preliminary results with simulations show that we need $\sim$ 10%

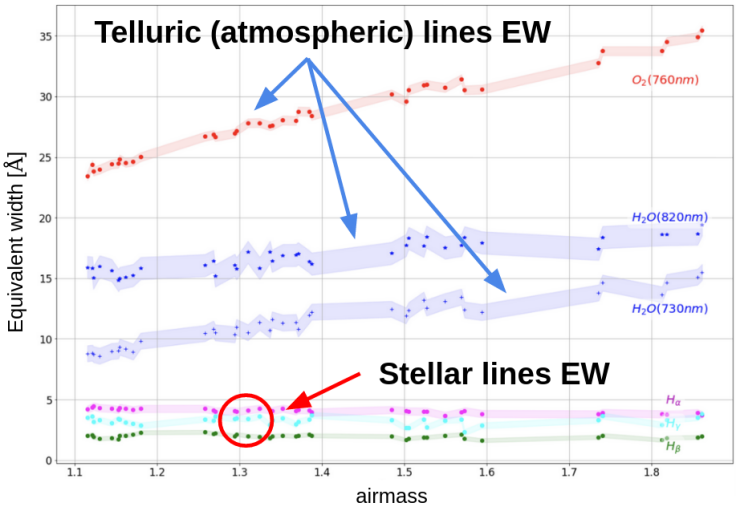

Figure 4: Equivalent width of stellar and telluric absorption lines. The former does not depend on the airmass and other atmospheric parameters, while the telluric ones show a clear dependence, proving our sensitivity to variations on the atmospheric parameters.

precision on the determination of atmospheric parameters to achieve 5 mmag precision in the photometric corrections. This is especially important for SNe Ia cosmological analyses carried out within Rubin-LSST. To apply this method, we use spectra of objects observed from space to compare them with the results obtained after passing through the atmosphere. This allows us to compute the correction on the colours to recover a reference photometry, such as that of a standard atmosphere for the site of observations.

Since AuxTel is slower than LSST, it will be usually pointing to a different position on the sky from LSST. Thus, we will use the atmospheric parameters derived by AuxTel to model the atmosphere in the direction that LSST is pointing to and then we will apply our method to obtain the corresponding correction. If both telescopes are observing the same position of the sky at the same time, we will directly obtain the atmospheric transparency by evaluating the ratio of the TOA and observed spectra of the standards on the field of view and we will correct the photometry consequently. Finally, the estimations of atmospheric parameters provided by AuxTel can serve as a prior to FGCM, allowing to use both in combination.

References

[1] Abell, P.A. et al. [LSST Science Collaboration], 2009, arXiv, arXiv:0912.0201

[2] Burke, D. L. et al., 2018, AJ, 155, 41

[3] Ivezić, Z. et al., 2019, ApJ, 873, 111

[4] Mayer, B. & Kylling, A., Atmos. Chem. Phys., 5: 1855-1877, 2005

[5] Moniez, M., Neveu, J. Dagoret-Campagne, S., Gentet, Y., Le Guillou, L., 2021, MNRAS, 506, 5589

Highlights of Spanish Astrophysics XI, Proceedings of the XV Scientific Meeting of the Spanish Astronomical Society held on September 4–9, 2022, in La Laguna, Spain. M. Manteiga, L. Bellot, P. Benavidez, A. de Lorenzo-Cáceres, M. A. Fuente, M. J. Martínez, M. Vázquez- Acosta, C. Dafonte (eds.), 2023

Do machines dream of modelling AGB stars?.

Santander-García, M.[1], Manuel Julián, J. A.[1,2], Alcolea, J.[1], Bujarrabal, V.[1], and Asensio Ramos, A.[3,4]

[1] Observatorio Astronómico Nacional (OAN-IGN), Alfonso XII, 3, 28014, Madrid, Spain
[2] Universidad Internacional de Valencia (VIU), c/del pintor Sorolla, 21, 46002, Valencia
[3] Instituto de Astrofísica de Canarias, c/Vía Láctea s/n, 38205 La Laguna, Tenerife
[4] Departamento de Astrofísica, Universidad de La Laguna, 38206 La Laguna, Tenerife

Abstract

It is very common in astrophysics that certain relevant parameters of the objects studied cannot be obtained directly from observations, but require numerical models that simulate the relevant physical mechanisms, often through an iterative process of trial and error. This is often lengthy and consumes a large part of the human and material resources of the research process. This is the case in the characterisation of the circumstellar envelopes of Asymptotic Giant Branch (AGB) stars, which could greatly benefit from the use of Artificial Intelligence Deep Learning (DL) techniques. We present the preliminary results of this project as an illustrative example of what can be achieved by (and expected from) the application of DL to numerical modelling in astrophysics.

For this project we have trained a convolutional neural network (CNN) to predict the physical conditions of these envelopes (mass loss, molecular abundance, temperature distribution, expansion velocity pattern, and distance) from a reduced set of single-dish observations of ^{12}CO rotational transitions including J=1–0, J=2–1, as observed with IRAM 30m, and J=6–5, J=10–9, and J=16–15 as observed with HERSCHEL/HIFI. The network has been trained by building a complete library of numerical models covering a large range of parameters using a custom radiative transfer 1D code, which computes the excitation of CO using the Large Velocity Gradient (LVG) approximation and then solves the radiative transfer problem via ray tracing, thus generating synthetic CO profiles from a detailed description of the physical structure of a circumstellar envelope. Once the learning is completed, the system should be able to determine these fundamental parameters from observations without the need for 'manual' model fitting.

1 Introduction

The goal of this work is to evaluate the feasibility of using Deep Learning (DL) techniques in the study and characterization of evolved star envelopes, specifically stars in the Asymptotic Giant Branch (AGB) phase. The objective is to determine if we can predict the most important physical parameters of these systems from observations in radio of certain emission

lines of the CO molecule. The specific goal is to characterize the envelope, determining its mass loss rate, the terminal velocity of the gas, the spatial distribution of the velocity and temperature, the CO abundance, and the distance to the star.

The preliminary work presented here will be further discussed in the Master's Thesis by one of the authors, José Antonio Manuel Julián, to be presented in early 2023.

2 Artificial neural networks

In the last 10 years significant progress has been made in the development of Artificial Neural Networks (NN), due to advancements in computing capacity and the growing trend in the availability of public data sets. A NN is defined as a set of nodes, called neurons, connected to each other that apply a non-linear transformation to input data to produce an output data. The original idea of NNs dates back to the late 1950s with the invention of the perceptron by Frank Rosenblatt [5], but could not be properly developed until decades later due to the limitations of early computers.

Just like in a biological neuron, an artificial neuron receives multiple inputs, from all of the outputs of the neurons it is connected to, it applies weights to those inputs, also applies an activation function, usually non-linear, and generates a specific output that is propagated to the neurons connected to its output. Normally the different neurons are organized in layers, where neurons only connect from one layer to another layer. This way, we will have an input layer, an output layer, and in between a series of layers that we usually call hidden layers. Depending on the number of hidden layers, we will have deeper or shallower networks. Signals are propagated from the input layer to the final output layer where the desired results are obtained.

One of the most successful applications of NNs has been image processing. This has been possible thanks to the development of a neural network architecture called Convolutional Neural Network (CNN), which are able to extract specific features from images and establish correlations between them, as well as their spatial distribution in the image by applying convolutional filters. However, the price to be paid is that they are much deeper and require more computing and memory capacity. In recent years, various companies dedicated to the development of artificial intelligence, such as Google, Facebook, etc., have developed different CNN architectures, training them with image datasets and making them available to the community. Some of them have represented a notable advance in the analysis and identification of objects in images and video.

Basically, the operation of a CNN is to accept a data tensor as input (the RGB values at each pixel of the image), apply a series of convolutional filters to that input, extract a feature map of the image and establish relationships between them, using fully connected neuron layers as output. Some of the most popular CNNs are capable of recognizing objects in images as well or even better than a human, for certain very specific tasks for which they have been conveniently trained.

The training process of an NN is very demanding in terms of computation and memory, as it consists in minimizing an error function between the output of the network and the

expected output. The error is calculated through an equation and it is sought to minimize it by adjusting the weights of the connections between the neurons using the gradient descent method. This process is repeated until the errors are small. The use of graphic cards (GPU) has significantly improved the training time, as they are specially designed to handle tensor operations and can improve performance by a factor of 20.

3 Methodology

The main idea behind this work is to take advantage of the success of CNN networks, specifically those that have already been shown to be efficient in extracting and identifying patterns in images. By using a pre-trained CNN network, it is expected that the training performance will be improved so that it can learn new patterns that will identify our images.

The goal is to perform simultaneous fitting of sets of single-dish observations of ^{12}CO rotational transitions including J=1–0, J=2–1, as observed with IRAM 30m, and J=6–5, J=10–9, and J=16–15 as observed with HERSCHEL/HIFI. The data of each set of lines is transformed into an image where the most outstanding line features can be seen thus taking advantage of the power of CNN networks. A large set of images, built from synthetic modelling by a 1D radiative transfer code using the Large Velocity Gradient (LVG) approximation [1], are used to train the network by associating each image with a point in the physical parameter space. The challenge now is to create an appropriate image from the line profiles. To do this, a 3D surface is created by representing the lines in that 3D space, repeating each line 10 times, and placing each set of repeated lines one after the other. A gap of 3 additional values, whose values are the interpolation of the data, is added between each block of repeated lines in order to achieve a smooth surface. Once the surface is created, it is projected onto the plane Z = 0 as a density map of the height of this surface. See Fig. 1 for an example of 3D surface construction.

These meta-images are associated with the set of physical parameters and are used to train the CNN network. In order to have a broader set of images, and to face the network with the noise that we will probably have in the real data obtained from a radio telescope, we generate 10 meta-images for each point in the parameter space. Each of these 10 images is the same version but adding noise to the data of each line, spanning a range of S/N similar to those typically found in real observations. This allows the CNN to learn the fundamental features that distinguish one image from another without being biased or affected by noise in the spectra.

3.1 The parameter hyperspace

The first important decision is how to discretize the space of physical parameters and how many simulations we needed to do to populate the parameter hyperspace. Initially, we considered a range of values that resulted in 10^7 simulations, where in each simulation the profile of 5 lines for 12CO and other 5 lines for 13CO must be calculated. In this scenario, despite having 16 double thread cores available from a machine at the Observatorio Astronómico

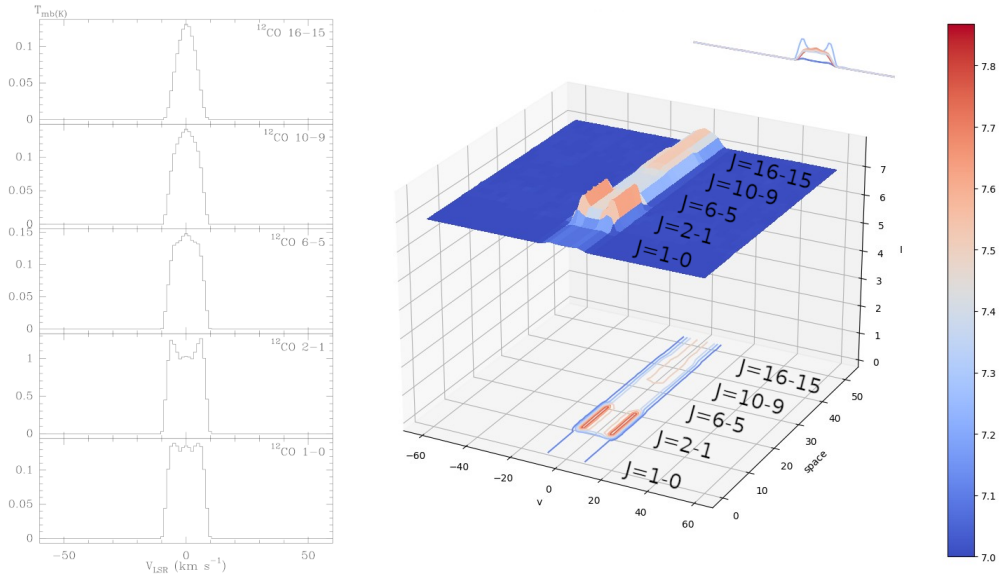

Figure 1: **Left**: Synthetic line set corresponding to a model AGB with $\dot{M}$=3.16×10^{-7} $M_{\odot}$ a^{-1}, X$_{^{12}CO}$=2×10^{-4},v$_{\infty}$=8 km s^{-1}, α_T=0.8, β_v=2.0, D=316 pc. α_T and β_v refer to the exponent of the radial distribution of the gas temperature and velocity, respectively. **Right:** 3D surface or meta-image built by stacking each of the lines on the left, each of them cloned 10 times, with a 3-pixel interpolation between successive lines.

Nacional (OAN), and being able to run 32 processes in parallel, the time it would take for our code to perform all the scenarios was more than 30 days, just to calculate the data of the lines. To this we would have to add the time necessary to create the meta-image, which would make the total process take more than 120 days of CPU, something unviable for a Master's Thesis work.

We therefore decided to further restrict the scope of the problem and focus only on 12CO, thus reducing the number of necessary simulations and the parameter space. We priorised discretization in those parameters with a greater impact on the shape of the spectra, that is, $\dot{M}$, v$_{\infty}$, X$_{^{12}CO}$, and D, ending up with a discretely randomized parameter space with fine granularity in the most relevant dimensions (see Table 1). A dataset of 290,000 images was generated to train the CNN, testing different models and modifying the final layers to adapt them to the desired output. We also introduced a modification so that the CNN would not only accept the meta-image as input, but also the maximum value of the signal present in the line data.

With regard to the CNN used, several tests were performed with different architectures, modifying the final layers to adapt them to our output. This is a common practice in DL, using a network that has already been created and previously trained, which we modify the final layers to make the output what we are looking for and retraining it with our image dataset. In this way, the network learns to extract the features of our images, in our case the meta-images.

Table 1: Range of model parameters covered. $\alpha_{\rm T}$ and $\beta_{\rm v}$ refer to the exponents of the radial distribution of the gas temperature and velocity, respectively. The term 'Scale' refers to the type of distribution between the minimum and maximum values.

Parameter	Minimum value	Maximum value	# values	Scale
$\dot{M}$	10^{-7} $M_\odot$ a^{-1}	10^{-5} $M_\odot$ a^{-1}	10	Logarithmic
$X_{^{12}CO}$	2×10^{-4}	8×10^{-4}	10	Lineal
v_∞	8	18	10	Lineal
$\alpha_{\rm T}$	0.8	1.25	5	Lineal
$\beta_{\rm v}$	0.8	2.0	5	Lineal
D	100 pc	1000 pc	5	Logarithmic

4 Preliminary results and conclusions

The DenseNet169 network [4] was ultimately selected for its superior performance. When training the network to focus on and predict the most relevant parameters only (i.e. $\dot{M}$, v_∞, $X_{^{12}CO}$, and D), the process reached an accuracy of 99.85% in sucessfully predicting the parameters of a validation set of 10,000 meta-images made from synthetic spectra lying within the sampled hyperspace volume, but never seen by the CNN before. We consider a prediction sucessful if the normalized distance between the predicted and real parameter vectors is within 10% of the normalized modulus of the real parameter vector. This training took 2 hours using GPU resources provided by the Instituto de Astrofísica de Canarias (IAC).

Figure 2 shows the relative error distribution of the validation image set in each parameter. Negative values in the figure are simply due to the way the error is defined, thus the sign can largely be ignored. As can be seen, the CNN accurately predicts v_∞ within a 6% uncertainty, while the error in the distance ranges between 10% for the smaller distances (∼100 pc) to 60% for the largest ones (∼1 kpc). The error in the ^{12}CO abundance, on the other hand, is ∼50% for abundances typical of O-rich stars, and ∼20% for those typical of C-rich stars. Finally, the CNN accurately predicts high mass losses (∼10^{-5} $M_\odot$ a^{-1}) within a ∼20%, and low ones (∼10^{-7} $M_\odot$ a^{-1}) with an expected, larger error around 100%.

Put together, these results have nothing to envy in comparison to the modelling work of an expert human (e.g. [6, 3]), which would also have taken a significantly larger amount of time. Future work, which we will detail in a forthcoming paper, consists of testing the trained CNN with data from a sample of real stars in order to evaluate its prospects in this field, including a detailed treatment of the errors and correlations between parameters following strategies tested in other fields [2]. In the meantime, in the light of present results, we can preliminary conclude that the prospects for the use of CNN for modelling AGB star envelopes are promising.

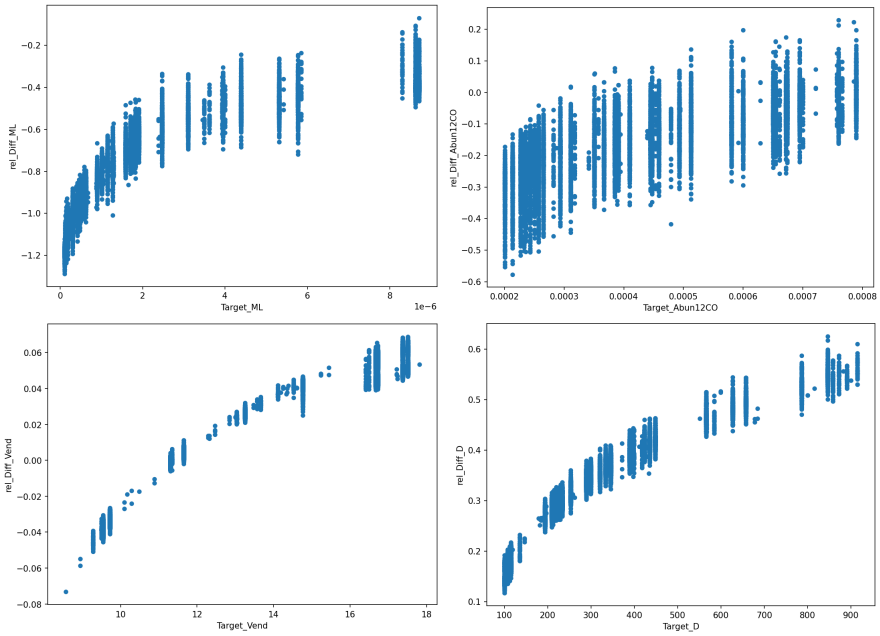

Figure 2: Relative error distribution of the image validation set in each of the most relevant parameters. From top to bottom and left to right, parameters are $\dot{M}$, $X_{^{12}CO}$, v_∞, and D.

Acknowledgments

M.S.G., J.A., and V.B. acknowledge support by the Spanish Ministry of Science and Innovation (MICINN) through project EVENTs/Nebulae-Web (grant PID2019-105203GBC21). The authors wish also to acknowledge the IAC for their kind disposition in the use of their IT resources.

References

[1] Castor, J. I., 1970, MNRAS, 149, 111

[2] Díaz Baso, C. J., Asensio Ramos, A., de la Cruz Rodríguez, J., 2022, A&A, 659, 165

[3] Díaz-Luis, J. J., et al., 2019, A&A, 629, 94

[4] Huang, G., et al., 2018, arXiv:1608.06993v5

[5] Rosenblatt, F., 1958, Psychological Review, 65, 386

[6] Santander-García, M., et al., 2012, A&A, 545, 114

Highlights of Spanish Astrophysics XI, Proceedings of the XV Scientific Meeting of the Spanish Astronomical Society held on September 4–9, 2022, in La Laguna, Spain. M. Manteiga, L. Bellot, P. Benavidez, A. de Lorenzo-Cáceres, M. A. Fuente, M. J. Martínez, M. Vázquez- Acosta, C. Dafonte (eds.), 2023

EMIR upgrade: installing a new Hawaii 2RG detector.

Garzón, F.[1,2], **Joven, E.**[1,2], **Rodríguez, H.**[1,2], **and Mato, Á.**[1,2] **and Rosich, J.**[1,2]

[1] Instituto de Astrofísica de Canarias, IAC, Vía Láctea s/n, 38205, La Laguna (S.C. Tenerife), Spain
[2] Departamento de Astrofísica, Universidad de La Laguna, 38206, La Laguna (S.C. Tenerife), Spain

Abstract

EMIR is one of the first common user instruments for the GTC, the 10 meter telescope operating at the Roque de los Muchachos Observatory (La Palma, Canary Islands, Spain). EMIR has been built by a Consortium of Spanish and French institutes led by the Instituto de Astrofísica de Canarias (IAC). The instrument is primarily designed to be operated as a MOS in the K band, but offers a wide range of observing modes, including imaging and spectroscopy, both long slit and multi-object, in the wavelength range 0.9 to 2.5 μm.
EMIR had its first light on June 2016 and started routine observation in 2017, while the MOS mode was commissioned and offered to the community in 2018. Since the beginning, EMIR performances were hampered by the high noise and instabilities of its detector, a Hawaii2 2048^2 array. We had no option but to use this low quality item as the original detector, much superior in virtually every aspect, was flagged with potential risk of explosion due to a defect in the fabrication procedure, that was corrected in subsequent fabrication batches. At that time, there were no more detectors available of the same type, a PACE architecture in the hybrid Silicon chip plus MCT. The lack of sensitivity due to the signal instabilities is more pronounced in spectroscopic mode, while the data frames taken in image mode could be cleaned to a large extent.
With support from the Spanish national funding agency, GRANTECAN has acquired two Teledyne Hawaii2 RG + ASIC to be used in the EMIR and FRIDA instruments. We are characterising the arrays in the lab and are executing a complex plan to permit the replacement of the EMIR detector in short time. This plan includes changes in the control software and a new detector assembly with piezoelectric actuators for remote control and adjustment of the alignment.
In this contribution we will provide a short description of the main problems of the current detector and will show how the new detector will improve significantly in all of these. We will also mention the current plans for installation.

1 Introduction

Among the large instrumental suite in each of these new telescope stations, multi-object spectrographs (MOS) play a prominent role and are always in the top rank of the most demanded

instruments. The near-infrared (NIR) MOS is particularly interesting for large telescopes as the NIR permits the detection of objects in the optical bands hidden by massive material clouds, and because of the effect of redshift in objects at cosmological distances. Given the next and upcoming generation of ground- and space-based observatories (e.g. JWST, E-ELT), NIR spectroscopy is of increasing importance. To support 30m class telescopes, well-established NIR spectrographs on 8–10m class telescopes are a vital resource, and are scientifically viable in their own right. EMIR ([4, 5, 6, 2, 3]) is occupying this niche at the Gran Telescopio Canarias (GTC).

EMIR is a NIR wide-field spectrograph, similar to other instruments developed in the 2000s for 10m class telescopes, such as KMOS/VLT[1], MOSFIRE/Keck[2], and Flamingos2/GEMINI[3]. The concept of the instrument corresponds to a classical camera and spectrograph design, but with several novelties. Its spectral working range is dictated by the spectral response of the detector, hence it spans from 0.9 to 2.5 μm. From the beginning the top priority mode of EMIR was set as multi-object spectroscopy in the K band, due to the requirements of the instrument main scientific driver, the Galaxy Origins and Young Assembly (GOYA) Survey ([7], [1]). This imposed a fully cryogenic layout of the instrument that, in addition, set a severe restriction for the multi-object capability of EMIR.

It is one of the common user instruments at the GTC, and offers observing capabilities in imaging and spectroscopy in both long-slit and multi-object modes, over a field of view of $6.67 arcmin \times 6.67 arcmin$ in image mode and $6.67 arcmin \times 6.67 arcmin$ in spectroscopy. It had its first light at the GTC in mid-2016 and was initially offered to the community in late 2017 after a long period of commissioning and science verification phases. The control system of EMIR was constantly tuned during the first years to permit a smooth coordination with the telescope and proper functioning of the different observing modes. EMIR was tested in the lab with a Hawaii2 FPA detector of the initial architecture, but we were forced to replace it, rather close to the shipping date to the GTC, due to the high risk of explosion that had happened in other similar arrays. The new detector, while free from the risk of explosion thanks to the new manufacturing process, was less adequate than the original one, due to higher read-out noise and instabilities in the signal. All together, these features led to an overall instrument performance below what was expected, in particular for faint sources. This unforeseen problem forced the instrument team to devote substantial efforts to try to alleviate the lower effective sensitivity. While in image mode we developed methods to clean the frame with remarkable success, in spectroscopy only minor improvements were achieved despite the many attempts using different approaches. It should be noted that this caveat is of particular importance, but only for faint objects. Finally, new funds arrived that permit the replacement of the detector by a new Hawaii2RG, which is currently being tested at the IAC. In the rest of the paper, we will describe the main problems observed in the current detector, will compare the performances of the two slates as they have been measured so far, and will summarise the status of the replacement project and expected schedule.

[1] http://www.eso.org/public/teles-instr/paranal-observatory/vlt/vlt-instr/kmos
[2] https://www2.keck.hawaii.edu/inst/mosfire/home.html
[3] https://www.gemini.edu/instrumentation/flamingos-2

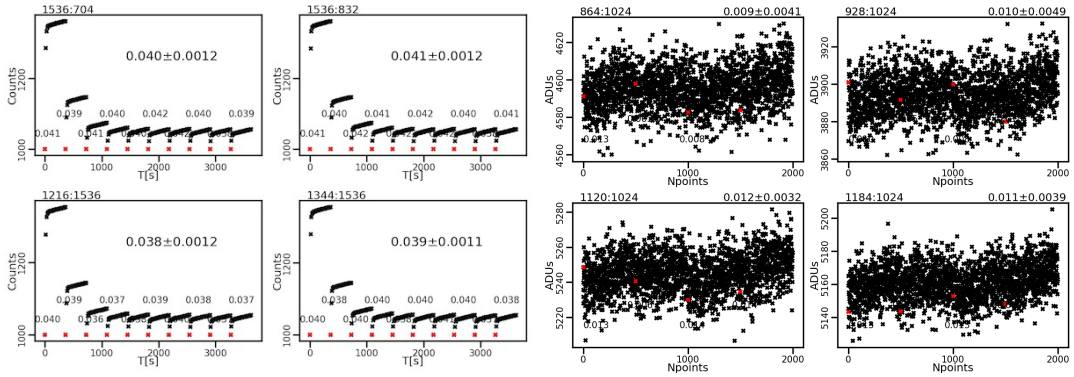

Figure 1: DC measurement test where ramps were taken with the instrument was fully closed to avoid any illumination onto the detector. Left panel: 4 channels of the current detector, with 10 ramps. Right panel: same test, but with the new detector mounted in the testing cryostat at the IAC, and with 4 ramps in total. See text for details.

2 The problem with the current detector

As it has been mentioned above, during the AIV phase of the EMIR instrument at the IAC, we had to replace the detector array, mounted on EMIR during a large fraction of the testing phases, for a new one due to the reasons already mentioned. Since the beginning, this new array exhibited an abnormal behaviour, particularly marked at low signal levels. Needles to say that the target objects at the faintest possible limit are of utmost interest for the observing programmes in 10 m class telescopes as the GTC.

Figure 1-left shows an example of the main caveat in the performances of the current EMIR detector. This is the result of a Dark Current (DC) test. During this measurement, the instrument was closed to the maximum possible extent – external window, CSU, grism and filter wheels in closed positions – to ensure complete darkness inside the cryostat. Then, the detector registers the signal produced by itself, that is called dark current. This current sets typically the sensitivity limit of the detector, together with the read-out noise (RON). In fig. 1 , each panel shows the result of one of the 4 central panel out of the 32 readout channel of the detector, as its architecture permits the simultaneous read through 32 separated channels, each one in charge of a subset of the full detector pixel set, hence diminishing the readout time by a factor of 32. On each panel, the average signal of the central 5000 pixels of each subset is marked as a single point in black. The red points correspond to the initial read of each ramp that are followed by 27 reads, totalling 28 non-destructive reads on each ramp in the left panels. 10 ramps were taken on this test. Each panel shows the trend of the 10 ramps in counts vs. time from the start of the test. The ramps were taken without any time shift in between them, as in the routine measurements on sky objects. What is of interest for the user is the slope of the ramp, from which the incident flux can be derived after proper calibration.

Two main features can be seen in fig. 1-left. At first, there is a clear shoulder on the

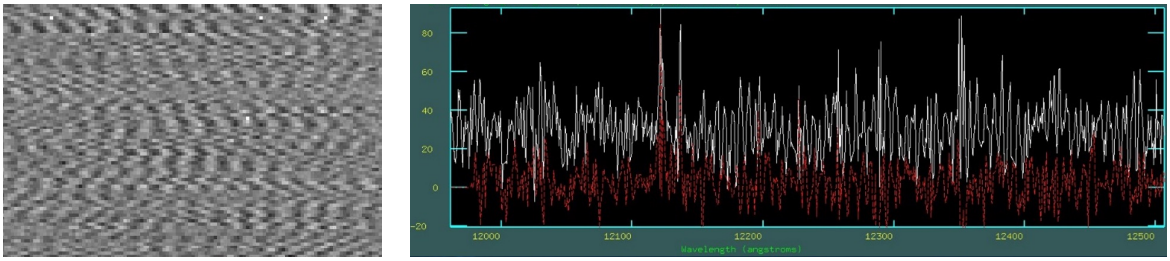

Figure 2: Left panel: detail of an area of the detector free of target signal during an observation. Right panel: portion of an object spectrum without cleaning, in white, and after cleaning, in red.

ramps, with the first 3–4 points climbing much steeper than the rest of the ramps. This effect is mostly due to a parasitic signal in the detector, that is added to signal produced by the target object. As a result, the first points cannot be used to derive the slope of the ramp, hence this calculation has to be performed with a smaller set of points than the total number of reads, that yields a poorer signal to noise ratio. The numbers close to each individual ramp are the slopes calculated using only the second half of the read points. And the numbers in the middle of each panel represent the average of the 10 measurements plus the standard deviation. The second issue is the fact the the first ramps behaves differently than the last ones. Depending upon the incident flux, which in this test is virtually null, there are a number of ramps that show a more pronounced shoulder than the rest of the series. In fig. 1-left, the first 3–4 ramps show this effect. Fortunately, the second half of this abnormal ramps are aligned with the rest of the set, so they can be used in the calculations. A third issue that is not visible in fig. 1-left consists in marked jumps in the reset level, that sets the initial level for the integration. Figure 1-left has all these pedestal level, marked in red, arbitrarily set to 1000 adu, hence displacing vertically each ramp a different amount. Without this artificial manipulation, that does not change the slopes, the comparative analysis of the ramps would have been a bit more difficult, as these jumps are of the order of a few hundred counts.

The above described effects are associated to intrinsic currents within the detector and to the reading procedure. So it is not unexpected that they show as a correlated pattern in the read frame. Figure 2 shows this pattern in a section of the frame free of spectral lines that would otherwise make more difficult to see the *regularity* of the pattern. We have taken advantage of this similarity to design cleaning procedures that works until a given extent, as can be seen in the right panel of fig. 2. The reduction in the spectrum noise in this case is a factor of 3. Regrettably, the cleaning fails in the presence of abundant sky lines, as in the H and K spectral bands, as there is no section of the detector frame free of input flux of sufficient extent to derive the pattern noise.

All in all, plus other less important features that are not commented in this paper, result of an irregular and unstable behaviour of the detector, which a clear impact in the performances of the whole instrument so, after receiving additional funds, we are now in the process of replacing the current detector for a new model of a modern and different technology and free of these flaws.

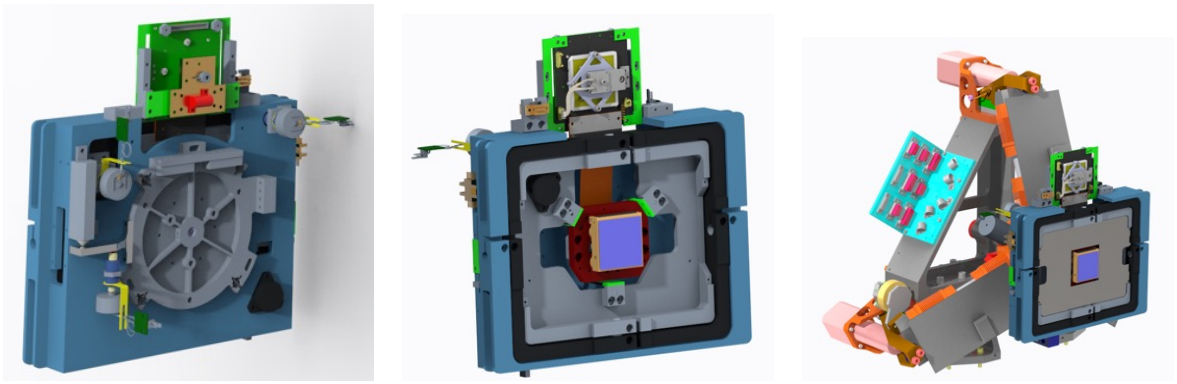

Figure 3: Several views of the design of the new detector mount. The green card on top the mount represent the ASIC unit of the new detector, that takes care of much of the detector driving. The right panel shows the complete set detector plus mount assembled onto the EMIR DTU.

3 New detector: short summary of performances and current installation plans

GRANTECAN received funds from the national agency to purchase two complete sets of detector array Hawaii2RG, which are currently been tested at the IAC. The item that will replace the EMIR detector is now fully tested in lab, and its performances, as far as DC is concerned, can be compared with that the current one in fig. 1. The right panel shows the DC measurements of 4 channels, with the same color code as in the left panel explained in Section 2, but with 500 reads on each ramp. In this case, the ramp points are depicted without correction for pedestal level. It can be seen that the red points aligned within a few counts, and that there is no shoulder in the ramps, that are mostly pure noise, as it should be. Also the average DC levels, showed on top of each panel in the right side of fig. 1, are much smaller than in the left side. And additional good feature of this new array resides on its flatness, that has been measured to be as small as 11μm peak-to-valley, that has to be compared with the figure of around 100μm in the current detector, that should result in a better image quality once mounted in EMIR. In addition, the new detector will be seated in a new gimbal mount, see fig. 3, equipped with remote controlled piezo-electric actuators to permit an fine tilt alignment once integrated onto the instrument.

At this time, we are finalising the construction of the new mount that will be assembled and tested in the next months. Also, the engineering team is updating the EMIR control software to cope with the driving of new detector, which is now controlled through a dedicated SIDECAR ASIC provided by the detector vendor.

We are expecting to be able to initiate tests on sky, with the new detector mounted in EMIR, during the first semester of 2023, but this tentative schedule has to be put in context with GRANTECAN and IAC capabilities and availabilities.

Acknowledgments

EMIR has been funded by GRANTECAN S.L. via a procurement contract; by the Spanish funding agency grants AYA2001-1656, AYA2002-10256-E, FIT-020100-2003-587, AYA2003-01186, AYA2006-15698-C02-01, AYA2009-06972, AYA2012-33211, AYA2015-63650-P, AYA2015-70498-C2-1-R and PGC2018-102249-B-I00; and by the Canarian funding agency grant ACIISI-PI 2008/226.

References

[1] Balcells, M. 2003, Revista Mexicana de Astronomía y Astrofísica Conference Series, 16, 69-72

[2] Garzón, F., 2016, Astronomical Society of the Pacific Conference Series, 507, 297

[3] Garzón, F., Abreu, D., Barrera, S., Becerril, S., Cairós, L. M., Díaz, J. J., Fragoso, A. B., Gago, F., Grange, R., González, C., López, P., Patrón, J., Pérez, J., Rasilla, J. L., Redondo, P., Restrepo, R., Saavedra, P., Sánchez, V., Tenegi, F. & Vallbé, M. . 2006, SPIE, 6269, 626918

[4] Garzón, F., Balcells, M., Gallego, J., Gry, C., Guzmán, R., Hammersley, P., Herrero, A., Muñoz-Tuñón, C., Pelló, R., Prieto, M., Bourrec, É., Cabello, C., Cardiel, N., ez, C., Laporte, N., Milliard, B., Pascual, S., Patrick, L. R., Patrón, J., Ramírez-Alegría, S. & Streblyanska, A. . 2022, A&A, 667, A107

[5] Garzón, F., Castro, N., Insausti, M., Manjavacas, E., Miluzzio, M., Hammersley, P., Cardiel, N., Pascual, S., ez, C., Molgó, J., Barreto, M., ez, P., Joven, E., López, P., Mato, A., Moreno, H., Núnez, M., Patrón, J., Rosich, J. & Vega, N. . 2017, Highlights on Spanish Astrophysics IX, 652-659

[6] Garzón, F., Castro, N., Insausti, M., Manjavacas, E., Miluzio, M., Hammersley, Peter, Cardiel, N., Pascual, S., ez, C., Molgó, J., Barreto, M., ez, P., Joven, E., López, P., Mato, A., Moreno, H., Núñez, M., Patrón, J., Rosich, J. & Vega, N. . 2016, SPIE, 9908, 99081J

[7] Guzmán, R.2003, Revista Mexicana de Astronomía y Astrofísica Conference Series, 16, 209-212

Highlights of Spanish Astrophysics XI, Proceedings of the XV Scientific Meeting of the Spanish Astronomical Society held on September 4–9, 2022, in La Laguna, Spain. M. Manteiga, L. Bellot, P. Benavidez, A. de Lorenzo-Cáceres, M. A. Fuente, M. J. Martínez, M. Vázquez- Acosta, C. Dafonte (eds.), 2023

Fully Adaptive Bayesian Algorithm for Data Analysis. FABADA.

Sánchez-Alarcón, Pablo M.[1,2], **and Ascasibar, Yago**[3]

[1] Instituto de Astrofísica de Canarias, c/ Vía Láctea s/n, E-38205, La Laguna, Tenerife, Spain
[2]Departamento de Astrofísica, Universidad de La Laguna, E-38206, La Laguna, Tenerife, Spain
[3]Departamento de Física Teórica, Universidad Autónoma de Madrid, E-28049 Madrid, Spain

Abstract

The discovery potential from astronomical and other data is limited by their noise. We introduce a novel non-parametric noise reduction technique based on Bayesian inference, `FABADA`, that automatically improves the signal-to-noise ratio of one- and two-dimensional data, such as astronomical images and spectra.
The algorithm iteratively evaluates possible smoothed versions of the data, the smooth models, estimating the underlying signal that is statistically compatible with the noisy measurements. Iterations stop based on the evidence and the χ^2 statistic of the last smooth model. We then compute the expected value of the signal as a weighted average of the whole set of smooth models. We evaluate its performance in terms of the peak signal to noise ratio using a battery of real astronomical observations.
Our Fully Adaptive Bayesian Algorithm for Data Analysis (`FABADA`) yields results that, without any parameter tuning, are comparable to standard image processing algorithms whose parameters have been optimized based on the true signal to be recovered, something that is impossible in a real application. On the other hand, state-of-the-art non-parametric methods, such as BM3D, offer a slightly better performance at high signal-to-noise ratio, while our algorithm is significantly more accurate for extremely noisy data, a situation usually encountered in astronomy. The source code of the implementation of the method, is publicly available at https://github.com/PabloMSanAla/fabada.

1 Introduction and Methodology

The acquisition of any experimental data is affected by several sources of statistical error, which ultimately translate into a random noise component in the measurements to be recorded. In astronomy, the noise introduced can sometimes be comparable to or even larger than the signal, and different image processing algorithms may be used to recover the information that is buried deep in the data.

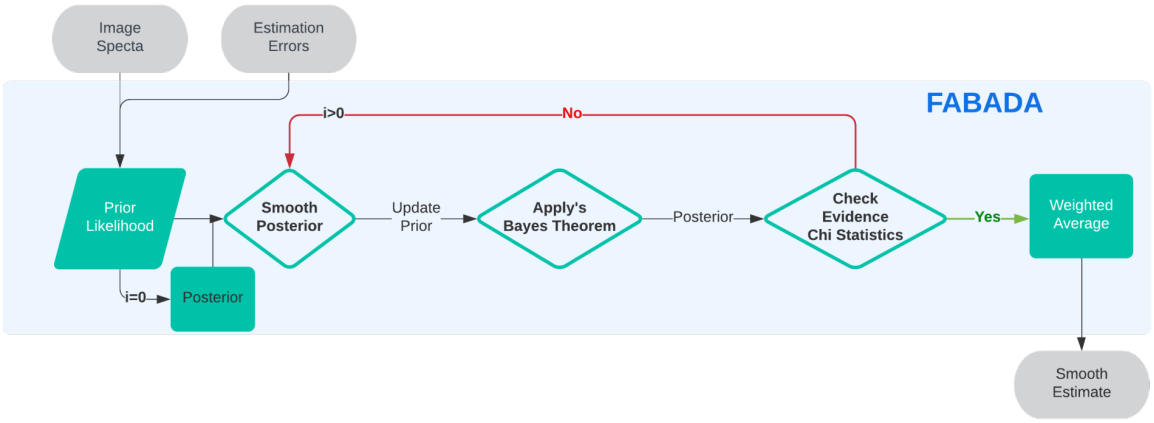

Figure 1: Visual layout of the Fully Adaptive Algorithm for Data Analysis.

The purpose of our Fully Adaptive Algorithm for Data Analysis is the estimation of the underlying signal in a way that is compatible with the measurements and the variance associated with it. Then, the inputs of our algorithm are the one- and two-dimensional data (such as astronomical spectra and images) and the variance associated with it (which can be heterogeneous). In Fig. 1 we show the layout of the method. `FABADA` is a novel non-parametric technique that reduces the noise in the image by applying Bayes' theorem in an iterative way. Therefore, we must define a suitable likelihood function to evaluate the models to be tested, and specify a prior probability distribution for the signal to initiate the process. Our likelihood is based on the statistics of a Gaussian process, and we start from an improper, constant prior. Then, we evaluate different smooth versions (by using the average of the surrounding points) of the posterior probabilities until a certain condition is reached. This new Bayesian technique incorporates an automatic selection criterion based on the statistical properties of the residuals, and therefore it yields a fully non-parametric method.

2 Astronomical Examples

In Fig. 2 we show two examples of the performance of `FABADA` in comparison with optimized standard algorithms (LOWESS [8], WIENER [7], and Gaussian Filter [3] and the state-of-the-art no parametric method, the Block-matching and 3D filtering, BM3D [5] of one-dimensional data (a-left) and two-dimensional images (b-right).

In figure 2-a we present the recoveries obtained for two random realizations with high, and low signal-to-noise ratios (SNR) for the spectrum of a pair of interacting galaxies, *Arp 256* [2]. At high SNR (left column), all algorithms display not only a similar performance, but actually converge to very similar solutions. All algorithms are able to correctly trace the presence of the most prominent emission lines, as well as the strong absorption line near the peak at the left end of the spectrum. Nevertheless, it is important to note that, while the

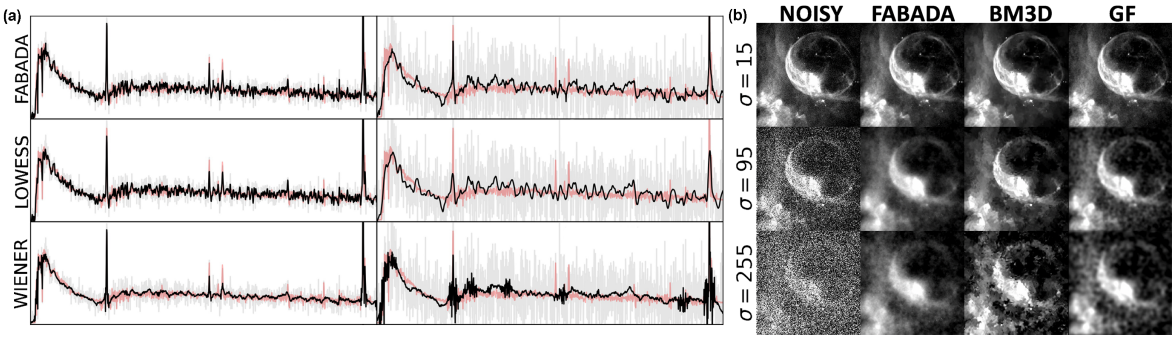

Figure 2: Examples of the recoveries obtained by FABADA on one-dimensional astronomical data (a-left) spectra, and two-dimensional images (b-right).

Wiener filter provides the best recovery in terms of to the overall noise reduction, `FABADA` tends to preserve the true intensity of these features slightly better than any of the other algorithms. This trend becomes more significant as the noise increases, and it is more difficult to discriminate significant spectral features from Gaussian random fluctuations. In the right panel, at low SNR, all models are able to reproduce the overall shape of the continuum. However, they fail to recover even the strongest absorption and emission lines, although hints of the brightest emission lines are still present in the standard methods. Only our prescription is able to provide a good description of these prominent features with this level of noise in the input data, albeit weaker absorption and emission lines are completely lost.
Similar trends are observed in the results obtained for the 2D data. Figure 2-b shows the recovery of the *Bubble* nebula image, taken from the Hubble Space Telescope gallery produced by NASA and the Space Telescope Science Institute (STScI). We compare the recovery with the state-of-the-art method (BM3D) and an optimized Gaussian Filter (GF) represented in each column, with three different noise levels ($\sigma = 15\,95,\ 255$ out of a dynamical range of 255) along the rows. All models yield fairly similar reconstructions for the highest signal-to-noise case ($\sigma = 15$). In particular, several edges in `FABADA` and GF seem to be a little bit more blurry compared to BM3D, together with a clearly visible *salt and pepper* noise component. Once again, the advantages of our algorithm become more evident as the noise increases. It is remarkable how the state-of-the-art BM3D method starts to add some artificial edges to the recovered image while `FABADA` is able to trace smoothly the global structure of the nebula. The GF can trace the structure but shows a preference for circular regions that can be related to the radius of the filters. These trends become more prominent if we push the noise even further, as is often the case in practical astrophysical applications, the signal itself is comparable to or even lower than the statistical uncertainties ($\sigma = 255$). While BM3D and the GF introduce some kind of artifacts, rectangular sharp gradients and circle regions, respectively, `FABADA` recovers the global structure in a smooth way.

3 Comparison Results

In Fig. 3 we show the results of the comparison between `FABADA`, the optimized standard methods, and the state-of-the-art BM3D method (only in 2D). We use the Peak Signal to Noise Ratio (PSNR) to evaluate the quality of the reconstruction by each algorithm. For simplicity we merge all the optimized standard methods (LOWESS, Savitzky–Golay filter [6], Gaussian filter, Wiener filter, and median filter) in one line (orange line), showing the region from the lowest to highest values of the metric obtained with this methods. Fig. 3-a (top panel) show the results for one-dimension for the three different spectra used in the comparison. The first, second and third column shows the results for a Kurucz stellar model [4], a emission line spectra from a supernova remnant SN132D [1], and for an interacting pair of galaxies, the pair group Arp256. Taking into account these results, one can see how `FABADA` performs as well as the best possible solutions of the standard methods typically used in astronomy.

Fig. 3-a (bottom panel) show the PSNR obtained for all the methods for different images. We consider eight different targets that are intended to sample the wide range of features that may be encountered in the field, including planets (Saturn), stars, diffuse nebulae (bubble, crab, ghost and eagle), and galaxies, either alone or in potentially blended groups (cluster). We can see similar behavior as the one-dimensional results. `FABADA` seems to offer the best solution possible obtained by the standard methods without the fine tuning of any parameter. However, in general, BM3D stands over the other methods, including `FABADA`, at high SNR ($\sigma \lesssim 95$ dB), in particular for the *Saturn* image. Its collaborative filter is particularly well suited for periodic data, or images with repetitive patterns, which are virtually absent in other test cases. The *stars* image would be a paradigmatic example, and the difference in this test is insignificant. On the other hand, `FABADA` perform better than BM3D at low signal-to-noise ratios.

4 Conclusions

In this work, we present the theory and implementation of a novel automatic algorithm for noise reduction: the Fully Adaptive Bayesian Algorithm for Data Analysis (`FABADA`). Our method iteratively evaluates progressively smoother models of the underlying signal and then combines them according to their Bayesian evidence and χ^2 statistic. The source code is publicly available at https://github.com/PabloMSanAla/fabada.

We compare `FABADA` with other methods that are representative of the current state of the art in image analysis and digital signal processing. For this comparison, we used the most typical metrics, the Peak-Signal-to-Noise-Ratio (PSNR), which is a measure of the Mean Square Error (MSE). One important advantage of our method, shared by BM3D over classical algorithms is the absence of free parameters to be tuned by the user. Our results suggest that `FABADA` and BM3D achieve values of PSNR comparable to or better than the best possible solution attainable by the classical methods.

Beyond the precise values of the global quantitative metrics, both `FABADA` and BM3D are

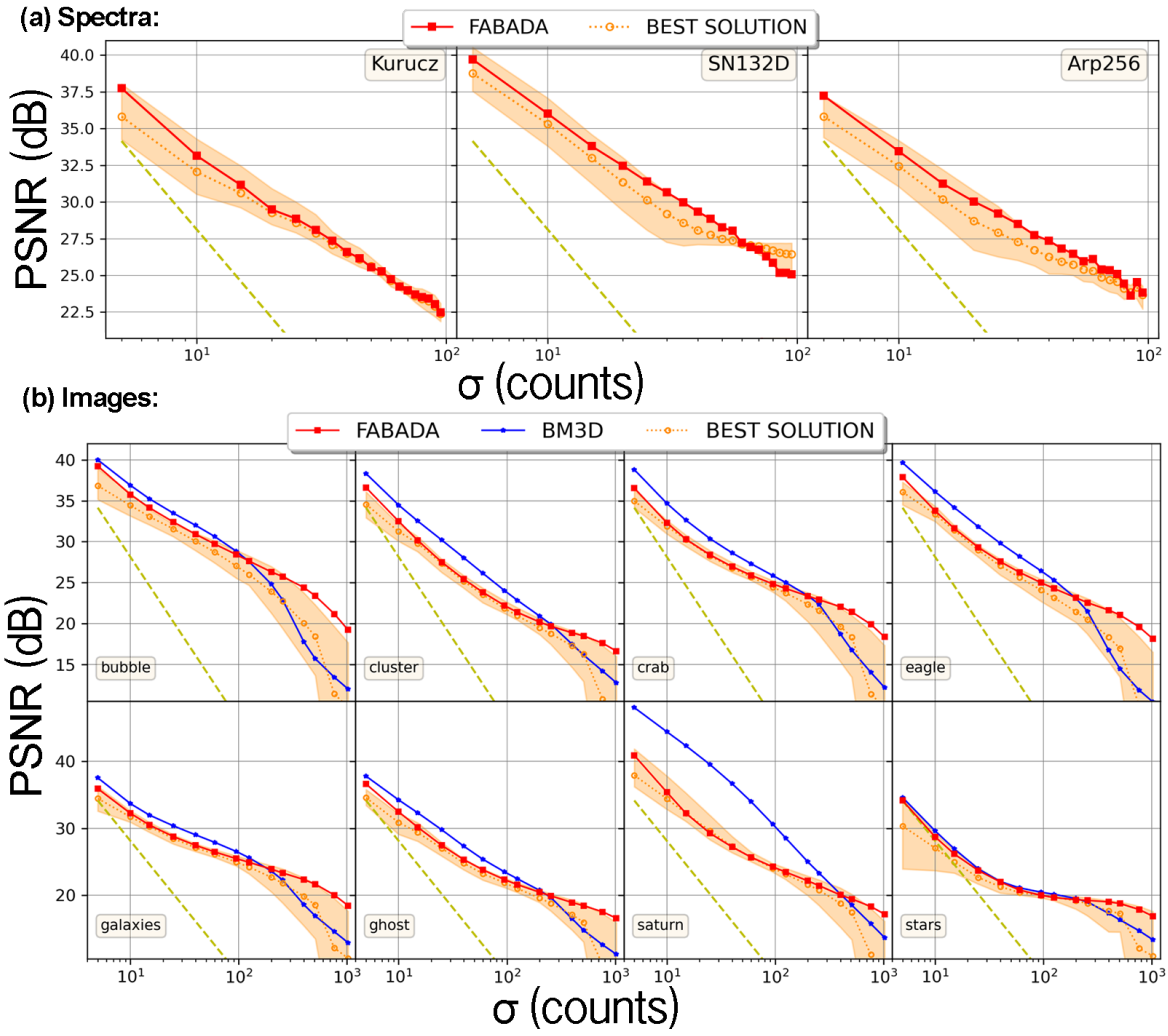

Figure 3: Results of the PSNR comparison between standard and state-of-the-art algorithms with respect to FABADA on one-dimensional astronomical data (a-top) spectra, and two-dimensional images (b-bottom).

quite successful in adapting to the structures present in the input data. Perhaps the most significant difference between them is that `FABADA`'s priors assume that the signal is smooth, whereas BM3D uses block-matching to look for repetitive patterns. This might be relevant when one must recover the height and shape of the spectral features in 1D or the gradients and boundaries in 2D. We argue that `FABADA` appears to offer a trade-off between noise reduction, increasing the metric values significantly, in a way that is statistically compatible with the data, keeping significant features without introducing considerable artifacts.

Acknowledgments

PMSA acknowledge financial support from the State Research Agency (AEI-MCINN) of the Spanish Ministry of Science and Innovation under the grant "The structure and evolution of galaxies and their central regions" with reference PID2019-105602GB-I00/10.13039/501100011033, from the ACIISI, Consejería de Economía, Conocimiento y Empleo del Gobierno de Canarias and the European Regional Development Fund (ERDF) under grant with reference PROID2021010044, and from IAC project P/300724, financed by the Ministry of Science and Innovation, through the State Budget and by the Canary Islands Department of Economy, Knowledge and Employment, through the Regional Budget of the Autonomous Community. Yago Ascasibar acknowledges financial support from grant "Starbursts throughout the evolution of the Universe" (PID2019-107408GB-C42/AEI/10.13039/501100011033) from the AEI-MICINN, Spain.

References

[1] Blair, W., Morse, J., Raymond, J., Kirshner, R., Hughes, J., Dopita, M., Sutherland, R., Long, K. & Winkler, P. Hubble Space Telescope Observations of Oxygen-rich Supernova Remnants in the Magellanic Clouds. II. Elemental Abundances in N132D and 1E 0102.2-7219. *Astrophysical Journal.* **537**, 667-689 (2000,7)

[2] Brown, M., Moustakas, J., Smith, J., Da Cunha, E., Jarrett, T., Imanishi, M., Armus, L., Brandl, B. & Peek, J. An Atlas of Galaxy Spectral Energy Distributions from the Ultraviolet to the Mid-infrared. *Astrophysical Journal, Supplement.* **212**, e18 (2014,6)

[3] Bromiley, P. Products and Convolutions of Gaussian Distributions. *Division Of Informatics, Imaging And Data Sciences, School Of Health Sciences, University Of Manchester.* pp. 1-2 (2003,1)

[4] Castelli, F. & Kurucz, R. New Grids of ATLAS9 Model Atmospheres. *Modelling Of Stellar Atmospheres.* **210** pp. A20 (2003,1)

[5] Dabov, K., Foi, A., Katkovnik, V. & Egiazarian, K. Image Denoising by Sparse 3-D Transform-Domain Collaborative Filtering. *IEEE Transactions On Image Processing.* **16**, 2080-2095 (2007)

[6] Savitzky, A. & Golay, M. Smoothing and Differentiation of Data by Simplified Least Squares Procedures.. *Analytical Chemistry.* **36**, 1627-1639 (1964),

[7] Lim, J. Two-dimensional signal and image processing. (Englewood Cliffs, N.J. ; Prentice Hall,1990)

[8] William S. Cleveland Robust Locally Weighted Regression and Smoothing Scatterplots. *Journal Of The American Statistical Association.* **74**, 829-836 (1979),

Highlights of Spanish Astrophysics XI, Proceedings of the XV Scientific Meeting of the Spanish Astronomical Society held on September 4–9, 2022, in La Laguna, Spain. M. Manteiga, L. Bellot, P. Benavidez, A. de Lorenzo-Cáceres, M. A. Fuente, M. J. Martínez, M. Vázquez- Acosta, C. Dafonte (eds.), 2023

Increasing the technological maturity of a low-noise magnetic measurement subsystem with IOD/IOV CubeSat Platforms.

Mateos, I.[1], Maria-Moreno, C.[1], Pacheco-Ramos, G.[2], Quirós-Olozábal, A.[1], Guerrero-Rodríguez, J.M. [1], Cifredo-Chacón, M.A. [1], Del Sol, I.[1], Cobos-Sánchez, C.[1], Vílchez-Membrilla, J.A.[1], and Rivas, F.[3]

[1] Escuela Superior de Ingeniería, Universidad de Cádiz, 11519 Cádiz, Spain
[2] Dpto. de Ingeniería Aeroespacial y Mecánica de Fluidos, Universidad de Sevilla, 41092 Sevilla, Spain
[3] Universidad de Loyola, 41704 Sevilla, Spain

Abstract

With the purpose of advancing the technological maturity of novel magnetic sensing techniques, in-orbit platform opportunities (IOD/IOV experiments) offer the possibility to assess their in-flight capabilities. Magnetic Experiments for the Laser Interferometer Space Antenna (MELISA) are a series of in-flight demonstrators that intend to characterize the low-frequency noise behavior of a magnetic measurement system under the harsh space environment. One of these undergoing experiments developed by the University of Cádiz is MELISA-III, an improved payload based on magnetoresistive sensors embarked on the first CubeSat mission of the Horizon 2020 IOD/IOV program with the support of the European Space Agency (ESA). After the successful environmental test campaign on the Qualification Model and the acceptance-level testing, the MELISA-III Flight Model was delivered to the prime contractor in February 2022 for its integration into a 6U CubeSat. A review of the main performances of the payload, the test campaigns, and the planned scientific operations at LEO will be described in this paper.

1 Introduction

LISA (Laser Interferometer Space Antenna) is the future space-borne gravitational wave (GW) observatory under the lead of the European Space Agency (ESA) in collaboration with NASA [1]. LISA will be constituted by three drag-free spacecraft forming a laser interferometer with 2.5-million-kilometer optical arms. Each spacecraft contains free-floating test masses (TMs) that behave as inteferometer end mirrors and follow a Geodesic trajectory. Hence, GWs passing through the LISA costellation will slightly change the distances between TMs shifting the inter-satellite optical arms of the laser interferometer. The top-level requirement for the LISA scientific payload is defined in terms of free-fall noise density as

$$S^{1/2}_{\delta a,\mathrm{LISA}}(\omega) \leq 3\times 10^{-15}\left\{\left[1+\left(\frac{\omega/2\pi}{8\ \mathrm{mHz}}\right)^4\right]\left[1+\left(\frac{0.1\ \mathrm{mHz}}{\omega/2\pi}\right)\right]\right\}^{\frac{1}{2}}\ \frac{\mathrm{ms}^{-2}}{\sqrt{\mathrm{Hz}}} \tag{1}$$

in the frequency band between $0.1\,\mathrm{mHz} \leq \omega/2\pi \leq 100\,\mathrm{mHz}$. One of the non-gravitational forces that can disturb the free-fall requirement is the magnetic environment caused by the interplanetary magnetic field and the spacecraft's magnetic sources, such as the electronics units or the solar panels. Therefore, to allow the accurate functioning of the GW detector, proper low-noise magnetometers are required to discern the magnetic contribution from the total acceleration budget.

2 CubeSat mission for in-orbit demonstration

To increase the technological maturity of chip-scale magnetic sensing techniques under harsh conditions in space, further experiments with In-orbit Demonstration and Validation (IOD/IOV) platforms need to be done for future space-based GW observatories. For this end, MELISA (Magnetic Experiments for the Laser Interferometer Space Antenna) are a series of compact magnetic measurement payloads with a detectivity capable of distinguishing interplanetary magnetic field fluctuations down to 100 μHz [2, 3].

MELISA-III is a technology demonstrator that intends to characterize the low-frequency noise behavior of a magnetic measurement system based on anisotropic magnetoresistive (AMR) sensors by applying low-noise bias fields with a built-in Printed Circuit Board (PCB) coil. With this purpose, the environmental magnetic field fluctuations will be diminished during in-flight operations by using a cylindrical shield with three concentric mu-metal layers enclosing the triaxial AMR sensors.

MELISA-III was selected by the European Union on the H2020 IOD/IOV mission, a 6U CubeSat with the support of ESA called CSC-2. The mission goal is to provide flight heritage to MELISA-III and two other selected experiments.

3 MELISA-III Payload: design and analysis

3.1 Analog signal conditioning circuit

The output from a full Wheatstone bridge of AMR elements is modulated at 5 Hz to reduce the $1/f$ noise of the sensor and electronics. The signal then goes through a precision instrumentation amplifier and is synchronously demodulated. Once the signal is integrated, a feedback controller helps to minimize the thermal dependence of the payload. This will decrease the excess noise in the lower end of the frequency bandwidth that is coupled to the long-term thermal drifts [2, 3]. Figure 1 displays the physical architecture of the experiment.

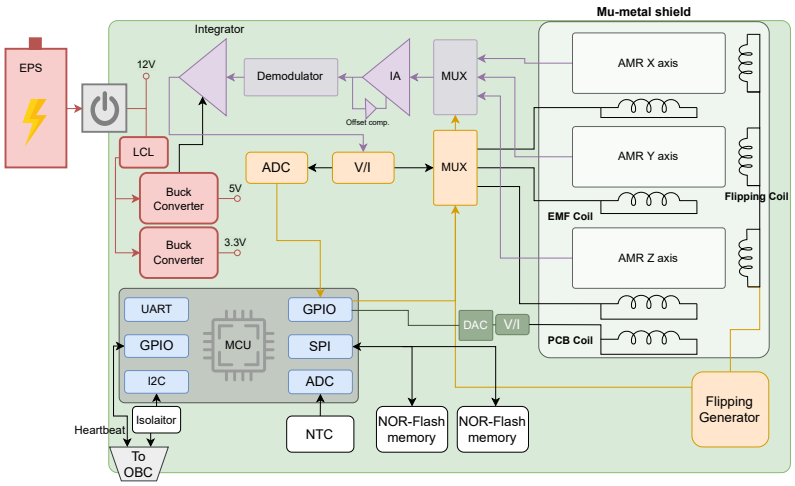

Figure 1: Block diagram of MELISA-III.

3.2 Compact PCB coil optimization

A transducer coil is built into the inner layers of the PCB to inject ultra-stable magnetic fields in the three axes of the AMR sensors. The purpose is to obtain noise curves along the whole magnetic field range of the payload during the in-flight scientific operations. The circuit that produces the current to feed the PCB coil contains a Digital-to-analog converter (DAC) followed by a low-noise floating current source. The DAC that sets the amplitude of the current applied to the coil is configured with bipolar operation.

An adapted Inverse Boundary Element Method (IBEM) has been utilized to optimize the multilayer PCB coil considering different geometrical and performance constraints, such as magnetic field maximization in the region where the AMR sensitive axes are located. The theoretical results were compared to numerical simulations using COMSOL Multiphysics and experimental measurements. Those results were deemed to be in good agreement [4].

3.3 Structural assessment

The design of MELISA-III is analyzed and validated from the structural point of view by means of Finite Element Analysis (FEA) using Ansys. The loading scenarios considered include: quasi-static loading, sine vibrations, random vibration, and shock response spectrum. The load levels are established according to the information supplied by the prime contractor. Moreover, a lower limit of 135 Hz is established for the first natural frequency. Given the dynamic nature of the loads, the numerical analyses are carried out based on modal decomposition and all the vibration modes within range of interest are considered. Based on the CAD, a simplified geometrical model is developed where design details not impacting structural analysis are removed. The geometrical entities and parts considered are showed in Fig. 2. Additionally, punctual and distributed masses are included to compensate the mass neglected due to geometry simplifications and modeling approach. A 3D finite element mesh-

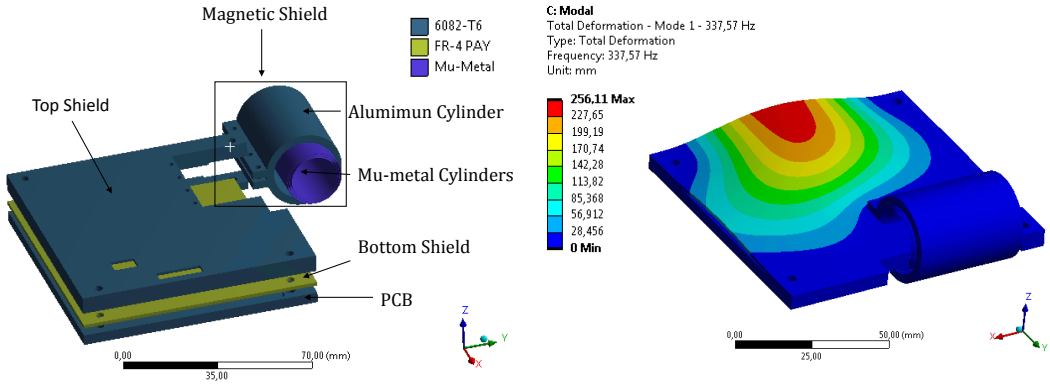

Figure 2: Left: MELISA-III geometry description. Exploded view. Right: First natural mode.

ing, based on tetrahedral/hexahedral SOLID185 elements, is created with the help of ANSYS meshing tools. With regards to properties, with the exception of FR4, which is modeled as an orthotropic material, isotropic properties are considered and applied to the modeled parts. In reference to connection, Multi Point Constraint (MPC) elements are used in order to model mechanical connections such as the bonding between cylinders or the connections to the PCB stack rods. Bolted joints are modeled as a combination of MPC and bar elements.

The results obtained from analysis allow to conclude the fulfilment of the structural requirements: i) the minimum natural frequency computed is 337.57 Hz, represented in Figure 2; ii) the stress levels and displacements obtained provide positive Margins of Safety for both metallic and FR4 parts, being the shock loading the most critical case.

4 Qualification and acceptance tests

The model and test philosophies were agreed upon with ISISpace as the System Integrator and ESA. The Qualification Model (QM) and Flight Model (FM) approach was selected for the MELISA-III payload. An overview of the required tests that were successfully performed at subsystem level is shown in Table 1. The environmental tests (EMC, TVAC/Bakeout, Vibration, and shock) were carried out in collaboration with ALTER Technology at their facilities.

5 Low-frequency environmental noise contributions at LEO

5.1 Magnetic impact of LEO environment

The LEO magnetic fluctuations that the magnetic shielding can not cancel out will be perceived by the measurement system. Therefore, the subtraction of these contributions must be applied during postprocessing. As a result, a simulation of the in-orbit environment is

Table 1: Qualification and acceptance tests performed in MELISA-III QM and FM.

Test	QM	FM
Functional and performance	✓	✓
EMC	✓	✓
Bakeout/TVAC	✓	
Thermal ambient		✓
Burn-in		✓
Vibration	✓	
Shock Response Spectrum	✓	

needed in order to foresee the influence of these conditions in the magnetic measurements, and elaborate an approach for the subtraction [5].

The LEO orbit is simulated in GMAT (General Mission Analysis Tool), providing the position of the satellite during a number of days. The orbital parameters are implemented according to the current information about the Sun-synchronous orbit provided by the CubeSat Operator. From these data, the magnetic environment that the CubeSat will experience is calculated during that time using the World Magnetic Model in MATLAB. The attitude, which will be nadir pointing, is simulated by applying a rotation matrix

$$R_Z = \begin{bmatrix} \cos(\omega) & -\sin(\omega) & 0 \\ \sin(\omega) & \cos(\omega) & 0 \\ 0 & 0 & 1 \end{bmatrix} \tag{2}$$

while $\omega = 7.66$ deg. On-ground triaxial Helmholtz coils are fed using controlled currents that provide the previously-determined magnetic field. MELISA-III is placed inside these coils along with an unshielded fluxgate magnetometer.

The in-orbit fluctuations are simulated in the three axes, while the scientific data of MELISA-III is produced at 5 Hz for 42 hours. The results are displayed in Figure 3, with and without the environment simulation. In this Amplitude Spectral Density (ASD), the fundamental frequency appears at approximately 93 min, which is the period of the orbit. Besides, the peak at ≈ 100 mHz is associated to the quantization noise due to the control of the currents through the Helmholtz coils. Eventually, ongoing postprocessing techniques will allow to disentangle these contributions from the scientific data provided in orbit through correlation with measurements of the platform's magnetometers.

5.2 Excess noise caused by temperature fluctuations

Variations in the ambient temperature may result in changes in the magnetic field generated by other components of the satellite, impacting the measurements of sensors. For instance, a rare-earth magnet is located in the same platform as MELISA-III for other experimental purposes. A test was performed in order to assess the magnetic field generation of that magnet

based on the in-orbit temperature fluctuations. Thus, variations of approximately 20°C in the magnet conditions were induced by a heater with the aim of assessing the magnetic influence on MELISA-III.

The results of the test are shown in Figure 3. The peak located at 0.35 mHz corresponds to the fundamental frequency of the thermal cycle of the magnet. Therefore, results provided by MELISA-III at mHz frequencies are significantly influenced by the temperature of this magnet, resulting in a possible in-orbit surpassing of the mission requirements. A suitable magnetic shielding for the payload is required for the mitigation of these contributions, otherwise postprocessing techniques are also needed.

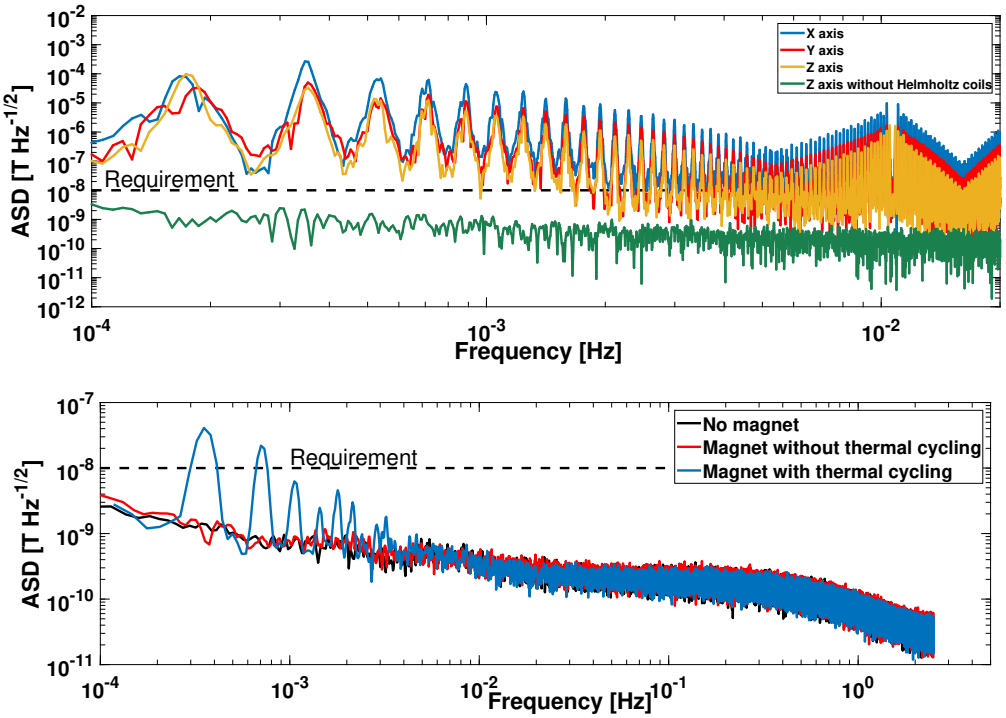

Figure 3: Top: ASD for the MELISA-III during the orbit simulation with the Helmholtz coils. The black dashed line indicates the instrument requirement. Bottom: Comparison between MELISA-III measurements with and without the influence of the magnet that is part of another on-board experiment.

6 Conclusions

MELISA-III, a low-noise magnetic measurement system based on AMR sensors with dedicated noise reduction techniques, has been designed, developed, and tested for a 6U CubeSat mission of the Horizon 2020 program. The MELISA-III payload has successfully passed the

qualification and acceptance test campaigns at subsystem level before its final assembly, integration, and validation on the platform. The CubeSat is scheduled to be launched from Kourou in ESA's Vega-C rocket before mid-2023.

During scientific operations, ongoing post-processing analyses will enable discerning thermal and magnetic contributions from the scientific data provided in orbit. The in-flight characterization of MELISA-III will allow reaching an unprecedented noise performance and expand the frequency range for magnetic sensing in space-based gravitational wave detectors, pushing the technological discipline beyond its previous state of the art.

Acknowledgments

We wish to thank ALTER Technology for their collaboration during the environmental tests and Laboratorio de Corrosión y Protección (UCA) and Navantia for the black anodizing process of the MELISA-III shield. Support for this work came from the Department of Economy, Knowledge, Business and University of the Regional Government of Andalusia under Project P18-FR-2721 (PAIDI-2020 Programme), Project FEDER-UCA18-107380, and Project FEDER-UCA18-105867. The MELISA-III experiment will be embarked on the first mission of the H2020 IOD/IOV program of the EU.

References

[1] Amaro-Seoane P. et al. 2017, https://arxiv.org/abs/1702.00786

[2] Mateos I. et al. 2015, Sens. Actuator A-Phys., 224, 147

[3] Mateos I. et al. 2018, Sens. Actuator A-Phys., 273, 311

[4] Vilchez-Membrilla J. A. et al. 2022, IEEE Trans. Instrum. Meas., 71, 9512509

[5] Maria-Moreno C. et al. 2023, Zenodo, https://doi.org/10.5281/zenodo.7050680

Highlights of Spanish Astrophysics XI, Proceedings of the XV Scientific Meeting of the Spanish Astronomical Society held on September 4–9, 2022, in La Laguna, Spain. M. Manteiga, L. Bellot, P. Benavidez, A. de Lorenzo-Cáceres, M. A. Fuente, M. J. Martínez, M. Vázquez- Acosta, C. Dafonte (eds.), 2023

Parameters for >300 million *Gaia* stars: Bayesian inference vs. machine learning.

Anders, F.[1], Khalatyan, A.[2], Queiroz, A.[2,3], and Nepal, S.[2], and Chiappini, C.[2]

[1] Institut de Ciències del Cosmos (IEEC-UB), Dept. Física Quàntica i Astrofísica (FQA), Universitat de Barcelona, C Martí i Franqués, 1, 08028 Barcelona, Spain
[2] Leibniz-Institut für Astrophysik Potsdam (AIP), An der Sternwarte 16, 14482 Potsdam, Germany
[3] Institut für Physik und Astronomie, Universität Potsdam, Haus 28 Karl-Liebknecht-Str. 24/25, D-14476 Golm, Germany

Abstract

The *Gaia* Data Release 3 (DR3), published in June 2022, delivers a diverse set of astrometric, photometric, and spectroscopic measurements for more than a billion stars. The wealth and complexity of the data makes traditional approaches for estimating stellar parameters for the full *Gaia* dataset almost prohibitive. We have explored different supervised learning methods for extracting basic stellar parameters as well as distances and line-of-sight extinctions, given spectro-photo-astrometric data (including also the new *Gaia* XP spectra). For training we use an enhanced high-quality dataset compiled from *Gaia* DR3 and ground-based spectroscopic survey data covering the whole sky and all Galactic components. We show that even with a simple neural-network architecture or tree-based algorithm (and in the absence of *Gaia* XP spectra), we succeed in predicting competitive results (compared to Bayesian isochrone fitting) down to faint magnitudes. We will present a new *Gaia* DR3 stellar-parameter catalogue obtained using the currently best-performing machine-learning algorithm for tabular data, `XGBoost`, in the near future.

1 Introduction

The *Gaia* mission [14] has triggered an enormous increase in astronomical data that is revolutionising not only stellar and Galactic science but also has implications for cosmology and fundamental physics. The latest *Gaia* data release, DR3 [17], for the first time contains also low-resolution spectra, taken with *Gaia*'s blue and red photometer (BP/RP), for 219 million sources. These so-called XP spectra [10] represent the biggest homogeneous spectroscopic dataset (albeit at very low resolution; $R \sim 25$) available to date. Efficient methods to extract information from this dataset are starting to appear (e.g. [28, 3]).

2 Bayesian inference of stellar parameters with `StarHorse`

In the past years, our group has been developing an efficient Bayesian isochrone-fitting code, `StarHorse` [27, 24, 25], to infer stellar parameters, distances, and extinctions, to be able to analyse the ever-growing stellar spectroscopic survey datasets.

In [1], we applied the code for the first time to the *Gaia* data without spectroscopic information. The first experiments proved to be so promising that a big-data analysis run (285 million *Gaia* DR2 stars with $G < 18$, cross-matched with the Pan-STARRS1, 2MASS, and WISE photometric catalogues) was carried out using the computing cluster of the Leibniz-Institut für Astrophysik Potsdam (AIP). Our results doubled the number of Gaia DR2 sources with astrophysical parameters, improved the accuracy of the geometric distances, and revealed the presence of the Galactic bar in the Gaia data in a direct and completely unexpected manner (see Fig. 1).

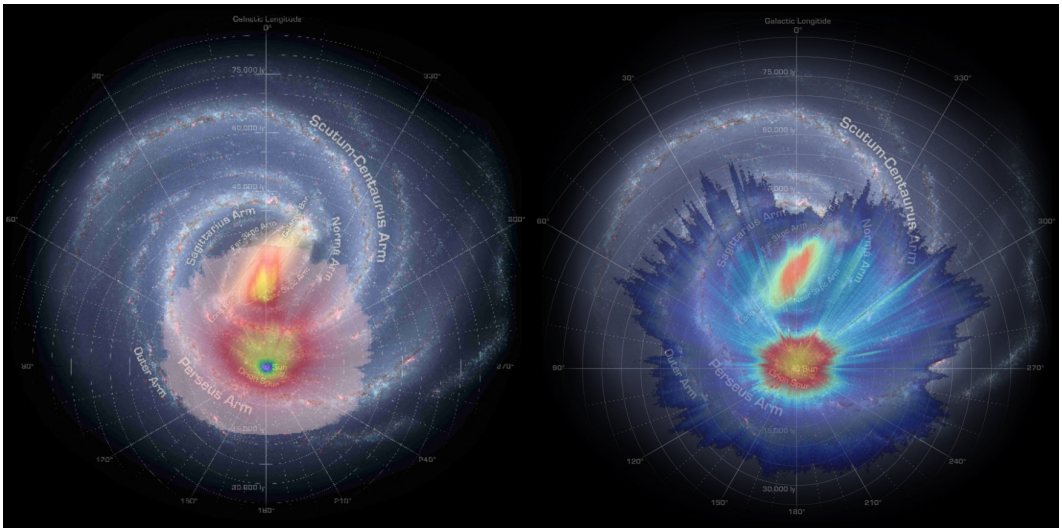

Figure 1: Comparison of the 5-year mission expectation for the Galactic coverage of the *Gaia* data before launch (left; [23]) with the results from `StarHorse` for *Gaia* DR2 ($G < 18$, 22 months of observation, right; [1]).

After the release of *Gaia*'s Early Data Release 3 in 2021 [16], and building on the success of the previous `StarHorse` catalogue, we ran our code on Gaia EDR3 data coupled with other large-area photometric surveys (now also including SkyMapper data). This resulted in an improved catalogue of 362 million stars, down to magnitude $G < 18.5$ (published in [2]). Thanks to the more precise EDR3 parallaxes and drastically reduced systematics [22], the Galactic density maps derived from it now probe a much greater volume than in [1], extending to regions beyond the Galactic bar and to Local Group galaxies, with a larger total number density.

The code was also sped up by using a less dense stellar model grid and a new computing cluster, which improved the CO_2 footprint of the project by factor ~ 6, but still consumed

around 1 month of computing time on a 1000-core cluster. At latest with the upcoming LSST surveys, this type of endeavour will therefore become unfeasible. In addition, `StarHorse` is unable to process spectroscopic measurements (such as the XP spectra) directly, which is an obvious drawback given that these data contain valuable information on the stellar parameters [13].

3 Predicting stellar parameters with a simple neural network

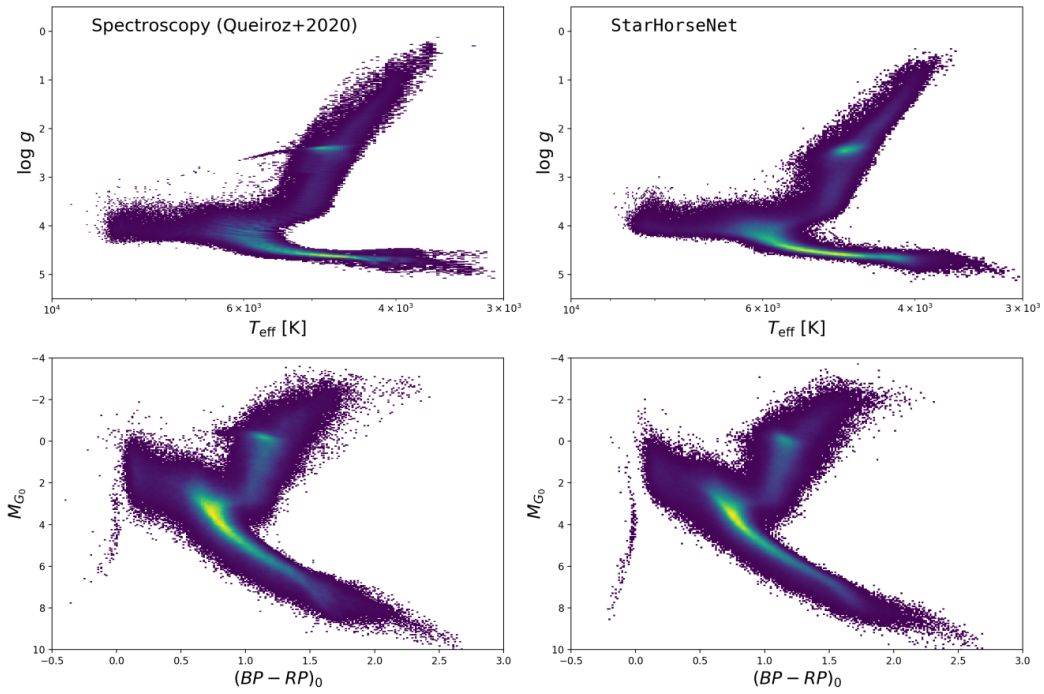

Figure 2: Results of the neural-network approach to stellar parameter estimation. Comparison between the colour-magnitude and Kiel Diagrams produced by the ANN model (right) with the spectroscopic test dataset [25]. Plot from the MSc thesis of Rany Assaad (University of Surrey, 2021).

In view of the computational drawbacks of traditional isochrone-based methods, in 2020 we started testing artificial neural networks (ANN) to predict stellar parameters for *Gaia* DR2 stars together with R. Assaad, an Erasmus+ MSc student visiting from the University of Surrey. As a training and test dataset, we used the `StarHorse` labels for various large-scale spectroscopic stellar surveys available at the time [25] (see Fig. 2).

This experiment was also surprisingly successful: with respect to [1] the ANN technique (even a very basic multi-layer perceptron architecture) doubled the number of stars (now more tha 300 million) considered to be of good quality. The full pipeline (including training

and prediction) could now be run on a 48-core machine within only 3 days, and it produced competitive posterior uncertainties (using a Monte-Carlo drop-out technique). The median uncertainties amounted to 16% in distance, 0.15 mag in V-band extinction A_V, 155 K in effective temperature $T_{\rm eff}$.

After cleaning the results of our Gaia DR2 run for poor input and output data, a sample of 373 million converged stars remained, for which we achieve a median uncertainty of 16% in distance, 0.15 mag in V-band extinction, and 155 K in effective temperature. Our experiment showed that even with a simple neural-network structure, one can succeed in predicting competitive results based on *Gaia* DR2 down to fainter magnitudes compared to classical isochrone or spectral-energy distribution fitting methods. Independent recent work [12] reached similar concluisons.

4 Improved results with tree-based algorithms

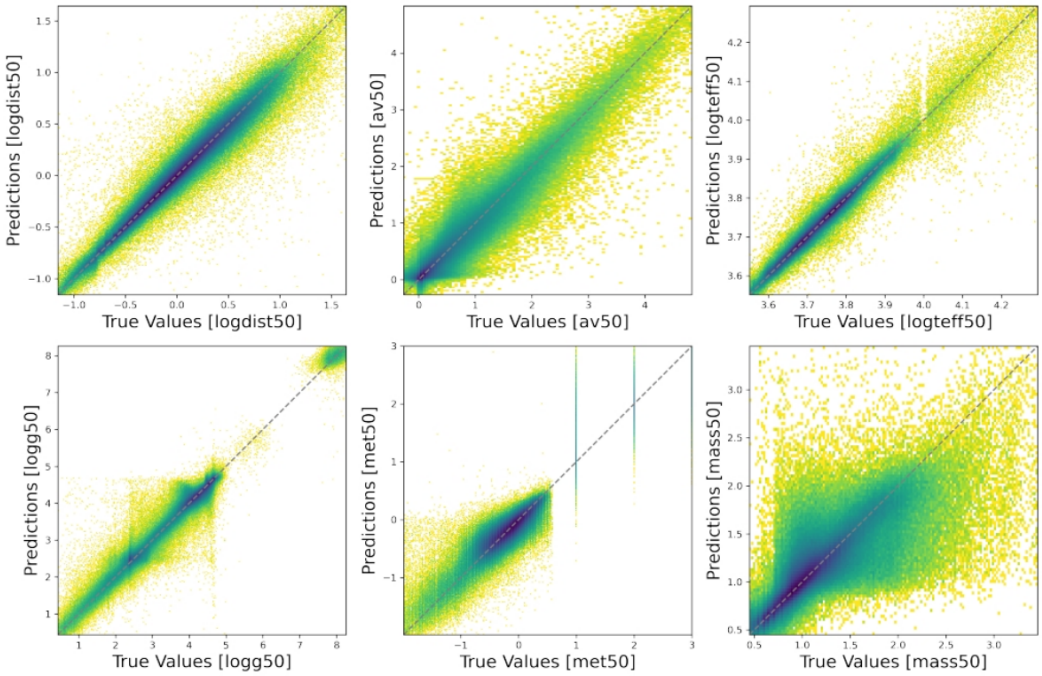

Figure 3: First results (June 2022) of the `XGBoost` approach to stellar parameter estimation for the case of stars with available *Gaia* DR3 XP spectra. One-to-one comparisons between the predicted stellar parameters and the spectroscopic test dataset [26] (labelled "true values").

The *Gaia* DR3 XP spectra are not delivered in the form of classical spectra, but come in the form of internally-calibrated spectral coefficients [6]. They can therefore be treated as tabular data and easily fed to a supervised learning technique. [5] benchmark-tested several

regression algorithms (including several neural network architectures) for tabular data and found that the most efficient and accurate technique was the tree-based algorithm Extreme Gradient-Boosted Trees (`XGBoost`, [7]). This technique is implemented in the `python` package `xgboost` that is widely used for classification tasks in astronomy (e.g. [4, 29, 20, 9]). Examples for the use of `XGBoost` for regression tasks in astronomy are sparser, but also start to appear, e.g. for photometric redshifts [8, 21], predicting the number of sunspots [11], or determining spectroscopic stellar ages [19].

For our first tests, we assembled a training set of 4 million *Gaia* DR3 stars with XP spectra that have also been observed by spectroscopic stellar surveys and have `StarHorse` stellar parameters [26]. As training columns we used the normalised XP coefficients, as well as *Gaia* astrometry and broad-band optical and infra-red photometry. The training set was complemented with spectroscopically observed white dwarfs from [18]. The predicted labels include distance, A_V, $T_{\rm eff}$, surface gravity $\log g$, metallicity [M/H], and stellar mass.

The first tests yielded the following precisions and accuracies for unseen test data: $\Delta \log d = -0.002 \pm 0.075$, $\Delta A_V = +0.001 \pm 0.145$, $\Delta \log T_{\rm eff} = 0.000 + -0.011$ (see Fig. 3). The computational cost is even lower than in the case of the simple neural network (Sect. 3), and robust to both the choice of hyperparameters and the scaling of the input data. For the first time, our group is also able to deliver acceptable stellar parameters for white dwarfs.

5 Conclusions

While traditional (and genuinely astrophysical) methods continue to be both useful and necessary to understand the new astronomical data, machine-learning techniques are needed to handle the sheer amounts of present and future data, and to lower the total CO_2 budget of astronomical research. Here we showed that both neural-network and tree-based algorithms, once sufficiently well trained, can be successfully employed to infer stellar parameters, distances, and extinctions in the absence of high-resolution spectroscopic data. In the near future, we will present a new `StarHorse`-like catalogue for *Gaia* DR3 stars based on `XGBoost` trained on high-resolution spectroscopic data.

Acknowledgments

This work was (partially) funded by the Spanish MICIN/AEI/10.13039/501100011033 and by "ERDF A way of making Europe" by the "European Union" through grant RTI2018-095076-B-C21, and the Institute of Cosmos Sciences University of Barcelona (ICCUB, Unidad de Excelencia 'María de Maeztu') through grant CEX2019-000918-M. FA acknowledges financial support from MICINN (Spain) through the Juan de la Cierva-Incorporcion programme under contract IJC2019-04862-I.

This work has made use of data from the European Space Agency (ESA) mission *Gaia* (`http://www.cosmos.esa.int/gaia`), processed by the *Gaia* Data Processing and Analysis Consortium (DPAC, `http://www.cosmos.esa.int/web/gaia/dpac/consortium`). Funding for the DPAC has been provided by national institutions, in particular the institutions participating in the *Gaia* Multilateral Agreement.

References

[1] Anders, F., Khalatyan, A., Chiappini, C., et al. 2019, A&A, 628, A94

[2] Anders, F., Khalatyan, A., Queiroz, A. B. A., et al. 2022, A&A, 658, A91

[3] Andrae, R., Fouesneau, M., Sordo, R., et al. 2023, A&A, in press, arXiv:2206.06138

[4] Bethapudi, S. & Desai, S. 2018, Astronomy and Computing, 23, 15

[5] Borisov, V., Leemann, T., Seßler, K., et al. 2021, arXiv e-prints, arXiv:2110.01889

[6] Carrasco, J. M., Weiler, M., Jordi, C., et al. 2021, A&A, 652, A81

[7] Chen, T. & Guestrin, C. 2016, arXiv e-prints, arXiv:1603.02754

[8] Chong, K. & Yang, A. 2019, arXiv e-prints, arXiv:1901.07544

[9] Cunha, P. A. C. & Humphrey, A. 2022, A&A 666, A87

[10] De Angeli, F., Weiler, M., Montegriffo, P., et al. 2023, A&A, in press, arXiv:2206.06143

[11] Dang, Y., Chen, Z., Li, H., Shu, H. 2022, Applied Artificial Intelligence, 2022, 36, arXiv:2203.05757

[12] Fallows, C. P. & Sanders, J. S. 2022, MNRAS 516, 5521

[13] Fouesneau, M., Frémat, Y., Andrae, R., et al. 2023, A&A, in press, arXiv:2206.05992

[14] Gaia Collaboration, Prusti, T., de Bruijne, J. H. J., et al. 2016, A&A 595, A1

[15] Gaia Collaboration, Brown, A. G. A., Vallenari, A., et al. 2018, A&A 616, A1

[16] Gaia Collaboration, Brown, A. G. A., Vallenari, A., et al. 2021, A&A 649, A1

[17] Gaia Collaboration, Vallenari, A., Brown, A. G. A., et al. 2021, A&A, in press, arXiv:2208.00211

[18] Gentile Fusillo, N. P., Tremblay, P. E., Cukanovaite, E., et al. 2021, MNRAS, 508, 3877

[19] Hayden, M. R., Sharma, S., Bland-Hawthorn, J., et al. 2022, MNRAS 517, 5325

[20] Li, C., Zhang, Y., Cui, C., et al. 2021, MNRAS, 506, 1651

[21] Li, C., Zhang, Y., Cui, C., et al. 2022, MNRAS, 509, 2289

[22] Lindegren, L., Bastian, U., Biermann, M., et al. 2021, A&A 649, A4

[23] Luri, X., Palmer, M., Arenou, F., et al. 2014, A&A, 566, A119

[24] Queiroz, A. B. A., Anders, F., A., Santiago, B. X., et al. 2018, MNRAS 476, 2556

[25] Queiroz, A. B. A., Anders, F., A., Chiappini, C., et al. 2020, A&A, 638, A76

[26] Queiroz, A. B. A., Anders, F., A., Chiappini, C., et al. 2023, A&A, subm.

[27] Santiago, B. X.; Brauer, D. E., Anders, F., et al. 2016, A&A 585, A42

[28] Weiler, M., Carrasco, J. M., Fabricius, C., Jordi, C. 2022, A&A, accepted, arXiv:2211.06946

[29] Yi, Z., Chen, Z., Pan, J., et al. 2019, ApJ, 887, 241

Highlights of Spanish Astrophysics XI, Proceedings of the XV Scientific Meeting of the Spanish Astronomical Society held on September 4–9, 2022, in La Laguna, Spain. M. Manteiga, L. Bellot, P. Benavidez, A. de Lorenzo-Cáceres, M. A. Fuente, M. J. Martínez, M. Vázquez- Acosta, C. Dafonte (eds.), 2023

Road to the stars, promoting the ESO Chile fellowships.

Corral-Santana, J.M.[1]

[1] European Southern Observatory (ESO), Alonso de Córdova 3107, Casilla 19, Vitacura, Santiago, Chile

Abstract

The European Southern Observatory (ESO) invites applications for the ESO-Chile Fellowship Programme every year around mid-October. The Programme provides a unique opportunity for young scientists to develop their independent research programs and successfully reach the next step of their scientific careers. With this contribution, we aim at promoting the ESO-Chile fellowship among the Spanish and Italian community. ESO Fellowships in Chile are granted for 4 years. During the first three years, the Fellows are assigned to one of the Science Operation groups of Paranal or ALMA, where they contribute at a level of 80 nights per year, corresponding to 50% of the working time. ESO Chile Fellows may choose to spend the fourth year at any astronomy/astrophysics institute in an ESO member, Chile or ESO's strategic partner, Australia, with 100% of their time devoted to scientific research. ESO Chile Fellows will benefit from developing their scientific profiles and becoming mature and independent researchers in a rich, collaborative and structured environment. In summary, this unique mix of technical knowledge and their close contact with the science carried out at the Observatories, ESO Chile Fellows can build a solid research programme that can boost their future career.

1 Introduction

The ESO fellowship program has been running since 1977. It is one of most recognized postdoctoral positions and an important component of ESO's mission, with positions open both in Germany and Chile. In the latter, ESO offers 5 to 6 positions every year open for young postdocs, who can spend part of their time working at ALMA or Paranal and carry out their independent research in the Vitacura premises in Santiago. These positions are open to all nationalities but preference is given to nationals of ESO member states.

2 The ESO Fellowship Program

The ESO Fellowship is a postdoctoral position for young researchers that can develop an independent research in combination with working at the ESO facilities and acquiring large

technical experience operating state-of-the-art instrumentation.With time, the fellow will also have the possibility to train new arrivals to the team.

During the duration of the position, the fellow will be part of the Office for Science which has a generous budget to support the fellow in travelling to conferences, science leaves or observing runs. In addition, the fellow have the possibility to co-supervise and mentor students or interns.

3 The ESO Fellowship in Chile

ESO operates 3 observatories in Chile: ALMA, La Silla and Paranal with about 70 staff and fellows which complement a larger team of engineers, students and colleagues working in administration and logistics. Around 300 people are currently working in Chile, divided between the observatories and the Vitacura campus in Santiago, where we have the ESO and ALMA headquarters.

The ESO Fellowship in Chile is a 4 years contract During the first 3 years, fellows will spend up to 50% of their working time performing duties either at ALMA or at Paranal. This corresponds to up to 80 nights per year. The remaining 50% of the working time to carry on and independent research.

During the 4th year, the fellow have different possibilities that they can choose according to their convenience:

- The fellow can decide to stay in any institution of any ESO Member State, Australia (as strategic partner) or in a Chilean institution, doing 100% research time.
- The fellow can also choose to stay at ESO Chile doing 25% operational duties (up to 40 nights) and 75% research.

There are 5 - 6 positions opened per year that are divided between Paranal and ALMA. The number of positions assigned to each observatory changes every year based on the observatories needs. The functional duties are mostly on-site for Paranal and partially on-site for ALMA, which is currently running many operations remotely from Santiago. These duties are performed in shifts: typically 8 days/nights in the case of ALMA and shifts of 6–14 days/nights (length chosen by the Fellow) in the case of Paranal. After each shift there are compensation days of similar length.

The duties of the fellows at Paranal include supporting astronomers for service and visitor runs, carrying out the execution of the observations (choosing which observing block can be executed in the current weather conditions, operating the instrument, analysing the quality control of the observed data, ...) and providing advice to the visitors. In addition, they will become instrument fellow acquiring in-depth knowledge of a given instrument. They will participate in engineering activities as recommissioning of instruments, will/can develop improvements of instrument performance, operation or data reduction.

Fellows that choose to perform the duties at ALMA are similar to the Paranal ones. They will be the astronomer on duty observing at the array and they will be working on the data

Figure 1: Left: Sunset at the Paranal observatory. Right: View of the Paranal residencia

processing and software testing. The fellow will also assist in the ALMA proposal review process and could also develop new capabilities.

Figure 2: Left: ALMA array. Right: View of the ALMA residencia

During the research time, the fellow will be in the Vitacura campus in Santiago where they will engage in a great scientific and social environment, attending and organizing talks, lectures and workshops as well as topic-related coffees and other social events. Being in Santiago will also allow the fellow to make connections with the growing Chilean astronomical community.

Fellows can co-supervise ESO students or interns with other ESO staff. They can also request funds to the Visitor program to bring students or senior collaborators to Chile or participate in organizing committees of workshops. The fellow will also benefit of working in a true international environment working closely with people from different cultures and disciplines.

ESO personnel do not have privilege access to any telescope time, However, if the fellow decides to stay in a Chilean institution during the 4th year, they will be eligible to apply for time on all telescopes in Chile through the 10% Chilean observing time.

There are other benefits that makes this post-doc position very competitive:

- Access to an international health insurance

Figure 3: ESO and ALMA Headquarters in Vitacura, Santiago.

- A plane ticket to the home station for all the fellow's family members paid by ESO (starting on the 2nd year)
- Education grant for fellow's children
- Paid relocation and installation grant
- And of course being in an amazing country and continent while working in a successful and recognized position.

The deadline for submitting applications is every year on Oct 15th using ESO's Recruitment Portal https://recruitment.eso.org

For more information about the ESO Fellowship program, please visit eso.org/fellowship or the talk uploaded to zenodo.org that can be found here.

Acknowledgments

We thank the ESO Chile Office for Science for their help and support.

Figure 4: Posters with more information about the ESO Fellowship.

Highlights of Spanish Astrophysics XI, Proceedings of the XV Scientific Meeting of the Spanish Astronomical Society held on September 4–9, 2022, in La Laguna, Spain. M. Manteiga, L. Bellot, P. Benavidez, A. de Lorenzo-Cáceres, M. A. Fuente, M. J. Martínez, M. Vázquez- Acosta, C. Dafonte (eds.), 2023

Status of the SKA project and the SKA Regional Centre Network.

Julián Garrido[1], Lourdes Verdes-Montenegro[1], and Susana Sánchez[1] and Julio Gallardo[1]

[1] Instituto de Astrofísica de Andalucía (CSIC)

Abstract

The aim of this contribution is to present the status of the SKA (Square Kilometre Array) project and the SKA Regional Centre Network (SRCNet). The SKA project is an international effort to build two radio-interferometers that will be able to make revolutionary contributions to Astrophysics, Astrobiology, and Fundamental Physics. In January 2021, the SKA Observatory (SKAO) was established as the second intergovernmental organisation in astronomy (after the European Southern Observatory). For SKA1, the first phase of the telescopes, SKA-Low will consist of more than 130.000 low-frequency dipoles in Australia, and SKA-Mid will consist of 197 dishes in South Africa (including MeerKAT's 64 antennas). The construction commenced in July 2021 and the procurement for its contracts have already been initiated with 5 contracts pre-allocated to Spain. In addition, the SKAO is planning to start a development program for new instrumentation development.

The high data-rate and complexity of SKAO will necessarily transform how scientists access, analyse and share data from observations, being considered a Big Data machine. A network of SKA Regional Centres (SRCs) is being established to take the science data products that will emerge from the SKA telescopes to the final state required for science analysis.

1 Introduction

The SKA Observatory (SKAO) is an ESFRI (European Strategy Forum on Research Infrastructures) Landmark aimed to build two radio interferometers with the potential to make revolutionary contributions to astrophysics, astrobiology and fundamental physics. The unprecedented sensitivity of the Square Kilometre Array (SKA) telescopes pursues a number of scientific goals, like understanding the evolution of galaxies and how dark energy works or searching for complex molecules that are fundamental to the formation of life, among others. The Spanish scientific community has showed a strong interest in the project by drafting the Spanish SKA White Book [1], gathering the national scientific interest in SKA.

The two radio interferometers will complement each other over a wide range of the radio spectrum. In their first phase one will have 197 dish antennas with a maximum baseline of 150 km (SKA-mid, 350MHz - 15.4GHz) located in the Karoo Desert in South Africa, and the

other more than 131000 2-metre high dipole antennas located in Western Australia, grouped into 512 stations with maximum separation of 65 km (SKA-low, 50-350 MHz).

The SKA Regional Centres (SRCs) will receive data from the SKAO and will be responsible for maintaining its scientific archive. The SRCs will be distributed around the world, forming a global network to provide computational resources and collaborative tools to allow the international SKA community to take full advantage of the SKA telescopes. The SRC Network (SRCNet) will also provide scientific support in the use of the instruments and in the analysis of their data, being the SRCs the place where SKA science will take place.

In the following sections it is explained the overall summary of the international SKA journey so far (section 2) and the national scientific preparatory work (section 2.1), the design and construction activities (section 2.2) and the communications and outreach effort (section 2.3). The section 3 includes the activities related with the SRCNet (Section 3.1), the Spanish SRC prototype and the Open Science (section 3.2) and the SKA Data Challenges (Section 3.3). At the end, a section with the conclusions is also included (section 4).

2 The SKA Observatory journey

In 2008, the preparatory phase of the SKA (PREPSKA: A Preparatory phase proposal for the Square Kilometre Array, European Union FP7 2008-2012) officially started with the goal of preparing for the pre-construction activities. The SKA Organisation was established in 2011 as the entity in charge of the coordination of the pre-construction activities. The detailed design of the SKA telescopes were carried out by 12 international engineering consortia, formed in 2013, which were responsible for the fulfillment of the design requirements defined for the telescopes. The System Critical Design Review (CDR), a review of an independent external panel for the SKA telescopes' overall design, succeeded in December 2019.

A few months before the CDR, in March 2019, 7 countries signed the SKAO Convention with the aim to establish the Observatory as an intergovernmental organisation (IGO), which would tackle the construction and operations of the telescopes. This milestone started a transition phase from the SKA Organisation to the SKA Observatory, concluding in January 2021 with the ratification of the needed signatures to establish the SKAO. The first Council meeting was held a few days later and two high-level documents were approved: 1) the Construction Proposal, the plan to build the SKA Phase 1 and 2) the SKAO establishment and Delivery Plan, which establish the SKAO as a scientifically productive entity. They cover the first decade of SKAO's planning, from its establishment until two years after the end of the construction phase. More than 26 contracts with a total value of €216M have already been tendered and, once operational, a lifetime of more than 50 years is foreseen.

At the time of writing, eight countries[1] have joined the SKAO so far and another eight[2] are expected to join the IGO in the coming years. Spain became the 11th member of the SKA Organisation in June 2018 and the SKAO Council approved the Spanish membership in July 2021, being the accession process very advanced. While the process is on going, the

[1] Australia, China, Italy, the Netherlands, Portugal, South Africa, Switzerland and the United Kingdom.
[2] Canada, France, Germany, India, Japan, South Korea, Spain and Sweden.

country has already started contributing to fund the SKAO.

Researchers from Spanish institutions have expressed their interest in the SKA since the 90's. From 2011 on, the *Instituto de Astrofísica de Andalucía* (IAA-CSIC) coordinates the national participation in the project, and receives direct economical support from the Spanish Science and Innovation Ministry (MCIN) since 2020. The coordination team gives support to academic groups, industry and MCIN in matters related to the project and interacts with the SKAO office. It also coordinates proposals and disseminates calls for funding and promotes the Spanish representation in SKAO committees, the scientific preparation and the participation in the SKAO construction. The group also coordinates communications and outreach at national level, being members of the SKA Communications and Outreach Network (SKACON) and its Steering Committee (SKACOSC).

2.1 Scientific preparatory work

The Spanish community participates in projects and observatories across the entire electromagnetic spectrum in synergy with SKA science. The participating in SKA precursors (telescopes located at future SKA sites) and pathfinders (telescopes using SKA preparatory technology) observation programmes (GASKAP, WALLABY, MIGHTEE, MHONGOOSE,...) is one of the major ongoing preparatory activities. Figure 1 shows two examples of the unprecedented science that SKA precursors are already delivering.

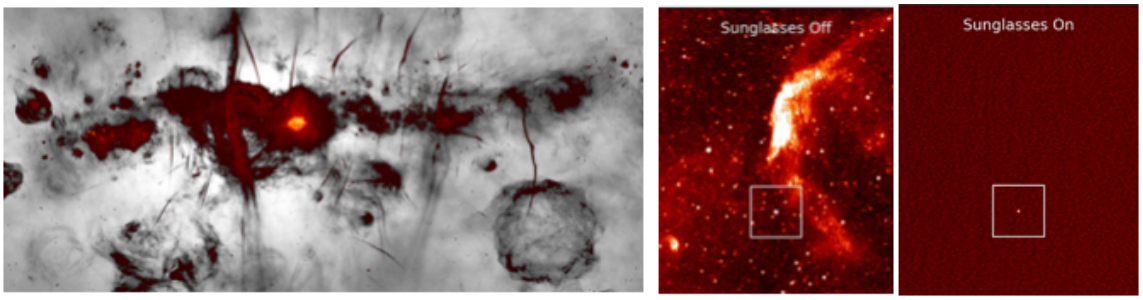

Figure 1: On the left, the deepest, most resolved image of the Milky Way centre (Heywood et al. [2], MeerKAT). On the right, the brightest ever pulsar found in the Magellanic Cloud (Wang et al. [3], ASKAP, Australian Square Kilometre Array Pathfinder)

The SKA-Mid and SKA-Low commissioning phase is expected to initiate in early 2024, with the finalisation of the construction of the first Array Assembly (AA - batch of antennas or stations), and science verification is scheduled to start by 2027. A series of SKA Data Challenges are being and will continue to be launched at the same time to help the community prepare for the analysis of the SKA data products that the SKA telescopes will deliver (sect. 3.3). Many astronomers from Spanish centres currently carry out research projects aligned with the SKA Science Drivers an have expressed a huge interest in SKA Science over the years specially by: 1)publishing the Spanish SKA White Book [1] in 2015 through the collaborative effort of 119 Spanish astronomers affiliated to 25 Spanish centres and 15 foreign ones; 2) organising and contributing in more than 10 SKA specific conferences in Spain; 3) being part

of 13 out of the 14 SKA Science Groups with the participation, at the time of writing, of 58 scientist from 18 Spanish research centres; and 4) establishing the Spanish SKA Network with national funds for national groups interested in the SKA project at scientific, technological and industrial levels to maintain contact and get involved in the initiative.

2.2 Design and Construction activities

In November 2011, the former MCIN funded a feasibility study for Spain's participation in SKA. As part of its results, the Spanish industry was interviewed to elaborate a Capability Map and identify stakeholders that could have relevant technological profiles for the SKA project. Two years later, eleven consortia were formed in order to carry out the design the specific elements of the telescopes between 2013 and 2019. At national level, more than 20 Spanish research centres and companies participated in 8 out of the 11 SKA design consortia.

The time period between the system CDR and the start of the telescopes' construction was defined as the 'bridging' phase, aimed at improving the design of different elements. Spain contributed to the Science Data Processor (IAA-CSIC and GMV through the project 'Supporting Open Science in the SKA by collecting Provenance from its Science Data processor') and to the Signal and Data Transport element ('White Rabbit Switch de alta fiabilidad de interoperabilidad 10G' project led by University of Granada and Seven Solutions).

Once the SKAO was established, its Council approved the start of the telescopes' construction in July 2021. This phase will last about 8 years and, in this period, the scientific community will begin to use part of the instrument to carry out the commissioning and verification of the instrument. As the MCIN has started the process to join the SKAO, Spain agreed with the SKAO on different technological areas for the Spanish industry to participate in i.e. synchronisation and distribution of signals, SKA-Mid dish antennas' sub-reflectors and different elements for the Band 1 (0.58–1.015GHz) and Band 5 (4.60–15.4GHz) receivers.

2.3 Communication and outreach

In 2022, the Spanish representatives at the SKACON and SKACOSC participated in the design of the SKAO Communication Strategy document, it covers the whole construction phase (2022-2029). In the same year, the SKAO website was published, including a page for Spanish national information about the SKA project.

Since last Spanish Society of Astronomy meeting, the SKA Spanish coordination team have been granted with funds from the International Astronomical Union (IAU) for two outreach projects. The IAU Office for Astronomy Outreach funded the 'From SKA to the World' project, aiming at developing online science communication and education products while targeting high school students. The 'Education for all' project, funded by the Office of Astronomy for Development, aimed to promote education in internally displaced communities in Burkina Faso. A collaboration has also been initiated in November 2022 during the Spanish Childhood day with the international Non-Governmental Organization, 'Aldeas Infantiles SOS' ('SOS Children Villages') with the intention to keep it growing.

3 SKA Regional Centre Activities

3.1 The SKA Regional Centre Network

In September 2016 the SKA organization established the SRC Coordination Group (SRCCG), with the mandate to define the requirements of the SRCNet. At that time, different international initiatives started contributing to the design of the SRCs, analyzing the requirements from a regional point of view, highlighting among them the European project "Advanced European Network of E-infrastructures for Astronomy with the SKA" (AENEAS). At the end of 2018, the SRC Steering Committee (SRCSC) took over from the SRCCG to take the SRCNet from design to implementation on a global basis. To this end, 7 working groups were established, focused on the following areas: SRCNet architecture, data logistics, operations, federated computing and data software services, SKA science archive, compute, and science user engagement. All these groups included a total of 12 Spanish members from 7 institutions. Among these groups the Science User Engagement Working Group was in charge to engage the community during the identification of requirements for the SRCNet

In early 2022, the SRCSC, with the support of the SRC Architect, defined nine international teams to carry out the SRCNet prototyping phase following an agile methodology. Five of these teams were focused on identifying and explore solutions in different areas (data management, science platform, Authetication and Authorisation, High Performance Computing (HPC) platforms and Visualisation). Two agile teams are in charge of building testbeds to provide feedback and a formal assessment of the technologies considered for the different SRC components. One of these teams is lead by the Spanish group in charge of the development of the Spanish SRC prototype (SPSRC). Two teams have not started their activity yet.

3.2 The Spanish SRC prototype and the Open Science

The IAA-CSIC is leading the development of the SPSRC as part of the program associated to its Severo Ochoa distinction. The SPSRC is providing support to scientific activities related to the SKA precursors and pathfinders, while promoting synergies and best practices on Open Science. The SPSRC initiative aims to build a transversal facility and uses Open Science as a tool to reach the whole astronomical community beyond that of radio astronomy.

As acknowledged by the United Nations Educational, Scientific and Cultural Organization (UNESCO), Open Science impacts on areas related to some of the Sustainable Development Goals (SDGs). The engagement of the SPSRC with Open Science is aligned with the position of SKA in this topic. SKAO is the first facility including reproducibility as a scientific metric of success. SKA project is aware of how Open Science impacts on areas related to some of the SDGs and the SKA's foundational principles include the adoption of Open Science values.

3.3 The SKA Data Challenges

The SKA Data Challenges (SDCs) are exercises designed and published by the SKAO. They entail analysis of simulated SKA data products and their aim is to prepare the scientific

community for the analysis of the SKA data. The SDC1 was published in 2018, the SDC2 ran during the first part of 2021 and SDC3 will do in the first part of 2023. Since the SDC2 several international computing facilities provide support to the SDC participants, so the community get familiar to analyse the data using external platforms, in a similar way as when the SRCNet will be functioning. The SKAO offered reproducibility award for those SDC2 participants who demonstrated reusable methods and reproducible results.

4 Conclusions

The SKAO started the construction of the two telescopes in 2021 and Spain was allocated with 5 contracts in the areas of synchronisation and distribution of signals, SKA-Mid antennas' sub-reflectors and different elements for the bands 1 and 5. The SRCNet will be part of an end-to-end system composed by the SKAO and the SRCs. The SRCs will provide the community with access to data, computational resources and support to produce SKA science, as well as a platform for collaborative science. Spain is contributing to the development of the SRCNet and the SPSRC is supporting ongoing preparatory scientific activities.

Acknowledgments

The authors acknowledge financial support from the grant CEX2021-001131-S funded by MCIN/AEI/ 10.13039/501100011033, from the grants RTI2018-096228-B-C31 and PID2021-123930OB-C21 funded by MCIN/AEI/ 10.13039/501100011033, by "ERDF A way of making Europe", by the "European Union", by the grant TED2021-130231B-I00 funded by MCIN/AEI/ 10.13039/501100011033 and by the "European Union NextGenerationEU/PRTR", and from the grant IAA4SKA (R18-RT-3082) funded by the Economic Transformation, Industry, Knowledge and Universities Council of the Regional Government of Andalusia and the European Regional Development Fund from the European Union. They also acknowledge financial support from The coordination of the participation in SKA-SPAIN, funded by the Ministry of Science and Innovation (MCIN) and the grant RED2018-102587-T funded by MCIN/AEI/ 10.13039/501100011033.

References

[1] The Spanish Square Kilometre Array White Book. Editors: Pérez-Torres, M. et al.

[2] Heywood, I. et al., 2022, ApJ, 925, 165

[3] Wang, Y., et al., 2022, ApJ, 930, 38

Highlights of Spanish Astrophysics XI, Proceedings of the XV Scientific Meeting of the Spanish Astronomical Society held on September 4–9, 2022, in La Laguna, Spain. M. Manteiga, L. Bellot, P. Benavidez, A. de Lorenzo-Cáceres, M. A. Fuente, M. J. Martínez, M. Vázquez- Acosta, C. Dafonte (eds.), 2023

The ExoLife Finder project: a prototype hydrid interferometer telescope to be installed at Teide Observatory.

Nicolas Lodieu[1,2], Rafael Rebolo[1,2,3], Jeff Kuhn[4,5], Gil Moretto[6], Ye Zhou[7], Maud Langlois[6], and Kevin Lewis[8]

[1] Instituto de Astrofísica de Canarias (IAC), Calle Vía Láctea s/n, E-38200 La Laguna, Tenerife, Spain
[2] Departamento de Astrofísica, Universidad de La Laguna (ULL), E-38206 La Laguna, Tenerife, Spain
[3] Consejo Superior de Investigaciones Científicas (CSIC), Madrid, Spain
[4] IfA/ATRC, University of Hawaii, Maikalani, Kula, HI 96790 USA
[5] MorphOptics, Kula, HI 96790 USA
[6] Centre de Recherche Astrophysique de Lyon, CNRS, Saint-Genis-Laval 69230, France
[7] Dynamic Intelligent Structures Ltd. Vancouver, BC, Canada
[8] Buble Studios, Kula, HI 96790 USA

Abstract

The IAC in Tenerife is collaborating with an international consortium involving the University of Hawaii, MorphOptic (USA), Dynamical Intelligent Structures (DiSL, Canada) and two institutes in Lyon (CRAL@CNRS + INSA; France), to design the future ≥40m ExoLife Finder (ELF), an optical hybrid interferometer telescope. The objectives of ELF are both scientific and technological: the discovery of biomarkers in the atmospheres of exoplanets and patenting tensegrity and ultra-light ultra-thin mirrors to reduce the weight of future large telescopes by at least a factor of ten.

The consortium embarked in building a 3.5-m prototype (nicknamed Small-ELF) as a demonstrator for ELF, made of 15 mirrors of 0.5m in diameter mounted on a "bicycle wheel" structure. Small-ELF will have high angular resolution astronomical capabilities in the near-infrared and will also serve as a technology demonstrator for the much larger ELF. The installation is planned in the coming years at Teide Observatory. The detailed design, which provides optical, mechanical, and electronic solutions with bottom-up cost estimates, is presented.

1 Introduction

Since the announcement of the first planet orbiting the 51 Peg star outside of our Solar system by Mayor & Queloz (1995) who received the Nobel prize in Physics in 2019 [1], the field of

exoplanets have evolved dramatically with the discovery of more than 5000 exoplanets with a wide variety of physical properties. The main objective has now shifted to the detection and characterization of telluric exoplanets. The search for biomarkers in their atmospheres and imaging of continents on their surfaces motivate the construction of dedicated giant telescopes capable of unprecedented contrast, angular resolution, and spectral stability.

2 The ExoLife Finder

To be able to image exoplanets, several key observational and technical requirements are mandatory, including:

1. high spatial resolution = angular separation to detect close companions to the star
2. high dynamic range i.e. contrast photometry to detect faint companions
3. high sensitivity or depth to detect faint companions
4. never mind the field-of-view because the planet is close to its host star
5. observe in the infrared where the planet is brighter

There is a specific need for a large but light and cheap telescope dedicated to exoplanet science with the above characteristics. This new telescope, nick-named the "ExoLife Finder" (ELF), is an hybrid optical interferometer planned with a minimum diameter of 40m [4]. It will be the lightest and unique telescope world-wide dedicated to high-resolution high-contrast infrared imaging. The challenges of ELF to reduce the weight, hence, the cost by a factor of approximately ten, are both technological and scientific.

The main scientific goals of ELF is to detect biomarkers in the atmospheres of exoplanets orbiting the nearest and brightest stars to the Sun and reconstruct the surface of extrasolar planets in the near-infrared with inversion techniques [3, 2].

ELF will work as a hybrid optical interferometer. Its contruction and success relies on three major technological challenges outlined below:

- Tensegrity will use cables instead of trusses to join the bicycle wheel shape of the mechanical structure to the mirror support structure [5]
- Ultra-light, self correcting, "Live" Mirrors lowering mirrors aerial density and maximizing performance with non-abrasive, additive, 3D-printed novels technology [6]
- Wavefront sensing and control technologies to reach unprecedented planet-to-star contrast ($>10^8$) by correcting on the fly the atmospheric turbulence together with telescope co-phasing and nulling [7]

3 The Small-ELF prototype

The consortium, made of the Hawaii Institute for Astronomy, MorphOptic Inc, and Georgia State University in the US, DiSL in Vancouver (Canada), and the Centre de Recherche

d'Astrophysique de Lyon (CNRS/CRAL) along with the Institut National des Sciences Appliquées (INSA) in Lyon (France), and the Instituto de Astrofísica de Canarias (IAC) is currently designing a 3.5-m prototype to be installed at Teide Observatory to develop, prove, and validate the three aforementioned key technologies. Small-ELF is a 3.5 m telescope that will have high angular resolution astronomical capabilities with bright sources that will serve as a technology demonstrator and prototype for ELF.

Our consortium has now a detailed design delivered and funded by the Spanish Ministry of Science's recovery plan that provides optical, mechanical, and electronic solutions with cost estimates. The basic optical design of the Small-ELF consists of a ring of 0.5m diametre lightweight primary mirrors (Figure 1). The ultra-light mirrors and the wavefront sensing technologies have recently been funded through European and french-national funds, respectively. The Small-ELF develops opto-mechanical and interferometric capabilities that are critical for the next generation of ultra-large optical telescopes and instruments. In particular, Small-ELF will demonstrate that new technologies such as synthetic optical aperture, light-weight mirrors, and tensegrity can be manufactured, assembled, tested, and installed efficiently and cost-effectively.

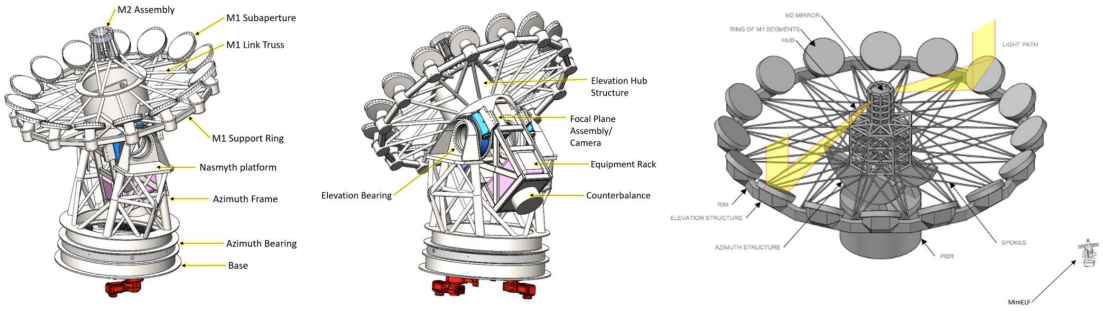

Figure 1: Detailed design of the Small-ELF 3.5-m prototype. *Copyright DiSL, IAC*

The construction of the mechanical structure of Small-ELF is planned in-house for the second half of 2024 and its installation a year later at Teide Observatory in Tenerife, Canary Islands (Spain). Small-ELF will provide a unique coronographic capability to the Spanish astronomical community to obtain high-contrast images of sources visible from the Northern Hemisphere. There is no other facility capable of provide images with such high contrast in the near-infrared available to the Spanish community.

4 Conclusions

Modern ground-based optics will far surpass space experiments for exoplanet observations. A dedicated exoplanet research facility like ELF is sorely needed to achieve both low scattered light and high photometric dynamic range in the next decades. We believe that ELF can be built in the next 10–20 years so that the new generation of astronomers can detect exolife during their career.

Acknowledgments

The design and construction of the Small-ELF prototype is partially finance by the European Union - NextGenerationEU - and the Recovery and Resilience Facility plan of the Spanish ministry. NL acknowledge support from the Agencia Estatal de Investigación del Ministerio de Ciencia e Innovación (AEI-MCINN) under grant PID2019-109522GB-C53.

References

[1] Mayor, M. & Queloz, D. 1995, Nature, 702, 27

[2] Berdyugina, S. V. & Kuhn, J. R. 2019, AJ, 158, 246

[3] Berdyugina, S. V. et al. SPIE, 10700E, 4IB

[4] Kuhn, J. R., Berdyugina, S. V., Capsal, J. -F., Gedig, M., Langlois, M., Moretto, G., Thetpraphi, K. 2018, SPIE, 10700E, 15K

[5] Zhou, Y. et al. 2022, SPIE, 12182E, 2JZ

[6] Moretto, G. et al. 2022, SPIE, 12188E, 0DM

[7] Moretto, G. et al. 2017, EPSC, 11, 893M

Highlights of Spanish Astrophysics XI, Proceedings of the XV Scientific Meeting of the Spanish Astronomical Society held on September 4–9, 2022, in La Laguna, Spain. M. Manteiga, L. Bellot, P. Benavidez, A. de Lorenzo-Cáceres, M. A. Fuente, M. J. Martínez, M. Vázquez- Acosta, C. Dafonte (eds.), 2023

The upcoming spectroscopic powerhouses at the Isaac Newton Group of Telescopes.

Balcells, M.[1,2,3]

[1] Isaac Newton Group, 38700 Santa Cruz de La Palma, Spain
[2] Instituto de Astrofísica de Canarias, 38200 La Laguna, Tenerife, Spain
[3] Universidad de La Laguna, 38200 La Laguna, Tenerife, Spain

Abstract

The Isaac Newton Group of Telescopes is completing a strategic change for the scientific use of its two telescopes, the 4.2-m William Herschel Telescope (WHT) and the 2.5-m Isaac Newton Telescope (INT). After more than 30 years operating as multi-purpose telescopes, the telescopes will soon complete their shift to nearly-single instrument operation dominated by large surveys.

At the WHT, the WEAVE multi-fibre spectrograph is being commissioned in late 2022. Science surveys are expected to launch in 2023. 30% of the available time will be offered in open time. For the INT, construction of HARPS-3, a high-resolution ultra-stable spectrograph for extra-solar planet studies, is underway, with deployment planned for late 2024. The INT itself is being modernised and will operate as a robotic telescope. An average of 40% of the time will be offered as open time.

The ING will maintain its student programme. Plans call for moving student work from the INT to the WHT once the INT starts operating robotically.

1 Introduction

Since the mid 1980's, the Isaac Newton Group[1] (ING) operates the 4.2-m William Herschel Telescope (WHT) and the 2.5-m Isaac Newton Telescope (INT) at the Observatorio Roque de los Muchachos on the Canarian island of La Palma. The telescopes have provided front-line multi-instrument observing capabilities to the ING astronomical communities of the UK, Spain and the Netherlands. Instrumentation comprised facility instruments (most recently ISIS, LIRIS, ACAM, PF, AF2, WYFFOS, INGRID, LDSS, NAOMI, OASIS, TAURUS-II, WFC, IDS), as well as powerful visiting instruments for science or for technology demonstration (AOLI, CANARY, DIPOL, GASP, GHaFaS, HiPERCAM, iQuEyE, LEXI, PAUCAM, PN.S, SPIFS, CIRPASS, CIRSI, ExPo, INTEGRAL, MAOJCam, PLANETPOL, PWFS, SAURON, ULTRACAM, Stereo-SCIDAR, Sodium Profiler).

[1] www.ing.iac.es

In 2010, following a strategic review and community consultation[2], and following the Astronet Roadmap for European Astronomy [5] and the European Telescope Strategy Review Committee 2010 report [15], ING started making steps to allow the WHT to become a powerful spectroscopic survey facility. This transformation had been announced at previous SEA conferences[3].

This paper provides a much needed update, after the pandemia years, coinciding with the exciting times when the WHT is starting to collect sky light with its new instrumentation.

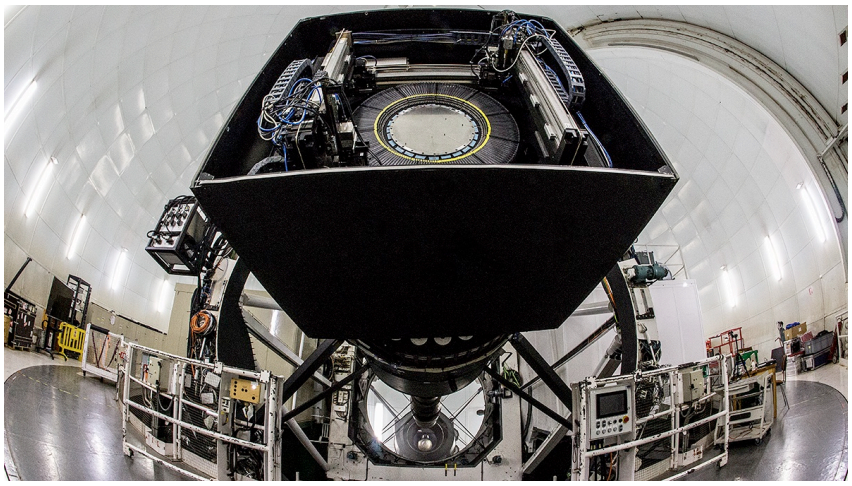

Figure 1: The WHT prime focus equiped with the WEAVE fibre positioner. Photo credit: J. Méndez, ING.

2 The new WHT

With a strategic view focused on science from massive spectroscopic surveys doable on a 4-m class telescope, there were clear design drivers for new instrumentation[1]. The WEAVE instrument (Fig. 1) is the result of that strategy. Three main elements comprise the new WHT:

Prime-focus corrector. A new optical corrector delivers a corrected field of view (FOV) of 2 degree (40 cm) diameter, with good transmission from 360 nm to 1000 nm.

Fibre positioner. A pick-and-place system, based on the 2dF system at the AAT, employs two robots to place up to 960 fibres on the focal plane. In addition to the standard single-fibre multi-object mode, the instrument comprises 20 fully-deployable mini-integral-field units (mIFU) of 10 arcsec FOV, as well as a monolithic integral-field unit (LIFU) with field of view 90 arcsec. A total of 3243 fibres transmit the light from the MOS system, the mIFU system and the LIFU to the spectrograph.

[2]https://www.ing.iac.es/about-ING/strategy/

Spectrograph. A new two-arm spectrograph provides spectroscopy at resolving power of either 5,000 (LR) or 20,000 (HR). Wavelength coverage at LR is the entire optical range, 366 – 959 nm.

2.1 WEAVE highlights

The WEAVE instrument has been described elsewhere [7][8][17][2]. The definitive description of the as-built instrument, at the time of integration at the telescope, pre-commissioning, is given in [12]. And an updated description is being maintained at the ING web site[3].

We direct the reader to the above references, and here just note the three input modes: multi-object mode (MOS), the large-integral field mode (LIFU) and the mini-integral field mode (mIFU). We discuss WEAVE's main highlights in the global context of multi-object spectroscopy instruments.

Table 1: WEAVE highlights

Parameter	Interest
MOS lowres $R = 5,000$	$\delta v \sim 3\,\mathrm{km\,s^{-1}}$ @ $V \sim 20$, match to Gaia v_T
MOS highres $R = 20,000$	Improved continuum for line strengths
MOS, mIFU FOV $\sim 2\,\mathrm{deg}$	High multiplex
LIFU highres $R = 10,000$	Resolving vertical vel. disp. of galaxy disks
LIFU FOV $\sim 90\,\mathrm{arcsec}$	Evolution of PPAK
20 mIFU, FOV $\sim 11\,\mathrm{arcsec}$	MANGA but on a 4-m, $R = 5,000$
End-to-end pipeline	Science-ready data
Offered for surveys and open time	Accommodates both large and small projects

When compared to other MOS instruments on 4-m class telescopes, WEAVE shines in a number of aspects. The more salient of them are noted in Table 1:

- In its default, low-resolution mode, WEAVE's resolving power $R = 5000$ is high among high-multiplex MOS instruments built for galactic and extra-galactic science, and makes WEAVE ideal for Milky Way dynamics and archaeology, as it provides stellar radial velocities with accuracies similar to those of tangential velocity data from Gaia.

- In its high-resolution mode, WEAVE's resolving power $R = 20,000$, when combined with its high multiplex, represents a significant step forward for stellar line strength determinations, as continua adjacent to the lines are less affected by instrumental broadening.

- The MOS FOV, 2 degree diameter, is unique in its mIFU mode and in the high-resolution MOS.

[3] https://www.ing.iac.es/astronomy/instruments/weave/weaveinst.html

- The LIFU high-resolution configuration, which delivers R=10,000 spectra, can resolve the vertical velocity structure of galaxy disks.

- The LIFU FOV, which was patterned after the PPAK LIFU[13], has 50% higher FOV, and higher wavelength coverage ($3660 - 9590$ $\AA$), and represents a true next-generation large IFU for the study of extended sources.

- The mIFU FOV matches the smaller end of the distribution of FOV for the MANGA units[4]. With their wide wavelength coverage and with spectral resolutions 2.5[10] times higher than the SDSS-III spectrographs in the low[high] WEAVE resolutions, the WEAVE mIFU's will be powerful tools for low-mass galaxies and for compact star-forming regions in our Galaxy.

- Data will be delivered fully reduced and containing a range of science-ready products.

2.2 WEAVE surveys

Eight surveys (Table 2) have been approved for execution over 5 years of WEAVE operation; they will be allocated 70% of the available time on WEAVE. As of this writing, the most comprehensive description of the surveys is given in [12]. For updates and contact points for the surveys and for WEAVE science, the reader is directed to the WEAVE web site[4].

Table 2: The eight WEAVE surveys

	Title		Title
GA	Galactic Archaeology	SCIP	Stellar, Circumstellar and Interstellar Physics
WC	Galaxy Clusters[6]	StePS	Stellar Populations At Intermediate Redshift[11]
WA	WEAVE Apertif [10]	WL	WEAVE LOFAR[16]
WQ	WEAVE QSO[14]	WD	WEAVE White Dwarfs

2.3 Using the WHT: surveys and open time

ING is offering time on WEAVE for large surveys as well as through the ING national time-allocation committees. The International Time programme of the Canarian Observatories[5] provides an additional means of obtaining up to 15 WEAVE nights per year in addition to time on any of the other ORM telescopes.

WEAVE is due to start commissioning in the fall of 2022. We anticipate LIFU science verification observations in early 2023, and aim for starting science in the middle of 2023.

[4]https://ingconfluence.ing.iac.es/confluence/display/WEAVEDEV/WEAVE%3A+The+Science

[5]https://www.iac.es/en/observatorios-de-canarias/observing-time/observing-time/international-time-programme

3 The third life of the Isaac Newton Telescope

ING is in the middle of transforming the 2.5-m Isaac Newton Telescope (INT) by installing HARPS3[6] [18], an enhanced version of the HARPS and HARPS-N spectrographs aimed at achieving 10 $\mathrm{cm\,s^{-1}}$ radial velocity precision on nearby stars to search for Earth-like planets. HARPS3 differs from its predecessors by a stabilised beam feed and a polarimetric sub-unit[9] which will provide a powerful tool for characterising stellar activity. The Terra Hunting Experiment (THE) consortium, P.I. Didier Queloz, is building HARPS3 and making it available in exchange for ∼50% of every night over 10 years; the remaining time will be offered as open time through the usual national time allocation channels. The consortium is also modernising the INT, which will become a robotic telescope. This will be the third encarnation of the venerable INT, after its first installation in Herstmonceux in 1967 and it re-deployment in La Palma in 1982.

With this transformation, we expect the INT will provide the UK, ES and NL astronomical communities with a much needed tool for extra-solar planet science.

Current plans call for the robotic INT to be commissioned during the summer of 2024, and for HARPS3 to start scientific operations before the end of 2024.

4 Opportunities for students

ING will continue to welcome 4 to 6 students for year-long stays at the ING. Building on the success of this highly-demanded programme, we are hoping to increase the number of student positions in the near future.

When the INT closes down for reforms and becomes a robotic telescope, students will dominantly work at the WHT, partaking in WEAVE survey and open-time observations. This will open up opportunities for the students to become familiar with the execution of large projects and to develop expertise in WEAVE data.

Acknowledgments

The Isaac Newton Group of Telescopes is operated on behalf of the UK Science and Technology Facilities Council (STFC) the Nederlanse Organisatie voor Wetenschappelijk Onderzoek (NWO), and the Instituto de Astrofísica de Canarias (IAC).

WEAVE construction was funded from generous grants from STFC, NWO, Spanish Science Ministry, the French CNRS, and the Italian INAF. Additional contributions were received from Konkoly Observatory in Hungary, INAOE in Mexico, and PI grants from Lund Observatory, IAP Potsdam, MPIA Heidelberg.

The HARPS3 instrument is being built by the Terra Hunting Experiment Consortium led by University of Cambridge Cavendish Laboratory.

[6] https://www.terrahunting.org/harps3.html

References

[1] Balcells, M., Benn, C. R., Carter, D., et al. 2010, in Ground-based and Airborne Instrumentation for Astronomy III, Proc. SPIE, 7735, 77357G

[2] Balcells, M. 2014, EAS Pub. Ser., 67, 227

[3] Balcells, M. 2015, in Highlights of Spanish Astrophysics VIII, 776

[4] Bundy, K., Bershady, M.Ă., Law, M. R., et al. 2015, ApJ, 798, 1

[5] ASTRONET infrastructure roadmap, 2009, http://www.astronet-eu.org/IMG/pdf/Astronet-Book_light.pdf

[6] Cornwell, D. J., Kuchner, U., Aragón-Salamanca, A., et al. 2022, MNRAS, 517, 1678

[7] Dalton, G., Trager, S. C., Abrams, D. C., et al. 2012, in Ground-based and Airborne Instrumentation for Astronomy IV, Proc. SPIE, 8446, 84460P

[8] Dalton, G., Trager, S. C., Abrams, D. C., et al. 2014, in Ground-based and Airborne Instrumentation for Astronomy V, Proc. SPIE, 9147, 91470L

[9] Dorval, P., Snik, F., Piskunov, N., et al. 2018, in Ground-based and Airborne Instrumentation for Astronomy VII, Proc. SPIE, 10702, 107026B

[10] Hess, K. M., Falcon-Barroso, J., Ascasibar, Y., et al. 2020, AAS, 235, 459.03

[11] Iovino, A., Poggianti, B. M., Mercurio, A., et al. 2023, A&A, accepted

[12] Jin, S., Trager, S. C., Dalton, G., et al. 2022, MNRAS, accepted, arXiv:2212.03981

[13] Kelz, A., Verheijen, M.Ă. W, Roth, M., et al. 2006, PASP, 118, 129

[14] Kraljic, K., Laigle, C., Pichon, C., et al. 2022, MNRAS, 514, 1359

[15] Report of the European Telescope Strategy Review Committee, 2010, http://www.astronet-eu.org/IMG/pdf/PlaquetteT2_4m-final-2.pdf

[16] Smith, D. J. B., Best, P. N., Duncan, K. J., et al. 2016, in SF2A-2016: Proceedings of the Annual meeting of the French Society of Astronomy and Astrophysics, 271

[17] Terrett, D. L., Lewis I. J., Dalton, G., Abrams, D. C., et al. 2014, SPIE, 9152, 216

[18] Thompson, S. J., Queloz, D., Baraffe, I., et al. 2016, in Ground-based and Airborne Instrumentation for Astronomy VI, Proc. SPIE, 9908, 99086F

Highlights of Spanish Astrophysics XI, Proceedings of the XV Scientific Meeting of the Spanish Astronomical Society held on September 4–9, 2022, in La Laguna, Spain. M. Manteiga, L. Bellot, P. Benavidez, A. de Lorenzo-Cáceres, M. A. Fuente, M. J. Martínez, M. Vázquez- Acosta, C. Dafonte (eds.), 2023

Update of FastCam, the lucky imaging instrument at the Observatorios de Canarias (OCAN).

Nespral, D.[1], Clavero-Jimenez, R.[1], Puig-Subira, M.[1], Lopez-Lopez, R.[1], Soria-Hernandez, E.[1], Oscoz, A.[1], and Zamora-Sanchez, O.[1]

[1] Instituto de Astrofisica de Canarias (IAC), C/ Vıa Lactea s/n, 38205 La Laguna, Spain

Abstract

FastCam is an instrument designed to obtain high spatial resolution images in the optical wave- length range from ground-based telescopes by using the Lucky Imaging technique. This technique is based on the idea of registering the instants of atmospheric stability, typically lasting just some milliseconds, using very short exposures. The instrument consists of a very low noise and very fast readout speed EMCCD camera capable of reaching the diffraction limit of medium-sized telescopes from 380 to 1000 nm. At the beginning of 2019, a new camera was commissioned. Now the instrument makes use of an Andor iXon DU-888U3-CSO#BV back-illuminated system containing a 1024x1024 pixel frame transfer CCD sensor from E2V Technologies. The pixel size is 13 microns and the camera allows up to 30 exposures per second. A new update of the camera acquisition software is currently being worked on. A complete characterization of the detector is also being carried out in order to better understand and exploit all the performances of the instrument, applying particular configurations for each scientific case. A standard reduction of the data is also being implemented in order to offer it to all users of the instrument. The first FastCam was an instrument jointly developed by the Spanish Instituto de Astrofísica de Canarias (IAC) and the Universidad Politécnica de Cartagena which started in 2006. Since then, the IAC assumed the instrument and tested it on several telescopes of the OOCC, among them the Nordic Telescope (NOT) where images were obtained in the optical domain diffraction-limited with high contrast, reaching a resolution of 0.1"/px. Currently FastCam is a common-user instrument at the Cassegrain focus of the 1.52-meter Carlos Sánchez Telescope (TCS, Teide Observatory) where observations are being made to calibrate the detector with sky tests. The idea is that in the near future it will be installed in the NOT to finish the commissioning process of the new camera and the whole acquisition system so that this instrument can be used by the international community.

1 Introduction

Fastcam is an instrument that uses the Lucky Imaging (LI) technique to obtain high spatial resolution images in the optical range. It has been developed by the Instituto de Astrofísica

de Canarias (IAC) in collaboration with other institutions [1]. This technique is based on recording the instants of atmospheric stability through very short exposures (30-50 ms). The selection of those images minimally affected by turbulence allows to reach the resolution limit of the telescope in the optical range, offering results similar to those of space telescopes (Figure 1).

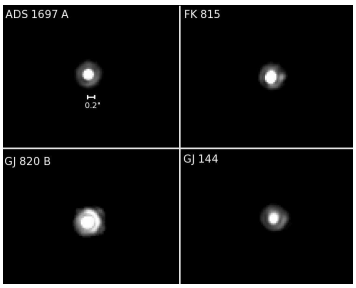

Figure 1: I-band images taken at the TCS showing the first Airy disc.

2 UPDATE OF THE INSTRUMENT

Fastcam consists of a commercial EMCCD (Electron Multiplying Charge Coupled Device) detector with fast-reading and low-noise together with an optical system and the acquisition, selection and process software packages. A new camera has been purchased and based on it we are carrying out a complete upgrade of the instrument and associated software (Figure 2).

3 A NEW CAMERA

The new Fastcam camera is an Andor iXon Ultra 888 detector, model DU-888U3-CS0-#BV (Back-illuminated, standard AR coated): 1024 x 1024 active pixels, 13 um pixel size, 30 MHz max readout time, $\ll$1 e- readout noise (with EM gain), 26 fps full frame, 93 fps at 512x512 (Cropped mode), $\gg$ 95% QE. Some features of the detector are the frame transfer mode. This option is a special acquisition mode that contains 2 areas of approximately equal size as shown below: 1. The Image Area, which is at the top and farthest from the readout register. This is the light sensitive area of the CCD. 2. The Storage Area is located between the Image Area and the readout register. This section is covered by an opaque mask, usually a metal film, and is therefore not sensitive to light. Frame transfer devices typically have faster frame rates than full frame devices, and have the advantage of a high duty cycle, meaning the sensor is always collecting light (Figure 3).

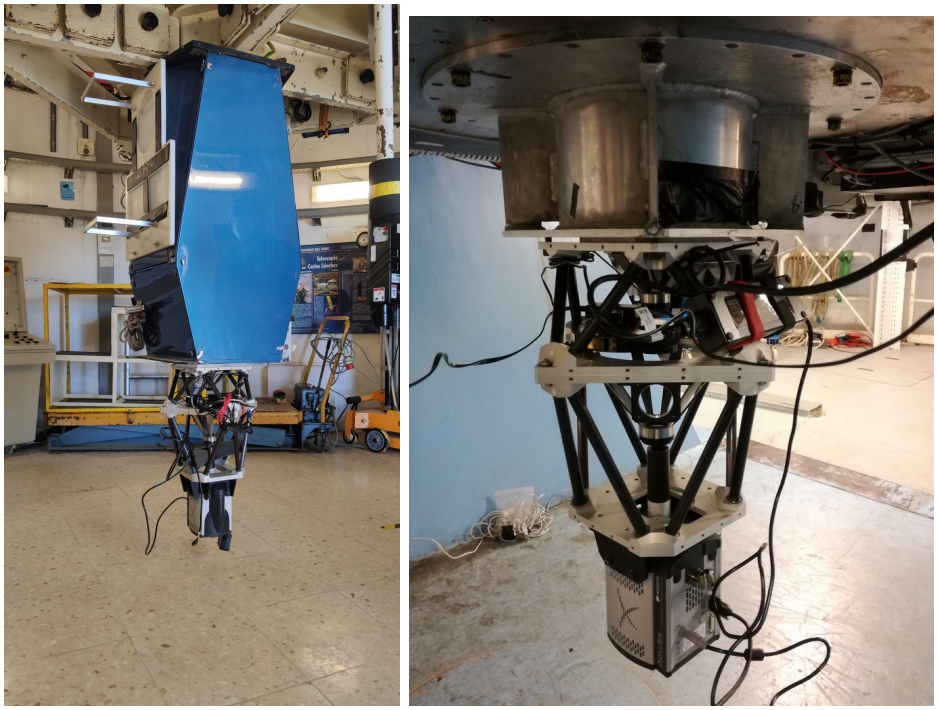

Figure 2: Left image: Fastcam at TCS, Right image: Fastcam at NOT

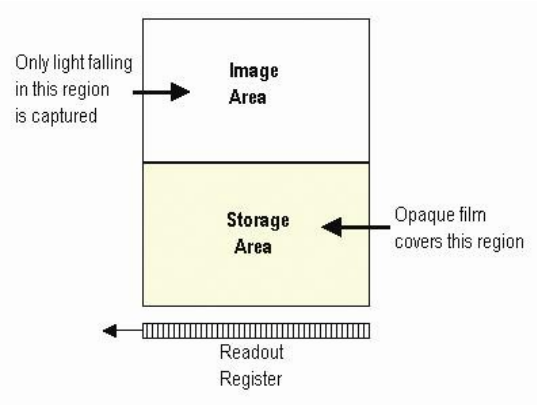

Figure 3: Frame transfer mode.

4 DETECTOR CHARACTERISATION

In addition to the new hardware, we are carrying out a complete characterization of the system both in the laboratory and in test nights at the Carlos Sanchez Telescope. Basically, the new generation of this type of optical detectors has the great advantage of performing the electron multiplication of the signal before the readout of the detector, which means that, proportionally, the readout noise can be significantly reduced in each pixel compared

to useful signal, down to 1 e- rms. Using Electron Multiplication, the iXon is capable of detecting single photons, therefore the actual detection limit of the camera is set by the number of 'dark' background events. These events consist of thermally generated residual electrons and Clock Induced Charge (CIC) electrons (also referred to as Spurious Noise), each appearing as random single spikes above the read noise floor. This total characterization of the system will allow optimization of the camera configurations according to the scientific objective (Figure 4).

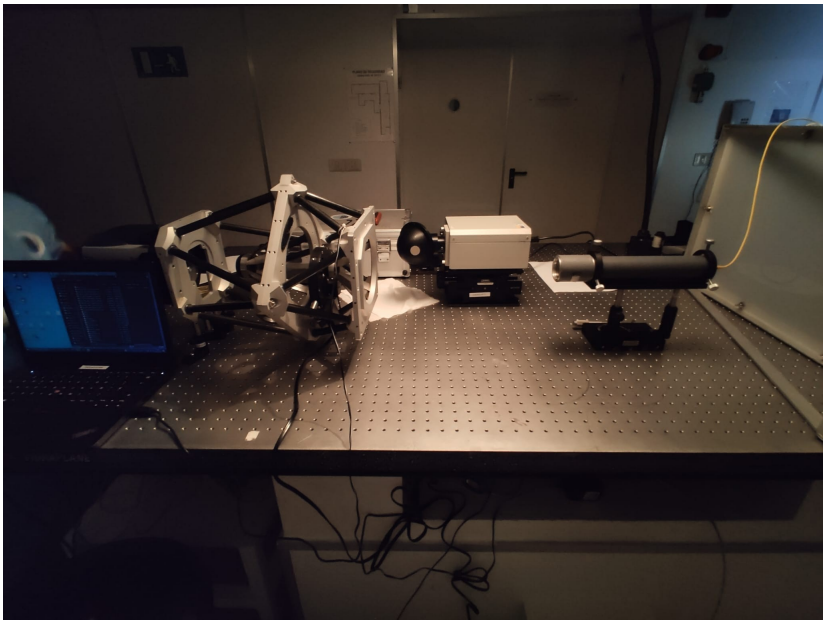

Figure 4: The system in the laboratory for a complete characterization.

5 SOFTWARE UPGRADE

Finally, we are carrying out a complete upgrade of the following software packages: New acquisition and control software. More robust user interface. Optimisation of the reduction software. In the LI algorithm, the images that suffered less atmospheric distortion are detected according to a quality criterion, then re-centered and added together into a single image [2]. A limitation of the LI technique is that a corrected image of a star shows a diffraction-limited central core with a residual halo corresponding to the atmospheric turbulence that could not be corrected as it can be seen in the figure. The new COELI algorithm (COvariancE of Lucky Images) [3, 4] has been designed to overcome that improving the detectability of faint objects falling inside the residual halo by analyzing the correlation between the peak pixel and the rest of the pixels of each lucky image (Figure 5).

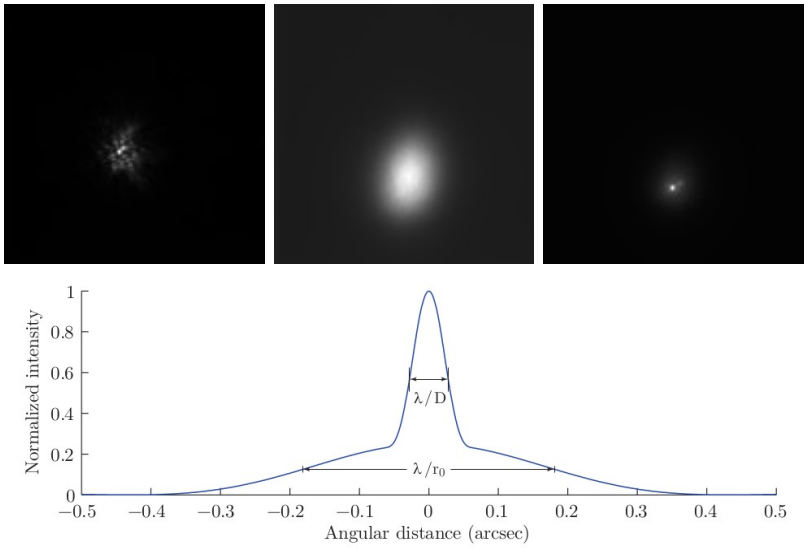

Figure 5: Left images: a 30ms exposure; natural seeing; 1% of 4,000 aligned and averaged images. Bottom image: profile of a partially corrected image of a star, showing a diffraction-limited central core and the residual halo..

6 CONCLUSIONS AND FUTURE WORK

The project started in March 2006 and, since then, FastCam has been successfully tested on different OCAN telescopes and the theoretical diffraction limit of the following telescopes has been reached in the I band (850nm), 0.17 at TCS, 0.10 at NOT and 0.07 arcsec at WHT, and similar resolutions have been also obtained in the V and R bands. For this update process we are performing observations that help us in the commissioning of the instrument to define the most appropriate configuration for each scientific case. The instrument can offer competitive observations in multiple fields of astronomy: Solar System with asteroids and comet; Exoplanets; Studies of stellar formation and dynamics; Multiplicity of stars in a wide range of masses and evolutionary states; Extragalactic resolution studies (quasars, AGNs, etc). Fastcam is a common-user instrument at TCS since 2008 and will be offered for installation at NOT in the near future.

References

[1] Oscoz, A. et al. 2008, Proc. SPIE, 7014
[2] Law N.M. et al., 2006, A&A 446
[3] Cagigal M.P. et al., 2016, MNRAS 455.3
[4] Cagigal M.P. et al., 2022, MNRAS 512.2

Highlights of Spanish Astrophysics XI, Proceedings of the XV Scientific Meeting of the Spanish Astronomical Society held on September 4–9, 2022, in La Laguna, Spain. M. Manteiga, L. Bellot, P. Benavidez, A. de Lorenzo-Cáceres, M. A. Fuente, M. J. Martínez, M. Vázquez- Acosta, C. Dafonte (eds.), 2023

Web-based telluric correction made in Spain: spectral fitting of Vega-type telluric standards.

de la Fuente, D.[1,2], Marco, A.[1], Patrick, L. R.[1,3,4], Rübke, K.[1], López, I.[1], Fernández, A.[1], Conejero, S.[1], Navarro, J.[1], Palazón, M.[1], and Negueruela, I.[4]

[1]Departamento de Física, Ingeniería de Sistemas y Teoría de la Señal, Universidad de Alicante, San Vicente del Raspeig, Spain
[2]CREOL, The College of Optics and Photonics, University of Central Florida, Orlando, FL, USA
[3]Departamento de Astrofísica, Centro de Astrobiología (CSIC-INTA), Torrejón de Ardoz, Spain
[4]Departamento de Física Aplicada, Universidad de Alicante, San Vicente del Raspeig, Spain

Abstract

Infrared spectroscopic observations from the ground must be corrected from telluric contamination to make them ready for scientific analyses. However, telluric correction is often a tedious process that requires significant expertise to yield accurate results in a reasonable time frame. To solve these inconveniences, we present a new method for telluric correction that employs a roughly simultaneous observation of a Vega analog to measure atmospheric transmission. After continuum reconstruction and spectral fitting, the stellar features are removed from the observed Vega-type spectrum and the result is used for cancelling telluric absorption features on science spectra. This method is implemented as `TelCorAl` (Telluric Correction from Alicante), a Python-based web application with a user-friendly interface, whose beta version will be released soon.

1 Introduction

Infrared spectra that are observed from ground-based facilities are heavily contaminated by absorption features from the Earth's atmosphere. The accuracy of the decontamination process, known as telluric correction, is crucial for producing reliable results from subsequent spectroscopic analyses.

Telluric correction basically consists in dividing the science spectra by atmospheric transmission. However, the latter cannot be easily determined because the atmosphere behaves in a complex and unpredictable manner. The intensities and shapes of telluric absorptions depend not only on observational settings (airmass, instrumental profile, the observer's altitude) but also on atmospheric properties that can change dramatically (abundances for the involved molecules, precipitable water vapor, seeing).

The currently available methods mainly differ on how this transmission spectrum is obtained. On the one hand, theoretical methods (e.g. [11]) fit a transmission model to the observations. On the other hand, observational methods (e.g. [12]) extract the transmission spectrum from a roughly simultaneous observation of a standard star whose intrinsic features are well known and easily separated from telluric absorptions. There also are some hybrid approaches (e.g. [2]). The user often has to make a complex choice, based on instrumental and operational features (spectral resolution, exposure times, observation schedule, etc.), and other requirements related to the planned treatment (intended signal-to-noise ratio, integration into a pipeline, etc.).

The majority of publicly available algorithms are designed for specific instruments or tailored to the scientific goals of some particular team. A few others have a more general purpose and are targeted to a wider community, although they have practical disadvantages in common. For example, users often complain about problems for installation and usability of these software, or about the amount of experience needed to obtain accurate results in a reasonable amount of time.

This situation has encouraged us to create a cross-platform, user-friendly application for telluric correction. To avoid the complications of fitting sky models or empirical libraries to the telluric component of science spectra, we have chosen the approach of measuring atmospheric transmission on an Observed Standard Star Spectrum (OSSS). We refer to [10] and [12] for the theoretical background for this kind of methods.

2 Methodology

Vega-type standards (i.e. spectral types around A0V) are preferred, as their intrinsic spectra only display wide hydrogen absorptions in most cases (see [9] for a notable counterexample). These lines are usually well described by Voigt functions (see [8] and references therein), which facilitates the modeling and removal of the OSSS stellar features. Model fitting, however, cannot be directly performed within wavelength regions where the continuum disappears from the observation (owing to broad telluric bands or to overlapping high-order hydrogen lines).

The extraction of the atmospheric transmission spectrum in such a way is the first phase of telluric correction, and is carried out in five steps:

1. A “default telluric correction” of the standard star is made by dividing the OSSS by a synthetic trasmission spectrum (respectively shown in black and light blue in Fig. 1). To generate the latter, the [4] telluric models for average atmospheric conditions are interpolated at the airmass of the OSSS, convolved with a Gaussian profile that matches the spectral resolution of the instrument, and resampled into the OSSS wavelength axis. The [4] models also provide variability information that is used for computing the uncertainty of the default correction.

2. A simple model of hydrogen absorption spectrum is created as a combination of Voigt profiles whose widths and relative intensities are preset for the spectral type of the OSSS. The profile heights are then multiplied by a scaling constant to match the line

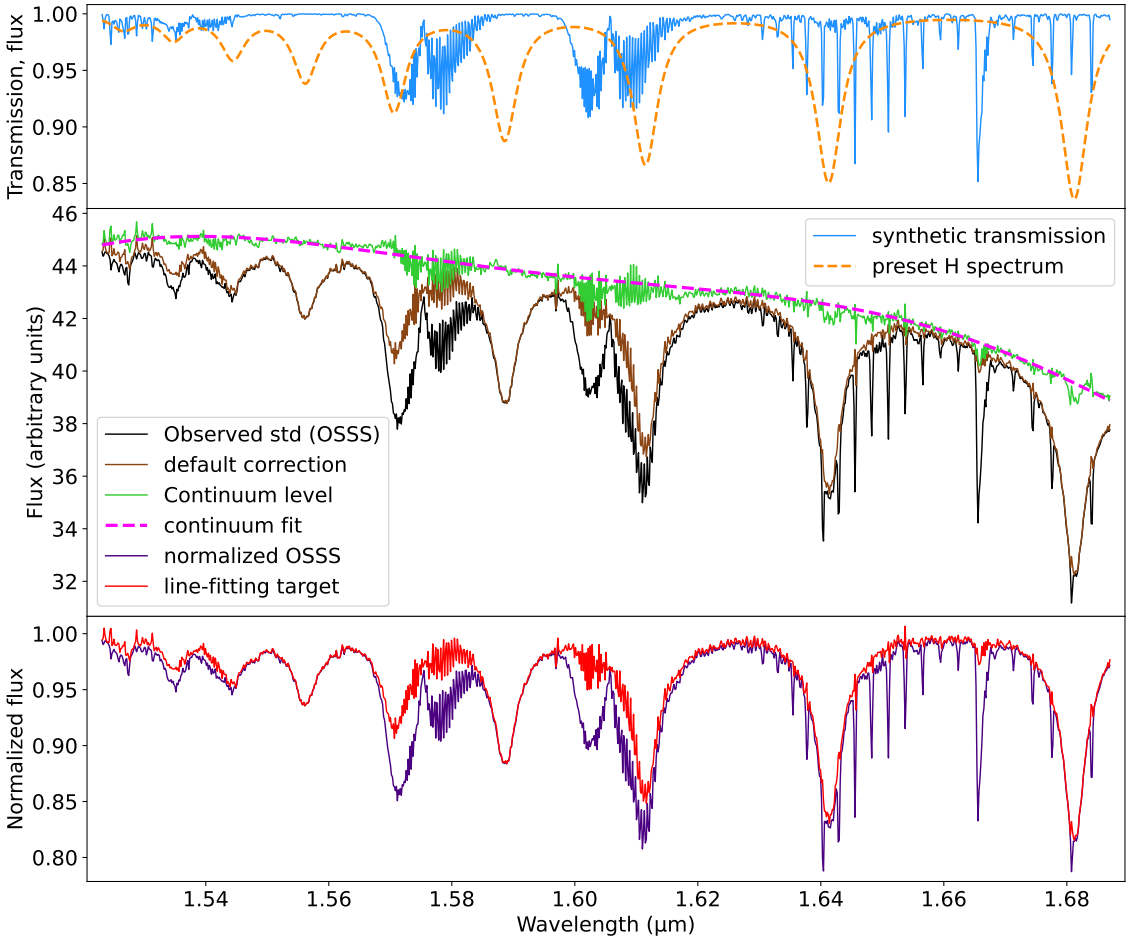

Figure 1: Spectra involved in the process of fitting a spectrum of a telluric standard star, as well as the normalized version of the OSSS for comparison purposes.

heights of the default telluric correction (brown line in Fig. 1), thus obtaining a first model of the standard star (dashed orange line).

3. The ratio between the results of previous steps (i.e. brown line divided by orange line) is used as an approximation for the continuum level (shown in green in Fig. 1). Weighted least-squares polynomial fits with boundary conditions are performed for increasing degrees of the polynomial, and the optimal result (magenta dashed line) is chosen on the basis of a goodness-of-fit test.

4. The spectrum that results from the default correction is normalized (i.e. brown/magenta = red in Fig. 1) and used for fitting a model for the combination of all H line profiles. The result is multiplied by the continuum fit (magenta dashed line) to produce a full model for the intrinsic features of the OSSS (See upper graph in Fig. 2).

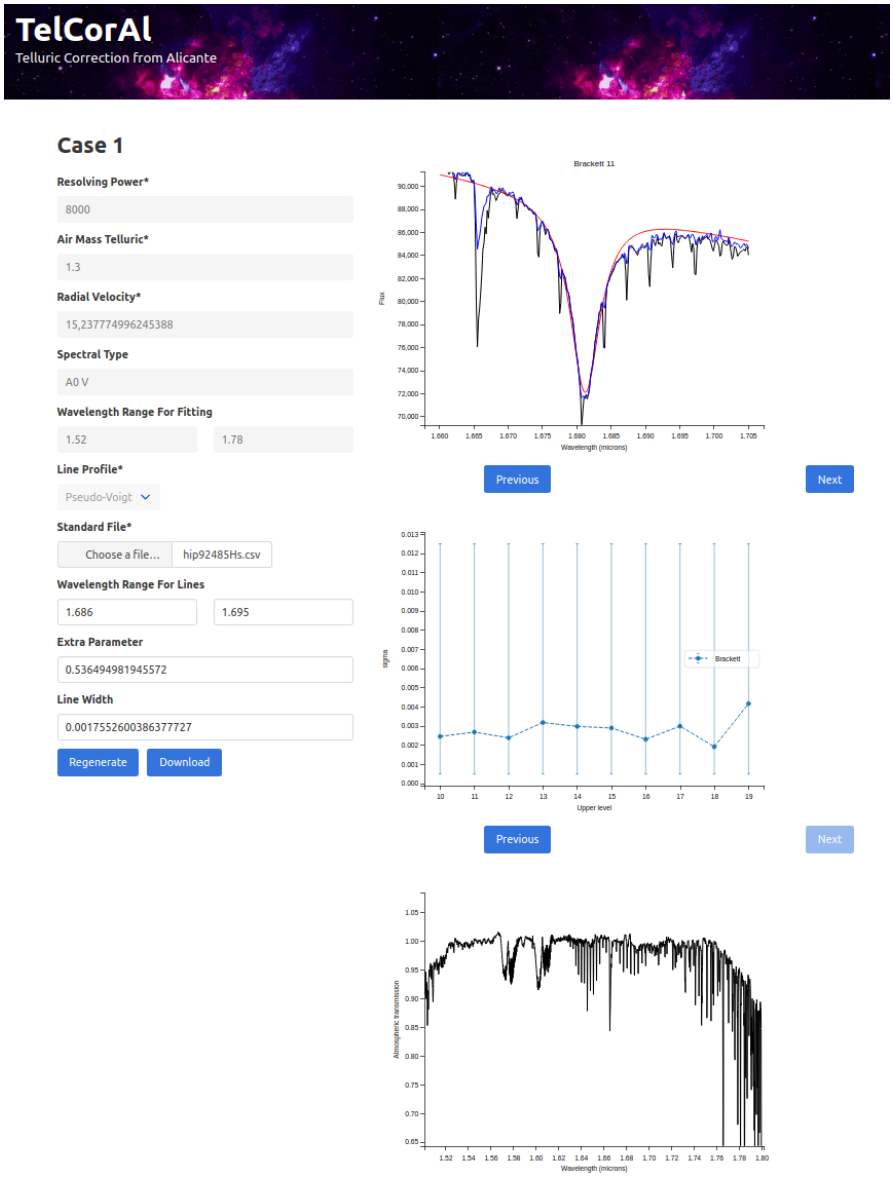

Figure 2: `TelCorAl` interface, showing an example of the fitting process for intrinsic features of a telluric standard star.

5. The telluric transmission spectrum (Fig. 2, lower plot) is obtained as the ratio of the OSSS to its full model.

If one or both of the initial synthetic spectra (like those in Fig. 1, top pannel) diverges significantly from the OSSS features, the fitting procedures will produce inaccurate results. In this case, the method will iterate on steps 1–5 so that the model and transmission results of an iteration are used as initial spectra for the next one.

Once an accurate result for telluric transmission is achieved, the second phase consists in using the resulting spectrum for correcting the science spectra. In an ideal case, the telluric features imprinted on all these spectra would be identical, and could be perfectly removed by dividing each science spectrum by the transmission. In practice, however, there are intensity and shape variations, caused not only by variability of the sky (for non-simultaneous observations), but also by factors related with the reduction process (e.g. wavelength calibrations of co-added frames) or with implicit approximations (e.g. the definition of airmass). To deal with these differences, the following tasks are carried out for each science spectrum:

- The transmission spectrum is slightly red- or blue-shifted according to a factor that corresponds to the maximum cross-correlation with the science spectrum. As far as possible, the cross-correlation function should be computed in a wavelength range where telluric features dominate over the intrinsic features of the science spectrum.

- The ratio between airmass factors for the science and transmission spectra is used for scaling the strength of telluric features through an exponential relation ([7]). The result can be manually fine-tuned by the user until optimal telluric cancellation is achieved.

3 Implementation and current status

We have developed `TelCorAl` (Telluric Correction from Alicante), a user-friendly web application that performs telluric correction in a semiautomatic way. Apart from carrying out all the telluric correction process as explained in Sect. 2, the users may choose to perform just one phase, or both phases independently, in order to test the method or make the correction in a more customized way. In all cases, the users are required to upload their input spectra in comma-separated value format, and the results are delivered in the same format together with information on the parameters used throughout the process. All calculations are internally made by a `Python 3` code, and users interact with it through a web interface that also displays helpful plots (Fig. 2). Everything is processed in the RAM of the server, and no data or results are ever stored outside it, thus keeping them private at all times.

The combined H line models are built and fitted through `lmfit 1.0.3` ([6, 5]), by employing a line profile function of the user's choice. Based on our experience, the pseudo-Voigt approximation ([14]) is usually the option that works better in general, although Gaussian or Lorentzian profiles are also offered, as they are more suitable under certain circunstances (e.g. extreme values for resolution and $v \sin i$ of the standard star). Other critical components of fitting and processing the spectra for telluric correction make use of the `SciPy` ([13]), `PyAstronomy` ([1]), and `specutils` ([3]) libraries.

A preliminary version of `TelCorAl` is currently running on the server of our group, although being only accessible from the University of Alicante network for the moment. Once the final telluric correction code is fine-tuned and comprehensive testing is carried out, a beta version will be released to the public.

4 Concluding remarks

Our forthcoming web application solves issues that make other telluric correction software impractical for widespread use. The user-friendly webpage format, which does not require installation, along with the semiautomatic approach, makes our software suitable even for inexperienced users that aim at promptly getting a decent correction of their infrared data. `TelCorAl` is also capable of dealing with a wide variety of instrumental and observational features of the input data.

Compared to other telluric correction methods that are based on spectral fitting of Vega-type stars ([12, 10]), our code uses a novel approach that consists in reconstructing the continuum level (green line in Fig. 1). This allows us to achieve accurate fits on regions where hydrogen line profiles overlap with each other or with wide telluric bands (e.g. between 1.54 and 1.62 μm, see Fig. 1).

Acknowledgments

This work has been financially supported by Generalitat Valenciana through grants APOSTD/2020/228, APOSTD/2020/247, and PROMETEO/2019/041. The Spanish Ministerio de Ciencia e Innovación and Agencia Estatal de Investigación (MCIN/AEI/10.13039/501100011033/FEDER, UE) has also provided financial support through grants PGC2018-093741-B-C21 and PID2021-122397NB-C22.

References

[1] Czesla, S., Schröter, S., Schneider, C. P., et al. 2019, ascl:1906.010

[2] Cook, N. J., Artigau, É., Doyon, R., et al. 2022, arXiv:2211.01358

[3] Earl, N., Tollerud, E., Jones, C., et al. 2022, Zenodo

[4] Moehler, S., Modigliani, A., Freudling, W., et al. 2014, A&A 568, A9

[5] Newville, M., Otten, R., Nelson, A., et al. 2021, Zenodo

[6] Newville, M., Stensitzki, T., Allen, D. B., et al. 2014, Zenodo

[7] Perliski, L. M. & Solomon, S. 1993, JGR, 98, 10363

[8] Posener, D. W. 1959, AuJPh., 12, 184

[9] Sameshima, H., Ikeda, Y., Matsunaga, N., et al. 2018, ApJS, 239, 19

[10] Sameshima, H., Matsunaga, N., Kobayashi, N., et al. 2018, PASP, 130, 074502

[11] Smette, A., Sana, H. Noll, S. et al. 2015, A&A 576, A77

[12] Vacca, W. D., Cushing, M. C., & Rayner, J. T. 2003, PASP, 115, 389

[13] Virtanen P., Gommers R., Oliphant T. E., et al. 2020, NatMe, 17, 261

[14] Whiting, E. E. 1968, JQSRT, 8, 1379

Highlights of Spanish Astrophysics XI, Proceedings of the XV Scientific Meeting of the Spanish Astronomical Society held on September 4–9, 2022, in La Laguna, Spain. M. Manteiga, L. Bellot, P. Benavidez, A. de Lorenzo-Cáceres, M. A. Fuente, M. J. Martínez, M. Vázquez- Acosta, C. Dafonte (eds.), 2023

A Day in the *LIFE*.

José A. Caballero[1], Daniel Angerhausen[2], Sascha P. Quanz[2], Antonio García-Muñoz[3], and the *LIFE* collaboration[4]

[1] Centro de Astrobiología, CSIC-INTA
[2] Institute for Particle Physics and Astrophysics, ETH Zürich
[3] Université Paris-Saclay
[4] https://life-space-mission.com/

Abstract

We briefly outline the basic ideas behind *LIFE*, the *Large Interferometer For Exoplanets*, a proposed space mission which topic coincides with one of those recently selected for ESA's Voyage 2050. *LIFE* is a project initiated in Europe with the goal to consolidate various efforts and define a roadmap that eventually leads to the launch of a large, space based mid-infrared nulling interferometer to investigate the atmospheric properties of a large sample of (primarily) terrestrial exoplanets. We summarise the current scientific and engineering efforts related to *LIFE*.

My poster is available at https://zenodo.org/record/7043679

Highlights of Spanish Astrophysics XI, Proceedings of the XV Scientific Meeting of the Spanish Astronomical Society held on September 4–9, 2022, in La Laguna, Spain. M. Manteiga, L. Bellot, P. Benavidez, A. de Lorenzo-Cáceres, M. A. Fuente, M. J. Martínez, M. Vázquez- Acosta, C. Dafonte (eds.), 2023

Analysis of Kepler light curves using the wavelet transform to discriminate with machine learning the astrophysical nature of the eclipsing object.

Guirado-Fuentes, L.[1], **and Baena-Gallé, R.**[1]

[1] UNIR - Universidad Internacional de la Rioja. Avenida de la Paz, 137, 26006 Logroño, La Rioja, Spain. https://orcid.org/0000-0001-5214-7408

Abstract

The Kepler mission has been the most successful so far in the search and characterization of exoplanets by transit. With this technique, the intensity of light emitted by the star is measured at regular intervals to detect periodically recurring photometric reductions, from which the presence of an object can be inferred. We introduce an approach to analyse light curves by using the Discrete Wavelet Transform (DWT) for exoplanet classification.

Our method consists of four stages. Firstly, light curves are phase folded distinguishing odd and even events. Secondly, a symlet 5 DWT is applied to the resulting curves creating up to 7 wavelet scales. Thirdly, noise filtering is applied to high-frequency scales. Finally, statistical features from the reconstructed curves are extracted by means of *tsfresh*. This information is used to perform supervised classification (LightGBM and AutoSklearn methods) as well as unsupervised statistical learning (t-SNE and UMAP non-linear dimensionality reduction techniques) to discriminate exoplanets from false positives (e.g., binary systems, pulsating stars, etc.). Our approach achieves an accuracy of 81%, beating by $5-6\%$ its non-wavelet counterpart.

Further evaluation of more complex extracted features and enlargement of the data set through simulated curves is required. The present work is a first approach to the identification of the nature of the eclipsing objects in light curves, by extracting features after a wavelet pre-processing.

Acknowledgements: This communication summarizes the results obtained by LGF in his Master's Degree final project entitled "Análisis de curvas de luz Kepler mediante la transformada *wavelet*", defended in the Master's Degree in Astrophysics and Observational Techniques in Astronomy at UNIR. RBG is funded by the UNIR research project "ADELA: Deep Learning Applications for Astrophysics", no. B0036.

.

My poster is available at https://doi.org/10.5281/zenodo.7326640

Highlights of Spanish Astrophysics XI, Proceedings of the XV Scientific Meeting of the Spanish Astronomical Society held on September 4–9, 2022, in La Laguna, Spain. M. Manteiga, L. Bellot, P. Benavidez, A. de Lorenzo-Cáceres, M. A. Fuente, M. J. Martínez, M. Vázquez- Acosta, C. Dafonte (eds.), 2023

Deep Learning for Artifact Removal in Galaxy Images.

Javier Hernández-Afonso[1], and Roberto Baena-Gallé[1]

[1] UNIR - Universidad Internacional de la Rioja. Avenida de la Paz, 137, 26006 Logroño, La Rioja, Spain. https://orcid.org/0000-0001-5214-7408

Abstract

In astronomical image acquisition, it is common to find artifacts and anomalies due to the particularities of the studied objects as well as the acquisition process. Two of these aberrations are, firstly, an object random light distribution that is usually modeled with a Poisson distribution, and, secondly, the loss of spatial resolution due to the optical and atmospheric point spread function (PSF).

Motivated by the recent advances in the field of Deep Learning in image reconstruction, we have built a solution based on convolutional neural network (CNN) for astronomic image aberrations removal. Our model is based on architectures with auto-encoders to extract fundamental image features, skip-connections to recover lost features during the compression stage, and two branches in parallel to perform the reconstruction task at different levels of resolution.

Our results over simulations of galaxy images show an improvement of up to 8dB in PSNR, and an increasement from ~ 0.45 to ~ 0.95 in SSIM for noise removal. However, weaker galaxy structures such as the halo, filaments and point-like structures associated with star formation regions are not well reconstructed yet. We are now researching to design and apply more complex deep learning models, such as U-Nets and GANs, to improve the quality in galaxy image recovery.

Acknowledgements: This communication summarizes the results obtained by JHA at his Master's Degree final project entitled "Redes Neuronales Convolucionales para la Reconstrucción de Imágenes de Galaxias", defended in Master's Degree in Artificial Intelligence at UNIR. RBG is funded by the UNIR research project "ADELA: Deep Learning Applications for Astrophysics", no. B0036.

My poster is available at https://zenodo.org/record/7048828#.Y3N3YHbP3cc

Highlights of Spanish Astrophysics XI, Proceedings of the XV Scientific Meeting of the Spanish Astronomical Society held on September 4–9, 2022, in La Laguna, Spain. M. Manteiga, L. Bellot, P. Benavidez, A. de Lorenzo-Cáceres, M. A. Fuente, M. J. Martínez, M. Vázquez- Acosta, C. Dafonte (eds.), 2023

Follow-up observations of time-domain science cases at ESO.

Corral-Santana, Jesús M.[1], **and Mehner, Andrea**[1]

[1] European Southern Observatory (ESO), Alonso de Córdova 3107, Casilla 19, Vitacura, Santiago, Chile

Abstract

Time-domain astrophysics comprises a vast array of phenomena, spanning from solar system objects to periodic variables, massive star eruptions, novae, supernovae, gamma-ray bursts, tidal disruption events, fast radio bursts, active galactic nuclei, and microlensing. Multi-messenger astrophysics is starting to become a powerful investigative tool and within the next decade several missions and facilities will explore the timevarying Universe. ESO's instrumentation suit is ideal for coordinated follow-up efforts, but are we prepared for it in terms of tools and procedures?.

My poster is available at https://zenodo.org/record/7046721

Highlights of Spanish Astrophysics XI, Proceedings of the XV Scientific Meeting of the Spanish Astronomical Society held on September 4–9, 2022, in La Laguna, Spain. M. Manteiga, L. Bellot, P. Benavidez, A. de Lorenzo-Cáceres, M. A. Fuente, M. J. Martínez, M. Vázquez- Acosta, C. Dafonte (eds.), 2023

Light pollution evolution around the Cíes Islands.

Xabier Pérez-Couto[1], Ana Ulla Miguel[2], and Carmen Bao-Varela[3] and Salvador Bará[1]

[1] A. Astronómica ÍO, A Coruña (Galicia)
[2] Universidade de Vigo, Área de Astronomía e Astrofísica, Departamento de Física Aplicada
[3] Universidade de Santiago de Compostela, Área de Óptica, Departamento de Física Aplicada

Abstract

Control and monitoring of light pollution is key to environmental and human wellbeing. To address a proper study of the many factors involved in this research area is mandatory, as well, for particular geographical regions with protected dark skies. In this context, the worldwide famous Cíes Islands, in the Spanish Galician Autonomous Community, hold since 2016 a Starlight Touristic Destination certificate that must be audited every 4 years. A summary of the results obtained for historical series and recent observational campaigns are here presented.

My poster is available at https://zenodo.org/record/7038615#.Y8GXvHbMK5d

Highlights of Spanish Astrophysics XI, Proceedings of the XV Scientific Meeting of the Spanish Astronomical Society held on September 4–9, 2022, in La Laguna, Spain. M. Manteiga, L. Bellot, P. Benavidez, A. de Lorenzo-Cáceres, M. A. Fuente, M. J. Martínez, M. Vázquez- Acosta, C. Dafonte (eds.), 2023

Magnetic impact of LEO environment on a magnetoresistive-based measurement system for a CubeSat.

C. Maria-Moreno[1], G. Pachecho-Ramos[2], A. Quirós-Olozábal[1], J.M. Guerrero-Rodríguez[1], M.A. Cifredo-Chacón[1], I. del Sol[1], C. Cobos-Sánchez[1], J.A. Vílchez-Membrilla[1], F. Rivas[3], and I. Mateos[1]

[1] School of Engineering, Universidad de Cádiz, 11519 Cádiz, Spain
[2] Dpto. de Ingeniería Aeroespacial y Mecánica de Fluidos, Universidad de Sevilla, 41092 Sevilla, Spain
[3] Universidad de Loyola, 41704 Sevilla, Spain

Abstract

Some space missions require a thorough control of the spacecraft's magnetic environment. With the aim of reducing risks, novel magnetic measurement designs that are likely to be included in these ambitious satellites might be previously tested in CubeSats as a cost-effective alternative. However, the adverse environment that these nanosatellites undergo at LEO altitudes may impact on the measurements that on-board magnetic sensors perform. For instance, continuously orbiting the Earth and changing the spacecraft's attitude entail undesired contributions to the noise estimation of the measurements. Therefore, this research elaborates on an approach to simulate these in-orbit magnetic variations at LEO orbit in order to identify the contributions generated by these conditions and to subtract them, so that just the intrinsic noise of the sensor can be assessed. The system tested for this purpose is Magnetic Experiment for LISA (MELISA), an AMR-based design. A version of this system, MELISA-III, is featured in the CubeSat Carrier-2 (CSC-2) platform as part of the Horizon 2020 programme. Additionally, MELISA-II is included in UCAnFly, a CubeSat developed under the FYS programme of the ESA. An on-ground Helmholtz Coil is fed to generate a suitable magnetic field according to the orbit simulations provided by tools like GMAT. Thus, SSO orbit conditions, which are typical scenarios for CubeSats, are represented in a laboratory environment along with the corresponding attitude variations. As a result, contributions in the measurements of the magnetic sensor are reflected at the frequencies that correspond to the orbit and attitude control simulated by the Helmholtz coils, which can be useful for foreseeing and cancelling out this effect for future missions.

My poster is available at https://zenodo.org/record/7050680#.Y3UhNJDMJD8

Highlights of Spanish Astrophysics XI, Proceedings of the XV Scientific Meeting of the Spanish Astronomical Society held on September 4–9, 2022, in La Laguna, Spain. M. Manteiga, L. Bellot, P. Benavidez, A. de Lorenzo-Cáceres, M. A. Fuente, M. J. Martínez, M. Vázquez- Acosta, C. Dafonte (eds.), 2023

Present and future of the IRAM 30-meter millimeter telescope.

Miguel Sánchez-Portal[1]

[1] Institut the Radioastronomie Millimétrique (IRAM), Granada, Spain

Abstract

The IRAM 30-meter millimeter radio telescope is placed at 2850 m above the sea level in the Loma de Dílar, a slope of Pico Veleta in Sierra Nevada, Granada, Southern Spain. The facility has been continuously operating around the clock since its inauguration in 1984. It is still one of the most sensitive and powerful telescopes worldwide in its frequency range. It has been recognised as one of the facilities within the Spanish Map of Singular Scientific and Technical Infrastructures (ICTS). IRAM has undertaken an ambitious project to upgrade the 30-meter to keep it in the research leading edge in the coming years. The planned improvement actions include a new servo control system for the mount and sub-reflector, comprising hardware (motors, amplifiers, sensors etc.) and low-level software components, and upgrades in the primary reflector to improve the thermal behaviour, surface accuracy and gain-elevation curve. The upgrade of the servo system, in advanced progress state, is supported by the Spanish Instituto Geográfico Nacional (IGN) and is co-financed by European Regional Development Fund (ERDF) programme. For the improvement of the primary reflector, different options are being considered, although the most important action being assessed is in-situ re-painting the surface with a high accuracy (50 μm with a tolerance of $\pm 5\,\mu$m peak-to-peak). The on-site upgrade work will start in late February 2023 and will extend for several months (likely until the end of the Summer semester 2023).

My poster is available at https://zenodo.org/record/7047921#.Y78DgOzMKek

Highlights of Spanish Astrophysics XI, Proceedings of the XV Scientific Meeting of the Spanish Astronomical Society held on September 4–9, 2022, in La Laguna, Spain. M. Manteiga, L. Bellot, P. Benavidez, A. de Lorenzo-Cáceres, M. A. Fuente, M. J. Martínez, M. Vázquez- Acosta, C. Dafonte (eds.), 2023

Proposal of a preliminay Planetary Protection protocol for the development of future Mars missions at the University of Vigo.

Alejandro Ramírez Ramos[1], Alejandro Cardesin Moinelo[2], Ana Ulla Miguel[1], Andoni Moral Inza[3], Alicia Berrocal Bravo[3], Carlos Briones Llorente[4], Stefano Chiussi[1], Alejandro Camanzo Mariño[1], Carmen Sieiro Vázquez[1], and Fernando Aguado Agelet[1]

[1] Universidade de Vigo, Vigo, Spain
[2] European Space Astronomy Centre, Villanueva de la Canada, Madrid, Spain
[3] Instituto de Tecnica AeroEspacial, Torrejon de Ardoz, Spain
[4] Centro de Astrobiologia, Torrejon de Ardoz, Spain

Abstract

We present here a research collaboration between the University of Vigo, ESA and INTA/CAB to analyse, adapt and test standard Planetary Protection (PP) protocols to avoid biological contamination during the development of future Mars exploration instrumentation.
This project is based on the standard PP requirements, procedures and techniques currently used for Mars science instruments, in particular for the Raman Laser Spectrometer (RLS) developed at INTA/CAB for the ESA ExoMars mission. The goal of the project is to compile, adapt and test these procedures in the current instrumentation facilities at the University of Vigo, so they could be used for the development of science payload in a potential future mission to Mars surface.
We will summarize in this contribution the standard requirements and procedures followed by ExoMars RLS team (biological contamination prevention, monitoring and cleaning methods) and how these techniques can be adapted to the University, including the preliminary study of various samples taken at the UVigo SpaceLab and CINTECX FA3 lab facilities to assess the current state of biological contamination.
Acknowledgements: This study has been supported by the ESA Science Faculty at ESAC, INTA/CAB RLS team, UVigo SpaceLab, CINTECX FA3 group and the Faculty of Biology of the University of Vigo.

My poster is available at https://zenodo.org/record/7040309#.Y6R8HHaZOUk

Highlights of Spanish Astrophysics XI, Proceedings of the XV Scientific Meeting of the Spanish Astronomical Society held on September 4–9, 2022, in La Laguna, Spain. M. Manteiga, L. Bellot, P. Benavidez, A. de Lorenzo-Cáceres, M. A. Fuente, M. J. Martínez, M. Vázquez- Acosta, C. Dafonte (eds.), 2023

Six years supporting the *Athena* Community Office.

Martínez-Núñez, S.[1], Carrera, F.J.[1], Ceballos, M.T.[1], Barret, D.[2], Rau, A.[3], and Bozzo, E.[4]

[1] Instituto de Física de Cantabria (CSIC-Universidad de Cantabria), 39005, Santander, Spain
[2] Institut de Recherche en Astrophysique et Planétologie, Université de Toulouse, CNRS, UPS, CNES 9, Avenue du Colonel Roche, BP 44346, F-31028, Toulouse Cedex 4, France
[3] Max-Planck-Institut für extraterrestrische Physik, Gießenbachstraße 1, D-85748 Garching, Germany
[4] Département d'Astronomie, Université de Genève, Chemin d'Ecogia 16, CH-1290 Versoix, Switzerland

Abstract

The *Athena* Community Office has been supporting the ESA's *Athena* Science Study Team and the broad *Athena* scientific community since June 2016. Currently, the community counts more than 1000 researchers spread around the world.
In this talk, we will present some of the most relevant projects carried out in the last two years, such as: supporting the production of the multimessenger-*Athena* and Rubin-*Athena* white papers; coordinating the *Athena* science monthly webinars; developing simulation software; assisting members of the community and other astronomers in performing science simulations; and last but not least keeping the development of communication and outreach activities openly distributed to the astronomical community.

Acknowledgments

ACO activities are being funded by project RTI2018-096686-B-C21 funded by MCIN/AEI/10.13039/501100011033 and by "ERDF A way of making Europe".

My poster is available at https://zenodo.org/record/7038422#.Y5sH36fMLpg

Highlights of Spanish Astrophysics XI, Proceedings of the XV Scientific Meeting of the Spanish Astronomical Society held on September 4–9, 2022, in La Laguna, Spain. M. Manteiga, L. Bellot, P. Benavidez, A. de Lorenzo-Cáceres, M. A. Fuente, M. J. Martínez, M. Vázquez- Acosta, C. Dafonte (eds.), 2023

The 40m radiotelescope of the Yebes Observatory.

Gómez-Garrido, M.[1,2], Tercero, B.[1,2], Beltrán, F.[2], González-García, J.[2], Gallego, J.D.[2], López-Pérez, J. A.[2], Tercero, F.[2], García, O.[2], Patino-Esteban, M.[2], López-Fernández,I.[2], Gómez-Molina, G.[2], Diez, M.[2], García-Carreño, P.[2], Bautista, M.[2], Malo, I.[2], Amils, R.[2], Serna, J.M.[2], Albo, C.[2], Hernández, J.M.[2], Vaquero, B.[2], Barbas, L.[2], López-Fernández, J.A. Bujarrabal, V.[1], Chacón-Tanarro, A.[1,2], Esplugues, G[1,2], García-Miró, C.[2], Jiménez-Donaire, M.J.[1,2], Marcelino, N.[1,2], Pardo, J.R.[3], Santander-García, M.[1,2], Tarrío, P.[1,2], Cernicharo, J.[2], and de Vicente. P.[2]

[1] Observatorio Astronómico Nacional (OAN-IGN), C/ Alfonso XII, 3, 28014 Madrid, Spain
[2] Observatorio de Yebes, IGN, Cerro de la Palera s/n, 19141 Yebes, Guadalajara, Spain
[3] Instituto de Física Fundamental, CSIC, Calle Serrano 123, 28006 Madrid, Spain

Abstract

The Yebes Observatory is one of the six Spanish "Infraestructuras Científicas y Técnicas Singulares" (ICTS) in astronomy and manages a 40m radio telescope as its main facility with open and competitive access. Since 2019, thanks to the Nanocosmos project, observations at 31.5–50 GHz and 72–90.5 GHz with an instantaneous bandwidth of 18 GHz are available, making it possible to observe many molecular transitions with single tunings in single-dish mode. This reduces the observing time and maximises the output from the telescope. The most remarkable result bringing by this upgrade is the detection of more than 50 new molecular species in space in the last three years in a wide variety of astrophysical environments. In addition, Yebes Observatory has recently built and installed a new C band receiver which covers the frequency range 4.5–9 GHz. Its main goal is to be used for very long baseline interferometry (VLBI), cover the two main European VLBI network (EVN) observing bands and provide a wide band of 4 GHz. This is a transition receiver which will work until an ultra wide one between 4 and 18 GHz (VLBI global observing system) is built and installed. One of the main goals is the design, construction, measurement, installation and commissioning of a high sensitive cryogenic receiver with an instantaneous bandwidth between 18 GHz and 32 GHz that will be deployed at the Yebes 40m radio telescope. This receiver will be a step forward in an ultimate goal that consists in having a full observable frequency coverage between 4 and 90 GHz at the 40m radio telescope.

My poster is available at https://zenodo.org/record/7035743#.Y8Juj3bMKUk

Highlights of Spanish Astrophysics XI, Proceedings of the XV Scientific Meeting of the Spanish Astronomical Society held on September 4–9, 2022, in La Laguna, Spain. M. Manteiga, L. Bellot, P. Benavidez, A. de Lorenzo-Cáceres, M. A. Fuente, M. J. Martínez, M. Vázquez- Acosta, C. Dafonte (eds.), 2023

The European JWST archive and associated tools.

A. Labiano[1], A. Marston[2], M. López-Caniego[3], M. Arévalo[4], J. Espinosa[4], and and J. Ballesteros[4]

[1] Telespazio UK for ESA
[2] Euroepan Space Agency (ESA)
[3] Aurora Technology for ESA
[4] RHEA for ESA

Abstract

The European archive of the James Webb Space Telescope (eJWST) is designed to be a service to the European scientific community, but open to all scientists around the world, enabling the most direct and useful access to the JWST science data products. eJWST forms part of ESA's science archives. It is therefore searchable in combination with data from any other ESA science mission. The eJWST holdings consist of all public data from the JWST mission and allows access to proprietary data, as produced by the official pipeline software at STScI. eJWST provides multiple methods for searching and filtering products and calibration data. The data can be downloaded directly from the UI or using ADQL, CURL, WGET or Astroquery scripts.

My poster is available at https://zenodo.org/record/7017065#.Y1f2Fi1h3UI

Highlights of Spanish Astrophysics XI, Proceedings of the XV Scientific Meeting of the Spanish Astronomical Society held on September 4–9, 2022, in La Laguna, Spain. M. Manteiga, L. Bellot, P. Benavidez, A. de Lorenzo-Cáceres, M. A. Fuente, M. J. Martínez, M. Vázquez- Acosta, C. Dafonte (eds.), 2023

Using cumulative distribution functions to characterize X-ray line complexes.

Cardiel, N[1], Ceballos, M.T.[2], and Cobo, B.[2]

[1] Departamento de Física de la Tierra y Astrofísica, Universidad Complutense de Madrid
[2] Instituto de Física de Cantabria, CSIC-Universidad de Cantabria

Abstract

The X-ray Athena (Advanced Telescope for High-Energy Astrophysics) mission, selected in 2014 by ESA within its Cosmic Vision Program to address the Hot and Energetic Universe scientific theme, will offer spectroscopic and imaging capabilities exceeding those of currently operating X-ray astronomy satellites. In particular, X-IFU (the X-ray Integral Field Unit), one of the two instruments to be on board the Athena Observatory, will provide unprecedented spectral resolution (2.5 eV at 7 keV) with 5 arcsec pixels.
As part of the Spanish contribution to this mission, an important effort has been invested in the detailed study of the impact of different algorithms devoted to the proper characterization of the energy of each photon that will be detected by X-IFU (see e.g., Ceballos et al. 2019ab, Cobo et al. 2020, Vega-Ferrero et al. 2022). The spectral resolutions achieved with the different strategies are evaluated by fitting X-ray line complexes corresponding to laboratory data generated with calibrated X-ray sources. Traditionally these data are binned in order to generate histograms which are subsequently fitted using the familiar chi-squared statistic or a maximum-likelihood approach (Fowler 2014).
In this work, we show how the use of cumulative distribution functions can be employed to determine the fit of X-ray line complexes constituted by several lines without the need to perform an a priori data rebinning. The method has been checked using simulated data, and the results indicate that it can recover photons beyond the fitting range. The procedure has been programmed in Python and the source code is publicly available.

My poster is available at https://zenodo.org/record/6922198#.Y1beYuxBxB0

Highlights of Spanish Astrophysics XI, Proceedings of the XV Scientific Meeting of the Spanish Astronomical Society held on September 4–9, 2022, in La Laguna, Spain. M. Manteiga, L. Bellot, P. Benavidez, A. de Lorenzo-Cáceres, M. A. Fuente, M. J. Martínez, M. Vázquez- Acosta, C. Dafonte (eds.), 2023

VIOMASS: Virtual Observatory Integration Of Madcuba And SLIM Spectra.

J. R. Rizzo[1,2], C. Blanco[2], and J. Martín-Pintado[2]

[1] ISDEFE, Spain
[2] Centro de Astrobiología (CAB/CSIC-INTA), Spain

Abstract

MADCUBA is an astronomical package primarily aimed to reduce and analyze data from many radio astronomical facilities. MADCUBA is not only able to process individual spectra, but also data cubes. In addition, it is able to identify thousands of molecular rotational transitions and radio recombination lines by consulting the most important molecular databases. One of its tasks -SLIM- simulates LTE conditions and makes a semi-automatic fitting of many lines simultaneously.
Under a collaborative effort of Virtual Observatory (VO) and MADCUBA groups, we are implementing new functionalities in MADCUBA to make it VO-compliant. The final objective is to profit the robustness of MADCUBA and the versatility of VO in order to increase visibility of MADCUBA and allow users to enhance results through the interaction with the pleiad of VO tools and available data sets.
In this e-poster we present the scope of the project, changes already implemented and future work. In detail, we show the data model which will be implemented and the options that the user will have to export their work adhering to the VO standards.

My poster is available at https://doi.org/10.5281/zenodo.7046116

Highlights of Spanish Astrophysics XI, Proceedings of the XV Scientific Meeting of the Spanish Astronomical Society held on September 4–9, 2022, in La Laguna, Spain. M. Manteiga, L. Bellot, P. Benavidez, A. de Lorenzo-Cáceres, M. A. Fuente, M. J. Martínez, M. Vázquez- Acosta, C. Dafonte (eds.), 2023

AB Aur: A Rosetta stone for planet formation theories. System chemistry.

Rivière-Marichalar, P.[1], Fuente, A.[1], Navarro-Almaida, D.[1,2], Baruteau, C. [3], and Le Gal, R.

[1] Observatorio Astronómico Nacional (OAN,IGN), Calle Alfonso XII, 3. 28014 Madrid, Spain
[2] Département d'Astrophysique (DAp), Commissariat à l'Énergie Atomique et aux Énergies Alternatives (CEA), Orme des Merisiers, Bât. 709, 91191 Gif sur Yvette, Paris-Saclay, France
[3] IRAP, Université de Toulouse, CNRS, UPS, Toulouse, France
[4] Institut de Radioastronomie Millimétrique, 300 rue de la Piscine, F-38406 Saint-Martin d'Hères, France

Abstract

AB Aur is a Herbig Ae star that hosts a well-known protoplanetary disk in which a series of interesting features are observed. Such features (a large inner cavity, a dust trap, and spiral arms) can be attributed to the presence of a forming planet, making AB Aur an interesting target to study planet formation and the interactions between a disk and a forming planet. We present NOEMA observations of molecular species towards the transition disk around AB Aur, including CO, ^{13}CO, C^{18}O, HCN, HCO$^+$, SO, H_2CO, and H_2S. These observations reveal a complex chemistry with strong chemical differentiation in the radial and azimuthal directions and the presence of a cavity-crossing filament. We have computed a series of Nautilus models to help us interpret our observations. Our astrochemical models point to a disk with a low gas-to-dust ratio and strong sulfur depletion. These Nautilus models helped us to understand the sulfur budget in the disk and the role of sulfuretted species in the system chemistry, and more generally in planet-forming disks.

1 Introduction

Planets are born in circumstellar disks made of gas and dust that surround young stellar objects, implying that a planet's composition is, at least partially, inherited from the protoplanetary disk. Therefore, characterizing the physical conditions and the chemical composition of protoplanetary disks is key for understanding planet formation. Furthermore, to study the chemical complexity of planetary atmospheres, it is mandatory to understand that of protoplanetary disks.

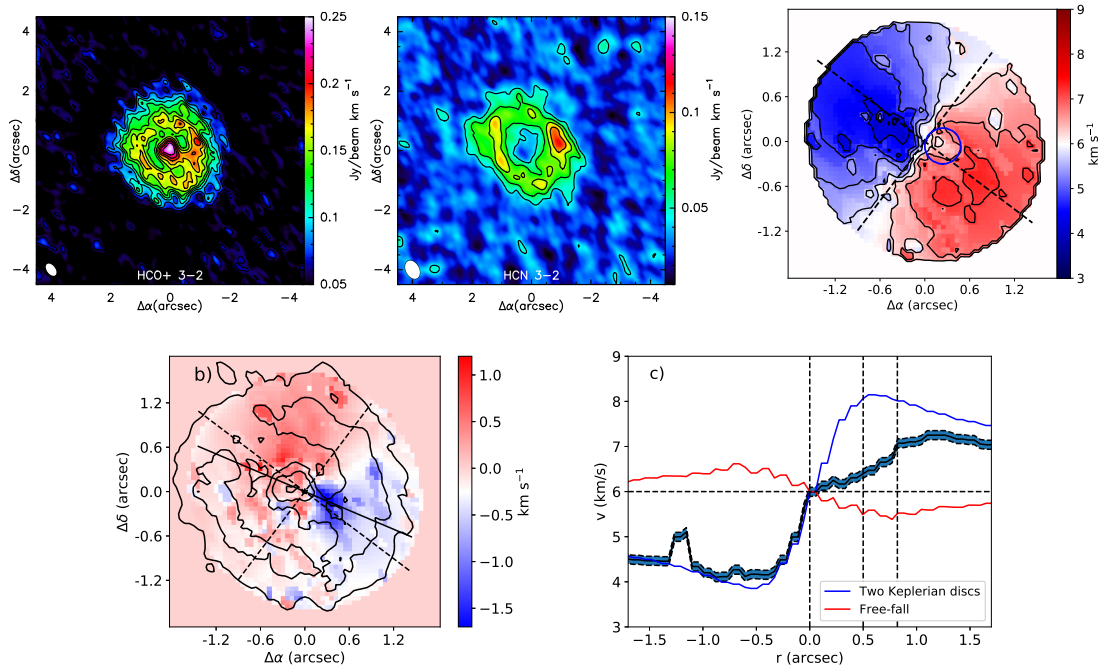

Figure 1: Top: from left to right we show the velocity-integrated intensity maps of HCO^+ (left) and HCN (right) 3-2 emission, and the HCO^+ 3-2 first-moment map. In the HCO^+ 3-2 first-moment map, the dashed lines indicate the direction of the major and minor axes. The blue circle contains a region with large anomalies with respect to a Keplerian rotation velocity field. The synthesized beam is shown in the bottom left corner of each map. Bottom: from left to right we show the residuals of a model consisting of two Keplerian disks and a cut along the velocity anomaly for the HCO^+ first-moment map (black lines with dashed region). Solid contours in the left panel depict 5σ to 25σ levels of the integrated line intensity. The black solid line shows the direction of the cut through the bridge used for the right panel. In the right panel, the blue line depicts a model consisting on two Keplerian disks (blue line), and a free-falling component (red line). The dashed vertical lines mark the positions of the center, the bridge, and the inner edge of the dust disk. From [30].

Statistical studies are key to understanding planet formation, but the detailed characterization of individual sources can provide deep insights into the physical properties and chemical reaction networks that are present in protoplanetary disks. AB Aur is a widely studied Herbig A0 star that hosts a transitional disk. At a distance of ∼160 pc [14], the system is well suited to study the distribution of gas and dust in circumstellar environments. The system presents a series of features that can be attributed to planet formation, such as a large inner cavity [29, 37, 38, 11], spiral arms [13, 17, 38, 31], and a dust trap [29, 11]. The source has been observed at all wavelengths from visible to centimetric. Low-resolution spectral observations are available from ∼1 μm up to ∼ 400 μm. The detection of lines of O I, C II, C, OH, as well as rovibrational lines of CO and H_2 demonstrates the existence of warm gas in the source. The origin of these emission lines is, however, uncertain due to the moderate

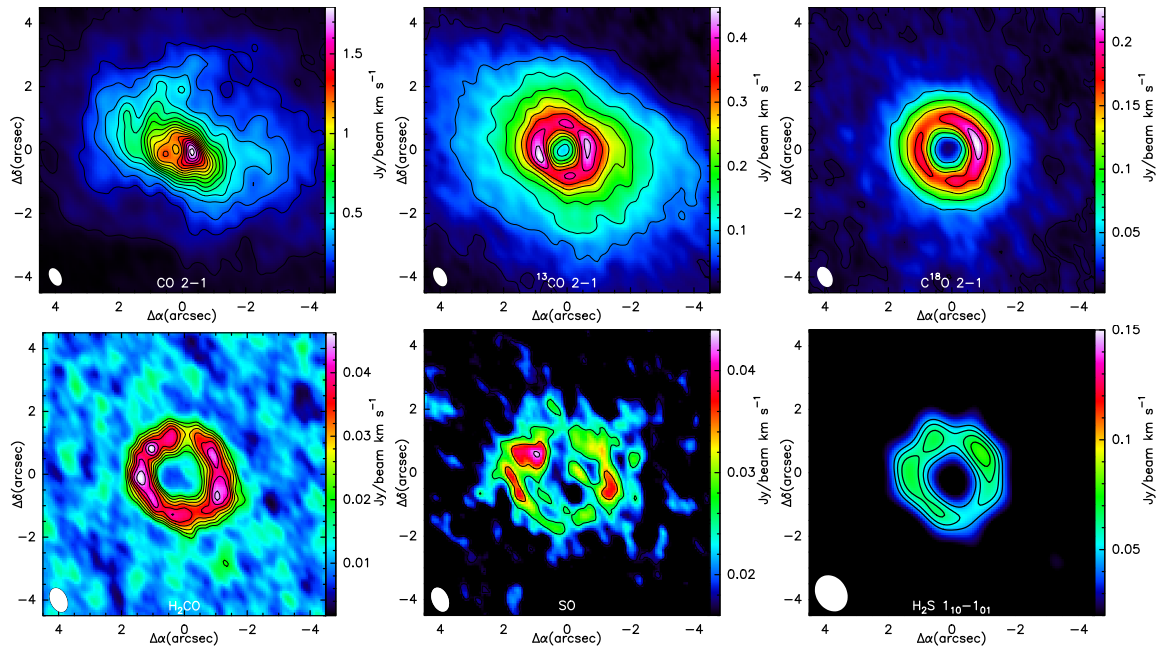

Figure 2: From left to right and top to bottom the panels show the velocity integrated intensity maps of ^{12}CO 2-1, ^{13}CO 2-1, C^{18}O 2-1, H_2CO 3_{03}-2_{02}, SO 5_6-4_5, and H_2S 1_{10}-1_{01}. The synthesized beam is shown in the bottom left corner of each map. From [31] and [32].

angular resolution of the observations. A few molecular species have been detected in AB Aur, including CO, SO, HCO^+, HCN, H_2CO, and H_2S [36, 29, 37, 38, 9, 25, 26, 30, 31, 32]. The first detection of SO in a protoplanetary disk was reported towards AB Aur [9, 25, 26]. Our team is performing a large observational effort to study the dust and gas content in this interesting object [11, 30, 31]. In this proceedings, we summarize the main results of our study.

2 NOEMA observations of HCN and HCO^+: accretion within the dust cavity?

We observed AB Aur with NOEMA in 2017 [30] to map the emission of HCO^+ 3-2 and HCN 3-2. Velocity-integrated intensity maps are shown in Fig. 2. Both maps look vey different. While HCN is detected in an annular ring spatially coincident with the dust ring, HCO^+ is detected in the outer ring and also features intense emission towards the central position. But the most striking feature of the HCO^+ 3-2 map is a bright HCO^+ emission bridge that connects the outer disk with the inner structure [30].

We show in the right panel of Fig. 2 the first-moment map of HCO^+ J=3-2. The outer parts of the disk are close to Keplerian rotation, but twisted isophotes are observed towards the center (r<0.6"). Two mechanisms have been proposed to explain twisted isophotes: two

Table 1: Peak position in radial profiles, and angle peak in azimuthal profiles of the continuum and the different species surveyed before de-projection. The last column gives the binding energy of the different species surveyed. References are: [1] [8]; [2] [24]; [3] [16]

Species –	Peak position (")	Peak position (au)	Peak. angle (°)	E_D (K)
Cont 1mm	0.96	157	269	–
^{12}CO	0.292	52	279	1575[1]
^{13}CO	0.80	130	279	1575[1]
$C^{18}O$	0.89	146	275	1575[1]
p$-H_2CO$	1.20	195	279	3260[2]
SO	1.41	229	105	2600 [3]
HCO^+	0.00	0.0	92	–
HCN	1.02	166	99	2050[3]

misaligned Keplerian disks [17] and the presence of an outflow [34]. We created a simple model consisting of two misaligned disks. This model provides a good fit across the disk except in the position of the bridge region, where prominent residuals are observed. Visual inspection of spectra at this position demonstrates the presence of material moving at forbidden velocities, most likely infalling material moving at free-fall velocities. By including a free-fall velocity component in our model we get a much better fit to the first-moment map. At the position of the bridge, the free-fall model has a velocity of 5.5 km s^{-1}, compared to the velocity of 5.3 km s^{-1} of the blue-shifted component observed towards the bridge. According to this, the material in the bridge seems to be infalling at a velocity close to free-fall. Assuming that this component was due to accretion, we derived a mass accretion rate in the range $3{\times}10^{-8}$ to $3{\times}10^{-7}$ $M_\odot$ yr^{-1}, comparable to previous measurements [35].

Radial inflows crossing dust cavities have been invoked before to explain a series of features observed in protoplanetary disks, such as gas and dust streamers and twisted isophotes [4, 7, 27, 43, 20, 21, 42]. Radial inflows were proposed to explain absorption features in CO ro-vibrational lines towards AA Tau [43], with material moving at free-fall velocities in regions between the inner and outer disk. These gap-crossing radial inflows could explain the high accretion levels derived in transitional disks, such as those observed in AB Aur [15, 35]. A compact and collimated bipolar jet was detected by [33] in the continuum at 7 mm suggesting the existence of a disk-jet system. In order to sustain it, the gas must flow through the cavity and reach the inner regions of the system. Otherwise, accretion would drain the inner disk very fast.

3 Spatial distribution of chemical species

We continued our research by studying the spatial distribution of ^{12}CO, ^{13}CO, $C^{18}O$, HCN, HCO^+, SO, H_2CO [31], and H_2S [32], by means of high angular resolution NOEMA observa-

Table 2: Nautilus 1D model parameters.

Parameter	Value
Molecular cloud	
T_{gas} (K)	10
T_{dust} (K)	10
n_H	10^4
A_v	20
f_{UV} (Draine units)	1
ζ_{H_2} (s^{-1})	10^{-17}
Gas-to-dust mass ratio	100
AB Aur at r=200 au	
T_{mid} (K)	39
T_{atm} (K)	65
A_v	2
f_{UV}(Draineunits)	1.2×10^4
ζ_{H_2} (s^{-1})	10^{-17}
Gas-to-dust mass ratio	40

tions. The species surveyed showed strong radial segregation, with differences as large as 100 au in the positions of their radial peaks. The only species that peaked toward the center was HCO^+. The emission from all gaseous species was more extended than that of the dust, ^{12}CO and ^{13}CO being the most extended ones, with 5σ emission detected at distances larger than 4" due to pollution by envelope emission. It sounds reasonable to postulate that this radially layered structure is related to the snow lines of the different species, which are determined by their binding energies. If thermal desorption is the main desorption mechanism in the mid-plane, one would expect that the radius of the snow line anti-correlates with the binding energy. However, this was not the behavior observed (see Table 2), which suggests that thermal desorption is not the main driver of the surface chemistry in this system. Furthermore, our data revealed that different species are probing different regions of the disk and the envelope. Species such as ^{12}CO and ^{13}CO trace the disk surface and the remnant envelope. Other species, such as $C^{18}O$ and HCN, are tracing the dusty disk, with a radial profile that almost overlaps with that of the continuum. H_2CO and SO trace the outer regions of the disk, and SO is likely to arise from shocked regions, such as the centrifugal barrier.

We also observed differences in the azimuthal profiles of the different species. $C^{18}O$ peaks close to the position of the dust trap, while SO peaks at $\sim180°$ from the position of the dust trap, and other species such as HCN, H_2CO, and HCO^+ are mostly flat along the ring.

Using H_2CO lines we derived a mean gas temperature of 39 K. Using SO lines we derived a temperature of 37 K, in good agreement with the value from H_2CO lines. This average temperature of 39 K is larger than the typical value for disks around T Tauri stars. By combining observations of the continuum, ^{13}CO, and $C^{18}O$ we computed a gas-to-dust ratio map, with a mean value of 40.

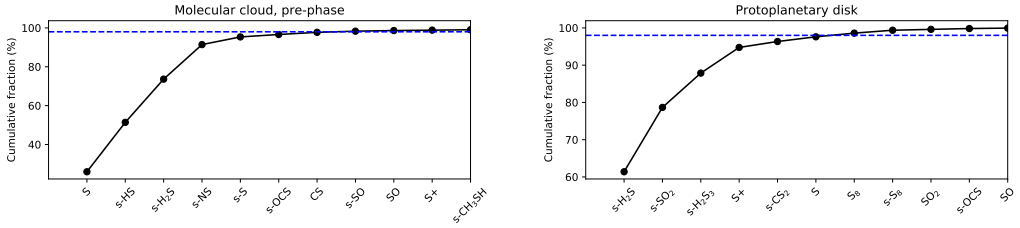

Figure 3: Cumulative sulfur abundance fraction of the ten main sulfur carriers from `Nautilus` models. Left: molecular cloud. Right: AB Aur protoplanetary disk at r=200 au. The horizontal blue dashed line depicts the position of the 98% cumulative fraction. From [32].

4 Chemical modeling and sulfur budget

To help us interpret our interferometric data, we developed a series of 1+1D Nautilus models [41], following the prescriptions used by [19]. The details of the model can be found in [31] and [19]. The elemental gas phase sulfur abundance is a controversial issue [10, 40, 39, 12, 23]. In our models, we considered a high-S abundance case, with the sulfur elemental abundance equal to the solar one [2], and a low-S case with S/H$\sim 8\times10^{-8}$, which is the value usually adopted to fit the abundances of S-bearing species in dark clouds [1]. We varied three parameters: the gas-to-dust ratio (40 and 100), the sulfur abundance (solar, [S/H]$=1.5\times10^{-5}$, and depleted, [S/H]$=8\times10^{-8}$), and the carbon to oxygen relative abundance (C/O=0.7 and C/O=1). By comparing the model abundances with that derived from our observations, we concluded that the best model was one with a low gas-to-dust ratio (thus supporting our estimated value), strong sulfur depletion ([S/H]$=8\times10^{-8}$), and C/O=1, supporting the idea that evolved disks are oxygen depleted [3, 5, 18, 22].

The previous models aimed at reproducing our observations of sulfuretted species in AB Aur. After our detection of H_2S we decided to model again the chemistry of AB Aur using Nautilus, but this time our focus was on understanding the budget of sulfur, as well as of molecular species in general. Instead of producing a 1D+1 model, we estimated the abundances at 200 au, where all the observed species are detected, allowing us to study the chemical budget and the evolution with height. The values adopted for the different parameters are summarized in Table 2. To set our initial abundances we first modeled the chemistry of a 10 K molecular cloud for 1 Myr, and used the output abundances from that model as input for the protoplanetary disk model. The parameters for the molecular cloud are also shown in Table 2. The details of the model can be found in [32].

In Fig. 3, we show the total cumulative fraction for the 10 most abundant sulfuretted species for the cold molecular cloud (left) and the AB Aur protoplanetary disk (right). In our protoplanetary disk model, 98% of the sulfur budget is contained in six species: g-H_2S, g-SO_2, g-H_2S_3, S^+, g-CS_2, and S, where g- stands for molecular species in the surface of dust grains. The budget is dominated by surface species, with 90.5% of the sulfur contained in molecular species on the surface of grains, and 9.5% in species in the gas phase. We show in Fig. 4 the 10 most abundant species for the different phases of the model. Surface H_2S

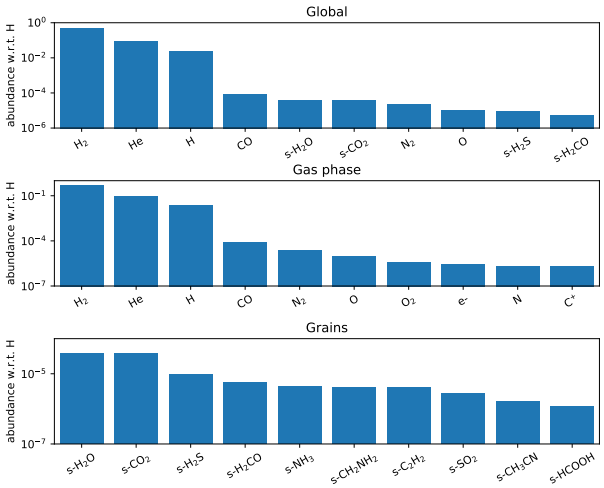

Figure 4: Abundances of the ten most abundant species in our `Nautilus` model for the global content (top), the gas phase (middle), and the surface of grains (bottom). From [32].

is the third most abundant species in the surface of grains, after H_2O and CO. Considering all phases, g-H_2S is the ninth most abundant species in the model, making H_2S a relevant component of dust grains, whose abundance in different protoplanetary systems is worth modeling to understand the chemical budget.

To test the stability of our sulfur budget model we computed new models where key parameters were changed, including the temperature of the cold cloud prephase, the UV field, the grain size, and the temperature of the mid-plane. For the temperature of the cold prephase, we computed a second model with a cloud temperature of 18 K, instead of 10 K. The abundance of all molecular species remained the same within an order of magnitude, exception made of $HSCN^+$. To test the impact of the UV -field, we computed a model with $f_{UV} = 12$ instead of $f_{UV} = 1.2 \times 10^4$, and observed that 85% of the sulfur species remained the same within an order of magnitude. To understand the role of the grain size distribution we computed a model where we assumed a different grain size at each height, with 1 mm grains in the mid-plane, 0.1 μm grains in the atmosphere, and a logarithmic interpolation in between. Again, most of the species (92%) remained the same within an order of magnitude. Finally, to test the impact of varying the mid-plane temperature we computed a model with a mid-plane temperature of 10 K. We show in the top panel of Fig. 5 the cumulative sulfur abundance fraction of the ten most relevant sulfur carriers from this model. The most relevant sulfur carrier, g-HS, is not among the 10 most abundant sulfur carriers in the original model. Most species that are important sulfur carriers in the original model are irrelevant to the sulfur budget in the 10 K model. In the mid panel of Fig. 5 we show a comparison of the abundances of all the sulfuretted species in both models. The large scatter observed indicates that varying the temperature of the mid-plane gas has an important impact on

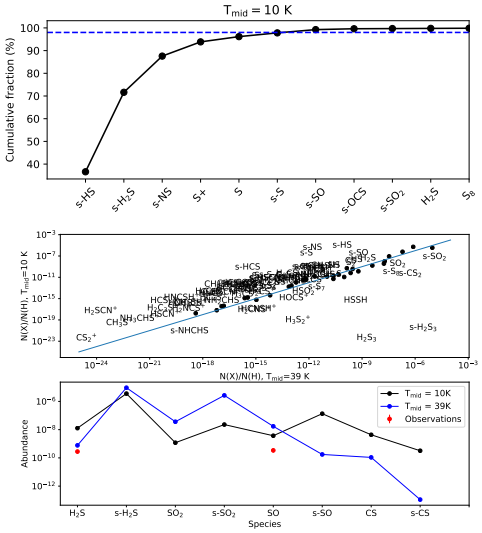

Figure 5: Impact of varying the mid-plane temperature on the model results. Top: cumulative sulfur abundance fraction of the ten main sulfur carriers for the `Nautilus` model with T_{mid}=10 K. Middle: abundance of sulfuretted species computed assuming T_{mid}=10 K versus the abundance computed assuming T_{mid}=39 K. We show the names of the species when there is an order of magnitude difference between both models, and plot black dots otherwise. Bottom: abundance of a subset of the most relevant sulfur carriers for the two mid-plane temperatures used. From [32].

the derived sulfur abundances. In the bottom panel of Fig. 5 we show the abundance of a subset of important sulfuretted species in both models. These species include H_2S, g-H_2S, SO_2, g-SO_2, SO, g-SO, CS, and g-CS. Large differences are observed, indicating the power of simultaneously observing this set of species to derive the mid-plane temperature.

5 Summary

AB Aur's protoplanetary disk presents a series of interesting phenomena that could be the result of the interaction between the disk and an embedded planet, including a cavity in the inner disk, a dust trap, and spiral arms. Thus, studying AB Aur can help us to get insight into the physical and chemical properties during the process of planet formation. For the last few years we have been driving an observational program to characterize the gaseous content of this system using observations with the NOEMA interferometer, the ALMA interferometer, and the IRAM 30 m telescope.

Our observations of HCO^+ revealed the presence of a gap crossing filament that connects the inner and outer disk. The material in this bridge appears to be moving at free-fall velocities and it is likely due to the material being accreted onto the central source. Assuming

that this component was due to accretion we derived an accretion rate in good agreement with previous estimates from the literature. Such radial inflow has been observed before and could explain the high accretion levels observed in transitional disks.

Our NOEMA observations showed strong radial segregation of chemical species in the disk. The positions of the radial peaks of the different species surveyed thus far suggest that thermal desorption is not driving the chemical evolution of the disk, and other mechanisms such as chemical desorption seem to be playing an important role. We derived an average gas-to-dust ratio of 40, significantly smaller than the value of 100 assumed for the ISM, in agreement with recent studies. We used observations our of H_2CO and SO to estimate a mean temperature of 39 K for the gas in the disk.

To help us to interpret the data, we modeled the chemical content of the protoplanetary disk using Nautilus. In our first attempt, we aimed at reproducing the abundance of the sulfuretted species detected thus far in the gas phase. Our best model was one with a gas-to-dust ratio of 40, in agreement with our estimate, strong sulfur depletion ([S/H]=8×10^{-8}), and a relative abundance of carbon to oxygen C/O=1, in agreement with recent studies that show an overabundance of carbon with respect to oxygen in evolved protoplanetary disks. After the detection of H_2S we aimed at deriving the evolution of the sulfur budget with height and to understand the role of sulfuretted species in the global chemistry of the system. According to our NAUTILUS model, H_2S is the main sulfur carrier on the surface of grains. It is also the third most abundant species on the surface of grains, after H_2O and CO_2. Our results show that H_2S observations are an essential diagnostic to determine the level of sulfur depletion in protoplanterary disks. Observations of H_2S and other sulfuretted species toward more young stellar objects are needed to understand sulfur depletion and put our observations of AB Aur in context. Our results also show the relevance of the mid-plane temperature for sulfur chemistry, illustrating to what extent the chemistry of T Tauri and HAeBe are different.

Future observations with NOEMA will help us to grow our database to study the protoplanetary disk around AB Aur and contribute to our global knowledge of the chemistry of protoplanetary systems.

Acknowledgments

PRM and AF thank the Spanish MINECO for funding support from PID2019-106235GB-I00.

References

[1] Agúndez, M. & Wakelam, V., Chemical Reviews, 113, 8710 (2013)

[2] Asplund, M., Grevesse, N., & Sauval, A. J., in Astronomical Society of the Pacific Conference Series, Vol. 336, ed. T. G. Barnes, III & F. N.Bash, 25 (2005)

[3] Bergin, E. A., Du, F., Cleeves, L. I., et al., ApJ, 831, 101 (2016)

[4] Casassus, S., van der Plas, G., M, S. P., et al. , Nature, 493, 191 (2013)

[5] Cleeves, L. I., Öberg, K. I., Wilner, D. J., et al., ApJ, 865, 155 (2018)

[6] Daflon, S., Cunha, K., de la Reza, R., et al., AJ **138**, 1577-1583 (2009)

[7] Dutrey, A., di Folco, E., Guilloteau, S., et al., Nature, 514, 600 (2014)

[8] Fayolle, E. C., Balfe, J., Loomis, R., et al., ApJL, 816, L28 (2016)

[9] Fuente, A., Cernicharo, J., Agúndez, M., et al., A&A **524**, A19 (2010)

[10] Fuente, A., Cernicharo, J., Roueff, E., et al., A&A, 593, A94 (2016)

[11] Fuente, A., Baruteau, C., Neri, R., et al., A&A **846**, L3 (2017)

[12] Fuente, A., Navarro, D. G., Caselli, P., et al., A&A, 624, A105 (2019)

[13] Fukagawa, M., Hayashi, M., Tamura, M., et al., ApJL **605**, L53-L56 (2004)

[14] Gaia collaboration, Vizier Online Data Catalog, I345 (2018)

[15] Garcia-Lopez, R., Natta, A., Testi, L., et al. A&A, 459, 837, (2006)

[16] Garrod, R. T. & Herbst, E., A&A, 457, 927 (2006)

[17] Hashimoto, J., Tamura, M., Muto, T., et al., ApJ **729**, L17 (2011)

[18] Le Gal, R., Brady, M. T., Öberg, K. I., et al., F., ApJ, 886, 86 (2019a)

[19] Le Gal, R., Öberg, K. I., Loomis, R. A., Pegues, J., & Bergner, J. B. , ApJ, 876, 72, (2019b)

[20] Loomis, R. A., Öberg, K. I., Andrews, S. M.,MacGregor, M. A., ApJ, 840, 23 (2017)

[21] Mendigutía, I., Oudmaijer, R. D.,Garufi, A., et al., A&A, 608, A104 (2017)

[22] Miotello, A., Facchini, S., van Dishoeck, E. F., et al., A&A, 631, A69 (2019)

[23] Navarro-Almaida, D., Le Gal, R., Fuente, A., et al., A&A, 637, A39 (2020)

[24] Noble, J. A., Theule, P., Mispelaer, F., et al., A&A, 543, A5 (2012)

[25] Pacheco, S., Fuente, A., Agúndez, M., et al., A&A, **578**, A81 (2015)

[26] Pacheco, S., Fuente, A., Baruteau, C., et al., A&A, **589**, A60 (2016)

[27] Perez, S., Casassus, S., Ménard, F., et al., ApJ, 798, 85 (2015)

[28] Phuong, N. T., Chapillon, E., Majumdar, L., et al., A&A **616**, L5 (2018)

[29] Piétu, V., Guilloteau, S., Durtey, A., A&A **443**, 945-954 (2005)

[30] Rivière-Marichalar, P., Fuente., A., Baruteau, C., et al., ApJL **879**, L14 (2019)

[31] Rivière-Marichalar, P., Fuente, A., Le Gal, R., et al., A&A **642**, A32 (2020)

[32] Rivière-Marichalar, P., Fuente, A., Esplugues, G., A&A **652**, A46 (2022).

[33] Rodríguez, L. F., Zapata, L., A., Dzib, S. A., et al., ApJ **793**, L21 2014

[34] Rosenfeld, K., A., Chiang, E., Andrew, S. M., ApJ **782**, 62 (2014)

[35] Salyk, C., Herczeg, G. J., Brown, J. M., et al., ApJ **769**, 21 (2013)

[36] Schreyer, K., Guilloteau, S., Semenov, D., et al., A&A, **491**, 821-827 (2008)

[37] Tang, Y. -W., Guilloteau, S., Piétu, V., et al., A&A **547**, A84 (2012)

[38] Tang, Y. -W., Guilloteau, S., Durtey, A., et al., ApJ **84**, 32 (2017)

[39] Vastel, C., Quénard, D., Le Gal, R., et al., MNRAS, 478, 5514 (2018)

[40] Vidal, T. H. G., Loison, J.-C., Jaziri, A. Y., et al., MNRAS, 469, 435 (2017)

[41] Wakelam, V., Ruaud, M., Hersant, F., et al., A&A **594**, A35 (2016)

[42] Walsh, C., Daley, C., Facchini, S., Juhász, A., A&A, 697, A114 (2017)

[43] Zhang, K., Crockett, N., Salyk, C., et al. ApJ, 805, 55, (2015)

Highlights of Spanish Astrophysics XI, Proceedings of the XV Scientific Meeting of the Spanish Astronomical Society held on September 4–9, 2022, in La Laguna, Spain. M. Manteiga, L. Bellot, P. Benavidez, A. de Lorenzo-Cáceres, M. A. Fuente, M. J. Martínez, M. Vázquez- Acosta, C. Dafonte (eds.), 2023

Formation of ring-like structures in flared α-discs with X-ray/FUV photoevaporation.

Vallejo, Juan C.[1,2], **and Gómez de Castro, Ana I.**[1,2]

[1] AEGORA research group - Joint Center for Ultraviolet Astronomy, Universidad Complutense de Madrid, Plaza de Ciencias 3, 28040, Madrid, Spain
[2] Departamento de Física de la Tierra y Astrofísica, Fac. de CC. Matemáticas, Plaza de Ciencias 3, 28040 Madrid, Spain

Abstract

Understanding the evolution of protoplanetary discs is key to understand the formation of planets around young stars. However, modelling these protoplanetary discs is not an easy task as several complex dynamical processes must be included in the numerical models. In this work, we analyse the impact of adding a progressive flattening in protoplanetary flared discs combined with different photoevaporative winds in the creation of ring-like structures, using a simple semi-analytical 1D α-disc. Our results show that such a progressive flattening may favour the formation of ring-like features resembling those observed in real systems. Depending on the control parameters, these features are created with proper disc masses and accretion rates at the right evolutionary times. However, further enhancements are still needed for better matching all the evolutionary times seen in real systems.

1 Introduction

The protoplanetary discs are the natural scenario for planet formation processes. Analysing their dispersal time-scales constraint the time in which those planets must form, while computing their masses at given times provide the mass available for planet formation.

We will focus here on modelling the so-called transitional discs. These discs have relatively short-lived inner cavities and gaps. Hence, analysing their creation and lifetimes will help in refining the model parameters.

Because of the complexity of the problem, we take an approach based on a semi-analytical 1D viscous α-disc, with a flaring profile that changes with time added to a photoevaporative term.

Viscous momentum transport is of interest in disc modelling from disc-possessing to discless status even when other transport alternatives are possible. In principle, the molecular viscosity of the gas is too small to produce significant evolution. Despite of above, a viscous approach is still quite common when ones interprets the viscosity as the outcome of a turbulent process.

Hence, the surface density $\Sigma(r,t)$ evolves as per the laws of mass and momentum conservation, with a diffusion coefficient regulated by the viscosity ν as follows,

$$\frac{\partial \Sigma}{\partial t} = \frac{3}{r}\frac{\partial}{\partial r}[r^{1/2}\frac{\partial}{\partial r}(\nu \Sigma r^{1/2})] - \dot{\Sigma}_w, \tag{1}$$

where $\dot{\Sigma}_w$ denotes the mass loss by a given photoevaporative wind, functionally equivalent to have a sink in this diffusion equation.

The photoevaporation can explain the two time-scales behavior observed in real systems, the shutdown of the mass accretion and disc dispersion at proper time scales. And an inside-out dispersal model produced by photoevaporation can naturally produce the observed internal cavities and gaps in the disc,

This can be considered a may be too simple model. There is not magnetic field, envelopes or other 2D/3D structures. Moreover, it does not include hydrodynamics, chemical processes, radiative or MHD processes. Many of these different mechanisms could create the observed ring-like features.

Despite of this, simple 1D (semi-)analytical models are still in use nowadays. They complement more complex models meanwhile offer simplicity in interpreting the results. And, because they can incorporate further details in a bottom up approach, they are ideally suited for the α-parametrization and numerical winds.

We extend the initial analyses carried out in [14], and we will evolve a set of models corresponding to a grid of physically meaningful systems covering some of the typical parameter values. Among all possible parameters, we will focus on those defining the disc (disc mass, host star mass, accretion rate, disc age), viscosity values, the time scales when the progressive flattening of the flared disc takes place and the different efficiencies of the photoevaporative winds.

The final goal will be to crosscheck the results with the ring-like features observed in some reference real systems located in the Taurus star forming region, aiming to see how different parameter affect their creation.

2 The numerical α-discs

The α-parametrisation was firstly introduced as a convenient scaling factor of the friction between adjacent rings. This parametrisation was firstly used in [12] and later refined in [13]. It hides the details of the specific viscous transport mechanism while reflecting the impact of the transport in the disc evolution. Therefore, as this parametrisation simplifies the implementation of the viscosity in numerical models, it has been widely used for many years and it is still in common use today [8, 9, 2].

This model relies on an optically thick accretion disc and a turbulent fluid described by a viscous stress tensor, with this stress tensor being proportional to the total pressure. When the eddy size (mean free-path) is less than the disc height and the turbulent velocity smaller than the sound speed c_s, one can write the viscous profile as $\nu(r) = \alpha c_s H(r)$, with $H(r)$ the

scale height profile that models the disc thickness, presuming $H(r) << r$ for a thin disc.

Considering hydrostatic equilibrium perpendicular to the disc plane and a simple relationship between the disc and surface temperatures, the sound speed can be written as $c_s = H(r)\Omega$, with Ω is the circular keplerian velocity [7]. Hence, the ν viscosity at a given distance r depends on rotation, with a linear dependency on the mass of the star M_* and on the flaring of the disc,

$$\nu(r) = \alpha \frac{c_s^2}{\Omega} = \alpha \Omega H^2(r). \tag{2}$$

Note that Magneto Rotational Instability (MRI) was a widely used candidate for modelling turbulence and angular moment transport, but MRI can be suppressed by non-ideal MHD. Other mechanisms such as outflows, gravitational instabilities or magnetic winds can also play a fundamental role in the evolution of the disc, but they do not exclude the viscous transport.

So, α-parametrisation can be seen as a mere (re)parametrisation of the viscosity, but also as a value that models the whole disc reflecting the different effectiveness of the different hidden processes.

A value of $\alpha = 0.01$ was typically used because it usually provides evolutionary time-scales in line with known properties of discs [5, 4]. Later on, values ranging from $\alpha = 0.1$ to 0.001 have been also used [1, 3, 7]. Nowadays, even lower values $\alpha = 10^{-4}$ can be found [2, 10], and these seems to better agree the observed discs [14, 15].

3 The photoevaporative wind

A simple 1D model can incorporate different radiation fields and be at the same time a convenient way for exploring the role of the different parameters. The photoevaporative wind will be different depending on the different heating radiation mechanisms. These winds can be dominated by EUV radiation, with energies from 13.6 eV to 0.1 keV, capable of ionising an Hydrogen atom. But also by fields dominated by X-rays radiation, with photons of energies ranging from 0.1 keV up to $1 - 2$ keV. These much energetic photons can penetrate large hydrogen columns but provide small heatings. Finally, one can also consider winds dominated by FUV radiation, embracing energies from 6 eV to 13.6 eV, capable of dissociating the H_2 molecule.

As a consequence, the wind term physics can be very complex. However, it can be included on the model as a simple mass sink term in the density surface evolution equation, in the form of numerical fits to the results coming from more complex simulations (as those from [11], [7] or [6]). The profiles corresponding to these results can be seen in the Fig. 1.

3.1 The progressive flattening of the disc

The flaring profile is a key parameter that defines the sound speed c_s profile, and, in turn, the temperature profile of the disc. The temperature depends on the amount of stellar radiation

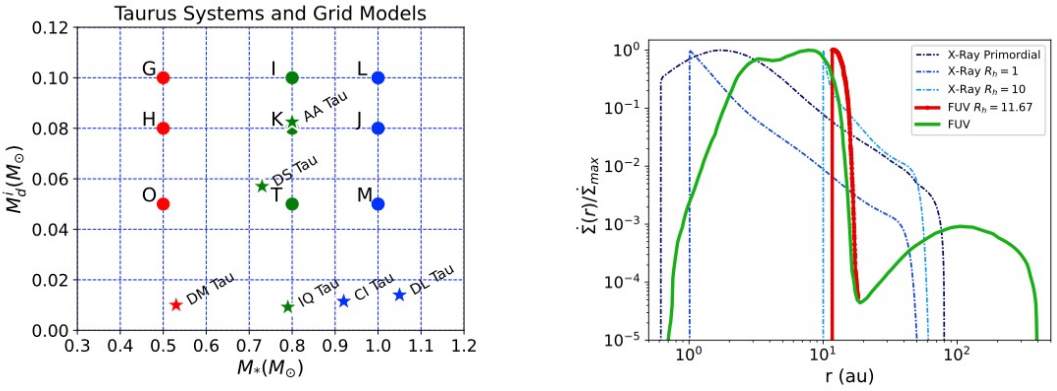

Figure 1: (left) The selected grid of discs models in the M_*–M_d^i plane. The initial disc masses M_d^i decrease as the discs evolve. Hence, these initial points move downwards in the diagram, approaching to the parameters observed in real Taurus systems. (right) Normalised photoevaporative wind mass losses corresponding to the FUV wind profiles described in [6] and the X-ray wind profiles from [11].

impacting the disc, which also rests on its geometry again. Hence, the resulting scale height $H(r)$ can follow an approximate power law dependence,

$$H(r) = \kappa\, r^h. \tag{3}$$

Even when it is customary to keep constant the flaring profile of the disc, it seems reasonable to consider that this flaring may change with time, with a progressive flattening of the disc as the age increases. Therefore, we will include in our simulations a changing profile for the flared disc, by decreasing the κ parameter in Equation 3 at given times.

4 Results

We have solved the evolution of the surface density derived from Equation 1, for different stellar masses and disc masses. We can observe in Fig. 2 that some features resembling the observed ring-like structures can be obtained with our simple photoevaporative models.

Further details and results can be seen in [15]. A progressive flattening of the disc seems to support the production of ring-like features at the observed ages. For certain viscosities, discs with large gaps and strong accretion rates, which have been linked to giant planet formation, can be also obtained.

However, our simple models do not reproduce in full all reference real systems. The produced features seem to be short-lived and some additional mechanism may be needed for carving faster the dents and create real gaps with proper lifetimes. This points to add further flattening laws and new winds evolution in a broader grid, and may be to extend the available wind efficiencies.

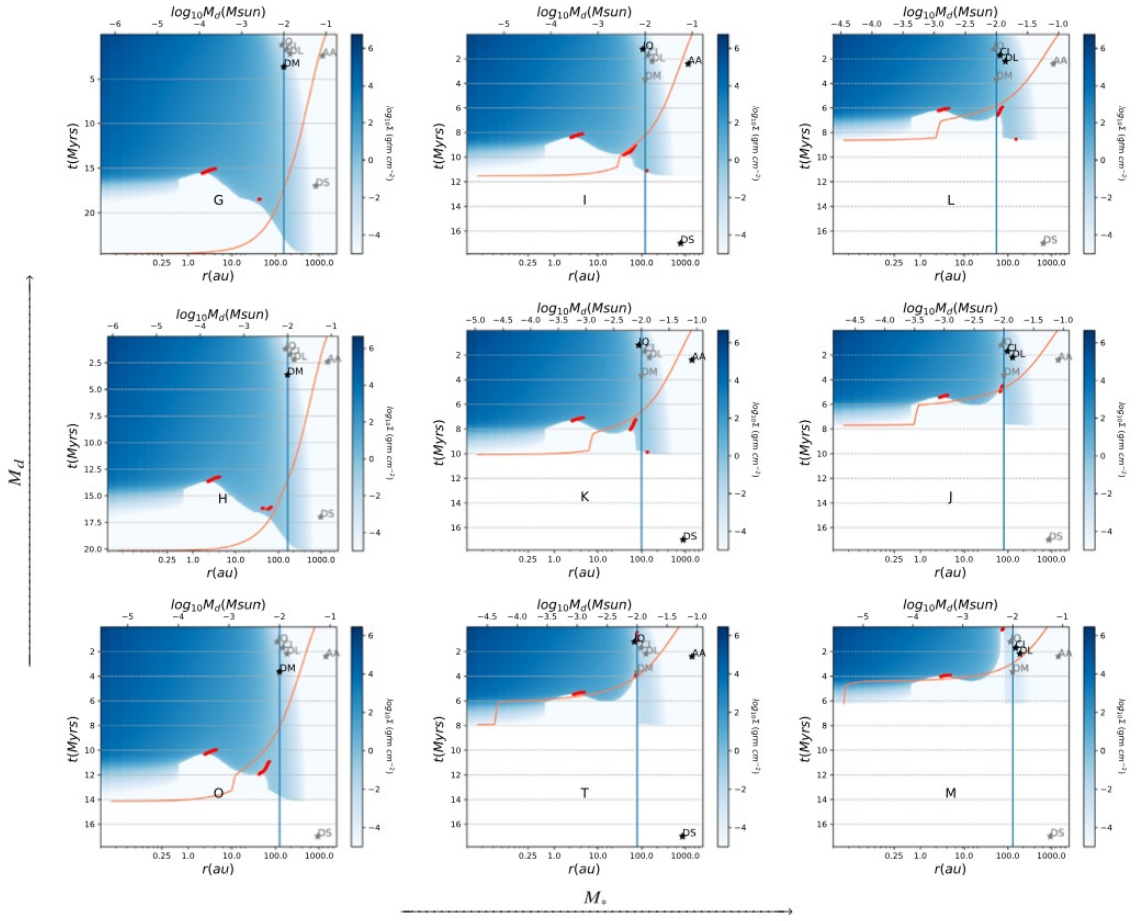

Figure 2: Evolution of the grid of models for a fiducial photoevaporation controlled by X-ray heating, efficiency factor=1.0, a viscosity value of $\alpha = 10^{-4}$ and a progressively flattened flaring profile. The surface density in blue gets lighter as the disc is eroded. The red points indicate local minima in the density profiles. The second dent can be carved at the same time or even at earlier times than the the inner dent. These two dents can produce ring-like features when exist at the same time. Sometimes, these two dents can be accompanied by a third outer dent. Some Taurus discs are also plotted for reference. They appear in black when their stellar masses are similar to the mass of the analysed synthetic model. Otherwise, they appear in grey.

Acknowledgments

The authors thank the Spanish Ministry of Economy, Industry and Competitiveness for grants ESP2015-68908-R and ESP2017-87813-R.

References

[1] Andrews, S.M., Wilner, D.J., Hughes, A.M., Qi, C., Dullemond, C.P., 2009, ApJ, 700, 1592.

[2] Ercolano, B., Jennings, J., Rosotti, G., Birnstiel, T., 2017, MNRAS, 472, 411.

[3] Gorti, U., Hollenbach, D., 2009, ApJ, 690, 1539.

[4] Hartmann L., Calvet, N., Gullbring, E., and D'Alessio, P., 1998, ApJ, 495, 385.

[5] Hawley, J.F., Balbus, S.A., 1995, PASA, 12, 159H.

[6] Jennings, J., Ercolano, B., and Rosotti, G.P., 2018, MNRAS, 477, 131.

[7] Jones, M.G., Pringle, J.E., Alexander, R.D., 2012, MNRAS, 419, 925.

[8] Kimura, S.S., Kunitomo, N., Takahashi, S.Z., 2016, MNRAS, 461, 2257.

[9] Lodato, G., Scardoni, Ch.E., Manara, C.F., Testi, L., 2017, MNRAS, 472, 4700.

[10] Martin R.G., Nixon, C.J., Pringle, J.E., Livio M., 2019, NewA, 70, 7M.

[11] Owen, J.E., Clarke, C.J. and Ercolano, B., 2012, MNRAS, 422, 1880.

[12] Shakura, N.I., Sundayev, R.A., 1973, A&A, 24, 337.

[13] Shakura, N.I., Sundayev, R.A., 1976, MNRAS, 175, 613.

[14] Vallejo, J.C., Gómez de Castro, A.I., 2018, APSS, 363, 246.

[15] Vallejo, J.C., Gómez de Castro, A.I., 2021, MNRAS, 508, 950.

Highlights of Spanish Astrophysics XI, Proceedings of the XV Scientific Meeting of the Spanish Astronomical Society held on September 4–9, 2022, in La Laguna, Spain. M. Manteiga, L. Bellot, P. Benavidez, A. de Lorenzo-Cáceres, M. A. Fuente, M. J. Martínez, M. Vázquez- Acosta, C. Dafonte (eds.), 2023

Here comes the GJ 486.

Caballero, José A.

Centro de Astrobiología, CSIC-INTA
caballero@cab.inta-csic.es

Abstract

At a distance of only 8.1 pc, GJ 486 b is the third closest transiting planet. The relatively bright, very weakly active, M-dwarf host star, its visibility from both Earth hemispheres, and the short orbital period and warm expected surface temperature make this planet one of the best targets for planet atmosphere emission and transit spectroscopy with *Webb* and future ground-based extremely large telescopes. Caballero et al. (2022) slightly improved the precision and accuracy of the planet mass and radius determination, with which they developed different planet interior and atmosphere scenarios. There are a few differences with respect to previous work that made this analysis unique. Instead of estimating the stellar radius from luminosity and model-dependent spectral synthesis, they directly measured the angular radius of the planet host star with MIRC-X at the CHARA Array. They reduced the input data error contribution by gathering extremely precise radial-velocity data collected by CARMENES and MAROON-X and transit data obtained by *TESS* and, presented there for the first time, *CHEOPS*. The selected joint radial-velocity and transit fit model with a Gaussian process was supported by an independent photometric monitoring with small and medium-size telescopes for determining the stellar rotation period. As a novelty in M dwarfs, they determined Mg, Si, V, Fe, Rb, Sr, and Zr abundances of the stellar host, which constrained two of the three considered planet interior scenarios. They also considered different planet atmosphere scenarios and their detectability with forthcoming *Webb* observations with NIRSpec and MIRI after taking into account different possibilities on composition and planet surface temperature and pressure. In the most probable combination of scenarios, GJ 486 b is a warm Earth-like planet of $R \sim 1.343\,R_\oplus$ and $M \sim 3.00\,M_\oplus$ with a relatively low-mass, metallic core surrounded by a silicate mantle with dissolved water, and an upper layer probably composed of a mixture of water steam and carbon dioxide.

1 Introduction

Instead of developing what is concisely summarised in the abstract just above or what is reported and discussed extensively in the discovery publication by Trifonov et al. (2021) [1] and the follow-up publication by Caballero et al. (2022) [2], here I just sum up the unpublished novelties on the rocky planet GJ 486 b (plotted with a black star symbol in Fig. 1)

in the last few months, for avoiding overlapping of forthcoming works. Environmentally-aware and busy readers may welcome this approach to avoid the never-ending repetition of content in conference proceedings and refereed papers.

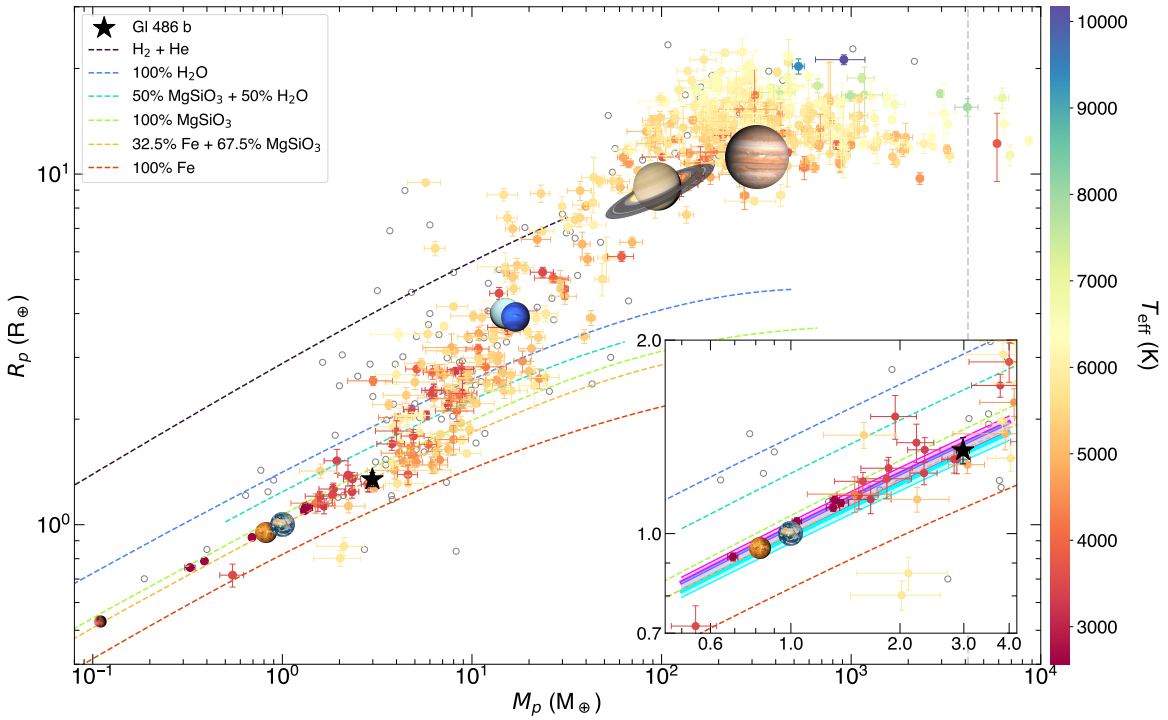

Figure 1: Mass–radius diagram of all transiting exoplanets with mass determination (from RV or transit time variations) known in Summer 2022, in comparison with the Solar System planets. Filled circles with error bars colour-coded by their host's $T_{\rm eff}$ are planets with mass and radius uncertainties of less than 30%, and open grey circles are the others. The filled black star is GJ 486 b. Dashed coloured curves are theoretical models, as specified in the legend. The Earth-like model is orange. The grey vertical dashed line is the deuterium burning mass limit at 13 $M_{\rm Jup}$ ('planet'-brown-dwarf boundary). The inset zooms in around the smallest planets and add mass-radius relationships informed by stellar abundances with median and 1σ error regions following nominal relative abundances of Fe, Mg, and Si of the host star without (pink) and with (cyan) empirical correction based on well-characterised super-Earths. The original figure, references, and details were provided by Caballero et al. (2022) [2].

2 What?

On the one hand, *TESS* revisited the star with its Camera 1 during Sector 50 observations between late March and late April 2022; these data are public. Besides, *CHEOPS* made three

additional visits in early March and early April 2022; these data have a one-year proprietary time (PI: J. A. Caballero). The early-April *CHEOPS* visit, simultaneous to *TESS* observations, will be very useful for direct spacecraft data comparison purposes; this is, however, a secondary objective. The new dataset, which virtually doubles the number of transits and enlarges the time baseline of the precise photometry by several orders of magnitude, is ideal for investigating transit time variations in the GJ 486 system. To date, previous searches (radial velocity, high resolution imaging, space astrometry) have, though, failed to find any additional planetary companion besides GJ 486 b [2]. As a bonus, together with the previously used CARMENES and MAROON-X radial velocities, the new precise photometry dataset will help further improving the stellar-to-planet radius ratio and other planetary parameters. All this analysis is being done by a team in Spain.

On the other hand, a team in the Netherlands is implementing an exhaustive planet modelling that includes both the structure, composition, and dynamics of the interior and a grid of global circulation models for different hypothetical atmospheres, while another team in Spain has proposed to use PIONIER at the ESO's Very Large Telescope Interferometer for covering the current observational gap in spatial frequency and, thus, determine a precise and accurate radius of the host star. New improved parameters of both the star (via interferometric data) and planet (via new *TESS* and *CHEOPS* data) will be excellent inputs for additional planet characterisation and modelisation works.

All this work in preparation is on time for the forthcoming publication of the analysis of the NIRSpec/*Webb* transmission spectra taken on 25 and 29 December 2022 with the filter F290LP, which are already available at the *Webb* archive (`jwst.esac.esa.int/archive`), and under analysis by a team in the USA. If you are interested in developing new projects on the GJ 486 planetary system on, for example, a wider grid of global circulation models with very different atmosphere compositions, structures, and dynamics, or the generation of magnetic fields in the liquid planet outer core, which may interact with the stellar magnetic field, feel free to contact the author of this proceeding.

3 Who?

Last but not least, the host star GJ 486 and the exoplanet GJ 486 b were one of the 20 star-planet pairs for which the International Astronomical Union offered all countries to name in the 2022 edition of the NameExoWorlds competition (`nameexoworlds.iau.org`). Other offered planetary systems pairs were, for example, GJ 1214, HD 95086, and WASP-69; all of them had, as well as GJ 486, been scheduled for observations by *Webb*.

In recognition of the United Nations Decade of Indigenous Languages (2022–2032), speakers of Indigenous languages were encouraged to propose names drawn from those languages. The Universidad del País Vasco/Euskal Herriko Unibertsitatea and the Centro de Astrobiología (CSIC-INTA) presented a proposal in Spain to name "Gar" and "Su" to the star GJ 486 and the planet GJ 486 b, respectively. In Basque[1], Gar means "flame", the luminous

[1]In Spain, in addition to Spanish, there are three co-official languages: Catalan/Valencian, Galician and Basque. All of them are Romance languages that evolved from Vulgar Latin, except for Euskara, which is a

gas coming from a burning object, while Su means "fire", a dual being (as it is good – it provides protection – but it can also be dangerous) as the selected planet. In Basque mythology, the fire of the hearth is the genie of the house and is asked for favours. Further details can be found at exoterrae.eu/gar+su. At the time of writing these lines, NameExoWorlds 2022 is in phase 2, namely national vetting process.

4 Why?

Finally, one may wonder why such a peculiar title for the proceeding of an oral contribution, "Here comes the GJ 486". Any reader with some musical rudiments will quickly realise of the reason when is told the titles of the other two contributions of the author in the same meeting: "A Day in the *LIFE*", on the *Large Interferometer For Exoplanets*, and "Radio Clásica's Longitud de Onda Club Band", the fifth item of the series "Music and astronomy". Actually, GJ 486 b has a soundtrack, which is the instrumental version of the CARMENES song[2] and that you can listen here.

Acknowledgments

I am in debt to Trifon Trifonov, Esther González-Álvarez, and all the coauthors of [1] and [2], Itziar Garate-Lopez and all the supporters of the gar+su NameExoWorlds 2022 proposal, and many other individuals with new research proposals on GJ 486, because without them this proceeding would not exist or would have been very different. I acknowledge financial support from the Agencia Estatal de Investigación 10.13039/501100011033 of the Ministerio de Ciencia e Innovación and the ERDF "A way of making Europe" through project PID2019-109522GB-C51.

References

[1] Trifonov, T., Caballero, J. A., Morales, J. C. et al. 2021, Science, 371, 1038

[2] Caballero, J. A., González-Álvarez, E., Brady, M. et al. 2022, A&A, 665, A120

unique linguistic case spoken in the north of the Iberian Peninsula and the south of France even before the arrival of the Indo-European languages. In fact, scientists have recently found a bronze piece with the oldest inscription in Basque, dating back to the 1st century BC.

[2]Contrary to what one might expect, it is not a song by the The Beatles, but by Antonio Arias and José A. Caballero.

Highlights of Spanish Astrophysics XI, Proceedings of the XV Scientific Meeting of the Spanish Astronomical Society held on September 4–9, 2022, in La Laguna, Spain. M. Manteiga, L. Bellot, P. Benavidez, A. de Lorenzo-Cáceres, M. A. Fuente, M. J. Martínez, M. Vázquez- Acosta, C. Dafonte (eds.), 2023

Mars Wind & Wave Mapping (MWWM) project: A global view of Martian atmosphere from Earth telescopes, Space missions and 3D climate models.

Cardesin-Moinelo, A.[1], Machado, P.[2], Brasil, F.[2], Martin, P.[1], and MWWM team (Silva, R., Riu, L., Grotheer, E., Breitfellner, M., Titov, D., Wilson, C., Gonzalez-Galindo, F., Gilli, G., Gondet, B., Spiga, A., Sanchez-Lavega, A., Hernandez-Bernal, J., Maattanen, A., Tirsch, D.)

[1] European Space and Astronomy Centre, Madrid, Spain
[2] Instituto de Astrofisica e Ciencias do Espaco, Lisboa, Portugal

Abstract

The Mars Wind & Wave Mapping project is an ESA-funded research activity with the objective of extending our current knowledge in the dynamics of Martian atmosphere, comparing remote sensing data from Mars Express (MEX) spacecraft, Earth telescopes and simulations of the Mars Global Climate Model (GCM) and mesoscale models. The expected outputs of this project are a map of wind velocities, based on Doppler measurements during the 2018 Global Dust Storm, and a database of atmospheric gravity waves.

1 Introduction

There is currently a considerable effort from the science community to study planetary atmospheres to understand the role of the climate change in planetary evolution. In particular for Mars, the climate history plays a key role to understand the conditions that could have allowed the presence of liquid water in the past and its consequences for comparative planetology and potential past life habitability. Nevertheless, the knowledge of the mechanisms dominating the planetary atmospheres is still limited. An understanding of the dominant factors and key elements controlling the atmospheric general circulation is a prerequisite for our understanding of terrestrial planets' variability and evolution.

2 Objectives

This new project aims to extend our current research activities in the dynamics of Martian atmosphere and compare data from Earth Telescopes and Space Missions with the Mars Global Climate Model (GCM) and mesoscale models. The proposal is mainly based on the

existing collaboration with IA Lisbon and their expertise in processing atmosphere dynamics data. The main two outputs of this project will be a map of wind velocities, based on Doppler measurements during the 2018 Global Dust Storm, and a database of atmospheric gravity waves that can be used to foster the science exchange between observations, global climate and mesoscale models.

3 Winds

Measuring winds on Mars is a challenge for remote observations but a global dust storm offers a unique opportunity to use an innovative technique, measuring the Doppler effect of solar Fraunhofer lines back-scattered on the Mars dust cloud. This innovative Doppler technique, never used on Mars before, has been developed by the research group at IA Lisbon and successfully implemented by retrieving winds at Venus cloud top region [7], producing the first ground-based direct mapping of Venus wind velocities. Although the Martian atmosphere is optically thinner, it is possible to adapt the Doppler method and retrieve wind velocities using the solar radiation back-scattered on the dust particles during a Global Dust Storm. The first ground observations using this technique were already performed as a Target of Opportunity proposal with the Very Large Telescope (VLT) UVES instrument in June/July 2018 [1], and coordinated with simultaneous MEX remote sensing measurements. The first efforts to retrieve a Martian wind velocity field have already demonstrated the proof of concept with promising results Figure 1 [8]. In this contribution we will describe the progress in the preparation of the first global map of Martian winds retrieved from Earth, measured at the altitude of the dust layer using the VLT/UVES data obtained during the past global dust storm in 2018.

4 Waves

The second part of this project is a characterisation of the Gravity Waves in the atmosphere of Mars. These waves have already been detected by MEX OMEGA instrument [9], [13], although there is still an important dataset of unexploited atmospheric observations [6] to be analysed. The second task (MWWM-T2) aims to build the first catalogue of atmospheric gravity waves and morphological parameters using Mars Express OMEGA data. Preliminary work has already started to validate the methodology Figure 2 [2] adapting the technique that was already used successfully for Venus [10],[11],[12]. This task will provide the main wave parameters: time, spatial coordinates, packet length/width, orientation and phase speed, to be analysed in correlation with mars topography, illumination conditions, local time and Mars seasonal climate variability.

5 Expected Results

Both winds and waves induce temporal and spatial variations in the atmosphere and the complete interpretation is only possible with the application of 3D climate models and con-

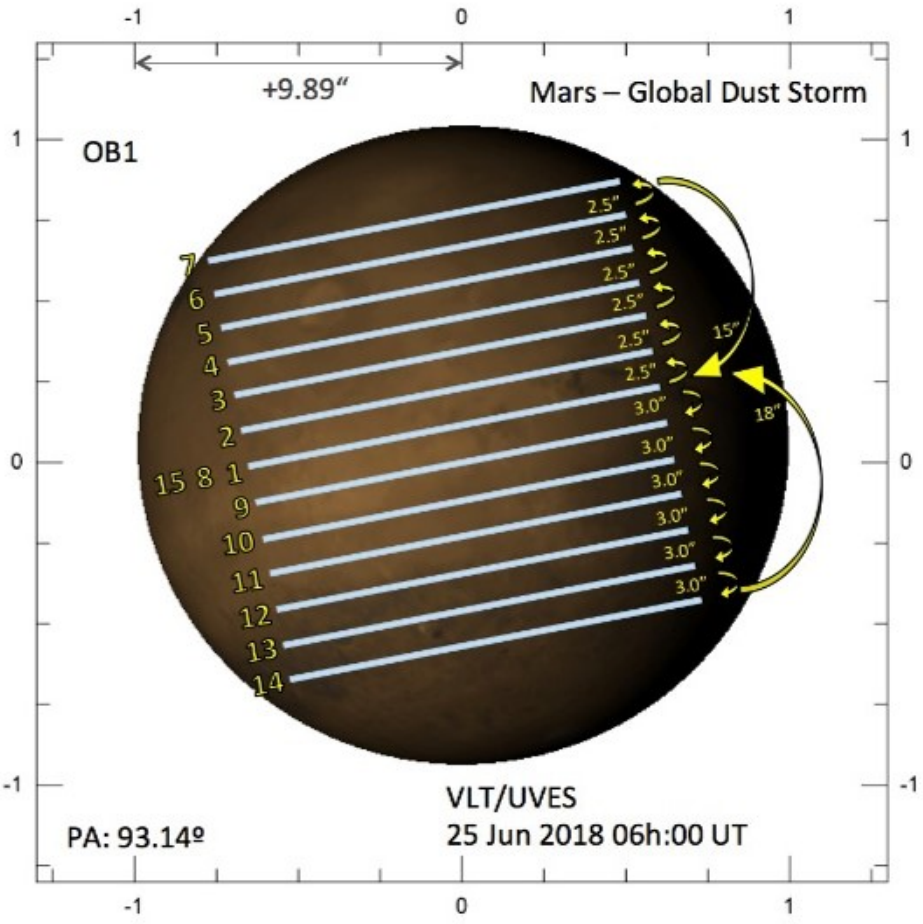

Figure 1: VLT/UVES Observations of Mars Global Dust Storm 2018. [8]

textual information. For this reason this project aims to cover an extensive science exchange with the experts that have analysed the contribution of winds and gravity waves in the Mars climate circulation [13], [4],[5], and strengthen the research collaboration promoting the use of observations performed from Earth and simultaneously from Mars Express and Trace Gas Orbiter [3].

6 Acknowledgments

We acknowledge support from ESA Faculty Science Exchange MWWM - Mars Wind and Wave Mapping project via ESA EXPRO RFP/3-17570/22/ES/CM and support from the Portuguese Fundacao Para a Ciencia e a Tecnologia (ref. PD/BD/128019/2016, ref. 2021.05455.BD. and ref. PTDC/FIS-AST/29942/2017) through national funds and by FEDER through COMPETE 2020 (ref. POCI-01-0145 FEDER-007672).

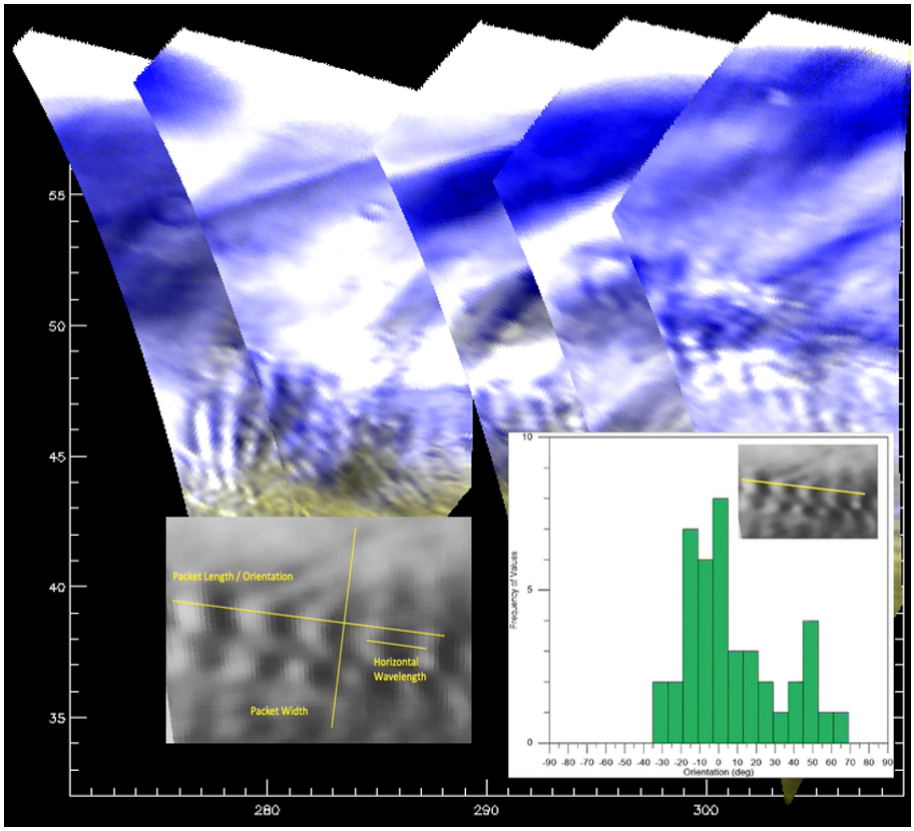

Figure 2: . Preliminary analysis of Gravity Waves [2]

References

[1] ESO VLT Observation Programme: Dust Storm on Mars, 2101.C-5029(A)

[2] Brasil, F., Machado, P., Gilli, G., et al. 2022, EGU General Assembly Conference Abstracts. doi:10.5194/egusphere-egu22-8087

[3] Cardesin-Moinelo, A., Geiger, B., Lacombe, G., et al. 2021, Icarus, 353, 113707. doi:10.1016/j.icarus.2020.113707

[4] Gonzalez-Galindo, F., Lopez-Valverde, M. A., Forget, F., et al. 2015, Journal of Geophysical Research (Planets), 120, 2020. doi:10.1002/2015JE004925

[5] Gilli, G., Forget, F., Spiga, A., et al. 2020, Journal of Geophysical Research (Planets), 125, e05873. doi:10.1029/2018JE005873

[6] Gondet, B. & Bibring, J.-P. 2018, European Planetary Science Congress. Vol. 12, EPSC2018-313

[7] Machado, P., Widemann, T., Peralta, J., et al. 2017, Icarus, 285, 8. doi:10.1016/j.icarus.2016.12.017

[8] Machado, P., Valido, H., Cardesin-Moinelo, A., et al. 2020, European Planetary Science Congress. doi:10.5194/epsc2020-221

[9] Määttänen, A., Montmessin, F., Gondet, B., et al. 2010, Icarus, 209, 452. doi:10.1016/j.icarus.2010.05.017

[10] Peralta, J., Hueso, R., Sánchez-Lavega, A., et al. 2008, Journal of Geophysical Research (Planets), 113, E00B18. doi:10.1029/2008JE003185

[11] Piccialli, A., Titov, D., Sanchez-Lavega, A., et al. 2014, Icarus, 227, 94. doi:10.1016/j.icarus.2013.09.012

[12] Silva, J. E., Machado, P., Peralta, J., et al. 2021, Astronomy & Astrophysics, 649, A34. doi:10.1051/0004-6361/202040193

[13] Spiga, A., González-Galindo, F., López-Valverde, M.-Á., et al. 2012, Geophysical Research Letters, 39, L02201. doi:10.1029/2011GL050343

Highlights of Spanish Astrophysics XI, Proceedings of the XV Scientific Meeting of the Spanish Astronomical Society held on September 4–9, 2022, in La Laguna, Spain. M. Manteiga, L. Bellot, P. Benavidez, A. de Lorenzo-Cáceres, M. A. Fuente, M. J. Martínez, M. Vázquez- Acosta, C. Dafonte (eds.), 2023

Martian CO profiles from the solar occultation experiment of NOMAD on board TGO.

Modak, A.[1], López-Valverde, M.A.[1], Brines, A.[1], Stolzenbach, A.[1], Funke, B.[1], González-Galindo, F.[1], Liuzzi, G.[2,5] Aoki, S.[2,3] Thomas, I.[3] Villanueva, G.[2] Erwin, J.[3] Lopez-Moreno, J.J. [1] Yoshida, N.[6] Grabowski, U.[7] Forget, F.[8] Daerden, F.[3] Ristic, B,[3] Belucci, G,[9] Patel, M.[10] Trompet, L.[3], and Vandaele, A.C.[3]

[1]Instituto de Astrofísica de Andalucia, Granada, Spain
[2]NASA Goddard Space Flight Center, USA
[3]Belgian Royal Institute for Space Aeronomy, Brussels, Belgium
[4]Japan Aerospace Exploration Agency (JAXA), Japan
[5]American University, Washington DC, USA
[6]Graduate School of Science, Tohoku University, Sendai, Japan
[7]Karlsruhe Institute of Technology, Institute of Meteorology and Climate Research, Karlsruhe, Germany
[8]Laboratoire de Météorologie Dynamique, IPSL, Paris, France
[9]Institute for Space Astrophysics and Planetology, Italy
[10]Open University, Milton Keynes, UK

Abstract

Carbon monoxide is one of the important minor species in the Martian atmosphere due to its role in the photochemical stability of the CO_2 atmosphere and can also be used as a dynamical tracer. The SO spectrometer onboard the Trace Gas Orbiter (TGO) scans the Martian limb in the infrared provides transmittances with fine vertical sampling ($\sim$ 1km). In the spectral region, the sounding of CO is found to be reliable due to its strong and well separated absorption lines. Here, we present the retrieval scheme for CO from the solar occultation observation. Our scheme obtains density profiles up to 100 km with a vertical resolution better than 5km and errors below 15%. The observations for the last two seasons of Mars Year 34 (MY34, April 2018 - March 2019) are analyzed here. We found important results such as a strong depletion of CO density during the global dust storm (GDS) and a clear dynamical influence of global Hadley circulation on the CO distribution.

1 Introduction

Untill the arrival of TGO, detailed systematic mapping of the Martian CO density and its variation in the vertical was essentially absent. The instrument NOMAD (Nadir and Occul-

tation for MArs Discovery) and ACS (Atmospheric Chemistry Suite) have proved themselves as successful instruments in terms of measuring atmospheric trace gases. The CO retrieved from the mid-infrared (MIR) channel of ACS showed a depletion in CO density during the global dust storm (GDS) of MY 34 [13]. A detailed quantitative comparison study based on the retrieved profiles from the ACS MIR, NIR, and TIRVIM can be found in [3]. Here, we present vertical profiles of CO retrieved from the measurements recorded by NOMAD solar occultation (SO) for the first year of TGO observations from April 2018 to March 2019, for the first time. This covers the last two seasons of MY 34 with fine latitudinal coverage. An extended version of this work can be found in a recently submitted manuscript [12].

2 The NOMAD Solar Occultation Channel

NOMAD is a suite of three spectrometers SO (Solar Occultation Channel), LNO(Limb and Nadir Occultation) and UVIS(The Ultraviolet and Visible Spectrometer) [16] onboard TGO. In this study, we only have used the SO observations. The SO spectrometer operates in the spectral range of 2.2-4.3μ m with a nominal resolving power $\sim$ 20,000. The spectrometer is primarily composed of an echelle grating in Littrow configuration which means the incident, the reflected and the blaze angles are equal. The other important components of the spectrometer are the detector, parabolic mirrors, and the Acousto Optical Tunable Filter (AOTF). The AOTF, controlled by radio frequency, works as a bandpass filter and should ideally, allow only one selected diffraction order to fall onto the detector. In practice, AOTF introduces contamination from the adjacent diffraction orders due to which we only process the spectra in selected microwindows (MWs)(see [12] for details).

The components of the SO spectrometer such as the detector, the AOTF, and the grating are characterized by numerical parametric functions. These functions are respectively, the Instrumental Line Shape (ILS), AOTF transfer function, and the blaze function. The blaze function is taken from [8] and the ILS and AOTF are determined by our team in collaboration with other NOMAD teams which is described in [17]. The AOTF transfer function has been further finetuned by our retrieval method as described in [12]. These parameters are essential for theoretical simulation of the SO spectra and have been convolved within forward model called KOPRA(Karlsruhe Optimized and Precise Radiative transfer Algorithm)[14] to determine the incoming solar radiation received by the spectrometer. Both the preprocessing and the inversion which are described next make use of the line-by-line forward model KOPRA.

3 Preprocessing and Inversion

The SO spectra used for this study are Level 1 calibrated data which provides atmospheric transmittances along with the measurement noises at all altitudes in every scan or orbit. The left panel of Figure 1 shows an example of these spectra for a given scan. The spectra clearly suffer from several residual calibration effects like spectral bending and shift. As an initial step, we clean these calibration issues before feeding the spectra into our retrieval scheme. We call this internal step preprocessing. The preprocessing is described in detail in [9, 1, 12].

The right panel of Figure 1 shows the cleaned/preprocessed spectra which are corrected for the spectral bending and the spectral shift.

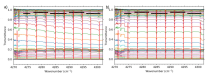

Figure 1: Example of our cleaning method applied to diffraction order 190 in one specific scan. Panel (a), all the original spectra (Level 1 calibrated transmittances) taken in this scan, showing clear bending effects and spectral shifts. Panel (b), spectra after cleaning.

Here we describe, in brief, the working principle of our retrieval scheme managed by a Retrieval Control Program (RCP) which performs a global fit (spectra at all altitudes) iteratively. The preprocessing and the retrieval scheme are common to our group targetting other atmospheric quantities such as temperature [10], water vapor [2], and aerosols [15]. The RCP runs KOPRA iteratively keeping the CO, continuum, and spectral shift as free parameters and compares the simulated spectra with the cleaned measured spectra until the best fit is obtained. The continuum is simulated by a spectrally constant transmittance level, adjusted to account for the impact of aerosol absorption. The goodness of our fit is characterized by $\boldsymbol{\chi^2}$ value obtained from the global fit method. For a more detailed description of this retrieval scheme the reader should refer to [12].

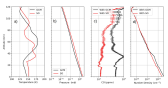

Figure 2: The effect of the reference thermal structure on the retrieved CO.

Retrieved CO values are highly dependent on the *a priori* temperatures [7]. To quantify the effect of temperature, we use simulated and retrieved climatologies[9] in the example depicted in Figure2. Figure2 shows two sets of atmospheric quantities; pressures, temperatures, mixing ratios, and number densities. Pressures and temperatures are referring to the apriori climatologies while the mixing ratios and the number densities are the results of the retrievals with those climatologies. The black curves are corresponding to the GCM scenario while the red curves are to the retrieval with SO T/P. The differences in CO number densities and the mixing ratios are indicating the sensitivity of CO retrievals on the apriori climatologies. This demonstrates that it is very important to use realistic temperatures profiles from a previous inversion from the same scan.

4 CO profiles and Variability

Above 60 km CO is produced by the photolysis of the CO_2 and the variability in these mesospheric altitudes is dominated by the production and atmospheric circulation while the lower atmosphere (below 60 km) is dominated by the loss of CO[6, 4, 11]. This inspires us to describe the CO variability of these two altitude regions separately with the help of an arbitrary marker fixed at the orange iso contour representing a CO VMR value of 2500 ppm (see Figure 3). There are two different seasons where the upper atmospheric CO distribution reflects the Martian dynamical behavior. During the northern autumn equinox (L_S = 160° - 180°) when the two Hadley cells extend from the equator to the high latitudes over both the hemispheres, CO enriched air from the low latitude regions most likely to downwell over the high latitude regions. Thus the increase in the CO mixing ratio is observed over the high latitudes during this period. During the southern soltice in the period $L_S \sim 280°$, the reference orange contour seems to reach down to altitudes near 60 km over the northern hemisphere (NH) whilst over the southern hemisphere (SH), this contour seems to retract towards altitudes above 80 km. This kind of upper atmospheric CO distribution points towards an interhemispheric circulation from SH to NH. The behavior of CO distribution in the lower atmosphere is mostly controlled by its loss. The loss is apparent during the onset of the GDS when CO is depleted due to the rise in water content of the atmosphere. This loss again becomes dominant during the southern summer but in this period the depletion might be due to a combined effect of the release of water vapor and CO_2 from the southern polar cap due to their annual sublimation. The release of CO_2 increases the total atmospheric mass thus depleting the CO mixing ratio.

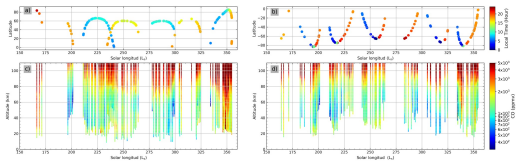

Figure 3: All CO profiles retrieved for this study. The upper panels ((a) and (b)) show the L_S-latitude distribution of the dataset used, with the colors on scale indicating the localtime. The bottom panels show L_S-altitude distribution of the CO profiles corresponding to the location shown in the top panels.

Figure 4 shows the latitudinal distribution of the CO profiles for small L_S periods. The left-hand panels of the Figure 4 show the retrieved CO distribution for fixed L_S periods corresponding to the northern equinox and southern summer while the right-hand panels

(panels (b),(d),(f) & (h)) show the corresponding CO distribution from the GCM simulations. The GCM simulated CO distributions are shown in order to illustrate the departure from apriori and to predict possible dynamical effects. During the northern equinox, the Martian dynamics is dominated by the two Hadley cells extending from the equatorial regions to the high latitude regions. The SO observations, in panel (a) suggest an increase in the low altitude CO abundance over high latitude due to the hemispheric Hadley cells which are also depicted in panel (b). At the beginning of the southern summer(panels (c) & (d)), there seems to be an increase in CO density in the upper altitudes which is probably a result of the increased photodissociation due to the increased solar insolation. The next panel (e) shows a globally developed interhemispheric Hadley cell which is not apparent in the simulation panel (f). According to our results, and despite the patchy maps obtained, it seems that the Hadley cell originates over the southern latitude $> 40°$S and downwells over the 60°N.

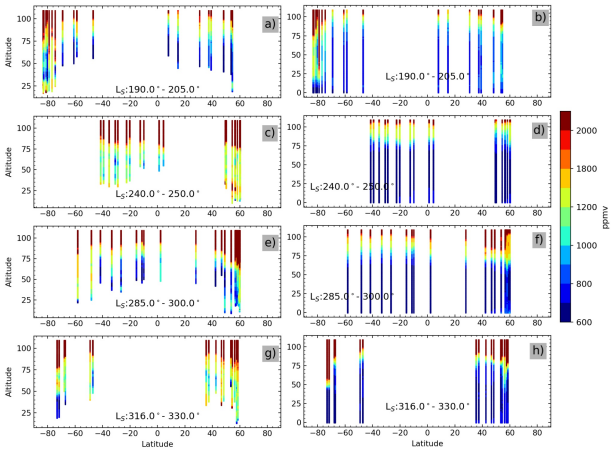

Figure 4: Latitudinal distribution of the retrieved, on the left panels ((a), (c), (e), & (g)) and GCM-simulated CO profiles on the right panels ((b),(d),(f), & (h)) Each panel corresponds to a fixed L_S period.

Acknowledgments

The IAA/CSIC team acknowledges financial support from the State Agency for Research of the Spanish MCIU through the 'Center of Excellence Severo Ochoa' award for the Instituto de Astrofsica de Andaluca (SEV-2017-0709) and funding by grant PGC2018-101836-B-100 (MCIU/AEI/FEDER, EU) and PID2019-110689RB-I00/AEI/10.13039/501100011033 Grant PRE2019-088355 funded by MCIN/AEI/ 10.13039/501100011033 and by 'ESF Investing in your future'. F.G.G. is funded by the Spanish Ministerio de Ciencia, Innovacion y Universidades, the Agencia Estatal de Investigacion and EC FEDER funds under project RTI2018-100920-J-I00.

References

[1] Brines, A., López-Valverde, M. A., Stolzenbach, A., Modak, A., Funke, B., Galindo, F. G., ... & Vandaele, A. C., 2022, JGR Planets, e2022JE007273

[2] Brines, A., López-Valverde, M. A., Stolzenbach, A., Modak, A., Funke, B., Galindo, F. G., ... & Bellucci, G., 2022, In Seventh International Workshop on the Mars Atmosphere: Modelling and Observations, (p. 2402)

[3] Fedorova, A., Trokhimovskiy, A., Lefèvre, F., Olsen, K. S., Korablev, O.,Montmessin, F., . . . others, 2022, JGR Planets, e2022JE007195

[4] González-Galindo, F., Forget, F., López-Valverde, M., Angelats i Coll, M., & Millour, 2009, JGR Planets, 114(E4)

[5] Gordon, I. E., Rothman, L. S., Hill, C., Kochanov, R. V., Tan, Y., Bernath, P. F.,. . . others, 2017, JQSRT, 203 , 3–69

[6] Krasnopolsky, V. A., 1995, JGR Planets, 100 (E2), 3263–3276

[7] Krasnopolsky, V. A., 2003, JGR, Planets, 108 (E2)

[8] Liuzzi, G., Villanueva, G. L., Mumma, M. J., Smith, M. D., Daerden, F., Ristic, B., . . . others, 2019, Icarus, 321 , 671–690

[9] López-Valverde, M.-A., Funke, B., Brines, A., Stolzenbach, A., Modak, A., Hill, B., . . . others 2022, JGR: Planets, e2022JE007278

[10] López-Valverde, M. A., Funke, B., Brines, A., Modak, A., Stolzenbach, A., Gonzalez-Galindo, F., ... & Vandaele, A. C., 2022, In Seventh International Workshop on the Mars Atmosphere: Modelling and Observations, (p. 1406)

[11] Modak, A., Sheel, V., & Lefèvre, F., 2020, PSS, 181

[12] Modak, A., López-Valverde, M. A., Funke, B., Brines, A., Stolzenbach, A., Gonzalez-Galindo, F., & others, 2022, JGR Planets, submitted

[13] Olsen, K., Lefèvre, F., Montmessin, F., Fedorova, A., Trokhimovskiy, A., Baggio, L., & others, 2021, Nature, Geoscience, 14(2), 67–71

[14] Stiller, G. P., 2000

[15] Stolzenbach, A., Lopez Valverde, M. A., Brines, A., Modak, A., Funke, B., Gonzalez-Galindo, F., ... & Aoki, S., 2022, In Seventh International Workshop on the Mars Atmosphere: Modelling and Observations, (p. 2206)

[16] Vandaele, A. C., Lopez-Moreno, J.-J., Patel, M. R., Bellucci, G., Daerden, F., Ristic,B., . . . others, 2018,Space Science Reviews, 214 (5), 1–47

[17] Villanueva, G. L., Liuzzi, G., Aoki, S., Stone, S. W., Brines, A., Thomas, I. R., . . .others, 2022 Geophysical Research Letters, 49 (12), e2022GL098161

Highlights of Spanish Astrophysics XI, Proceedings of the XV Scientific Meeting of the Spanish Astronomical Society held on September 4–9, 2022, in La Laguna, Spain. M. Manteiga, L. Bellot, P. Benavidez, A. de Lorenzo-Cáceres, M. A. Fuente, M. J. Martínez, M. Vázquez- Acosta, C. Dafonte (eds.), 2023

The KOBE experiment - `KOBEsim`: improving RV detection through efficient scheduling.

O. Balsalobre-Ruza[1], J. Lillo-Box[1], and A. Berihuete[2]

[1] Centro de Astrobiología (CAB), CSIC-INTA, Camino Bajo del Castillo s/n, 28692, Villanueva de la Cañada, Madrid, Spain
[2] Depto. Estadística e Investigación Operativa, Universidad de Cádiz, Avda. República Saharaui s/n, 11510 Puerto Real, Cádiz, Spain

Abstract

At present, detecting new rocky planets within the habitable zone and the radial velocity follow-up of transiting candidates are priority objectives of the exoplanetary field. Both, require a great effort including high-precision instruments and state-of-the-art analysis techniques. Additionally, a proper observing strategy is crucial to ensure the effectiveness of the observations, avoiding unnecessary measurements that waste invaluable telescope time. In this talk, we present the `KOBEsim` algorithm, a Bayesian-based strategy for the detection of planets in radial velocity surveys. It is developed within the KOBE experiment, aspiring at maximizing the detection of potential habitable exoplanets orbiting late K-dwarfs. The algorithm uses the first data obtained for a given star to choose a target orbital period (usually the highest power periodicity) and uses Bayesian inference to propose the optimum next observing date, thus accelerating the detection/rejection of such period. This new approach has demonstrated to improve the detection efficiency in comparison with a conventional strategy of monotonic cadence, reaching a detection in ∼50% less observations and timespan. `KOBEsim` has the potential to save expensive telescope time in current and upcoming instruments, and to allow the detection of light planets further away from their host star in reasonable timespans.

1 Introduction

Over the last decades, exoplanetary exploration has been focused on filling the census of exoplanet properties. Currently, the number of confirmed planets according to the NASA Exoplanet Archive overtakes the figure of 5200 [1]. The reason for this rush is that we need statistics. Only if we have a representative sample of the planet diversity we could create reliable models, for instance on planet formation, migrations, or dependencies with the host star properties. But it is undeniable that the planets that most yearn to detect are potentially habitable. Finding life beyond the Solar System is what guides the actions of the field.

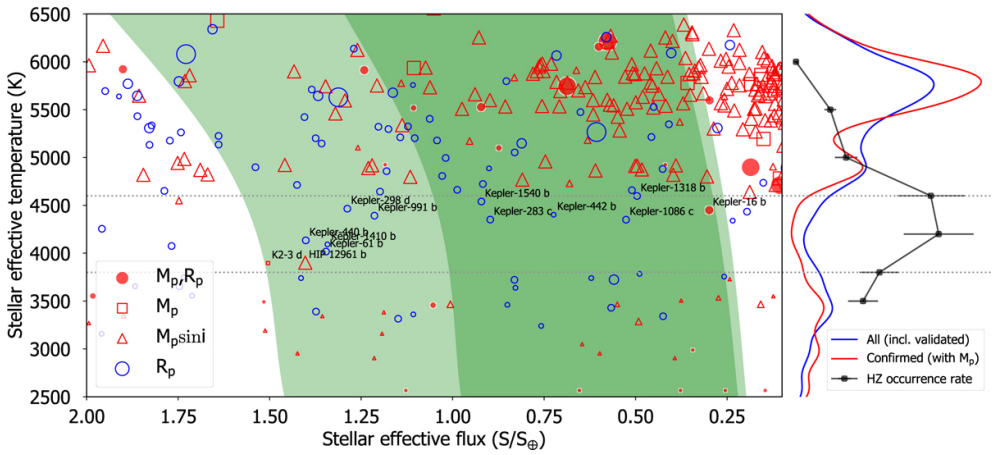

Figure 1: Exoplanet population within the HZ for different stellar types. Source [4].

2 The KOBE experiment

The majority of the efforts dedicated to searching for habitable planets have preferred two spectral types as host stars: M and G-dwarfs. The M-dwarfs are an interesting target from the detectability point of view. Since they are cold and less massive stars, their habitable zone (HZ) is closer and thus inducing higher radial velocity (RV) semiamplitudes and requiring less time to infer their presence. As an example, the high-resolution spectrograph CARMENES [2] is optimized to find planets orbiting M-dwarf stars. In parallel, since the only planet that we are certain to be habitable is the Earth, G-dwarfs (solar-type stars) seem the perfect target from an astrobiological point of view. One of the most fruitful missions, Kepler, was specifically designed for finding Earth-type worlds around solar-type stars [3].

Nonetheless, we are missing what might be the perfect target. Putting the focus on M and G stars has resulted in an observational bias around K-dwarfs (see Fig. 1). This spectral type is in the middle of the other two, thus finding a trade-off between habitability and detectability. Moreover, theoretical studies have shown that the highest occurrence rate of habitable planets is around the quiet late-K-dwarfs [15]. These reasons have inspired to start the first RV survey devoted specifically to late-type K-dwarfs. The K-dwarfs Orbited By habitable Exoplanets (KOBE) [4] experiment, a legacy program of the Calar Alto Observatory (CAHA; Almería, Spain), making use of CARMENES at the 3.5 m telescope. Its observations began in January 2021 and will be monitoring 50 late K-dwarf stars over five consecutive semesters.

The aim of KOBE is to detect a handful of habitable planets around K-type stars to ease the paucity. Reaching such an ambitious goal requires an observational strategy designed accordingly to the needs. `KOBEsim` [5] is an open-source algorithm written in Python language that we have developed to make more efficient the detection of planets in blind-RV surveys.

3 Observational strategy of KOBEsim

The proposed observational strategy consists of two steps. First, the star is monitored with the usual survey strategy until the periodogram shows a predominant periodicity ($P_{\rm peak}$). For example, a conventional strategy would be following a monotonic cadence that consists of gathering data every N days. Second, $P_{\rm peak}$ is targeted by the KOBEsim algorithm to speed up the confirmation or rejection of a planetary origin. The algorithm uses the prior knowledge (the observations gathered so far) to predict future measurements and makes a ranking of the dates available to observe the target again. The criterion for the ranking is based on the expected knowledge gain. In the following sections, we see in more detail the method.

3.1 Statistical framework

The mathematical tool we use is the Bayes factor. Basically, it compares two models to assess from which one is more likely that our data come[1]. We compute this quantity by comparing 1) the null hypothesis in which we assume there is no planet in the system (H_0), and 2) a 1-planet model orbiting with a periodicity near to $P_{\rm peak}$ (H_1). The Bayes factor is frequently used in planetary searches to claim a detection when it is higher than a threshold [6], [7], [8]. In our case, we opt for a conservative criterion considering a detection at $\ln(B_{10}) > 6$ [9].

3.2 Code methodology

The algorithm is composed of three steps: estimation of the orbital parameters, simulation of the next RV measurement at different orbital phases, and selection of the optimum observing date according to the expected increase of the Bayes factor.

1. **Parameter inference and evidence of the models:** In order to infer the orbital parameters from the observations, KOBEsim explores the parameter space and samples the posterior distribution by using the Markov chain Monte Carlo (MCMC) affine invariant ensemble sampler emcee [12]. The model used for the 1-planet hypothesis is a single Keplerian from the python module RadVel [13], meanwhile for the null-hypothesis the RV takes a constant value equal to the systemic velocity. Next, it calculates the Bayes factor metric employing the bayev [14] code to quantify how much evidence we have with the current observations on the existence of the planet at the selected period.

2. **Simulation of the future dates:** To find the candidate dates we divide the period under study into a total of $N_{\rm phases}$ orbital sub-phases. We choose the next assigned date from the schedule at the telescope that matches each sub-phase. Next, from the posterior probability distributions inferred through the MCMC algorithm in the previous step, KOBEsim predicts the RVs at each potential observing date. Running again emcee and bayev over each of the datasets (our already gathered RV plus one additional datapoint corresponding to each predicted RV at a proposed date), we end

[1] B_{10} is the notation for a Bayes factor comparing a hypothesis H_1 over another H_0.

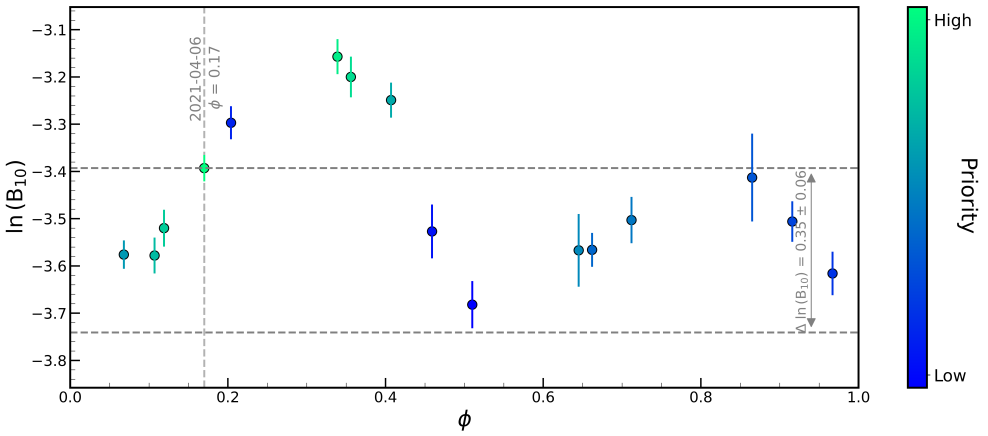

Figure 2: KOBEsim output figure. Predicted Bayes factor for each candidate date (orbital phase). Source [5].

up with an estimation of the expected increase in the Bayes factor ($\Delta \ln(B_{10})$) for each of the proposed future dates.

3. **Ranking of the candidate observing dates:** `KOBEsim` sorts the tested dates according to the Bayes factor giving the maximum priority to the highest $\Delta \ln(B_{10})$. However, the largest $\ln(B_{10})$ increase may occur at a very distant date, which is against the efficiency of the observations. To prevent this situation, we introduce a weight to the increase of the Bayes factor with the shape of a density function of a beta distribution. Hence, the ranking is done according to the Bayes factor weighted with this function to find a trade-off between the number of observations and timespan. In Fig. 2 we show an example of the output figure of `KOBEsim`. Additionally, it delivers a table with these results sorted by the priority of the the candidate dates.

4 `KOBEsim` efficiency test

In this section, we show a test with simulated data to quantify the efficiency improvement when using this strategy. We use ten mock RVs for a $5\,M_\oplus$ planet orbiting within the HZ of a late-K-dwarf with a 59-days period, corresponding to an RV semiamplitude of $1.2\,\mathrm{m\,s^{-1}}$. We estimate how long it would take to detect this planet following different strategies: with a monotonic cadence (MC), following the recommendations of `KOBEsim` (`K`) every new observation, and `KOBEsim` using the beta function ($\mathtt{K}_\beta$, see step 3 of Sect. 3.2).

In Fig. 3 we show the evolution of the Bayes factor (y-axis) as a function of the number of observations (x-axis) for each strategy (color-code). From a quick visual inspection, it is easy to perceive that the number of observations is greatly reduced when using the algorithm in comparison with the MC strategy. It is also highlighting the timespan (see legend at

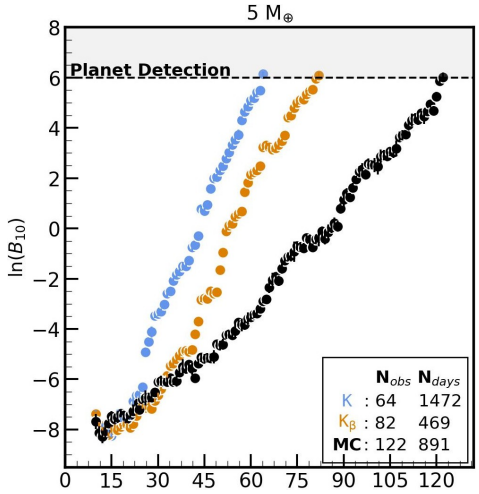

Figure 3: Prediction in the evolution of the logarithm of the Bayes factor for a 5 $M_\oplus$ simulated planet. Source [5].

the right bottom of Fig. 3) is only improved when using the $\mathtt{K}_\beta$ strategy, thus finding the optimum trade-off in sake of efficiency. The improvement is, therefore, a 33 % in the number of observations and a 47 % in timespan.

5 Conclusions

The biggest conclusion is that there is room for improving the efficiency of observations. Reducing the observational time required to achieve our scientific goals means being capable of including additional targets or even achieving goals that otherwise would be inaccessible. In particular, our approach demonstrates speeding up detections up to a 50 % in both number of observations and timespan. The more challenging the target is, the higher the efficiency gain when using `KOBEsim`. Therefore, its use could be decisive to detect rocky planets within the HZ in reasonable timespans.

GTO programs can be highly benefited from the use of this algorithm since they enjoy wider freedom in their schedule. An opportunity for saving time and favor the detection of the most elusive planets for the upcoming generation of instruments such as HARPS3 [16] or NIRPS [17]. We want to note that, even designed for blind-search surveys, it also can be highly useful in the RV follow-up of transiting candidates since the orbital period is clear since the very beginning of the observations. Furthermore, by customizing the code, one could optimize other problems such as discerning between competing periodicities, or the number of planets in the system. Indeed, the strategy could be used to schedule the observation of time series in any other field than exoplanets just by modifying the models.

Acknowledgments

We want to thank to all KOBE team members, which includes (apart from the authors) N. C. Santos, A. Santerne, A. M. Silva, D. Barrado, J. Faria, A. Castro-González, M. Morales-Calderón, A. Saavedra, E. Marfil, S. G. Sousa, V. Adibekyan, S. C. C. Barros, E. Delgado-Mena, N. Huélamo, M. Deleuil, O. D. S. Demangeon, P. Figueira, and S. Grouffal.

References

[1] Akeson, R. L., Chen, X., Ciardi, D., et al. 2013, Publications of the Astronomical Society of the Pacific, 125, 989–999

[2] Quirrenbach, A., CARMENES Consortium, Amado, P. J., et al. 2020, in Society of Photo-Optical Instrumentation Engineers (SPIE) Conference Series, Vol. 11447, Society of Photo-Optical Instrumentation Engineers (SPIE) Confer- ence Series, 114473C

[3] Borucki, W. J., Koch, D., Basri, G., et al. 2010, Science, 327, 977

[4] Lillo-Box, J., Santos, N. C., Santerne, A., et al. 2022, Astronomy & Astrophysics, 667, A102

[5] Balsalobre-Ruza, O., Lillo-Box, J., Berihuete, A., et al. 2022, A&A, accepted [arXiv:2210.11207]

[6] Lillo-Box, J., Figueira, P., Leleu, A., et al. 2020, A&A, 642, A12

[7] Mortier, A., Zapatero Osorio, M. R., Malavolta, L., et al. 2020, MNRAS, 499, 5004

[8] Faria, J. P., Suárez Mascareño, A., Figueira, P., et al. 2022, A&A, 658, A115

[9] Jeffreys, H. 1961, 3rd Edition, Clarendon Press, Oxford

[10] Mackay, D. J. C. 2003, Information Theory, Inference and Learning Algorithms Mayor, M. & Queloz, D. 1995, Nature, 378, 355

[11] Thrane, E. & Talbot, C. 2019, PASA, 36, e010

[12] Foreman-Mackey, D., Conley, A., Meierjurgen Farr, W., et al. 2013, emcee: The MCMC Hammer

[13] Fulton, B. J., Petigura, E. A., Blunt, S., & Sinukoff, E. 2018, PASP, 130, 044504

[14] Díaz, R. F., Ségransan, D., Udry, S., et al. 2016, A&A, 585, A134

[15] Kunimoto, M., & Matthews, J. M. 2020, AJ, 159, 248

[16] Thompson, S. J., Queloz, D., Baraffe, I., et al. 2016, in Society of Photo-Optical Instrumentation Engineers (SPIE) Conference Series, Vol. 9908, Ground- based and Airborne Instrumentation for Astronomy VI, ed. C. J. Evans, L. Simard, & H. Takami, 99086F

[17] Wildi, F., Blind, N., Reshetov, V., et al. 2017, in Society of Photo-Optical Instrumentation Engineers (SPIE) Conference Series, Vol. 10400, Society of Photo-Optical Instrumentation Engineers (SPIE) Conference Series, 1040018

Highlights of Spanish Astrophysics XI, Proceedings of the XV Scientific Meeting of the Spanish Astronomical Society held on September 4–9, 2022, in La Laguna, Spain. M. Manteiga, L. Bellot, P. Benavidez, A. de Lorenzo-Cáceres, M. A. Fuente, M. J. Martínez, M. Vázquez- Acosta, C. Dafonte (eds.), 2023

The search for gas in debris disks: ALMA detection of CO gas in HD 36546.

Isabel Rebollido,[1] Álvaro Ribas[2], Itziar de Gregorio-Monsalvo[2], Eva Villaver[3], Benjamín Montesinos[3], Christine Chen[1], Héctor Canovas[4], Thomas Henning[5], Attila Moór[6], Marshall Perrin[1], Pablo Rivière-Marichalar[7], and and Carlos Eiroa[8]

[1]Space Telescope Science Institute, 3700 San Martin Drive, Baltimore, MD 21218, USA
[2]European Southern Observatory (ESO), Alonso de Córdova 3107, Vitacura, Casilla 19001,Santiago de Chile,Chile
[3] Centro de Astrobiología (CAB, CSIC-INTA), ESAC Campus Camino Bajo del Castillo, s/n, Villanueva de la Cañada, 28692 Madrid, Spain
[4] Telespazio UK for the European Space Agency (ESA), European Space Astronomy Centre (ESAC), Camino Bajo del Castillo s/n, 28692 Villanueva de la Cañada, Madrid, Spain
[5] Max-Planck-Institut für Astronomie (MPIA), Königstuhl 17, 69117 Heidelberg, Germany
[6] Konkoly Observatory, Research Centre for Astronomy and Earth Sciences, Eötvös Loránd Research Network (ELKH), Konkoly-Thege Miklós út 15-17, H-1121 Budapest, Hungary
[7] Observatorio Astronómico Nacional (OAN-IGN)-Observatorio de Madrid, Alfonso XII, 3, 28014 Madrid, Spain
[8] Private Researcher (formerly at Universidad Autónoma de Madrid)

Abstract

Debris discs represent the last stages of planet formation and as such are expected to be depleted of primordial gas. Nonetheless, in the last few years the presence of cold gas has been reported in $\sim$ 20 debris discs from far-IR to (sub-)mm observations and hot gas has been observed in the optical spectra of debris discs for decades. While the origin of this gas is still uncertain, most evidences point towards a secondary origin, as a result of collisions and evaporation of small bodies in the disc. In this paper, we present ALMA observations aimed at the detection of CO gas in a sample of 8 debris discs with optical gas detections. We report the detection of CO (^{12}CO and ^{13}CO) gas in HD 36546, the brightest and youngest disc in our sample, and provide upper limits to the presence of gas in the remaining seven discs.

1 Introduction

As exoplanetary studies progress, with more than 5000 planets confirmed, we tend to imagine planetary systems as simple associations of a central body (or more than one in some cases),

i.e. a star, and a few to several planet sized objects revolving around it, much like our own Solar System. In doing so, we usually forget the plethora of other bodies that are present: moons, asteroids, comets, etc.; as well as the non-negligible amounts of dust and gas that are released via interactions of those components, mostly through collisions and evaporation.

However, minor bodies play a key role in the chemical and dynamical evolution of planetary systems, as they interact with each other and the proto-planets being formed. The Earth itself is thought to have been heavily impacted by small bodies in the system during the moon formation process and during the Late Heavy Bombardment event, possibly having its early atmosphere altered by volatiles (i.e., water) deposited by comets and asteroids. The study of the gaseous component of planetary systems in debris disks can help us investigate these kind of interactions, and have a significant impact in the study of habitability.

2 Circumstellar gas in debris disks

Gas has been classically expected to be depleted after the protoplanetary phase, and therefore not detectable around stars that have reached the main sequence already (i.e., debris disks). In the past 5-10 years, the increasing sensitivity of interferomertic facilities, such as ALMA, have led to multiple detections of CO gas in debris disks, challenging the classic view, and raising the question about why this gas is present in debris disks. While the community still investigates the possibility of this gas being a remnant of the protoplanetary phase, the general agreement is that secondary processes, such as evaporation and collisions of minor bodies, are acting as replenishment mechanisms of both the gas and dust components [9, 6].

The gas we find in debris disks can be separated in two populations. As mentioned above, (sub-)mm interferometric facilities have revealed the presence of CO emission in over 20 debris disks so far. This gas is usually located in the outer regions of the systems (¿10 au and up to several hundreds) and it has very low temperatures (a few Kelvin). Using optical spectroscopy, we can detect the gas located in the inner regions, at very high temperatures (over 1000 K) and most likely released by exocomets as they sublimate at very small distances from the star. This gas is mostly from highly refractory elements (e.g. Ca II) but has also been detected in multiple species in the ultraviolet region [15].

In both cases, the most likely origin of the gas is collisions or evaporation of minor bodies in the system, i.e. exocomets. The first detection of exocomets is reported in 1987 [4], where they observe variable absorption features overimposed to the Ca II line at 3933.66 Å. These absorptions were suggested to be originated by *Falling Evaporating Bodies* or FEBs, and later explained as bodies similar to the comets from the solar system [1].

3 Co-existence of hot and cold gas

In order to determine if cold and hot gas are co-existing and possibly connected to the presence of exocomets, I led a study presented in [12] that investigated the presence of absorption gas in systems with emission gas detection. At the time of the study, cold emission gas had been detected in 17 debris disks, out of which we selected 15 (excluding β Pic and Fomalhaut,

due to their spectra being analyzed in previous research work). For those 15 sources, we obtained high resolution spectra containing the Ca II doublet. We collected inclinations for all the sources, with only one being unresolved. We separated the spectra between those with a non-photospheric absorption (i.e. a narrow absorption that is not originated in the stellar photosphere) and those without non-photospheric absorptions in the Ca II K line. After investigating if the origin of the absorptions is either from the circumstellar or interstellar environment by checking the radial velocities and the neighboring stars, we found out that ∼90% of the debris disks with edge on orientations (¿ 70°) showed a circumstellar absorption, and similarly ∼90% of the debris disks with face on orientations (¡ 70°) did not show any circumstellar absorption [1]. This is explained simply by a geometrical effect, meaning that the inner gas detected in absorption needs to transit the star in order to be detectable. The fact that cold and hot gas are simultaneously present in the majority of systems where both are detectable seems to be proof that they co-exist in debris disks, and they might have a common origin.

4 Results from ALMA observations

Given the presence of hot and cold gas seems to be simultaneous in debris disks, we designed the reverse experiment, where we selected a sample of stars with narrow circumstellar absorptions in the Ca II K line and searched for the cold gas counterpart [14].

We performed ALMA Band 6 (1.3 mm) observations in a sample of 8 debris disks with infrared luminosities between 10^{-5} and 10^{-3} and ages between 3 and 890 Myr.

We report detections in the dust continuum for 3 sources (HD 36546, HD 110411 and HD 158352) and ^{12}CO and ^{13}CO detections around HD 36546. We also report the detection of background sources in the field of view of HD 37306 and HD 182919. Detections around HD 36546 are shown in the top panel of Fig. 1, and the values for the fluxes, along with the rest of the detections can be found in [14].

The continuum detections allow to constrain the disk masses by assuming optically thin disks and a temperature of the dust consistent with the black body temperature of the thermal excess. The dust mass estimates of HD 36546 and HD 158352 are consistent with other debris disks, while the dust mass of HD 110411 appears to be particularly low, with less than 10^{-3} $M_{\oplus}$. CO gas mass was also estimated for HD 36546 using the optically thin ^{13}CO transition, yielding a gas mass of $(3.2 \pm 1.2) \times 10^{-3}$ M $\oplus$.

The line profile of the detected ^{12}CO line shows an asymmetric profile, with a larger flux in the blue-shifted velocities. Although the signal to noise is not enough to confidently measure any asymmetry in the ^{13}CO, a similar feature is observed (see bottom pannels of Fig. 1). This could indicate a significant asymmetry in the disk caused by disk perturbations from internal (self-stirring, planets) or external (binary, flybys) agents.

[1] β Pic and Fomalhaut were not included in this study, but also follow this trend.

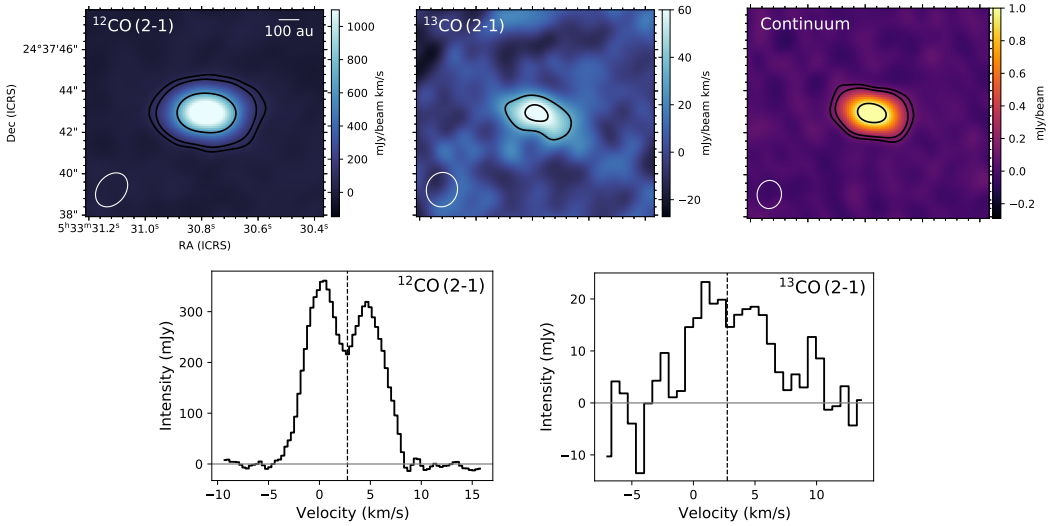

Figure 1: Figure from [14]. Emission observed in HD 36546. Top panels, left to right: Integrated emission of ^{12}CO (230.538 GHz), ^{13}CO (220.398 GHz) and continuum (1.33 mm). In all panels the size of the beam is indicated in the lower left corner. Contours indicate 5, 10 and 50 σ. Bottom panel, left to right: Spectra of ^{12}CO and ^{13}CO. The ^{12}CO panel shows the double peaked profile, characteristic of Keplerian rotation, and less visible in the ^{13}CO panel. The continuous horizontal line marks the continuum (at 0 mJy) and the vertical dashed line shows the systemic velocity of the disc.

4.1 HD 36546

The detection of large amounts of CO around HD 36546 fits in the overall picture we have of this system based on previous work.

Spectroscopic work by [8] showed a prominent feature at 8-9 μm, indicative of an over-abundance of carbon that could be due to a large collision of rocky bodies. [2] presented scattered light observations later re-analyzed in [7] where they reported the first estimation of the morphology of the disk (consistent with our findings in ALMA). They also included planet detection limits based on an estimated age of 3-10 Myr, with upper limits of 5-6 M_J at 23 au, and $\sim$ 2.5 M_J at larger separations. This system also has exocometary activity reported in [13], and a significant amount of Ca gas in the inner region of the system.

All these findings put together seem to indicate considerable dynamical activity in the system, and likely the presence of large bodies; i.e., planets.

4.2 The general picture

The detection of CO around HD 36546 puts this disk in context with previous detections, and shows a similar behaviour as other CO rich debris disks, with a high infrared luminosity and dust mass.

The overall result of the observations yielded a 12% of gas detections with only one out of 8 in the total sample. This appears to show that these systems lack a cold gas component, and therefore the rejection of the hypothesis of co-existence of hot and cold gas in them. However, theoretical predictions for gas production in debris disks depend on the amount of small bodies and dust particles in the system. [5] presented a model that predicted the CO mass in debris disks based on their infrared luminosity. Looking at Fig. 2, all our non detection have much lower dust masses than the disks with CO detections. It is thus possible that the low number of cold gas detections is instead due to insufficient sensitivity of our observations, rather than the lack of cold gas in these systems.

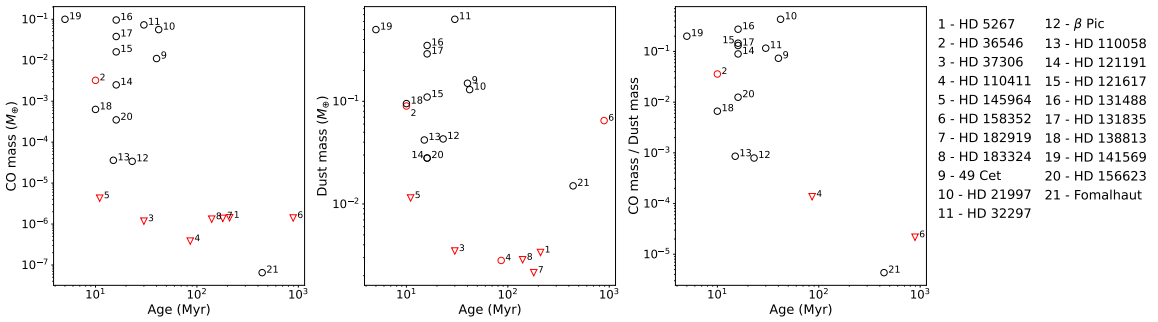

Figure 2: Figure from [14]. Context of the sample compared to other debris discs around A-type stars with detected CO gas. Red symbols mark the positions of the stars in the sample, numbered from 1 to 8. Triangles indicate upper-limits for non-detections. Black circles mark other debris discs with detections in the literature numbered from 9 to 21 [10, 11, 3].

5 Summary

The work presented in this contribution summarized the ALMA observations of project 2019.1.01517.S (PI: I. Rebollido). We report the detection of ^{12}CO and ^{13}CO in the debris disk HD 36546, which confirms this is a complex and interesting system with cold gas [14], hot gas and exocomets[13] and a debris disk with several belts and a carbon enhancement [8]. We also report continuum detections for HD 158352 and HD 110411. The rest of the disks observed within the same ALMA program showed no gas or dust detections, which is probably linked to their low dust content as suggested by [5]. This analysis and results can be found in [14].

We intend to follow up with ALMA observations for the HD 36546 disk to improve the spatial resolution, and recent observations with JWST (GO 2053, PI: I. Rebollido) will allow to investigate the presence of volatiles in the warmer regions of the disk and delivery mechanisms.

References

[1] Beust, H., Lagrange, A.-M., Crawford, I. A., Goudard, C., Spyromilio, J., & Vidal-Madjar, A., 1998, A&A, 338, 1015

[2] Currie, T., Guyon, O., Tamura, M., Kudo, T., Jovanovic, N., Lozi, J., Schlieder, J. E., Brandt, T. D., Kuhn, J., Serabyn, E., Janson, M., Carson, J., Groff, T., Kasdin, N. J., McElwain, M. W., Singh, G., Uyama, T., Kuzuhara, M., Akiyama, E., Grady, C., Hayashi, S., Knapp, G., Kwon, J.-. mi ., Oh, D., Wisniewski, J., Sitko, M., & Yang, Y., 2017, ApJL, 836, L15

[3] Di Folco, E., Péricaud, J., Dutrey, A., Augereau, J.-C., Chapillon, E., Guilloteau, S., Piétu, V., & Boccaletti, A., 2020, A&A, 635, A94

[4] Ferlet, R., Hobbs, L. M., & Vidal-Madjar, A., 1987, A&A, 185, 267

[5] Kral, Q., Matrà, L., Wyatt, M. C., & Kennedy, G. M., 2017, MNRAS, 469, 521

[6] Kral, Q., Marino, S., Wyatt, M. C., Kama, M., & Matrà, L., 2019, MNRAS, 489, 3670.

[7] Lawson, K., Currie, T., Wisniewski, J. P., Tamura, M., Augereau, J.-C., Brandt, T. D., Guyon, O., Kasdin, N. J., Groff, T. D., Lozi, J., Deo, V., Vievard, S., Chilcote, J., Jovanovic, N., Martinache, F., Skaf, N., Henning, T., Knapp, G., Kwon, J., McElwain, M. W., Pyo, T.-S., Sitko, M. L., Uyama, T., & Wagner, K., 2021, AJ, 162, 293

[8] Lisse, C. M., Sitko, M. L., Russell, R. W., Marengo, M., Currie, T., Melis, C., Mittal, T., & Song, I., 2017, ApJL, 840, L20

[9] Marino, S., Flock, M., Henning, T., Kral, Q., Matrá, L., & Wyatt, M. C., 2020, MNRAS, 492, 4409

[10] Moór, A., Curé, M., Kóspál, Á., Ábrahám, P., Csengeri, T., Eiroa, C., Gunawan, D., Henning, T., Hughes, A. M., Juhász, A., Pawellek, N., & Wyatt, M., 2017, ApJ, 849, 123

[11] Moór, A., Kral, Q., Ábrahám, P., Kóspál, Á., Dutrey, A., Di Folco, E., Hughes, A. M., Juhász, A., Pascucci, I., & Pawellek, N., 2019, ApJ, 884, 108

[12] Rebollido, I., Eiroa, C., Montesinos, B., Maldonado, J., Villaver, E., Absil, O., Bayo, A., Canovas, H., Carmona, A., Chen, C., Ertel, S., Garufi, A., Henning, T., Iglesias, D. P., Launhardt, R., Liseau, R., Meeus, G., Moór, A., Mora, A., Olofsson, J., Rauw, G., & Riviere-Marichalar, P., 2018, A&A, 614, A3

[13] Rebollido, I., Eiroa, C., Montesinos, B., Maldonado, J., Villaver, E., Absil, O., Bayo, A., Canovas, H., Carmona, A., Chen, C., Ertel, S., Henning, T., Iglesias, D. P., Launhardt, R., Liseau, R., Meeus, G., Moór, A., Mora, A., Olofsson, J., Rauw, G., & Riviere-Marichalar, P., 2020, A&A, 639, A11

[14] Rebollido, I., Ribas, Á., de Gregorio-Monsalvo, I., Villaver, E., Montesinos, B., Chen, C., Canovas, H., Henning, T., Moór, A., Perrin, M., Rivière-Marichalar, P., & Eiroa, C., 2022, MNRAS, 509, 693

[15] Roberge, A., Feldman, P. D., Weinberger, A. J., Deleuil, M., & Bouret, J.-C., 2006, Nature, 441, 724

Highlights of Spanish Astrophysics XI, Proceedings of the XV Scientific Meeting of the Spanish Astronomical Society held on September 4–9, 2022, in La Laguna, Spain. M. Manteiga, L. Bellot, P. Benavidez, A. de Lorenzo-Cáceres, M. A. Fuente, M. J. Martínez, M. Vázquez- Acosta, C. Dafonte (eds.), 2023

Water vapor vertical distribution in the Martian atmosphere from TGO/NOMAD observations.

Brines, A.[1], Lopez-Valverde, M.A.[1], and Sotlzenbach, A.[1] Modak, A.[1] Funke, B.[1] Galindo, F.G.[1] Aoki, S.[2,3] Villanueva, G.L.[4] Luizzi, G.[4,5] Thomas, I.[2] Erwin, J.T.[6] Grabowski, U.[6] Forget, F.[7] Lopez Moreno, J.J.[1] Rodriguez-Gomez, J.[1] Daerden, F.[2] Trompet, L.[2] Ristic, B.[2] Patel, M.R.[8] Bellucci, G.[9] and Vandaele, A.C.[2]

[1] Instituto de Astrofísica de Andalucía (IAA/CSIC), Spain
[2] Royal Belgian Institute for Space Aeronomy, Belgium
[3] Department of Complexity Science and Engineering, University of Tokyo, Japan
[4] NASA Goddard Space Flight Center, USA
[5] American University, Washington DC, USA
[6] Karlsruhe Institute of Technology, Karlsruhe, Germany
[7] Laboratoire de Météorologie Dynamique, IPSL, Paris, France
[8] Open University, UK
[9] Istituto di Astrofisica e Planetologia, Italy

Abstract

The water vapor in the Martian atmosphere plays a significant role in the planet's current and past climate, being crucial in important chemical processes like those involved in the stability of the CO_2. The recent ExoMars 2016 mission, with its NOMAD Solar Occultation channel spectrometer onboard the Trace Gas Orbiter, allowed us to measure the H_2O vertical distribution with unprecedented resolution. Recent studies of vertical profiles have shown that high dust concentration in the atmosphere, in particular during dust storms, induces an efficient transport of the H_2O to higher altitudes, from 40 km up to 80 km. Here we present the water vapor vertical distributions obtained for the Martian Years 34 and 35, covering the Global Dust Strom (GDS) event of 2018 (during MY 34) and hence, characterizing how it varies under very different dusty conditions. The direct comparison of the same season in these two consecutive Martian Years allowed us to confirm the strong impact of the GDS in the water distribution.

1 Introduction

Water vapor is present in the Martian atmosphere in relatively low abundances. Being a trace gas, its vertical distribution is affected by numerous processes, from the surface interactions to atmospheric chemistry and transport to escape to space at high altitudes.

[12]. Recent observations have proven that the ancient Mars was wetter than today, meaning that processes like the escape of water to the space have driven the planet to its current state. Also, previous works have pointed out how important is the vertical distribution of the water in the atmosphere for the evolution of the planet and for the understanding of the physical and chemical processes driving the water cycle [9]. Recent studies with the Atmospheric Chemistry Suite (ACS) and NOMAD revealed an enhancement of water vapor at high altitudes during dust events such as the Global Dust Storm during MY 34 [4, 5, 1, 2]. Other works focused on the hydrogen escape [20, 21] have suggested that the dust enhancement has a strong effect on the escape processes. Here we apply an state-of-the-art retrieval scheme to derive precise vertical profiles from NOMAD observations. Then we analyze the seasonal and latitudinal variation of the water in the atmosphere during the first half of the perihelion season of two consecutive Martian Years (MY), sampling an altitude range from the surface of the planet up to 110 km, along with an estimation of the water vapor saturation ratio.

2 NOMAD SO Measurements and Analysis

2.1 NOMAD Instrument and Dataset

The Nadir and Occultation for MArs Discovery (NOMAD) is an infrared spectrometer on-board the ExoMars Trace Gas Orbiter (TGO) that covers the spectral range between 0.2 and 4.3 μm [19]. The instrument consists of three independent channels, Limb Nadir and Occultation (LNO) operating between 2.3 and 3.8 μm, Ultraviolet and Visible Spectrometer (UVIS) operating at 200-600 nm, and Solar Occultation (SO) operating in the range between 2.3 and 4.3 μm and designed only for solar occultation measurments. This channel with a spectral resolution $\Delta\lambda/\lambda \simeq$2000, uses an echelle grating with a density of $\sim$ 4 lines/mm in a litrow configuration. It contains an Acousto-Optical Tunable Filter (AOTF) which permits to select different diffraction orders with a width that varies from 20 to 35 cm^{-1}. During each atmospheric scan, a solar occultation is measured every $\sim$1 s, allowing a vertical sampling of $\sim$1 km. In addition, the AOTF is able to change the observed diffraction order quasi-instantaneously so the SO channel can measure up to 6 diffraction orders every observation. For this study we selected a subset of measurements taken during 180° - 270° of solar longitude (L_s) during MY 34 and 35, corresponding to the first half of the Martian perihelion season. For the retrievals of water vapor we used diffraction order 134 (3011-3035 cm^{-1}) to study the the lower atmosphere (below 60 km) and order 168 (3775-3805 cm^{-1}) to study higher altitudes (above 60 km), due to the difference in the strength of the water vapor absorption lines present in these two orders. The selected dataset includes simultaneous observation of both diffraction orders, allowing us to analyze the atmosphere from $\sim$10 km above the surface up to $\sim$100 km.

2.2 Data Anaylsis and Inversion of Vertical Profiles

The NOMAD SO data used in this work are Level 1a calibrated transmittances processed at the Belgian Institute of Space Aeronomy (ISAB-BIRA) [18]. These data need to be furthermore processed in order to identify and correct for residual calibration features including spectral shifts and spectral bending across each diffraction order. At IAA we have developed tools (pre-processing phase) to clean the measured transmittances (T) corrected for the spectral shift ($\Delta\lambda$) as a proportional combination of the modeled transmittance (T_0) scaled by a factor (k), the residual bending (T_b) and the aerosol extinction along the slant path (τ). This cleaning of the data can be summarized with the following expression $T(\lambda+\Delta\lambda) = T_0^k(\lambda)\cdot T_b(\lambda)\cdot e^{-\tau}$. After this pre-processing we performed the water vapor inversion using the Retrieval Control Program (RCP), which is a fully-tested multi-parameter non-linear least squares fitting of measured and modeled spectra [22], which incorporates the state-of-the-art line-by-line radiative transfer model KOPRA (Karlsruhe Optimized Radiative transfer Algorithm) [16]. The a priori atmosphere used for RCP during the retrievals was taken from specific runs of the Mars Planetary Climate Model (LMD Mars PCM)[6], using the recent implementations of the water cycles [14] and the dust scenarios appropriate for MY 34 and 35 [10, 11]. This inversion of H_2O profiles was done with two different diffraction orders, 134 and 168. When both were measured simultaneously, in this work we built a full water vapor vertical profile merging information from order 134 below 60 km and from order 168 above.

3 Results and Discussion

3.1 Water Vapor Seasonal Variation

The maturation phase of the 2018 Global Dust Storm (GDS) occurred during L_s ~190° - 210° with a long decay phase until L_s ~270° of MY 34. In Figure 1 we show the seasonal variation of the water vapor at 50 km and 90 km for MYs 34 and 35. During the GDS maturation phase, we observe an intense peak in the water vapor volume mixing ratio (VMR) showing abundances <150 ppm at 50 km in both hemispeheres and ~50 ppm at 90 km in the Southern hemisphere. This enhancement of the water vapor at high altitudes is not present during the same period of MY 35, when a GDS was not present. At the end of the analyzed period at $L_s > 240°$ we observe a progressive increase of the water vapor abundances in the Southern hemisphere during both MYs due to the seasonal temperature increase and the sublimation of the southern polar cap, allowing more water to be present in the atmosphere.

3.2 Water Latitudinal Variation

The effects of the GDS during MY 34 in contrast with MY 35 can also be observed at different latitudes. This is shown in Figure 2. During the period of strong activity of the GDS we observe a clear increase of the water vapor VMR with the water confined mostly between 60°N and 75°S and reaching altitudes up to 80 km at mid latitudes with abundances about 150 ppm. Regardless of the poor coverage of the northern hemisphere, this same period

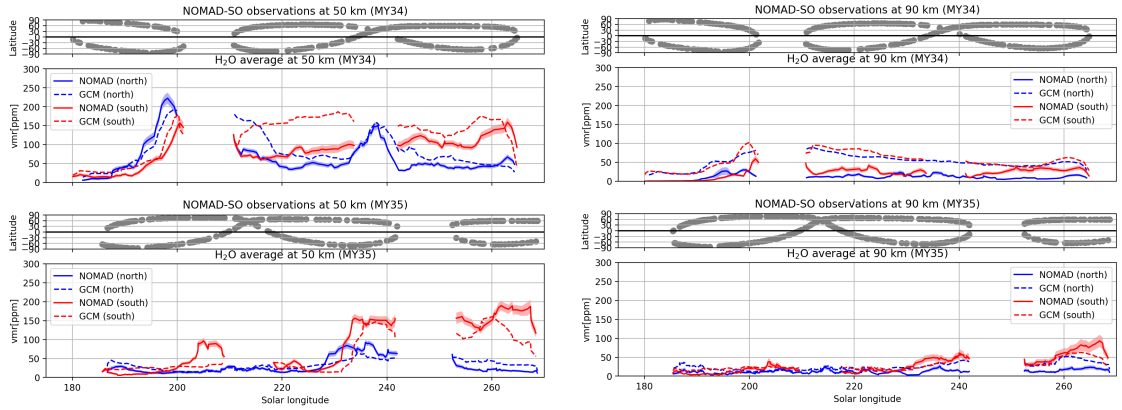

Figure 1: Seasonal variation of water vapor at 50 km (left) and 90 km (right) during L_s = 180° - 270° of MY 34 (top) and MY 35 (bottom). See text for details.

during MY 35 shows that water vapor is mostly confined below 45 km and in latitudes lower than 50°S.

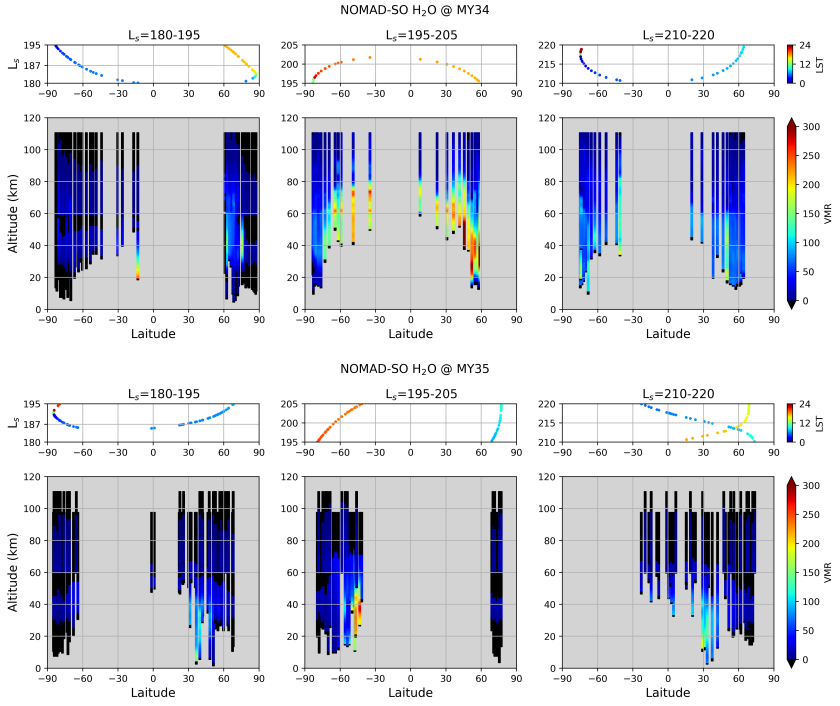

Figure 2: Latitudinal distribution of the water vapor during L_s = 180° - 220° of MY 34 (top) and MY 35 (bottom). See text for details.

3.3 Water Vapor Saturation and Water Ice

The water vapor saturation ratio (S) can be calculated as the ratio of the water vapor present in the atmosphere (retrieved water vapor μ_{H_2O}) over the expected saturated water vapor (μ_{sat}) under certain pressure and temperature conditions. In order to estimate the saturation pressure over water ice we used the well known relation of saturation vapor pressure with temperature for H_2O [13] and applied it to the NOMAD SO retrieved temperatures as obtained in our team [8], only applied when coincident retrievals of H_2O and temperature were available for MY 34. In addition, using the aerosol information obtained by [17] for the same period we identified several saturation events occurring in presence of water ice and two events of saturaiton occurring towards the top of ice clouds layers, supporting the schematic model proposed by [15]. An example of saturation in presence of water ice is shown in Figure3 (top panels) and an event of saturation observed at the top of an ice cloud is shown in Figure3 (bottom panel).

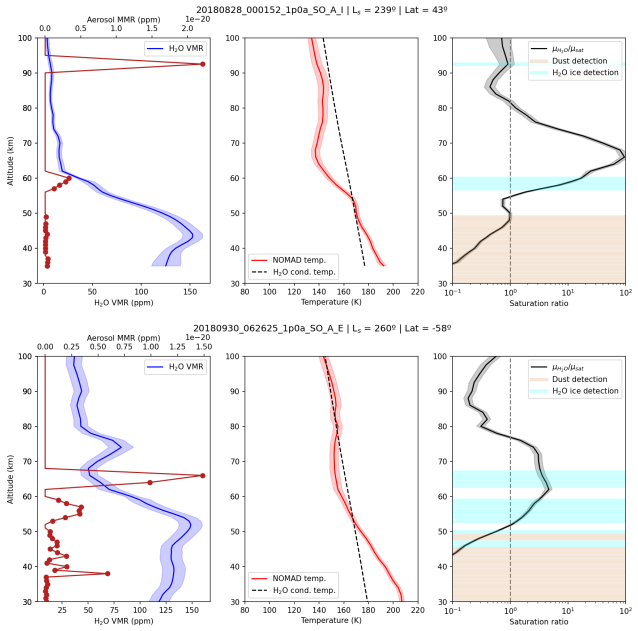

Figure 3: Profiles of water vapor, aerosols mass mixing ratio (MMR), temperature and water saturation ratio for two NOMAD SO observations. Left panels: Water vapor VMR (blue) and aerosol MMR (dark red). Center panels: NOMAD temperature (red) and water vapor condensation temperature (dashed). Right panels: Water saturation ratio (black), water ice detections (light blue) and dust detections (light brown). Vertical dashed line shows saturation ratio equal to 1. See text for details.

4 Conclusions

In this study we have presented the water vapor vertical distributions obtained for the first half of the perihelion season during Martian years 34 and 35 characterizing the water vapor under GDS and non-GDS conditions. The main results we found are:
- During the strong activity of the GDS, we observe an intense peak in the water vapor showing abundances about 150 ppm at 50 km in both hemisphere. In contrast, during MY 35, water vapor does not exceed abundances of 50 ppm above 50 km in the northern hemisphere.
- During northern winter solstice, at high southern latitudes, we observe high water vapor abundances to altitudes as high as 60 km, indicative of a progressive temperature increase. This feature is observed in both Martian Years.
- We identify saturated layers in presence of water ice, indicative of a condensation process going on at the terminator at the precise moment and local time of the NOMAD observations.
An extended version of this paper can be found in [3]. Application of these methods to an extended dataset of NOMAD solar occultations, covering the whole MY 34 and MY 35 are ongoing at our team and will be presented in future works.

Acknowledgments

The IAA/CSIC team acknowledges financial support from the State Agency for Research of the Spanish MCIU through the 'Center of Excellence Severo Ochoa' award for the Instituto de Astrofísica de Andalucía (SEV-2017-0709) and funding by grant PGC2018-101836-B-100 (MCIU/AEI/FEDER, EU) and PID2019-110689RB-I00/AEI/10.13039/501100011033 Grant PRE2019-088355 funded by MCIN/AEI/ 10.13039/501100011033 and by 'ESF Investing in your future'. F.G.G. is funded by the Spanish Ministerio de Ciencia, Innovación y Universidades, the Agencia Estatal de Investigación and EC FEDER funds under project RTI2018-100920-J-I00. ExoMars is a space mission of the European Space Agency (ESA) and Roscosmos. The NOMAD experiment is led by the Royal Belgian Institute for Space Aeronomy (IASB-BIRA), assisted by Co-PI teams from Spain (IAA-CSIC), Italy (INAF-IAPS), and the United Kingdom (Open University). This project acknowledges funding by the Belgian Science Policy Office (BELSPO), with the financial and contractual coordination by the ESA Prodex Office (PEA 4000103401, 4000121493) as well as by UK Space Agency through grants ST/V002295/1, ST/V005332/1 and ST/S00145X/1 and Italian Space Agency through grant 2018-2-HH.0. This work was supported by the Belgian Fonds de la Recherche Scientifique-FNRS under grant number 30442502 (ET-HOME). This project has received funding from the European Union's Horizon 2020 research and innovation program under grant agreement No 101004052 (RoadMap project). US investigators were supported by the National Aeronautics and Space Administration. We want to thank M. Vals, F. Momtmessin, F. Lefevre and the broad team supporting the continuous development of the LMD Mars PCM.

References

[1] Aoki, S., Vandaele, A. C., Daerden, F., Villanueva, G. L., Liuzzi, G., Thomas, I. R., ... & NOMAD team. 2019. JGR: Planets, 124(12), 3482-3497.

[2] Aoki, S., Vandaele, A. C., Daerden, F., Villanueva, G. L., Liuzzi, G., Clancy, R. T., ... & Fedorova, A. A. 2022. JGR: Planets, 127(9), e2022JE007231.

[3] Brines, A., Lopez-Valverde, M. A., Funke, B., Stolzenbach, A., Modak, A., Gonzalez-Galindo, F., et al. 2022. JGR: Planets (accepted)

[4] Fedorova, A., Bertaux, J. L., Betsis, D., Montmessin, F., Korablev, O., Maltagliati, L., & Clarke, J. 2018. Icarus, 300, 440-457.

[5] Fedorova, A. A., Montmessin, F., Korablev, O., Luginin, M., Trokhimovskiy, A., Belyaev, D. A., ... & Wilson, C. F. 2020. Science, 367(6475), 297-300.

[6] Forget, F., Hourdin, F., Fournier, R., Hourdin, C., Talagrand, O., Collins, M., ... & Huot, J. P. 1999. JGR: Planets, 104(E10), 24155-24175.

[7] Jurado Navarro, Á. A. 2016. PhD. Thesis, Univ. Granada

[8] López Valverde, M. A., Funke, B., Brines, A., Stolzenbach, A., Modak, A., Hill, B., ... & NOMAD team. 2022. JGR: Planets, e2022JE007278.

[9] Maltagliati, L., Montmessin, F., Korablev, O., Fedorova, A., Forget, F., Määttänen, A., ... & Bertaux, J. L. 2013, Icarus, 223(2), 942-962.

[10] Montabone, L., Forget, F., Millour, E., Wilson, R. J., Lewis, S. R., Cantor, B., ... & Wolff, M. J. 2015. Icarus, 251, 65-95.

[11] Montabone, L., Spiga, A., Kass, D. M., Kleinböhl, A., Forget, F., & Millour, E. 2020. JGR: Planets, 125(8), e2019JE006111.

[12] Montmessin, F., Smith, M. D., Langevin, Y., Mellon, M. T., & Fedorova, A. 2017, The atmosphere and climate of Mars, 18, 338.

[13] Murphy, D. M., & Koop, T. 2005. Quarterly Journal of the Royal Meteorological Society, 131(608), 1539-1565.

[14] Navarro, T., Madeleine, J. B., Forget, F., Spiga, A., Millour, E., Montmessin, F., & Määttänen, A. 2014. JGR: Planets, 119(7), 1479-1495.

[15] Poncin, L., Kleinböhl, A., Kass, D. M., Clancy, R. T., Aoki, S., & Vandaele, A. C. 2022. Planetary and Space Science, 212, 105390.

[16] Stiller, G. P. 2000 .Vol. FZKA 6487. Forschungszentrum Karlsruhe

[17] Stolzenbach, A., Lopez-Valverde, M. A., Funke, B., Brines, A., Modak, A., Gonzalez-Galindo, F., et al. 2022. JGR: Planets (submitted)

[18] Thomas, I. R., Aoki, S., Trompet, L., Robert, S., Depiesse, C., Willame, Y., ... & NOMAD Team. 2022. Planetary and Space Science, 218, 105411.

[19] Vandaele, A. C., Lopez-Moreno, J. J., Patel, M. R., Bellucci, G., Daerden, F., Ristic, B., ... & Wolff, M. 2018. Space Science Reviews, 214(5), 1-47.

[20] Villanueva, G. L., Liuzzi, G., Crismani, M. M., Aoki, S., Vandaele, A. C., Daerden, F., ... & NOMAD team. 2021. Science Advances, 7(7), eabc8843.

[21] Villanueva, G. L., Liuzzi, G., Aoki, S., Stone, S. W., Brines, A., Thomas, I. R., ... & Vandaele, A. C. 2022. GRL, 49(12), e2022GL098161.

[22] von Clarmann, V., Glatthor, N., Grabowski, U., Höpfner, M., Kellmann, S., Kiefer, M., ... & López-Puertas, M. 2003. JGR: Atmospheres, 108(D23).

Highlights of Spanish Astrophysics XI, Proceedings of the XV Scientific Meeting of the Spanish Astronomical Society held on September 4–9, 2022, in La Laguna, Spain. M. Manteiga, L. Bellot, P. Benavidez, A. de Lorenzo-Cáceres, M. A. Fuente, M. J. Martínez, M. Vázquez- Acosta, C. Dafonte (eds.), 2023

Are pit craters habitable? Geological analysis and description of their structural potential as lunar bases.

López-Martínez, G.[1] **and M. Parro, L.**[2,3,4]

[1] Valencia International University, Spain
[2] Universidad Complutense de Madrid, E-28040 Madrid, Spain
[3] Lunar and Planetary Laboratory, University of Arizona, Tucson, AZ, USA
[4] Instituto de Física Aplicada a las Ciencias y las Tecnologías. Universidad de Alicante, Sant Vicent del Raspeig, Spain

Abstract

Pit craters, also known as subsidence or collapse craters, are circular-shaped holes in the terrain found throughout the Solar System. Their formation does not relate to any impact, in some planetary bodies, the surface collapses over a lava tube [1], [2], [3] or magma chamber, generating a natural entrance of a planetary cave. The presence of these lava tubes on the Moon has been proposed since the sixties [4], using as evidence the sinuous rilles. More recently, attempts have been made to evaluate the dimensions of lava tubes using the Lunar Radar Sounder of Kaguya [5] and gravimetry data from GRAILS, to detect huge mass deficits under the surface [6]. These studies give strong indications that sublunarean caves might exist, and they could be related to pit craters [5], also known as skylights. Caves could become the first human settlements on the Moon because they provide a natural and safe refuge for astronauts, technology and resources [7]. However, the connection between pit craters and caves is not demonstrated.

We located the best skylight candidates by overlaying pit crater locations from the LROC atlas to the global geologic map of the Moon (USGS), getting information on the properties of the lunar regions (material type and age); the Kaguya (SELENE) mission maps, covering latitudes from -60° to 60°; and the north and south pole LOLA LRO lunar topographic maps. A wrinkle ridges layer is also added to find some clues about how the pit craters in an area might be connected and how large the subsurface caves would be.

A sublunarean lava cave accessible from one of these four skylight candidates would be a promising astrobiological region due to its own microclimate preservation capabilities and its shielding against radiation [8] and meteorites. Additionally, a pristine lava tube would be helpful to better understand the Lunar geological history.

.

My poster is available at https://doi.org/10.5281/zenodo.7032407

Highlights of Spanish Astrophysics XI, Proceedings of the XV Scientific Meeting of the Spanish Astronomical Society held on September 4–9, 2022, in La Laguna, Spain. M. Manteiga, L. Bellot, P. Benavidez, A. de Lorenzo-Cáceres, M. A. Fuente, M. J. Martínez, M. Vázquez- Acosta, C. Dafonte (eds.), 2023

Exploring stable lithium isotope ($\delta 7Li$) concentration on the lunar surface.

S. Fernández Menéndez [1], R.S. Anangonó-Tutasig [1], J.M. Fernández Díaz [1], J. Fernández Calleja [2], E. Diez Alonso [1], and F. J. De Cos Juez [1]

[1] Instituto Universitario de Ciencias y Tecnologías Espaciales de Asturias (ICTEA), C. Independencia 13, E-33004 Oviedo, Spain
[2]Dpto. Física Universidad de Oviedo

Abstract

We explore the concentration of Lithium and $\delta 7Li$ in the lunar surface (out rocks and regolith) using spectral data obtained from the Clementine mission (images UV–VIS with 450, 750, 900, 950 and 1000 nm bands), that provide 100 % coverage of the lunar surface at resolution of 100 to 300 m, between latitudes of 70° S to 70° N. In order to extract quantitative abundance of Lithium, ground truth sites must be used to calibrate the sensor. Lithium composition of samples (12045, 15058, 15475, 15555, 70035, 74220 and 75075) returned from Apollo missions 12, 15, 16 and 17 have been compared to the Clementine UV-Vis-Nir bands. We find an excellent linear correlation between the spectral parameters and Lithium content of samples. The analysis presented here further explores the presence of Lithium and $\delta 7Li$ in areas with different exposures to solar wind, as shadowed craters or elevated areas of lunar crust with different exposure age, trying to elucidate the possibility of Lithium enrichment of lunar regolith by spallation processes.

My poster is available at https://zenodo.org/record/7042762

Highlights of Spanish Astrophysics XI, Proceedings of the XV Scientific Meeting of the Spanish Astronomical Society held on September 4–9, 2022, in La Laguna, Spain. M. Manteiga, L. Bellot, P. Benavidez, A. de Lorenzo-Cáceres, M. A. Fuente, M. J. Martínez, M. Vázquez- Acosta, C. Dafonte (eds.), 2023

Formation of structures due to the presence of planets in the discs of young solar-like stars.

Canet, A.[1,2], and Gómez de Castro, A.I.[1,2]

[1] AEGORA Research Group. Fac. de CC. Matemáticas. Universidad Complutense de Madrid, Plaza de Ciencias 3, 28040, Madrid, Spain
[2] Departamento de Física del a Tierra y Astrofísica. Fac. de CC. Físicas. Universidad Complutense de Madrid, Plaza de Ciencias 1, 28040, Madrid, Spain

Abstract

Forming planets around young, fast-rotating solar-like stars are exposed to strongly magnetized stellar winds, as a consequence of the enhanced magnetic activity of these stars. In addition to the action of these winds, transient energetic events such as coronal mass ejections (CMEs) are believed to be frequent in these environments, increasing the density, velocity, and magnetic field of the background stellar wind. The interaction of winds and CMEs with orbiting planets around active stars may lead to the formation of observable signatures due to the formation magnetic field and density disturbances in the vicinity these planets, such as comet-like tails or large bow-shocks, and may play a fundamental role in shaping the geometry of the possible present young planetary atmospheres. In this work, we study the interaction between the stellar winds and CMEs of very active, young stars with planetary obstacles through numerical 2.5D simulations using the PLUTO MHD code. The case of study is AB Doradus, a nearby young star, with a small rotation period (0.51 days) and a strong flaring activity. From these simulations, we characterize the formation of density and magnetic field disturbances in the vicinity of the planetary obstacles for different stellar wind configurations, in the case of close-in Earth-like planets. These results may contribute to the study of the temporal variability in UV and sub-mm ranges in young-protoplanetary discs due to the presence of planets.

My poster is available at https://doi.org/10.5281/zenodo.7044634

Highlights of Spanish Astrophysics XI, Proceedings of the XV Scientific Meeting of the Spanish Astronomical Society held on September 4–9, 2022, in La Laguna, Spain. M. Manteiga, L. Bellot, P. Benavidez, A. de Lorenzo-Cáceres, M. A. Fuente, M. J. Martínez, M. Vázquez- Acosta, C. Dafonte (eds.), 2023

Geomorphological characterisation and Spectroscopy analysis of the Gusev and Jezero craters on Mars: Landing sites of NASA's Mars exploration missions.

R.S Anangonó-Tutasig [1], S. Fernández Menéndez [1], E. Diez Alonso [1], and F.J. De Cos Juez[2]

[1] Instituto Universitario de Ciencias y Tecnologías Espaciales de Asturias (ICTEA), C. Independencia 13, E-33004 Oviedo, Spain

Abstract

Gusev Crater, landing site of the MER-A mission, and Jezero Crater, site of the Mars2020 mission, were possibly two past fluvial-lacustrine systems, and have therefore been of great interest to understand the past of Mars. The mapping of both craters has been carried out by the Context Camera (CTX) and the High-Resolution Imaging Experiment (HiRISE) on board the Mars Reconnaissance Orbiter (MRO), improving the resolution of previous studies. Also the analysis of the data collected by The Compact Reconnaissance Imaging Spectrometer for Mars (CRISM, on board MRO), shows the mineralogy present on the surface. These are complemented by data from the Thermal Emission Imaging System (THEMIS) and the Mars Orbiter Laser Altimeter (MOLA), both on board the Mars Global Surveyor mission (MGS). CTX and HiRISE provide visible images with detailed information related with the surface features of morphological units. CRISM produces images from visible, infrared and near-infrared (VNIR) spectra, where it records the residual mineralogy present on the surface. In both craters shows mineralogy associated with Fe and Carbonates by spectral signatures and RGB composition. THEMIS images collect information in the infrared range, showing the temperature variation in materials during the day and night. With MOLA data has been possible to determine the stratigraphic position of the mapped units and to obtain information on the slopes and elevations of the units. With the analysis and combination of all the data, we have been able to describe the geological characteristics, such as the presence of fluvial-lacustrine, aeolian, glacial and volcanic deposits present in craters Gusev and Jezero, of great importance in the former, since new units have been defined and are described in this research. For Jezero, slight modifications are proposed to some of the units already described in previous studies.

My poster is available at https://zenodo.org/record/6903296

Highlights of Spanish Astrophysics XI, Proceedings of the XV Scientific Meeting of the Spanish Astronomical Society held on September 4–9, 2022, in La Laguna, Spain. M. Manteiga, L. Bellot, P. Benavidez, A. de Lorenzo-Cáceres, M. A. Fuente, M. J. Martínez, M. Vázquez- Acosta, C. Dafonte (eds.), 2023

Mineralogical and morphological characterization and optimization of extractive techniques applied to minor bodies of the Solar System.

J. Rodríguez Rodríguez[1], E. Díez Alonso[1], S. Fernández Menéndez[1], S. Iglesias Álvarez[1], J. Gracia Rodríguez[1], and F. J. de Cos Juez[1]

[1] Instituto Universitario de Ciencias y Tecnologías Espaciales de Asturias (ICTEA)

Abstract

In this work we review what are the demands related to critical elements in technological areas in the near future, being its extraction from asteroids the main target. We study how frequently those critical elements appear in different asteroid taxonomies by comparing the asteroid taxonomies with meteor remains on Earth, concluding that the best candidates to be mined in a future mission would be M/X type asteroids. We have selected several NEA's and asteroids from the Main Belt belonging to this taxonomy as optimal candidates to be mined, studying their composition by spectroscopy. We also analyse their available dense and sparse photometry in databases in order to obtain their physical parameters (pole orientation, rotation period, size) and also apply the light curve inversion method, complemented with radar images, if available, to estimate their shape, which is fundamental to determine which mining method is the optimal in each particular asteroid. In this work we have focused on (4660) Nereus.

My poster is available at https://doi.org/10.5281/zenodo.7016560

Highlights of Spanish Astrophysics XI, Proceedings of the XV Scientific Meeting of the Spanish Astronomical Society held on September 4–9, 2022, in La Laguna, Spain. M. Manteiga, L. Bellot, P. Benavidez, A. de Lorenzo-Cáceres, M. A. Fuente, M. J. Martínez, M. Vázquez- Acosta, C. Dafonte (eds.), 2023

Modelling activity-induced radial velocities through STELLA/WiFSIP simultaneous photometry.

Castro-González, A[1], Lillo-Box, J[1], and the KOBE team[1−6]

[1] Centro de Astrobiología (CAB, CSIC-INTA), Depto. de Astrofísica, ESAC campus, 28692 Villanueva de la Cañada (Madrid), Spain
[2] Instituto de Astrofísica e Ciências do Espaço, Universidade do Porto, CAUP, Rua das Estrelas, 4150-762 Porto, Portugal
[3] Aix-Marseille Univ., CNRS, CNES, LAM, Marseille, France
[4] Depto. Estadística e Investigación Operativa, Universidad de Cádiz, Avda. República Saharaui s/n, 11510 Puerto Real, Cádiz
[5] Observatoire astronomique de l'Université de Genève, Chemin Pegasi 51, 1290 Versoix, Switzerland
[6] Centro Astronómico Hispano en Andalucía, Observatorio de Calar Alto, Sierra de los Filabres, 04550 Gérgal, Almería, Spain

Abstract

The search for habitable worlds is a challenging process but key in our search for life beyond Earth. In this context, the KOBE experiment is aimed at searching for new worlds within the habitable zone of K-dwarf stars through the radial velocity method using the CARMENES instrument. When searching for low-amplitude radial velocity signals, as those produced by rocky worlds, stellar activity is one of the major contaminants. A widely-used procedure to overcome this is to use activity indicators from the spectroscopic data, simultaneously modelling the stellar activity and the radial velocity. However, our simulations show that the KOBE long cadence (∼9 days) is not enough to properly do so. To overcome this, we are performing a high-cadence photometric monitoring of the KOBE sample stars over the duration of the CARMENES observations (until 2023A) through the robotic telescope STELLA/WiFSIP located in Tenerife. This way, we are able to obtain contemporary and time-resolved information about activity that allows us to use it as a proxy to account for activity in the radial velocity time series. In this contribution we show our modelling procedure, current results, and discuss the capabilities of the CARMENES-WiFSIP synergy in order to facilitate and improve planet detection and characterization.

My poster is available at https://doi.org/10.5281/zenodo.7041400

Highlights of Spanish Astrophysics XI, Proceedings of the XV Scientific Meeting of the Spanish Astronomical Society held on September 4–9, 2022, in La Laguna, Spain. M. Manteiga, L. Bellot, P. Benavidez, A. de Lorenzo-Cáceres, M. A. Fuente, M. J. Martínez, M. Vázquez- Acosta, C. Dafonte (eds.), 2023

New compositional proposals to asteroid (121) Hermione based on spectroscopic and photometric analysis.

S. del Carmen Fernández [1], E. Díez Alonso [1], J. Rodríguez Rodríguez [1], and F. J. de Cos Juez [1]

[1] Instituto Universitario de Ciencias y Tecnologías Espaciales de Asturias (ICTEA), C. Independencia 13, E-33004 Oviedo, Spain

Abstract

(121) Hermione is a Cybele group asteroid discovered in 1872 with a km-size moonlet detected in 2002. Based on bulk density (1.4 ± 0.2 g/cm^3) and albedo values, the derived Hermione's taxonomic class is C-type with a low albedo, making the CI and CM carbonaceous chondrites the best meteoritic analogs. Nowadays our knowledge on the mineralogy of asteroids is based on remote-sensing photometry and spectroscopy in the visible and near-infrared, radar polarimetry and comparison with meteorites studied in the laboratory. Spectral observations of Hermione at VIS-NIR wavelengths will help to refine its taxonomic classification and state of weathering. In this work we review the mineralogy assignation of Hermione comparing JPL spectral libraries of minerals and meteorites (ultramafic rocks, pyrites, piroxenes, diamonds, olivine, hematites, carbons and carbonaceous meteorites) resampled to the wavelengths of VIS-NIR spectrum of Hermione from SMASSII. In order to quantify similarities between resampled spectra and Hermione SMASSII spectrum, we performed a Factor Análisis (PCA). The same analysis was carried out with spectra resampled to wavelengths of 367, 436, 545, 638 and 797 nm, which correspond to effective central wavelengths of U, B, V, R and I photometric filters used to observe (121) Hermione from ICTEA observatory (mpc code L94). Pyrite, Sphalerite and Goethite are the mineral species with more similar spectra to Hermione's SMASSII spectrum. In the same way, chondrite carbonaceous and troillite are the meteorites more similar. The same results were found using our photometric analysis, but olivine also was included in the same group of (121) Hermione.

My poster is available at https://doi.org/10.5281/zenodo.7044370

Highlights of Spanish Astrophysics XI, Proceedings of the XV Scientific Meeting of the Spanish Astronomical Society held on September 4–9, 2022, in La Laguna, Spain. M. Manteiga, L. Bellot, P. Benavidez, A. de Lorenzo-Cáceres, M. A. Fuente, M. J. Martínez, M. Vázquez- Acosta, C. Dafonte (eds.), 2023

Numerical simulations of polarized microwave emission from cosmic particles in the upper atmosphere of the Earth.

López-Viejobueno, J.[1], Beitia-Antero, L.[2], and Gómez de Castro, A. I.[1]

[1] AEGORA Research Group, Facultad de Ciencias Matemáticas, Universidad Complutense de Madrid, Madrid, Spain
[2] Observatorio Astronómico Nacional, Instituto Geográfico Nacional, Madrid, Spain

Abstract

Tons of cosmic material enter the Earth atmosphere every year, most of them being leftovers and debris from comets and shattered asteroids. Many of the estimates of this material influx rely on measurements carried out by observations of meteor showers and by ground-based searches of meteorites in deserted areas, either in hot deserts or in Antarctica. However, global space-based surveys are still missing; these surveys will provide valuable clues on the chemistry and physical properties of near-Earth bodies prior to its fragmentation in the Earth's atmosphere and its later shock with the surface. The thermal emission from this space dust is expected to be polarized due to the alignment of the grains with the solar radiation field and/or the Earth's magnetic field by radiative torques (RATs), depending on their properties (size and composition). In this work, we analyse the expected properties (strength and polarization) of space dust as seen from space. This is done at microwave wavelengths in the context of the project MARTINLARA funded by the Comunidad Autónoma de Madrid, to build a cubesat operating in the 80-220 GHz range, to test new technologies and probe the properties of space dust. The calculations have been carried out using the Monte Carlo code RADMC-3D for a grid of models simulating various possible properties of the dust grains and of their spatial distribution.

My poster is available at https://doi.org/10.5281/zenodo.7044485

Highlights of Spanish Astrophysics XI, Proceedings of the XV Scientific Meeting of the Spanish Astronomical Society held on September 4–9, 2022, in La Laguna, Spain. M. Manteiga, L. Bellot, P. Benavidez, A. de Lorenzo-Cáceres, M. A. Fuente, M. J. Martínez, M. Vázquez- Acosta, C. Dafonte (eds.), 2023

Probing star-planet interaction in Proxima Centauri with radio observations.

L. Peña-Moñino[1], M. Pérez-Torres[1], J.F. Gómez[1], J.L. Ortiz[1], G. Anglada[1], P.J. Amado[1], and F. Murgas[2]

[1] Instituto de Astrofísica de Andalucía-CSIC (IAA-CSIC), Glorieta de la Astronomía s/n, E-18008 Granada, Spain
[2] Instituto de Astrofísica de Canarias (IAC), C. Vía Láctea s/n, E-38205 La Laguna, Santa Cruz de Tenerife, Spain

Abstract

Recent MHD 3D modelling of the Proxima system predicts that the interaction of the planet Proxima b with its host star, Proxima, would be proceeding in the supra-Alfvénic regime. In this case, no radio emission from the star-planet interaction should be observed.
In this poster, we present multi-epoch radio observations of the Proxima Centauri system obtained with the Australia Telescope Compact Array (ATCA) in 2017 and 2021, at frequencies between from 1 to 3 GHz.
We also present a relatively simple modelling, which indicates that Proxima b is in the sub-Alfvénic regime, and therefore can induce radio emission from the interaction with its host star.
We find that the radio emission is highly circularly polarized in many epochs, with the maxima of emission happening at about twice per orbital period of Proxima b. The radio emission is consistent with being produced by the electron-cyclotron maser emission mechanism, and we suggest it is originated as a consequence of the interaction between Proxima b and its host star, Proxima. If confirmed, this result would validate the use of radio observations to detect new exoplanets. In addition, this would contradict the predictions from some 3D MHD modelling. This could in turn suggest that some of the stellar wind parameters in the region where Proxima b is located may need to be revised.

My poster is available at https://doi.org/10.5281/zenodo.7043419

Highlights of Spanish Astrophysics XI, Proceedings of the XV Scientific Meeting of the Spanish Astronomical Society held on September 4–9, 2022, in La Laguna, Spain. M. Manteiga, L. Bellot, P. Benavidez, A. de Lorenzo-Cáceres, M. A. Fuente, M. J. Martínez, M. Vázquez- Acosta, C. Dafonte (eds.), 2023

Search for warm gas in debris disks with JWST.

Isabel Rebollido[1], Christine Chen[1], Marshall Perrin[1], Aki Roberge[2], Cicero X. Lu[3], John H. Debes[1] and Amaya Moro-Martin[1,3]

[1] Space Telescope Science Institute, 3700 San Martin Dr., Baltimore, MD 21218, USA
[2] NASA Goddard Space Flight Center, Greenbelt, MD 20771, USA
[3] Department of Physics and Astronomy, The Johns Hopkins University, 3400 N. Charles Street, Baltimore, MD 21218, USA

Abstract

Observations in far-infrared and (sub-)mm wavelengths have found evidence for a non-negligible amount of gas around 20 nearby main-sequence stars with debris disks. This gas, located in the outer regions of the systems, is likely to have originated via collisions or evaporation of planetesimals due to dynamical instabilities. Gas detected in the optical range with spectroscopy, located much closer to the star, and attributed to the presence of evaporating bodies, has also been found in these systems, pointing towards these objects, also known as exocomets, as a possible transportation mechanism for volatiles from the outer regions of planetary systems, beyond the snowline, to the inner regions where rocky planets are located.However, observations thus far have not been able to identify warm gas in intermediate regions, or the presence of water, and therefore we don't yet understand how the transportation mechanisms might compare to those observed in the solar system. We propose to use NIRSpec fixed slit mid-resolution observations in the 3 to 5 micron range to look for volatiles in a sample of 5 debris disk stars with known millimetric and optical gas, in particular targeting the 4.5-5 micron water features that is not observable from the ground. The detection of CO and water could not only help constrain the amount and temperature of gas, key in planet formation studies, but also shed light into the dynamics and architecture of planetary systems, and have implications in astrobiological studies, such as water delivery theories.

My poster is available at https://doi.org/10.5281/zenodo.7048301

Highlights of Spanish Astrophysics XI, Proceedings of the XV Scientific Meeting of the Spanish Astronomical Society held on September 4–9, 2022, in La Laguna, Spain. M. Manteiga, L. Bellot, P. Benavidez, A. de Lorenzo-Cáceres, M. A. Fuente, M. J. Martínez, M. Vázquez- Acosta, C. Dafonte (eds.), 2023

Search of Exoplanets in steLLar streAms (SELLA).

S. Iglesias Álvarez [1], E. Díez Alonso [1], M. L. Sánchez [1], A. Castro-González [2], J. Rodríguez Rodríguez [1], and C. Rodríguez Pereira [1]

[1] Instituto Universitario de Ciencias y Tecnologías Espaciales de Asturias (ICTEA), C. Independencia 13, E-33004 Oviedo, Spain
[2] Centro de Astrobiología (CAB, CSIC-INTA), Depto. de Astrofísica, ESAC campus, 28692, Villanueva de la Cañada (Madrid), Spain

Abstract

In this work we search and characterize exoplanets orbiting members of stellar streams, structures in the Galaxy composed of stars with similar dynamic and chemical properties, and with galactic or extragalactic origin. With current facilities, the detection of exoplanets in extragalactic stellar streams, resulting from merger events, could be the only way to study in detail exoplanets formed outside the Milky Way. This could help to understand better the impact of the merger events in the planetary systems of these stars, and also to compare their planetary properties and statistics with the ones from the Milky Way. We used Gaia DR2 to select stellar candidates of the Arcturus stream, an over density of stars suspected to have an extragalactic origin, and we obtained their photometry from the TESS Full Frame Images. We found several transiting planetary candidates and present three of them which are being studied in detail.

My poster is available at https://doi.org/10.5281/zenodo.7016515

Highlights of Spanish Astrophysics XI, Proceedings of the XV Scientific Meeting of the Spanish Astronomical Society held on September 4–9, 2022, in La Laguna, Spain. M. Manteiga, L. Bellot, P. Benavidez, A. de Lorenzo-Cáceres, M. A. Fuente, M. J. Martínez, M. Vázquez- Acosta, C. Dafonte (eds.), 2023

The search for exocomets in photometry using CHEOPS.

Isabel Rebollido[1], Sebastian Zieba[2], Daniela Iglesias[3], Vincent Bourrier[4], Flavien Kiefer[5] and Alain Lecavelier Des Etangs[6]

[1]Space Telescope Science Institute, Baltimore, MD 21218, USA
[2]Max-Planck-Institut für Astronomie, Königstuhl 17, D-69117 Heidelberg, Germany
[3]Leiden Observatory, Leiden University, Niels Bohrweg 2, 2333CA Leiden, The Netherlands
[4]School of Physics and Astronomy, Sir William Henry Bragg Building, University of Leeds, Leeds LS2 9JT, UK
[5]Observatoire Astronomique de l' Universitè de Genève, Chemin Pegasi 51b, CH-1290 Versoix, Switzerland
[6]Institut d' Astrophysique de Paris, Sorbonne Universitè, 98bis boulevard Arago, Paris, 75014, France

Abstract

The interest in minor bodies has grown significantly in the past decade, thanks to the growth of the exoplanetary field and their relevance in planetary system formation and architecture. Particularly, the presence of exocomets has been detected in spectroscopy as variable absorption events in metallic lines (mainly Ca II K and Na D) in several A-type stars. While spectroscopy allows the detection of the gas component of cometary tails, it wasn't until the appearance of intensive exoplanet search photometric missions that the dust counterpart of these events was found, first with Kepler and then with TESS.

Still, there is only one star where exocomets have been detected simultaneously using the two different techniques: Beta-Pic. In an attempt to enlarge this number, we proposed observations of the bright exocomet-host star, 5 Vulpeculae, with CHEOPS for a time span of almost 2 full days. We present here the negative results of the observations, and what have we learned from the experiment.

My poster is available at https://doi.org/10.5281/zenodo.7048264

Highlights of Spanish Astrophysics XI, Proceedings of the XV Scientific Meeting of the Spanish Astronomical Society held on September 4–9, 2022, in La Laguna, Spain. M. Manteiga, L. Bellot, P. Benavidez, A. de Lorenzo-Cáceres, M. A. Fuente, M. J. Martínez, M. Vázquez- Acosta, C. Dafonte (eds.), 2023

A tactile model of the night summer northern sky for the teaching of astronomy to the BVI.

Pérez-Montero, E.[1], **Lanzara, M.**[2], **Ortiz-Gil, A.**[2], **Villaverde, M.**[1], **García-Benito, R.**[1], **Gallego-Calvente, T.**[1], **and García Gómez-Caro, E.**[1]

[1] Instituto de Astrofísica de Andalucía - CSIC. Apdo. de correos 3004, E-18080, Granada (Spain)
[2] University of Valencia, Astronomical Observatory, Paterna (Valencia), Spain

Abstract

Astroaccesible is an outreach project hosted by the Instituto de Astrofísica de Andalucía - CSIC aimed at the teaching and popularisation of the astronomy among all publics independently of their capabilities and abilities, paying special attention to the collective of blind and visually impaired (BVI). Among the different strategies and resources using in our project, we have developed new 3D models representing in relief some of the stars, constellations and deep sky objects that can be observed during night from the Northern hemisphere in spring and summer. These models can be used by BVI to transmit to them the spatial configuration of the sky during night, but can be also used as an additional resource for all kind of publics to complement their sensorial experience. We also describe additional resources based on sounds that can also be employed to get deeper into this multisensorial experience. Finally, we summarize some of the activities and the context in which this new material has been used in the last 2 years.

1 Introduction

The outreach project *Astroaccesible*[1] [5] has the objective of bringing astronomy to every public, using all kind of resources based on the senses other than that of sight in order to reach to the collective of blind and visually impaired (BVI). The objective of using this material and strategies for every public, independently of their abilities, is fundamented on that many of these complementary resources strength and deepen the attention and the clarity of the transmitted contents [3]. Therefore, *Astroaccesible* has also the objective of convincing other scientists and teaching professionals to incorporate an inclusive aspect to their projects, as this largely benefit the collective of impaired people, helping at the same time to improve the quality of their contents for everyone.

Among the different activities carried out by *Astroaccesible* in the last years there are thus sessions devoted to BVI, mainly in collaboration with the *Organización Nacional de Ciegos*

[1] http://astroaccesible.iaa.es

de España (ONCE), but also to all kind of publics at different educational levels, covering from primary to college, always using an inclusive methodology in any case. In all these activities it is common to resort to complete oral descriptions of the presented material, in combination with adequate comparisons, highlighting the relative weight of the sense of sight in the acquisition of the explained information.

Another important resource used in all the activities of *Astroaccesible* is the tactile material, under the form of both sheets in relief or 3D models, as those developed by the project *A Touch of the Universe* [2], representing some of the rocky planets and moons of the Solar System.

In addition, 3D models of the night sky printed on the outer surface of an hemisphere, and representing stars in relief, with lines joining stars of the same constellations have been also widely used in our activities. These models help BVI to establish a spatial mental image of the distribution of these elements on the sky, but can also help people able to see the same figures projected onto a screen, to identify and to put them in the context of the whole sky. We have used in the last years 3D models representing the night sky visible from the Northern hemisphere during autumn and winter (i.e. from Orion to Gemini constellations), an epoch when public observations are not frequent due to the adverse weather conditions. For this reason, in this contribution, we present a new model representing the night sky during spring and summer, with most of the constellations observable during this period that can be used by both the collective of BVI and people without problems of vision during outdoors or indoors inclusive activities.

2 Description and goals of the 3D models

The 3D models described here consists of an hemisphere whose outer surface presents different elements in relief representing stars and deep sky objects that can be observed in the night sky from the Northern hemisphere, at a latitude similar to that of southern Europe, during spring and summer.

The different elements in relief include points representing stars. The size of these points is proportional to the brightness of the corresponding star. Stars belonging to a same constellation are joined by solid lines. The represented constellations include Virgo, Scorpius, Sagitarius, Lyra, Cygnus, Andromeda, Perseus, Ursa Major, and Ursa Minor. These are also joined between them with dashed lines that serve as a guide to travel throughout the model using the sense of touch. In addition, a coarse band goes through the surface representing the Milky Way, as observed during the same epoch. Finally, there are some other coarse extended circles representing deep sky objects, such as the Virgo cluster, the Ring Nebula, or the Andromeda galaxy. This portion of the night sky is easily observable from places without an excess of light pollution during spring and summer, when most of public observations made with an outreach purpose are carried out. Therefore, this material can supply a valuable additional source of information for people of the BVI collective and, at same time, an additional source of information to identify the same objects to those able to see them directly in the sky.

A prototype using different elements in relief was designed, manually elaborated and finally digitalized. From this, we printed several models that could be later used in face-to-face activities thanks to the financial support from the Sociedad Española de Astronomía (SEA) through its annual program of grants to outreach projects. An image of one of the printed resulting 3D models can be seen in left panel of Figure 1. Additionally, the file necessary to create more copies of the same model, along with instructions describing the represented elements, both in English and Spanish, can be found in this link. The optimal diameter to print the models is 20 cm.

Figure 1: *Left:* Image of the printed 3D model representing the summer and spring northern night sky. *Right:* Image of one of the activities carried out within the project *Astroaccesible* using the set of printed models. This activity was done in the *Museo Casa de la Ciencia* of CSIC in Sevilla (Spain) in October 2022 as part of the Space Week organized by this museum and was addresed to students of secondary level without any problem of vision.

3 Additional sonic resources

Sounds constitute an additional resource that can largely contribute to complement the multisensorial aspect of the activities carried out by *Astroaccesible*, adding an extra dimension to all the treated material. The amount of available adaptations from astronomical data to sounds through their multiple techniques (e.g. audification, sonification, or musification) helps to incorporate them to different adapted activities, as those related with the use of the models, deepen on their inclusive aspect.

For instance, among the different available resources, the *Cosmonic* project [1], whose different products can be consulted in its webpage http://rgb.iaa.es/es/cosmonic/, provides different animations with sounds, that allow the BVI to access to the data and simultaneously help people able to see the graphical content to properly interpret them.

An additional resource developed in the framework of *Astroaccesible* is the project *El Universo en palabras* (*The Universe in words*) [4], a series of videos publicly available through a web channel in YouTube with images of different astronomical objects with an audio description in Spanish of both the context and the content of the image. Again, this resource can be useful for people of the BVI collective to overcome the barrier of the lack of information,

supplying at same time a valuable background to everyone who want to better understand the described objects.

Since many of the objects represented in the 3D model of the night summer sky can be also represented with either sonifications or audio descriptions, the simultaneous use of sounds in the activities focused on models ensures a much more efficiency in the teaching process when this material is used.

Moreover, the situation of pandemic suffered during most of 2020 and 2021, when most of in-person activities were cancelled and, therefore, the activities using tactile activities were not possible, the inclusive workshops participated by *Astroaccesible* were totally virtual and based exclusively on the use of sonic resources. This other modality of interaction, however, has also the advantage that it can be used for a more extended public involving participants from different geographical areas. Our experience from this period shows that a combination of both types of activities (i.e. in-person with models and virtual using only sounds) can be the best solution for the post-pandemic times.

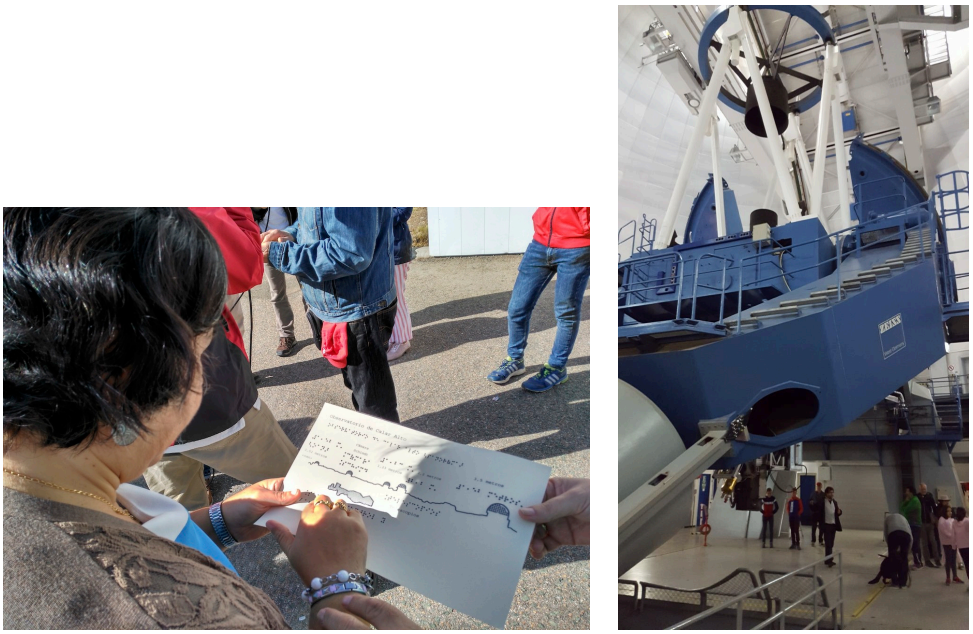

Figure 2: Images of one of the inclusive visits to the Calar alto Observatory *Left:* A person of the BVI collective exploring a sheet showing in relief some of the domes of the Observatory. *Right:* Picture of one of the groups under the dome of the telescope of 3.5 m.

4 Use of the 3D models in outreach activities

Although the 3D models representing the summer night sky were designed and printed during 2019, due to the global situation of pandemic, they could not be used in public outreach activities until the end of 2021. Fortunately, given the growing number of astronomical

resources based on sounds, as explained in the previous section, allowed us to continue our inclusive activities addressed to an impaired and non-impaired public, during the period when in-person activities and the use of tactile material was restricted. As an example, during April 2021 *Astroaccesible* took part in the organization of the *Month of Astronomy*, including several virtual activities addressed to members of ONCE in Spain. This program included virtual conferences using the sound as a resource to understand several astronomical objects, the public launch of the project *El Universo en palabras*, or the organization of a round table with several professional astronomers to describe without the use of images, different fields or problems of the astronomy. The conference using sounds was repeated for several educational institutions and scientific associations encouraging people to get interest about astronomy using sensorial channels complementing the sight.

Once some in-person activities could be organized and the new 3D models could be used again, they were employed in scholar activities at different educational levels, such as the event *Noche Europea de los Investigadores*, or the *Aula Científica* in the University of Granada, with a high level of acceptance among the students and the teachers, even if these collectives did not include any participant with a visual disability. An example of these activities can be seen in right panel of Figure 1 taken during the *Week of Space* organized by the *Casa Museo de la Ciencia* in Sevilla (Spain) for students of secondary level.

Among the other activities for which this set of models were used and exclusively addressed to people of the BVI collective, it is important to highlight the program of inclusive visits to the Observatory of Calar Alto (Almería, Spain) financed by CSIC. We made three visits to this Observatory for BVI people in ONCE in the region of Andalusia, and another one for a intellectual disability association. The combined used of the models, sounds, images and inclusive explanations, along with the presence under the dome of several of the telescopes of the observatory was a complete experience that helped to fight against the idea that astronomy can only be learnt by people without any sight problem and reinforces the argument that multisensorial resources can be always applied to better transmit any scientific concept to any public. Two images of one of these inclusive visits are shown in Figure 2, one showing one person of the BVI collective exploring one sheet in relief showing the different domes present in the Observatory, and another one taken in the moment of the visit to the dome of the telescope of 3.5 m, the largest of the Observatory.

Therefore, the production of new tactile and sonic resources, not just in the outreach ambit, but also at a higher educational and research level can largely benefit the teaching process and the transmission of ideas and knowledge of all type of public and researchers.

Acknowledgments

We acknowledge the *Sociedad Española de Astronomía* (SEA) for its financial support to print most of the 3D models described in this proceeding, without its use the inclusive activities carried out by *Astroaccesible* would not be possible. We also thank to *Consejo Superior de Investigaciones Científicas* (CSIC) for its help to finance the inclusive visits to the Observatory of Calar Alto through its program *Cuenta la Ciencia*, during 2020. EPM also thanks his guide dog Rocko, without whose daily help his both research and outreach activities would be much more difficult.

References

[1] García-Benito, R. & Pérez-Montero, E. 2022, Revista Mexicana de Astronomia y Astrofisica Conference Series, 54, 28. doi:10.22201/ia.14052059p.2022.54.06

[2] Ortiz-Gil, A., Burguet-Castell, J., Pérez-Montero, E., et al. 2019, EPSC-DPS Joint Meeting 2019

[3] Pérez-Montero, E. 2019, Nature Astronomy, 3, 114. doi:10.1038/s41550-019-0693-3

[4] Pérez-Montero, E., Barnés-Castaño, C., & García Gómez-Caro, E. J. 2022, Revista Mexicana de Astronomia y Astrofisica Conference Series, 54, 111. doi:10.22201/ia.14052059p.2022.54.25

[5] Pérez-Montero E., García Gómez-Caro E., Sánchez Molina Y., Ortiz-Gil A., López de Lacalle S., Tamayo A., 2017, hsa9.conf, 742

Highlights of Spanish Astrophysics XI, Proceedings of the XV Scientific Meeting of the Spanish Astronomical Society held on September 4–9, 2022, in La Laguna, Spain. M. Manteiga, L. Bellot, P. Benavidez, A. de Lorenzo-Cáceres, M. A. Fuente, M. J. Martínez, M. Vázquez- Acosta, C. Dafonte (eds.), 2023

Educational Project with Robotic Telescopes (PETeR): robots looking to the future.

Rodríguez Eugenio, N.[1,2]

[1] Instituto de Astrofísica de Canarias (IAC), E-38205 La Laguna, Tenerife, Spain
[2] Universidad de La Laguna (ULL), Departamento de Astrofísica, E-38206 La Laguna, Tenerife, Spain

Abstract

The "Proyecto Educativo con Telescopios Robóticos" (PETeR) of the Instituto de Astrofísica de Canarias is an online inquiry-based laboratory that allows school students to carry out their own observations and research projects in astronomy using professional robotic telescopes. The availability of observing time on several telescopes, which also offer different types of observations through user-friendly portals, has allowed us to open the project to the entire Spanish educational community, from primary to secondary school and vocational training. This paper outlines the project's goals, materials and educational approaches used, as well as the teacher training programmes we provide in the framework of PETeR.

1 Introduction

Student lack of interest in STEM (Science, Technology, Engineering and Mathematics) studies and careers is a growing concern in many European countries [2]. In Spain, the demand for enrolment in these university studies is five percentage points below the European average [1]. Factors influencing students' disenchantment with STEM include: the way these subjects are taught in schools, the perception that they are difficult studies, and the apparent lack of sufficiently attractive career opportunities [5].

Therefore, in order to engage students in these areas, it is necessary to focus on three aspects: 1) promoting hands-on science education; 2) providing teachers with the necessary resources, training and support to enable them to develop a more attractive and stimulating STEM education for their students; and 3) contributing to improving the social perception of science and technology professions.

Astronomy is the perfect engine to arouse interest in STEM subjects [6]. In addition to its aesthetic and general appeal, the development of robotic telescopes in recent decades, together with tools that allow their use by non-professional observers, has opened up this science to the participation of the educational community [4]. Robotic telescopes also allow developing an inquiry-based approach to teaching-learning STEM, which translates into a better understanding and assimilation of concepts [3].

The Instituto de Astrofísica de Canarias (IAC) has made a firm commitment to STEM education deciding to allocate part of its guaranteed time on some robotic telescopes to the Spanish educational community. To this end, it launched the Educational Project with Robotic Telescopes (known by its Spanish acronym PETeR), linked to its Outreach and Communication Unit.

PETeR seeks to foster the interest of pre-university students in science and the development of their STEM skills through their participation in real research experiences using professional robotic telescopes. Our objectives also include training teachers in astronomy and inquiry-based learning methods, as well as contributing to the dissemination of astronomy and astrophysics.

2 PETeR robots

PETeR was launched in 2006, following the installation of the Liverpool Telescope (LT) at the Roque de los Muchachos Observatory (Canary Islands). The LT was the first of the fully autonomous 2-metre robotic telescopes and it is one of the largest and most advanced even today. The IAC decided to allocate 25% of its observing time with the LT to PETeR, which is 5% of the total observing time on this telescope.

Figure 1: Some of the robotic telescopes available through PETeR. Left: the Liverpool Telescope, credit: Daniel López / IAC. Middle: worldwide distribution of the LCO 0.4 m telescopes (bottom) and image of those at the Teide Observatory (top, credit: Daniel López / IAC). Top right: PIRATE and COAST telescopes, credit: IAC. Bottom right: SARA telescope at the Roque de los Muchachos Observatory, credit: ING / IAC.

In addition to the LT, other "robots" have been added to the project in recent years. In 2018, PETeR joined as educational partner of Las Cumbres Observatory (LCO) through the Global Sky Partners programme, which gives access to its network of 40 cm telescopes located in six observatories around the world, in both the Northern and Southern Hemispheres

(see Fig. 1). Since 2019, PETeR users can also observe with the 0.5-metre-class PIRATE and COAST telescopes of the Open University, installed at the Teide Observatory (Canary Islands). The latest telescopes that we have incorporated into the project are those of the Southeastern Association for Research in Astronomy (SARA) network, of 1-metre class, located in the Canary Islands, Chile and the USA.

All the telescopes available at PETeR are fully autonomous, except for the SARA telescopes, which are controlled remotely. In the first case, users can access the portals of the different telescopes through the PETeR website to request their queued observations and download the images once they have been obtained. At the SARA network telescopes, we request half nights at the Kitt Peak (USA) and Cerro Tololo (Chile) observatories to coincide with school hours in Spain, allowing schools to connect live to the remote observations.

3 Target audience

The availability of observing time on several telescopes, which also offer different types of observations through user-friendly portals, has allowed us to open the project to all levels of pre-university education, from primary to high school and vocational training. The observation time is offered to schools completely free of charge and, for the time being, with no limitation other than the division of the available time among the registered schools.

At present, PETeR's users include more than 300 schools throughout Spain, some 25 secondary schools in other countries that collaborate in specific projects with Spanish schools, as well as some 40 non-formal schools and associations of amateur astronomers that participate in the project by carrying out educational and outreach activities with children and young people. The scope of the project is currently around 10,000 students per year.

4 PETeR approaches

PETeR works as an online inquiry-based laboratory (www.iac.es/peter) that allows students to discover the Universe by carrying out their own astronomical observations and research. To do this, we offer different tools, resources and formats.

In 2012, we launched a survey among Spanish teachers, active and potential users of PETeR, to find out their needs and the project models they found most interesting and appropriate. Based on the results of that study [7], we proposed three active learning approaches, complementary to each other, which try to cover most of the demands of the educational community. Below we present the different models that we offer in the project.

4.1 Pre-defined observations

This model consists of obtaining and analyzing one- or three-color images of different types of objects that can be selected from a list. The observing interface sets, for each object, the appropriate instrument, filter(s), and exposure time. Therefore, this is the easiest option to integrate into teaching practice, as it requires less prior knowledge and is less time-consuming.

For this approach, we use the LT and the observing portal of the National Schools' Observatory (NSO), which allows observations of regions of the Moon, planets, nebulae, stellar clusters and galaxies. On the PETeR website, we also offer a programme for visualising and analysing astronomical images, PeterSoft, which is specially designed for education.

4.2 Didactic Units

Each Unit introduces several astronomy concepts related to primary and secondary school curricula, and provides one or more activities, which make use of pre-observed data and serve as a practical introduction to the different tools of the image processing software. Some of the topics proposed are the structure of the Solar System, the movements of planets and satellites or the determination of distances in the Universe. The aim of this approach is for students to develop their STEM skills while assimilating knowledge about the topic presented.

4.3 Research Projects

This format corresponds to real scientific processes, either guided or open enquiry. In the first case, we propose to teachers the type of objects to be studied and the possible methodology to select the objects, programme the observations and analyse the data obtained, providing them with the teaching resources and software necessary to carry out the research. Some examples of guided research projects we offer are the search for supernovae and for variable stars, the characterisation of exoplanets with transits or the confirmation of asteroid orbits.

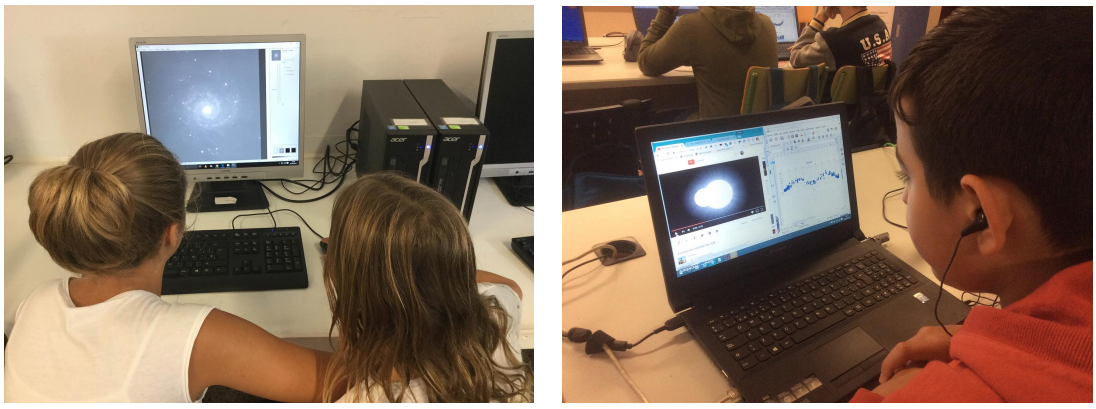

Figure 2: Sixth grade primary school students (left) and 12-year-old secondary school students (right) developing different research projects with PETeR. Image credits: Aleix Roig, Escola GEM (left), IES El Calero (right).

In open research projects, it is the groups of students plus their teacher who decide what they want to investigate and how. In all cases, we provide scientific and technical advice to the users for the development of the project.

The observations required for these types of projects can be performed directly by our users through the LCO observation portal, the Open University's public portal, and the advanced

interface of the NSO portal. By requesting their observations autonomously, PETeR users have a real experience of obtaining data in astronomy. The strength of this approach is that students experience the scientific process in all its phases. Collaborative work is also encouraged, both within the classroom and with other schools in Spain and other countries.

5 Teachers: a key factor

During the first years of the project, few observations were made. One of the reasons given by teachers was their lack of knowledge in astronomy to guide their students in the research projects. Thus, in 2015 we started to run teacher trainings that introduce astronomy and astrophysics concepts but are eminently practical. Our courses focus on the use of robotic telescopes, software and web resources to visualize and analyse astronomical images, inquiry-based learning methods, and examples of research projects that can be develop with PETeR.

One of our main target groups is teachers in the Canary Islands, as we aim for the local educational community to identify the scientific culture and sky of the Archipelago as part of their own heritage. We offer them extensive training along the school year, both in person and online, in collaboration with the Department of Education of the Canarian Government. During the school year, we also run online training sessions for teachers from all over Spain.

In summer we run the international school "Astronomy Education Adventure in the Canary Islands" (AEACI), which celebrated its eighth consecutive edition in 2022. This teacher training is organized with the collaboration of NUCLIO, the NSO, the Faulkes Telescope Project and, in the last four editions, the CESAR project. It consists of a week of intensive training that includes lectures, workshops, visits to the IAC facilities and activities that allow participants to establish links with teachers from other schools in Spain and other countries, fostering cooperation between schools around the world.

Figure 3: Pictures taken during the AEACI 2019 and AEACI 2022 international schools. Credit: IAC.

We have trained more than 1,200 teachers and educators from over 60 countries of the five continents (more than 800 of them from Spain) through the different courses that we organize or in which we participate.

6 Conclusions

Educational projects with robotic telescopes require a significant investment of technological resources (telescope time, observation portals, educational software, etc.) and human resources (staff dedicated to developing teaching materials and research projects, advising and training teachers, etc.), but the benefits are considerable. PETeR and other similar projects democratise access to the sky and to astronomy, allowing hundreds of schools to observe with telescopes located in some of the best observatories on the planet, regardless of their economic level and without the light pollution of the region where they are located being an impediment. In addition, queued observations as well as remote observations during school hours greatly facilitate the participation of schoolchildren aged 6 to 12, for whom night-time observing activities are not usually organised.

In the field of STEM education, the results show that the educational use of robotic telescopes can effectively develop inquiry-based teaching-learning processes, foster students' interest in these areas and stimulate scientific thinking. In Astronomy, we often say that our tools, the telescopes, allow us to look into the past. At PETeR, we use them to encourage the scientific minds of the future.

Acknowledgments

This work has been supported in part by the agreement between the Liverpool John Moores University and the Instituto de Astrofísica de Canarias for the installation and operation of the Liverpool Telescope, and by the Spanish Ministry of Economics, Industry and Competitiveness (MINECO) under the Severo Ochoa Centres of Excellence Programmes 2012 – 2015 and 2016 - 2019.

References

[1] CRUE Spanish Universities (2019). ISBN 978-84-09-18182-7

[2] European Commission, Directorate General for Education and Culture – Higher Education (2015). Publications Office of the European Union, doi: 10.2766/000444

[3] Furtak, E. M., Seidel, T., Iverson, H., & Briggs, D. C. (2012). Review of Educational Research, 82(3), 300-329

[4] Gomez, E. L., & Fitzgerald, M. T. (2017). Astronomical Review, 13(1), 28–68

[5] Obra Social La Caixa, FECYT and everis (2015)

[6] Pasachoff, J., & Percy, J. (Eds.) (2005). Teaching and Learning Astronomy: Effective Strategies for Educators Worldwide. Cambridge University Press

[7] Rodríguez Eugenio, N. (2019). Proceedings of the IAU Astronomy Education Conference, 83-89

Highlights of Spanish Astrophysics XI, Proceedings of the XV Scientific Meeting of the Spanish Astronomical Society held on September 4–9, 2022, in La Laguna, Spain. M. Manteiga, L. Bellot, P. Benavidez, A. de Lorenzo-Cáceres, M. A. Fuente, M. J. Martínez, M. Vázquez- Acosta, C. Dafonte (eds.), 2023

Martian Science and Technology in the Research High School.

Ordóñez-Etxeberria, Iñaki[1]

[1] Pamplona Planetarium, Navarra - Spain

Abstract

The project described is an initiative undertaken by the Pamplona Planetarium and high school students from several different institutions. The goal of the project was to construct and assemble a 1:4 scale replica of the Perseverance rover. This project was carried out over the course of a school year, with the participation of 12 students from 4 different institutions. Each institution was responsible for a different part of the model, and monthly sessions were held to discuss the progress and any challenges encountered. In addition to building the rover replica, each student also conducted their own small-scale scientific research on Mars and the context in which the Perseverance rover operates. This project appears to be a unique opportunity for high school students to engage in hands-on learning and teamwork, while also gaining a deeper understanding of Mars and the science behind the Perseverance mission. This can help to foster students' interest in science and technology, and may be a valuable experience that prepares them for future studies and careers in these fields.

1 Introduction

In June 2021, a collaboration agreement was established between the Pamplona Planetarium and several high schools institutes in order to promote an initiative called "Bachillerato I+". This type of research high school has been implemented in the institutes of Barañáin, Plaza de la Cruz, Ribera del Arga and Valle del Ebro, and constitutes an educational option within the high school aimed at students who are interested in delving into the different research methods and in the analysis of the problems of any investigation.

The rover replica construction project was carried out during a school year, with the participation of 12 students from 4 different institutes, with equal participation between male and female students. However, the total number reached by the project has been higher, due to the participation of the leading students in different outreach sessions within their own institutes. Each institute has been in charge of a different part of the model, and during this course there have been monthly sessions in which the work done and the difficulties encountered were shared. In addition to the construction of the rover, each student has carried out a scientific investigation about Mars and the context in which the Perseverance

rover is located. This is a project in which the students have participated very actively and in which both technological and scientific concepts of missions to Mars have been worked on.

2 Development of the project

The way of working has consisted of simulating the operation of NASA or another space agency, in the construction of these kind of vehicles, with the distribution of the different components between the different centers. The project has been articulated in monthly sessions divided between the technical and scientific fields, in which the students have shared the development of the parts for the assembly of the rover that they had assigned by institute, and the difficulties in their construction and/or acquisition. Also in these sessions, each student has exposed to the rest of the participants the details of the scientific topics that they are analyzing, such as the meteorology on Mars, geology, impact craters, polar caps, water on the planet, storms from dust etc. In the development of their scientific investigations, the students have been working with data from the missions to Mars, downloading the information from the public repositories of the PDS, processing the data and relating the results to their own investigations.

The rover model selected for the project is publicly available on the informative web space howtomechatronics.com and consists of the assembly of different parts made with 3D printers, installation of the vehicle's electronic system and programming and connection of the devices.

In total, more than 150 parts have been printed with 3D printers and the manufacturing of these parts was divided equally among the four institutes (Figure 1). This part of the project allowed the students to gain experience in this type of tool, since it was the first time for all the students that they had to get involved in the use of this type of tool. The students also made a 1:1 scale Perseverance rover wheel to compare with the wheels on our model and get an idea of the rover's actual dimensions.

3 Results

After 9 months of diligent work, the team successfully completed the construction of the replica of the Perseverance rover (Figure 2). However, the scientific research projects related to the project are currently ongoing, and will soon be presented and defended at their respective institutions. This multi-faceted project has been a valuable learning experience for the students involved, and we look forward to seeing the results of their research.

The rover is equipped with motors and electronic components that allow it to move across the terrain avoiding obstacles. It also has a camera that allows you to observe the situation from the rover's perspective. All these pieces of equipment can be handled and controlled with a radio control joystick.

Figure 1: Two types of sessions in the project: The engineering sessions (left) ordering the more than 150 pieces made by the different institutes. The scientific sessions (right) with the presentation of the different topics to the rest of the students.

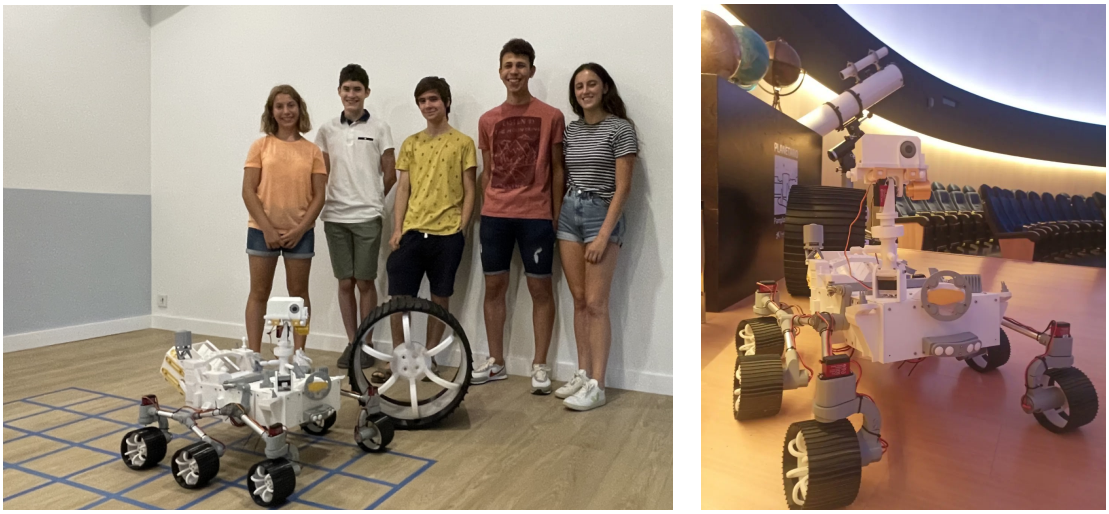

Figure 2: Final result of the construction of the rover model, which is currently on display at the Pamplona Planetarium.

4 Conclusions and Next Steps

Among the direct benefits focused on the students who have participated, we can highlight::

1. Hands-on learning experience for high school students.
2. Opportunity to apply technological and scientific concepts to a concrete project.
3. Collaborative teamwork among students from different institutions.

4. Development of deeper understanding of Mars and the Perseverance mission.
5. Enhancement of students' interest in science and technology.
6. Preparation for future studies and careers in these fields.
7. Positive impact on students' engagement and motivation.

We can conclude that this project in order to build a replica of the Perseverance rover has been successful in terms of engaging and motivating students, as well as providing a practical application of technological and scientific concepts. Additionally, the project has contributed to a deeper understanding of Mars and the Perseverance mission, and has fostered students' interest in science and technology. To which we must add that as a result of the project we have a replica of the Perseverance rover on which to continue working.

4.1 Next Steps

We have proposed to the students of the following course the possibility of including a robotic arm and a weather station in the rover.

The decision to continue the project and add a robotic arm to the front of the rover shows a long-term commitment to educational and practical learning for students. The addition of a robotic arm also offers the opportunity to continue exploring and experimenting with technologies and processes used in Mars exploration. Overall, this project seems to be a valuable initiative that benefits students and promotes their interest in science and technology.

In addition, there is the possibility of the inclusion of a weather station (similar to MEDA weahter station, [1]) inside the rover replica also offers the opportunity to address topics related to meteorology and climate change with students, which can help to increase their knowledge and interest in these important subjects. Overall, this project seems to be an excellent opportunity for students to gain practical skills and scientific knowledge while working on a collaborative and engaging project.

We highly encourage other schools to replicate this project. The construction and assembly of a replica of the Perseverance rover offers a unique and engaging learning opportunity for students, and allows them to apply technological and scientific concepts to a tangible project. Additionally, the project promotes collaboration among students from different schools, and encourages a deeper understanding of Mars and the Perseverance mission.

References

[1] J. A. Rodriguez-Manfredi, M. de la Torre Juárez, & The MEDA team, Space Sci Rev 217, 48 (2021). https://doi.org/10.1007/s11214-021-00816-9

Highlights of Spanish Astrophysics XI, Proceedings of the XV Scientific Meeting of the Spanish Astronomical Society held on September 4–9, 2022, in La Laguna, Spain. M. Manteiga, L. Bellot, P. Benavidez, A. de Lorenzo-Cáceres, M. A. Fuente, M. J. Martínez, M. Vázquez- Acosta, C. Dafonte (eds.), 2023

Mentoring Program for Female Astronomers of the Spanish Astronomical Society: *Walking together Towards the Stars.*

Manjavacas, E.[1,2], Rebollido, I.[3], Barrado-Izagirre, N.[4], Agís-González, B.[5], Bonoli, S.[6], Cerviño, M.[7], de Lorenzo-Cáceres, A.[8], Martínez-Núñez,S.[9], Ospina, N.[10], Pintos-Castro, I.[11], Rodríguez-Baras, M.[12] Rouco Escorial, A.[13,14], Suso, J.[15], Varela, J.[11], and Vidal-García, A.[12]

[1] AURA for the European Space Agency (ESA), ESA Office, Space Telescope Science Institute, 3700 San Martin Drive, Baltimore, MD 21218, USA
[2] Department of Physics and Astronomy, Johns Hopkins University, Baltimore, MD 21218, USA
[3] Space Telescope Science Institute, 3700 San Martin Drive, Baltimore, MD 21218, USA
[4] UPV/EHU, Escuela de Ingeniería de Bilbao, Fisica Aplicada, Bilbao, Spain
[5] Instituto de Astrofísica de Andalucía-CSIC, Glorieta de la Astronomía s/n, 18008, Granada, Spain
[6] Donostia International Physics Center (DIPC), Manuel Lardizabal Ibilbidea, 4, San Sebastián, E-20018 Donostia, Spain; Ikerbasque, Basque Foundation for Science, E-48013 Bilbao, Spain
[7] Centro de Astrobiología (CAB), CSIC-INTA, Carretera de Ajalvir km 4, E-28850 Torrejón de Ardoz, Madrid, Spain
[8] Instituto de Astrofísica de Canarias, Calle Vía Láctea s/n, E-38205 La Laguna, Tenerife, Spain; Departamento de Astrofísica, Universidad de La Laguna, E-38200 La Laguna, Tenerife, Spain
[9] Instituto de Física de Cantabria (CSIC-Universidad de Cantabria), 39005, Santander, Spain
[10] Department of Theoretical Physics, University Autonoma Madrid, 28049 Madrid, Spain
[11] Centro de Estudios de Física del Cosmos de Aragón (CEFCA), Plaza San Juan 1, 44001, Teruel, Spain
[12] Observatorio Astronómico Nacional (OAN), Alfonso XII, 3, 28014, Madrid, Spain
[13] Center for Interdisciplinary Exploration and Research in Astrophysics (CIERA) and Department of Physics and Astronomy, Northwestern University, Evanston, IL 60208, USA
[14] European Space Agency (ESA), European Space Astronomy Centre (ESAC), Camino Bajo del Castillo s/n, 28692 Villanueva de la Cañada, Madrid, Spain
[15] Observatorio Astronómico de la Univ. de Valencia, C/Catedrático Jose Beltran, 2, 46980, Paterna, Valencia, Spain

Abstract

Mentoring programs for career and personal development have shown to be incredibly beneficial for mentees, boosting their work and life satisfaction. Mentoring programs are particularly important for women in academia, where they are usually a minority. In 2021, in the context of the commission of Women in Astronomy of the Spanish Society of Astronomy, we started a mentoring program for female astronomers to support their careers. In the first two editions, we have more than 50 participants between mentors and mentees. In the mentoring program, we assigned a mentor to each mentee, according to their preferences and objectives. To encourage networking, we carry on group peer-mentoring sessions among mentors and mentees. Finally, we organized training sessions for mentors and mentees with the aim of boosting their career development.

1 Introduction

Mentoring is the act or process of helping and giving advice to a younger or less experienced person in your field. The benefits of mentoring programs in career development, personal development and mental health have been widely shown: mentoring allows the mentees to gain practical advice, encouragement and support, learn from the experiences of others, increase academic confidence, establish a support network, and ultimately increase work and life satisfaction. Thus, mentoring is particularly important in the case of women in academia, who often feel more isolated and unsupported in a work environment than their male counterparts, where they are a minority [1]. This is probably one of the reasons explaining the lack of women in academia beyond the postdoctoral stage [2]. Mentoring programs that aim at increasing diversity in academia are therefore crucial since it has been demonstrated that diverse research groups produce stronger research [3].

The Commission of Women and Astronomy of the Spanish Astronomical Society is the peer support group for women in the Society, which advocates raising awareness of the role of women in astronomy, and it is leading the change toward a less-biased academic environment (see Rodríguez-Baras et al. in this Proceedings series). In the context of the Commission of Women and Astronomy, we started a mentoring program in May 2021 for female astronomers members of the Spanish Astronomical Society. This year we started the second edition of the program, with about 50 participants (25 mentor-mentee pairs). In this proceeding, we will describe the activities we have carried out in this mentoring program during the first two editions.

2 Aims of the Mentoring Program

The aims of the mentoring program for female astronomers are focused on providing the support and tools to the younger female astronomers that are given by default to their male counterparts by the academic system since it has traditionally been male-dominated. The

three main objectives of this mentoring program are the following:

- Provide role models of female astronomers that support the younger generation of women astronomers to succeed in academia.
- Build a solid network among women of different academic environments members of the Astronomical Spanish Society across the globe.
- Help younger female astronomer to gain confidence in their skills and abilities.

3 Flow of the Mentoring Program

Any female member of the Spanish Astronomical Society may apply to be part of the mentoring program as mentor, under the requirement that they have a postdoctoral experience of at least 2 years, and a mentee, under the requirement that they have been accepted in a PhD program inside or outside Spain. The minimum time-requirement to stay in the program is 1 year, with the possibility of staying longer if they wish, and to follow the code of conduct as stated in the program webpage[1]. These are the annual different stages of the mentoring program that repeat every year after we receive all mentees and mentor applications:

- We put in contact mentors and mentees, according to the preferences and career/personal objectives of the mentees.
- We offer training to the mentors and the mentees at the beginning of the program. The aim of these trainings is to clarify the role and support that mentors might offer, and prepare mentees to make the most of the mentoring relationship.
- Each trimester of the academic year, we organise a peer-mentoring session among mentors and mentees separately. The aim of these sessions is to allow engagement on networking, and to provide a space for support among mentors and mentees.
- After 4–6 months in the mentoring program, we offer another training session to further guide the mentors into the mentoring relationship with their respective mentees.
- Finally, we offer additional, non-mandatory trainings during the academic year to further support the careers of the mentoring program, with special focus in the mentees. In the next section, we will specify some of the activities during the first edition of the program.

4 Activities

These are the extraordinary activities we carried on as part of the mentoring program in its first edition:

[1] https://www.sea-astronomia.es/programa-mentoria

- Training for Mentors: we offered a training for all mentors in the mentoring program by Yolanda García[2], an expert in leadership development, diversity & inclusion, executive coaching, project management, and business consulting. The training had three sessions in which the mentors were trained to guide their mentees through the program.

- Special Chat with Dr. Jocelyn Bell-Burnell: As part of the visit of Dr. Jocelyn Bell-Burnell to the European Space Agency Center (ESAC) in Madrid, the members of the SEA mentoring program for female astronomers had the chance of chatting with one of the most relevant female role-models in Astronomy, and ask her for advise on how to further advance academy to be more inclusive for women.

- Impostor Syndrome Workshop: Dr. Paola Pinilla[3], Associate Professor of Astrophysics at University Collegue London gave a workshop in which we talked about what is the Impostor Syndrome, and how it affects women in academia and other minorities. The aim of this workshop was to raise awareness of this issue to mitigate the impact in women within our mentoring program.

- How to prepare your Postdoc Application: Dr. Violeta González Pérez[4] gave an introductory training session for our mentees on how to write your postdoc applications. This training session was particularly useful for the mentees that were applying the first time for postdoc positions.

5 Conclusions

After the closing of the first edition of the SEA mentoring program for female astronomers, the great majority of the participants showed to be highly satisfied with the SEA mentoring program. 9 of the survey respondents graded the program with a 10/10, 12 graded as 9/10, and 6 graded the program with a 8/10. In addition, the great majority were extremely satisfied with their mentors: 16 respondents gave a 10/10 to their mentors, 3 gave a 9/10, 4 gave a 8/10, and 3 gave a 7/10. Finally, about 76% is willing to participate in the second edition of the mentoring program as well, and an extra 14% may be also participating. The second edition of the mentoring program for female astronomers is already ongoing until June 2023. The call to participate in the third edition of the program is scheduled to open in September 2023.

Acknowledgements

We would like to acknowledge the Spanish Astronomical Society Board of Directors for their unconditional support in the development of the Mentoring Program.

[2]http://www.ahorayo.es
[3]https://paola-pinilla.com
[4]https://viogp.github.io

References

[1] Ivie, Rachel and White, Susan and Chu, Raymond Y. 2018, https://ui.adsabs.harvard.edu/abs/2018arXiv181111836I

[2] Pérez Sedeño, Eulalia and Kiczkowski, Adriana and Márquez Pérez, Isabel, 2018, NatAs, 2, 628-633

[3] Nielsen, M.W., Bloch, C.W. & Schiebinger, L., 2018, Nat Hum Behav 2, 726–734. https://doi.org/10.1038/s41562-018-0433-1

Highlights of Spanish Astrophysics XI, Proceedings of the XV Scientific Meeting of the Spanish Astronomical Society held on September 4–9, 2022, in La Laguna, Spain. M. Manteiga, L. Bellot, P. Benavidez, A. de Lorenzo-Cáceres, M. A. Fuente, M. J. Martínez, M. Vázquez- Acosta, C. Dafonte (eds.), 2023

Per aspera ad astra simul: ERASMUS+ strategic partnerships for international education and outreach.

Jones, D.[1,2], Kabáth, P.[3], García-Rojas, J.[1,2], Hanuš, J.[4], Jakubík, M.[5], Janík, J.[6], Nagy, R.[7], and and Tóth, J.[7]

[1] Instituto de Astrofísica de Canarias, E-38205 La Laguna, Tenerife, Spain
[2] Departamento de Astrofísica, Universidad de La Laguna, E-38206 La Laguna, Tenerife, Spain
[3] Astronomical Institute, Czech Academy of Sciences, Fričova 298, 25165, Ondřejov, Czech Republic
[4] Charles University, Faculty of Mathematics and Physics, Institute of Astronomy, V Holešovičkách 2, CZ-18000, Prague 8, Czech Republic
[5] Astronomical Institute, Slovak Academy of Sciences, 05960 Tatranská Lomnica, Slovakia
[6] Department of Theoretical Physics and Astrophysics, Faculty of Science, Masaryk University, Kotlářská 2, CZ-611 37 Brno, Czech Republic
[7] Faculty of Mathematics, Physics and Informatics, Comenius University, Bratislava, Slovakia

Abstract

Most researchers and educators are familiar with the Erasmus+ programme of the European Commission through its support for spending a semester or two abroad during an undergraduate degree programme. However, the programme also provides funding for other activities including multinational strategic partnerships between research and educational institutions. Here, we outline the details of two such strategic partnerships, demonstrating that they can prove to be an incredibly valuable resource for supporting and promoting educational projects as well as furthering the development of early career researchers.

1 Introduction

When most people think of the European Commission's Erasmus+ programme, they think of semesters abroad during undergraduate degrees. However, this is only part of what is supported by the programme. Key Action 2 of the Erasmus+ programme includes financial support for multinational strategic partnerships to carry out projects in line with the programmes aims: the promotion of educational, professional and personal development. Such strategic partnerships are applied for on a national level by the lead institution in their home

country - in our case by the Astronomical Institute of the Academy of Sciences of the Czech Republic (AI ASCR). We have been fortunate enough to be two awarded consecutive projects – "Per Aspera Ad Astra Simul" (2017- 2020, 2017-1-CZ01-KA203-035562) and its (currently active) successor "European Collaborating Astronomers Project: España-Czechia-Slovakia" (2020-2023, 2020-1-CZ01-KA203-078200) – which we describe here with the hope of encouraging others to make use of these opportunities to fund educational and outreach projects might otherwise be difficult to undertake.

2 Partners

The complete list of partners involved in the two strategic partnerships is given in table 1. Charles University joined as a partner only for the second instance of the project, while GranTeCan was an Associate Partner for the first. AI ASCR was the lead institute of both projects, with key involvement in all activities from all partners. For example, all partners participated in mobilities and in local outreach and educational activities. Financially, the projects were managed by the lead institute with funds transferred to the partners in accordance with the planned activities.

Table 1: List of partner institutions

Institution	Country
Astronomical Institute of the Academy of Sciences of the Czech Republic (AI ASCR)	Cz
Instituto de Astrofísica de Canarias (IAC)	Es
Comenius University Bratislava	Sk
Masaryk University	Cz
Astronomical Institute of the Slovak Academy of Sciences (AI SAS)	Sk
Astronomical Institute of Charles University (AI CU)	Cz
GranTeCan (GTC)	Es

3 Mobilities

Erasmus+ strategic partnerships offer excellent financial support for mobilities of researchers for periods ranging from a few weeks to several months. As part of our strategic partnerships, we supported short term exchanges for senior researchers, in order to build and strengthen collaborations, and longer term exchanges for early career researchers, for their personal and professional development. To date, we have been able to support more than 30 mobilities (in spite of the COVID-19 pandemic striking towards the end of the first strategic partnership and adversely affecting travel).

Many of the mobilities have led to very tangible outcomes, like continued longterm collaboration and publications (see [1] for more details). One special example is the case of one long-term mobility of a Czech student to GranTeCan, where she combined her doctoral research with support astronomer activities. This offered the student a unique opportunity to gain experience in a world-leading observatory, something which has proved invaluable in her subsequent career as she has gone on to obtain highly competitive positions as both the European Space Agency and the European Southern Observatory following graduation.

4 Summer schools and educational resources

To date, the projects have supported the organisation of three summer schools targeting early career researchers. The first of these was organised in Tatranská Lomnica (Slovakia) in collaboration with OPTICON in 2019 [2]. "Observational astrophysics: from proposals to publication" comprised hands-on research projects for the attendees using archival data, as well as more traditional lectures on astronomical techniques and how to obtain observing time. The school was attended by approximately 40 students, with all local costs covered by the strategic partnership.

A second school, "GAIA and TESS: Tools for understanding the Local Universe" was held online (due to the COVID-19 pandemic) in 2022 with 17 students in attendance [4]. The school comprised a number of talks by experts on the TESS and Gaia missions (all of which were archived online and are available to the public), as well as detailed example research projects making use of the public data products of these missions.

"Eclipsing Binaries and Asteroseismology: Precise fundamental stellar parameters in the golden age of time-domain astronomy" was held in a hybrid format with 18 in-person attendees being hosted at the IAC's offices on La Palma. The school featured a combination of practical tutorials using publicly available resources as well as more traditional lectures from both in-person and remote presenters.

A final school focusing on dynamics in the Universe is planned to be held in 2023 in Slovakia.

In addition to the summers schools, a brief workshop on échelle spectroscopy was organised for masters students from the Charles University and AI ASCR in September 2021. Furthermore, senior researchers from all institutes contributed to a book of review papers, each designed to provide a graduate-level introductions to their respective topics, ranging from stellar evolution through to the standard cosmological model [3].

5 Outreach

A key component of both strategic partnerships was outreach, with funding being used to support activities in schools and for the general public. Preschoolers in Ondvrejov were invited to visit the observatory and tour the 2-m telescope there, before listening to a talk by one of the researchers of the AI ASCR. The children then created art projects based on what

they had seen and learned during the visit, with the results presented in a small gathering with their parents invited. In the Canary islands, a number of talks in local schools were organised catering to audiences ranging from six years old through to seventeen years old.

Talks for the general public were also presented in both the Czech and Slovak republics. Similarly, a YouTube channel was created hosting bilingual (English and Spanish) videos presenting basic astronomical concepts and interviews with astronomers[1]. Partners at the Comenius University also contributed to a pre-existing YouTube channel as part of the project[2].

6 Conclusions

We have briefly outlined some of the activities undertaken as part of two strategic partnerships carried out under the auspices of the Key Action 2 of the Erasmus+ programme of the European Commission. Such strategic partnerships offer substantial financial support for educational and outreach activities and we strongly encourage other astronomy educators to consider how they too might make use of the scheme in future calls.

Acknowledgments

This work was supported by the Erasmus+ programme of the European Union under grant numbers 2017-1-CZ01-KA203-035562 and 2020-1-CZ01-KA203-078200.

References

[1] Jones, D., Kabáth, P., García-Rojas, J., et al., 2022, Astronomy Education Journal, 2, 1, 041resa

[2] Kabáth, P., Korhonen, H., & Jones, D., 2019, Contributions of the Astronomical Observatory Skalnate Pleso, 49, 522

[3] Kabáth, P., Jones, D., & Skarka, M., 2020, Reviews in Frontiers of Modern Astrophysics: From Space Debris to Cosmology, Springer

[4] Skarka, M., Janík, J., Paunzen, E., & Glos, V., 2021, Contributions of the Astronomical Observatory Skalnate Pleso, 51, 41

[1] https://www.youtube.com/channel/UCXBLE1tzrL2mhY3Kb0ELieQ/videos
[2] https://www.youtube.com/playlist?list=PLqiGU4u5LkCF2YYU450gssOPPhE-4jOfI

Highlights of Spanish Astrophysics XI, Proceedings of the XV Scientific Meeting of the Spanish Astronomical Society held on September 4–9, 2022, in La Laguna, Spain. M. Manteiga, L. Bellot, P. Benavidez, A. de Lorenzo-Cáceres, M. A. Fuente, M. J. Martínez, M. Vázquez- Acosta, C. Dafonte (eds.), 2023

RECA: Mentoring, internship and educational programs as tools to overcome inequalities for Astronomy students in Colombia.

Ospina, N.[1], Agudelo-Vásquez, M.[2], Buitrago-Casas, J. C.[3,4] Diaz-Castillo, S. M.[5,6], Garavito-Camargo, N.[7], Oliveros-Gomez, N.[8], Pinilla-Jurado, S.[2], Quiroga-Nunez, L. H.[9], Rojas-Ruiz, S.[10], Salazar-Manzano, L. E.[11], Uchima-Tamayo, J. P.[12] Plazas Malagón, A. A.[13,14,15], Abril-Melgarejo, V.[16], Bonilla-Rivera, A.[17], Cardenas-Avendaño, A.[18,19], Cardona-Torres, L.[20], Chaparrro, G.[21], Fernandez-Arenas, D.[22], Gonzalez-Sanchez, J.[23], Gutierrez, C. P.[24,25], Peña-Ramirez, K.[26], Quitian-Lara, H.[27,28], Ramírez-Agudelo, O.H.[29] Suarez-Perez, J.F.[30] Vargas-Bastidas, A.[2] Villa-Vélez, J.A.[31], and Villamil Sastre, M.[32]

[1] Department of Theoretical Physics, University Autonoma of Madrid
[2] Instituto de Física, Universidad de Antioquia
[3] Space Sciences Laboratory, University of California Berkeley
[4] Physics Department, University of California, Berkeley
[5] Leibniz-Institut für Sonnenphysik (KIS)
[6] Physikalisches Institut, Albert-Ludwigs-Universität Freiburg
[7] Center for Computational Astrophysics, Flatiron Institute. 162 5th Ave, New York, NY 10010, USA
[8] Departamento de Astronomía, Universidad de Guanajuato, Mexico
[9] Department of Aerospace, Physics, and Space Sciences, Florida Institute of Technology
[10] Max-Planck-Institut für Astronomie, Königstuhl 17, D-69117, Heidelberg, Germany. Fellow of the International Max Planck Research School for Astronomy and Cosmic Physics at the University of Heidelberg (IMPRS–HD)
[11] University of Texas Rio Grande Valley
[12] Departamento de Astronomía, Universidad de La Serena, Av. Juan Cisternas 1200, La Serena, Chile
[13] Department of Astrophysical Sciences, Princeton University, Peyton Hall, Princeton, NJ 08544, USA
[14] Kavli Institute for Particle Astrophysics and Cosmology, P.O. Box 20450, MS29, Stanford, CA 94309, USA
[15] SLAC National Accelerator Laboratory, 2575 Sand Hill Road, MS29, Menlo Park, CA 94025, USA
[16] Space Telescope Science Institute, 3700 San Martin Drive, Baltimore, MD, 21218, USA
[17] Departamento de Física, Universidade Federal de Juiz de Fora, 36036-330, Juiz de Fora, MG, Brazil
[18] Princeton Gravity Initiative, Princeton University, Princeton, NJ 08544, USA

[19] Programa de Matemática, Fundación Universitaria Konrad Lorenz, 110231 Bogotá, Colombia
[20] Instituto Nacional de Astrofísica, Óptica y Electrónica, Luis Enrique Erro 1, Sta. Ma. Tonantzintla, 72840, Puebla, Mexico
[21] SEAP/FACom, Instituto de Física - FCEN, Universidad de Antioquia Calle 70 No. 52-21, Medellín, Colombia
[22] Canada–France–Hawaii Telescope,CFHT 65-1238 Mamalahoa Hwy Kamuela,Hawaii 96743, USA
[23] Universidad de Manizales, Colombia
[24] Finnish Centre for Astronomy with ESO (FINCA), FI-20014 University of Turku, Finland
[25] Tuorla Observatory, Department of Physics and Astronomy,FI-20014 University of Turku, Finland
[26] Centro de Astronomía (CITEVA), Universidad de Antofagasta, Av. Angamos 601, Antofagasta, Chile
[27] School of Physical Sciences, Ingram Building, University of Kent, Park Wood Rd, Canterbury CT2 7NH, United Kingdom
[28] Observatório do Valongo, Universidade Federal do Rio de Janeiro, Ladeira do Pedro Antônio 43, 20080-090 Rio de Janeiro, Brazil
[29] German Aerospace Center(DLR), Institute for the Protection of Terrestrial Infrastructures, Rathausallee 12, 53757 Sankt Augustin, Germany
[30] Departamento de Física, Universidad de los Andes, Cra. 1 No. 18A-10, Bogotá, Colombia
[31] École Normale Supérieure, Laboratoire de Physique de l'Ecole normale supérieure 24 Rue Lhomond, 75005 Paris, Île-de-France, France
[32] Astronomical Observatory of Geneva, Geneva, Switzerland

Abstract

The Network of Colombian Astronomy Students (Red de Estudiantes Colombianos Astronomía, RECA – in Spanish) is a civil association that seeks to create and maintain strong links among Astronomy students in Colombia. One of the RECA's main goals is to build a strong collaborative community of early-career Astronomers and professional Astronomers to enhance the scientific development of the country. Since 2020, RECA has successfully implemented two programs targeting last year undergraduate and master students looking to take their next step in their professional career. These are the mentoring and summer internship programs. With these two programs together with an educational project for schools, RECA intends to foster in the students the essential capacities to carry out scientific research, contribute to their academic training and encourage vocations. An overview of these activities implemented by RECA is presented, as well as the preliminary impact of these activities.

1 Introduction

RECA[1] began in the framework of the III Colombian Congress of Astronomy and Astrophysics (Congreso Colombiano de Astronomía y Astrofísica, COCOA – in Spanish) held in 2012, from the need of physics and astronomy students to create spaces to generate extracurricular environments for dissemination, discussion, and interaction, with the purpose of creating an astrophysical community that would provide academic opportunities and social connections for students. The network is part of the Colombian astronomers community (Comunidad de astrónomos de Colombia, AstroCO[2] – in Spanish) since 2021, which is also a member of the Colombian Academy of Exact, Physical and Natural Sciences (Academia Colombiana de Ciencias Exactas, Físicas y Naturales, ACCEFYN – in Spanish). Nowadays, RECA is a civil association that seeks to create and strengthen the links between astronomy students in Colombia and Colombian professional astronomers; promoting spaces that allow the exchange of ideas and significant experiences among its members, where collaboration prevails for the realization of diverse academic projects generating a professional and social impact.

The network is currently composed of 171 members, of which 111 are from more than 18 Colombian institutions and 60 are from different institutions in 22 foreign countries, with a percentage of 38.60% women, 60.82% men, and 0.58% non-binary.

RECA's operational functionality is based on a horizontal structure composed of nodes defined on the main projects developed by the network: organizational, mentoring, internship, education, census, communications, and institutional relations nodes. RECA works to have a very welcoming environment, especially for early-career researchers.

2 Mentoring

The Mentoring program[1] was conceived in response to the barriers experienced by Colombian students in getting access to postgraduate studies, especially due to the lack of information and guidance during undergraduate studies. The primary goal is to connect early-career students with astronomers who have developed a professional career. This program is focused on providing information on the different options to continue their career, guiding students during the application process to postgraduate programs in astronomy, and/or advising them to succeed in their following professional steps.

2.1 First edition

The first edition of the RECA Mentoring program was held in the 2020-2021 academic year and involved 24 students from 13 Colombian institutions, and 24 Mentors from 22 institutions of which 18 were international. The program consisted of 1:1 virtual mentorships in which students received personal advice in the process of applying to postgraduate studies. In

[1] https://www.astroreca.org/
[2] https://accefyn.com/microsites/nodos/astroco/

addition, weekly panels (8 in total) were carried out on CV preparation, exam preparation (e.g., the Graduate Record Examination, and the Test Of English as a Foreign Language), scholarships and funding opportunities, and time management, among other soft skills topics. All the panels are accessible to the community through the website and YouTube channel of RECA.

As a result of this first edition, 12 applications were made to international universities of which 10 were successful. However, not all students were able to finish the application process to universities or start their postgraduate studies due to financial hardship (need for scholarship) and the lack of research experience in astrophysics.

2.2 Second edition

The second edition of the RECA Mentoring program was carried out in 2021-2022 with a considerable increase in the number of applications to the program, from 24 in the past edition to 46 in this edition, from 14 universities in 7 different cities in Colombia. Meanwhile, the number of Mentors remained similar to the first edition, with 20 Mentors for this edition, from 18 institutions in 8 different countries.

Because of the increase in the number of students and the small decrease in the number of Mentors, an advisory mode was included for the first time in the program. This advisory mode consisted in 23 students who were not yet at the stage of applying for postgraduate studies but wanted to learn more about the process a couple of semesters in advance. These students had full advice from the RECA Mentoring node members and access to the panels but were not involved in the 1:1 mentoring. The remaining 23 students had a 1:1 mentoring. As part of the activities developed in this edition, there were the panels as in the first edition. This time, thanks to a grant of 5000€, from the Office of Astronomy for Development of the International Astronomical Union (IAU-OAD) in 2022 to improve the program, it was possible to recruit experts for the panels and improve the quality of the videos.

As feedback from this edition, the students expressed their satisfaction with the program and highlighted learning about writing motivational letters as well as helping to organize and prepare their applications to postgraduate studies.

2.3 Third edition

The third edition of the mentoring program started in September 2022 and follows the same scheme that the second version. In this case, 47 early-career students applied for advising and 20 later-career applied for 1:1 mentoring. The students are from 20 universities in 13 different cities in Colombia. For the first time, a decentralization of applications has been observed, with students coming from regions of the country where access to education is more challenging (e.g. applications from students coming from the Amazon region, a region that is considered difficult to access due to communication problems, limited education, and poor health). In addition, for the first time, 2 Colombian students from international institutions were allowed to participate.

Regarding the Mentors, for this edition, the program currently has 17 Mentors, from 17

institutions in 9 different countries. This third edition is still ongoing and is expected to finish before July 2023.

3 RECA Internship

Currently, there are many research internship programs around the world aimed at undergraduate students, but many of them are highly competitive and citizenship-limited. With the idea of enriching the curriculum of Colombian students to make them more competitive when applying to international programs, the RECA internship program was created to promote scientific research and create networks to establish collaborations. The summer internship consists zof a 10-week training program in scientific research in Astronomy, aimed at students from Colombian institutions who are in their final years of undergraduate studies under the supervision of scientists inside and outside Colombia.

3.1 First edition

The first edition of the internship program took place in the summer of 2021. Over 60 applications were received from Colombian students in astronomy, physics, chemistry, and engineering, of which 13 were selected (6 men and 7 women). Besides, there were 13 selected research projects proposed by researchers from 10 different countries. The projects covered a variety of current topics in Astronomy and the results were presented at the 1st RECA Internship Symposium[3], held virtually, and published in Astrobitos[4].

The work was carried out over a period of 10 weeks in which each student worked one-to-one with each researcher and also had the opportunity to participate in remote observations using the Nordic Optical Telescope (NOT) and the Mercator Telescope, located at the Roque de los Muchachos Observatory, in Canary Islands (Spain).

Some of the research projects done during this internship have been published in high-impact journals in Astronomy, have been presented as undergraduate theses, and have been the beginning of collaborations between Colombian and foreign researchers.

3.2 Second edition

The second edition of the program was held in the summer of 2022. In particular, this edition was supported by funding from different organizations such as The LSST Corporation[5], The Flatiron Institute, Platzi, and the IAU-OAD[6]. This funding was used entirely to pay research stipends to the students because, in the first edition, some students commented that it was financially difficult to balance work and internship. In this edition, there were more than 40 applications from students from 13 different Universities and 9 research projects proposed by

[3] https://www.astroreca.org/internship-simposio-2021
[4] Spanish version of Astrobites: https://astrobitos.org/
[5] https://www.lsstcorporation.org/node/270
[6] https://www.astro4dev.org/category/a-virtual-community-mentorship-program-for-development-in-colombia/

Supervisors from 5 countries. On this occasion, 9 participants were selected (4 men and 5 women).

In addition to the research projects, the students had the opportunity to participate in different activities organized by the RECA Internship Committee such as a Python Bootcamp, lectures given by experts on current topics in astrophysics, and remote observations. This time the observations were performed with the VLT Telescope at the Paranal Observatory and the IAC80 Telescope at the Teide Observatory. As in the last edition, the results were presented at the 2nd RECA Internship Symposium[7] and will be published in Astrobitos.

4 RECA Education

The RECA educational node was created in 2021 with the aim of bringing Astronomy to schools in all socio-economical contexts (rural and urban) around Colombia to promote links between professional Astronomers and schools and encourage scientific inquiry from an early age. Among the activities that the education node organizes with teachers in schools, RECA has the project "Astronomy goes to your School". This consists of creating spaces for schools to have the opportunity to interview an Astronomer or attend a talk related to diverse topics of Astronomy and Women Scientists.

During 2021, 14 talks were given in different public and private schools in cities such as Bogota, Medellin, Cali, and Bucaramanga. The main problem we encountered was communication with teachers and the use of virtual platforms such as Zoom or Meet. In the case of 2022, 30 talks were held throughout different regions of Colombia, including 5 schools in rural areas. These talks were a great challenge for the RECA team and the teachers because there was no internet access in the schools, so the sections were recorded on weekends. Nevertheless, there was an overall 14% increase of talks finalized compared to 2021, and a 22% of talks given in schools from rural areas. However, there were still a number of issues and delays in the final encounter between the astronomer and the school because of the lack of connectivity.

Additionally, we have implemented the "Accompanying schools" program that is focused on school clubs. In the major cities of Colombia where the schools have more resources to implement programs outside the general curriculum, some teachers have initiated astronomy clubs. However, they often do not know how to access resources for workshops or activities and therefore the RECA Education Node offers help in this matter. For example, we have worked closely with the Abraham Maslow School in Bogota, which has an observatory with two 12" and 16" and a meteorological station. We have made motivational talks for students in primary and secondary school to make use of these resources at their school. Moreover, we have helped the teacher in charge of the astronomy curriculum in implementing ideas and resources in the classroom. Finally, the 2023 version is in preparation and we hope to reach more schools and cities in the country.

[7] https://www.astroreca.org/internship-simposio-2022

Acknowledgments

RECA acknowledges the support and funding from the IAU-OAD astronomy for development grant 2022, the LSST Corporation Enabling Science Award 2021-51, and the Simons Foundation. RECA also acknowledges the collaboration and partnership with ACCEFYN, Astroco, Platzi, ScienteLab, astrobitos, Alpha-Cen, SEA. RECA acknowledges the Mentors and Supervisors who have contributed with their work to make the RECA programs possible. RECA thanks to Instituto de Astrofísica de Canarias for allowing the use of the facilities of the Roque de los Muchachos Observatory and the Teide Observatory, as well as the European Southern Observatory for the use of the Very Large Telescope at the Paranal Observatory. N.O. acknowledges funding from the Ministry of Universities of Spain, the Recovery, Transformation and Resilience Plan (PRTR), and the UAM though the Grant CA3/RSUE/2021-00559 and the Grant PID2021-124050NB-C31 funded by MCIN/AEI/10.13039/501100011033 and by the European Union NextGenerationEU/PRTR. S.R.R. acknowledges financial support from the International Max Planck Research School for Astronomy and Cosmic Physics at the University of Heidelberg (IMPRS–HD). J.P.U.T. acknowledges support from the National Agency for Research and Development (ANID)/Scholarship Program/Doctorado Nacional/2021-21210732. The work of A.A.P.M. was supported by the U.S. Department of Energy under contract number DE-AC02-76SF00515.

References

[1] Quiroga-Nunez, L.H., Garavito-Camargo, N., Plazas Malagón, A.A., Gonzalez-Sanchez, J., Bonilla-Rivera, A., Salazar-Manzano, L., Quitián-Lara, H., Buitrago-Casas, J., Chaparro, G., Rojas-Ruiz, S. and Ospina, N., 2022, American Astronomical Society Meeting Abstracts, 54, 315.

Highlights of Spanish Astrophysics XI, Proceedings of the XV Scientific Meeting of the Spanish Astronomical Society held on September 4–9, 2022, in La Laguna, Spain. M. Manteiga, L. Bellot, P. Benavidez, A. de Lorenzo-Cáceres, M. A. Fuente, M. J. Martínez, M. Vázquez- Acosta, C. Dafonte (eds.), 2023

Remote Virtual Observatory schools.

Mas-Buitrago, P.[1], Solano, E.[1], Aller, A.[1], Cortés-Contreras, M.[1], Cruz, P.[1], Gálvez-Ortiz, M. C.[1], Jiménez-Esteban, F.[1], López-Martí, B.[1,2], Murillo-Ojeda, R.[1] Rizzo, J. R.[3], and Rodrigo-Blanco, C.[1]

[1] Centro de Astrobiología (CAB), CSIC-INTA. Camino Bajo del Castillo s/n. E-28692, Villanueva de la Cañada, Madrid, Spain
[2] Universidad CEU San Pablo, Boadilla del Monte, E-28668 Madrid, Spain
[3] ISDEFE, Beatriz de Bobadilla 3, E-28040, Madrid, Spain

Abstract

The Spanish Virtual Observatory (SVO) is an initiative whose main goal is to boost and coordinate Virtual Observatory activities in Spain. SVO has a large experience organising VO schools and workshops both at national and European level.
In the context of the pandemic situation caused by COVID-19, we made a large effort to carry on with these educational activities by making them virtual. At the time of writing these proceedings (December 2022), six VO schools have been carried out remotely.
The main conclusion that can be drawn from the online schools is that neither a negative impact on the follow-up of the tutorials nor on the communication with the participants was detected. Moreover, the online activities benefited from the advantages that remote teaching presents in particular in terms of number of attendants and geographical flexibility.

1 Introduction

National and international ground- and space-based observatories produce terabytes of data per year, which are publicly available all around the world from data centres. Theoretical models, as well as results, published in electronic journals are also available on line.

The Virtual Observatory (VO) is the e-infrastructure necessary to efficiently exploit the scientific contents of the huge databases that populate the distributed worldwide astronomical data centres. VO is an ecosystem of interoperable tools and services that enable discovery, access, and subsequent analysis of multi-wavelength, multi-epoch data. Underpinning the VO are data discovery and access protocols that enable archives to interoperate through common interfaces. The protocols themselves are negotiated on behalf of the worldwide astronomy community by the International Virtual Observatory Alliance (IVOA). This is a diverse organization, consisting of 21 nationally funded VO projects on all continents and two intergovernmental organizations (ESA and SKAO). The IVOA has been promoting Open Science and what have become formalized as FAIR (*Findable, Accesible, Interoperable, Reusable*) [1] principles since its founding in 2002.

VO's ultimate goal is to produce better, new, and more efficient science. To work toward this aim, IVOA established in 2009 the Standing Committee on Science Priorities. However, the lack of familiarity of the astronomical community with the VO tools and services may limit the scientific impact of the VO. Also, the absence of strong links between VO and the research groups may lead to futile efforts. So, for instance, if the services and tools developed by the VO are not scientifically oriented, they will not be used by the community.

Training is, thus, considered a key element to ensure the adoption of the VO framework by the astronomical community. This is why, since its early times, IVOA has explored different approaches to reach astronomical researchers. The so-called *Research Initivatives*, an activity aiming at actively supporting research projects which require the unique capabilities offered by VO tools and services, was conducted in the framework of the European Virtual Observatory Astronomical Infrastructure for Data Access FP7 project (EuroVO-AIDA, 2008-2010)[1]. A couple of workshops on spectroscopy and multi-wavelength astronomy were also organised in the framework of the same project. Nevertheless, schools have proven to be the most effective mechanisms to attract astronomers to the VO. The Euro-VO initiative began to organise regular VO schools during the EuroVO-AIDA project. The usefulness of these schools was immediately obvious, and they were continued in the framework of the projects EuroVO-ICE (2010-2012), CoSADIE (2012-2015), ASTERICS (2015-2019) and ESCAPE (2019-2023). SVO is, among all VO projects, the most active one in the organisation of VO schools, with 22 schools held in Spain since 2009 and nine schools (in collaboration with Euro-VO[2] partners) at European level.

2 The schools

In all cases, both for the national and international schools, the goals were twofold: On one hand, to expose astronomers to the variety of currently available VO tools and services so that they can use them efficiently for their own research, and, on the other hand, to gather their feedback on the VO tools and services and the school itself. Although schools are mainly aimed at targeting early-career scientists, other profiles (senior researchers, technical staff, amateurs,...) showing a clear interest on the use of VO tools and services are also accepted.

The programme of the schools is typically structured around four main topics:

- Introductory presentations about the VO in general and the school itself in particular, to ensure that all participants are well informed of the organisational background before the hands-on sessions start.
- Hands-on sessions where VO experts guide participants on the use of the tools through a series of predefined science cases. This is the activity that takes most of the allocated time. Different tutorials adapted to the participants' profile (beginners, intermediate, advanced) are offered. In these tutorials, the most important functionalities of the most used VO tools and services (Aladin, TOPCAT, VOSA,...) are described. Thanks to the

[1] http://cds.u-strasbg.fr/twikiAIDA/bin/view/EuroVOAIDA/WebHome
[2] http://euro-vo.org

feedback gathered in previous schools, tutorials are continuously updated to best suit specific scientific cases and their duration fitted to match the mean time users need to go through them for the first time. The latest functionalities implemented in VO tools and services and the latest data releases of publicly available data are also taken into account when improving the tutorials.

- Use cases proposed by the participants. In schools with a duration longer than two days, each participant is encouraged to propose a scientific case related to his/her research and, if possible, a case in which his/her own data could be used. During the school, they can work on it under the guidance of VO tutors. This session is conducted on the last day of the school to profit the knowledge gained throughout the previous days. Also on the last day, a selection of the projects is made and participants give a short presentation on their scientific use cases and how VO tools and services helped for their projects. Examples of science cases proposed by the participants can be found here.

  To ensure that all participants get the best out of this session, each one is asked to fill in a questionnaire before the school. The purpose of this is to better understand the science cases proposed by the participants, along with the type of data (images, spectra, catalogues, data cubes,...) and wavelength range to be used, and also to assess their feasibility using VO tools and services. This way, a picture of the participants' interest and needs is obtained. Based on this information, a suitable tutor is assigned to each participant. Every tutor typically coaches two to three students.

- Feedback. Participants are requested to anonymously fill in a feedback survey with questions about the quality, length and level of difficulty of the tutorials, about their previous knowledge of VO tools and services, their plans to use them in the own research as well as on other aspects of the school. The results of the survey are commented before the closure session. They help us to improve the organisation and programme of subsequent schools.

After the schools, participants are encouraged to act as VO-ambassadors in their research institutes by giving informal talks with colleagues, seminars, scientific workshops and conferences, and making use of the material employed during the school, which remain publicly available.

Detailed information on the schools organised by the SVO can be found at the SVO portal[3].

3 Virtual Observatory schools become virtual

The COVID-19 lockdown that affected many countries in the Spring of 2020 and the long period in which the pandemic situation was far from being under control, made us to move the schools to an online format.

The online school sessions are carried out using Zoom[4]. To provide an adequate response

[3] https://svo.cab.inta-csic.es/docs/index.php?pagename=Meetings
[4] https://zoom.us/

to the needs of the participants, tutors are assigned to cover the following roles:

- Host tutor: Responsible for setting up sessions, organising breakout rooms, taking care of the chat and delivering participant's questions to the main tutor and backup tutors.
- Main tutor: Runs the tutorial and answers questions of general interest in the main room.
- Backup tutors: Support participants via chat and breakout rooms. While the main tutor conducts the tutorial at the main room for all participants, backup tutors are available to answer the participants' question through the Zoom chat. In case of complex questions, the backup tutor and the participant are sent by the chair to a breakout room for a closer interaction. In these breakout rooms the participant is able to directly talk to the tutor and shares his/her screen if necessary. Typically, 3-4 backup tutors are assigned per tutorial.

Once the school session is finished and the Zoom connection is closed, a Slack[5] channel is, sometimes, open for off-line communication between the students and tutors. At the beginning of each day, 5-10 minutes are devoted to comment on the most relevant topics discussed on Slack the previous day. The Slack channel remains open to allow tutors - students interactions well after the school. Finally, "virtual" coffee-breaks are also conducted using the Slack platform to allow for informal interactions between participants and tutors in a relaxed atmosphere.

Six virtual VO schools have been organised so far. Four schools were oriented towards MSc and PhD students from Spanish universities and research centres, one focused on the Spanish amateur community, and one targeted at the Brazilian astronomical community. The main result that can be drawn from the organisation of these events is that they have allowed us to reach a more numerous and more geographically distributed audience (Fig. 1). Being more accessible, they increase the participation for those who may experience travel restrictions due, for instance, to financial restraints. The organisation of a school for the Brazilian astronomical community with more than 100 participants from different centres or the participation in the last school of two students from Ethiopian research institutes are good examples of the strength of virtual meetings.

4 Conclusions

Running a high-level interactive event in an online setting is a challenging task and the SVO has pioneered this format in the IVOA environment. The experience is being extremely successful and no negative impact on the schools has been observed. On the contrary, we are taking advantage of the benefits of the virtual format to reach a larger audience and geographical flexibility and to lower economic and environmental costs.

[5] https://slack.com/

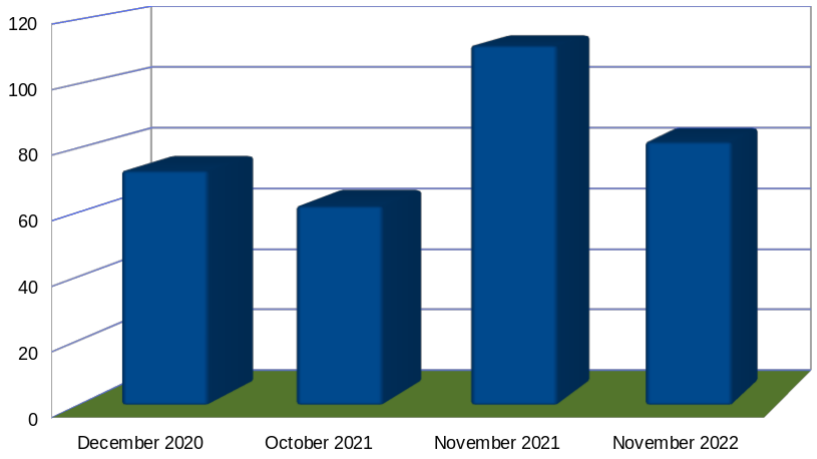

Figure 1: Number of participants in the last four online schools. As a comparison, the average number of participants in physical meetings was typically below 35-40.

Now that the pandemic is becoming part of the past, we plan to conduct future VO schools in an hybrid format, combining face-to-face and virtual participation. This way, in-person attendants would benefit from the more natural face-to-face interaction, while the option of remote learning remains open for those unwilling or unable to travel without losing access to a high quality VO formation program.

Acknowledgments

This research has made use of the Spanish Virtual Observatory (https://svo.cab.inta-csic.es) project funded by MCIN/AEI/10.13039/501100011033/ through grant PID2020-112949GB-I00 and ESCAPE, a project supported by the European Commission Framework Programme Horizon 2020 Research and Innovation action under grant agreement n. 824064.

References

[1] Wilkinson, M. D., Dumontier, M., Aalbersberg, I. J., et al. 2016, NatSD, 3600, 18W

Highlights of Spanish Astrophysics XI, Proceedings of the XV Scientific Meeting of the Spanish Astronomical Society held on September 4–9, 2022, in La Laguna, Spain. M. Manteiga, L. Bellot, P. Benavidez, A. de Lorenzo-Cáceres, M. A. Fuente, M. J. Martínez, M. Vázquez- Acosta, C. Dafonte (eds.), 2023

Universo Complutense: a blog for astronomy and astrophysics students.

Beitia-Antero, L.[1,2], Canet, A.[2], Marfil, E.[3,4], Gómez de Castro, A.I.[2], and Montes, D.[3] and de Castro, E.[3]

[1] Observatorio Astronómico Nacional, Instituto Geográfico Nacional
[2] Departamento de Física de la Tierra y Astrofísica, Facultad de CC. Matemáticas, Universidad Complutense de Madrid
[3] Departamento de Física de la Tierra y Astrofísica, Facultad de CC. Físicas, Universidad Complutense de Madrid
[4] Hamburguer Sternwarte, Universität Hamburg, Gojenbergsweg 112, 21029 Hamburg, Germany

Abstract

Astronomy and astrophysics students in the last degree and Master courses often encounter difficulties in dealing with astronomy specific software that hampers their progress during the practical lessons. In an effort to ease their way and provide complementary resources, we started a teaching innovation project at Universidad Complutense de Madrid that consisted on a wordpress blog and an associated YouTube channel with video-tutorials. Based on our own teaching experience at all academic levels, we identified what we considered the main weak points of the students that would benefit from supplementary material and published a series of entries and videos focused on the use of UNIX systems, Python packages, and specific astrophysical software and databases. The characteristic feature of this material is that it is available completely in Spanish.

1 Introduction

At Universidad Complutense de Madrid, we have a large number of students interested in specialising in astronomy and astrophysics. Students in the Physics faculty are offered a series of subjects to introduce them into astrophysics at the last courses of their degree, while those in the Mathematics faculty are taught position astronomy and celestial mechanics at a very high level, and many of these students do an End-Of-Degree project in astrophysics and later choose to study the Astrophysics Master at the Physics faculty. As former students of that Master programme and teachers involved in the courses, we had first-hand information on the main weak points of the students that made their introduction into practical astrophysics difficult. Although it depended strongly on their background, we found that students commonly struggled working with UNIX-based systems (in many cases without a supporting

graphical interface) and their programming skills were at a level much lower than desired. Therefore, in 2019 we applied for a teaching innovation project at our university entitled 'Soft skills for degree and master students' with the objective of elaborating additional supporting material for these students. In that framework, during the academic year 2019/2020 we created a Wordpress blog, Universo Complutense, and an associated YouTube channel where we uploaded a series of video-tutorials as supporting material for the written entries. In the following sections we present an overview of the contents of both sites (Secs. 2 and 3) and an overview of the envisioned future content of the blog (Sec. 4).

2 Wordpress blog

The Wordpress blog can be accessed via this link. In a first stage, we elaborated a list of potential contents for the blog classified into four blocks:

- UNIX systems. How to use the terminal for remote connections and file edition (vi).
- Python. Basic usage of the commonly-used packages pandas and numpy, graphical representation with matplotlib, and the specific package astropy.
- Databases: VizieR, MAST, ESA Archive, SIMBAD, and Virtual Observatory tools such as TopCat.
- Specific software: Aladin Sky Atlas, EsaSky, Wobble, iSpec.

We started covering the contents of the first two blocks, which were the most technical ones and the most needed by our students for their projects. First, we introduced UNIX at a very low level and provided a virtual machine with a basic Lubuntu installation that could be run on Windows systems, which is the most popular operating system. On subsequent publications, we explained what a terminal was and the mostly used shortcuts for creating files and folders, renaming and moving them, and updating the software, and devoted one entry to remote connections and basic file edition using 'vi'. Once this part was finished, we moved towards more specific written tutorials from the last two blocks. We provided a page with a list of useful links and then we moved to Python (how to perform a basic installation with and without anaconda). With that, we finished the introduction and immersed ourselves in the main contents of the blog focusing on specific software and working with real astrophysical data. At the time of writing this contribution, we have published more than ten entries classified into different categories to help the readers to find the desired content, as is shown in Fig. 1. Apart from the direct feedback received from our students, it is also possible for any reader to leave their comments on the blog, but up to now we have not received any suggestions for new content.

Figure 1: Preview of some entries of the blog (left) and the categories available on January 3, 2023 (right).

3 YouTube channel

The YouTube channel is also public and available through this link. On January 3, 2023, it counts with 19 suscribers and 8 videos (Fig. 2). There is not a one-to-one correspondence between blog entries and videos, since sometimes the written content in wordpress was self-consistent and self-explanatory, while other times we decided to provide supporting videos showing different functionalities (for instance, the two versions of Aladin, Desktop and Lite). As a general rule, we have opted for a format of short (less than 15 minutes) videos that are easy to follow and reproduce, where we explore either the general features of the software or one very specific example.

4 Future steps

So far, we have covered roughly three quarters of the contents we envisioned when we proposed the teaching innovation project, but we have several ideas to continue. Among them, we can list: a tutorial on the use of EsaSky, specific entries for an advanced use of SIMBAD and other CDS tools such as the cross-match catalogue service, basic use of DS9 for FITS preview and apperture photometry, and more Python-related entries for sofisticated plots with matplotlib or line fitting with specutils. Besides, since some of us are also involved in teaching space science to students of Mathematics Engineering, we are also planning to expand our horizons with new content focused on positioning, signal and image processing, that might catch the interest of engineering students in other fields outside astronomy, making Universo Complutense a fundamental tool for unifying space astronomy and astrophysics for the Spanish-speaker community.

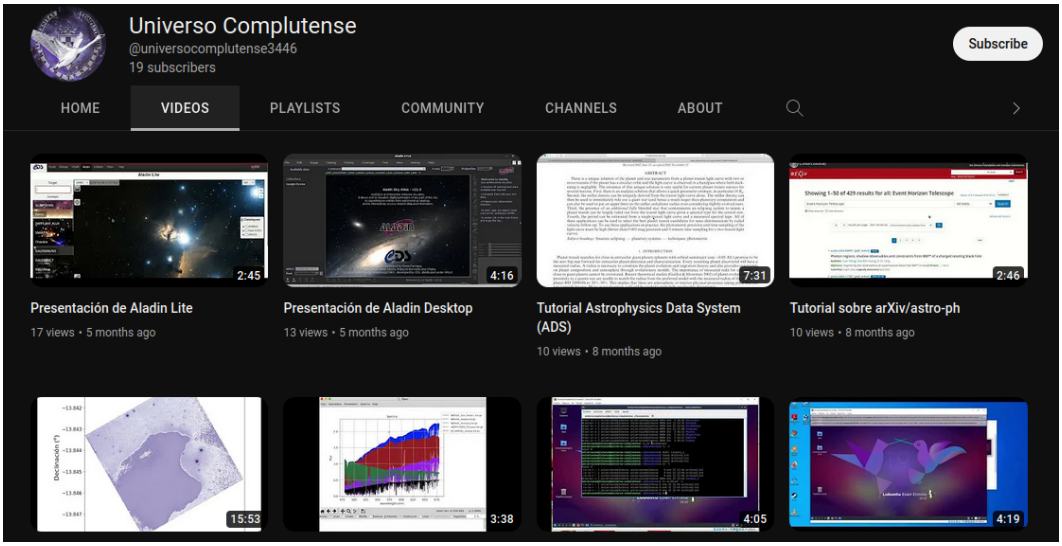

Figure 2: Snapshot of the videos available on the YouTube channel on January 3, 2023.

Acknowledgments

L. Beitia-Antero acknowledges Universidad Complutense and Banco Santander for the receipt of a 'Periodo de Orientación Postdoctoral' grant that supported her during the development of the blog. L. Beitia-Antero and E. Marfil are currently supported by a Margarita Salas postdoctoral fellowship from Universidad Complutense de Madrid, funded by 'Ministerio de Universidades' with NextGeneration EU Funds

Highlights of Spanish Astrophysics XI, Proceedings of the XV Scientific Meeting of the Spanish Astronomical Society held on September 4–9, 2022, in La Laguna, Spain. M. Manteiga, L. Bellot, P. Benavidez, A. de Lorenzo-Cáceres, M. A. Fuente, M. J. Martínez, M. Vázquez- Acosta, C. Dafonte (eds.), 2023

Astronomy Communication in a Time of Confinement: #AstroatHome.

Montes, D.[1]

[1] Departamento de Física de la Tierra y Astrofísica & IPARCOS-UCM (Instituto de Física de Partículas y del Cosmos de la UCM), Facultad de Ciencias Físicas, Universidad Complutense de Madrid, E-28040 Madrid, Spain

Abstract

During the confinement (in Spain from March to June 2020) the usual observations at the UCM (Universidad Complutense de Madrid) observatory (Observatorio UCM) were not possible. There were no public observations and was impossible to take pictures with the telescopes or teleobjetives. To solve this problem, I started to make observations from the window on my root at home. I got up with a scale, installed on a small tripod my digital camera and started to take pictures of the more relevant ephemerides and shared the images on internet in order a lot of people could enjoy from these events. These observations included: phases of the Moon night and day, the supermoon, timelapses, startrails and Moontrails, pass of the Moon close to Mars, Jupiter and Saturn, pass of Venus across the Pleyades, conjunction of Mars and Mercury, pass of the *ISS* and *Starlink* satellites, etc... and later, when the confinement finished, I also took pictures of the penumbral Moon eclipse in June and comet C/2020 F3 (NEOWISE) at the observatory but without public . All the resulting images are available in several picture galleries and on *Twitter* accounts @DMontesG and @ObservaUCM and *Instagram* (@dmontesg_fotos_astro) with hashtags: #AstronomiaenCasa #AstroatHome #AstronomiaContraElVirus and part of @IAU_Outreach.

My poster is available at https://doi.org/10.5281/zenodo.7036127

Highlights of Spanish Astrophysics XI, Proceedings of the XV Scientific Meeting of the Spanish Astronomical Society held on September 4–9, 2022, in La Laguna, Spain. M. Manteiga, L. Bellot, P. Benavidez, A. de Lorenzo-Cáceres, M. A. Fuente, M. J. Martínez, M. Vázquez- Acosta, C. Dafonte (eds.), 2023

Difundiendo eventos astronómicos desde el Observatorio UCM.

Montes, D.[1], colaboradores del Dpto. FTA[2], and ASAAF-UCM[3]

[1] Departamento de Física de la Tierra y Astrofísica & IPARCOS-UCM (Instituto de Física de Partículas y del Cosmos de la UCM), Facultad de Ciencias Físicas, Universidad Complutense de Madrid, E-28040 Madrid, Spain
[2] Departamento de Física de la Tierra y Astrofísica, Facultad de Ciencias Físicas, Universidad Complutense de Madrid, E-28040 Madrid, Spain
[3] ASAAF-UCM, (Asociación de Astrónomos Aficionados de la UCM)

Abstract

Desde el Observatorio de la Universidad Complutense de Madrid (UCM) se realizan diferentes labores de divulgación ademas se su utilización para actividades docentes en la Facultad de Ciencias Físicas con alumnos del Grado en Física y el Master en Astrofísica. Todos los años se organizan con motivo de la Semana de la Ciencia de la Comunidad de Madrid visitas guiadas por las instalaciones con observaciones solares y nocturnas con una gran afluencia de público. Asimismo, los telescopios e instrumentación con los que cuenta actualmente el Observatorio han permitido organizar otras actividades de divulgación como la observación en tiempo real, y su difusión a través de Internet, o en las redes sociales como *Twitter* (@ObservaUCM) e *Instagram* (@observaucm) de los eventos astronómicos de mayor interés como eclipses de Sol y de Luna, tránsitos de Mercurio y Venus, alineaciones de planetas, ocultaciones, etc... En esta contribución se hace un resumen de estas actividades mostrando algunas de las imágenes obtenidas.

My poster is available at https://doi.org/10.5281/zenodo.7036204

Highlights of Spanish Astrophysics XI, Proceedings of the XV Scientific Meeting of the Spanish Astronomical Society held on September 4–9, 2022, in La Laguna, Spain. M. Manteiga, L. Bellot, P. Benavidez, A. de Lorenzo-Cáceres, M. A. Fuente, M. J. Martínez, M. Vázquez- Acosta, C. Dafonte (eds.), 2023

Music and astronomy. IV. The Astrophysical Brothers.

Cifuentes, C.[1], **and Caballero, J. A.**[1]

[1] Centro de Astrobiología (CAB), CSIC-INTA, ESAC Campus, Camino bajo del castillo s/n, 28692 Villanueva de la Canñada, Madrid, Spain

Abstract

The separation between music and astronomy is only superficial, as Pythagoras already noted in his *Musica Universalis*. Artists from Gustav Holst to Lady Gaga, going through David Bowie or Rob Zombie have been inspired by the planets of the Solar System, by space travel, and by ideas of life beyond Earth. Bowie claimed to be based on *2001: A Space Odyssey* to narrate the story of Major Tom in *Space Oddity*. Antonio Vega imagined the vastness of the Universe in *Lucha de Gigantes*, as a "recollection of the location of the dimensions of the human being in a cosmic environment, of the relativity between the greatness of humans and their smallness in a grandiose and infinite environment". For instance, within the project *Cultura con C de Cosmos: Astromúsica* (`www.culturaccosmos.es`), we proposed a journey through time, space, and music, to reach with the imagination what our eyes sometimes cannot.

My poster is available at https://zenodo.org/record/7034801

Highlights of Spanish Astrophysics XI, Proceedings of the XV Scientific Meeting of the Spanish Astronomical Society held on September 4–9, 2022, in La Laguna, Spain. M. Manteiga, L. Bellot, P. Benavidez, A. de Lorenzo-Cáceres, M. A. Fuente, M. J. Martínez, M. Vázquez- Acosta, C. Dafonte (eds.), 2023

Music and astronomy. V. Radio Clásica's *Longitud de Onda* Club Band.

José A. Caballero[1], Fernando Blázquez[2], and Yolanda Criado[2]

[1] Centro de Astrobiología, CSIC-INTA
[2] Radio Clásica, Radio Nacional de España

Abstract

"¡Hola y saludos a todos!". Does listening to Mozart make us smarter? How could Beethoven going on composing when he became deaf? How are the places with the best acoustics? Is there music outside our planet? Music, science and new technologies, and their relation, are the central axis of *Longitud de Onda* (Wavelength), a unique radio programme in Spanish radio. The LDO *"astrónomo de cabecera"* recounts his wanderings and adventures at the Radio Clásica studio, accompanied by microphones, two awarded presenters and a grand piano (and, from time to time, some guests). *"Y que la Fuerza os acompañe"*.

My poster is available at https://zenodo.org/record/7038085

Highlights of Spanish Astrophysics XI, Proceedings of the XV Scientific Meeting of the Spanish Astronomical Society held on September 4–9, 2022, in La Laguna, Spain. M. Manteiga, L. Bellot, P. Benavidez, A. de Lorenzo-Cáceres, M. A. Fuente, M. J. Martínez, M. Vázquez- Acosta, C. Dafonte (eds.), 2023

Más allá de Madame Curie: iniciativas IFCA para todos los públicos por la visibilización de científicas.

M.T. Ceballos[1], R. García[1], C. E. Graafland[1], D. Herranz[1], S. Martínez-Núñez[1], J. Piedra[1], M. Seror[1], and R. Vilar[1]

[1] Instituto de Física de Cantabria, CSIC-Universidad de Cantabria

Abstract

Es una situación en la que seguro que muchos/as nos hemos encontrado alguna vez... en una charla pública preguntamos por el nombre de científicas importantes y el único nombre que surge es el de Marie Curie. Pero las personas que hacemos ciencia cada día sabemos que ella solo fue la punta del iceberg.

El Instituto de Física de Cantabria a través de su comisión de igualdad y diversidad en colaboración con el departamento de difusión cuenta con una larga trayectoria de actividades enfocadas a dar visibilidad a las científicas tanto del presente como del pasado, en los campos relacionados con la ciencia de las diferentes líneas de investigación del centro. El público al que esta labor va destinada incluye desde escolares en la etapa de infantil hasta estudiantes de universidad, pasando por todas las etapas educativas, además del público general.

El objetivo de esta labor es conseguir transmitir que no solo Madame Curie tuvo un papel relevante en la Física (en la ciencia en general) sino que el nombre y el trabajo de otras muchas científicas esté presente en la cultura científica de la sociedad.

Desde la divulgación y como primer campo de actuación, abordamos el papel de las científicas en nuestro programa "Expandiendo la ciencia: investigadores/as en la escuela", de charlas en los centros educativos. La visibilización tiene una doble vertiente, ciencia contada por científicas del IFCA y charlas específicas visibilizando las "gigantas" del pasado en cuyos hombros nos apoyamos las personas en ciencia del presente.

Con este objetivo en mente, anualmente participamos también en la celebración del "Día internacional de las mujeres y las niñas en la ciencia" con dos iniciativas concretas: el concurso de cómics sobre mujeres científicas (que ha celebrado en 2022 su V edición) y el ciclo de conferencias científicas "Ateneas" en colaboración con el Ateneo de Santander.

El balance a lo largo de los años en que llevamos realizando estas actividades es realmente positivo. Aunque somos conscientes de que son pequeños granitos de arena, hemos podido constatar que cuando ahora preguntamos en los colegios o en charlas públicas por nombres de científicas importantes, no solo aparece el nombre de Madame Curie... ¿será que algo está(mos) realmente cambiando?

My poster is available at https://doi.org/10.5281/zenodo.6913197

Highlights of Spanish Astrophysics XI, Proceedings of the XV Scientific Meeting of the Spanish Astronomical Society held on September 4–9, 2022, in La Laguna, Spain. M. Manteiga, L. Bellot, P. Benavidez, A. de Lorenzo-Cáceres, M. A. Fuente, M. J. Martínez, M. Vázquez- Acosta, C. Dafonte (eds.), 2023

Online Master in Astrophysics and Observational Techniques in Astronomy.

Roberto Baena-Gallé[1]

[1] UNIR - Universidad Internacional de la Rioja. Avenida de la Paz, 137, 26006 Logroño, La Rioja, Spain. https://orcid.org/0000-0001-5214-7408

Abstract

The 2021/2022 academic year, the Master's Degree in Astrophysics and Observational Techniques in Astronomy, at *Universidad Internacional de la Rioja* (UNIR), was instituted. This master's degree is structured in one academic year and 60 ECTS credits (one credit corresponds to between 25 and 30 hours of student's work), 12 of them devoted to the realization of a final master's project. This official study (MECES level 3) provide access to doctoral programs, and it is designed to give a broad view of numerous astrophysical processes that occur in nature, as well as instrumentation and main data reduction techniques. Hence, it is the beginning of a professional career focused on astrophysics and astronomy, for example, as a researcher, telescope operator, science communicator, etc.

The main particularity of UNIR is its purely online methodology. In this way, from any laptop, students can access PDF materials, recorded pills and interact with professors in live classes and through an online forum. Online teaching has numerous advantages to extend knowledge by canceling geographical distances. Therefore, in its first year of teaching, the Master's Degree in Astrophysics and Observational Techniques in Astronomy at UNIR has been taught to students residing in Spain, Panama, Ecuador, Chile, etc. One of the most obvious examples that this methodology does not involve any training handicap is in the fact of having offered access to astronomical facilities remotely, so students were able to acquire their own astrophysical data from their homes by themselves, no matter in which country they lived.

Acknowledgements: More information can be found on the official website. RBG is funded by the UNIR research project "ADELA: Deep Learning Applications for Astrophysics", no. B0036.

My poster is available at https://doi.org/10.5281/zenodo.7019079

Highlights of Spanish Astrophysics XI, Proceedings of the XV Scientific Meeting of the Spanish Astronomical Society held on September 4–9, 2022, in La Laguna, Spain. M. Manteiga, L. Bellot, P. Benavidez, A. de Lorenzo-Cáceres, M. A. Fuente, M. J. Martínez, M. Vázquez- Acosta, C. Dafonte (eds.), 2023

Teaching astronomy during the pandemics.

Vicent Martinez-Badenes[1], Lorena Nieves-Seoane[1], Pere Blay Serrano[1], Nestor Sanchez[1], and Marta Gonzalez Garcia[1]

[1] Universidad Internacional de Valencia, C/Pintor Sorolla 21, E-46002 Valencia, Spain

Abstract

In this poster, we are presenting a qualitative study on the way that teaching of astronomy in Spain was adapted to the situation generated by the COVID-19 pandemics. We have selected several cases of study corresponding to a Physics Degree (UV), Master Degree (UGR, VIU) and university courses for elder people (UVigo). As it could be expected, the models applied were built and implemented on the fly, as there were no plans for such a situation.

In the case of the Valencia International University, a complete online university, its methodology was already well settled once the Master Degree had completed 9 previous editions. This led to a dramatic increase in the number of students, reaching a 30% increase in the edition starting in April 2020 and a 55% in the October 2020 edition. Apart from some minor issues generated by the larger number of students, there were no critical problems, with the students refering a 9/10 satisfaction.

In the case of the presential university, the migration to the online teaching, apart from obvious initial problems, was not bad, but it has not led to major changes in the teaching methodologies of those universities, apart from students choosing the online model for "tutoría" or professor attending hours. In general, the impact of the switch to an online model has been lower as the digital competence of the students was higher.

My poster is available at https://zenodo.org/record/7044523#.Y72KyxXMJD8

Highlights of Spanish Astrophysics XI, Proceedings of the XV Scientific Meeting of the Spanish Astronomical Society held on September 4–9, 2022, in La Laguna, Spain. M. Manteiga, L. Bellot, P. Benavidez, A. de Lorenzo-Cáceres, M. A. Fuente, M. J. Martínez, M. Vázquez- Acosta, C. Dafonte (eds.), 2023

Hyper-Kamiokande: the next generation of neutrino detectors.

Ospina, N.[1] on behalf of the Hyper-Kamiokande Collaboration

[1] Department of Theoretical Physics, University Autonoma of Madrid

Abstract

The next generation of water Cherenkov neutrino detector, Hyper-Kamiokande will take a unique role in neutrino astrophysics. The detector which has an effective volume 8.4 times larger than its predecessor, Super-Kamiokande, will be capable of observing proton decay, atmospheric neutrinos, and neutrinos from astronomical sources. The detector will be instrumented with new technology photo-sensors, faster and with higher quantum efficiency than the ones in Super-Kamiokande, its improved photon yield will enable superior signal efficiency and background rejection. This is particularly relevant for astrophysical neutrinos, such as the supernova burst neutrinos, supernova relic neutrinos, and solar neutrinos, allowing a much more precise study of their physics phenomena.

1 Introduction

Hyper-Kamiokande[1]-[3] is the next experiment, approved by the Japanese government, in the successful Kamiokande neutrino program. In 2020, the collaboration transitioned from a proto-collaboration to a real collaboration. Accordingly, the collaboration structure was reorganized for the construction work in the coming years. The number of collaborators has been increasing rapidly since the project approval, and it now involves a total of 493 researchers from 99 institutes in 20 countries participate as of January 2022.

Hyper-Kamiokande will be devoted to the search for nucleon decay as well as the study of neutrino phenomena and neutrino sources. Over the years, a series of water Cherenkov neutrino detectors have been built, beginning with the original Kamiokande detector[5] (1983-1996) and continuing with the Super-Kamiokande detector[4] (1996-). Hyper Kamiokande, like its predecessor Super-Kamiokande, will use the T2K long-baseline neutrino oscillation experiment as a far detector to measure the oscillations of neutrino and anti-neutrino beams generated at the Japan Proton Accelerator Research Complex (J-PARC)[6]. The detector will be capable of observing - far beyond the sensitivity of the Super-Kamiokande detector - precision neutrino oscillation with accelerator neutrinos and sun and atmospheric neutrinos, and neutrinos from astronomical sources. The expected potential for physics research and more detailed discussion are reported in [3].

2 Experiment design

2.1 The Far detector

The Hyper-Kamiokande detector will be located 600 m under the Mount Nijugo-yama in the Tochibora-mine at Kamioka, Japan. It will consist of a cylindrical tank with a diameter of 68 m and a height of 71 m, the schematic view of Hyper-Kamiokande tank is shown in Fig. 1. The experiment, which will be 8.4 times the size of its predecessor, Super-Kamiokande, will be filled with ultra-pure water, providing a fiducial volume of 188 kton. The tank is optically separated into 2 regions: the Inner-Detector (ID) and the Outer-Detector (OD). The ID consists of an array of 20,000 50 cm diameter photo-multiplier tubes (PMTs) which detect the Cherenkov light generated from events in the detector. This PMTs will provide 20% surface area coverage and have been developed by Hamamatsu (Hamamatsu R12860) with a high Quantum Efficiency photo-cathode and with a large Box & Line (B&L) type dynode to give 2.6 ns timing resolution. In addition to the 50 cm PMTs, 1,000 8 cm multi-PMTs (mPMTs) grouped in modules of 19 PMTs will be include to provide unique and complementary information to the 50 cm PMTs. Improving the position, timing and direction resolution of the detected events.

The OD will act as both, a passive shield for low energy backgrounds and an active veto for cosmic ray muons. The expected cosmic ray muon rate through Hyper- Kamiokande is around 45 Hz so this system is required to veto nearly 4 million muons per day. The OD region surrounds the inner detector, and is 1 m wide in the barrel region and 2 m deep at the top and bottom of the cylinder. It consist of 8,000 8 cm PMTs, each mounted within a $\sim$ 30% cm sided Wave Length Shifter (WLS) plates that serves to increase the coverage and collection efficiency.

2.2 The Neutrino Beam

The J-PARC beam-line that currently provides a 500 kW neutrino (anti-neutrino) beam to the T2K experiment will be upgraded over 1.3MW beam power in 2028. This will be achieved in two stages with a main ring power supply upgrade and a subsequent radio frequency upgrade to allow the repetition rate to be doubled.

2.3 Near detectors

There are near detector suites for monitoring the neutrino beam and studying neutrino interactions at the J-PARC site: The INGRID on-axis detector and the ND280 magnetized tracker. These detectors are an essential component of the long baseline experiment, allowing measurements to constrain the flux and neutrino interaction model uncertainty. The Hyper-Kamiokande project include upgrades of this detectors to improve the angular acceptance of the ND280 tracking detector.

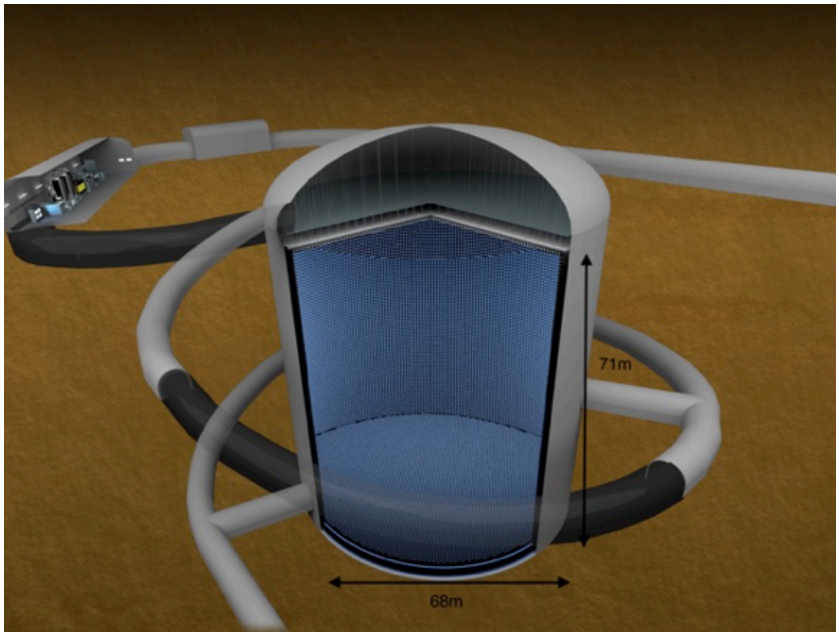

Figure 1: Schematic view of the Hyper-Kamiokande water Cherenkov detector. The tank will provide a volume of 260 kton of ultrapure water, with the dimensions of the 71 m $\times$ 68 m.

3 Current status of construction

Hyper-Kamiokande ground-breaking ceremony was held in May 2021. But in 2020, construction of the entrance yard and intensive geological surveys were carried out. The results indicated that the rock quality at the location of the main Hyper-Kamiokande cavity was excellent. The basic design of an underground facility was determined. Important milestones have been achieved since then: excavation of the access tunnel (1873 m) was initiated in November of 2021 and completed in February 2022. In 2021, mass production of the new 20-inch PMT commenced and was followed by the delivery of electronics and other equipment. In June of 2022, the tunnel excavation reached the center of the cavern dome and, the cavern dome excavation started in October of the same year. The construction of the tank structure is scheduled in 2024 and 2025, and the PMT installation will occur in 2026. Simultaneously, the power upgrade of the neutrino beam at J-PARC began during the shutdown period in 2021 and 2022. It is expected that the experiment start operations in 2027. The status of the experiment construction is shown in Fig. 2.

Acknowledgments

N.O. acknowledge funding from the Ministry of Universities of Spain, the Recovery, Transformation and Resilience Plan (PRTR), and the UAM though the *Grant CA3/RSUE/2021-00559* and the *Grant PID2021-124050NB-C31* funded by MCIN/AEI/10.13039/501100011033 and by the European

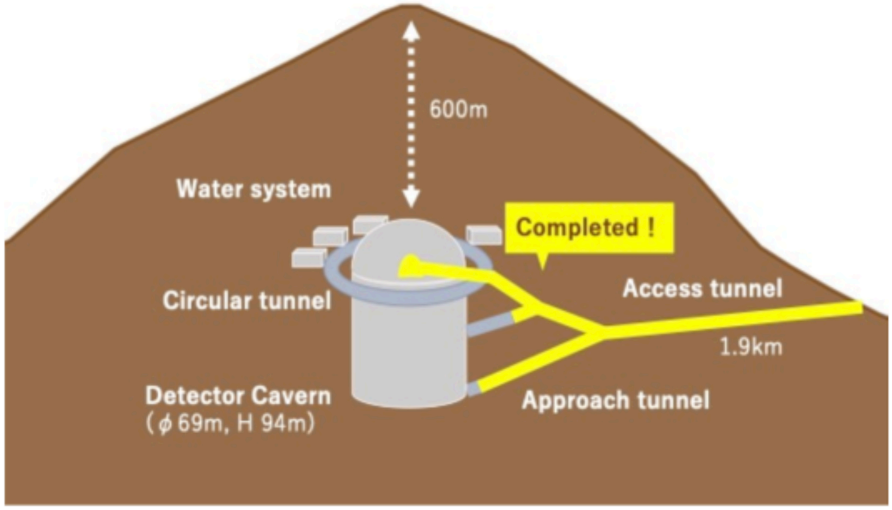

Figure 2: Construction status of Hyper-Kamiokande as of the summer of 2022.

Union NextGenerationEU/PRTR and the European Union's Horizon 2020 Research and Innovation Programme under the Marie Sklodowska-Curie 2020-MSCA-RISE-2019 SK2HK grant agreement no. 872549.

References

[1] Abe, K., Abe, T., Aihara, H., et al. 2011, arXiv:1109.3262.

[2] Hyper-Kamiokande Working Group, :, Abe, K., et al. 2014, arXiv:1412.4673.

[3] Hyper-Kamiokande Proto-Collaboration, :, Abe, K., et al. 2018, arXiv:1805.04163.

[4] Fukuda, S., Fukuda, Y., Hayakawa, T., et al. 2003, Nuclear Instruments and Methods in Physics Research A, 501, 418. doi:10.1016/S0168-9002(03)00425-X.

[5] Arisaka, K., Kajita, T., Kifune, T., et al. 1984, Low Energy Tests of Conservation Laws in Particle Physics, 114, 54. doi:10.1063/1.34507.

[6] Kudenko, Y. 2020, Journal of Instrumentation, 15, C07029. doi:10.1088/1748-0221/15/07/C07029.

Highlights of Spanish Astrophysics XI, Proceedings of the XV Scientific Meeting of the Spanish Astronomical Society held on September 4–9, 2022, in La Laguna, Spain. M. Manteiga, L. Bellot, P. Benavidez, A. de Lorenzo-Cáceres, M. A. Fuente, M. J. Martínez, M. Vázquez- Acosta, C. Dafonte (eds.), 2023

Mining the unrevealed population of red-nugget relics in disk galaxies.

Costantin, L.[1], Pérez-González, P.[1], Méndez-Abreu, J.[2,3], and Huertas-Company, M.[2,3,4]

[1] Centro de Astrobiología (CAB/CSIC-INTA), Ctra. de Ajalvir km 4, Torrejón de Ardoz, E-28850, Madrid, Spain
[2] Instituto de Astrofísica de Canarias, 38200, La Laguna, Tenerife, Spain
[3] Departamento de Astrofísica, Universidad de La Laguna, 38205, La Laguna, Tenerife, Spain
[4] LERMA, Observatoire de Paris, CNRS, PSL, Université de Paris, France

Abstract

Do galaxies that quenched at early epochs remain passive since then or do they rejuvenate, experiencing further episodes of star formation? We apply a structure spectro-photometric decomposition method to obtain the spectral energy distributions for bulges and disks in a representative sample of massive galaxies at redshift $0.14 < z \leq 1$. This opens the possibility to study the star formation history of each morphological component, a novelty in the characterization of galaxy evolution at this redshift. We find that bulges display a bimodal distribution of mass-weighted ages, i.e., they form in two waves. The first wave of bulges could start to form as early as $z = 10$ and evolve passively for as long as 6 Gyr before re-entering the star-forming main sequence at later times, after acquiring a stellar disk. Being very massive and compact systems, which formed through a very intense episode of star formation, we identify first-wave bulges to be the result of a compaction event that occurred at a very high redshift. These results allow extending to late-type galaxies the two-phase formation scenario currently accepted to shape early-type galaxies: first-wave bulges represent a complementary channel for the evolution of the blue and red-nugget systems observed at cosmic noon, which could enter the main sequence and acquire a stellar disk while evolving in massive disk galaxies as we observe them at $z < 1$.

1 Introduction

The formation of the first galaxies is supposed to take place in the largest dark matter halos at $z \sim 10$ when highly-perturbed systems form through accretion-driven violent instabilities and very efficient starbursts ([1], [2]). They are supposed to undergo a fast dissipative process characterized by an impressive star formation rate ($\sim 1000 M_{\odot}$ yr^{-1}) resulting at $z \sim 4$ into blue and centrally-concentrated galaxies, called blue nuggets ([3], [4], [5]). Then, they

probably suffer violent compaction, exhaust their gas, stop forming stars, and passively evolve by $z \sim 2$ into red, spheroidal, and dense stellar systems named red nuggets ([6], [7]). At this stage, they are quite small (effective radii $r_e < 2$ kpc) but very massive stellar systems ($M_\star > 3 \times 10^{10} M_\odot$; [8], [9]).

Despite the major effort produced, the hunt for the relics of red nuggets still has not provided reasonable answers. Only a few of these systems survived intact until today and were spectroscopically observed at $z \sim 0$ in the form of ultra-compact massive ellipticals ([10], [11], [12]), but their number density is much less than predicted ([13], [14]). While some of them could possibly hide in the cores of ellipticals (e.g., [15]), their characterization is very complicated because of the mix of the different stellar populations that result from the multiple mergers and the chaotic star formation history that early-type galaxies experienced ([16], [17], [18]).

In [19] and [20] we proposed a novel approach based on the two-dimensional bulge/disk photometric decoupling of the galaxy light across wavelength (spectrophotometric decomposition) to derive the spectral energy distribution (SED) for individual morphological components in galaxies. This technique allowed us to study the interplay between the bulge and disk properties through cosmic time, identifying a fraction ($\sim 20\%$) of bulges in massive disk galaxies as candidate red-nugget relics.

2 Data

We studied the assembly history of bulges and disks in a sample of 91 massive ($M_\star > 10^{10} M_\odot$) galaxies at redshift $z \leq 1$ in the North field of the Great Observatory Origins Deep Survey (GOODS-N). For this study, we combine data from the Survey for High-z Absorption Red and Dead Sources (SHARDS; [21]) and the Cosmic Assembly Near-infrared Deep Extragalactic Legacy Survey (CANDELS; [22]; [23]). In particular, we used 25 filters for SHARDS data in the optical wavelength range $500 - 941$ nm and seven filters for HST images ($\sim 500 - 1600$ nm). This data set was complemented with the K-band information at ∼2100 nm (Canada-France-Hawaii Telescope WIRCam data; [24]).

The combined dataset allowed us to take advantage of SHARDS spectral resolution and HST spatial resolution and perform a spectro-photometric decomposition of the morphological structures of our galaxies (Fig. 1). This technique, extensively described in [19], consists of a two-dimensional photometric decomposition across wavelength using the `GASP2D` algorithm ([25], [26]), where high spatial resolution broadband images (i.e., HST) are used to robustly constrain "spectroscopic data" (i.e., SHARDS) with a lower spatial resolution (see also [27, 28]).

The SED of each bulge and disk component was fitted with the Bruzual & Charlot (2003) stellar population library ([29]) by means of the `synthesizer` fitting code ([30], [31]). We assumed a Chabrier (2003) initial mass function ([32]) and parametrized the star formation history (SFH) of each morphological component with a declining delayed exponential law. Models were chosen to have subsolar, solar, or super-solar metallicity ($Z/Z_\odot = [0.4, 1, 2.5]$). The V-band attenuation was parametrized by the extinction law of Calzetti et al. (2000)

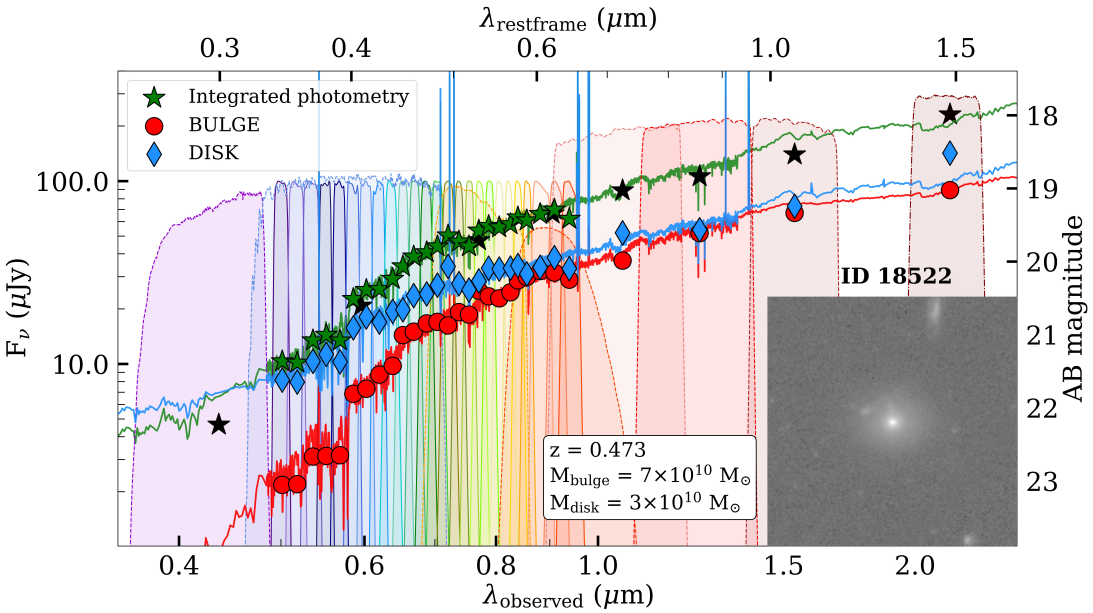

Figure 1: Example of SED for galaxy ID 18522. Green and black stars stand for SHARDS and HST integrated photometry, respectively (apart from the latest K-band WIRCam data point). Red dots and blue diamonds and red dots represent the individual photometric results of our decoupling analysis of the bulge and disk components, respectively. The best models for the bulge, disk, and galaxy are shown as red, blue, and green lines, respectively. HST, SHARDS, and WIRCam filters are shown as dashed, solid, and dashed-dotted profiles.

([33]) with values ranging from 0 to 3 mag.

As an example, in Fig. 1 we presented the best model for the bulge and disk SED for the galaxy ID 18522.

3 Results and Conclusions

The characterization of each bulge and disk SFH allows us to derive their stellar masses ($M_{\rm b}$ and $M_{\rm d}$), mass-weighted ages ($\bar{t}_{M,{\rm b}}$ and $\bar{t}_{M,{\rm d}}$), as well as their corresponding redshift (i.e., the mass-weighted formation redshift $\bar{z}_{M,{\rm b}}$ and $\bar{z}_{M,{\rm d}}$). In Fig. 2 we show the correlation between mass-weighted formation redshift and stellar mass of bulges and disks in our sample. We found that bulges form in two waves: first-wave bulges have median $\bar{z}_{M,{\rm b}} = 6.2^{+1.5}_{-1.7}$, while second-wave bulges have median $\bar{z}_{M,{\rm b}} = 1.3^{+0.6}_{-0.6}$ ([19]). On the other hand, the majority of

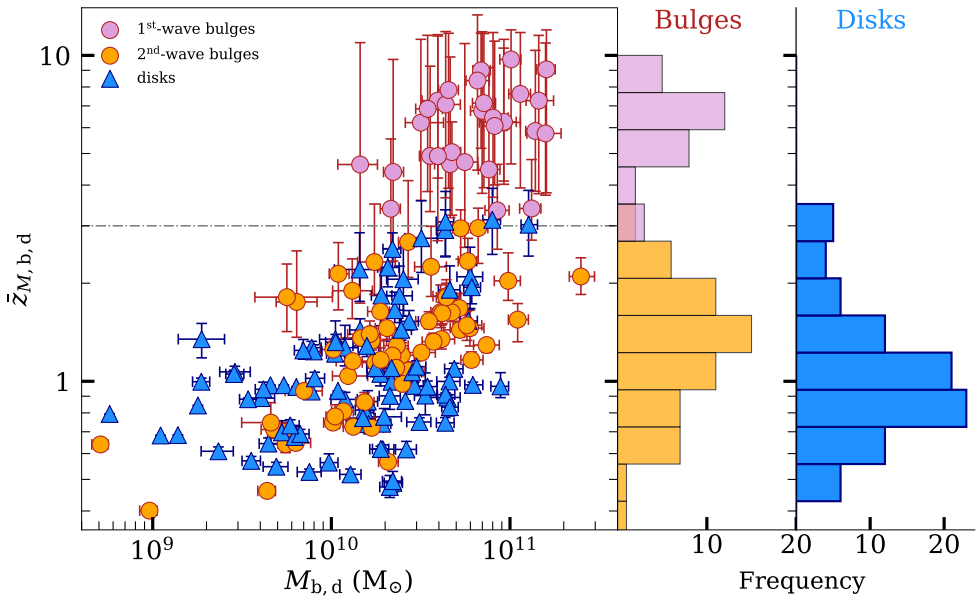

Figure 2: Mass-weighted formation redshift of bulges (dots) and disks (triangles) as a function of their stellar mass. Bulges are separated into first-wave (purple) and second-wave (orange) ones. Errors are reported as a 16th–84th percentile interval. The gray dashed-dotted horizontal line marks $\bar{z}_{M,\mathrm{b}} = 3$. The histograms represent the frequency of the mass-weighted formation redshifts of the bulge and disk populations. Purple and orange histograms stand for first- and second-wave bulges, while the blue histogram stands for the disk population.

our disks formed at similar cosmic times as second-wave bulges ($\bar{z}_{M,\mathrm{d}} = 1.0^{+0.6}_{-0.3}$), since only 10 out of 91 disks have $\bar{z}_{M,\mathrm{d}} > 2$ ([20]).

First-wave bulges are fast-track spheroids (i.e., short formation timescale) and have similar sizes but higher masses compared to second-wave bulges. Thus, we interpret the population of bulges formed at $\bar{z}_{M,\mathrm{b}} > 3$ as relics of the early Universe, formed by compaction events driven by violent disk instabilities and clump migration, in agreement with predictions from numerical simulations ([34], [35], [36]).

Finally, we quantified the differences in mass-weighted ages between each bulge and disk, finding a median $\Delta\bar{t}_{M,\mathrm{bd}} = \bar{t}_{M,\mathrm{b}} - \bar{t}_{M,\mathrm{d}} = 1.6^{+5.4}_{-0.7}$ ([20]). In particular, first-wave bulges and their disks have $\Delta\bar{t}_{M,\mathrm{bd}} = 5.2^{+1.1}_{-1.9}$, while the age difference for second-wave bulges is $\Delta\bar{t}_{M,\mathrm{bd}} = 0.7^{+1.5}_{-1.6}$ ([20]). In this context, we argue that a fraction of massive disk galaxies, hosting a compact core (first-wave bulge), went through a blue and red nugget phase and grew an extended stellar disk at later cosmic times. This could allow one to extend the two-phase paradigm to late-type galaxies, as already proposed by recent studies ([37], [38], [39], [40]).

Acknowledgments

L.C. acknowledges financial support from Comunidad de Madrid under Atracción de Talento grant 2018-T2/TIC-11612. L.C. and P.G.P.G. acknowledge support from the Spanish Ministerio de Ciencia, Innovación y Universidades through grant PGC2018- 093499-B-I00.

References

[1] Blumenthal, G. R., Faber, S. M., Primack, J. R. 1984, Nature, 311, 517

[2] Bromm, V., & Yoshida, N. 2011, ARAA, 49, 373

[3] van der Wel, A., Rix, H.-W., Wuyts, S. 2011, ApJ, 730, 38

[4] Barro, G., Faber, S. M., Pérez-González, P. G. 2013, ApJ, 765, 104

[5] Tacchella, S., Dekel, A., Carollo, C. M. 2016, MNRAS, 458, 242

[6] Daddi, E., Renzini, A., Pirzkal, N. 2005, ApJ, 626, 680

[7] Damjanov, I., McCarthy, P. J., Abraham, R. G. 2009, ApJ, 695, 101

[8] Van Dokkum, P. G., Franx, M., Kriek, M. 2008, ApJL, 677, L5

[9] Werner, N., Lakhchaura, K., Canning, R. E. A. 2018, MNRAS, 477, 3886

[10] Trujillo, I., Cenarro, A. J., de Lorenzo-Cáceres, A. 2009, ApJ, 692, L118

[11] Ferré-Mateu, A., Trujillo, I., Martín-Navarro, I. 2017, MNRAS, 467, 1929

[12] Spiniello, C., Tortora, C., D'Ago, G. 2020, A&A, 654, A136

[13] Hopkins, P. F., Hernquist, L., Cox, T. J. 2008, ApJS, 175, 356

[14] Buitrago, F., Ferreras, I., Kelvin, L. S. 2018, A&A, 619, 137

[15] Spiniello, C., Tortora, C., D'Ago, G. 2021, A&A, 646, A28

[16] Naab, T., Johansson, P. H., & Ostriker, J. P. 2009, ApJ, 699, L178

[17] McDermid, R. M., Alatalo, K., Blitz, L. 2015, MNRAS, 448, 3484

[18] Beasley, M. A., Trujillo, I., Leaman, R. 2018, Nature, 555, 483

[19] Costantin, L., Pérez-González, P., Méndez-Abreu, J. 2021, ApJ, 913, 125

[20] Costantin, L., Pérez-González, P., Méndez-Abreu, J. 2022, ApJ, 929, 121

[21] Pérez-González, P. G., Cava, A., Barro, G. 2013, ApJ, 762, 46

[22] Grogin, N. A., Kocevski, D. D., Faber, S. M. 2011, ApJS, 197, 35

[23] Koekemoer, A. M., Faber, S. M., Ferguson, H. C. 2011, ApJS, 197, 36

[24] Hsu, L.-T., Lin, L., Dickinson, M. 2019, ApJ, 871, 233

[25] Méndez-Abreu, J., Aguerri, J. A. L., Corsini, E. M. 2008, A&A, 478, 353

[26] Méndez-Abreu, J., Debattista, V. P., Corsini, E. M. 2014, A&A, 572, A25

[27] Méndez-Abreu, J., Sánchez, S. F., & de Lorenzo-Cáceres, A. 2019a, MNRAS, 484, 4298

[28] Méndez-Abreu, J., Sánchez, S. F., & de Lorenzo-Cáceres, A. 2019b, MNRAS, 488, L80

[29] Bruzual, G., & Charlot, S. 2003, MNRAS, 344, 1000

[30] Pérez-González, P. G., Gil de Paz, A., Zamorano, J. 2003, MNRAS, 338, 525

[31] Pérez-González, P. G., Rieke, G. H., Villar, V. 2008, ApJ, 675, 234

[32] Chabrier, G. 2003, PASP, 115, 763

[33] Calzetti, D., Armus, L., Bohlin, R. C. 2000, ApJ, 533, 682

[34] Dekel, A., Sari, R., & Ceverino, D. 2009, ApJ, 703, 785

[35] Zolotov, A., Dekel, A., Mandelker, N. 2015, MNRAS, 450, 2327

[36] Ceverino, D., Klessen, R. S., & Glover, S. C. O. 2018, MNRAS, 480, 4842

[37] Graham, A. W. 2013, in Planets, Stars and Stellar Systems, ed. T. D. Oswalt & W. C. Keel, Vol. 6 (Berlin: Springer), 91

[38] de la Rosa, I. G., La Barbera, F., Ferreras, I. 2016, MNRAS, 457, 1916

[39] Costantin, L., Méndez-Abreu, J., Corsini, E. M. 2020, ApJL, 889, L3

[40] Hua, G., Ho, L. C., Li, Z. Y. 2022, ApJS, 262, 54

Highlights of Spanish Astrophysics XI, Proceedings of the XV Scientific Meeting of the Spanish Astronomical Society held on September 4–9, 2022, in La Laguna, Spain. M. Manteiga, L. Bellot, P. Benavidez, A. de Lorenzo-Cáceres, M. A. Fuente, M. J. Martínez, M. Vázquez- Acosta, C. Dafonte (eds.), 2023

Planet formation in extreme conditions.

Osorio, M.[1]

[1] Instituto de Astrofísica de Andalucía (CSIC), Glorieta de la Astronomía s/n, 18008 Granada, Spain
osorio@iaa.es

Abstract

After the discovery of more than 5,000 exoplanets, one of the most striking aspects is the diversity of types found, as well as the diversity of architectures of exoplanetary systems. It is therefore reasonable to expect that a similar diversity should also be observed in their progenitors, the protoplanetary disks. I will focus on the observed diversity of protoplanetary disks, presenting some unique examples, taken from our recent research, that show planetary formation under extreme conditions. I will then present our work on dwarf protoplanetary disks around M-type dwarf stars, disks around very massive stars, and disks in multiple star systems, and discuss the implications for planetary formation.

1 Introduction

In the current paradigm ([20]), the stars are formed through the collapse of a fragment of a molecular cloud. At the very beginning of this process a central object is formed. This is the protostar. At the same time, because of the angular momentum conservation, a flattened structure is developed around the protostar, the accretion disk. In addition to accretion, a fraction of material is ejected in a direction perpendicular to disk. In this way, the excess of mass and angular momentum is removed. During the evolution of the process accretion and outflow coexist and are the hallmark of the current star formation paradigm. As time goes by, the envelope is being removed, accretion decreases and the star reaches its final mass. Also, the accretion disk becomes a planetary system. For this reason, these disks are called protoplanetary disks.

In the last 10 years, the focus of study of the earliest stages of star formation has shifted to the earliest stages of planet formation. This is because of the advent of the ultra-sensitive radio interferometers, such as the Atacama Large Millimeter/submillimeter Array (ALMA), the Very Large Array (VLA), and large infrared telescopes that have completely revolutionized the field. Thanks to these instruments, we have been able to detect several signatures of the onset of the planet formation process in many of these disks. Examples of these signatures are cavities, gaps, spirals, rings, walls, and azimuthal asymmetries. These signatures are attributed to the presence and perturbations produced by one or several planet embryos

within the disk. A confirmation of this interpretation is the detection of infrared point sources within the cavities of some disks ([21], [11], [28]).

The most compelling case may be that of the PDS70 disk, where an infrared source at 20 au from the star is found inside the cavity. This has been interpreted as a protoplanet or substellar companion with an estimated mass of 10 Jupiter masses. The orbital period of this object is about 120 years. Another example is HD 169142, where a protoplanet candidate has been detected inside its cavity at similar distance and with a similar mass. These candidates can be confirmed if orbital proper motions are measured. Given the period of about 100 years, this can be done in the next few years.

The distinctive characteristic of the standard star formation paradigm is the presence of a disk-jet system. The presence of a disk makes the formation of a planetary system possible. However, the standard paradigm assumes isolated low-mass star formation. After the consolidation of this paradigm, it is worth asking whether it could also be extrapolated to other cases. Are disk-jet systems also present in other scenarios, for instance in multiple or even in high-mass star formation? Can planetary systems be formed in these scenarios? How are these planetary system expected to be?

Certainly, the study of these additional star/planet forming scenarios may provide the clues for a better understanding of the striking diversity of all the known exoplanetary systems that are being discovered. In this paper, I will present some striking results on protoplanetary disks associated with multiple or high-mass protostars, and discuss the possibility of planet formation under these extreme physical conditions.

2 Disks in binary or multiple systems

In the case of multiple star formation, the standard star formation scenario is not completely valid. Each protostar may develop its own disk and jet system, but the whole system is more complex. In a binary system, there might be up to three protoplanetary disks: two circumstellar disks (CS), and a circumbinary disk (CB) surrounding the two stars. In the case of a close binary, there may also be strong interaction between stars, even with matter exchange. The evolution of one star may affect the other one; actually, one of the protostars may be formed from the fragmentation of the disk of its companion. High angular resolution data (< 1") are needed to disentangle the emission of each component, especially for those systems separated by less than 100 au. In summary, the standard paradigm of star formation may be used for the study of binary star formation, but it is more complex.

The development of different kinds of disks is confirmed by hydrodynamic simulations, demonstrating that the key parameter in disk formation is the specific angular momentum of the infalling gas [3]. This can be seen in Figure 1 which shows the distribution of material as a function of the specific angular momentum. According to these simulations, systems with low specific angular momentum, the material will only fall toward the primary (the more massive), forming a circumstellar disk. Systems with increasing specific angular momentum, part of material will also fall toward the secondary star, forming another circumstellar disk. If the specific angular momentum increased even more, circumbinary disk starts to appear,

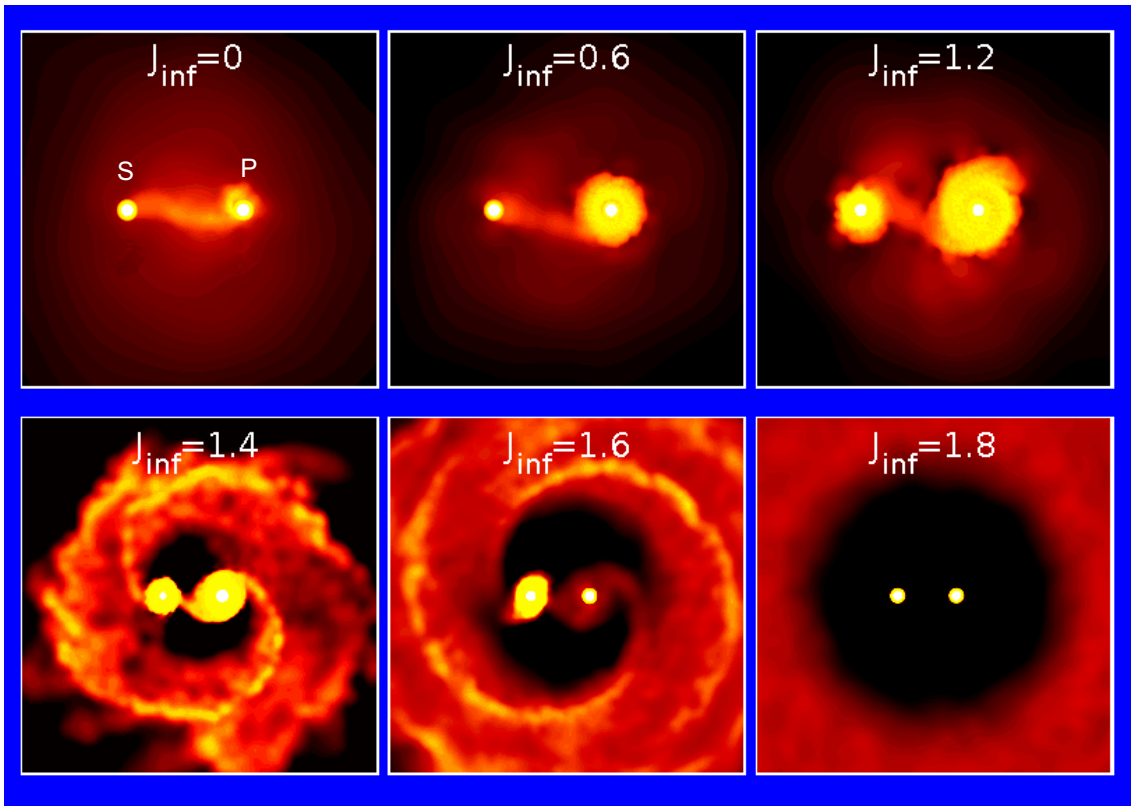

Figure 1: Hydrodynamic simulations of disk formation in a binary system as a function of angular momentum per unit mass, $J_{\rm inf}$. The more massive star is labeled as P (primary) and the less massive star is labeled as S (secondary). Credit:[3].

and if the specific angular momentum is very high all the material goes to the CB disk. In summary, a protobinary system might develop one, two or three protoplanetary disks.

The results of simulations are supported by ALMA observations as can be seen in Figure 2, which shows millimeter observations revealing a protobinary system where one circunstellar disk is brighter than the other, a system with two circumstellar disks of similar brightness and an example in which a circumbinary disk, in addition to the two CS disks is present. One of these cases is the L1551 IRS5 system, which is the first binary in which a clear disk/jet system associated with each star was discovered, suggesting that the formation of binary systems has shown similarities with the formation of isolated stars. VLA observations of L1551 IRS 5 show two disks ([22]), separated by 45 au, and two jets ([23]), so that each of two protostars is associated with a disk/jet system. The disks have a radius of only 10 au, which is one order of magnitude smaller than the typical radii of disks around single stars. The small radii of the disks can be explained as the result of tidal interactions between the stars. For this reason, the disks could be truncated at a size that is a fraction of the maximum

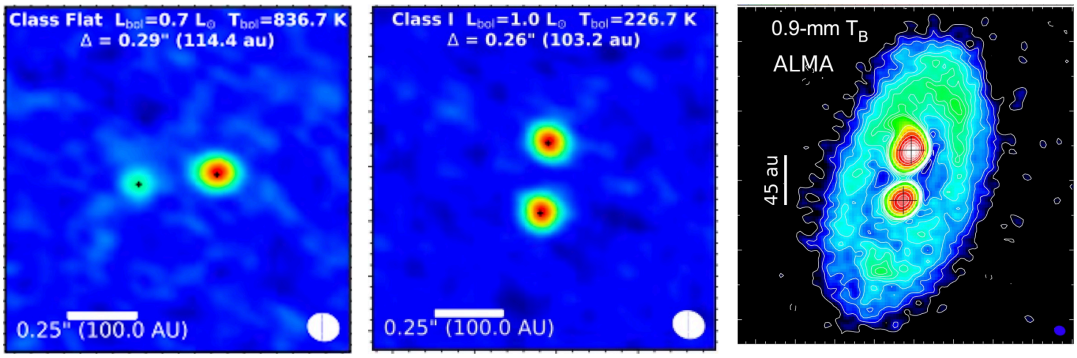

Figure 2: Dust emission of HOPS 242 (left) and HOPS 193 (center) circunstellar disks detected by ALMA at 870 μm in the Orion star forming region. Circunstellar and circumbinary dust disks of the L1551 IRS 5 protobinary system (right), in Taurus, detected by ALMA at 0.9 mm. Figures adapted from [26] and [24]. Other examples can be found on the website: *https://planetstarformation.iaa.es*.

separation between the stars. Twenty years ago, the system was modeled in great detail [18]. The model predicted that in addition to the CS disks a CB disk is required to explain the SED and mm images properly. Interestingly, ALMA has detected the circumbinary disk very recently ([24], [8]).

The SVS 13 proto-binary system is another case with a circumbinary disk. The CB disk shows prominent spiral arms extending up to $\sim$ 500 au (see left panel of Figure 3) that appear to converge mainly toward the position of the western source ([9]). Each source has a circumstellar disk with radius of $\sim$ 10 au. We have recently conducted a comprehensive observational study of this system to derive the physical and chemical properties of the disks as well as their kinematics ([9]). Compiling data from 30 years of observations, we have measured the orbital proper motions of the stars and found that they rotate counterclockwise. Combining the proper motions with the line of sight velocities, inferred from the molecular line observations, we obtained the 3D kinematics of the system.

Figure 3 (top-right panel) shows the mean velocity (in color scale) overlaid on the integrated intensity of the CS (J=7-6) rotational transition. The image clearly illustrates an east-west velocity gradient in the CB disk with a peculiar "yin-yang" shape. We interpreted this morphology as a combination of infall and rotation motions in this structure. Interestingly, there are a few Etylene Glycol transitions which are only detected in the western circumstellar disk (Figure 3, bottom-right panel), allowing the isolation of the western disk kinematics at scales of the order of 10 au, and to infer the stellar mass of this component ($0.3 M_\odot$) by fitting a Keplerian rotating disk model to these transitions. We are currently working on radiative transfer models to further characterize the properties of the CS disks (see [16]) and on analyzing in detail the properties of the very high velocity outflow driven by this source ([6]).

The existence of planets around one of the stars or around each star of a binary, or even around the two stars, circumbinary planets, as predicted by the simulations and observations

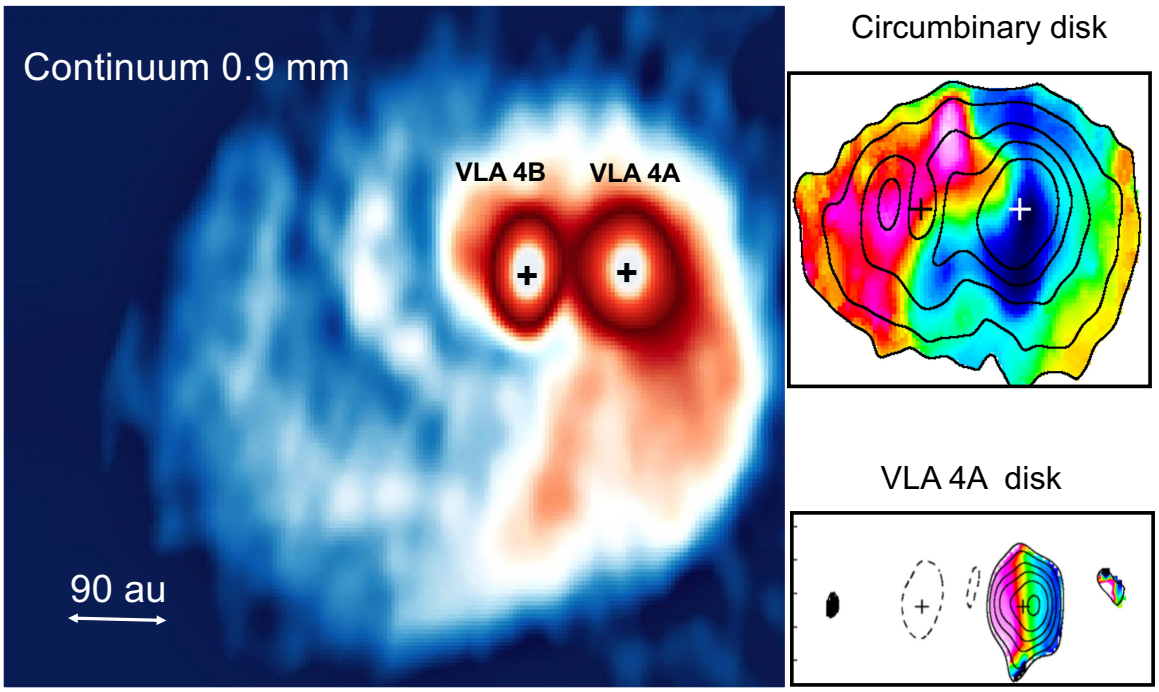

Figure 3: Dust emission of SVS 13 protobinary system in Perseus molecular cloud complex observed by ALMA at 9mm. Two circumstellar disks and a spiraling circumbinary disk are clearly detected in dust continuum emission (Left panel). Velocity-integrated emission (contours) overlaid on intensity-weighted mean velocity (color scale) of the CS (7–6) molecular lines observed with ALMA toward the circumbinary disk (Top-right panel). Velocity-integrated emission (contours) and intensity-weighted mean velocity (color scale) of the ethylene glycol lines associated with VLA 4A disk (Bottom-right panel). Figures adapted from [9].

of protobinaries has been confirmed by exoplanet observations. Recently, the TESS satellite has discovered a planet orbiting two stars in the system Kepler 34 ([12]).

In addition to the presence of several types of disks, another factor that increases the complexity of multiple star formation is the interaction between the stars. Recent simulations performed by ([4]), depicted in Figure 4, illustrate the matter exchange due to tidal interactions in the formation of multiple systems and also show spiral arms, fragmentation, merges, etc. These simulations take into account the formation of a cluster of about 100 stars. Each panel of Figure 4 is a close-ups of several groups of stars (white points), corresponding to a snapshot of the whole system at a given time.

In some cases there are two very close protostars and a third more separated one. Also there are tidal tails with a shape of spirals, produced by the interaction between components. The simulations also show four protostars, but they are grouped in close pairs, so that, at large scale appears as two stars. There is matter exchange between the protostars, and as the systems evolves, the relative masses of the disks and stars may change. Merging of two

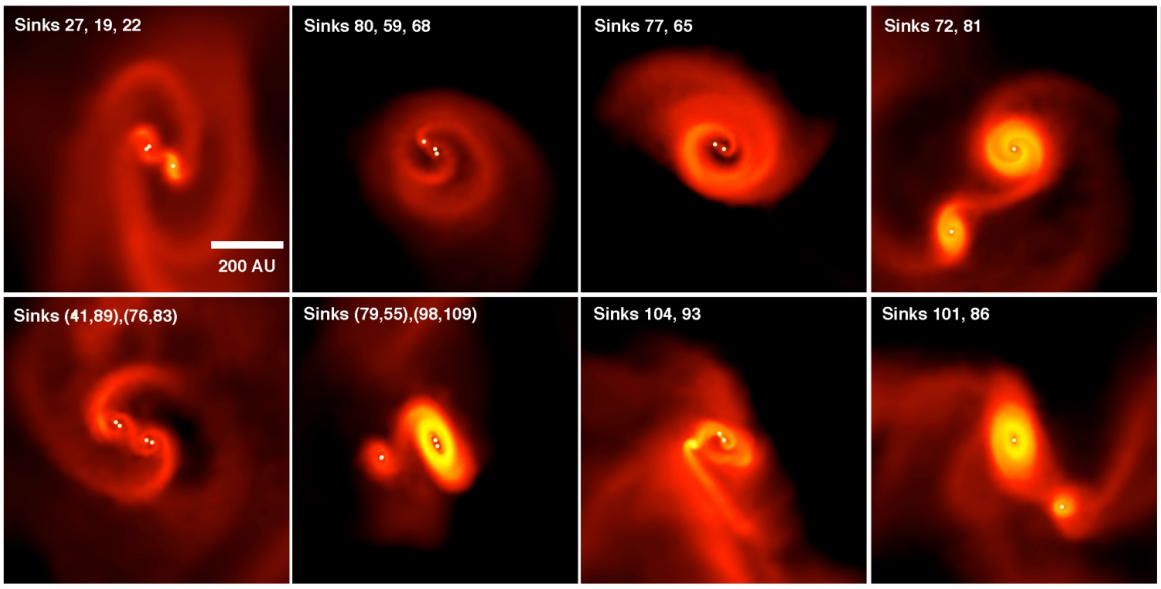

Figure 4: Hydrodynamic simulations of disk formation in binary systems and in multiple systems that take account matter exchange. Protostars or sink particles are plotted as white filled circles. Credit: ([4])

stars is also possible. Fragmentation of the disks also occurs, originating new stars. This is exactly what observations show, as can be seen in a gallery of disks observed with ALMA (Figure 5), where the formation of double, triple and high order stellar systems is revealed. In the protobinary system SVS 13 spiral arms can be observed ([9]), while in BHB 2007 system tidal tails ([1]) are observed. In fact, there is evidence of fragmentation, from which new stars are formed in L1448 system ([25]) and flybys in UX Tau A/C disk system ([27]). Even, in the most extreme cases, the interaction of a triple hierarchical system usually results in the ejection of the less massive star, while the other two stars remain gravitationally bound in a closer orbit. This may be the case o of our nearest neighbor Alpha Centauri, where the less massive component, Proxima, is located at a much larger distance ($\sim$ 10000 au) from the other two components. These interactions will be reflected in the final result: the exoplanetary systems.

3 Dwarf disks

One of the most striking results of the study of exoplanets is the diversity of planets from super-Earth to mini-neptunes and their configurations. It is particularly noteworthy, the small exoplanetary systems discovered by Kepler mission. Although there may be strong observational biases, Kepler has found planetary systems really small planetary systems, with many planets orbiting within a radius smaller than 1 au. Kepler 11 ([15]) is a prototypical example of the so-called closely packed exoplanetary system, in which a large number of

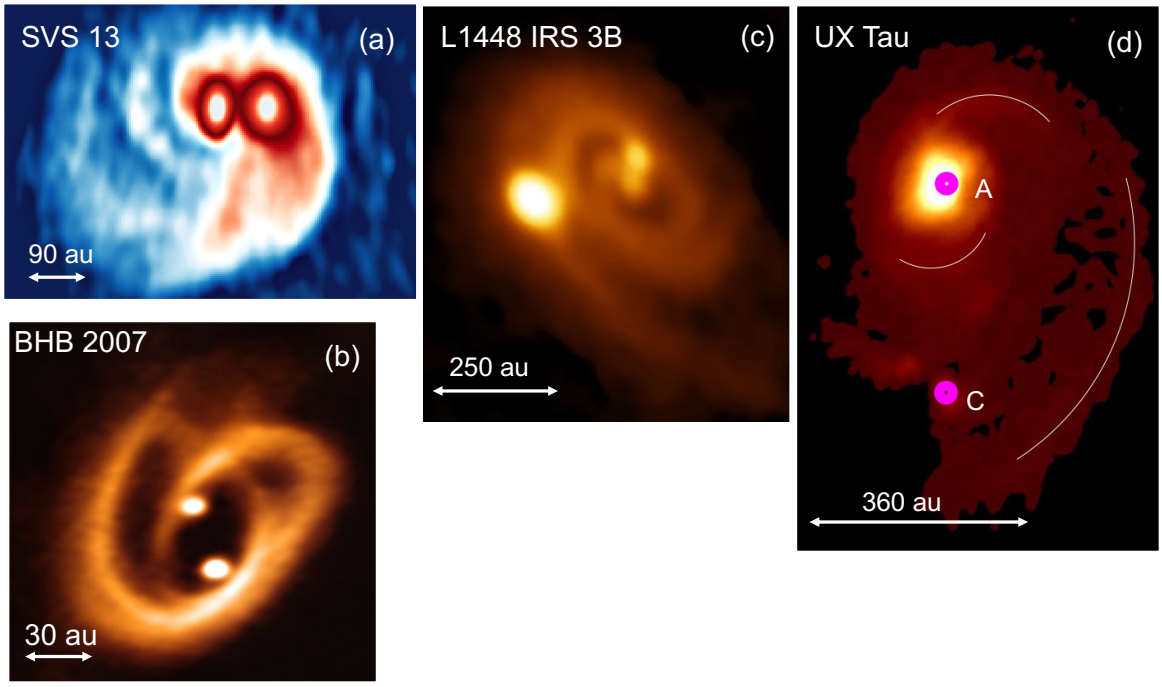

Figure 5: Gallery of disks in multiple young stellar systems observed by ALMA in the submillimeter regime. Panel a) protobinary system SVS 13 ([9]), Panel b) protobinary system BHB 2007 ([1]), Panel c) triple system L1448 IRS 3B ([25]), and Panel d) multiple system UX Tau ([27])

.

planets are found within a small radius. In fact, in these systems all the stable orbits are occupied by a planet. Within the orbit of Venus our Solar system has only Mercury, while Kepler 11 has 6 planets. Trappits 1 also fall into this category. Which is the origin of these compact exoplanetary systems? Do compact exoplanetary systems originate from dwarf protoplanetary disks? There is evidence of an extremely small disk from which the compact exoplanetary systems may originate.

A few years ago we reported the detection of a circumstellar disk of only 3 au radius ([19]). This disk belongs to the protobinary system XZ Tau (located at 4200 au from the well-known HL Tau disk), whose components are separated by 40 au. The large improvement in the angular resolution of ALMA allow us to probe scales of only 2 au. Figure 6 shows HL Tau and XZ Tau B disks at the same scale in order to see how small XZ Tau B is. Interestingly in this small disk signs of the onset of planet formation can be seen, e.g., the decrease in the emission towards the center may be indicating a small cavity and the slight azimuthal asymmetry, with the SW side brighter than the NW side, could be a dust trap. To test the disk interpretation, we modeled ([19]) the compact dust emission to reproduced the SED and the 1.3mm spatial profile obtained by ALMA. Despite the scarcity of data, for which many solutions are posible, we see the model predicts a disk with enough mass to form

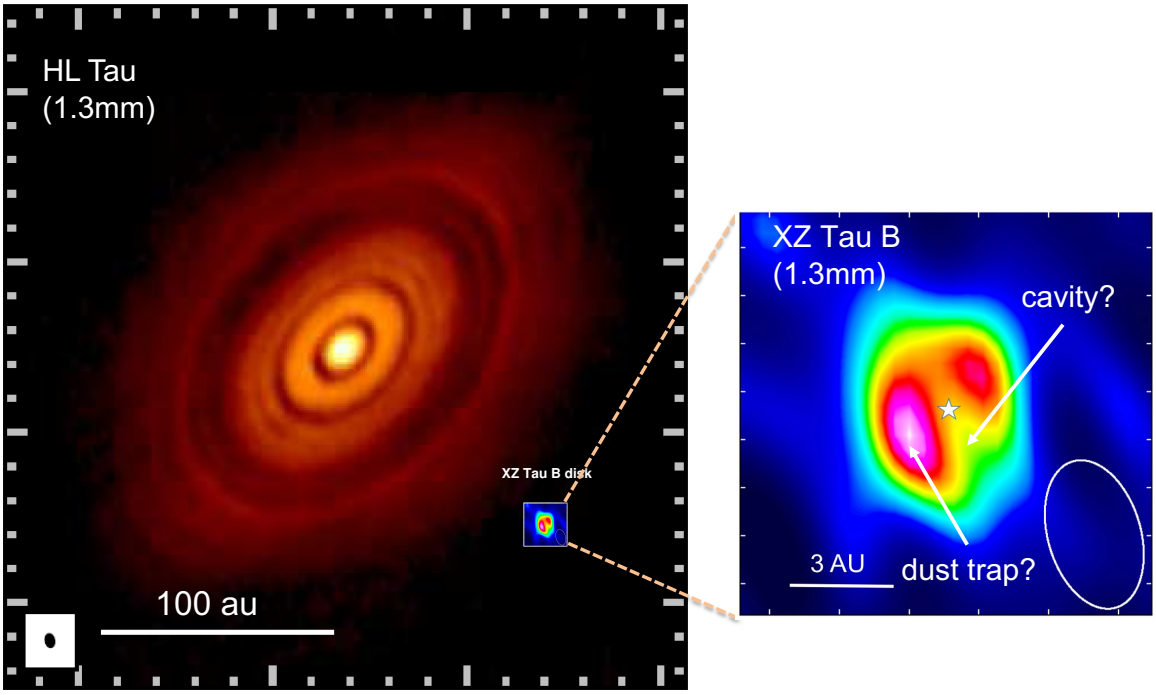

Figure 6: Left: Comparison of the HL Tau and XZ Tau B disks at the same scale. Right: Close-up of XZ Tau disk showing some possible features of planet formation.

planets (Mass >9 M_{Jup}) even though it is very small.

If planet formation is feasible in XZ Tau B, such disks could be the precursors of compact exoplanetary systems. A large population of these very small disks could exist, but has remained hidden because only a few extremely high angular resolution observations have been made so far.

4 Disks around high-mass protostars

Finally, the case of high-mass star formation and the possibility of planet formation in these stars is discussed. If massive stars could be formed by accretion, with a disk/jet system, then, in principle, a planetary system could be formed from the circumstellar disk. However, there are some important differences between low-mass star and high-mass star formation, for example, the evolution of massive stars is faster than that of low-mass stars, massive stars reach the main sequence when they are still accreting material from their maternal cloud, and in addition they are born in crowded regions, which makes the process more complex. Massive stars develop HII regions with a high UV photon rate. Radiation pressure and intense stellar winds of these stars may halt the collapse, so that the star cannot continue growing and reach a high mass. Therefore, it has been debated in recent years whether it is possible to form high-mass stars by accretion.

Two main mechanisms have been proposed to form high-mass stars: the coalescence scenario in which a massive star is formed by collisions of low-mass stars. The other scenario is the monolithic accretion, which is a scaled version of the standard scenario for low-mass stars formation. The coalescence scenario has the problem that the time between collisions is much longer than age of the cluster where the massive star is born, however, it may be the only way to form extremely massive stars ($\sim$ 100 $M_\odot$).

As mentioned before, the accretion scenario may have a problem with the radiation pressure, however, detailed radiative transfer calculations ([17]) show that it is possible to form stars up to 30 $M_\odot$. Moreover, the observations show that massive stars are associated with disk/jet systems ([5]) similar to those found in low-mass stars. Since disks and jets are not expected to survive after the collisions, their detection is taken as a strong argument in favor of the accretion scenario.

One of the most remarkable cases is that of the high-mass protostar HH80, where a clear disk/jet system is associated with a star of 20$M_\odot$. Figure 7 shows this spectacular system, consisting of a disk (observed by ALMA at 1.14mm, [13]) with a radius of 200 au and a radio-jet clearly perpendicular to the disk (observed by the VLA at 3.6 cm, [7]). We believe this is a genuine accretion disk around a 20 $M_\odot$ protostar. We have also carried out polarization observations ([13]) from which dust properties can be inferred using the polarization pattern and assuming that scattering is the dominant mechanism. This is important to model the disk. We have performed radiative transfer models to reproduce the image at 1.14mm obtained by ALMA ([2]). The model takes into account stellar irradiation, viscosity dissipation and the accretion shock which is a relevant source of heating due to the high-mass accretion rates of high-mass stars ([17], [10]).

From the modelling, several disk parameters can be inferred, for instance, the disk mass (5 $M_\odot$), its stability, the ratio between mass accretion rate and viscosity and also its physical structure (see [2]). We found that this disk is very hot, with temperatures above 100K everywhere. As a consequence of the high temperature of the disk, no solid-phase molecules, such as water or CO, are expected to survive. Condensation fronts, also called snow lines, must be near the edge of the disk, in the envelope surrounding it. Therefore, the formation of giant gas planets, such as Jupiter, within the disk is not expected unless they form at great distances from the star. This is consistent with the recent finding of an exoplanet at a distance of 500 au from the massive b Centauri star ([14]), that has been detected by direct imaging.

5 Summary of the results:

The diversity observed in exoplanetary systems can reflect the diversity of scenarios in the formation of protoplanetary disks.

We find that disks in binary protostars are in agreement with exoplanet observations, since exoplanets have been discovered around already formed binary stars.

We propose that dwarf disks are possible precursors of closely packet compact exoplanetary systems discovered by Kepler mission.

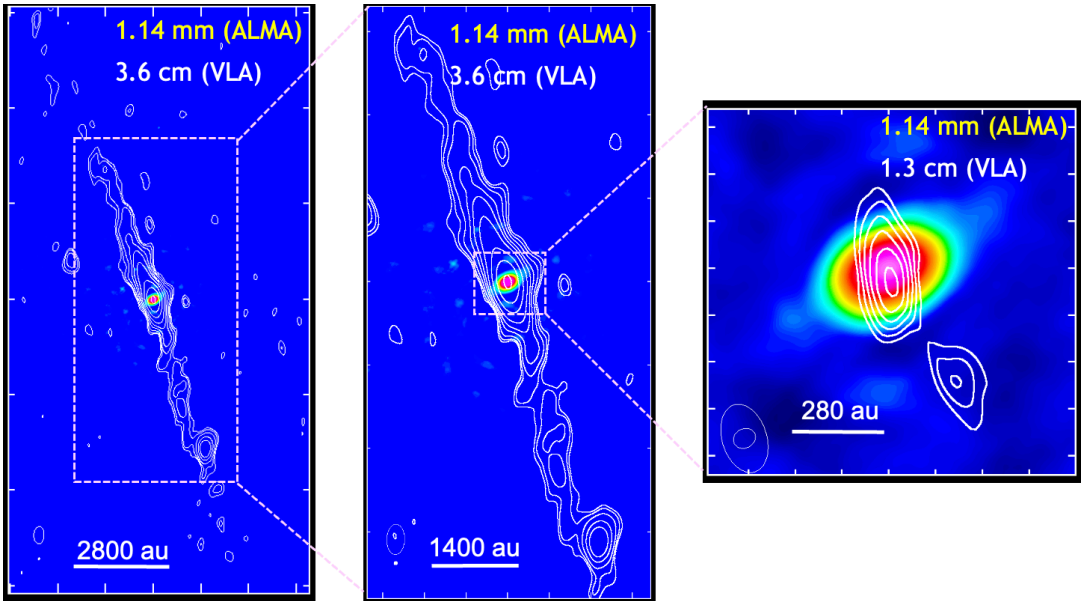

Figure 7: Sequence of amplifications of the disk/jet system associated with the high-mass protostar HH80. The dust continuum emission from the disk (ALMA at 1.14 mm, color scale) has a radius of $\sim$ 200 au. The free-free emission (contours) associated with the radio-jet, traced by the VLA at 3.6 cm (left and center panels) and 1.3 cm (right panel), is seen clearly perpendicular to the disk. The ALMA and VLA beams are shown in the lower left corner of each panel. Figures adapted from [13], [7], [2].

Finally, we find that disks in massive protostars can form Jupiter planets only at large distances from the star, which is supported by the recent finding of an exoplanet candidate, orbiting a 6 $M_{\odot}$ star, at a large distance of 500 au.

Acknowledgments

M.O. acknowledges financial support from PID2020-114461GB-I00 and CEX2021-001131-S grants, funded by MCIN/AEI/ 10.13039/501100011033, and Junta de Andalucía (Spain) grant P20-00880 (FEDER, EU).

References

[1] Alves, F. O., Caselli, P., Girart, J. M. et al. 2019, Science, 366, 90

[2] Áñez-López, N., Osorio, M., Busquet, G. et al. 2020, ApJ, 888, 452

[3] Bate, M., Bonnell, I.A. 1997, MNRAS, 285, 33

[4] Bate, M. 2018, MNRAS, 475, 561

[5] Beltran, M. T., de Wit, W. J. 2016, A&ARv, 24, 6

[6] Blázquez-Calero et al. 2023, in "Highlights of Spanish Astrophysics XI, Proceedings of the XV Scientific Meeting of the Spanish Astronomical Society (La Laguna, Spain 2022), M. Manteiga, L. Bellot, P. Benavidez, A. de Lorenzo-Cáceres, M. A. Fuente, M. J. Martínez, M. Vázquez- Acosta, C. Dafonte (eds.), 2023

[7] Carrasco-González, C., Galván-Madrid, R., Anglada, G. et al. 2012, ApJL, 752, L29

[8] Cruz-Sáenz de Miera, F., Kóspál, Á., Ábrahám, P., Liu, H. B., Takami, M. 2019, ApJL, 882, L4

[9] Diaz-Rodriguez, A. K., Anglada, G., Blázquez-Calero, G., et al. 2023, ApJ, 930, 91

[10] De Buizer, J.M., Osorio, M., Calvet, N. et al. 2005, ApJ, 635, 452

[11] Keppler, M., Benisty, M., Müller, A. et al. 2018, A&A, 617, 44

[12] Kostov, V. B., Powell, B. P., Orosz, J. A. et al. 2021, AJ, 162, 234

[13] Girart, J. M., Fernández-López, M., Li, Z. -Y., et al. 2018, ApJL, 586, L27

[14] Janson, M., Gratton, R., Rodet, L. et al. 2021, Nature, 600, 231

[15] Lissauer, J. J., Fabrycky, D. C., Ford, E. B. et al. Nature, 470, 53

[16] Navarro, R., Osorio, M., Blázquez-Calero, G. et al. 2013, poster number: DOI 10.5281/zenodo.7050035 in "Highlights of Spanish Astrophysics XI, Proceedings of the XV Scientific Meeting of the Spanish Astronomical Society (La Laguna, Spain 2022), M. Manteiga, L. Bellot, P. Benavidez, A. de Lorenzo-Cáceres, M. A. Fuente, M. J. Martínez, M. Vázquez- Acosta, C. Dafonte (eds.), 2023

[17] Osorio, M., Lizano, S., D'Alessio, P. 1999, ApJ, 525, 808

[18] Osorio, M., D'Alessio, P. Muzerolle, J., Calvet, N., Hartmann, L., 2003, ApJ, 586, 1148

[19] Osorio, M., Macías, E., Anglada, G. et al. 2016, ApJ, 825, 10

[20] Shu, F. H., Adams, F. C., Lizano, S. 1987, ARA&A, 25, 23

[21] Reggiani, M., Quanz, S. P., Meyer, M. R., et al. 2014, ApJL, 792, L23

[22] Rodríguez, L. F., D'Alessio, P., Wilner, D. J., et al. 1998, Nature, 395, 355

[23] Rodríguez, L. F., Porras, A., Claussen, M. J., et al. 2003, ApJL, 586, L13

[24] Takakuwa, S., Saigo, K., Matsumoto, T. et al. 2020, ApJ, 898, 10

[25] Tobin, J. J., Kratter, K. M., Persson, M. V. 2016, Nature, 538, 483

[26] Tobin, J. J., Sheehan, P. D., Megeath, S. T. et al. 2020, ApJ, 890, 130

[27] Zapata, L. A.; Rodríguez, L. F.; Fernández-López, M. et al. 2020, ApJ, 896,132

[28] Zhou, Y., Sanghi, A., Bowler, B. P. et al. 2022, ApJ, 934, 13